TAL TECH

DOCTORAL THESIS

Dynamics Modeling and Optimization of Locally Resonant Metastructures for Vibration Suppression and Energy Harvesting

Hossein Alimohammadi

TALLINNA TEHNIKAÜLIKOOL
TALLINN UNIVERSITY OF TECHNOLOGY
TALLINN 2025

TALLINN UNIVERSITY OF TECHNOLOGY
DOCTORAL THESIS
79/2025

Dynamics Modeling and Optimization of Locally Resonant Metastructures for Vibration Suppression and Energy Harvesting

HOSSEIN ALIMOHAMMADI

TAL TECH PRESS

TALLINN UNIVERSITY OF TECHNOLOGY
School of Information Technologies
Department of Computer Systems

The dissertation was accepted for the defence of the degree of Doctor of Philosophy on September 24, 2025

Supervisor: Associate Professor Kristina Vassiljeva,
Department of Computer Systems, School of Information Technologies,
Tallinn University of Technology,
Tallinn, Estonia

Co-supervisor: Associate Professor Peeter Ellervee,
Department of Computer Systems, School of Information Technologies,
Tallinn University of Technology,
Tallinn, Estonia

Co-supervisor: Associate Professor Seyed Hassan HosseinNia Kani,
Department of Precision and Microsystem Engineering,
Faculty of Mechanical Engineering,
Delft University of Technology,
Delft, The Netherlands

Opponents: Associate Professor Andrei Lobov,
Department of Mechanical and Industrial Engineering, Faculty of Engineering,
Norwegian University of Science and Technology,
Trondheim, Norway

Assistant Professor Raine Viitala,
Department of Energy and Mechanical Engineering, School of Engineering,
Aalto University,
Helsinki, Finland

Defence of the thesis: November 7, 2025, Tallinn

Declaration:
Hereby I declare that this doctoral thesis, my original investigation and achievement, submitted for the doctoral degree at Tallinn University of Technology, has not been submitted for any academic degree elsewhere.

Hossein Alimohammadi _____
signature

Copyright: Hossein Alimohammadi, 2025
ISSN 2585-6898 (publication)
ISBN 978-9916-80-396-7 (publication)
ISSN 2585-6901 (PDF)
ISBN 978-9916-80-397-4 (PDF)
DOI https://doi.org/10.23658/taltech.79/2025
Printed by Koopia Niini & Rauam

Alimohammadi, H. (2025). *Dynamics Modeling and Optimization of Locally Resonant Metastructures for Vibration Suppression and Energy Harvesting* [TalTech Press]. https://doi.org/10.23658/taltech.79/2025

TALLINNA TEHNIKAÜLIKOOL
DOKTORITÖÖ
79/2025

Dünaamiline modelleerimine ja optimeerimine kohalikult resonantsete metastruktuuride jaoks vibratsiooni summutamiseks ja energia kogumiseks

HOSSEIN ALIMOHAMMADI

TAL TECH
KIRJASTUS

Contents

List of Publications 9

Author's Contributions to the Publications 10

Abbreviations 11

Terms 12

Symbols 13

1 Introduction 15
- 1.1 Locally Resonant Metamaterials 16
- 1.2 Application 17
- 1.3 Problem Statement 17
- 1.4 Significance of the Research 18
- 1.5 Research Gap 18
- 1.6 Research Objectives and Questions 19
- 1.7 Scope of the Research 21
- 1.8 Contributions 21
- 1.9 Dissertation Outline 22

2 Relevant Studies 23
- 2.1 Lumped Parameter Metastructures 23
- 2.2 Distributed Parameter Metastructures 24
  - 2.2.1 Mechanical Locally Resonant Metamaterials 24
  - 2.2.2 Electromechanical Locally Resonant Metamaterials 25
- 2.3 Streamlining Metastructure Modeling: More Techniques for Enhanced Functional Diversity 26
  - 2.3.1 Enabling Distributed Metastructures with Internally Coupled Resonators 26
  - 2.3.2 Developing Closed-Form Distributed Models with Piezo Actuators to Compensate Structural Damping 27
  - 2.3.3 Formulating Closed-Form Transfer Function Equations for Notched-Piezo Actuators 27

3 Modeling of Flexible Metastructures with Mechanical Resonators 29
- 3.1 Lumped Parameter Modeling 29
- 3.2 Linear Lumped Parameter Modeling 29
  - 3.2.1 Nonlinear Lumped Parameter Modeling 30
  - 3.2.2 Dispersion Curve 32
  - 3.2.3 Numerical Studies 34
- 3.3 Distributed Parameter Modeling 36
  - 3.3.1 Modal Analysis and Bandgap Formation in Mechanical Metastructures 36
- 3.4 Dispersion Analysis by Plane Wave Expansion Method 42
- 3.5 Numerical Studies 43
- 3.6 Finite Element Study 45
- 3.7 Experimental Study 46
- 3.8 Summary 48

4 Modeling of Flexible Metastructures with Electromechanical Resonators .. 50
4.1 Lumped Parameter Modeling 50
4.1.1 Linear Electromechanical Resonators 50
4.1.2 Analysis of Power Output of Standard Piezoelectric Circuit for Energy Harvesting 53
4.1.3 Nonlinear Electromechanical Resonators 54
4.1.4 Theoretical Models for the Nonlinear Energy Harvesting 55
4.2 Numerical Studies 56
4.2.1 Investigation on Energy Harvesting Performance in Linear Electromechanical Metamaterial 56
4.2.2 Model NL:1 - Polynomial Nonlinearity in Resonators 58
4.2.3 Model NL:2 - Nonlinear Capacitance in Voltage-Dependent Scenarios 60
4.2.4 Model NL:3 - Cubic Nonlinearities 60
4.3 Distributed Parameter Modeling 61
4.3.1 Electromechanical Resonators for Energy Harvesting 62
4.4 Numerical Studies 67
4.5 Summary 71

5 Streamlining Metastructure Modeling: Internally Coupled Resonators ... 73
5.1 Lumped Parameter Model of Mechanical Internally Coupled Resonators 73
5.1.1 Stability Analysis for Mechanical Internally Coupled Metamaterial 75
5.2 Lumped Parameter Model of Electromechanical Internally Coupled Resonators 77
5.2.1 Internal Coupling Through Shunt Capacitance Circuit Techniques 77
5.2.2 Stability Analysis of Electromechanical Internally Coupled Resonators Using Shunt Capacitance 80
5.3 Numerical Studies 83
5.3.1 Nonlinear Mechanical Resonators and Internal Coupling Dynamics 83
5.3.2 Internally Coupled Resonators with Electromechanical Nonlinearity 85
5.4 Distributed Parameter Model of Mechanical Internally Coupled Resonators 87
5.5 Numerical Studies 92
5.6 Experimental Study 94
5.6.1 Transmittance Measurements 95
5.6.2 Observations from FEM Analysis: 96
5.7 Summary 99

6 Streamlining Metastructure Modeling: More Techniques for Enhanced Functional Diversity 101
6.1 AI-Driven Optimization of Metastructures: Analytical and Experimental Approaches for Parameter Estimation of Metastructure 101
6.1.1 Estimation of Damping Ratio in Metastructures 101
6.1.2 Structural Damping Impact on Metastructural Dynamics 102

6.1.3 Numerical Studies and Experimental Approaches for Parameter Estimation of Metastructur ... 103
6.1.4 Noisy Signal: Case Study #1 ... 103
6.1.5 Experimental Setup: Case Study #2 ... 106
6.1.6 Experimental Setup: Case Study #3 ... 108
6.1.7 Experimental Setup: Case Study #4 ... 111
6.2 Methodology for Structural Damping Compensation in Distributed Parameter Metastructures through Piezo Actuation with Constant Voltage ... 113
6.2.1 Enabling Methodology for Damping Compensation of Metastructure ... 114
6.3 Methodology for Structural Damping Compensation in Distributed Parameter Metastructures via Notched Piezo Actuation ... 118
6.3.1 Numerical Studies ... 119
6.4 Summary ... 124

7 Conclusions, Contributions, and Future Work ... 126
7.1 Summary and Conclusions ... 126
7.1.1 Modeling of Flexible Metastructures with Mechanical Resonators ... 126
7.1.2 Modeling of Flexible Metastructures with Electromechanical Resonators ... 127
7.1.3 Streamlining Metastructure Modeling: Internally Coupled Resonator ... 128
7.1.4 Streamlining Metastructure Modeling: More Techniques for Enhanced Functional Diversity ... 128
7.2 Contributions ... 129
7.3 Future Work ... 132

List of Figures ... 134

List of Tables ... 141

References ... 142

Acknowledgements ... 149

Abstract ... 150

Kokkuvõte ... 151

Appendix 1 ... 153

Appendix 2 ... 179

Appendix 3 ... 201

Appendix 4 ... 217

Appendix 5 ... 225

Appendix 6 ... 233

Appendix 7 241
Appendix 8 255
Appendix 9 275
Appendix 10 283
Curriculum Vitae 293
Elulookirjeldus 294

List of Publications

The present Ph.D. thesis is based on the following publications that are referred to in the text by Roman numbers.

I Alimohammadi, H., Vassiljeva, K., HosseiniNia, S. H., Petlenkov, E. (2024). Nonlinear Dynamics in PEH for Enhanced Power Output and Vibration Suppression in Metastructures. Nonlinear Dynamics.

II Alimohammadi, H., Vassiljeva, K., HosseiniNia, S. H., Petlenkov, E. (2024). Bandgap Dynamics in Locally Resonant Metastructures: A General Theory of Internal Resonator Coupling. Applied Sciences, 14(6), 2447.

III Alimohammadi, H., Vassiljeva, K., HosseiniNia, S. H., Petlenkov, E. (2024). Stability analysis and energy harvesting in lumped parameter systems with internally coupled resonators. Journal of Vibration and Control.

IV Alimohammadi, H., Vassiljeva, K., HosseiniNia, S. H., Petlenkov, E. (2024). Harvesting Energy and Stability Insights in Internally Coupled Resonator Systems. The 18th IEEE International Conference on Advanced Motion Control (AMC), 1-6.

V Alimohammadi, H., Vassiljeva, K., HosseiniNia, S. H., Petlenkov, E. (2024). Enhancing Bandgap Depth in Locally Resonant Metastructures via Notch-filtered Piezoelectric Actuation, The 25th IEEE International Conference on Industrial Technology.

VI Alimohammadi, H., Vassilyeva, K., HosseiniNia, H., Petlenkov, E. (2023). Band gap tuning based on adjustable stiffness of local resonators. The 13th International Conference on Metamaterials, Photonic Crystals and Plasmonics.

VII Alimohammadi, H., Vassiljeva, K., HosseiniNia, S. H., Ellervee, P, Petlenkov, E. (2024). Piezoelectric Compensation of Structural Damping in Metamaterial Beams: Stability and Performance Analysis. Active and Passive Smart Structures and Integrated Systems XVIII (SPIE).

VIII Alimohammadi, H., Vassiljeva, K., HosseiniNia, S. H., Petlenkov, E. (2024). Exploring Internally Coupled Resonator's Dynamics and Spatial Variability in Metamaterials for Vibration Suppression. Active and Passive Smart Structures and Integrated Systems XVIII (SPIE).

IX Alimohammadi, H., Vassiljeva, K., HosseiniNia, S. H., Ellervee, P, Petlenkov, E. (2024). Exploring the Real-World Challenges and Efficacy of Internal Coupling in Metastructures: An Experimental Perspective. The 4th International Conference on Electrical, Computer and Energy Technologies, ICECET.

X Alimohammadi, H., Vassiljeva, K., HosseiniNia, S. H., Ellervee, P, Petlenkov, E. (2024). Damping Optimization in Locally Resonant Metastructures via Hybrid GA-PSO Algorithms and Modal Analysis. Conference on Smart Materials, Adaptive Structures and Intelligent Systems , ASME SMASIS.

Author's Contributions to the Publications

In I, I conceptualized and designed the study, wrote the simulation program, and carried out the simulations and the analysis of the results.
In II, I conceptualized and designed the study, derived new mathematical representations, developed the analytical models, performed data analysis, and was a major contributor in writing the manuscript.
In III, I conducted the simulation, analysis of the piezoelectric effects, and significantly contributed to the drafting and revising of the manuscript.
In IV, I conducted the simulation, analyzed the piezoelectric effects, and significantly contributed to the drafting and revising of the manuscript.
In V, I conceptualized and designed the study, adapted and designed notch filters to compensate damping, and wrote the simulation program.
In VI, I was responsible for the setup of the experimental design, data collection, FEM simulations, and data analysis, and was instrumental in the manuscript preparation and revision.
In VII, I conducted the simulation, analysis of the internally coupled resonator effects, and significantly contributed to the drafting and revising of the manuscript.
In VIII, I performed all simulations, analyzed data, and wrote substantial sections of the manuscript.
In IX, I was responsible for the setup of the experimental design, designed and built the prototype, assembled the equipment, and conducted the experiments.
In X, I designed the optimization experiments, executed the simulations using Hybrid GA-PSO algorithms, analyzed the results, and contributed to writing the manuscript.

Abbreviations

ABC Artificial Bee Colony.

AI Artificial Intelligence.

DDPG Deep Deterministic Policy Gradient.

FEM Finite Element Method.

GA Genetic Algorithm.

MEMS Microelectromechanical Systems.

MPPT Maximum Power Point Tracking.

ODE Ordinary Differential Equation.

PDE Partial Differential Equation.

PSO Particle Swarm Optimization.

RL Reinforcement Learning.

RMSE Root Mean Square Error.

RMS Root Mean Square.

SECE Synchronized Electric Charge Extraction.

SSE Sum of Squared Errors.

SSHI Synchronized Switch Harvesting on Inductor.

TMD Tuned Mass Damper.

Terms

Bandgap A range of frequencies in which wave propagation is forbidden or significantly attenuated; A range of frequencies in which waves cannot propagate through a structure, often created deliberately in metamaterials for vibration suppression.

Damping The effect of reducing the amplitude of oscillations in a dynamic system.

Energy Harvesting The process by which energy is derived from external sources (e.g., solar power, thermal energy, kinetic energy), converted to electrical energy, and stored or used immediately.

Metamaterial A material engineered to have properties not found in naturally occurring materials.

Modal Analysis The process of determining the natural frequencies, mode shapes, and damping ratios of a structure.

Notch Filter An electronic filter that passes most frequencies unaltered but attenuates those in a specific range to very low levels.

Piezoelectric Effect The ability of certain materials to generate an electric charge in response to applied mechanical stress.

Resonator A device or system that naturally oscillates at some frequencies.

Transmittance The ratio of transmitted wave intensity to incident wave intensity in a material.

Symbols

Greek Symbols

β Coefficient representing a proportionality factor.

γ Nonlinear stiffness coefficient.

$\delta(x - x_r)$ Dirac delta function indicating resonator location.

δ_{mn} Kronecker delta function for modes m and n.

ζ Damping ratio.

θ Electromechanical coupling coefficient (N/V).

$\vartheta_{p,r}$ Piezoelectric coupling coefficient for resonator r (N/V).

κ Internal coupling stiffness (N/m).

λ Wavelength of the propagating wave (m).

μ Mass ratio.

ν Stiffness ratio.

ρ Density of the material (kg/m^3).

τ Time constant related to the resistor and capacitor in the circuit (s).

τ_r Transmittance of output displacement to input displacement.

Ψ_m Resonator's modal coordinate.

ω Angular frequency of oscillation; natural frequency of the system's modes (rad/s).

ϕ_m Mode shape function of the m-th mode.

ϕ_n Mode shape function of the n-th mode.

Other Symbols

A Cross-sectional area of the beam (m^2).

E Young's modulus of the beam material (Pa).

G_n Wave number of the n-th mode in the structure (rad/m).

I Moment of inertia of the beam cross-section (m^4).

$\mathcal{L}$ Structural flexibility parameter (N/m).

$\mathcal{M}$ Mass per unit length of the beam (kg/m).

m_r Mass of the r-th resonator (kg).

N_m Number of modes.

N_r Number of resonators.

$\mathcal{C}$ Damping coefficient (Ns/m).

$C^*_{p,r}$ Effective capacitance of the piezoelectric element in resonator r (F).

$\mathcal{F}_{b_m}$ External force distributed across the beam due to modals (N).

$\mathcal{F}_{b_r}$ External force distributed across the beam due to resonators (N).

x_r Position of the r-th resonator (m).

z_m Modal displacement amplitude (m).

z_r Displacement of the r-th resonator (m).

$_{2r-1}$ Subscript notation for odd-numbered resonators.

$_{2r}$ Subscript notation for even-numbered resonators.

1 Introduction

Vibration isolation is essential across multiple engineering disciplines such as robotics, precision manufacturing, seismic protection, and automotive engineering. In robotics, particularly with flexible manipulators, controlling vibrations is essential for precision and accuracy. In precision manufacturing, vibration isolation ensures the quality of production processes. Seismic vibration isolation protects structures during earthquakes, while in automotive engineering, reducing engine vibrations that reach the cabin enhances comfort and safety. For flexible space structures and telescopes in space, effective vibration isolation is crucial for maintaining structural integrity and functionality in harsh environments. In aircraft engines and wings, where lightweight structures are essential, metamaterials offer a significant advantage by providing effective vibration isolation while being lighter than traditional materials.

Traditional vibration control techniques, such as passive damping, tuned mass dampers, and active control methods, have been extensively used in various industries. However, they each come with inherent limitations. Damping materials, for instance, dissipate vibrational energy into heat but often add weight and complexity to the system, making them impractical for lightweight structures such as aircraft wings or flexible robotic arms. Additionally, damping materials can degrade over time due to environmental conditions such as temperature fluctuations, humidity, and mechanical fatigue. Additionally, it might not be efficient over a broad range of frequencies [1].

Another widely employed vibration control method is the Tuned Mass Damper (TMD), which consists of an auxiliary mass attached to a structure via a spring-damper system [2]. By introducing an anti-resonance at a specific frequency, TMDs effectively reduce vibrations at that frequency. However, their effectiveness is typically limited to a narrow frequency band, making them unsuitable for systems subjected to broadband or time-varying excitations. When a system is exposed to broadband excitation, such as turbulence in aircraft wings or road irregularities in vehicles, TMDs are insufficient in providing effective vibration mitigation. Furthermore, the tuning of mass dampers requires precision, and slight variations in structural properties or environmental conditions can render them ineffective.

To overcome these limitations, Mechanical Metamaterials (or Metastructures) offer a novel solution and significant advantages over traditional methods. Metamaterials are engineered with repeated lattices that manipulate wave propagation, creating vibrational bandgaps where elastic waves cannot propagate through the material.

Initially stemming from optical and electromagnetic waves [3, 4], the concept has expanded into domains such as acoustic [5, 6] and elastic waves [7]. The elastic metamaterials have emerged to control elastic waves, encompassing longitudinal, transverse, and rotational waves. This extension opens new avenues for applications in vibration control, seismic protection, and medical ultrasound imaging, demonstrating the versatile and far-reaching impact of metamaterial technology [7].

One of the primary mechanisms behind bandgap formation in metamaterials is Bragg scattering, a phenomenon observed in phononic crystals—composite materials characterized by periodically varying material properties. Bragg scattering occurs when wave reflections from periodic structures interfere destructively, preventing wave propagation at specific frequencies [8]. However, a major drawback of

Bragg scattering-based phononic crystals is that the bandgap frequency depends on the lattice size. To create bandgaps at low frequencies, which are essential for seismic vibration isolation or large-scale structures, the lattice size must be relatively large, making the structure impractical for real-world applications. A promising solution to overcome the limitations of Bragg scattering in phononic crystals is the use of locally resonant metamaterials.

1.1 Locally Resonant Metamaterials

Locally resonant metamaterials provide a superior alternative for practical applications, especially at low frequencies. This approach was first demonstrated by Liu et al. [5], who experimentally showed a bandgap at wavelengths significantly larger than the lattice size. Since then, numerous types of locally resonant metamaterials have been developed, broadly categorized into mechanical and electromechanical systems. These materials ingeniously incorporate resonant unit cells that enable the creation of band gaps at virtually any desired frequency by fine-tuning the resonator's frequency. This adaptation facilitates the mitigation of phase differences between the resonator and the lattice, allowing for effective vibration suppression across a broader range of frequencies.

To fully exploit the potential of locally resonant metamaterials, it is crucial to employ accurate and versatile modeling approaches. In the following sections, we delve into two primary modeling methodologies: Lumped Parameter Metastructures, and Distributed Parameter Metastructures. Lumped Parameter Modeling simplifies systems into discrete components like masses and springs, leading to Ordinary Differential Equations (ODEs) that depend solely on time. This modeling approach is represented by the equation:

$$F\left(t, z(t), \frac{\partial z(t)}{\partial t}, \frac{\partial^2 z(t)}{\partial t^2}, \ldots, \frac{\partial^n z(t)}{\partial t^n}\right) = g(t) \tag{1}$$

This methodology is suitable for preliminary designs and rapid analyses due to its straightforward computational nature.

On the other hand, Distributed Parameter Modeling treats systems as continuous media, leading to Partial Differential Equations (PDEs). This approach is expressed through the equation:

$$F\left(x, t, w, \frac{\partial w}{\partial x}, \frac{\partial^2 w}{\partial x^2}, \frac{\partial w}{\partial t}, \frac{\partial^2 w}{\partial t^2}, \ldots\right) = h(x, t) \tag{2}$$

Here, $w(x,t)$ represents the modal summation $\sum_{m=1}^{N_m} \phi_m(x) z_m(t)$, where $\phi_m(x)$ are the mode shapes and $z_m(t)$ are the modal coordinates. This method accounts for changes across both spatial and temporal coordinates, providing a comprehensive and accurate representation of dynamic behaviors in flexible structures and machines. It captures the potentially infinite number of natural frequencies due to minute variations in distributed masses and stiffnesses along the structure.

By implementing an effective methodology for metastructural vibration suppression with locally resonant units, the vibrations of the main structure are significantly attenuated, achieving the desired vibration control. Rather than being dissipated, the energy is transferred to the resonators, resulting in minimal vibrational energy in the primary structure while maximizing energy accumulation within the resonators. This fundamental mechanism underpins vibrational energy

harvesting, wherein the concentrated vibrational energy in resonators is efficiently converted into usable electrical power through piezoelectric, electromagnetic, or other transduction mechanisms.

A broader bandgap range in the main structure enhances energy harvesting efficiency by concentrating vibrational energy within the resonators, thereby optimizing energy conversion. Beyond establishing the transfer function of such metastructures for control applications, a key objective is to improve energy harvesting by expanding bandgap width, deepening existing bandgaps, or generating multiple distinct bandgaps. Advancing these capabilities necessitates a range of strategies, including multi-resonator configurations, internally coupled resonators, graded metastructures, nonlinear metamaterials, topology optimization, optimized energy harvesting circuits, and advanced filtering techniques such as notch filters. These methodologies collectively enhance vibration suppression and maximize energy conversion efficiency, enabling the development of high-performance metastructures for engineering applications.

1.2 Application

Classical vibration control techniques—such as passive damping, TMDs, and active control methods—are widely used in engineering applications. However, they often fall short in fully eliminating wave propagation or suppressing structural vibrations across a broad frequency range. Passive damping dissipates energy but cannot fully prevent wave transmission, while TMDs are typically narrowband and sensitive to parameter variations. Active methods require significant power and complexity, making them impractical in many scenarios.

In contrast, locally resonant metastructures are increasingly recognized as critical solutions across diverse engineering domains due to their tailored dynamic properties. Rather than merely reducing the amplitude of vibration, these systems are designed to create bandgaps—frequency ranges in which wave propagation is entirely suppressed. This enables superior vibration isolation, noise reduction, and structural control across a range of conditions.

Such metastructures are particularly valuable in high-precision manufacturing (e.g., nanopositioning systems), where even minimal vibrations can degrade performance. They also enhance durability and comfort in automotive and railway systems by suppressing vibration transmission and reducing noise. Furthermore, by integrating electromechanical components, metastructures can serve a dual purpose: simultaneously suppressing vibrations and harvesting ambient mechanical energy. This makes them ideal for powering autonomous monitoring systems and extends their utility to applications such as smart infrastructure and seismic protection.

1.3 Problem Statement

Despite these promising potentials, significant technical challenges remain unresolved. Most prior works rely on linear approximations of metastructure dynamics, which fail to capture the full complexity of real-world nonlinear phenomena—especially in systems with internal coupling or piezoelectric integration. These nonlinearities can significantly influence bandgap characteristics and energy harvesting behavior, yet are not adequately addressed in existing analytical frameworks. Moreover, although closed-form transfer functions are essential for control

and real-time tuning of metastructures, current literature primarily focuses on simplified unit-cell models. There is a lack of closed-form models that account for advanced configurations, such as internally coupled resonators or systems designed for structural damping compensation.

Additionally, multifunctional optimization, especially in closed-form presentation —balancing vibration suppression with energy harvesting and other structural or performance constraints—has not been sufficiently developed within a unified modeling and control framework. While some research has highlighted how structural damping reduces bandgap depth, few have proposed effective methods to compensate for this, particularly through active strategies such as piezoelectric actuation. Furthermore, although piezoelectric-based control has been explored to a degree, its stability boundaries, design trade-offs, and integration into distributed metastructure models remain open questions.

In summary, the nonlinear modeling of advanced metastructures, the development of closed-form transfer functions for real-time control, and the formulation of damping compensation strategies using electromechanical methods remain key challenges. These aspects have not yet been addressed within a cohesive and practically applicable framework. This thesis aims to fill that gap.

1.4 Significance of the Research

The increasing demand for high-performance, energy-efficient, and autonomous structural systems has made vibration suppression and energy harvesting critical in modern engineering. Locally resonant metastructures provide a lightweight, scalable foundation for both passive and actively controlled vibration suppression systems. However, their widespread adoption is limited by unresolved issues in nonlinear modeling, damping effects, and control implementation to enhance bandgap and harvesting energy performance. This thesis addresses these barriers by developing mathematically rigorous and practically oriented frameworks, contributing both to the theoretical understanding and to the future deployment of metastructures in real-world applications such as smart infrastructure, precision manufacturing, and transport systems.

1.5 Research Gap

Despite growing interest in locally resonant metastructures, several critical gaps remain that hinder their widespread practical adoption and multifunctional performance. This thesis identifies and addresses the following unresolved challenges in the current literature:

- **Nonlinear Dynamics:** The influence of nonlinearities—both mechanical and electromechanical—on bandgap behavior and energy harvesting potential is insufficiently understood, especially when internal coupling or piezoelectric actuation is involved.
- **Internal Coupling:** While internal resonators have been studied, the role of linear and nonlinear internal coupling in modifying bandgap depth, merging phenomena, and dynamic behavior remains underexplored, particularly in configurations beyond the fundamental unit-cell level.
- **Closed-form Modeling:** There is a lack of closed-form transfer function models that can describe distributed metastructures with complex config-

urations, such as internally coupled resonators and systems incorporating damping compensation or adaptive control.

- **Stability Under Piezoelectric Actuation:** Although piezoelectric elements have been used for vibration control, comprehensive analyses of how piezoelectric compensation for damping affects the system's stability boundaries, especially in the presence of feedback loops or nonlinearities, are limited.
- **Structural Damping Compensation:** The detrimental effect of structural damping on bandgap depth is known, but methods for actively compensating for it—especially using piezoelectric or electromechanical feedback—are not well established in the literature.
- **Experimental Scalability and Real-World Testing:** Although several analytical and numerical studies have examined internally coupled metastructures, experimental validation is still lacking. The absence of physical testing under realistic boundary conditions and dynamic loading highlights a significant gap, limiting the practical confidence and adoption of such advanced configurations.
- **AI-Driven Optimization:** Advanced AI techniques, such as reinforcement learning or evolutionary optimization, have only recently been introduced in this field. Their application in tuning piezoelectric actuators, optimizing damping profiles, and enhancing bandgap control remains limited.
- **Frequency Control through Notch Filtering:** While theoretical designs may achieve ideal bandgap performance, real-world implementations often deviate due to structural damping and energy losses. Various approaches have been proposed to overcome damping-induced degradation of bandgaps, including shunted piezoelectric circuits, resonator grading strategies, hierarchical unit cells, and nonlinear design techniques. While these methods have shown partial success, the integration of such mechanisms within closed-form, control-ready models remains limited. Notch filtering, in particular, though widely used, still lacks a general framework for dynamic and adaptive frequency control under realistic damping conditions.

This thesis addresses the above gaps by developing nonlinear and distributed models, introducing closed-form control-oriented formulations, and implementing both experimental validation and AI-based tuning approaches to advance the multifunctional performance of metastructures for vibration suppression and energy harvesting.

1.6 Research Objectives and Questions

The overarching goal of this thesis is to enhance the characteristics of band gaps (BG)—in particular, by increasing their width and depth—and to maximize energy harvesting in locally resonant metamaterials. Additionally, it aims to streamline the modeling methodology and develop closed-form transfer functions to enable real-time control of distributed metastructures.

To achieve this, the research addresses the following specific objectives:

1. Develop nonlinear mechanical and electromechanical models for resonant unit cells.

2. Formulate closed-form and control-theoretic transfer functions for distributed metastructures.

3. Investigate internal coupling effects, including bistability and frequency merging phenomena.

4. Explore spatial tuning strategies, such as mass distribution and center-of-mass shifting.

5. Propose and validate experimentally feasible methods for damping compensation, including piezoelectric actuation.

6. Analyze stability boundaries under nonlinear coupling and active control conditions.

7. Employ artificial intelligence-based optimization techniques for parameter estimation and adaptive tuning.

8. Validate the analytical model through numerical simulations and targeted experimental investigations.

To realize these objectives and to address the challenges of vibration suppression and energy harvesting in metastructures, this thesis is driven by the following main research question:

Main RQ: *How can the performance of bandgap formation and energy harvesting in metastructures be enhanced through nonlinear modeling, closed-form control techniques, and AI-based tuning, particularly in the presence of structural damping?*

To support this goal, the research is structured around a set of focused subquestions, grouped into four thematic areas: (1) Modeling and Dynamics, (2) Control and Closed-form Representation, (3) Experimental Validation, and (4) Optimization and Intelligence:

- **RQ1:** How do nonlinear mechanical and electromechanical effects influence bandgap formation and energy harvesting in metastructures? This question is elaborated in Chapter 3 and supported by the nonlinear modeling and energy harvesting framework presented in [9].

- **RQ2:** How do linear and nonlinear coupling mechanisms affect vibration suppression and bandgap evolution in metastructures? This is addressed in Chapter 4 and Chapter 5, and supported by [10, 9].

- **RQ3:** What closed-form analytical formulations best describe continuous metastructures with internal coupling, and how can they enable effective bandgap tuning? This is addressed in Chapter 5, and supported by the closed-form modeling work in [11].

- **RQ4:** What are the stability boundaries of metastructures under piezoelectric actuation, feedback loops, and nonlinear coupling, and how can they be analyzed analytically? These aspects are explored in Chapter 4 and Chapter 5, and analyzed in [12, 13].

- **RQ5:** How accurately do theoretical and numerical predictions of internally coupled metastructures match experimental results under realistic conditions? This validation is carried out in Chapter 5, and supported by [14].

- **RQ6:** How can artificial intelligence techniques (e.g., RL, GA, PSO) be used to estimate parameters, optimize bandgap depth, and enable real-time tuning in closed-form presentation of metastructures? This is presented in Chapter 6 and explored in [15, 16, 17].
- **RQ7:** How can notch filtering strategies be formulated and optimized for adaptive, closed-form control of bandgaps in damped, nonlinear, or uncertain metastructures? This control method is developed in Chapter 6 and detailed in [16].
- **RQ8:** How can spatial variation strategies, such as center-of-mass shifting and mass grading, passively tune or extend bandgap ranges? This is explored in Chapter 3 and discussed in [18].

These questions and objectives form the methodological foundation for the theoretical modeling, simulations, optimizations, and experimental studies presented throughout this thesis.

1.7 Scope of the Research

This thesis encompasses analytical modeling, numerical simulations, and selective experimental investigations relevant to locally resonant metastructures. The primary objective is to enhance vibration suppression through increased and deepened bandgaps while maximizing energy harvesting performance.

The research particularly emphasizes the development of generalized mathematical models that account for nonlinear behaviors, such as those arising from internally coupled resonators and piezoelectric actuation. While several analytical and numerical frameworks are presented to characterize piezoelectric-based systems, the experimental validation of nonlinear piezoelectric effects is not included within the scope of this work. This is due to practical limitations in accessing piezoelectric elements capable of exhibiting the specific nonlinear phenomena modeled in this study.

As such, the focus remains on providing a comprehensive theoretical and simulation-based foundation for understanding the performance and control potential of metastructures under a wide range of nonlinear and coupled conditions. The groundwork established here is intended to guide and motivate future experimental research, particularly involving nonlinear piezoelectric resonators.

1.8 Contributions

This thesis presents several novel contributions to the modeling, analysis, and control of locally resonant metastructures. In particular, the research introduces (i) generalized nonlinear modeling frameworks, (ii) closed-form analytical formulations for continuous systems, (iii) damping compensation strategies for closed-form metastructures, utilizing piezoelectric actuation, (iv) detailed stability analyses under nonlinear coupling, (v) AI-driven optimization methods for closed-form metastructure identification and tuning, and (vi) experimental validation of metastructure configurations as well as internally coupled designs. The primary contributions are detailed as follows:

- Development of generalized nonlinear mechanical and electromechanical models for locally resonant metastructures, enabling enhanced vibration suppres-

sion and improved energy harvesting performance;

- Derivation of novel closed-form analytical formulations for continuous (distributed) metastructures with internally coupled resonators, extending beyond traditional lumped models;
- Introduction of new functionalities enabled by closed-form solutions, such as active structural damping compensation via piezoelectric actuation, allowing significant improvements in bandgap depth and tunability;
- In-depth stability analyses for internally coupled metastructures, clearly defining safe operational limits for both mechanical and electromechanical coupling scenarios;
- Integration of artificial intelligence and optimization techniques for parameter estimation of mathematical models and optimization of metastructure functionalities;
- Experimental validation of theoretical and numerical predictions, clearly identifying and discussing real-world implementation challenges and practical limitations.

1.9 Dissertation Outline

Each chapter of the dissertation begins with a concise introduction, followed by a detailed explanation of the methodology and mathematical formulations related to metamaterial dynamics. This is succeeded by sections on simulation and experimental procedures, culminating in a thorough analysis of the results. The summary of each chapter provides insights and commentary on the findings, thereby enhancing the understanding of their implications.

The dissertation is organized as follows: Chapter 2 provides an overview of relevant studies and foundational concepts for understanding the advanced modeling techniques used throughout this research. Chapter 3 develops the formulation and general theory for modeling mechanical locally resonant metastructures through lumped parameter modeling and distributed parameter modeling, accompanied by experimental validation for a locally resonant beam. Chapter 4 extends the theoretical framework to electromechanical locally resonant metastructures, incorporating both lumped metamaterial models with piezoelectric resonators and distributed beam models in bending. Numerical validation is performed using the Finite Element Method (FEM). This chapter highlights the role of electromechanical resonators in vibration control and energy harvesting, and presents comprehensive modeling approaches including analytical formulations, lumped and distributed parameter models (linear and nonlinear), and modal analysis techniques. Chapter 5 describes the streamlining of a closed-form methodology for flexible metastructures with internally coupled resonators. It discusses the concept and theoretical benefits, challenges in practical application, and details the experimental setup and methodology, including FEM analysis. Chapter 6 focuses on streamlining more techniques for enhanced functional diversity, such as piezoelectric actuation and notch filter integration, utilizing AI-driven optimization, and conducting a set of experiments to estimate structural damping. Finally, Chapter 7 summarizes the contributions of this dissertation to the field of elastic metamaterials and outlines potential topics for future research.

2 Relevant Studies

Vibration control technologies have rapidly evolved to address the demands of modern engineering applications, ranging from automotive to civil engineering structures. The development of metastructures, especially those incorporating advanced material properties and geometrical designs, represents a significant leap in our ability to control and manipulate wave propagation. This section delves into various methodologies for modeling and optimizing such structures, focusing on both lumped and distributed parameter approaches. The insights gained from these studies not only enhance our understanding of dynamic systems but also pave the way for innovating new applications in noise reduction, energy harvesting, and beyond.

2.1 Lumped Parameter Metastructures

Lumped parameter metastructures are a simplified yet powerful approach to modeling and understanding the dynamic behavior of metamaterials. This method treats the metamaterial as a collection of discrete elements, each with its own distinct properties such as mass, stiffness, and damping. By focusing on these individual elements, lumped parameter models provide a clear and manageable framework for analyzing the resonant behavior and vibration suppression capabilities of metastructures [19, 20]. Central to these systems are chain oscillators, which both convert and suppress vibrational energy, enhancing the efficiency of energy extraction from ambient sources [21, 22, 23].

In the realm of electromechanical systems, lumped parameter models have been extended to include the effects of piezoelectric materials, which convert mechanical energy into electrical energy and vice versa. This integration allows for the development of advanced vibration suppression and energy harvesting devices. Researchers have extensively studied the use of piezoelectric elements in metastructures, highlighting their potential to create tunable bandgaps and improve the overall efficiency of energy conversion systems [24, 25, 26, 27, 28].

Moreover, lumped parameter models facilitate the incorporation of nonlinear dynamics, which are crucial for predicting the behavior of metastructures under real-world operating conditions [29]. Nonlinearities such as cubic stiffness and quadratic damping can significantly influence the formation and characteristics of bandgaps [30, 31]. The inclusion of bistable systems within these chains extends their wave control capabilities beyond conventional models, offering a broader attenuation of vibrations and an expanded operational bandwidth [32, 33].

The primary goal in integrating metamaterials into energy harvesting systems is to maximize bandgaps in the main structure, which leads to more energy being transferred to the resonators and, consequently, more harvested energy. This strategy enhances the resonators' energy harvesting capabilities and the overall system's efficiency [34, 35]. While traditional circuits [24, 25] directly connect the load to the harvesting component, advanced designs like SSHI, SECE, and MPPT improve energy conversion efficiency and adapt to environmental changes, significantly enhancing the performance of energy harvesting systems [36, 37, 38, 39, 40]. Data-driven methods, particularly neural networks, have been integrated into Piezoelectric Energy Harvesting (PEH) systems, significantly advancing their performance by allowing these systems to adapt dynamically to varying conditions, optimizing energy conversion efficiency in real-time [41, 42].

However, while lumped parameter models offer significant insights and practical advantages, they also have limitations. The simplification inherent in this approach means that some of the finer details of the wave propagation and interaction may be overlooked. This is where distributed parameter models, which will be discussed in the following section, come into play, providing a more detailed and comprehensive analysis of metastructures.

2.2 Distributed Parameter Metastructures

Distributed parameter metastructures represent a more detailed approach to modeling metamaterials, capturing the continuous nature of wave propagation through these engineered structures. Unlike lumped parameter models, which treat the system as a collection of discrete elements, distributed parameter models consider the material's properties as continuous functions over space and time. This allows for a more comprehensive analysis of the dynamic behavior of metastructures, particularly when dealing with complex geometries and material distributions. They are particularly relevant in various fields, including electromechanical [43] systems, fluid dynamics [44], biological systems [45], and data analysis systems [46].

The foundation of distributed parameter modeling lies in its ability to describe the spatially varying properties of a metamaterial, such as geometry, density, stiffness, and damping. One of the significant advantages of distributed parameter models is their ability to account for higher-order effects and interactions that are often neglected in lumped parameter models. This includes phenomena such as wave scattering, mode coupling, and the influence of boundary conditions. Developing closed-form expressions for the behavior of locally resonant units in metastructures significantly advances the field, offering new perspectives and methodologies for tuned dynamic response and control in engineering applications [47, 11].

Despite their advantages, distributed parameter models are often more computationally intensive than lumped parameter models. The continuous nature of these models requires solving partial differential equations, which can be challenging and time-consuming. However, advances in numerical methods and computational power have made it increasingly feasible to employ distributed parameter models for practical applications.

To further explore the potential of distributed parameter metastructures, it is essential to delve into the specific categories of these materials. The following sections will discuss mechanical and electromechanical locally resonant metamaterials, highlighting their unique properties and applications.

2.2.1 Mechanical Locally Resonant Metamaterials

Mechanical Locally Resonant Metamaterials (MLRMs) utilize resonant unit cells to achieve band gaps at wavelengths much larger than the size of their periodic structure. These materials typically consist of a host matrix embedded with resonant inclusions, which can be designed to target specific frequencies for vibration attenuation. By carefully tuning the mass, stiffness, and damping properties of these inclusions, MLRMs can be optimized to suppress vibrations across a wide range of frequencies.

One of the key advantages of MLRMs is their ability to create low-frequency band gaps without the need for large, impractical structures. This is achieved by leveraging the resonance of the inclusions, which interact with the host matrix to dissipate vibrational energy effectively. The resulting band gaps can be fine-tuned

by adjusting the properties of the resonant units, allowing for precise control over the vibrational characteristics of the material.

Recent research has focused on enhancing the performance of MLRMs through the development of advanced materials and fabrication techniques. For example, researchers have explored the use of lightweight, high-strength materials to create more efficient resonant inclusions, as well as novel fabrication methods such as additive manufacturing to produce complex metamaterial structures with high precision [48, 49]. Other researchers have examined various implementations of resonators for different types of elastic waves, such as longitudinal, shear, and surface waves. These studies include exploring the potential for harnessing such waves in applications ranging from seismic vibration control to advanced acoustic filtering [50, 51, 52, 53, 54].

Additionally, the integration of nonlinear resonators has been investigated to extend the operational bandwidth of MLRMs [55, 56, 57]. Nonlinear resonators can exhibit behaviors such as amplitude-dependent frequency shifts, which enable the creation of broader and more adaptable band gaps. This makes MLRMs particularly suitable for applications in dynamic environments where the frequency content of vibrations may vary over time [10, 58, 59].

2.2.2 Electromechanical Locally Resonant Metamaterials

Electromechanical Locally Resonant Metamaterials (ELRMs) combine mechanical resonators with electromechanical components, such as piezoelectric elements, to achieve enhanced vibration control and energy harvesting capabilities. These materials exploit the electromechanical coupling between the mechanical resonators and the piezoelectric elements to convert mechanical energy into electrical energy, which can then be dissipated or harvested for use in low-power electronic devices [43].

The incorporation of piezoelectric elements into the resonant unit cells of ELRMs allows for the active tuning of resonant frequencies through the application of electrical signals. This capability enables the dynamic adjustment of band gaps in response to changing environmental conditions, providing a more adaptable and responsive solution for vibration control [60, 61, 62].

ELRMs have been shown to be highly effective in both vibration suppression and energy harvesting applications. In vibration suppression, the piezoelectric elements can be used to shunt the electrical energy [63, 64] generated by the mechanical vibrations, effectively damping the resonant response of the system. This approach has been demonstrated to provide significant attenuation of vibrational energy across a wide frequency range [65].

In energy harvesting, ELRMs can convert ambient mechanical vibrations into usable electrical energy, offering a sustainable power source for low-power devices. The efficiency of energy harvesting can be optimized by tuning the resonant frequencies of the unit cells or resonators to match the dominant frequencies of the ambient vibrations. This makes ELRMs particularly suitable for applications in environments with abundant vibrational energy, such as industrial machinery or transportation systems [66, 67].

Furthermore, recent advancements in materials science and fabrication technologies have enabled the development of more efficient and durable piezoelectric materials, significantly enhancing the performance and longevity of ELRMs [68]. Additionally, research has highlighted the potential of employing active feedback

control in piezoelectric metastructures to create tunable bandgaps, enabling targeted vibration suppression across specific frequency ranges without relying on extensive parametric modeling [69]. Meanwhile, nonlinearities have been recognized for their beneficial role in broadening the effective bandwidth of vibratory energy harvesters, suggesting opportunities for improved energy conversion efficiency in environments characterized by variable excitation conditions [70].

The integration of nonlinear resonators has been investigated to extend the operational bandwidth of ELRMs. Research has examined the benefits of nonlinearities in vibratory energy harvesting, highlighting that nonlinear energy harvesters have a broader steady-state frequency bandwidth than linear ones [71]. This makes them more efficient in varying ambient conditions, potentially providing a better power source for low-power devices used in wireless sensing, data transmission, actuation, and medical implants. Diodes introduce a marked nonlinearity in the current-voltage relationship, significantly impacting energy harvesting efficiency. This effect is critical in rectifying the alternating current (AC) generated by piezoelectric elements into direct current (DC), which is more readily used by electronic devices [24, 25, 26]. Moreover, the interaction between mechanical structures and embedded piezoelectric materials leads to nonlinear behaviors such as amplitude-dependent frequency shifts, essential for enhancing the energy harvester's bandwidth [27, 28].

2.3 Streamlining Metastructure Modeling: More Techniques for Enhanced Functional Diversity

Developing closed-form expressions for the behavior of locally resonant units in metastructures significantly advances the field, offering new perspectives and methodologies for tuned dynamic response and control in engineering applications [47, 43, 72, 73, 74]. This section aims to enable different functionalities of the recent closed-form transfer function approach in metastructures, opening new avenues for control.

2.3.1 Enabling Distributed Metastructures with Internally Coupled Resonators

This involves developing models that incorporate internal coupling mechanisms to enhance the bandgap features of distributed metastructures [75, 11]. Internal coupling, both linear and nonlinear, can improve vibration control and energy harvesting by manipulating wave propagation characteristics. Studies on linear chains with nonlinear resonators [30, 76, 77] and nonlinear chains with linear resonators [30, 78] have demonstrated this phenomenon. Additionally, a novel metamaterial with a multiresonator mass-in-mass lattice system achieved internal coupling through a linear spring, forming two additional bandgaps over conventional designs [79]. Furthermore, coherent internally coupled distant magnonic resonators via superconducting circuits demonstrated operation at quantum-compatible scales [80]. Nonlinear internally coupled resonators have shown promising results, employing a distributed parameter model for the main structure while using a chain or lumped model for resonators. This approach introduces nonlinear internally coupled resonators, demonstrating enhanced wave manipulation capabilities. Modeling and analysis have highlighted the advantages of incorporating nonlinear dynamics into the design of metastructures [10].

2.3.2 Developing Closed-Form Distributed Models with Piezo Actuators to Compensate Structural Damping

Integrating piezoelectric actuators with applied voltage-dependent control can compensate for structural damping that influences bandgap features, particularly enhancing the depth of the bandgap. This approach seeks to refine control over bandgap properties, ensuring more effective vibration suppression [81, 82, 83]. Active control strategies have been explored as a means to adaptively tune vibration characteristics [84]. However, these methods often fall short in unstable ratios, where the active components can introduce additional poles and zeroes in the right-hand side of root locations without significantly improving isolation [85].

2.3.3 Formulating Closed-Form Transfer Function Equations for Notched-Piezo Actuators

Deriving mathematical equations for notched-piezo actuators aimed at frequency-dependent control of bandgap features is crucial for applications requiring precise control over the frequency response of the metastructures. This development leverages advanced control strategies and optimization algorithms to enhance system performance. The application of notch filters within the control loop of piezoelectric actuators has been less documented, with pioneering work suggesting potential improvements in bandgap depth [86]. The integration of AI and machine learning techniques into metastructure design further enhances the adaptability and efficiency of these systems. AI algorithms can optimize the parameters of notch filters in piezoelectric actuators, leading to significant improvements in bandgap depth and vibration isolation [87, 86, 88]. Enhancing bandgap depth in high-damping metastructures involves using piezoelectric actuators paired with notch filters, optimized through reinforcement learning algorithms to achieve improved vibration isolation [16].

Despite significant advancements, several gaps remain in the current understanding and application of distributed parameter metastructures, particularly those integrating nonlinear piezoelectric sensors for energy harvesting and piezoelectric actuators for applications such as structural damping compensation and internal coupling mechanisms. One major gap is the development and implementation of closed-form transfer functions for enhanced control and analysis in various applications, such as piezoelectric actuation and internally coupled resonators. This would enable more precise control over the dynamic responses of metastructures.

Another critical area is the validation of models to confirm their scalability and practicality. Real-world testing remains a crucial step to ensure these metastructures function effectively outside controlled laboratory settings. Alongside this, there is a need for an in-depth analysis of the effects of nonlinear dynamics on electromechanical metastructure performance.

The variable coupling effects in electromechanical systems, such as those involving piezoelectric materials, also require further study. These effects significantly influence bandgap characteristics, energy harvesting, and vibration control capabilities. Additionally, stability challenges need to be addressed when updating metastructures with various elements such as piezoelectric actuation, internally coupled resonators, mass asymmetry, piezoelectric feedback loops, and the introduction of nonlinear components.

Practical implementation limitations, such as accurately estimating and compensating for structural damping in real-world conditions, are another critical area

needing attention. Testing built metastructures in practical environments will refine these estimates and ensure the structures' applicability.

Finally, there is substantial potential in leveraging machine learning and AI-driven techniques to optimize these models. AI can provide accurate dynamic predictions, adjust damping ratios, and optimize piezoelectric actuation and notch filters, significantly enhancing the performance and adaptability of metastructures.

3 Modeling of Flexible Metastructures with Mechanical Resonators

This chapter explores the modal analysis of mechanical locally resonant metastructures through the use of lumped and distributed parameter models. The focus is placed on understanding and predicting the dynamic behaviors of these systems, which are relevant in various engineering applications due to their unique properties in manipulating wave propagation and vibration characteristics.

The fundamental concepts of modal analysis are introduced, utilizing differential operator notation to establish the governing equations. This approach simplifies the mathematical complexities involved and lays the groundwork for further analysis.

The bandgap frequency range and its edge frequencies are derived, predicated on the assumption of an infinite number of resonators. Furthermore, these theoretical predictions undergo validation through numerical approaches, notably the plane wave expansion method, to verify their practical relevance and applicability. Additionally, the chapter discusses experimental validation conducted to assess the performance of the metastructure.

Overall, the chapter aims to provide a detailed understanding of the dynamics of mechanical metastructures, emphasizing the importance of practical design and application to achieve desired dynamic properties through strategic manipulation of structural parameters.

3.1 Lumped Parameter Modeling

Lumped parameter modeling simplifies the analysis of complex physical systems by condensing key properties like inertia, elasticity, and damping into discrete, manageable components. These components, defined by characteristic parameters of mechanical or electrical systems—such as mass, damping, stiffness, resistance, capacitance, and inductance—are interconnected within a network governed by Ordinary Differential Equations (ODEs).

This modeling approach is particularly effective for systems where spatial variations in properties are minimal, thus allowing the simplification of the analysis to ordinary differential equations rather than more complex partial differential equations. It offers a clear, intuitive understanding of system dynamics by abstracting complex phenomena into simpler, discrete elements like springs, dampers, and masses.

3.2 Linear Lumped Parameter Modeling

Linear Lumped Parameter Modeling serves as the cornerstone for understanding wave propagation in metamaterials, laying the groundwork for more complex nonlinear analyses. This approach simplifies the dynamic behavior of a metamaterial system into a series of discrete masses, springs, and dampers, whose interactions can be described by linear differential equations. For a one-dimensional (1D) phononic medium, this linearized model provides an insightful preliminary assessment of wave transmission and reflection characteristics.

Consider a periodic structure consisting of an infinite series of identical unit cells, each comprising a primary mass m_m connected to its neighbors by springs of stiffness k_m, (see Fig. 1). This setup forms a monoatomic chain that can support wave propagation due to mechanical vibrations. Each unit cell is augmented

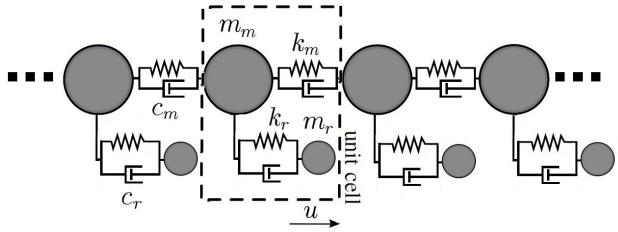

Figure 1: Foundational model of linear phononic media: a linear monoatomic chain with linear resonators of masses, spring, and damping. Dashed rectangle is unit cell.

with a linear resonator, characterized by a mass m_r and connected to the primary chain by a spring of stiffness k_r. For the linear model, we assume the resonator's response to displacement is proportional to the applied force, neglecting any form of nonlinearity or damping for simplicity. The interaction between the chain mass and the resonator can thus be represented as:

$$f_r = k_r \delta, \tag{3}$$

where δ denotes the relative displacement between the chain mass and the resonator.

Applying Newton's second law to both the chain mass and the resonator yields the following set of equations describing the system dynamics:

$$m_m \ddot{u}_m + k_m \left(2u_m - u_{m^-} - u_{m^+}\right) + k_r(u_m - u_r) = 0 \tag{4}$$

$$m_r \ddot{u}_r - k_r \left(u_m - u_r\right) = 0, \tag{5}$$

where u_m and u_r represent the displacements of the chain mass and the resonator, respectively, and u_{m^+} and u_{m^-} are the displacements of the neighboring chain masses. For the last mass in the chain: $u_m - u_{m^+} = 0, \quad \dot{u}_m - \dot{u}_{m^+} = 0$, and for the first mass in the chain: $u_{m^-} = u_b$.

The Linear Lumped Parameter Model elucidates the fundamental mechanics behind wave propagation and band gap formation in mechanical metamaterials. By revealing the influence of mass and stiffness ratios on the system's dynamic properties, this model guides the design of metamaterials with tailored wave manipulation capabilities.

3.2.1 Nonlinear Lumped Parameter Modeling

Transitioning from the foundational principles established in linear dynamics, we now delve into the complexities of Nonlinear Lumped Parameter Modeling, exploring how nonlinearity of resonators enriches the metamaterial's response to external stimuli. The simplest lumped model of a 1D nonlinear phononic medium repeating unit cell, as illustrated in Fig. 2, is characterized as a linear atomic chain with embedded nonlinear resonators. This chain comprises an infinite series of uniform unit cells. Each of these unit cells consists of a mass, m_m, pertaining to the monoatomic chain, interconnected through linear springs.

This primary linear chain is interfaced with nonlinear resonators, each identified by its mass, m_r. For simplicity, let us initially neglect both the damping element

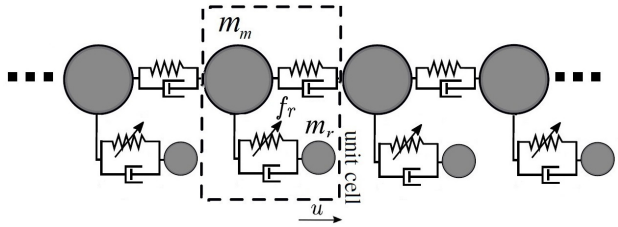

Figure 2: Foundational model of nonlinear phononic media: a linear monoatomic chain with nonlinear resonators of masses, spring, and damping. Dashed rectangle is unit cell.

and any external actuation or feedback mechanisms. The net force exerted by the nonlinear spring connecting the resonators can be represented as:

$$f_r = k_r\delta + \sum \gamma_q \delta^q, \tag{6}$$

where δ is the relative displacement between the adjacent masses (chain mass and resonator). Subsequently, the dynamics of the system can be expounded as follows:

$$\begin{aligned} m_m\ddot{u}_m + k_m\left(2u_m - u_{m^-} - u_{m^+}\right) + \sum \gamma_{q_m}\left((u_m - u_{m^-})^q + (u_m - u_{m^+})^q\right) \\ + k_r(u_m - u_r) + \sum \gamma_{q_r}\left(u_m - u_r\right)^q = 0 \end{aligned} \tag{7}$$

$$m_r\ddot{u}_r - k_r\left(u_m - u_r\right) - \sum \gamma_{q_r}\left(u_m - u_r\right)^q = 0, \tag{8}$$

where for the last mass in the chain: $u_m - u_{m^+} = 0, \quad \dot{u}_m - \dot{u}_{m^+} = 0$, and for the first mass in the chain: $u_{m^-} = u_b$.

Here, $\gamma_{q_m}, \gamma_{q_r}$ denote the nonlinear stiffness of the monoatomic chain and resonator, respectively. Here, u_m denotes the displacement of the m^{th} mass, k_m represents the stiffness of that mass, k_r is the resonator's stiffness, while u_{m^+} and u_{m^-} indicate the displacements of the succeeding and preceding masses, respectively, and u_b signifies the displacement of the excitation at the base or first mass chain.

The parameter q can assume values $(0, 1, 2, 3, \ldots)$, denoting the degree of system nonlinearity: linear $(q = 0, 1)$, quadratic $(q = 2)$, cubic $(q = 3)$, and so forth. Weakly and strongly nonlinear systems can be distinguished based on the relative magnitude of the nonlinear force term, expressed as $\sum \gamma_q \delta^q$. Essentially nonlinear systems are characterized by vanishing linear forces $(k_{m,r} \to 0)$ but non-zero nonlinear forces ($\gamma > 0$ for all q except $q = 0$ and $q = 1$).

Cubic nonlinearities can manifest as either purely hardening ($\gamma > 0$) or softening ($\gamma < 0$), while quadratic nonlinearities combine both softening and hardening behaviors. The versatility of this elementary discrete model extends to representing more intricate media configurations. These adaptations empower discrete modeling techniques to provide insights into the complexities of nonlinear phenomena.

Considering wave propagation in a system and applying boundary conditions with an input $u_b = e^{i\omega t}$, the transmittance of the system can be quantified as $\tau_r = \left|\frac{u_m^N}{u_m^1}\right|$, where u_m^{N} represents the displacement of u_m at the end of the chain sequence, while u_m^1 denotes the displacement of the mass at the first position in the sequence or the base excitation or the displacement at the initial position u_b.

The Laplace transform of nonlinear terms, specifically $\gamma_{q_r}(u_m - u_r)^q$, is not straightforward. While one could approach this by linearizing around a specific operating point, a more practical solution is often to address it numerically. Essentially, due to the complexities introduced by nonlinearity, numerical methods frequently provide the most feasible approach for analysis.

3.2.2 Dispersion Curve

To elucidate the influence of the resonator's mass and spring within these configurations, the dispersion curve is determined for linear mechanical resonators. A streamlined model, where mechanical damping and the effects of the piezoelectric transducer are neglected (refer to Fig. 17), is employed. In this model, both the stiffness of the monoatomic chain and the resonator are treated as linear. Assuming a harmonic wave solution and incorporating Bloch's theorem, the harmonic displacements of the masses can be expressed as:

$$u_m = u_{m_0} e^{i(G_n a - \omega t)} \tag{9}$$

$$u_r = u_{r_0} e^{i(G_n a - \omega t)}, \tag{10}$$

where u_{m_0} and u_{r_0} are the initial displacements or amplitudes for unit cell or main chain and resonator. Substituting into linear form of Eq. (7) and Eq. (8) results in:

$$\begin{aligned} &m_m m_r \omega^4 - \left(2k_m m_r \left(1 - \cos\left(G_n a\right)\right) + k_r m_m + k_r m_r\right) \omega^2 \\ &\quad - 2k_m k_r \left(\cos\left(G_n a\right) - 1\right) = 0 \end{aligned} \tag{11}$$

For wider scope and easy analysis, the normalized dimensionless parameters μ, ν, and ω_L, along with the natural frequency ω_0, are defined as follows:

$$\omega_L = \frac{1}{2}\sqrt{\frac{m_m}{k_m}\frac{k_r}{m_r}},\ \mu = \sqrt{\frac{m_r}{m_m}},\ \nu = \sqrt{\frac{k_r}{k_m}},\ \omega_0 = \sqrt{\frac{4k_m}{m_m}} \tag{12}$$

The parameters μ and ν represent the mass and stiffness ratios of the resonator relative to the main structure. Solving the Eq. (11) produces four roots for ω, which leads to Eq. (13) and (14) for the individual derivatives with respect to mass and stiffness ratios, μ and ν.

$$\begin{aligned} \omega_{\pm}(k) = \omega_0 \Bigg(\frac{1}{2} \Bigg\{ &\frac{1}{2}[1 - \cos(G_n)] + \omega_L^2(1 + \mu^2) \pm \\ &\sqrt{4\left(\mu\omega_L^2\right)^2 + \left[\frac{1}{2}[1 - \cos(G_n)] + \omega_L^2(\mu^2 - 1)\right]^2} \Bigg\} \Bigg)^{1/2} \end{aligned} \tag{13}$$

$$\begin{aligned} \omega_{\pm}(k) = \omega_0 \Bigg(\frac{1}{16} \Bigg\{ &\sin\left(\frac{G_n}{2}\right)^2 + \frac{1}{4}\nu^2 + \omega_L^2 \pm \\ &\sqrt{\left(\frac{1}{4}\nu^2 + \omega_L^2\right)^2 + \left(\frac{\nu^2}{4} - 4\omega_L^2\right)\sin\left(\frac{G_n}{2}\right)^2 + \frac{1}{4}\cos(G_n)^2 - \frac{1}{4}} \Bigg\} \Bigg)^{1/2} \end{aligned} \tag{14}$$

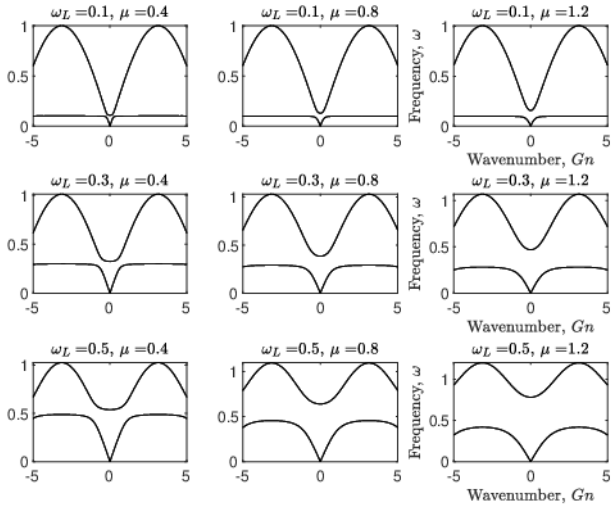

Figure 3: Dispersion in the periodic structure with varying resonance coupling, and mass ratio. The plots demonstrate the profound influence of resonance conditions on the emergence and width of band gaps, highlighting the potential for tuned wave propagation control by adjusting the μ parameter.

The dispersion relation in Eq. (13) emphasizes the effects of μ, profoundly affecting the value of ω at each wave vector G_n. On the other hand, the dispersion relation Eq. (14) focuses more on the stiffness ratio ν, playing a critical role as well in determining the behavior of the system.

From Fig. 3 and Fig. 4, it becomes evident that the properties of the periodic structure are intricately linked with the resonance conditions. One striking observation is that the emergence of a band gap isn't directly associated with a specific wave vector G_n. Instead, it's bound to certain conditions or parameters, possibly hinting at the importance of resonator properties in dictating wave propagation characteristics. This indicates a more complex interplay between the system parameters than just the wave vector, emphasizing the significance of resonator configurations in the system's acoustic properties.

Another pivotal observation is how the width of the band gap is influenced by ν. As the stiffness ratio becomes more pronounced, the width of the band gap enlarges. This suggests that by manipulating the stiffness of the resonator, one could have a direct influence on the system's acoustic insulation or filtering capabilities. The stronger the coupling, the more formidable the band gap, acting as a more robust barrier to certain frequency components.

Fig. 4 suggests that controlling the system by adjusting ν is a valuable approach. Online tuning with the mass ratio μ can be challenging and impractical, whereas tuning with ν is straightforward, even in real-time scenarios. This holds significant importance for real-time control applications. Changing the mass ratio typically requires halting the operation to physically modify the system—a process that is both time-consuming and may inadvertently alter other critical parameters like the bandgap width. On the other hand, stiffness can be dynamically altered by implementing mechanisms such as actuators that adjust the position of an attached mass on the resonator, facilitating on-the-fly tuning of the bandgap frequency edges

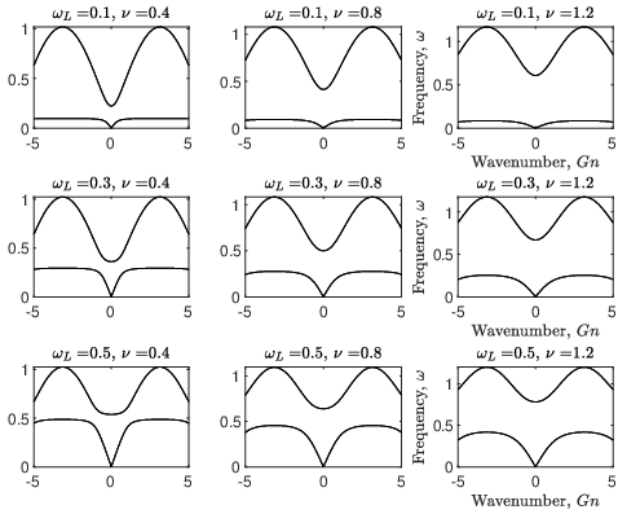

Figure 4: Dispersion in the periodic structure with varying resonance coupling, and stiffness ratio. The plots demonstrate the profound influence of resonance conditions on the emergence and width of band gaps, highlighting the potential for tuned wave propagation control by adjusting the ν parameter.

without needing to stop the system. This method provides a streamlined and practical solution for tuning the system's acoustic properties in real-time, enhancing its adaptability and effectiveness in various applications.

3.2.3 Numerical Studies

The dynamic behaviors of the proposed mechanical resonator models are characterized through simulations informed by parameters detailed in Table 1. The models incorporate sets of ordinary differential equations that capture the mechanical dynamics of the resonators. Solutions are numerically derived using the fourth-order Runge-Kutta method, ensuring accuracy and stability.

Table 1: Defined parameters for the lumped models

Parameter	Value
Mass of main chain (m_m)	0.056 kg
Mass of resonator (m_r)	0.0336 kg
Spring constant of main chain (k_m)	150 N/m
Spring constant of resonator (k_r)	129.6 N/m
Damping coefficient of main chain (c_m)	0.0464 Ns/m
Damping coefficient of resonator (c_r)	0.0334 Ns/m
Nonlinear stiffnesses quadratic coefficient (γ_2)	-500 N/m^2
Nonlinear stiffnesses cubic coefficient (γ_3)	15000 N/m^3

The focus on nonlinear resonators, characterized by quadratic and cubic stiffness terms, indicates a significant influence on the bandgap's extent. The quadratic nonlinearity is expressed as:

$$f_r = k_r u + \gamma_{r_2} u|u|, \tag{15}$$

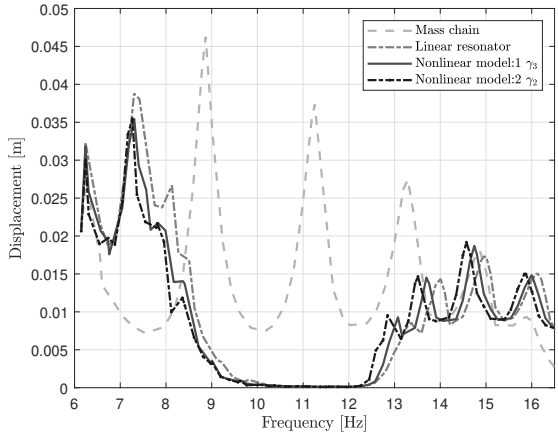

Figure 5: Comparative Analysis of Band Gap Behaviors in a 1-D Chain System: Insights from Mass Chain without Resonators, Conventional Metastructure, Linear, and Nonlinear Resonator Configurations

This simplified expression is utilized to simulate nonlinear effects and compare them against linearities. Bistable nonlinearities were excluded from the analysis to focus on single-state behavior and avoid the complexity of the system.

Simulations reveal the frequency range of natural vibrations extends from 6 to 17 Hz, with the integration of resonators delineating band gaps within this spectrum. These band gaps stem from the local resonance of the mechanical resonators and are depicted in Fig. 5. Fig. 6 (Right) shows the nonlinear spring force–displacement relation for cubic nonlinearities, and the influence of such a nonlinearity in the system. Distinctly, the nonlinearity is characterized by the coefficient γ_3, where its sign determines the hardening or softening nature of the system. Transmittance response in Fig. 6 (Left) demonstrates that the behavior of cubic nonlinear resonators, whether hardening or softening, is determined by the sign of the cubic stiffness coefficient, γ_{r_3}. In practical applications, these characteristics can be harnessed to design systems with desired dynamic responses, such as vibration isolators or mechanical filters, where the specific nonlinearity can be chosen to control the behavior of the system under varying load conditions. The cubic nonlinearity is modeled as:

$$f_r = k_r u + \gamma_{r_3} u^3, \tag{16}$$

By varying γ_{r_3} within a range of ± 15000 N/m^3 clearly exhibits the system's transition between hardening and softening behaviors. The analytical focus remains on the primary effects of cubic nonlinearity without delving into the complexities of bistability or tristability. By simplifying the approach, the need for comprehensive frequency sweeps typically necessary for analyzing nonlinear systems is effectively circumvented, streamlining the study of the system's dynamic response. Factors like excitation frequency and material properties influence the efficacy and persistence of this suppression.

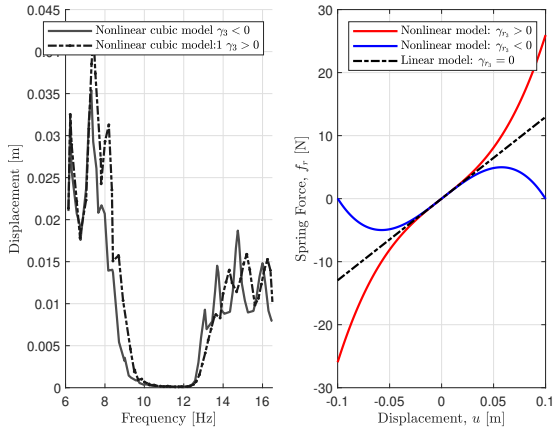

Figure 6: Impact of Cubic Nonlinearity on the 1-D Chain System: (a) Transmittance response influenced by cubic nonlinearity, and (b) Nonlinear spring force–displacement relationship for cubic nonlinearities.

3.3 Distributed Parameter Modeling

Distributed Parameter Modeling (DPM) stands in contrast to Lumped Parameter Modeling (LPM) by offering a more granular perspective on physical systems. Where LPM simplifies systems into discrete, point-like elements that aggregate mass, energy, or stiffness, DPM employs partial differential equations to reflect the continuous spatial distribution of these properties. This approach helps accurately capture the nuanced spatial variations inherent in complex metastructures, such as the vibration patterns of fluid flows, the temperature distribution in a body, acoustic behavior of the materials, or the vibration of a membrane or beam. By embracing the spatial heterogeneity of the system's properties, DPM enables a more precise simulation of real-world phenomena, enhancing our ability to design and analyze advanced metastructures that leverage spatial variation for innovative functionalities.

3.3.1 Modal Analysis and Bandgap Formation in Mechanical Metastructures

The research primarily employs modal analysis in the design and optimization of mechanical locally resonant metastructures. This analysis is crucial for identifying key vibration characteristics, such as natural frequencies, mode shapes, and modal damping ratios, under specific conditions. These insights enable the engineering of metastructures with tailored mechanical wave propagation behaviors.

The study employs a distributed parameter model approach, utilizing PDEs to capture the system dynamics more precisely than lumped parameter models. This methodology is particularly applicable to systems where spatial variations are non-negligible, affecting phenomena such as wave propagation, heat transfer, and fluid dynamics. Analytical models are derived using modal analysis through the frequency determinant method, providing a solid theoretical foundation for understanding the intricate behavior of internally coupled resonators within metastructures. This type of methodology has already been presented by Sugino et al.

[47] and serves as both background and input for our further investigation in this research, enabling its application to other functionalities and applications.

The standard distributed model of the metastructure under investigation, subject to base excitation and external forces, is illustrated in Fig. 7. Employing Newtonian mechanics and drawing from classical vibration textbooks, the behavior of the metastructure is captured by the following partial differential equation, as detailed in Eq. (17).

$$\mathcal{L}w(x,t)+\mathcal{C}\frac{\partial w(x,t)}{\partial t}+\mathcal{M}\frac{\partial^2 w(x,t)}{\partial t^2}-\sum_{r=1}^{N_r}\left(k_r z_r(t)+c_r\frac{\partial z_r(t)}{\partial t}\right)\delta\left(x-x_r\right)=\mathcal{F}_{b_m}(x,t) \tag{17}$$

which includes structural flexibility $\mathcal{L}$, damping $\mathcal{C}$, and inertia $\mathcal{M}$. The interaction with the resonators is represented by the summation term, encompassing the stiffness k_r, damping c_r, and location x_r of each resonator. The dynamic of the system is a linear homogeneous differential operator, exhibiting orders of $2p$ and $2q$, respectively, with $q \leq p$. The spatial coordinate x extends over domain D. The function $w(x,t)$ captures the system's relative transverse vibration compared to the base motion, essentially reflecting the displacement at specific points relative to the base's harmonic movement. On the other hand, $z_r(t)$ denotes the resonator's relative vibration in absolute coordinates, providing insight into its displacement to the overall structure's vibration. The $\delta(x-x_r)$ is the Kronecker delta function to pinpoint the resonators' locations on the beam, with x_r specifying the position of the r-th resonator. Moreover, $\mathcal{F}$ symbolizes the external force, distributed across D, and incorporates the impact of the base excitation on the beam.

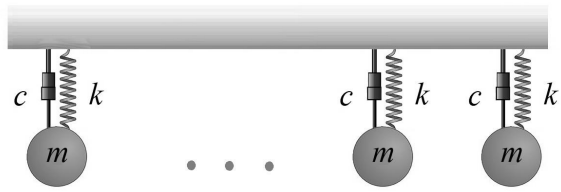

Figure 7: Example of standard locally resonant metastructures, where m represents the mass of the resonators, c is the damping, and k is the stiffness of the resonators.

Similarly, the governing equation for the resonators, derived from Newton's second law of motion, is expressed as follows:

$$m_r\frac{\partial^2 z_r(t)}{\partial t^2}+c_r\frac{\partial z_r(t)}{\partial t}+k_r z_r(t)+m_r\frac{\partial^2 w\left(x_r,t\right)}{\partial t^2}=\mathcal{F}_{b_r}(t) \tag{18}$$

The boundary conditions for the system, as outlined in Eq. (17), are defined by Eq. (19), where each $\mathcal{B}_i$ is a linear homogeneous differential operator of order no greater than $2p-1$.

$$\mathcal{B}_i[w(x,t)]=0, \quad i=1,2,\ldots,p \tag{19}$$

Proportional damping, a method often used in real-world structures for estimating natural frequencies and mode shapes, relates the damping matrix to the mass and stiffness matrices. This concept allows $\mathcal{C}$ to be expressed as a combination of mass and stiffness operators $\mathcal{L}$ and $\mathcal{M}$, as shown in Eq. (20), with c_1 and c_2 being non-negative constants, determined based on the physical properties

of the system. However, engineers usually use experimental modal analysis or fit data from vibration tests to find them. This approach, as referenced in [89], maintains consistent mode shapes and similar natural frequencies for both damped and undamped systems.

$$\mathcal{C} = c_1\mathcal{L} + c_2\mathcal{M} \tag{20}$$

The eigenfunctions $\phi_m(x)$ of the system are derived by solving the eigenvalue problem of the undamped version of Eq. (17), presented in Eq. (21).

$$\mathcal{L}\left[\phi_m(x)\right] = \lambda_m \mathcal{M}\left[\phi_m(x)\right], \quad m = 1, 2, \ldots, N_m \tag{21}$$

The symbol λ_m represents an eigenvalue associated with the mth eigenfunction $\phi_m(x)$ of the system. For structures like beams equipped with resonators, the system is defined by coupled differential equations for each resonator and the structure itself. These equations account for the mutual influence of each component on the system's dynamics. The mode shapes of the base structure alone are not the exact mode shapes of the entire metastructure, but using them simplifies the analysis significantly.

In the case of an Euler beam spanning domain $D = [0, L]$, assumed to be linearly elastic and homogeneous, the operators $\mathcal{L}$, $\mathcal{M}$, $\mathcal{C}$, $\mathcal{B}_1$, and $\mathcal{B}_2$ are defined in terms of the beam's physical properties: flexural rigidity (EI), density (ρ), and cross-sectional area (A).

$$\begin{aligned} &\mathcal{L} = EI\frac{\partial^4}{\partial x^4}, \quad \mathcal{M} = \rho A, \quad \mathcal{C} = c, \\ &\mathcal{B}_1 = 1, \quad \mathcal{B}_2 = EI\frac{\partial^2}{\partial x^2} \end{aligned} \tag{22}$$

In advancing the understanding of modal expansion in the system, the orthogonality of eigenfunctions is critical for solving Eq. (17). The self-adjoint (Hermitian) nature of the eigenvalue problem ensures this orthogonality. For any two eigenfunctions $\phi_m(x)$ and $\phi_n(x)$, the problem is self-adjoint if they satisfy the conditions given in Eq. (23), as highlighted by [90, 91].

$$\begin{aligned} \int_D \phi_m(x)\mathcal{L}\left[\phi_n(x)\right] dx &= \int_D \phi_n(x)\mathcal{L}\left[\phi_m(x)\right] dx \\ \int_D \phi_m(x)\mathcal{M}\left[\phi_n(x)\right] dx &= \int_D \phi_n(x)\mathcal{M}\left[\phi_m(x)\right] dx. \end{aligned} \tag{23}$$

When considering unique eigenvalues ω_m^2 and ω_n^2 with their respective eigenfunctions $\phi_m(x)$ and $\phi_n(x)$, these functions are normalized with respect to $\mathcal{M}$. This normalization leads to the generalized orthogonality condition outlined in Equations (24) and (25), with δ_{mn} being the Kronecker delta function.

$$\int_D \phi_m(x)\mathcal{M}\left[\phi_n(x)\right] dx = \delta_{mn} \tag{24}$$

and

$$\int_D \phi_m(x)\mathcal{L}\left[\phi_n(x)\right] dx = \delta_{mn}\omega_m^2 \tag{25}$$

Assuming proportional damping, the structural damping characteristics are captured by Eq. (26). Here, ζ_m denotes the damping ratio of the m-th mode, which is

precisely defined in Eq. (27) utilizing the constants c_1 and c_2. Equations (24)–(26) are integral to constructing a set of orthonormal eigenfunctions, which together form a complete basis for the solution space pertinent to the eigenvalue problem.

$$\int_D \phi_m(x)\mathcal{C}\left[w_m(x)\right] dx = c_1\delta_{mn}\omega_m^2 + c_2\delta_{mn} = 2\delta_{mn}\zeta_m\omega_m \tag{26}$$

with

$$\zeta_m = \frac{1}{2\omega_m}\left(c_1\omega_m^2 + c_2\right) \tag{27}$$

Modal decomposition is a method used to describe the structure's vibration across a domain D by representing it as a sum of modal shapes in one direction. This method assumes that the behavior of the structure can be accurately captured using a finite set of modes. For instance, the Euler–Bernoulli beam theory, commonly used in these analyses, may not provide sufficient accuracy in high-frequency situations. This technique, widely used in modal analysis, produces convergent solutions to the boundary value problem as formulated.

Using modal decomposition, the beam's deflection in the domain D is expressed as a sum of modal shapes in one direction. This assumes that the behavior of the beam can be accurately represented by a finite number of modes, as expressed in Eq. (28):

$$w(x,t) = \sum_{m=1}^{N_m} \phi_m(x) z_m(t), \tag{28}$$

Here, $\phi_m(x)$ denotes the spatial mode shape, and $z_m(t)$ is the time-dependent modal coordinate for the m-th mode. These modal representations are crucial in modeling the dynamics of a flexible beam with integrated discrete resonators.

Incorporating the modal expansion from Eq. (28) into the system's governing differential equation, given by Eq. (17), yields Eq. (29). This resultant equation effectively combines the modal decomposition with the system's differential operators, capturing the influence of the resonators. It provides a complete representation of the beam's dynamic response, encompassing both the modal characteristics and the interactive effects of the resonators.

$$\mathcal{L}\sum_{m=1}^{N_m}\phi_m(x)z_m(t)+\mathcal{C}\frac{\partial}{\partial t}\sum_{m=1}^{N_m}\phi_m(x)z_m(t)+\mathcal{M}\frac{\partial^2}{\partial t^2}\sum_{m=1}^{N_m}\phi_m(x)z_m(t)- \sum_{r=1}^{N_r}\left(k_r z_r(t)+c_r\frac{dz_r(t)}{dt}\right)\delta\left(x-x_r\right)=\mathcal{F}_{b_m}(x,t) \tag{29}$$

Multiplying Eq. (29) by $\phi_n(x)$ and integrating over the domain D, and applying the orthogonality conditions Equations (24)–(27) of the mode shapes, gives
-0cm

$$\ddot{z}_m(t)+2\zeta_m\omega_m\dot{z}_m(t)+\omega_m^2 z_m(t)-\sum_{r=1}^{N_r}m_r\omega_r^2 z_r(t)\phi_m\left(x_r\right)=\mathcal{Q}_{b_m}(x,t),\quad m=1,2,\ldots,N_m \tag{30}$$

Similarly for resonators, substituting the modal expansion Equations (28) into (18) yields

$$\ddot{z}_r(t)+2\zeta_r\omega_r\dot{z}_r(t)+\omega_r^2 z_r(t)+\sum_{m=1}^{N_m}\ddot{z}_m(t)\phi_m(x_r)=\mathcal{Q}_{b_r}(t),\quad r=1,2,\ldots,N_r \tag{31}$$

Here, N_m and N_r denote the number of modes and resonators, respectively. Each mode has a specific modal frequency ω_m, and each resonator has a mass m_r and its own natural frequency ω_r. The damping ratios ζ_m for the modes and ζ_r for the resonators quantify energy dissipation.

To simplify, the superscript "dot" indicates time derivatives, and "prime" indicates spatial derivatives. Each equation in the model represents the dynamics of modal coordinates or resonator displacement as a second-order ordinary differential equation. The dynamics are influenced by modal and resonator parameters (natural frequencies ω_m and ω_r, damping ratios ζ_m and ζ_r), their interactions, and base excitation forces ($\mathcal{Q}_{b_m}$ and $\mathcal{Q}_{b_r}$).

Decoupling of these equations is achieved through an orthogonal transformation, involving pre- and post-multiplication by the mode shape matrix. This leads to diagonalization of the mass and stiffness matrices, thanks to the orthogonality of eigenvectors to both matrices. The result is a set of decoupled ordinary differential equations. This normal mode method applies in the absence of damping or with proportional damping, where the damping matrix is a linear combination of the mass and stiffness matrices. The transformation becomes orthonormal when the mode shape is normalized to the mass matrix.

Combining the structural dynamics represented in Eq. (30) with the dynamics of resonators from Eq. (31) enables the coupling of inertial terms and decoupling of stiffness in the system, facilitating analysis in the frequency domain. This process is expressed in Eq. (32), where $\mathcal{H}_{b_m}(x,t)$ is determined by integrating the effects of external forces, base motion, and damping into a net external force, as shown in Eq. (33). Equations (31) and (32) together form a set of coupled second-order linear ordinary differential equations, which, upon solving, yield the mode shapes and resonant frequencies of the entire system and its steady-state response to harmonic excitation.

$$\ddot{z}_m(t) + 2\zeta_m\omega_m\dot{z}_m(t) + \omega_m^2 z_m(t) + \sum_{r=1}^{N_r} m_r\phi_m(x_r)\sum_{p=1}^{N_m}\ddot{z}_m(t)\phi_p(x_r) + \sum_{r=1}^{N_r} m_r\ddot{z}_r(t)\phi_m(x_r) + 2\sum_{r=1}^{N_r} m_r\phi_m(x_r)\zeta_r\omega_r\dot{z}_r(t) = \mathcal{H}_{b_m}(x,t), \quad m = 1,2,\ldots,N_m \tag{32}$$

$$\mathcal{H}_{b_m}(x,t) = \int_0^L \mathcal{F}_e(x,t)\phi_m(x)dx - \ddot{w}_b(t)\left(\int_0^L \mathcal{M}\phi_m(x)dx + \sum_{r=1}^{N_r} m_r\phi_m(x_r)\right) - \dot{w}_b(t)\int_0^L \mathcal{C}\phi_m(x)dx \tag{33}$$

The Laplace transform is applied to the system of equations, assuming zero initial conditions, to transition the analysis to the frequency domain, as seen in Equations (34) and (35). In these equations, $Z_m(s)$ and $Z_r(s)$ represent the Laplace transforms of the modal and resonator displacements, respectively. This transformation simplifies the algebraic manipulation and analysis of the system's dynamics.

$$Z_r(s) = \frac{\mathcal{Q}_{b_r}(s) - \sum_{m=1}^{N_m} s^2 Z_m(s)\phi_m(x_r)}{s^2 + 2\zeta_r\omega_r s + \omega_r^2}, \quad r = 1,2,\ldots,N_r \tag{34}$$

$$s^2 Z_m(s) + 2\zeta_m\omega_m s Z_m(s) + \omega_m^2 Z_m(s) + \sum_{r=1}^{N_r} m_r\phi_m(x_r)\sum_{p=1}^{N_m} s^2 Z_p(s)\phi_p(x_r) + \sum_{r=1}^{N_r} m_r s^2 Z_r(s)\phi_m(x_r) + 2\sum_{r=1}^{N_r} m_r\phi_m(x_r)\zeta_r\omega_r s Z_r(s) = H_{b_m}(s), \quad m = 1,2,\ldots,N_m \tag{35}$$

For a deeper analytical understanding, applying Eq. (34) to the Laplace transform of Eq. (30) yields the following expression in Eq. (36).

$$(s^2 + 2\zeta_m\omega_m s + \omega_m^2)Z_m(s) - \sum_{r=1}^{N_r} m_r\omega_r^2\left(\frac{\mathcal{Q}_{b_r}(s) - \sum_{p=1}^{N_m} s^2 Z_p(s)\phi_p(x_r)}{s^2 + 2\zeta_r\omega_r s + \omega_r^2}\right)\phi_m(x_r) = \mathcal{Q}_{b_m}(s), \quad m = 1,2,\ldots,N_m \tag{36}$$

The analysis focuses on the transfer function $\frac{Z_m}{\mathcal{Q}_{b_m}}$, particularly when the effect of $\mathcal{Q}_{b_r}$ is ignored. Here, the mass ratio μ, a dimensionless quantity, relates the mass of each resonator to a differential mass element of the system and is defined as $\mu = \frac{m_r}{m(x_r)dx_r}$, where $m(x_r)$ represents the mass per unit length at x_r and dx_r is an infinitesimal segment length at this point. To simplify the system of equations, it is assumed that an infinite number of resonators are distributed throughout the entire domain of x, and the regions represented by x_r become infinitesimally small.

$$\lim_{N_r\to\infty}\sum_{r=1}^{N_r} m\left(x_r\right)\phi_m\left(x_r\right)\phi_p\left(x_r\right)dx_r \approx \int_0^L m(x)\phi_m(x)\phi_p(x)dx = \delta_{mp}, \quad m,p = 1,2,\ldots \tag{37}$$

Applying these assumptions results in the following expression:

$$\frac{Z_m(s)}{Q_{b_m}(s)} = \frac{1}{s^2\left(1+\frac{\mu(2\zeta_r\omega_r s+\omega_r^2)}{s^2+2\zeta_r\omega_r s+\omega_r^2}\right)+2\zeta_m\omega_m s+\omega_m^2} \qquad m = 1,2,\ldots,N_m \tag{38}$$

Equation (38) indicates that resonators add a frequency-dependent mass to the system. With the assumption of an infinite resonator distribution, leading to continuous spatial displacements, similar reductions apply to the resonator displacements. By substituting Equations (38) into (34) and transitioning from the discrete x_r to a continuous spatial domain x, a simplified equation emerges as presented in Eq. (39).

$$Z_r(x,s) = -\frac{s^2}{s^2+2\zeta_r\omega_r s+\omega_r^2}\sum_{m=1}^{N_m}\frac{Q_{b_m}(s)\phi_m\left(x\right)}{s^2\left(1+\frac{\mu(\omega_r^2+2\zeta_r\omega_r s)}{s^2+2\zeta_r\omega_r s+\omega_r^2}\right)+2\zeta_m\omega_m s+\omega_m^2} \tag{39}$$

Equation (39) defines the motion $Z_r(x,s)$ of resonators along the beam in the Laplace domain, influenced by modal forces $Q_{b_m}(s)$. The displacement of the resonators is presented as a weighted sum of the beam's modal shapes:

$$Z_r(x,s) = \sum_{m=1}^{N_m}\Psi_m(s)\phi_m(x) \tag{40}$$

Equation (41) expresses the relationship between the modal force $Q_{b_m}(s)$ and the modal coordinate $\Psi_m(s)$ in the Laplace domain. It illustrates how resonator displacements are influenced by the modes of the structure:

$$\frac{\Psi_m(s)}{Q_{b_m}(s)} = \frac{-s^2}{\left[s^2+2\zeta_r\omega_r s+\omega_r^2\right]\left[s^2\left(1+\frac{\mu(\omega_r^2+2\zeta_r\omega_r s)}{s^2+2\zeta_r\omega_r s+\omega_r^2}\right)+2\zeta_m\omega_m s+\omega_m^2\right]}, \quad m = 1,2,\ldots,N_m \tag{41}$$

The transfer function in Eq. (41) clarifies how the input forces are transformed into modal responses. The function's poles, indicative of the system's natural frequencies, are the points at which the system exhibits peak responses.

3.4 Dispersion Analysis by Plane Wave Expansion Method

The Plane Wave Expansion (PWE) method is extensively utilized to analyze wave propagation in periodic structures. This technique provides critical insights into wave behaviors, which are crucial for designing and optimizing periodic structures in applications like vibration suppression and energy harvesting [92, 93].

Consider the transverse displacement of a conventional metastructure defined as follows: For the beam: $W_t(x,t) = \hat{W}_t e^{i(G_n x-\omega t)}$, and for resonators: $z_r(t) = \hat{z}_r e^{i(\omega t)}$

The dynamic behavior of the conventional metastructure and its resonators is described by the following differential equations:

$$EIG_n^4\hat{W}_t - \rho A\omega^2\hat{W}_t + k_r\hat{W}_t - k_r\hat{z}_r = 0, \tag{42}$$

$$-k_r\hat{W}_t + k_r\hat{z}_r - m_r\omega^2\hat{z}_r = 0. \tag{43}$$

Here, $\hat{W}_t$ and $\hat{z}_r$ denote the amplitudes of the transverse displacements for the beam and resonator, respectively; G_n is the wave number; ω is the frequency of interest; E is the modulus of elasticity; I is the second moment of area of the beam's cross-section; A is the cross-sectional area; ρ is the material density; k_r is the stiffness of the resonators; and m_r is the mass of each resonator.

The dispersion relation is derived by applying periodic boundary conditions and seeking non-trivial solutions. The characteristic equation relating frequency ω and wavevector G_n simplifies to:

$$(Am_r\rho)\omega^4 + (-EIm_rG_n^4 - k_rm_r - Ak_r\rho)\omega^2 + EIG_n^4k_r = 0 \tag{44}$$

The fourth-order dispersion equation in ω derived from the PWE method yields four solutions. However, considering that negative frequencies are non-physical in this context, we only focus on the positive solutions. Among these, two solutions on the positive frequency axis delineate the dispersion relationship, mapping frequency to wave number G_n. Notably, there are specific wave numbers for which the equation does not yield real frequency solutions; these ranges are identified as bandgaps. These bandgaps represent frequency intervals where wave propagation is inhibited due to the periodic structure of the metastructure. Hence, the dispersion curve computed for a given target frequency, such as $f_t = 31.2$ Hz, provides critical insights into the wave propagation characteristics of the metastructure, highlighting frequencies that correspond to propagating waves and those that fall within the bandgap regions, as shown in Fig. 8. The designated target frequency, (here, the resonator's frequency) delineates the frequency edge of the bandgap, marking the frequency range where local resonances substantially alter wave propagation. This initiation point heralds the emergence of a bandgap within the out-of-plane phase.

3.5 Numerical Studies

The numerical study presented here is derived from the analytical equations (Eq. 38) developed in the preceding sections, showcasing the dynamic behavior of a metamaterial beam through its transmittance plot. The parameters used in the simulation are detailed in Table 2. The excitation is applied at the base of the beam using a shaker, and the response is measured at the tip.

Table 2: Geometric and material properties of the studied rectangular aluminum beam

Parameter	Value	Parameter	Value
L_m	0.91 m	ζ_r	0.02
w_m	40 mm	ρ_m	2710 kg/m^3
h_m	3 mm	N_m	8
E_m	69.5 GPa	N_r	8
ζ_m	0.02	μ	1.04

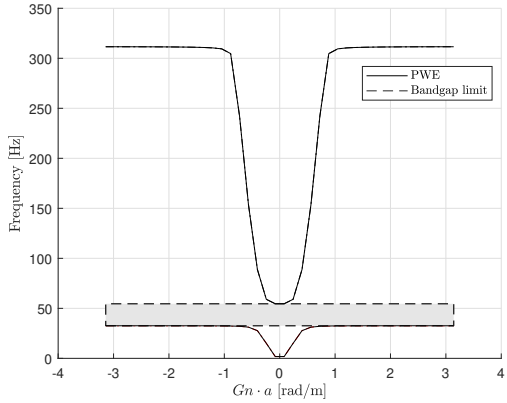

Figure 8: Dispersion curves computed using the plane wave expansion method for target frequency f_t=31.2 Hz

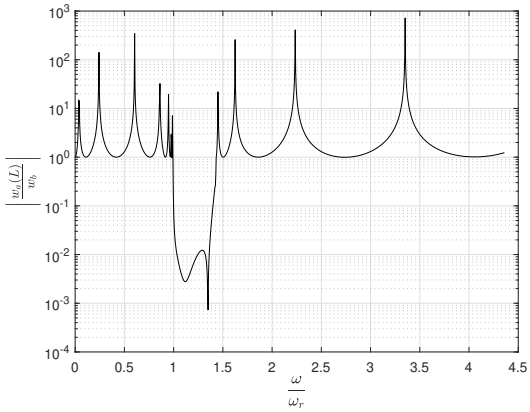

Figure 9: Transmittance plot for a metamaterial beam.

In Fig. 9, the depicted transmittance plot for the metamaterial beam reveals the bandgap regions. These regions are characterized by a dramatic decrease in transmittance, indicating effective vibration isolation. The beginning of the bandgap starts at the resonator's natural frequency, ω_r. Given the mass ratio $\mu = 1.04$, the width of the bandgap extends from the resonator frequency ω_r to a frequency less than $\omega_r\sqrt{1+\mu}$. Within this frequency span, the structural design effectively suppresses wave propagation, resulting in the bandgap observed. The depth and breadth of the bandgap are dependent on factors such as resonator damping and the physical properties of the metamaterial, which influence the degree of vibration attenuation. This behavior is essential for applications that require vibration isolation or wave filtering at specific frequencies.

The formation of a bandgap is closely linked to the resonators' natural frequency, ω_r. The resonant frequency acts as a critical threshold, marking the lower boundary of the bandgap. Serving as a modal response model, $G(s)$, as derived from Eq. 38 articulates the dynamic behavior of a beam within a negative feedback system where the proportional feedback gain is symbolized by ω_r^2. This transfer function systematically relates the input forces to the consequent displacements across the structure's modal frequencies, delineating the system's vibrational characteristics in relation to its inherent resonant behavior.

Given the mass ratio $\mu = 1.04$, the bandgap phenomenon in the system can be analyzed through the root locus method, which delineates the trajectories of the system's poles in response to variations in the feedback gain ω_r^2, with further details explained in Chapter 5. The zeros of the system, occurring at $s = \pm i\omega_t$, are fixed points in the s-plane, while the poles, initially at $s = \pm i\omega_t\sqrt{1+\mu}$, shift along the imaginary axis as ω_r^2 varies. Due to the symmetrical nature of the poles and zeros on the imaginary axis and the fundamental property that poles must migrate towards zeros or infinity, the frequency range defined by $\omega_t < \omega < \omega_t\sqrt{1+\mu}$ emerges as a forbidden zone for pole existence, thereby creating a bandgap.

3.6 Finite Element Study

The established methodology enables manipulation of the transfer function, thereby permitting exploration into how adjustments in the mass placement on a resonator affect bandgap traits, a key factor for refining bandgap properties within a closed-loop control system.

This section explores the impact of spatial variations on bandgap characteristics by adjusting resonator stiffness while maintaining constant mass, a method beneficial for heavy machinery applications where traditional piezoelectric solutions may fall short. Stiffness tuning, as opposed to piezoelectric adjustments, offers a more durable and practical solution for these demanding environments. The current study examines a conventional metastructure that does not incorporate internally coupled resonators. The resonators are of the cantilever type, with a mass that can be positioned along the length from the tip to the base. The specific parameters defining the metastructure and resonators are as follows: eight resonators ($N_r = 8$), with the beam dimensions being 300 mm in length, 25 mm in width, and 3 mm in height. The material density is 2710 kg/m^3, and the modulus of elasticity is 69.5 GPa. The damping ratio of the structure and resonators is the same at 0.01. An attached mass (m_a) of 3.8 grams is placed at distances that vary from 20 to 57.3 millimeters along the resonator. The natural frequency of the resonator (ω_r), when the attached mass is at the tip, is 32 Hz. This setup allows for an exploration of

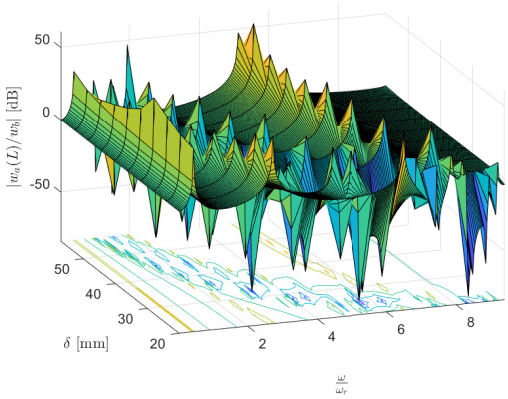

Figure 10: A 3D representation of the bandgap frequency shift as a function of the mass positioning along a resonator. Here, delta (δ) is indicative of the mass location on the resonator, increasing from the tip (lower δ) to the base (higher δ) of the cantilever beam. This spatial variation results in a downward shift of the bandgap edge frequency, moving from higher frequencies (approaching $8\omega_r$) to lower frequencies (close to ω_r), as the mass is repositioned towards the base, [18].

the resonator stiffness's impact on the bandgap properties of the metastructure.

Fig. 10 provides a 3D visualization of how the position of the attached mass along the length of a resonator affects the bandgap frequencies in a metastructure. The natural frequency at which the bandgap starts is denoted as ω_r, corresponding to the case when the mass is located at the tip of the resonator. The graph demonstrates that as the mass moves closer to the base of the resonator—decreasing δ—the resonator's stiffness increases, leading to a rise in ω_r and a subsequent shift of the bandgap towards higher frequencies.

The contour plot in the x-y plane clearly depicts the bandgap's initiation at the initial natural frequency ω_r when the mass is at the resonator's tip. From there, the bandgap expands and moves as the location of the mass changes. This shift is particularly crucial for applications requiring tunable vibration isolation, as it shows the potential to adjust the bandgap frequency by simply repositioning the resonator mass without altering the resonator or structure itself.

The binary representation in Fig. 11 illustrates the influence of the mass location along the resonator on the bandgap frequencies. With the bandgap depth limit set at a decibel ratio of output to input displacement of 0.2, the plot shows that when the attached mass is positioned at the tip of the resonator, the bandgap originates at the resonator frequency ω_r. The white areas in the binary representation correlate to the regions of significant transmittance reduction, effectively mapping the bandgap's presence and evolution as the mass moves closer to the resonator's base.

3.7 Experimental Study

The experimental investigations centered on a specifically designed cantilever beam setup, detailed in Table 3 and illustrated in Fig. 12. The beam, fabricated from aluminum, measured 3 mm in thickness, 40 mm in width, and 0.91 m in length. A nut and bolt assembly, weighing 19 grams, was affixed to the beam's tip to

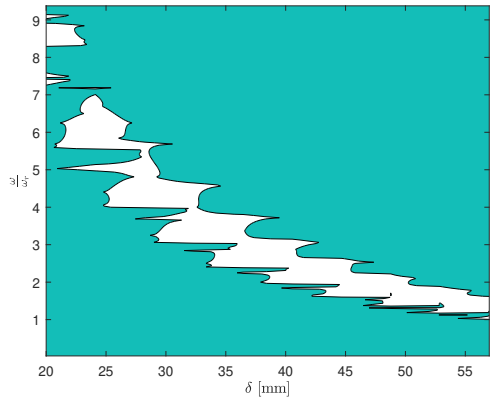

Figure 11: Binary mapping of the bandgap presence as a function of mass placement along the resonator, with δ indicating the distance from the cantilever beam's fixed end, versus normalized frequency (ω/ω_r), illustrating how the bandgap shifts with frequency and mass position. White areas denote regions where the transmittance falls below the threshold of 0.2 decibels, signifying the vibration isolation at these frequencies.

adjust the natural frequency to 64 Hz, thereby tuning the resonant characteristics essential for the study.

Vibration excitation was provided by a 100 N TIRA 51110 Shaker. Vibrational responses were precisely recorded using two Dytran Accelerometer 3055D21 units, each with a sensitivity of 100 mV/g, connected using wires designed for low electrical resistance and high signal integrity. One accelerometer was mounted at the beam's tip to measure acceleration, while another was positioned at the base to monitor and control input vibrations. The signal to the shaker was amplified using a Power Amplifier BAA 120, and a Vibration Controller VR9500 regulated the shaker's input and monitored the beam's response. Notably, the inclusion of accelerometer wiring introduced an additional mass approximately 1% of the accelerometer's mass, a factor considered in the experimental analysis to ensure the accuracy of the dynamic response measurements.

Table 3: Experimental parameters

Symbol	**Parameter**	**Value**
L	Length of the beam	91 cm
b	Width of the beam	4 cm
h	Thickness of the beam	3 mm
E	Young's modulus of the beam	70 GPa
ρ	Density of the beam	2710 kg/m^3
ω_r	Resonator's natural frequency	64 Hz
N_r	Number of Resonators	8

The experimental results displayed in Fig. 13 demonstrate the transmittance spectrum, which corresponds to the resonant frequencies of the standard metastructure with $\mu = 1.2$. The regions of low transmittance, which signify the bandgaps, commence at a frequency of $\omega_r = 64$ Hz, in line with analytical predictions. Additionally, the observed width of the bandgap is consistent with the anticipated value of $(1+\mu) = 2.2$. This data shows the existence of a bandgap between frequencies ω

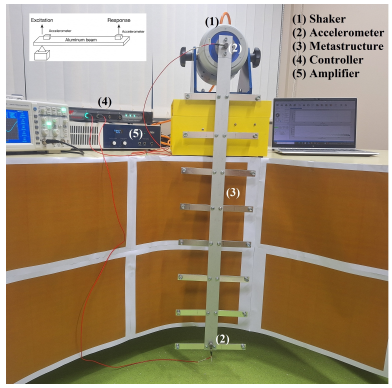

Figure 12: Experimental setup of a metastructure prototype equipped with 8 resonators, each tuned to a resonator's natural frequency using adjustable mass at the tip. Measurement accuracy is ensured with two Dytran Accelerometers, linked by low-resistance wires. Geometric and material properties of the beam and resonators used in the setup are provided in Table 3. A schematic in the top right illustrates the direction of excitation and response measurement.

and $\omega_r\sqrt{1+\mu}$, corresponding to the calculated bandgap limit of $\sqrt{1+\mu} = 1.484$. This observation confirms the presence of the primary bandgap, illustrating the dynamic behavior of the system across the spectrum.

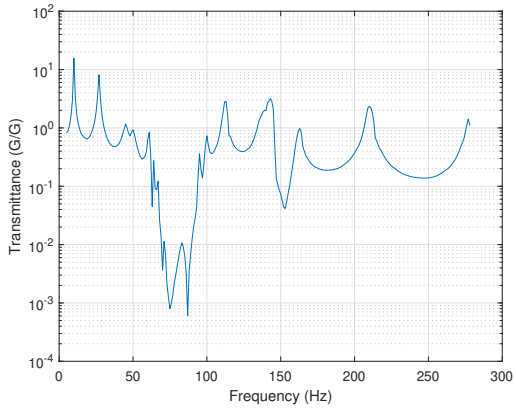

Figure 13: Experimental transmittance data versus excitation frequency for the metastructure, with $\mu = 1.2$. The plot highlights the bandgap region between 64 to 95 Hz, which corresponds to the analytical bandgap boundary $\omega_r\sqrt{1+\mu}$.

3.8 Summary

This chapter delved into the modal analysis of flexible metastructures equipped with mechanical resonators, employing both lumped and distributed parameter models to elucidate their dynamic behavior. The primary goal was to understand how these metastructures can be optimized to achieve desirable wave propagation characteristics, particularly the formation and manipulation of bandgaps. Through

a combination of analytical derivations, numerical studies, and experimental validations, this chapter provided a comprehensive examination of the influence of structural parameters on the metastructure's ability to control vibrational energy.

The lumped parameter modeling approach offered a simplified yet powerful tool for analyzing metastructures. By abstracting the system into discrete components, this model provided clarity on the fundamental dynamic interactions within the metastructure. Numerical simulations based on these models revealed how nonlinearity, specifically cubic nonlinearity, could be leveraged to modulate bandgap properties, paving the way for designing metastructures with custom-tailored dynamic responses.

Conversely, distributed parameter modeling presented a more detailed perspective by accounting for the spatial continuity of the system's properties. This approach was essential for capturing the nuances of wave propagation in metastructures, enabling the prediction of bandgap behavior with high fidelity. Analytical methods such as modal expansion and frequency determinant analysis, alongside numerical simulations, were key in assessing the impact of mechanical resonators on the bandgap characteristics.

Experimental studies served as the ultimate testbed, validating the analytical and numerical findings. The experiments confirmed the presence of bandgaps and their dependence on various parameters like the mass ratio and resonator positioning. By manipulating these parameters, the experiments demonstrated the feasibility of tuning the bandgap edges, offering practical insights for real-world applications.

Here are the key points summarizing the contributions and insights gained:

• Introduced a systematic approach for analyzing the wave propagation and dynamic behavior in mechanical metastructures using both lumped and distributed parameter models.

• Demonstrated the application of modal analysis for predicting bandgap behavior in metastructures, thereby facilitating the design of structures with enhanced vibration control capabilities.

• Showed how nonlinearity, especially cubic nonlinearity, affects the transmittance spectrum and bandgap properties, offering a pathway to custom-designed dynamic responses.

• Provided numerical validation of the bandgap phenomena and showcased the effects of spatial variations in resonator properties on the emergent bandgaps.

• Conducted experimental investigations to validate the analytical and numerical models, thus bridging the gap between theory and practical application.

• Established the practical feasibility of tuning bandgap properties by manipulating structural parameters such as resonator mass, stiffness, and placement.

• Revealed the potential of metastructures in a wide array of applications, from isolation of undesired vibrations to efficient energy harvesting solutions.

4 Modeling of Flexible Metastructures with Electromechanical Resonators

This chapter delves into the theoretical modeling of flexible metastructures with electromechanical resonators, exploring their dynamic properties through analytical approaches and numerical simulations. Particularly, piezoelectric materials are utilized within these electromechanical resonators, offering unique advantages in energy harvesting and vibration control due to their electromechanical coupling capabilities.

The chapter is structured into two main sections: lumped parameter modeling and distributed parameter modeling. In the lumped parameter section, models are presented that simplify the physical system into discrete elements whose dynamic behavior can be captured by algebraic equations.

Conversely, in the distributed parameter modeling section, the system is treated more holistically, considering the continuous distribution of mass, energy, and forces along the structure. This method provides a more detailed and accurate representation of the wave propagation phenomena inherent in flexible metastructures. By focusing on these theoretical models, it is aimed to provide a robust foundation for understanding how electromechanical resonators can influence the dynamic characteristics of metastructures, particularly in terms of vibration control and energy harvesting potential.

4.1 Lumped Parameter Modeling

This section explores the application of lumped parameter models to analyze linear and nonlinear behaviors of electromechanical resonators, emphasizing their role in energy harvesting and vibration attenuation. Through detailed mathematical modeling and simulation, the intricacies of how piezoelectric components can be optimized to enhance system performance, both in energy efficiency and dynamic response, are delved into. This approach not only elucidates the fundamental principles governing such systems but also provides insights into more practical investigations of more realistic structures through distributed parameter modeling.

4.1.1 Linear Electromechanical Resonators

Electromechanical systems can incorporate piezoelectric components that introduce additional nonlinearity to the system dynamics. These piezoelectric elements serve a dual purpose: they aid in attenuating vibrations within the unit cell, while simultaneously enhancing energy harvesting in the resonators. With reference to Fig. 17, let's take a scenario where resonators are equipped with piezoelectric elements. This incorporation couples the mechanical motion of the resonators with electrical dynamics, enriching the behavior and capabilities of the system but also complicating its dynamics.

To derive the dynamic equations of the harvester, the Lagrangian formulation for electromechanical systems is employed. The Lagrangian L is defined as:

$$L = T - U + W_e - D \tag{45}$$

Using Lagrange's equation, the governing dynamics are given by:

$$\frac{d}{dt}\frac{\partial L}{\partial \dot{q}_i} - \frac{\partial L}{\partial q_i} + \frac{\partial D}{\partial \dot{q}_i} = Q_i \tag{46}$$

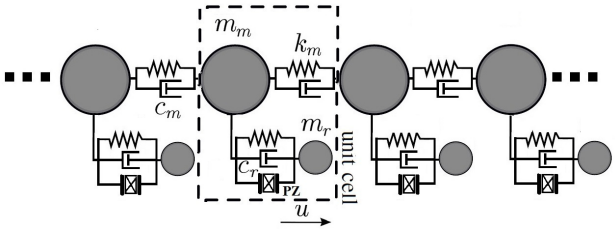

Figure 14: Foundational models of linear phononic media: a linear monoatomic chain with linear resonators of masses, spring, damping, and piezoelectric element, PZ. Dashed rectangle is unit cell.

Here, T represents the kinetic energy of the system, U is the potential energy, W_e denotes the coenergy of the piezoelectric module, and D is the dissipative function capturing both mechanical and electrical energy losses. In this formulation, q_i is the generalized displacement corresponding to a specific degree of freedom in the system. Q_i represents the external force or input acting on the respective degree of freedom. By applying this equation, a set of differential equations governing the behavior of the harvester can be derived, effectively capturing its mechanical and electrical characteristics. The mechanical damping, often referred to as Rayleigh damping, is represented by the term

$$D_m = \frac{1}{2}c_r\left(\dot{u}_r - \dot{u}_m\right)^2 + \frac{1}{2}c_m\left(\dot{u}_{m^-} - \dot{u}_m\right)^2 + \frac{1}{2}c_m\left(\dot{u}_m - \dot{u}_{m^+}\right)^2 \tag{47}$$

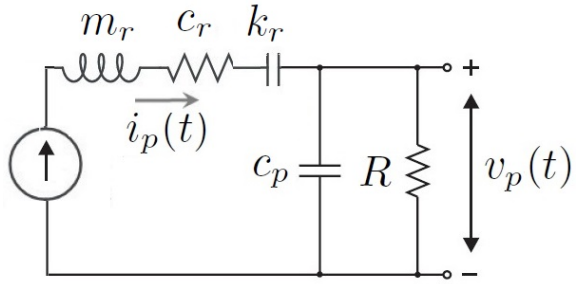

Figure 15: An equivalent circuit for piezoelectric device model with internal electrode capacitance and load resistance

Piezoelectric devices are often represented by a model where a current source is in parallel with their internal electrode capacitance c_p, as depicted in Fig. 15. Additionally, a simple resistance R is connected to the load in this configuration. The electrical damping arises from the piezoelectric coupling, and it represents the energy dissipation due to electrical losses, denoted by D_p :

$$D_p = \frac{1}{2}\frac{v_p^2}{R} \tag{48}$$

Thus, the total dissipation function for the electromechanical system is given by $D = D_m + D_p$. Considering the piezoelectric transducer integrated into the

resonator, the coenergy W_e of the piezoelectric module is given by:

$$W_e = \frac{1}{2}c_p v_p^2 - \theta v_p \left(u_m - u_r\right) - \frac{1}{2}k_p \left(u_m - u_r\right)^2 \tag{49}$$

Where c_p and k_p denote the equivalent free-body capacitance and stiffness of the piezoelectric element, respectively. θ represents the equivalent force-electric factor of the piezoelectric cantilever beam. The first term corresponds to the electrical coenergy in the capacitance c_p. The second term represents the piezoelectric coenergy. The third term signifies the elastic strain coenergy in a spring with stiffness k_p. Eqs. (46)-(49) detail the electrical behavior of the piezoelectric resonators within the system. It's essential to note that θ and k_p must be experimentally determined to ensure the proposed model aligns with the real setup. In the total mechanical stiffness, $k_r + k_p$, the stiffness contribution from the piezoelectric material, k_p, is significantly smaller in magnitude compared to the resonator's mechanical stiffness, k_r. Therefore, its contribution to mechanical stiffness is often disregarded in the analysis. The energy equations are characterized by linear representations. Given these linear forms of the energy equations, the associated governing equations of motion in metastructure are as follows:

$$\begin{aligned} &m_m \ddot{u}_m(t) + k_m \left(2u_m(t) - u_{m^-}(t) - u_{m^+}(t)\right) \\ &\quad + c_m \left(2\dot{u}_m(t) - \dot{u}_{m^-}(t) + \dot{m}_{m^+}(t)\right) + k_r \left(u_m(t) - u_r(t)\right) \\ &\quad + c_r \left(\dot{u}_m(t) - \dot{u}_r(t)\right) + \theta v(t) = 0 \end{aligned} \tag{50}$$

$$m_r \ddot{u}_r(t) - c_r \left(\dot{u}_m(t) - \dot{u}_r(t)\right) - k_r \left(u_m(t) - u_r(t)\right) - \theta v(t) = 0 \tag{51}$$

$$c_p \dot{v_p}(t) + \frac{v_p(t)}{R} - \theta(\dot{u}_m(t) - \dot{u}_r(t)) = 0 \tag{52}$$

Equations (50) to (52) are included with multiple parameters, adding to their complexity. For enhanced clarity and broader applicability, the model's governing equations are recast using the established normalized parameters as follows:

$$\begin{aligned} &\ddot{u}_m(t) + 4\zeta_m \omega_m \dot{u}_m(t) - 2\zeta_m \omega_m \left(\dot{u}_{m^-}(t) + \dot{u}_{m^+}(t)\right) + 2\omega_m^2 u_m(t) \\ &\quad - \omega_m^2 (u_{m^-}(t) + u_{m^+}(t)) + 2\mu\zeta_r \omega_r \left(\dot{u}_m(t) - \dot{u}_r(t)\right) + \nu^2 \omega_m^2 \left(u_m(t) - u_r(t)\right) \\ &\quad + k_e^2 \nu^2 \omega_m^2 \bar{v}(t) = 0, \end{aligned} \tag{53}$$

where for the last mass $u_m(t) - u_{m^+}(t) = 0, \quad \dot{u}_m(t) - \dot{u}_{m^+}(t) = 0$, and for the first mass $u_{m^-}(t) = u_b(t)$. The equation for the resonator becomes:

$$\ddot{u}_r(t) - 2\zeta_r \omega_r \left(\dot{u}_m(t) - \dot{u}_r(t)\right) - \omega_r^2 \left(u_m(t) - u_r(t)\right) - k_e^2 \omega_r^2 \bar{v}(t) = 0 \tag{54}$$

Lastly, the equation representing the piezoelectric effect is given as:

$$\dot{\bar{v}}(t) + \frac{\omega \dot{\bar{v}}(t)}{r_g} - \left(\dot{u}_m(t) - \dot{u}_r(t)\right) = 0 \tag{55}$$

where $k_e^2 = \theta^2 / \left(c_p k_r\right)$ indicates the electromechanical coupling coefficient, $\bar{v} = c_p v_p / \theta$ is the scaled piezoelectric output voltage, and $r_g = R c_p \omega_r$ designates the proportion of the actual load R to its optimal value R_{opt} . Additionally, $\zeta_m = c_m / \left(2 m_m \omega_m\right)$ and $\zeta_r = c_r / \left(2 m_r \omega_r\right)$ are the damping ratios of the main chain and the resonator, respectively. Furthermore, $v^2 = k_r / k_m$ represents the stiffness proportion between the resonator and the chain mass, while $\mu = m_r / m_m$ depicts the mass ratio between the resonator and the chain mass.

4.1.2 Analysis of Power Output of Standard Piezoelectric Circuit for Energy Harvesting

The primary objective of this research is to investigate the inherent properties of various types of nonlinearity in piezoelectric materials, rather than comparing different circuit models. For a consistent evaluation, every type of nonlinearity is paired with the same standard circuit, ensuring each nonlinearity is studied in isolation and without the influence of varying circuit efficiencies. A standard rectifier interface circuit with no electrical losses for energy harvesting is explored using a lumped parameter model. In design analysis for energy harvesting, a simplified circuit is frequently employed, as shown Fig. 16. In this configuration, the regulation circuit and battery are substituted with an equivalent resistor labeled as R, and the rectified voltage across it is denoted as v_e. It is assumed, for the purposes of this study, that the rectifying bridge is in an ideal and faultless state. A rectifying bridge circuit is integrated, targeting a stable output DC voltage v_e, which connects the load directly. It is assumed that the filter capacitor c_e is sufficiently large to render v_e essentially constant. In steady-state operation, the average rectified voltage and displacement are related. Governed by equations, the piezo voltage $v_p(t)$ is proportional to the displacement $u(t)$. Both variables are modeled as $u(t) = u_0 \sin(wt-\theta)$ and $v_p(t) = v_{p_0}(wt-\theta)$, where u_0 is the constant displacement magnitude, and $v_{p_0}(t)$ is a periodic function with $|v_{p_0}(t)| \leq v_e$.

During a semi-period $\frac{T}{2}$, defined as $T = \frac{2\pi}{w}$, the integral of the rate of change of $v_p(t)$ is $2v_e$. This yields

$$\int_{t_1}^{t_2} I(t)dt = \frac{T}{2}\frac{v_e}{R}, \tag{56}$$

delineating the relationship between the current and average rectified voltage [94]. The integral $\int_{t_1}^{t_2} \dot{v}_p(t)dt$ represents the total change in the piezoelectric voltage $v_p(t)$ from time t_1 to t_2. If $v_p(t)$ oscillates between $-v_e$ and v_e during this semi-period $\frac{T}{2}$, then the total change in $v_p(t)$ is $v_e - (-v_e) = 2v_e$. If $u(t)$ is oscillating from its minimum $-u_0$ to its maximum u_0 during the semi-period from time t_1 to t_2, then the change in $u(t)$ during this period is $u_0 - (-u_0) = 2u_0$. Assuming the standard

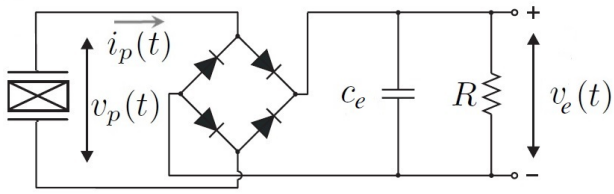

Figure 16: Classical energy harvesting circuit for the standard electronic interfaces.

linear form and rewriting Eq. (52) yields to:

$$c_p\dot{v}_p(t) + i_p(t) = \theta\dot{z}(t), \tag{57}$$

where $z(t)$ is the relative displacement of the mass chain with respect to the resonator in each unit cell. Integration of Eq. (57) from time t_1 to t_2 gives:

$$2c_pv_e + \frac{T}{2}\frac{v_e}{R} = 2\theta z_0 \tag{58}$$

This equation correlates the changes in stored electric charge, current, and mechanical displacement between times a and b. Given $\frac{T}{2} = \frac{\pi}{\omega}$, the equation for v_e expressed as:

$$v_e = \frac{R\theta\omega}{Rc_p\omega + \frac{\pi}{2}} z_0 \tag{59}$$

Furthermore, the average harvested power P can be well-defined as:

$$P = \frac{v_e^2}{R} = \frac{R\theta^2\omega^2}{\left(Rc_p\omega + \frac{\pi}{2}\right)^2} z_0^2 \tag{60}$$

Although it is possible to derive using only the absolute displacement of resonators z_r, the decision was made to use the relative displacement, z_0, instead. This method is preferred in this research because it simplifies the investigation of various piezoelectric configurations.

4.1.3 Nonlinear Electromechanical Resonators

The behavior of a linear piezoelectric element is described by Eq. (52). While linearized models offer simplicity and are often adequate for many applications, they may miss critical behaviors and limit our understanding and predictive capabilities. The study of nonlinearity provides a comprehensive and accurate view of systems, essential for both practical applications and scientific inquiry. When introducing any of these nonlinearities into the model, it is essential to ensure that they are grounded in physical reality or experimental observations relevant to the system. Modeling choices should be justified based on the underlying physics, empirical data, or both.

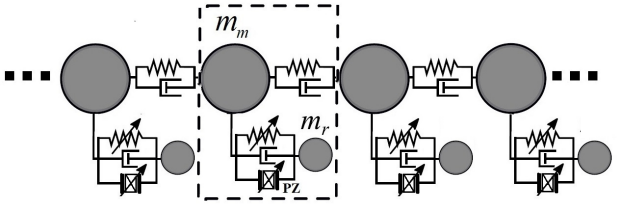

Figure 17: Foundational models of nonlinear phononic media: a linear monoatomic chain with nonlinear resonators of masses, spring, damping, and piezoelectric element, PZ. Dashed rectangle is unit cell.

Let's consider a metastructure system incorporating nonlinear piezoelectric elements, as depicted in Fig. 17. One common approach to introduce nonlinearity is by using a polynomial expansion. When considering the piezoelectric response, one possibility is a nonlinear dependency of the voltage, denoted as $v(t)$, on strain. Adding a simple quadratic nonlinearity to the piezoelectric equation, yields to:

$$c_p\dot{v}(t) + \frac{v(t)}{R} - \theta\left(\dot{u}_m(t) - \dot{u}_r(t)\right) - \beta\left(\dot{u}_m(t) - \dot{u}_r(t)\right)^2 = 0 \tag{61}$$

Where β is a coefficient of the nonlinear term. In this model, the piezoelectric response starts to deviate from linearity as the strain (differential displacement) increases. The term β dictates the strength of this nonlinearity. If β is zero, the system returns to the original linear behavior. In electronic circuits, transistors,

especially MOSFETs, can exhibit polynomial behavior with respect to gate-source voltage and drain current, leading to nonlinear amplification. Moreover, the dynamics of robotic arms can have nonlinear components due to joint friction, and these can be represented as polynomial functions of velocities.

Upon introducing nonlinearity, the system can be numerically simulated using techniques tailored for nonlinear differential equations, such as the Runge-Kutta method. Software packages, like MATLAB's Simulink or COMSOL, can also be employed. Initial conditions and boundary conditions need to be established based on the specific study.

Apart from polynomial expansion, there are several other types to introduce and study nonlinearity in a piezoelectric energy harvester.

4.1.4 Theoretical Models for the Nonlinear Energy Harvesting

The nonlinear behavior in energy harvesting can be succinctly captured in a generalized equation which encompasses multiple facets of nonlinearity. Consider the following expression [9]:

$$\alpha \frac{v(t)}{R(\omega)} + c_p \frac{d}{dt}[f(v(t))] - \theta \left[g\left(\frac{d^2}{dt^2} u_m(t) - \frac{d^2}{dt^2} u_r(t), v(t) \right) \right] - h\left(\int v(t) dt \right) = 0 \tag{62}$$

Here: $R(\omega)$ introduces nonlinearity as a function of frequency. Adjustable parameter, α can be varied to explore different system behaviors and regimes. $f(v(t))$ introduces nonlinearity as a function of the voltage across the impedance.

The term $g\left(\frac{d^2}{dt^2} u_m(t) - \frac{d^2}{dt^2} u_r(t), v(t) \right)$ represents a nonlinear function of the acceleration and voltage. $h\left(\int v(t) dt \right)$ is the nonlinearity introduced by an integral of voltage over time. It is important to note that this is a completely abstract and generalized equation that must be determined based on the system specifications and the physics involved.

The Eq. (62) exemplifies a multi-faceted nonlinear system that integrates various nonlinear dependencies into a comprehensive framework. $R(\omega)$ denotes a frequency-dependent nonlinearity, reflective of materials like semiconductors or piezoelectric elements under resonance. $f(v(t))$ embodies a voltage-dependent nonlinearity, typical in devices like diodes or transistors, where shifting voltage can alter operational regimes.

The term $g\left(\frac{d^2}{dt^2} u_m(t) - \frac{d^2}{dt^2} u_r(t), v(t) \right)$ encapsulates a coupled nonlinearity, hinting at a complex relationship between the accelerations of two system components and voltage. Lastly, $h\left(\int v(t) dt \right)$ introduces a memory effect, capturing historical influences on the system, akin to hysteresis or capacitive responses. To derive the standard linear form of a piezoelectric equation, the resistance is considered as not frequency-dependent, and the capacitance is assumed not to be influenced by voltage variations, simplifying the term $c_p \frac{d}{dt}[f(v(t))]$ to $c_p \dot{v}(t)$ by setting $f(v(t)) = v(t)$. The electromechanical coupling is taken to be linear, meaning the term with $g(\cdot)$ reduces to $\theta\left(\dot{u}_2(t) - \dot{u}_1(t)\right)$, indicating the coupling coefficient isn't influenced by displacement, velocity, or acceleration. Lastly, the term $h\left(\int v(t) dt \right)$ is disregarded, signifying that the integral of voltage over time does not significantly influence the system dynamics. Under these assumptions and simplifications, the generalized Eq. (62) reduces to Eq. (52), which is the standard linear form of a rectifier circuit.

4.2 Numerical Studies

This section presents a comprehensive numerical analysis of lumped linear and nonlinear electromechanical resonators. The analysis harnesses the parameters delineated in Table 4, addressing the electrical and electromechanical characteristics that influence the behavior of the resonators. The mechanical characteristics detailed in Table 1 have been enhanced with terms representing electromechanical parameters. Through simulation studies, the dynamic responses of the resonators are thoroughly investigated, revealing the impact of key parameters on the energy harvesting capabilities and vibration attenuation potential of the metamaterials in question. Various high-efficiency advanced rectifiers have been developed to maximize harvested energy, as reported in the literature [39, 95]. However, a standard rectifier is used in all cases of this investigation, as the goal is to examine various piezoelectric designs rather than different rectifiers. The objective here is to broaden the frequency of the bandgap and enhance harvested energy.

Table 4: Defined parameters for the lumped models

Parameter	Value
Mass of main chain (m_m)	0.056 kg
Mass of resonator (m_r)	0.0336 kg
Spring constant of main chain (k_m)	150 N/m
Spring constant of resonator (k_r)	129.6 N/m
Damping coefficient of main chain (c_m)	0.0464 Ns/m
Damping coefficient of resonator (c_r)	0.0334 Ns/m
Piezoelectric capacitance (c_p)	1.5 mF(C/m)
Electromechanical coupling coefficient (θ)	0.25 N/V
Nonlinear stiffnesses quadratic coefficient (γ_2)	-500 N/m^2
Nonlinear stiffnesses cubic coefficient (γ_3)	15000 N/m^3
Shunt capacitance (c_s)	-7.9 mF(C/m)
Internal resistance (R)	500 Ω

4.2.1 Investigation on Energy Harvesting Performance in Linear Electromechanical Metamaterial

In Fig.18, the transmittance for various values of k_e, representing the piezoelectric coupling coefficient (Eq. 55), is depicted. For the analysis, the stiffness of the piezoelectric element, represented by k_p, is considered negligible compared to the significantly greater stiffness of the resonator, denoted by k_r. This simplification enables a focus on the effects of other parameters without the interference of k_p.

A noticeable broadening of the band gap is observed as the electromechanical coupling coefficient k_e is increased, indicating an enhanced capacity of the system to suppress vibrations. The peaks of the transmittance adjacent to this band gap are notably sensitive to variations in k_e, while those further from the band gap show minimal alternations. This observation emphasizes the crucial role played by k_e in modulating the system's response when using piezoelectric materials, highlighting its significant contribution to vibration control in complex systems. Additionally, the parameter r_g, defined as $r_g = \omega_r c_p R$, can be adjusted to achieve minimal transmittance at each frequency.

The influence of the electromechanical coupling coefficient on energy harvest-

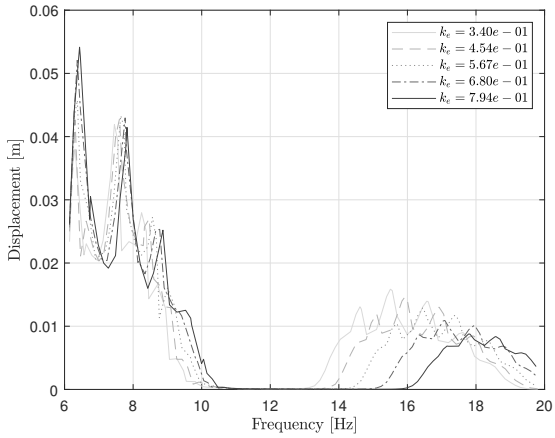

Figure 18: Band gap illustration for a monochain featuring linear local resonators with $n = 8$ mass chains, demonstrating the influence of k_e on band gap and metastructure response. The results are based on the electromechanical model described by Eq. 55, which corresponds to the schematic shown in Figure 14.

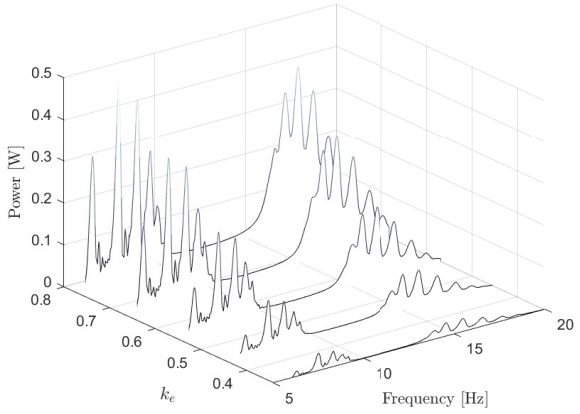

Figure 19: Electromechanical Coupling's Impact on Energy Harvesting: Illustration of the power harvested across varying k_e in an $n = 8$ unit cell monochain, showcasing the pivotal role of the electromechanical coupling coefficient in optimizing energy conversion and system dynamics.

ing, as it pertains to the relative displacement between the main structure and the resonator, is demonstrated in Fig. 19,. This parameter, essentially governs how efficiently piezoelectric materials convert mechanical energy to electrical energy and vice versa, exerting a significant influence on the outcomes of energy harvesting. In scenarios characterized by weak coupling, an increase in k_e results in a notable increase in power output. Conversely, in situations involving strong coupling, an increase in k_e leads to a power level that remains constant, preventing any additional improvements. For our subsequent analysis, a weak coupling value of $k_e = 0.567\,(c_p = 1.5\text{mF})$ is selected to avoid the complex power response patterns observed in strong coupling situations. To comprehensively assess overall energy harvesting performance, we uniformly adjust the resistors R, connected to the piezoelectric transducers, and consolidate power outputs from these resistors. High-capacitance (millifarad-level) piezoelectric materials have a wide range of applications, from energy-harvesting floor tiles in busy areas to vibration damping in machinery, structural monitoring, energy recapture in vehicle suspensions, self-charging personal electronics, and power sources for wearable health monitors. To enhance the capacitance of these materials, strategies include selecting materials with higher dielectric constants, optimizing element geometry, using multi-layer structures, and parallel capacitor configurations, aiming to boost energy harvesting capabilities and efficiency in diverse applications.

4.2.2 Model NL:1 - Polynomial Nonlinearity in Resonators

Polynomial nonlinearity finds practical applications in electronic circuits with diodes and in thermostats or temperature controllers. In diodes, the voltage-dependent behavior transitions from an open switch to a closed switch as voltage crosses a threshold, using piecewise linear approximations. In temperature controllers, piecewise linear models are employed to control heaters based on temperature thresholds, resulting in distinct on-off behavior points in the response curve. Introducing polynomial nonlinearity in resonators by adding a term with coefficient β fundamentally alters the voltage-strain relationship within the piezoelectric equation, encapsulating the nonlinear disposition of the piezoelectric material under substantial strains. The primary system equations for m_m and m_r persistently portray the dynamics of the masses along with their reciprocal interactions, which remain unaffected by the inherent nonlinearity of the piezoelectric element. This incorporation of a nonlinearity parameter, β, facilitates a discernable softening behavior when it is positive and a hardening behavior when negative, each having distinct implications on resonance frequency and amplitude of vibration. Optimization of the nonlinear polynomial parameters can be a viable strategy for maximizing energy harvesting within the outlined system. This can be achieved by defining a cost function, an integration of power across a desired frequency span, thereby quantifying the performance. Utilizing computational tools, such as MATLAB, enables optimization of this function concerning the nonlinear coefficient. By examining the system's eigenvalues to extract information about the bandgap, a thorough combination of analytical and numerical methods is used to enhance the system's performance to achieve optimal results.

Fig. 20 shows the relationship between the nonlinearity coefficient β and the harvested power in a monochain system. The $n = 8$ mass chain model is instrumental in depicting this correlation, serving as a concise yet representative framework to showcase the trends. Although a larger number of chains could enhance the meta-

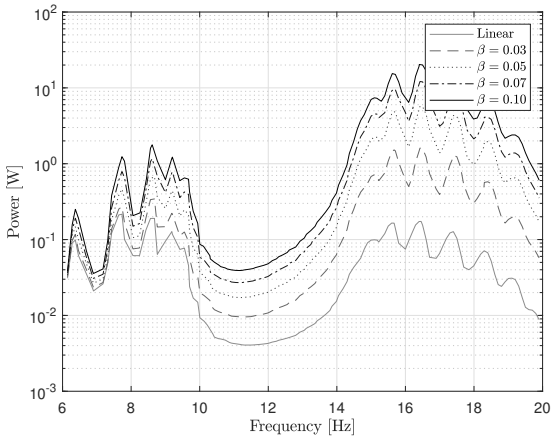

Figure 20: Harvested power from a monochain with polynomial nonlinear local resonators in an eight-mass chain configuration. The graph highlights the impact of varying the nonlinearity coefficient β on the piezoelectric response and the resultant band gap behavior.

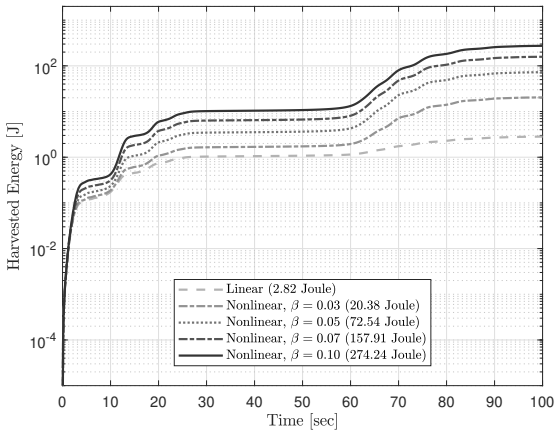

Figure 21: Temporal Evolution of Harvested Energy: A depiction of energy harvested from piezoelectric elements over time in a monochain with polynomial nonlinear local resonators, utilizing $n = 8$ mass chains. This visualization underscores the profound influence of polynomial nonlinearity on the system's energy-harvesting trajectory, revealing a substantial enhancement in energy accumulation even in the absence of notable bandgap alterations.

material characteristic, the chosen size suffices to capture the essential dynamics for this analysis, aligning with the findings from Eq. (60).

The interaction among β, vibration dynamics, and energy conversion can provide insights for enhancing energy collection in similar systems. Fig. 21 delves into this concept, demonstrating how energy harvested from piezoelectric elements evolves over time. Although the introduction of polynomial nonlinearity doesn't significantly alter the formation of bandgaps, it noticeably impacts power and energy harvesting because of the increased motion in the presence of nonlinearity.

4.2.3 Model NL:2 - Nonlinear Capacitance in Voltage-Dependent Scenarios

Starting with the general nonlinear equation in Eq. (62) and making a few simplifications, such as assuming consistent resistance, introducing voltage-dependent capacitance, transitioning from acceleration nonlinearity to velocity differences, and disregarding memory effects, the following model is derived to describe the nonlinear capacitance in the piezoelectric equation:

$$\frac{v(t)}{R} + c_p(v(t))\frac{dv(t)}{dt} - \theta\left(\frac{du_m(t)}{dt} - \frac{du_r(t)}{dt}\right) = 0 \tag{63}$$

Here, $c_p(v(t))$ represents the voltage-dependent capacitance, mathematically representing scenarios where capacitance shifts with applied voltage.

In practical applications, encountering nonlinear capacitance isn't rare and can be observed in various electronic components and systems like varactors, ferroelectric materials, and memristors. These systems showcase a capacitance that isn't static but modulates with the voltage applied, thereby exhibiting diverse behaviors across assorted operating regimes.

When simulating scenarios where capacitance nonlinearly shifts with voltage, an example relationship might be expressed as:

$$c_p(v(t)) = c_{p_0} + k_v v^2(t), \tag{64}$$

where k_v serves as a proportionality constant, illuminating and predicting how systems respond when capacitance dynamically interacts with applied voltage. In Fig. 22, a specific relationship between capacitance and voltage under the parameters $c_p = 1.5$ mF (base capacitance). The figure, composed of four subplots detailing Transmitance, Power, and Harvested Energy in relation to excitation frequency, and an illustration of the quadratic term coefficient of c_p piezo capacitance, provides a detailed overview of key data points. Notably, there's an evident increase in power when dealing with nonlinear capacitance compared to linear piezo capacitance. This observation is corroborated by the energy acquired during the simulation time, which is 3.67 Joules, in contrast to the 2.82 Joules observed in a linear framework.

Thus, in this scenario, not only is more energy harvested from the resonators, but there is also an expansion in the transmittance bandgap. The dual advantages of vibration suppression in the main chain and enhanced energy harvesting from the resonator open the door to potentially more effective approaches for optimizing energy extraction in comparable systems.

4.2.4 Model NL:3 - Cubic Nonlinearities

Cubic nonlinearities can be found in electromechanical systems, such as sensors and actuators. In micro electromechanical systems (MEMS), such as accelerometers

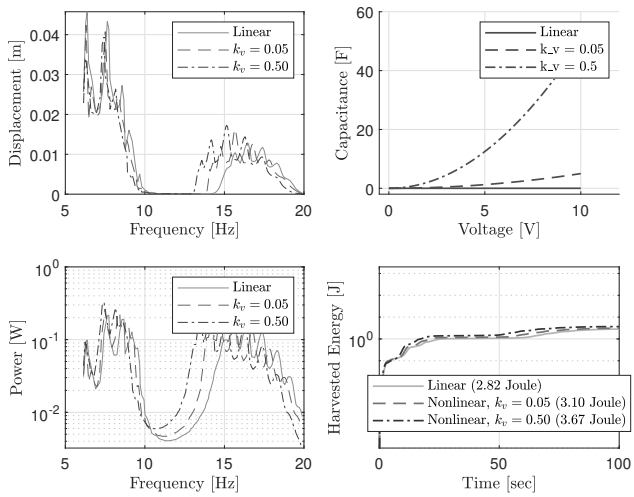

Figure 22: Influence of quadratic nonlinear piezo capacitance, c_p on transmittance and harvested energy

or gyroscopes, cubic nonlinearities can arise due to the miniaturized mechanical components. For nonlinear electromechanical coupling, the piezoelectric equation can be represented as:

$$\frac{v(t)}{R} + c_p \frac{dv(t)}{dt} - \theta \left(\frac{du_m(t)}{dt} - \frac{du_r(t)}{dt} \right)^3 = 0 \tag{65}$$

In Fig. 23, the relation between voltage $v(t)$ and relative displacement z is explored within the context of cubic nonlinearity. The subplot detailing the $v(t) - z(t)$ relationship illustrates that the equation simplifies to:

$$\frac{v(t)}{R} - \theta z(t)^n = 0 \tag{66}$$

To maintain comparable saturation characteristics between a conventional linear resonator and one with a cubic term, resistances of $R = 500\Omega$ and $192\,\mathrm{k}\Omega$ are utilized, respectively.

The case study demonstrates that introducing cubic nonlinear terms, linked to the relative velocities of the primary chain and resonator, significantly affects both harvested energy and transmittance. Specifically, the observed cubic nonlinearity contributes to a decline in harvested energy, posing noteworthy implications for optimization in energy-harvesting contexts, where strategies to circumvent or offset this reduction are crucial. Simultaneously, the incidence of these nonlinear terms provokes a contraction of the transmittance band gap, which could potentially affect the system's efficacy, inviting further exploration and mitigation strategy development.

4.3 Distributed Parameter Modeling

In this study, the dynamics of the metamaterial system are explored using a distributed parameter model. This approach considers spatial variations in param-

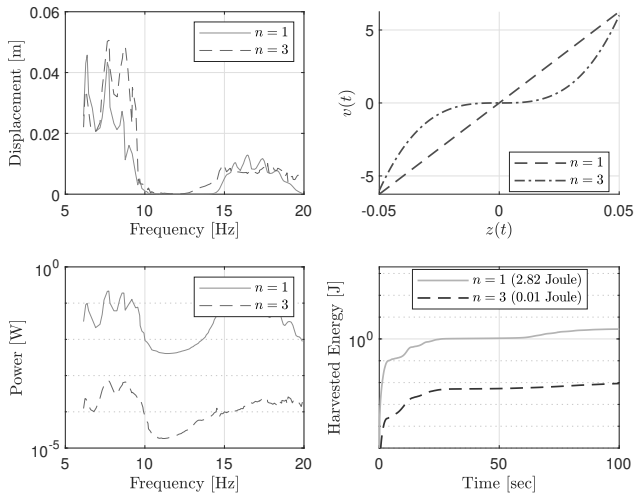

Figure 23: Illustrating the Interplay of $v(t)$ and $z(t)$ in the Presence of Cubic Nonlinearities. The figure demonstrates how cubic nonlinearity affects electromechanical coupling in a piezoelectric system, utilizing specific resistances for standard and cubic terms ($R = 500$ Ω and $R = 192$ kΩ, respectively) to maintain consistent saturation characteristics across scenarios.

eters, which is crucial for detailed analysis of wave propagation across the structure. Modal analysis is employed to determine the natural frequencies and mode shapes of the metastructure, critical for identifying and optimizing bandgaps. The previous section discussed how mechanical resonators facilitate bandgap creation. In this section, the focus shifts to electromechanical elements, specifically piezoelectric components attached to resonators. The aim is to investigate how these configurations influence the bandgap characteristics of the main plain structure. Additionally, this setup explores energy harvesting from significant fluctuations of the resonators. While the main plain structure suppresses vibrations within the bandgap region, the resonators experience maximal fluctuations, presenting opportunities for effective energy harvesting.

4.3.1 Electromechanical Resonators for Energy Harvesting

Proceeding with the methodology discussed in [48], Fig. 24 depicts the configuration of the locally resonant metastructure, which incorporates piezoelectric energy harvesters with admittance load G_r of the shunt circuit on the r-th resonator. Further deepening the analysis in this section, the effects of the resonator's damping are involved, which is essential for future investigations in subsequent chapters. The implementation of a distributed parameter model leads to a series of partial differential equations, accurately representing the system's dynamics. These equations are discretized and solved computationally to determine the modal properties of the metastructure. The system's dynamics are encapsulated by a set of partial differential equations, using principles of Newtonian mechanics as:

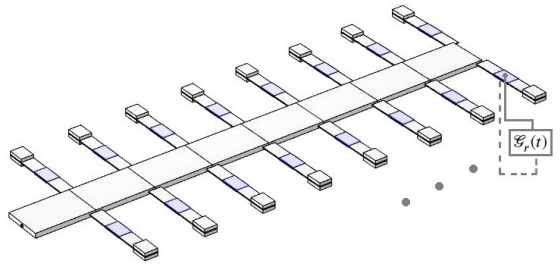

Figure 24: Schematic of the mechanical locally resonant energy harvesting metastructure. The design features cantilever beams with tip masses, serving as mechanical resonators attached to the primary beam structure. Piezoelectric elements are integrated with a resistive load admittance, denoted as G_r.

$$\mathcal{L}w(x,t)+\mathcal{C}\frac{\partial w(x,t)}{\partial t}+\mathcal{M}\frac{\partial^2 w(x,t)}{\partial t^2}-\sum_{r=1}^{N_r}\left(k_r z_r(t)+c_r\frac{\partial z_r(t)}{\partial t}\right)\delta\left(x-x_r\right)=\mathcal{F}_{b_m}(x,t) \tag{67}$$

$$m_r\frac{\partial^2 z_r(t)}{\partial t^2}+c_r\frac{\partial z_r(t)}{\partial t}+k_r z_r(t)+m_r\frac{\partial^2 w\left(x_r,t\right)}{\partial t^2}-\vartheta_{p,r}v_{p,r}(t)=\mathcal{F}_{b_r}(t) \tag{68}$$

$$C_{p,r}\frac{\partial v_{p,r}(t)}{\partial t}+G_r v_{p,r}(t)+\vartheta_{p,r}\frac{\partial z_r(t)}{\partial t}=0 \tag{69}$$

$\mathcal{L},\mathcal{C}$, and $\mathcal{M}$ denote the spatial, damping, and mass distribution characteristics, respectively. $\vartheta_{p,r}, C_{p,r}$, and G_r represent the electromechanical coupling, piezoelectric capacitance, and admittance of the r-th resonator's shunt circuit. $w(x,t)$ and $z_r(t)$ indicate the transverse vibration of the structure and the resonator's vibration, respectively. $\delta(x-x_r)$ is the Kronecker delta, signifying the location of resonators.

The system's boundary conditions are set using linear homogeneous differential operators. The damping matrix is a combination of the mass and stiffness matrices, resulting in the same mode shapes for both damped and undamped systems. These undamped system mode shapes, while not fully accurate, are employed for simplification in the metastructure with resonators. The operators are defined as $\mathcal{L}=EI\frac{\partial^4}{\partial x^4}$ (flexural rigidity), $\mathcal{M}=\rho A$ (mass distribution), $\mathcal{C}=c$ (damping), and the boundary conditions as $\mathcal{B}_1=1,\mathcal{B}_2=EI\frac{\partial^2}{\partial x^2}$. The modal expansion method utilizes orthogonal eigenfunctions to solve Eqs. (67), (68), and (69). This orthogonality stems from the self-adjoint (Hermitian) nature of the eigenvalue problem, as outlined by [96] and demonstrated in the integrals of mass and stiffness over domain D. For eigenvalues ω_m and ω_n with their respective eigenfunctions $\phi_m(x)$ and $\phi_n(x)$, orthogonality is established, as indicated in Eqs. (70) and (71), with the Kronecker delta function, δ_{mn}, confirming their orthogonal relationship.

$$\int_D \phi_m(x)\mathcal{M}\left[\phi_n(x)\right]dx=\delta_{mn} \tag{70}$$

$$\int_D \phi_m(x)\mathcal{L}\left[\phi_n(x)\right] dx = \delta_{mn}\omega_m^2 \tag{71}$$

In the context of proportional damping, the interplay between damping and orthogonal eigenfunctions is expressed in Eqs. (72) to (74). Here, ζ_m denotes the damping ratio of a mode, and constants c_1 and c_2 establish the linear damping relationship.

$$\int_D \phi_m(x)\mathcal{C}\left[w_m(x)\right] dx = c_1\delta_{mn}\omega_m^2 + c_2\delta_{mn} \tag{72}$$

$$\int_D \phi_m(x)\mathcal{C}\left[w_m(x)\right] dx = \delta_{mn}2\zeta_m\omega_m \tag{73}$$

$$\zeta_m = \frac{1}{2\omega_m}\left(c_1\omega_m^2 + c_2\right) \tag{74}$$

Utilizing the modal decomposition method, the Euler beam's deflection within domain $D = [0, L]$ is expressed as a series of modal shapes in a single direction, as shown in Eq. (75). This approach assumes that the beam's dynamics can be adequately represented by a finite number of modes:

$$w(x,t) = \sum_{m=1}^{N_m} \phi_m(x) z_m(t), \tag{75}$$

Here, $\phi_m(x)$ is the spatial mode shape, and $z_m(t)$ is the temporal modal coordinate for the m-th mode. This equation is part of the PDEs describing the motion of a flexible beam system integrated with individual resonators.

Substituting the modal expansion Eq. (75) into Eqs. (67) and (68), and applying orthogonal conditions Eqs. (70) and (71) yields to:

$$\begin{aligned}\ddot{z}_m(t) + 2\zeta_m\omega_m\dot{z}_m(t) + \omega_m^2 z_m(t) - \sum_{r=1}^{N_r} m_r\omega_r\left(\omega_r z_r(t) + 2\zeta_r\dot{z}_r(t)\right)\phi_m(x_r) \\ = \mathcal{Q}_{b_m}(x,t), \quad m = 1, 2, \ldots, N_m\end{aligned} \tag{76}$$

$$\ddot{z}_r(t)+2\zeta_r\omega_r\dot{z}_r(t)+\omega_r^2 z_r(t)+\sum_{m=1}^{N_m}\ddot{z}_m(t)\phi_m(x_r)-\frac{\vartheta_{p,r}}{m_r}v_{p,r}(t) = \mathcal{Q}_{b_r}(t), \quad r = 1, 2, \ldots, N_r \tag{77}$$

$$C_{p,r}\dot{v}_{p,r}(t) + G_r v_{p,r}(t) + \vartheta_{p,r}\dot{z}_r(t) = 0, \quad r = 1, 2, \ldots, N_r \tag{78}$$

where, N_m denotes the total number of structural modes under consideration, while N_r signifies the count of resonators present. The term $z_m(t)$ corresponds to the relative displacement observable in the system's m-th mode. Both ζ_m and ζ_r are the damping ratios for the m-th structural mode and the resonator, respectively, expressed as dimensionless quantities. The function $\phi_m(x_r)$ describes the shape of the m-th mode's deformation, assessed at the specific location x_r. Eqs. (76), (77), and (78) can be determined using standard techniques for linear multi-degree-of-freedom dynamical systems. By rearranging the equations and applying Laplace transforms under the assumption of zero initial conditions, a corresponding set of linear equations can be formulated as:

$$\left(s^2 + 2\zeta_m\omega_m s + \omega_m^2\right) Z_m(s) + \frac{s^2\left(\omega_r^2 + 2\zeta_r\omega_r s\right)\sum_{r=1}^{N_r} m_r\phi_m(x_r)\sum_{p=1}^{N_m}\phi_p(x_r)Z_p(s)}{s^2 + 2\zeta_r\omega_r s + \omega_r^2\left(1 + \frac{\kappa_h s}{s+g(s)}\right)} = \mathcal{Q}_{b_m}(s) \tag{79}$$

where, $Z_m(s)$ denotes the Laplace-transformed displacement of the structure's m th mode, while $\mathcal{Q}_{b_m}(s)$ represents the Laplace-transformed external disturbances. The admittance function $g(s)$ is defined as the ratio of the Laplace transform of G_r, denoted as $G_r(s)$, represented as: $g(s) = \frac{G_r(s)}{C_{p,r}}$, and the term κ_h is dimensionless of resonator electromechanical coupling factor expressed as $\kappa_h = \frac{\vartheta_{p,r}^2}{k_r C_{p,r}}$. The masses of the resonators (m_r) are set proportional to the structure's mass distribution at the resonator attachment points, scaled by a mass ratio (μ), which reflects the total resonator mass in relation to the mass of the underlying structure, as expressed by $m_r = \mu m(x_r)dx_r$. This simplification allows for the resonator masses to be directly linked to the structure's mass distribution, ensuring that the behavior of the resonators is closely coordinated with the dynamics of the structure to which they're attached. When the number of resonators is large, the system can be approximated accordingly as $\sum_{r=1}^{N_r} m(x_r)\phi_m(x_r)\phi_p(x_r)dx_r \approx \int_0^L m(x)\phi_m(x)\phi_p(x)dx = \delta_{mp}$, and the Eq. (79) derived to:

$$\left(s^2 + 2\zeta_m\omega_m s + \omega_m^2\right) Z_m(s) + \frac{s^2\left(\omega_r^2 + 2\zeta_r\omega_r s\right)\mu Z_m(s)}{s^2 + 2\zeta_r\omega_r s + \omega_r^2\left(1 + \frac{\kappa_h s}{s+g(s)}\right)} = \mathcal{Q}_{b_m}(s) \tag{80}$$

The transfer function representing the relationship between the displacement of the m-th mode of the structure and the excitation force on the m-th mode is given by:

$$\frac{Z_m(s)}{Q_{b_m}(s)} = \frac{1}{s^2\left(1 + \frac{\mu(2\zeta_r\omega_r s+\omega_r^2)}{s^2+2\zeta_r\omega_r s+\omega_r^2\left(1+\frac{\kappa_h s}{s+g(s)}\right)}\right) + 2\zeta_m\omega_m s + \omega_m^2} \tag{81}$$

This equation describes how the structural mode's displacement is influenced by the applied excitation force, taking into account various damping, frequency, and system parameters.

When a resonator is short-circuited ($g(s) \to \infty$), the piezoelectric element's impedance is effectively zero, which means that the mechanical and electrical systems are strongly coupled. This results in a significant alteration of the system's resonant frequencies and potentially enhances energy dissipation within the mechanical system. In an open-circuit condition ($g(s) = 0$), the electrical impedance is infinite, which minimizes the coupling between the mechanical and electrical systems. The alteration in the system's resonant frequencies is less pronounced compared to the short-circuit case. The bandgap shift due to the piezoelectric element is expected to be marginal in practical applications.

There are different shunt circuits (Purely Resistive Shunts, Resistive-Inductive-Capacitive, Switched Shunts, Nonlinear Shunts, etc.), each type introduces distinct dynamics to the system, influencing the energy harvesting performance in terms of frequency, bandwidth, and efficiency. The choice depends on the application requirements and the nature of the vibrational energy to be harvested.

To calculate the voltage output at a specific location x_r, the Laplace transform is applied to Eq. (77). Subsequently, integrating this result into Eq. (78) leads to the following expression for resonator voltage:

$$V_r(x_r, s) = \frac{\vartheta_{p,r}}{C_{p,r}} \frac{s}{s + g(s)} \frac{s^2 W(x_r, s)}{s^2 + 2\zeta_r \omega_r s + \omega_r^2 \left(1 + \frac{\kappa_h s}{s + g(s)}\right)} \tag{82}$$

Here, $W(x_r, s)$ is the Laplace transform of the resonator's absolute displacement at location x_r, determined via modal expansion. The power dissipated in each resonator, when considering the frequency domain with $s = i\omega$, can be determined through the admittance $G_r(s)$. The power, denoted as $\mathbb{P}(x_r, i\omega)$, is expressed as follows:

$$\mathbb{P}(x_r, i\omega) = |V_r(x_r, i\omega)|^2 G_r^*(i\omega) = \frac{\mu \kappa_h \omega^6 \omega_t^2 g^*(i\omega) |W(x_r, i\omega)|^2 m(x_r) dx_r}{\left| (i\omega + g(i\omega)) \left(\omega^2 - i2\zeta_r \omega_t \omega - \omega_t^2 \left(1 + \frac{i\kappa_h \omega}{i\omega + g(i\omega)}\right)\right)\right|^2} \tag{83}$$

Here, the term $()^*$ represents the complex conjugate. The power is calculated based on the voltage at the resonator, the admittance, and various parameters of the system, such as frequency, damping, and coupling coefficients. With the assumption that resonators become infinitesimally small, the total complex power of the system is approximated by integrating the power of individual resonators over the domain as: $\mathbb{P}_{tot}(i\omega) = \sum_{r=1}^{N_r} \mathbb{P}(x_r, i\omega) \approx \int_x d\mathbb{P}$. This integral equation represents the total power dissipation in the system, factoring in the cumulative effect of all resonators and yields to total power dissipation in the system as:

$$\mathbb{P}(x_r, i\omega) = \frac{\mu \kappa_h \omega^6 \omega_t^2 g^*(i\omega) \int_x m(x) |W(x, i\omega)|^2 dx}{\left| (i\omega + g(i\omega)) \left(\omega^2 - i2\zeta_r \omega_t \omega - \omega_t^2 \left(1 + \frac{i\kappa_h \omega}{i\omega + g(i\omega)}\right)\right)\right|^2} \tag{84}$$

The total complex power of the system, $\mathbb{P}_{\text{tot}}(i\omega)$, is derived by considering the modal weightings $Z_m(s)$ and applying the orthogonality condition of the mode shapes as stated in equations (70) to (73). This approach simplifies the integral in Eq. (84), leading to:

$$\int_x m(x) |W(x, i\omega)|^2 dx = \int_x m(x) \sum_{m=1}^{N_m} Z_m(i\omega) \phi_m(x) \sum_{k=1}^{N_m} Z_k^*(i\omega) \phi_k(x) dx = \sum_{m=1}^{N_m} |Z_m(i\omega)|^2 \tag{85}$$

With this simplification, the total complex power can be written as:

$$\mathbb{P}_{tot}(i\omega) = \frac{\kappa_h \mu \omega^6 \omega_t^2 g^*(i\omega) \sum_{m=1}^{N_m} |Z_m(i\omega)|^2}{\left| (i\omega + g(i\omega)) \left(\omega^2 - i2\zeta_r \omega_t \omega - \omega_t^2 \left(1 + \frac{i\kappa_h \omega}{i\omega + g(i\omega)}\right)\right)\right|^2} \tag{86}$$

For further simplification, it can be expressed as:

$$\mathbb{P}_{tot}(i\omega) = \frac{\kappa_h \mu \omega^6 \omega_t^2 g^*(i\omega) \sum_{m=1}^{N_m} |Z_m(i\omega)|^2}{\left| (i\omega + g(i\omega)) (\omega^2 - i2\zeta_r \omega_t \omega - \omega_t^2) - i\omega \omega_t^2 \kappa_h \right|^2} \tag{87}$$

4.4 Numerical Studies

This section presents a numerical study on vibration attenuation of distributed metastructure achieved by installing piezoelectric elements on resonators. It also explores how varying the damping ratios of these resonators influences both the attenuation of vibrations and the efficiency of energy harvesting. It delves into energy harvesting via resistive shunting, a method involving a resistor connected across electrodes, leading to a normalized admittance $g(i\omega) = 1/\tau$. Here, $\tau = R_p C_{p,r}$ signifies the time constant associated with the parallel resistance R_p. The study extensively investigates the impact of varying the resonator's damping ratios ζ_r and different load resistances (values of τ) on the system's performance. The analysis encompasses the structural response and power output of a cantilever beam under base excitation, characterized by an amplitude w_b at various frequencies ω. Key aspects of the study include the generation of heatmaps to display the beam's tip transmissibility and power output, with these visualizations highlighting the dependence on both the damping ratio ζ_r and the load resistance parameter τ, along with the frequency ω. This comprehensive analysis aids in understanding the intricate relationships between damping, load resistance, and the efficiency of energy harvesting.

Additionally, for each excitation frequency, the optimal value of τ_{opt} that maximizes the real part of the power output $P(i\omega) = \text{Re}\{\mathbb{P}_{\text{tot}}(i\omega)\}$ is determined. The resulting optimal real power is then plotted as a function of the excitation frequency alone. Alongside, the tip displacement at this optimal load is evaluated to verify the presence of the bandgap, even under optimal loading conditions. These findings are depicted in Figs 25 to 29, illustrating the behavior of the mechanical metastructure with energy harvesting resonators. This approach helps in identifying the most effective operating conditions for maximizing energy harvesting while ensuring the structural integrity and functionality of the metastructure.

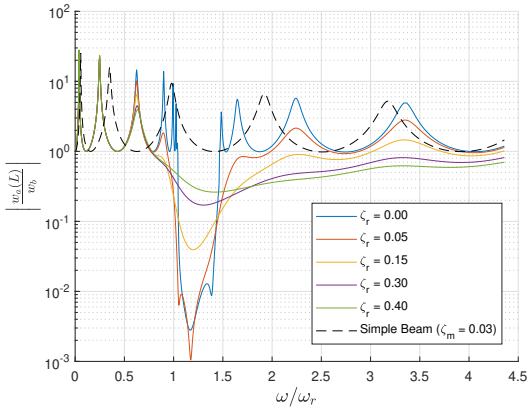

Figure 25: Beam tip response of a mechanical metastructure with variable damping ratios (ζ_r), demonstrating the effect on resonance peaks and bandgaps at optimal power output conditions. The responses are plotted as a function of normalized excitation frequency (ω/ω_r), with parameters set to $\kappa_h = 0.1, g = 1$, and $\mu = 1.4$, for a cantilever beam subjected to base motion. The comparison with a simple beam, which has a damping ratio of $\zeta_m = 0.03$, highlights the influence of the resonators on the formation of the bandgap and the system's pronounced sensitivity to ζ_r.

Figure 25 exhibits the beam tip response of a cantilever metastructure, under base excitation for various damping ratios ζ_r at optimal power output conditions. The responses, plotted against the normalized excitation frequency ω/ω_r, reveal the influence of damping on the amplitude and bandwidth of the resonant peaks. Increased damping ratios lead to broader and lower peaks, indicative of energy dissipation, while the presence of bandgaps-regions of reduced vibrational transmission-suggests the metastructure's capability for targeted vibration attenuation. Compared to a simple beam with $\zeta_m = 0.03$, the metastructure demonstrates altered dynamics due to the resonators, particularly under the conditions $\kappa_h = 0.1, g = 1, \mu = 1.4$, and $\omega_t = 3\omega_r$, signifying a system tuned for enhanced energy harvesting around the tripled resonant frequency. The figure underscores the critical role of damping optimization in maximizing the efficiency of energy harvesting within the metastructure.

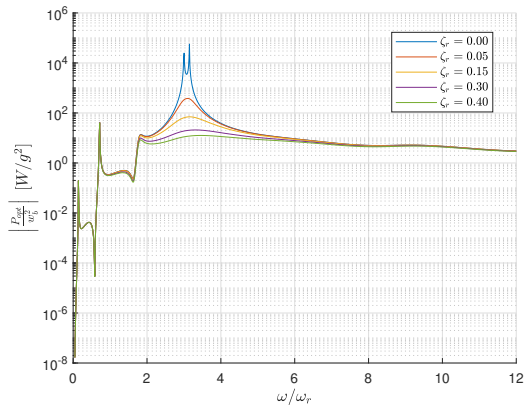

Figure 26: Optimal real power output of a cantilever beam in a mechanical metastructure with resistive shunting, presented across a spectrum of normalized metastructure with resistive shunting, presented across a spectrum of normalized excitation frequencies (ω/ω_r). The graph showcases the dependency of power output on various resonator damping ratios (ζ_r), with the parameter $\omega_t = 3\omega_r$ consistent with previous analyses. It highlights the influence of damping on energy harvesting efficiency, notably at and around the resonant frequency.

Figure 26 shows the optimal real power output of a cantilever beam in a mechanical metastructure with resistive shunting. Large, broadband power output is observed near the resonant frequency of the resonators. This occurs just before the targeterd locally resonant bandgap. Sudden peaks in displacement and power at optimal loading are noted. The frequency neighborhood where this occurs is affected by damping and system parameter variations. As the damping ratio ζ_r increases, the peak magnitude decreases and the curve flattens, signifying reduced power output efficiency. The significance of the damping ratio is emphasized for optimizing energy harvesting capability, with lower damping ratios being preferable for higher power outputs. A large but narrower-band power output is also seen near the system resonances.

Figure 27 showcases heatmaps of power output density across excitation frequencies and load resistances for different damping ratios. An optimal load resistance region is identified, where power output is maximized, showing a dependency on

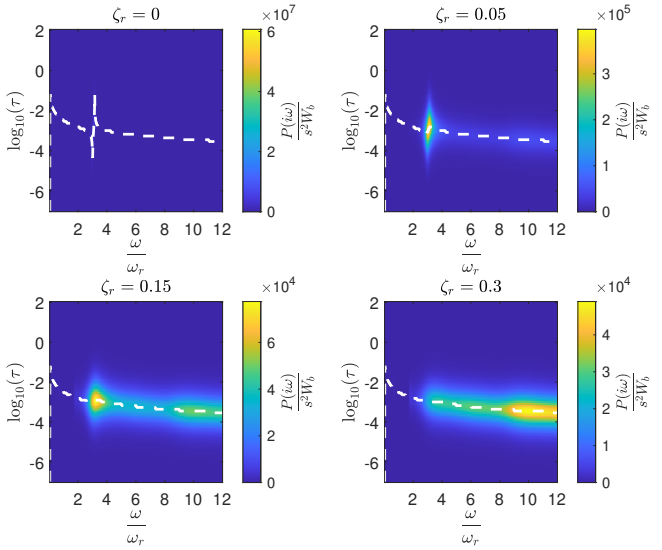

Figure 27: Heatmaps display the power output density variation with normalized excitation frequency and load resistance for different ζ_r. The dashed line indicates the optimal loading condition at each excitation frequency. Notable is the decrease in energy harvesting at higher frequencies with increased damping. Parameters: $g = 1, \kappa_h = 0.1, \omega_t = 3\omega_r, \mu = 1.4, \zeta_m = 0.027$.

mechanical damping and electrical loading. Increasing the damping ratio leads to decreased maximum power output and a less distinct optimal load resistance region. The necessity of selecting appropriate resistive loads for efficient power conversion at various frequencies is highlighted. At higher frequencies, there is a noticeable dissipation of energy, with a reduction in power output intensity in the heatmaps.

Figures 28 and 29 illustrate the impact of varying ζ_r on the beam tip response of a cantilever beam in a mechanical metastructure under base excitation. With increased damping, the resonant peaks at lower frequencies are reduced in intensity and sharpness, leading to a wider energy distribution. Higher damping ratios cause a pronounced broadening effect at frequencies just below the locally resonant bandgap, aiding in effective attenuation of the structural response. This damping behavior is important for reducing unwanted vibrations and for energy harvesting, as it enables a smoother transition from resonance to bandgap The resonant frequencies below the bandgap show strong attenuation, which correlates with high power output near the resonator's resonant frequency, suggesting efficient energy harvesting. The resonant frequencies below the bandgap show strong attenuation due to the energy harvesting, as suggested by the high power output near the resonator's resonant frequency.

Figure 30 illustrates a significant shift in the bandgap frequency range under varying conditions, from low to high electromechanical coupling. In cases of minimal coupling, the bandgap known for its high vibration damping shows little sensitivity to the optimal loading conditions of the energy harvester. With increased electromechanical coupling, the bandgap's influence grows, yet it remains narrow in bandwidth. Although the bandwidth for attenuation marginally decreases, the

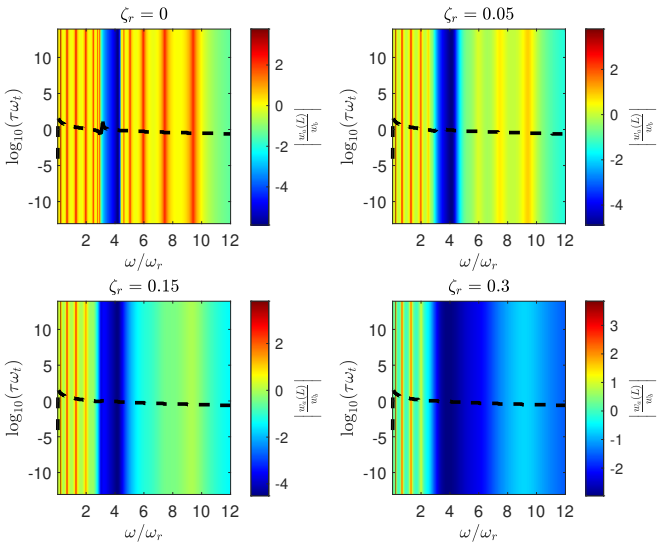

Figure 28: Influence of resonator damping on the beam tip response within a mechanical metastructure, visualized over RC time constant and normalized excitation frequency. The heatmaps depict attenuation effects at lower frequencies and the persistent bandgap stability despite varied damping, with dashed lines marking optimal energy harvesting conditions. Parameters: $g = 1, \kappa_h = 0.1, \omega_t = 3\omega_r, \mu = 1.4, \zeta_m = 0.027$.

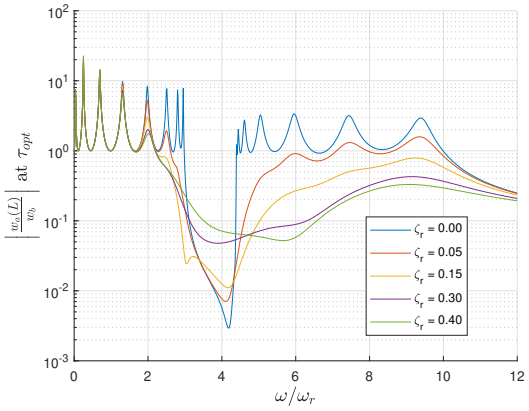

Figure 29: Beam tip response of a mechanical metastructure with varying ζ_r *at optimal power output, plotted against normalized excitation frequency. The graph illustrates the impact of damping on the vibrational response of a cantilever beam under base excitation, with parameters set to* $g = 1, \kappa_h = 0.1, \omega_t = 3\omega_r, \mu = 1.4,$ *and* $\zeta_m = 0.027$

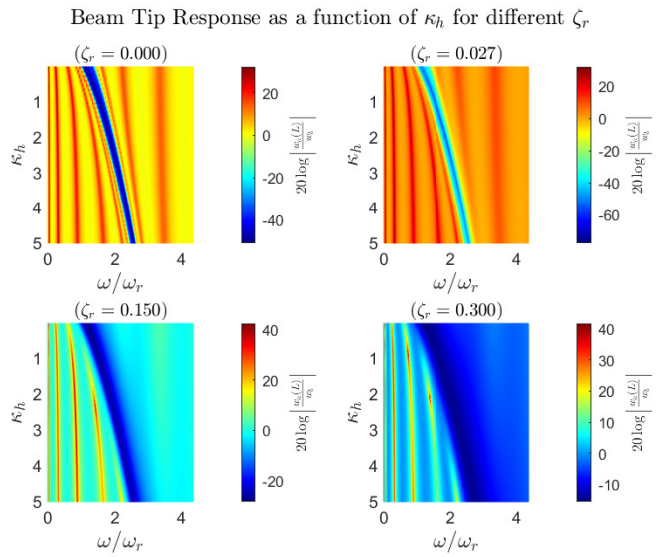

Figure 30: Bandgap frequency shifts and attenuation characteristics across different electromechanical coupling conditions. The heatmaps underscore the transition of the bandgap response with minimal to increased coupling (κ_h), highlighting the narrow bandwidth yet noticeable impact on vibration damping, especially under optimal energy harvester loading. The sensitivity of lower damping ratios to frequency changes and the broadened response at higher ratios are evident.

impact is noticeable. Higher levels of electromechanical coupling indicate a balance between bandwidth and amplitude, akin to the behavior of a damped vibration absorber. While higher electromechanical coupling in energy harvesters might seem advantageous, its desirability is limited by the availability of piezoelectric materials. The pattern of electromechanical coupling remains consistent across all damping ranges of the resonator. However, at high damping ratios, the electromechanical coupling is expected to shift the frequency edge of attenuation. The heatmaps reveal that for lower damping ratios, the response is highly sensitive to changes in the frequency ratio, as shown by the sharp, bright bands indicating significant peaks in the response. As the damping ratio increases, the peaks become less intense and more spread out, indicating a broader frequency range of response but with less pronounced peaks. This suggests that lower damping ratios are more effective for energy harvesting at specific resonant frequencies, while higher damping ratios may be better suited for applications that require a wider range of frequency responses.

4.5 Summary

This chapter established a robust theoretical foundation for understanding the dynamic characteristics of flexible metastructures with electromechanical resonators. The lumped parameter models offered simplicity and clarity in capturing the essential dynamics, while the distributed parameter models provided detailed and accurate representations of wave propagation and energy harvesting phenomena. The integration of piezoelectric elements within these models demonstrated significant potential for enhancing vibration control and energy harvesting efficiency. The

modal expansion method was employed to derive the natural frequencies and mode shapes of the metastructure, integrating electromechanical elements to study their influence on bandgap characteristics. The results demonstrated that piezoelectric elements, when attached to resonators, significantly affect the system's bandgap properties, offering substantial potential for energy harvesting from resonator fluctuations.

Here are the key points summarizing the contributions and insights gained from this chapter:

- Developed lumped and distributed parameter models for flexible metastructures with electromechanical resonators, providing a robust framework for analyzing dynamic behavior.
- Demonstrated the potential of piezoelectric elements to enhance energy harvesting and vibration control, particularly through the modulation of bandgap characteristics.
- Explored the impact of of various nonlinearities, including polynomial, voltage-dependent, and cubic forms, has revealed their critical roles in optimizing system performance. This investigation has shown how these nonlinearities can be adjusted to maximize energy harvesting and vibration attenuation.
- Extensive numerical studies have been conducted to evaluate the effects of key metastructure parameters such as resonator damping ratios and load resistances. These studies have provided valuable insights into designing these systems to achieve optimal conditions for energy harvesting and vibration control.

5 Streamlining Metastructure Modeling: Internally Coupled Resonators

Traditional metastructures enhance dynamic responses by incorporating periodic inclusions that disrupt and absorb wave energy. The introduction of internal coupling among resonators introduces a refined layer of control over these bandgap properties, potentially allowing for more bandgap creation.

The concept of internally coupled resonators refines the traditional designs by coupling resonators within the same unit cell or between neighboring cells. This adjustment alters the local dynamics, possibly leading to new secondary bandgaps and improved performance characteristics. The theoretical implications of such configurations are profound, suggesting potential benefits for industries like building construction, civil engineering, automotive manufacturing, and even consumer electronics, where precise control over vibrational energy is essential.

However, the transition from theory to practice with internally coupled resonators in metastructures is fraught with challenges. These include the need for precise manufacturing, sensitivity to structural variations, and the complexities involved in seamlessly integrating these systems. This chapter delves into these challenges through both lumped and distributed parameter models, employing experimental validations and numerical simulations to refine our understanding and application of these advanced theoretical models.

5.1 Lumped Parameter Model of Mechanical Internally Coupled Resonators

To clarify the dynamics within the mechanically internally coupled system, the analysis strategically simplifies the system by focusing exclusively on the springs, omitting damping effects and electromechanical elements. This approach allows for a concentrated examination of the system's behavior under the influence of linear springs in the primary chain and resonators, alongside nonlinear springs that facilitate internal coupling between resonators. As depicted in Fig. 31, the system consists of a nonlinear mechanical internally coupled chain, with the unit cell highlighted by the dashed rectangle. Consequently, the dynamic behavior of the system will be primarily dictated by this nonlinear internal coupling between resonators, even as the rest of the system retains its linearity. This configuration allows for a focused study on the impacts and potential advantages of having a nonlinear inter-resonator spring in an otherwise linear spring system.

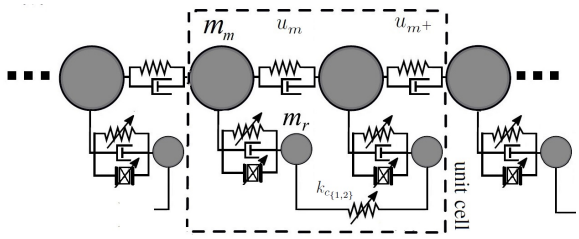

Figure 31: Mechanically internally coupled resonators. The dashed rectangle signifies a unit cell.

The kinetic energy, symbolized by T, includes the dynamic activities of both

the main chain and the resonators, and is expressed as follows:

$$T = \frac{1}{2} m_m \left(\dot{u}_m^2 + \dot{u}_{m^+}^2 \right) + \frac{1}{2} m_r \left(\dot{u}_r^2 + \dot{u}_{r^+}^2 \right) \tag{88}$$

The potential energy, denoted by U, encapsulates the energy stored in various components of a mechanically coupled system: the main chain's linear springs, coupling springs between the chain and resonators, and notably, the nonlinear springs internally coupling the resonators, providing a comprehensive view of energy distribution and interplay in a predominantly linear mechanical chain with specific nonlinear interactions.

$$\begin{aligned} U =& \frac{1}{2} k_m \left[(u_{m^-} - u_m)^2 + (u_m - u_{m^+})^2 + (u_{m^+} - u_{m^{++}})^2 \right] \\ &+ \frac{1}{2} k_r \left[(u_m - u_r)^2 + (u_{m^+} - u_{r^+})^2 \right] + \frac{1}{2} k_{c_1} (u_r - u_{r^+})^2 + \frac{1}{4} k_{c_2} (u_r - u_{r^+})^4 \end{aligned} \tag{89}$$

Here, k_{c_1} and k_{c_2} serve as linear and nonlinear coupling coefficients respectively. While k_{c_1} facilitates a linear coupling between resonators, k_{c_2} introduces a bistable nonlinearity due to its fourth-order nature among the resonators. If both k_{c_1} and k_{c_2} are positive ($k_{c_1} > 0$ and $k_{c_2} > 0$), the system achieves a traditional monostable state, thereby circumventing the need to identify and linearize around a stable point. Opting for this strategy not only guarantees straightforward and stable system dynamics but also commonly serves to sidestep the intricacies encountered when navigating through bistable systems, especially in scenarios where $k_{c_1} < 0$ and $k_{c_2} > 0$.

Utilizing the Lagrangian formulation, and defining $z_r(t)$ as relative displacement between chain mass and resonator, the resonator's equation of motion yields:

$$m_m \ddot{z}_r(t) + c_m \left(2\dot{z}_r(t) - \dot{z}_{r^-}(t) - \dot{z}_{r^+}(t) \right) + k_m \left(2z_r(t) - z_{r^-}(t) - z_{r^+}(t) \right) + k_r z_r(t) = f_{e_r} \tag{90}$$

$$m_m \ddot{z}_{r^+}(t) + c_m \left(2\dot{z}_{r^+}(t) - \dot{z}_r(t) - \dot{z}_{r^{++}}(t) \right) + k_m \left(2z_{r^+}(t) - z_r(t) - z_{r^{++}}(t) \right) + k_r z_{r^+}(t) = f_{e_{r^+}} \tag{91}$$

$$m_r \ddot{z}_r(t) + c_r \dot{z}_r(t) + k_r z_r(t) + k_{c_1} \left(z_r(t) - z_{r^+}(t) \right) + k_{c_2} \left(z_r(t) - z_{r^+}(t) \right)^3 = f_{e_m} \tag{92}$$

$$m_r \ddot{z}_{r^+}(t) + c_r \dot{z}_{r^+}(t) + k_r z_{r^+}(t) - k_{c_1} \left(z_r(t) - z_{r^+}(t) \right) - k_{c_2} \left(z_r(t) - z_{r^+}(t) \right)^3 = f_{e_{m^+}} \tag{93}$$

Here, m_m represents the mass of the main chain, and the coefficient k_m is the main chain's stiffness, interacting with the relative displacements between the resonator and its neighbors, while k_r characterizes the resonator's inherent stiffness. The resonator, with mass m_r, has a damping coefficient c_r that represents its resistance to motion due to velocity. The coefficients k_{c_1} and k_{c_2} represent the linear and nonlinear coupling stiffness between adjacent resonators, respectively. These couplings govern the interaction forces that depend on the relative displacement and displacement cubed between neighboring resonators, enhancing the dynamic response control. The forces f_{e_r} and $f_{e_{r^+}}$ indicate excitation on the primary mass

chain, influenced by the resonator and internal connections. f_{e_m} and $f_{e_{m^+}}$ are forcing on the resonators, sourced from the main chain mass and internal stiffness interactions.

The superscript '++' indicates the two adjacent mass-in-mass structures, where $u_{m^{++}}$ denotes the displacement of the mass or unit that is two positions away from mass m. Utilizing Bloch's theorem, the waveform of the harmonic displacements of masses can be expressed as:

$$\begin{aligned} u_m &= u_{m_0} e^{i(G_n x - \omega t)} \\ u_{m^+} &= u_{m_1} e^{i(G_n x + G_n a - \omega t)} \\ u_r &= u_{r_0} e^{i(G_n x - \omega t)} \\ u_{r^+} &= u_{r_1} e^{i(G_n x + G_n a - \omega t)} \end{aligned} \tag{94}$$

where G_n represents the wave number or spatial frequency, dictating the spatial periodicity of the wave over the unit cell with the dimension of a. The coefficients $u_{m_0}, u_{m_1}, u_{r_0}$, and u_{r_1} represent the complex wave amplitudes. Integrating these terms into the provided equations leads to the derivation of the dispersion relation. The associated matrix is determined for this purpose, and by setting its determinant to zero, a relationship between G_n and ω is established. For nonlinear scenarios, as presented in the above equations, a numerical approach is typically employed. From four inertias in a unit cell, an eighth-order dispersion equation arises when the determinant is zero. This results in four curves with three band gaps on the positive real axis, indicating that internally coupled metamaterials offer additional band gaps over conventional ones.

In this study, we focus on a specific frequency range. A comprehensive analysis of the effects of piezoelectric nonlinearities across the entire frequency spectrum is beyond the scope of this work.

5.1.1 Stability Analysis for Mechanical Internally Coupled Metamaterial

The Jacobian matrix is commonly used to analyze the stability of equilibrium points for nonlinear systems. The idea is to linearize the nonlinear system around its equilibrium points and then analyze the stability of the resulting linear system. This provides insight into the local behavior of the nonlinear system around those points.

Considering Eqs. (92) and (93) without the excitation force, the equilibrium points of the system can be ascertained. Setting the velocities $\dot{z}_r$ and $\dot{z}_{r^+}$, along with the accelerations $\ddot{z}_r$ and $\ddot{z}_{r^+}$, to zero provides the necessary conditions that define these equilibrium positions. The equilibrium points satisfy:

$$\begin{aligned} k_r z_{r_0} + k_{c_1}\left(z_{r_0} - z_{r_0^+}\right) + k_{c_2}\left(z_{r_0} - z_{r_0^+}\right)^3 = 0 \\ k_r z_{r_0^+} - k_{c_1}\left(z_{r_0} - z_{r_0^+}\right) - k_{c_2}\left(z_{r_0} - z_{r_0^+}\right)^3 = 0 \end{aligned} \tag{95}$$

Introducing small perturbations around these equilibrium points results in the following expressions [13]:

$$\begin{aligned} \delta z_r &= z_r - z_{r_0} \\ \delta z_{r^+} &= z_{r^+} - z_{r_0^+} \end{aligned} \tag{96}$$

Upon linearization of the equations of motion around the equilibrium, terms of higher order in δz_r and δz_{r^+} are neglected, leading to:

$$m_r\delta\ddot{z}_r + c_r\delta\dot{z}_r + k_r\delta z_r + k_{c_1}\left(\delta z_r - \delta z_{r^+}\right) + 3k_{c_2}\left(z_{r_0} - z_{r_0^+}\right)^2\left(\delta z_r - \delta z_{r^+}\right) = 0 \quad (97)$$

$$m_r\delta\ddot{z}_{r^+} + c_r\delta\dot{z}_{r^+} + k_r\delta z_{r^+} - k_{c_1}\left(\delta z_r - \delta z_{r^+}\right) - 3k_{c_2}\left(z_{r_0} - z_{r_0^+}\right)^2\left(\delta z_r - \delta z_{r^+}\right) = 0 \quad (98)$$

A state vector is introduced to convert the second-order system into a system of first order:

$$X = \begin{bmatrix} \delta z_r \\ \delta z_{r^+} \\ \delta\dot{z}_r \\ \delta\dot{z}_{r^+} \end{bmatrix} \quad (99)$$

Differentiating the state vector yields:

$$\dot{X} = \begin{bmatrix} \delta\dot{z}_r \\ \delta\dot{z}_{r^+} \\ \delta\ddot{z}_r \\ \delta\ddot{z}_{r^+} \end{bmatrix} \quad (100)$$

The objective is to represent $\dot{X}$ in the form AX, where A is a matrix constructed from the system parameters and possibly the equilibrium point. The matrix A is determined by linearizing the equations of motion. The eigenvalues of A indicate the stability of the system around the equilibrium.

The eigenvalue for the nonlinear internally coupled resonators is determined by Eqs. (101) and (102):

$$\lambda_{1,3} = -\frac{c_r \pm \sqrt{c_r^2 - 4k_r m_r}}{2m_r} \quad (101)$$

$$\lambda_{2,4} = -\frac{1}{2m_r}\left(c_r \pm \sqrt{c_r^2 - 4m_r k_r - 8m_r\left(k_{c_1} + 3k_{c_2}(\delta z_r - \delta z_{r^+})^2\right)}\right) \quad (102)$$

By omitting the nonlinear term k_{c_2}, the system transitions to a linear internally coupled resonator. This exclusion simplifies the stability analysis by removing the nonlinear component. Consequently, the system's behavior is analyzed linearly around its equilibrium point. After this simplification, the governing equation of motion becomes:

$$\lambda_{1,3} = -\frac{c_r \pm \sqrt{c_r^2 - 4k_r m_r}}{2m_r} \quad (103)$$

$$\lambda_{2,4} = -\frac{c_r \pm \sqrt{c_r^2 - 4m_r(k_r + 2k_c)}}{2m_r} \quad (104)$$

Stability scenarios for internally coupled systems, both nonlinear and linear, are summarized as follows:

Nonlinear Systems:

Case 1: For $c_r^2 - 4k_r m_r < 0$, $\lambda_{1,3}$ imply a stable focus.

Case 2: With $c_r^2 - 4k_r m_r > 0$ and all positive parameters, λ_1 and λ_3 ensure stability.

Case 3: Sign of $\lambda_{2,4}$ depends on term magnitudes and c_r.

Case 4: $c_r^2 - 4k_r m_r - 8m_r \left(k_{c_1} + 3k_{c_2} \left(\delta z_r - \delta z_{r^+}\right)^2\right) < 0$ denotes stability.

Linear Systems:

Case 1: For $c_r^2 - 4k_r m_r < 0$, $\lambda_{1,3}$ indicate a stable focus.

Case 2: With $c_r^2 - 4k_r m_r > 0$, signs of λ_1 and λ_3 are determined by c_r.

Case 3: In $c_r^2 - 4k_r m_r - 8k_c m_r > 0$, stability relies on signs of λ_2 and λ_4.

Case 4: Condition $c_r^2 - 4k_r m_r - 8k_c m_r < 0$ signals stability.

5.2 Lumped Parameter Model of Electromechanical Internally Coupled Resonators

In the preceding section, the metamaterial with internal resonator coupling was examined. Due to challenges in constructing and instructing the internal spring, especially when aiming for negative stiffness, an alternative is to utilize an electrical shunt circuit, specifically a prototype capacitance, offering behavior similar to the mechanically internally coupled resonator.

5.2.1 Internal Coupling Through Shunt Capacitance Circuit Techniques

In this section, the shunt capacitance circuit technique is employed to model a two-degree-of-freedom electrical system with internal coupling, as illustrated in Fig. 32. In this scenario, capacitance is incorporated as a key component instead of utilizing the previously formulated resistance (R). Fig. 32 presents two different

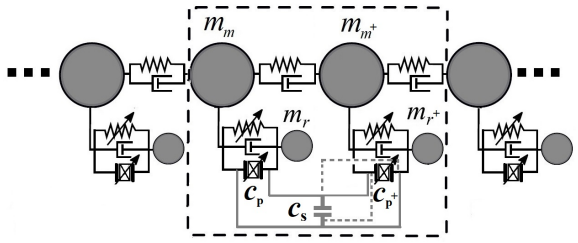

Figure 32: Internally coupled with electrical shunt circuit. Forward (dash) and reverse (solid) capacitance shunting configuration.

configurations of the shunt circuit: the forward and the reverse. For the forward setup, the top and bottom surfaces of the piezoelectric transducer on the left align with the analogous surfaces of its counterpart on the right. Conversely, the reverse configuration has the top and bottom surfaces of the two piezoelectric transducers connected in an opposite fashion. In both setups, a capacitor is connected in parallel to both piezoelectric transducers.

The analytical procedures for both configurations are analogous, leading to comparable conclusions. The distinction in circuit connectivity between these two setups only results in a sign reversal in the ultimate expression for equivalent coupling stiffness. Both forward and reverse connections can achieve the same functionality, albeit with differing capacitance tuning strategies. This investigation primarily focuses on the reverse connection configuration. In its absence of external capacitance, it exhibits characteristics akin to a standard spring with positive stiffness,

simplifying its interpretation in an equivalent mechanical context.

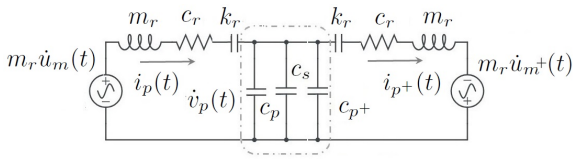

Figure 33: Equivalent Electrical System Representation of the Unit Cell Resonators with Capacitance Shunt Circuit Using the Impedance Analogy

Capacitance typically relates the change in electric charge to shifts in electric potential. With positive total capacitance, a discharge of current leads to a voltage decrease across the capacitor, whereas with negative total capacitance, the voltage increases. Utilizing the impedance analogy (current to velocity, charge to displacement, voltage to force), the circuit segments LRC and LRC^+ correspond to the resonators $m_r c_r k_r$ and $(m_r c_r k_r)^+$, respectively, as illustrated in Fig. 33. For simplicity, the mechanical properties of the resonators (mass, stiffness, and damping) are assumed to be identical.

The voltage across the total capacitance represents the force interaction between these resonators. Additionally, the current through total capacitance, representing the difference in currents in the loops' paths, indicates the difference in velocity between the resonators. The charge variation in total capacitance indicates the displacement difference between the resonators. Hence, the capacitor in the electrical system can be envisioned as a spring, k_s coupling the resonators in the mechanical domain, with positive total capacitance acting as a positive-stiffness coupling spring and negative total capacitance as a negative-stiffness spring.

Considering the reversed configuration of the two piezoelectric transducers, the voltages exhibit identical magnitudes but with opposite directions. Factoring in the current passing through the parallel-connected capacitance c_s, the relationship between the voltages is expressed as:

$$\frac{1}{c_s}\int \big(i_p(t) - i_{p^+}(t)\big)\, dt = v_p(t) \tag{105}$$

The design employs an internal shunt capacitance circuit to optimize the band gap behavior in resonators. When this capacitance acts as a negative capacitor and is finely tuned, it can offset the capacitances of linked piezoelectric transducers, enhancing the coupling between adjacent resonator.

Considering damping in the resonators and assuming identical stiffness, damping coefficients, and masses for all resonators, the governing equations for the motion of the two resonators within a unit cell (refer to Fig. 32) relative to the mass of the chain is as follows:

$$m_r\ddot{z}_r(t) + c_r\dot{z}_r(t) + k_r z_r(t) + \theta_r v_p(t) = m_r\ddot{u}_m(t) \tag{106}$$

$$m_r\ddot{z}_{r^+}(t) + c_r\dot{z}_{r^+}(t) + k_r z_{r^+}(t) + \theta_{r^+} v_{p^+}(t) = m_r\ddot{u}_{m^+}(t) \tag{107}$$

The relative displacements of these resonators with respect to the main chain structure are denoted by $z_r(t)$ and $z_{r^+}(t)$. The electromechanical coupling coefficients are θ_r and θ_{r^+}, and the voltages across the corresponding piezoelectric

transducers are $v_p(t)$ and $v_{p^+}(t)$. The excitation displacements are represented as $u_m(t)$ for the left and $u_{m^+}(t)$ for the right resonators.

The governing electrical domain equations for the piezoelectric transducers are as follows:

$$c_p\dot{v}_p(t) + i_p(t) - \theta_r\dot{z}_r(t) = 0 \tag{108}$$

$$c_{p^+}\dot{v}_{p^+}(t) + i_{p^+}(t) - \theta_{r^+}\dot{z}_{r^+}(t) = 0 \tag{109}$$

$$i_p(t) = \frac{c_{p^+}\theta_r\dot{z}_r + c_p\theta_{r^+}\dot{z}_{r^+} + c_s\theta_r\dot{z}_r}{c_p + c_{p^+} + c_s} \tag{110}$$

$$i_{p^+}(t) = \frac{c_{p^+}\theta_r\dot{z}_r + c_p\theta_{r^+}\dot{z}_{r^+} + c_s\theta_{r^+}\dot{z}_{r^+}}{c_p + c_{p^+} + c_s} \tag{111}$$

Substituting Eq. (110) and Eq. (111) into Eq. (105) and integrating with respect to time for zero initial condition yields:

$$v_p(t) = \frac{(\theta_r z_r - \theta_{r^+} z_{r^+})}{c_p + c_{p^+} + c_s} \tag{112}$$

$$v_{p^+}(t) = -\frac{(\theta_r z_r - \theta_{r^+} z_{r^+})}{c_p + c_{p^+} + c_s} \tag{113}$$

Substituting equations Eq. (112) and Eq. (113) into Eqs. (106) and Eq. (107) yields the following expressions:

$$m_r\ddot{z}_r(t) + c_r\dot{z}_r(t) + k_r z_r(t) + \frac{\theta_r(\theta_r z_r(t) - \theta_{r^+} z_{r^+}(t))}{c_p + c_{p^+} + c_s} = m_r\ddot{u}_m(t) \tag{114}$$

$$m_r\ddot{z}_{r^+}(t) + c_r\dot{z}_{r^+}(t) + k_r z_{r^+}(t) - \frac{\theta_{r^+}(\theta_r z_r(t) - \theta_{r^+} z_{r^+}(t))}{c_p + c_{p^+} + c_s} = m_r\ddot{u}_{m^+}(t) \tag{115}$$

Rearranging

$$m_r\ddot{z}_r(t) + c_r\dot{z}_r(t) + k_r z_r(t) + k_{s_1} z_r(t) - k_{s_2} z_{r^+}(t) = m_r\ddot{u}_m(t) \tag{116}$$

$$m_r\ddot{z}_{r+}(t) + c_r\dot{z}_{r+}(t) + k_r z_{r+}(t) - k_{s_2} z_r(t) + k_{s_3} z_{r+}(t) = m_r\ddot{u}_{m^+}(t), \tag{117}$$

where

$$k_{s_1} = \frac{\theta_r^2}{c_p + c_{p^+} + c_s} \tag{118}$$

$$k_{s_2} = \frac{\theta_r\theta_r^+}{c_p + c_{p^+} + c_s} \tag{119}$$

$$k_{s_3} = \frac{\theta_{r^+}^2}{c_p + c_{p^+} + c_s}. \tag{120}$$

For identical electromechanical couplings and after substituting the relevant equations into Eq. (105), the integrated result yields the following condensed motion equations:

$$m_r\ddot{z}_r(t) + c_r\dot{z}_r(t) + k_r z_r(t) + k_s\left(z_r(t) - z_{r^+}(t)\right) = m_r\ddot{u}_m(t) \tag{121}$$

$$m_r\ddot{z}_{r^+}(t) + c_r\dot{z}_{r^+}(t) + k_r z_{r^+}(t) - k_s\left(z_r(t) - z_{r^+}(t)\right) = m_r\ddot{u}_{m^+}(t) \tag{122}$$

where

$$k_s = \frac{\theta_r^2}{c_p + c_{p^+} + c_s} \tag{123}$$

Implementing coupling through piezoelectric transducers and a shunt capacitance circuit is practical, as it serves as an equivalent spring that relates the motions of two resonators via their relative displacements. This coupling mechanism, resulting from local resonances, creates additional band gaps in metamaterials by generating two resonant frequencies. The piezoelectric transducers, when shunted, act as an analogous internal coupling spring k_s, similar to the mechanical internal coupling that links the movement of two resonators.

However, it's important to note that using a negative shunt capacitor, which is a type of positive feedback in op-amp circuits, can increase the risk of system instability without the right parameter choices. Despite this, the design's strength is its tunability and ability to generate multiple band gaps, offering robust vibration suppression.

5.2.2 Stability Analysis of Electromechanical Internally Coupled Resonators Using Shunt Capacitance

The stability of the system hinges on k_s, denoting electromechanical coupling through the shunt circuit. Instability might arise with negative shunt capacitance. For the dual-resonator setup, stability is gauged by linearizing its equations of motion and inspecting the eigenvalues of the Jacobian matrix. A system is stable if all its eigenvalues possess negative real parts. By analyzing the Jacobian matrix derived from linearizing around equilibrium, we discern system behavior. The system remains stable with all eigenvalues in the left-half complex plane. Achieving negative stiffness necessitates k_{s_1}, k_{s_2}, and k_{s_3} to be negative. Uniform electromechanical coupling demands $k_s < 0$.

For a system with positive electromechanical coupling, achieving a negative k_s necessitates the combined c_p and c_s to be negative, indicating a need for negative capacitance. This can be realized using active circuits with operational amplifiers or ferroelectric capacitors. However, this introduces challenges such as potential destabilization. Ensuring system stability, especially with negative capacitance, is paramount, often verified using Jacobian analysis. Mathematically, a corresponding linear system is expressed as:

$$m\ddot{z}(t) + c\dot{z}(t) + kz(t) = f(t) \tag{124}$$

with

$$z(t) = \begin{bmatrix} z_r(t) \\ z_{r^+}(t) \end{bmatrix}$$

$$\lambda = \frac{-c_r \pm \sqrt{c_r^2 - 2k_{s_1}m_r - 2k_{s_3}m_r - 4k_r m_r \pm 2m_r\sqrt{k_{s_1}^2 - 2k_{s_1}k_{s_3} + 4k_{s_2}^2 + k_{s_3}^2}}}{2m_r} \tag{125}$$

The system's stability is influenced by the eigenvalues of the Jacobian matrix, determined by Eq. (125). These eigenvalues are shaped by the damping coefficient c_r and shunt coefficients k_{s_1}, k_{s_2}, and k_{s_3}. While damping can promote stability, spring coefficients introduce potential oscillations. The interplay of k_{s_1}, k_{s_3}, and coupling k_{s_2} deeply impacts the system dynamics. A system is stable when all eigenvalues have negative real parts. If the discriminant is negative, oscillatory behaviors emerge. Notably, the real component of λ, defined as $\frac{-c_r}{2m_r}$, predisposes the system to stability, but further analysis is essential for full understanding.

$$a = c_r^2 - 2k_{s_1}m_r - 2k_{s_3}m_r - 4k_r m_r \tag{126}$$

$$b = 2m_r\sqrt{k_{s_1}^2 - 2k_{s_1}k_{s_3} + 4k_{s_2}^2 + k_{s_3}^2} \tag{127}$$

Case 1: $a < 0$ and $b < 0$, the system is stable if $|a| > |b|$.

Case 2: $a > 0$ and $b > 0$, the system is stable if $a < b$.

Case 3: $a > 0$ and $b < 0$, stability would need to be ascertained by calculating the actual values and verifying the sign of λ. The system can lead to an unstable region.

Case 4: $a < 0$ and $b > 0$, the system is stable if $|a| > |b|$.

Case 5: $a = 0$ or $b = 0$, the system is stable.

For a marginally stable system, damping is typically disregarded to establish boundaries of stability. As per Eq. (128), when the system's eigenvalues are purely imaginary, it denotes a marginal stability condition. This equation delineates constraints on the stiffness coefficients k_r and k_s, defining the threshold between stable and unstable regimes.

$$2k_r > -k_{s_1} - k_{s3} - \sqrt{k_{s_1}^2 - 2k_{s_1}k_{s3} + 4k_{s_2}^2 + k_{s_3}^2} \tag{128}$$

The associated eigenvalues, representing the system's characteristic frequencies, are given by:

$$\lambda = \pm\frac{1}{\sqrt{2}}\sqrt{\frac{-\left(2k_r + k_{s_1} + k_{s_3} \pm \sqrt{k_{s_1}^2 - 2k_{s_1}k_{s_3} + 4k_{s_2}^2 + k_{s_3}^2}\right)}{m_r}} \tag{129}$$

To identify criteria for c_s that ensures a negative equivalent stiffness, Equations (118), (119), and (120) are substituted into (126) and (127). The derived expressions are then analyzed to determine the conditions for c_s that satisfy the stability conditions:

$$a - b < 0 \tag{130}$$

$$|a| > |b| \tag{131}$$

Substituting a and b into Eq. (130) for the stability condition of $a-b<0$ yields to:

$$c_r^2 - 4k_r m_r < 2m_r \left(\frac{\theta_r^2 + \theta_{r^+}^2 + \sqrt{\theta_r^4 + 2\theta_r^2\theta_{r^+}^2 + \theta_{r^+}^4}}{c_p + c_{p^+} + c_s} \right) \tag{132}$$

Taking into account the absolute values in Eq. (131), it becomes imperative to explore two scenarios due to the potential positivity or negativity of both a and b.

$$\left| c_r^2 - 4k_r m_r \right| > \left| 2m_r \frac{\sqrt{\theta_r^4 + 2\theta_r^2\theta_{r^+}^2 + \theta_{r^+}^4}}{c_p + c_{p^+} + c_s} \right| \tag{133}$$

The inequalities (133) and (132) should be satisfied for stability, and c_s appears in the denominator of the fractions in these expressions, implying that as c_s changes, the values of these expressions will alter, potentially changing the sign of the inequalities. To derive explicit criteria, one could further manipulate these expressions or, depending on the specific application or system, analyze them numerically by substituting values of other parameters (c_r, k_r, m_r, etc.) to explore how varying c_s affects the system's stability. solving for c_s results in:

$$c_s > \frac{2m_r \left(\theta_r^2 + \theta_{r^+}^2 + \sqrt{\theta_r^4 + 2\theta_r^2\theta_{r^+}^2 + \theta_{r^+}^4} \right)}{c_r^2 - 4k_r m_r} - c_p - c_{p^+} \tag{134}$$

In the case of identical electromechanical coupling, and capacitance, the criteria for c_s can be simplified as follows:

$$c_s > \frac{8m_r\theta_r^2}{c_r^2 - 4k_r m_r} - 2c_p \tag{135}$$

In the scenario devoid of damping, the eigenvalues of the system, representing its characteristic roots, are provided as follows:

$$\begin{aligned} \lambda_{1,2} &= \pm \frac{\sqrt{-k_r m_r}}{m_r} \\ \lambda_{3,4} &= \pm \frac{\sqrt{-m_r\left(k_r + 2k_s\right)}}{m_r} \end{aligned} \tag{136}$$

The system's stability is defined by the real parts of its eigenvalues. When $k_r+2k_s>0$, the system exhibits marginal stability, oscillating continuously without decay or growth. However, if $k_r + 2k_s < 0$, the system has both positive and negative eigenvalues, indicating instability. This highlights the critical relationship between the resonator's spring constant and the shunt capacitance stiffness (k_s). If the feedback from the shunt is overly negative, it can destabilize the system. In most applications, full stability is preferred over marginal stability. The stability criterion for c_s is:

$$c_s > -(\frac{2\theta_r^2}{k_r} + 2c_p) \tag{137}$$

In contrast to purely mechanical internally coupled resonators, electromechanical shunt capacitance circuits provide benefits over solely mechanical resonators by

allowing easy adjustments for negative stiffness. The system's flexibility is further amplified by altering parameters like c_p, c_{p^+}, θ_r, and θ_{r^+}, enabling advanced system behaviors and improved dynamic control.

For most practical applications, a strictly stable system, where all disturbances decay, is more desirable than a marginally stable one. Exploring stability in lumped parameter systems reveals that maintaining a strictly stable condition, preferable for practical applications, hinges on a fine balance within the system's parameters, as indicated by the derived criterion. For a detailed examination of stability analysis and energy harvesting within lumped parameter systems, particularly those incorporating internally coupled resonators, the study in [12] extends the discussion to encompass a variety of conditions.

5.3 Numerical Studies

This section delves into simulations that distinguish between mechanical and electromechanical systems, further bifurcated into linear and nonlinear models with internal coupling resonators. The exploration is grounded in the lumped parameter methodology, where the dynamics of these systems, including piezoelectric energy harvesters, are investigated. Simulations were conducted to analyze the dynamic behaviors of the proposed models featuring internally coupled electromechanical resonators, using parameters listed in Table 5. The mechanical and electromechanical characteristics, previously elaborated in Table 1 and Table 4, have been augmented with terms representing internal coupling.

Table 5: Defined parameters for the piezoelectric model

Parameter	Value
Mass of main chain (m_m)	0.056 kg
Mass of resonator (m_r)	0.0336 kg
Spring constant of main chain (k_m)	150 N/m
Spring constant of resonator (k_r)	129.6 N/m
Damping coefficient of main chain (c_m)	0.0464 Ns/m
Damping coefficient of resonator (c_r)	0.0334 Ns/m
Piezoelectric capacitance (c_p)	1.5 mF(C/m)
Electromechanical coupling coefficient (θ)	0.25 N/V
Nonlinear stiffnesses quadratic coefficient (γ_1)	-500 N/m^2
Nonlinear stiffnesses cubic coefficient (γ_3)	15000 N/m^3
Linear coupling coefficient (k_{c_1})	198(-20) N/m
Nonlinear coupling coefficient (k_{c_2})	2386(880) N/m^3
Shunt capacitance (c_s)	-7.9 mF(C/m)
Internal resistance (R)	500 Ω

5.3.1 Nonlinear Mechanical Resonators and Internal Coupling Dynamics

Figure 34 illustrates the transmittance responses and bandgap creation across a range of system configurations. For a comprehensive perspective, this figure integrates the outcomes from Chapter 2, juxtaposing the linear and nonlinear resonator, and internally coupled resonator analyses results to facilitate a direct comparison. The system's natural frequencies are analyzed within a range from 6 to 17 Hz. The introduction of locally resonating elements distinctly establishes a band gap, dif-

ferentiating these configurations from the conventional metastructure setup. This band gap characteristic is attributed to the linear local resonance, which undergoes out-of-phase motion when subjected to an external excitation frequency near its local resonance frequency.

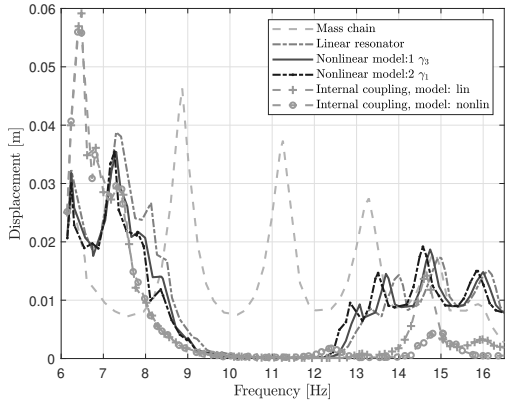

Figure 34: Comparative Analysis of Band Gap Behaviors in a 1-D Chain System: Insights from Linear, Nonlinear, and Internally Coupled Resonator Configurations

The nonlinear analysis focuses primarily on contrasting linear systems with their nonlinear counterparts, in addition to examining internally coupled systems. Effects arising from bifurcation and its influence on frequency sweeps are not explored in this context. With the substitutions $k_r \rightarrow k_{c_1}$ and $\gamma_{r_3} \rightarrow k_{c_2}$, the Eq. 16 modifies to:

$$f_r = k_{c_1} u + k_{c_2} u^3 \tag{138}$$

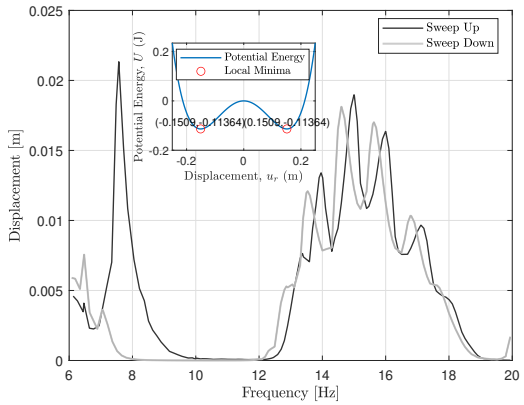

Figure 35: Displacement response of bistable nonlinear mechanical internal coupling resonators. Linear coupling coefficient $k_{c_1} = -20N/m$, and nonlinear coupling coefficient $k_{c_2} = 880N/m^3$. Inset: Resonator's potential energy profile for the specified coupling parameters.

Figure 35 shows the transmission response of a metastructure equipped with a nonlinear bi-stable internal coupling resonator.

The observed bifurcation is shaped by linear ($k_{c_1} = -20$ N/m) and nonlinear ($k_{c_2} = 880$ N/m^3) coupling coefficients, with the continuous sweep offering a detailed system response. The main graph underlines the system's potential energy dynamics, with an unstable origin indicating negative stiffness. This complexity is further highlighted by bifurcations between 14-16 Hz. The inset reveals various energy states the system can attain. Multiple local minima suggest system multi-stability, especially during large fluctuations. Hysteresis is evident from discrepancies in sweep traces, particularly in lower frequencies from 6 Hz and 10 Hz. However, it's vital to understand the intent behind the choice of parameters in this study. The deliberate restriction to a specific frequency range serves to mimic negative stiffness phenomena observed in specific electromechanical systems.

Cubic nonlinearities, with their symmetric properties, are observed to manifest either pure hardening or softening behaviors. This stands in contrast to the dual behavior inherent to asymmetric quadratic nonlinearities. The significance of optimal impedance matching is underscored, highlighting its role in achieving enhanced vibration suppression and energy harvesting. However, as theoretical constructs transition to tangible systems, certain compromises are often necessary to accommodate weakly and strongly coupled systems.

Setting both k_{c_1} and k_{c_2} to be positive (see Table 5) induces a classic monostable state, simplifying the system and avoiding the complications inherent in managing bistable systems, particularly when $k_{c_1} < 0$ and $k_{c_2} > 0$.

5.3.2 Internally Coupled Resonators with Electromechanical Nonlinearity

Fig. 36 visualizes the derived relationship of Eq. (137) and its implications for system stability. Based on the analysis, the threshold value of the equivalent internally coupled stiffness k_s for stability is given by $k_s > -\frac{k_r}{2}$. The relationship between k_s and shunt capacitance c_s is clearly illustrated, with the light gray region representing system stability and the dark gray region indicating system instability. The dividing threshold between these regions is represented by the line at $k_s = -\frac{k_r}{2}$. For the provided parameters, the system remains stable for c_s values ranging from negative infinity to approximately -0.004 Farad and resumes stability from around -0.003 Farad ($k_s = -3468$ to 5203 N/m) to positive infinity, with a brief interval of instability between these ranges. The magnified view offers a closer perspective on the critical transition points, emphasizing the pivotal c_s values at which the system's dynamical response alternates.

In the study of energy harvesting systems, understanding the behavior of different parameters is essential for optimization. Fig. 38 presents the harvested power and energy across a range of shunt capacitances. It clearly underscores the influential role of shunt capacitance on the system's overall efficiency.

An observation made from the results is the superiority of electrical internal coupling via shunt circuits in terms of tunability. Specifically, electrical coupling seems to allow for easier tuning of the band gap compared to its mechanical counterpart. This is evident in Fig. 37 and 38, where the chosen shunt capacitor facilitates a band gap at a notably lower frequency in comparison to a mechanically internally coupled system, as illustrated in Fig. 34. Choosing a shunt capacitance of $c_s = -5.08$mF results in an equivalent stiffness of k_s = -30. This specific choice

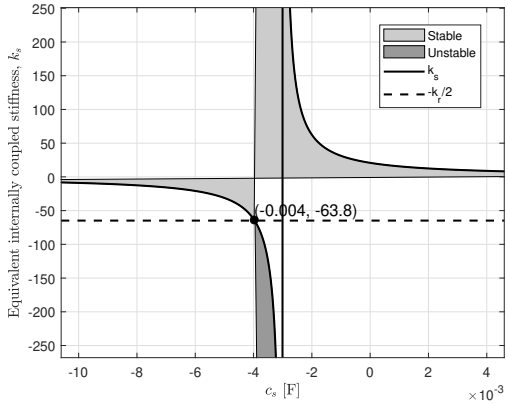

Figure 36: Stability Area of the Electromechanical Internally Coupled Lumped-Mass System: Exploring the Interplay Between Equivalent Stiffness k_s and Shunt Capacitance c_s. Parameters: $n = 4$, $m_m = 56$ g, $m_r = 33.6$ g, $k_m = 150$ N/m, $k_r = 129.6$ N/m, $\theta = 0.25$ N/V, $R = 500\ \Omega$, $c_p = 1.5 \times 10^{-3}$ F.

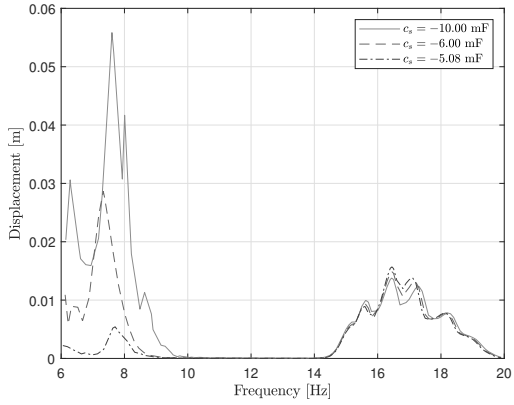

Figure 37: Transmittance Comparison of Electrical Internally Coupling with Shunt Circuit for $\theta = 0.25$ and $c_p = 1.5$mF, Demonstrating the Impact of an Equivalent Negative Stiffness.

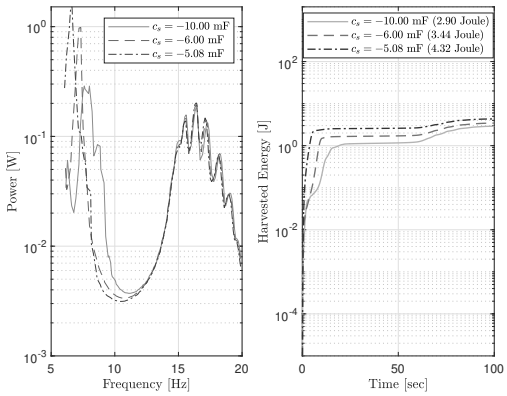

Figure 38: Harvested Power and Energy across Different Shunt Capacitances for $\theta = 0.25$ *and* $c_p = 1.5$mF

not only introduces an equivalent negative stiffness into the system, enhancing energy harvesting capabilities across varied frequency spectrums and enabling the creation of a lower-frequency band gap (see Fig. 37). Compared to mechanical internal coupling, this provides more flexibility in tuning the band gap across different frequencies.

The results underscore the intricate balance required between nonlinearity parameters and system efficiency, opening avenues for the optimization of energy harvesters in practical applications. Future studies are anticipated to delve deeper into electromechanical nonlinearity models, with an emphasis on scalability, parameter-specific impacts, and the development of feedback circuits for adaptive systems. The transition to distributed parameter models also stands out as a promising direction for achieving a closer representation of physical systems in piezoelectric energy harvesting research.

5.4 Distributed Parameter Model of Mechanical Internally Coupled Resonators

By introducing an internal linear coupling term, κ, within the resonators illustrated in Fig. 39, the system evolves into an interconnected pair of resonators. This transformation creates an environment where the displacements of the resonators are no longer independent but coupled. Specifically, the displacement of one resonator influences the displacement of the other, establishing a dynamic interaction. The energy associated with this coupling is quantified by the coupling potential energy, in which each pair of resonators (1 and 2, 3 and 4, 5 and 6, etc.) forms a system with two degrees of freedom:

$$V_c(t) = \frac{1}{2}\kappa \left(z_{r_1}(t) - z_{r_2}(t) + w\left(x_{r_1}, t\right) - w\left(x_{r_2}, t\right)\right)^2 \tag{139}$$

The equations for the coupled oscillator system can be formulated as follows:

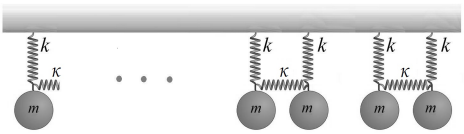

Figure 39: Locally resonant metastructures with internally coupled resonators. Each pair of resonators forms one unit cell, with m representing the mass of the resonators, c the damping, k the stiffness of the resonators, and κ the internal coupling stiffness between them.

$$\ddot{z}_m(t) + 2\zeta_m\omega_m\dot{z}_m(t) + \omega_m^2 z_m(t) - \sum_{r=1}^{N_r/2}\left(m_{2r-1}\omega_{2r-1}^2 z_{2r-1}(t)\phi_m\left(x_{2r-1}\right) + m_{2r}\omega_{2r}^2 z_{2r}(t)\phi_m\left(x_{2r}\right) = \mathcal{Q}_{b_m}, \quad m = 1, 2, \ldots, N_m, \text{ and } N_r \in 2\mathbb{N}\right) \tag{140}$$

Meanwhile, the equation for the resonators is given by:

$$\ddot{z}_{2r-1}(t) + 2\zeta_{2r-1}\omega_{2r-1}\dot{z}_{2r-1}(t) + \omega_{2r-1}^2 z_{2r-1}(t) + \sum_{m=1}^{N_m}\ddot{z}_m(t)\phi_m\left(x_{2r-1}\right) + \beta\frac{\kappa}{m_{2r-1}} = \mathcal{Q}_{b_{2r-1}}, \quad r = 1, 2, \ldots, N_r/2 \tag{141}$$

$$\ddot{z}_{2r}(t) + 2\zeta_{2r}\omega_{2r}\dot{z}_{2r}(t) + \omega_{2r}^2 z_{2r}(t) + \sum_{m=1}^{N_m}\ddot{z}_m(t)\phi_m\left(x_{2r}\right) - \beta\frac{\kappa}{m_{2r}} = \mathcal{Q}_{b_{2r}}, \quad r = 1, 2, \ldots, N_r/2 \tag{142}$$

where

$$\beta = z_{2r-1}(t) - z_{2r}(t) + \sum_{m=1}^{N_m} z_m(t)\phi_m\left(x_{2r-1}\right) - \sum_{m=1}^{N_m} z_m(t)\phi_m\left(x_{2r}\right) \tag{143}$$

These equations characterize the underlying dynamics of both the beam and the internally linear coupled resonator system. The Laplace transform of Eq. (140) with zero initial conditions results in Eq. (144).

$$(s^2 + 2\zeta_m\omega_m s + \omega_m^2)Z_m(s) - \sum_{r=1}^{N_r/2}\left(m_{2r-1}\omega_{2r-1}^2 Z_{2r-1}(s)\phi_m(x_{2r-1}) + m_{2r}\omega_{2r}^2 Z_{2r}(s)\phi_m(x_{2r})\right) = Q_{b_m}(s) \tag{144}$$

Given that the forces $\mathcal{Q}_{b_{2r-1}}$ and $\mathcal{Q}_{b_{2r}}$ are equal to $-\ddot{w}_b(t)$, and considering that $m_{2r-1} = m_{2r}$ or identical mass m_r for all resonators, along with the distribution of numerous resonators along a beam, it is assumed that the derivative of position

within each unit cell is the same, indicated by $dx_{2r-1} = dx_{2r}$. This reflects a uniform position derivative across all resonators. Furthermore, the following relationships are established: $m_{2r-1} = \mu m(x_{2r-1})dx_{2r-1}$, and $m_{2r} = \mu m(x_{2r})dx_{2r}$.

$$\lim_{N_r\to\infty} \sum_{r=1}^{N_r/2} m\left(x_{2r-1}\right)\phi_m\left(x_{2r-1}\right)\phi_p\left(x_{2r-1}\right)dx_{2r-1} = \frac{1}{2}\delta_{mp}, \quad m,p = 1,2,\ldots \tag{145}$$

$$\lim_{N_r\to\infty} \sum_{r=1}^{N_r/2} m\left(x_{2r}\right)\phi_m\left(x_{2r}\right)\phi_p\left(x_{2r}\right)dx_{2r} = \frac{1}{2}\delta_{mp}, \quad m,p = 1,2,\ldots \tag{146}$$

Taking the Laplace transform of equations (141) and (142), and applying the orthogonality of the mode shapes as demonstrated in Eqs. (145) and (146), results in the derivation of the transfer function for a metastructure with internally coupled resonators, as represented in Eq. (147).

$$\frac{Z_m(s)}{Q_{b_m}(s)} = \frac{1}{s^2\left(1+\frac{\mu\omega_{2r-1}^2}{s^2+\omega_{2r-1}^2}\right)\left(1+\frac{\frac{\mu}{4}\omega_{2r}^2}{s^2+\omega_{2r}^2}\right)+\omega_m^2}, \quad m = 1,2,\ldots,N_m \tag{147}$$

The transfer function presented in Eq. (147) incorporates coupling effects through the κ parameter, allowing for the interaction between multiple resonators, denoted as ω_{2r-1} and ω_{2r}. This interaction can lead to complex dynamic behavior, including the potential for multiple bandgaps or more pronounced resonant effects. The integration of damping elements for both the plain structure and the resonators can be conveniently executed at this stage.

In distributed parameter systems, such as beams, the resonators are two-degree-of-freedom (2 DOF) systems. It can be proven that $\omega_{2r-1} = \omega_r$, where ω_r is the natural frequency of a resonator when it is not coupled with its adjacent resonator. Additionally, $\omega_{2r} = \sqrt{\omega_{2r-1}^2 + \frac{2\kappa}{m_r}}$, where κ is the mechanical coupling coefficient and m_r is the mass of the resonator. This framework leads to the formation of secondary bandgaps in metastructures with internally coupled resonators. These bandgaps are associated with a 180-degree phase shift in the resonators. Consequently, such metastructures exhibit both primary and secondary bandgaps, a distinct feature compared to traditional structures. The condition of no stretching in the coupling spring essentially renders its influence negligible. Consequently, this scenario simplifies the equation, reducing it to a form that corresponds to the conventional metastructure dynamics, as established in Eq. (38). This simplification allows for a more straightforward analysis of the metastructure by reverting to a more basic, yet fundamental, form of the equation. On the other hand, if the resonators differ in frequency or have the same frequency but with a phase difference, the parameter κ experiences stretching. This results in an additional pole and zero, creating an extra bandgap.

Now, leveraging the transfer function method enables the utilization of the well-known root locus analysis. By considering the modal response as the closed-loop transfer function of a negative feedback system, which incorporates a proportional feedback gain of ω_m^2, and defining the feedforward transfer function as $G(s)$, as specified in Eq. (148), one can observe this interpretation.

$$G(s) = \frac{s^2 + \omega_{2r-1}^2}{s^2\left(s^2 + \omega_{2r-1}^2 + \mu\omega_{2r-1}^2\right)} \frac{s^2 + \omega_{2r-1}^2 + \frac{2\kappa}{m_r}}{\left(s^2 + (1 + (\frac{\mu}{4}))(\omega_{2r-1}^2 + \frac{2\kappa}{m_r})\right)} \tag{148}$$

The first transfer function accurately represents what is found in a conventional metastructure. This function has two poles at the origin, characteristic of a system's inherent response dynamics. It includes an additional pole at $\sqrt{1+\mu}\omega_{2r-1}$, influenced by the mass of the resonators. This pole is responsible for creating a bandgap with a length of $\sqrt{1+\mu}$, indicative of the system's frequency-selective behavior. The internal coupling of resonators introduces additional dynamics, particularly influencing the system's behavior near resonant frequencies. The second transfer function introduces terms that model the added poles and zeros in the metastructure due to the internal coupling of resonators. In this function, the roots progress from zero at ω_{2r} to a pole at $\sqrt{1+\frac{\mu}{4}}\omega_{2r}$, creating a bandgap with a length of $\sqrt{1+\frac{\mu}{4}}$.

The comparative analysis of the root locus plots for a conventional metamaterial and a metamaterial with internal resonator coupling, as depicted in Figures 40 and 41, clearly indicate the influence of the coupling term κ on the system dynamics. Figure 40 illustrates the resonance characteristics and bandgap frequencies of a metastructure, as indicated by the poles of its transfer function. The system's resonances correspond to the imaginary components of these poles. Modal responses of the plain beam are modeled as a closed-loop transfer function with proportional feedback. Bandgap edge frequencies are identified using root locus analysis, with specific zeros and poles on the imaginary axis determining these frequencies. Notably, within the bandgap defined by $\omega_{2r-1} < \omega < \omega_{2r-1}\sqrt{1+\mu}$, and $\omega_{2r} < \omega < \omega_{2r}\sqrt{1+\frac{\mu}{4}}$, no poles are present. Root locus analysis is advantageous for evaluating general linear attachments and facilitating the creation of multiple bandgaps.

As mentioned earlier, the introduction of κ in the coupled system leads to additional zeros and poles, as evidenced by the second root locus in Fig. 41. This modification is characterized by the resonant frequencies $\omega_{2r-1} = 1$(rad/s) and $\omega_{2r} = 1.7$(rad/s), suggesting the emergence of a second bandgap. Moreover, the root locus plot in Fig. 41 (left) indicates that the internal coupling parameter influences the system's pole trajectories. Conversely, the Bode plot (right) reveals a pronounced resonant peak, suggesting an increased selective sensitivity to certain frequencies. While the phase response indicates the overall system's stability under the new coupling condition must be carefully evaluated to ensure robustness, especially in control applications where stability is critical.

Following the approach in Chapter 3, the PWE method is utilized here to analyze wave propagation in metastructures with internally coupled resonators. In the unit cell, the transverse displacements for the first and neighboring resonators are expressed as $z_{2r-1}(t) = \hat{z}_{2r-1}e^{i(\omega t)}$ and $z_{2r}(t) = \hat{z}_{2r}e^{i(G_n a + \omega t)}$, respectively. Assuming equal stiffness and mass for both resonators, $k_{r_1} = k_{r_2} = k_r$ and $m_{r_1} = m_{r_2} = m_r$, the governing equations for the system simplifies as follows:

$$C_1\omega^6 + C_2\omega^4 + C_3\omega^2 + C_4 = 0 \tag{149}$$

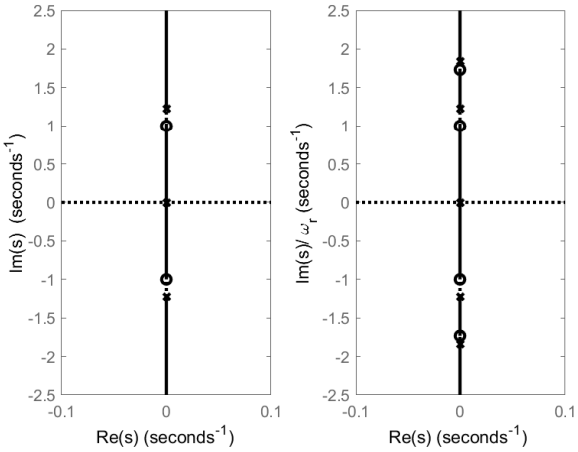

Figure 40: Left: Conventional metastructure root locus with $\omega_m = 0.5$, $\omega_{2r-1} = \omega_r = 1$, $k_r = 1$, $m_r = 1$, and $\mu = 0.5$. Right: Metastructure with internal coupling, exhibiting a narrow band gap, characterized by $\omega_m = 0.5$, $\omega_{2r} = 1.7$, $\kappa = k_r$ and $\mu = 0.5$. The internal coupling's impact on the system dynamics is highlighted by the additional band gap in the right plot.

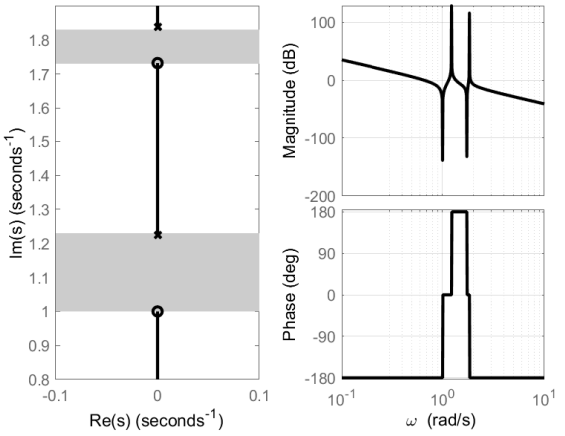

*Figure 41: Bode and root locus plots for Eq. (148). (**Left**) Root locus with $K = \omega_m^2$, showing conventional and internally coupled bandgap for $\mu = 0.5$ and $\kappa = 1$. Markers: system poles at $\omega_m^2 = 0$, solid lines: pole trajectory as ω_m^2 increases. Grey region: bandgap frequency range. (**Right**) Bode plot showing frequency response, including resonance from coupling effect.*

where:

$$
\begin{aligned}
C_1 &= -Am_r^2\rho, \\
C_2 &= m_r^2\left(EIG_n^4 + 2k_r\right) + 2A\rho m_r\kappa + 2A\rho m_r k_r, \\
C_3 &= -\left(2\kappa m_r k_r + A\rho k_r^2 + 2A\rho\kappa k_r + EIG_n^4 m_r^2\left(\kappa + 2k_r\right)\right), \\
C_4 &= EIG_n^4\left(2\kappa k_r + k_r^2\right).
\end{aligned}
\tag{150}
$$

5.5 Numerical Studies

The rectangular beam under analysis is characterized using the properties outlined in Table 2. Additionally, the stiffness of the internally coupled resonators, denoted by κ, is aligned with the resonator stiffness k_r, to ensure a harmonized response between the structural and resonant components of the system.

Figure 42 depicts the dispersion curve of the internally coupled metamaterial beam ($\kappa = k_r$) using the plane wave expansion method. The target frequency corresponds to the resonator frequency. The diagram illustrates two bandgaps: the first is associated with the in-plane behavior of both resonators within each unit cell, while the second bandgap emerges due to the out-of-plane behavior of the two resonators in each unit cell. Here, G_n represents the wave vector number and a denotes the lattice size.

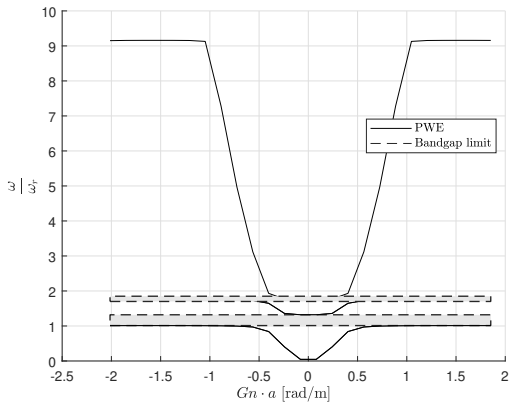

Figure 42: Dispersion curve of an internally coupled metamaterial beam, displaying two distinct bandgaps resulting from in-plane and out-of-plane resonator behavior.

Figure 43 illustrates the transmittance characteristics of a metamaterial beam with internal resonator coupling in terms of tip displacement relative to the base displacement in absolute coordinates. The presence of a common initial bandgap aligns with the theoretical expectations discussed earlier, assuming that all resonators resonate at the same frequency ($\omega_{2r-1} = \omega_{2r} = \omega_r$) and maintain identical phase relationships. In the case of the internally coupled metastructure, an additional bandgap is observed, which substantiates the theoretical premise that variations in resonator frequencies or phase differences can extend the parameter κ. This extension, facilitated by the assumption of a massless coupling spring, introduces new dynamics to the system by adding an extra pole and zero, resulting in the creation of an additional bandgap. The primary bandgap occurs at the target frequency, which corresponds to the resonator's frequency adjusted by the length

factor $\sqrt{1+\mu}$. The secondary bandgap's location is contingent upon the stiffness of the internal coupling and is defined by the length factor $\sqrt{1+\frac{\mu}{4}}$. Notably, the dips in the graph signify areas of low transmittance, indicating reduced vibration at the beam's tip and effectively marking the bandgap regions.

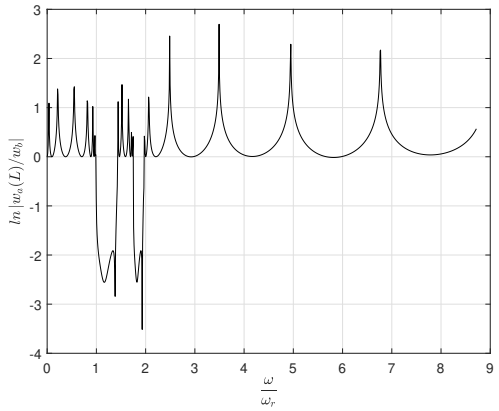

Figure 43: Transmittance plot for a metamaterial beam with internal resonator coupling ($k = k_r$) comprising eight resonators, which equates to four unit cells.

Figure 44 presents a graphical analysis illustrating the influence of varying internal coupling spring constant values, denoted as κ, on the bandgap frequencies within a metastructure. Notably, alterations in κ do not induce substantial shifts in the frequency edges of the primary first bandgap. However, as κ increases, it introduces additional, narrower gaps at frequencies above the rest of the second bandgap. These narrower gaps underscore the sensitivity of the metastructure's dynamic response to specific ranges of internal coupling strength.

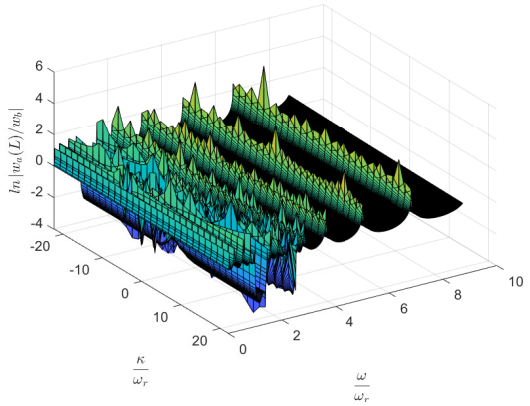

Figure 44: Analysis of the influence of internal coupling stiffness κ on the metastructure's bandgap frequencies in Eq. (147), showing the consistent edge of the first bandgap and the emergence of narrow higher frequency gaps within certain κ ranges.

Figure 45 presents a contour plot of the transmittance across the metastructure as a function of the normalized internal coupling strength, κ/ω_r, and normalized

frequency, ω/ω_r. The color gradient represents the logarithmic scale of transmittance, indicating the level of wave attenuation within the metastructure. Dark regions correspond to high attenuation levels, signifying the presence of bandgaps. As observed, the contour lines delineate the boundaries of the bandgaps, which become more distinct with specific values of internal coupling strength. This visualization provides a comprehensive understanding of how internal coupling affects the bandgap frequencies, offering insights into the precise tuning of the metastructure's vibrational properties. It can be seen that the emergence of additional bandgaps occurs within certain ranges of κ, demonstrating the metastructure's sensitivity to variations in internal coupling. The plot serves as a detailed map for predicting the dynamic behavior of the metastructure under varying conditions of internal coupling, which is critical for applications requiring targeted vibration isolation frequencies.

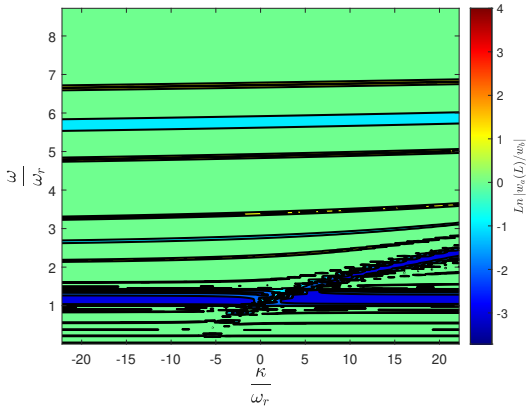

Figure 45: Transmittance contour plot against normalized internal coupling strength and frequency in Eq. (147), highlighting bandgap boundaries and the metastructure's sensitivity to κ variations.

The results reveal that metastructures with internally coupled resonators retain the primary bandgap found in conventional metastructures but also introduce an additional, thinner bandgap at a higher frequency. This secondary bandgap remains separate from the primary one, making it challenging to use internal coupling to merge both bandgaps for vibration isolation in continuous and distributed metastructures. This difficulty arises because the second bandgap's nature is linked to a 180-degree phase change in resonators with identical natural frequencies (ω_r). It would be beneficial to investigate the impact of varying ω_r in different unit cells. Despite these challenges, it is noteworthy that in lumped systems, metastructures with internally coupled resonators significantly widen the bandgap compared to conventional configurations.

5.6 Experimental Study

An experimental study detailed in Fig. 46 focuses on the crafting and integration of each resonator within the metastructure to scrutinize the effects of internal coupling on the system's dynamic behavior. The metastructure features internally coupled resonators made from pure aluminum, each with a thickness of 2 mm,

a width of 20 mm, and a length of 11.3 mm. The properties of the main plane and resonators align with those specified in Table 3. The natural frequency of the unitcell resonator, denoted as ω_{r_k}, is identified to be 85 Hz.

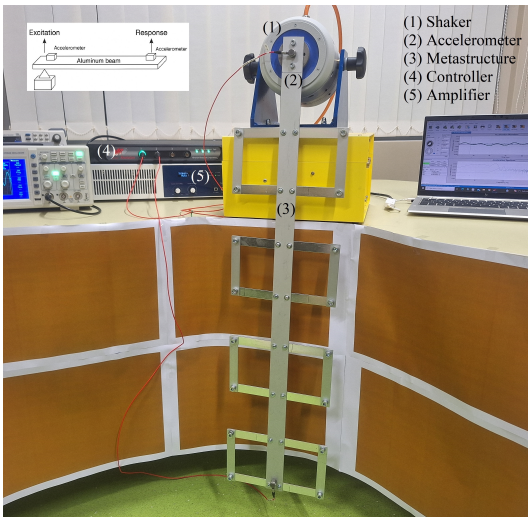

Figure 46: Experimental Design for a Prototype Metastructure Comprising Four Unit Cells of Internally Linked Resonators, Constructed from Pure Aluminum.

5.6.1 Transmittance Measurements

While the experimental outcomes for the standard metastructure corroborated the theoretical forecasts, the scenario markedly diverged with the introduction of internally coupled resonators. Fig. 47 encapsulates the experimental transmittance data, evidencing a distinct behavioral pattern for the metastructure endowed with internal coupling mechanisms. The manifestation of the initial bandgap at 85 Hz, slightly higher than what is observed in the standard metastructure (Fig. 13), aligns with the natural frequency of the coupled resonators. This is indicative of increased stiffness within the unit cell, a direct result of the resonators' collective configuration.

This measurement uncovers a scenario marked by chaos and irregularities in the transmittance spectrum, diverging from the uniform patterns expected based on theoretical projections by researchers in earlier studies, as highlighted in the introduction. Such manifestations underscore the sensitivity of the metastructure's dynamic behavior to the precise integration and configuration of internally coupled resonators, highlighting the challenges inherent in translating theoretical advantages into practical applications. It raises questions about the practical realization of internally coupled resonator benefits, such as significant bandgap widening or enhanced energy dissipation. The results imply that while the concept of internal coupling holds promise in theory, the transition to tangible applications faces challenges that may limit the effectiveness of such designs in real-world vibration control scenarios. Further investigation and refinement of the metastructure design and manufacturing processes are necessary to harness the full potential of internal coupling in metastructures for practical vibration suppression and energy harvesting applications. This claim is further supported by FEM analysis in the following

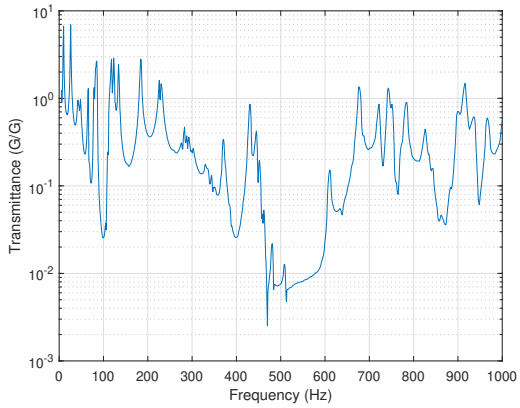

Figure 47: Experimental transmittance results for the metastructure with internally coupled resonators. The first bandgap is observed between 90-110 Hz. This shift can be attributed to the enhanced stiffness of the unit cell, which is composed of a pair of resonators. Measurement devices are located at the base and the tip of the metastructure to capture the full spectrum of its response.

section. FEM simulations here, aimed to offer an analytical view complementary to the experimental insights, especially concerning metastructures with internally coupled resonators. This shift towards numerical modeling serves as a crucial phase in corroborating experimental findings, with the primary aim of substantiating the observed behaviors in experiments, thereby deepening our comprehension of the metastructure's dynamic characteristics.

5.6.2 Observations from FEM Analysis:

Fig. 48 depicts the transmissibility across different internal coupling stiffness, κ, as a function of normalized frequency. These results highlight the appearance of a pronounced second bandgap at a specific internal coupling stiffness, κ, matched to the resonator's stiffness ($\kappa/\omega_r = 0.003$), pinpointing this condition as essential for optimal bandgap definition (see bottom left corner subplot). Such precise matching between the internal coupling and resonator stiffness is key to achieving the desired dynamic behavior in the metastructure.

However, deviations from this optimal κ value lead to significantly disordered responses, underlining the metastructure's acute sensitivity to variations in internal coupling stiffness. Such behavior showcases the challenges associated with achieving and maintaining this precision in stiffness alignment in practical applications. The observed irregularities and chaotic dynamics for non-optimal κ values highlight potential difficulties in predictability and replicability of the metastructure's performance in real-world settings. This sensitivity to the exactness of internal coupling stiffness calls for rigorous precision in the design and manufacturing of such metastructures to ensure their effective implementation and functionality in targeted vibration control applications.

Confirmed by Fig. 49, which provides different transmittance for κ, illustrates the necessity for precise tuning of κ to harness the desired vibration isolation capabilities of the metastructure. The results emphasize the critical nature of parameter optimization in designing metastructures with internally coupled resonators, where

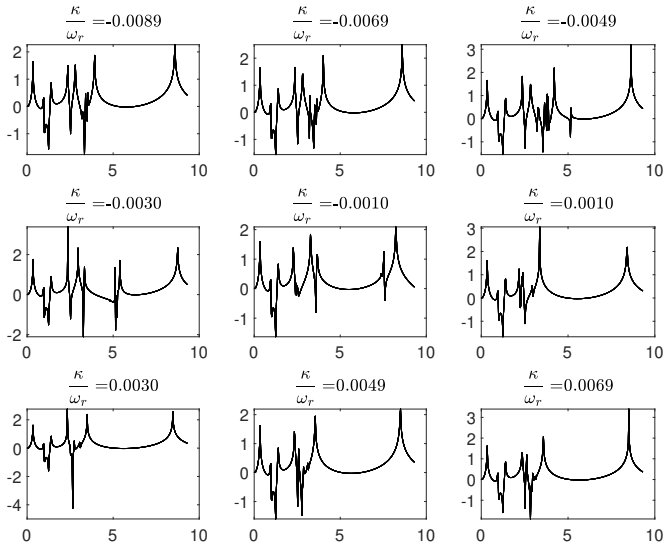

Figure 48: Transmissibility of a cantilever beam for varying stiffness ratios κ, showing system sensitivity and its effects. Subplots detail responses at different κ/ω_r ratios, highlighting a critical condition at $\kappa = k_r$ in the bottom left corner subplot for optimal internal coupling. The y-axis is absolute displacement of beam tip to base displacement, $\ln|w_a(L)/w_b|$, and the x-axis is normalized frequency ω/ω_r.

slight deviations from the optimal stiffness ratio can lead to notable changes in the system's transmissive behavior. The contour plot provided in Fig. 49 visualizes that there are distinct regions where the transmittance drops significantly, indicated by cooler colors, which are indicative of bandgap formation. These regions represent frequencies at which the metastructure effectively blocks wave propagation, a desired feature for vibration isolation applications. The figure indicates that the bifurcation of the bandgap from $\kappa = 0$ to higher values does not exhibit the clarity observed in analytical results, highlighting potential discrepancies between theoretical predictions and practical observations.

The necessity for precision in calibrating κ is evident, as small variations can lead to significant changes in the transmittance landscape. Achieving the exact bandgap properties requires careful adjustment of the metastructure's internal stiffness. While analytical models predict clear transitions and bandgap formations, the observed data might show more gradual changes and less distinct boundaries between bandgap regions. This disparity highlights the challenges in translating theoretical models into experimental or real-world scenarios.

The irregularities and variations presented in the FEM results underscore the imperative for experimental studies to authenticate and fine-tune the theoretical models, thereby confirming their relevance and effectiveness in real-world applications.

In Figs. 50 and 51, an internal coupling mechanism is demonstrated at work within the metastructure, where each pair of resonators acts as a unit cell. Fig. 50 demonstrates the initial out-of-plane oscillations that give rise to the primary

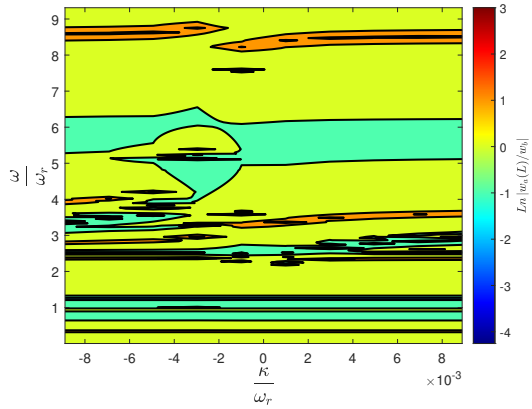

Figure 49: Contour plot of transmittance for varying κ, illustrating the frequency-dependent formation and bifurcation of the bandgap. The plot captures the perturbations and potential destabilization inherent to varying internal coupling stiffness, underscoring the need for precise κ calibration. It also highlights the discrepancies between analytical predictions and observed bandgap clarity.

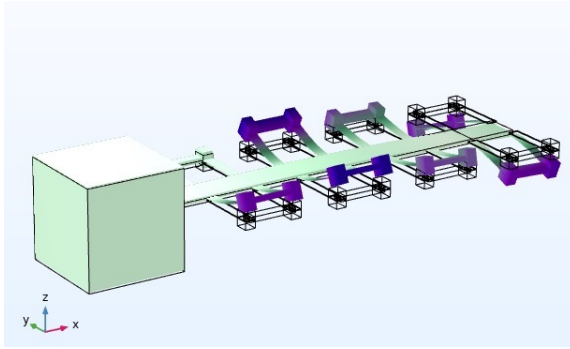

Figure 50: Metastructure with internally coupled resonators configured as unit cells.

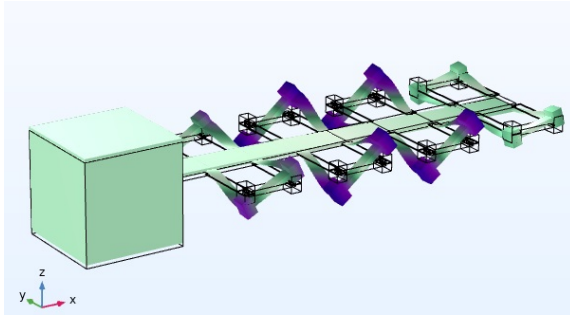

Figure 51: Visual representation of the mechanism leading to the second bandgap in the internally coupled metastructure.

bandgap, analogous to the behavior observed in conventional metastructures. As the excitation frequency increases, the system temporarily reverts to normal vibrational modes before encountering a specific frequency where the resonators within each cell commence vibration in opposing directions. This antiphase motion, depicted in Fig. 51, signifies the onset of the secondary bandgap due to the stiffness matching between the resonator and the internal coupling. However, the crucial insight is that despite the exact stiffness alignment (resonators and internal couple stiffness), merging the primary and secondary bandgaps to expand the bandgap width is not feasible. The inherent nature of the secondary bandgap's formation in such metastructures prevents the amalgamation of multiple bandgaps, thus questioning the practical application of internally coupled resonators in continuous metastructures.

To consolidate the findings, experimental assessments were meticulously executed in configurations devoid of gravitational bias, both vertical and horizontal, ensuring the authenticity of the dynamic behavior observed in the metastructures. The outcomes for the standard metastructure without internal coupling resonated well with the theoretical anticipations, affirming the models' predictive reliability.

Conversely, when internal coupling was introduced in the metastructures, the experimental data diverged from the theoretical expectations. The finer points of the FEM analysis brought to light the necessity for an exact match in the stiffness of the internal coupling and the resonators (κ to k_r). Replicating this precise parameter in a physical experimental setup posed substantial challenges due to the limitations inherent in manufacturing precision. Furthermore, the pursuit to merge multiple bandgaps into a wider singular bandgap was stymied by the intrinsic characteristics of the second bandgap's formation within these metastructures, thus calling into question the feasibility of utilizing internally coupled resonators in metastructures.

Future research could focus on developing new manufacturing techniques or material configurations that mitigate the current limitations. Innovations in precision engineering and design optimization may hold the key to successfully harnessing the full potential of internally coupled resonators. Further studies could also explore alternative mechanisms for bandgap manipulation that may offer more practical and flexible solutions for real-world applications.

5.7 Summary

This chapter has provided an in-depth exploration of metastructures incorporating internally coupled resonators, focusing on both theoretical modeling and practical applications. By employing mathematical models, finite element analysis, and experimental studies, the chapter has illuminated the dynamics and potential of using internally coupled resonators for enhanced vibration control and energy harvesting.

While the pioneering research by Hu et al. [75], and related studies [97], have highlighted the theoretical benefits of internal coupling in creating secondary bandgaps and boosting energy harvesting efficiency, our findings underscore the difficulties faced when translating these concepts into practical applications [14]. The challenges identified, such as the precision required in assembly and the limitations in merging multiple bandgaps, were substantiated through experimental observations and reinforced by FEM analysis, revealing a nuanced understanding of the real-world applicability of internally coupled resonator metastructures.

Here are the key points summarizing the contributions and insights gained:

• The chapter introduced and detailed lumped and distributed parameter models for analyzing the dynamics of metastructures with internally coupled resonators. The lumped models provided insights into unit cell interactions, while distributed models offered a more comprehensive view of wave propagation and bandgap behavior.

• Internal coupling mechanisms enabled the formation of secondary bandgaps and enhanced tunability. However, in distributed metastructures, merging multiple bandgaps to broaden the attenuation range remains challenging due to structural constraints and complex wave interactions.

• The transition from theoretical models to practical applications, substantiated by FEM analysis, revealed significant challenges, including the precision required in manufacturing and the sensitivity of system performance to structural variations. These findings underscore the importance of meticulous design and optimization.

• Numerical studies on lumped models clarified localized dynamics and demonstrated potential for enhanced vibration suppression and energy harvesting. Experimental and numerical validation of distributed models confirmed theoretical predictions but revealed practical limitations, such as structural sensitivity and limited bandgap merging.

• The exploration of internal coupling in metastructures presents a valuable case study of how advanced material concepts transition from theory to practice. While several limitations were identified, the findings open new directions for future research.

6 Streamlining Metastructure Modeling: More Techniques for Enhanced Functional Diversity

This chapter explores the integration of AI-driven optimization, piezoelectric actuation, and notch filter technology in the design and optimization of metastructures. It focuses on using machine learning and AI for parameter estimation and optimizing notch filters. The aim is to improve modeling accuracy by estimating mathematical models through experimental data. A new mathematical closed-form transfer function for piezoelectrically-actuated metastructure is derived, and stability analysis is performed. The chapter also discusses optimizing the parameters of piezoelectrically-actuated metastructures to enhance their performance, specifically by deepening the bandgap.

6.1 AI-Driven Optimization of Metastructures: Analytical and Experimental Approaches for Parameter Estimation of Metastructure

This section delves into the AI-driven optimization of metastructures through both analytical and experimental approaches, focusing on the precise estimation of damping ratios critical for effective vibration control. By employing a suite of optimization algorithms, this study integrates AI techniques with robust mathematical modeling to enhance the design and performance of metastructures. The methodologies adopted here bridge theoretical predictions with real-world experimental validations, thereby reinforcing the accuracy and applicability of the models. In this section, a Hybrid Genetic Algorithm–Particle Swarm Optimization (GA-PSO) method is applied to estimate damping parameters that influence the accuracy of metastructure response predictions. While all physical parameters of the metastructure were available and measurable, the structural and resonator damping ratios could not be directly obtained. Hence, optimization algorithms were employed for parameter estimation. This approach ensures the analytical model aligns closely with experimental observations and supports the development of accurate, control-oriented dynamic models.

6.1.1 Estimation of Damping Ratio in Metastructures

The study employs modal analysis within a distributed parameter model to explore the dynamic characteristics of a metastructure, consisting of an aluminum rectangular beam with integrated local resonators. This analytical approach facilitates the identification of natural frequencies and mode shapes, which are used for the control of the structure's bandgap properties.

The transfer function, detailing the relationship between the displacement of the structure's m-th mode and the corresponding excitation force, is presented earlier in Eq. (38) as follows:

$$\frac{Z_m(s)}{Q_{b_m}(s)} = \frac{1}{s^2\left(1+\frac{\mu(2\zeta_r\omega_r s+\omega_r^2)}{s^2+2\zeta_r\omega_r s+\omega_r^2}\right)+2\zeta_m\omega_m s+\omega_m^2}, \quad m=1,2,\ldots,N_m \tag{151}$$

In this context, $Z_m(s)$ represents the Laplace-transformed displacement of the structure's m-th mode, $Q_{b_m}(s)$ symbolizes the Laplace-transformed external force, ζ_m and ζ_r are damping ratio of structure's m-th mode and resonator, respectively.

ω_m and ω_r are the natural frequencies of the structure's m-th mode and the resonators, respectively.

In the study of metastructures, estimating the damping ratio ζ_r from experimental data is pivotal for the effective modeling of vibration suppression and dynamic response tuning. Various methods can be employed for this estimation, each with its specific advantages and requirements. These include Frequency Response Analysis, System Identification Techniques, Energy Decay Method, Optimization Algorithms, and Bayesian Inference.

To estimate the damping ratio, optimization algorithms are utilized due to their ability to navigate complex, multidimensional parameter spaces. These algorithms are particularly effective in situations where the objective function is nonlinear or nonsmooth, as often encountered in real-world data from metastructures. An objective function is defined to quantify the error between the experimental data and theoretical model predictions. Typically, the Sum of Squared Errors (SSE) is used for this purpose. Several algorithms are considered for algorithm Selection and configuration:

Nelder-Mead Simplex Algorithm: A heuristic search method ideal for nonsmooth functions, enabling robust initial parameter estimation without derivatives. Genetic Algorithm (GA): This algorithm excels in finding global solutions in complex problems characterized by multiple local minima.

Particle Swarm Optimization (PSO): It simulates a social process, effectively honing in on global optima, especially in continuous optimization scenarios.

Artificial Bee Colony (ABC) Algorithm: Inspired by the foraging behavior of bees, it balances local and global search effectively, useful for complex parameter estimation tasks.

Hybrid GA-PSO: Combining GA's exploration and PSO's exploitation efficiency, this approach aims to quickly and reliably find global optima in multi-modal data landscapes.

For implementation, each algorithm is configured with appropriate parameters such as learning rate, population size, mutation rates, and particle velocities. The choice and configuration of the algorithm depend on the specific requirements of the problem and the nature of the experimental data. The selected algorithm is run to optimize the ζ_r, using the objective function to guide the search. This process is iterative, involving continuous evaluation and refinement based on performance metrics.

6.1.2 Structural Damping Impact on Metastructural Dynamics

Before delving deeper into the estimation of damping in metastructures, it is first necessary to understand how they influence bandgap characteristics. It evaluates how changes in both structural and resonator damping ratios impact the effectiveness of vibration suppression in metastructures. Through detailed frequency response analyses of Equation 151, the study aims to clarify how various damping parameters affect the dynamic responses of metastructures, offering primary insights for optimizing design strategies to enhance vibration control.

Figure 52 depicts the frequency response functions illustrating the impact of varying damping ratios on the dynamic response of a metastructure. The upper plot reveals that altering the structural damping ratio influences the overall dynamic response but leaves the bandgap region largely unaffected. In contrast, the lower plot indicates that changes in the resonator damping ratio significantly alter the

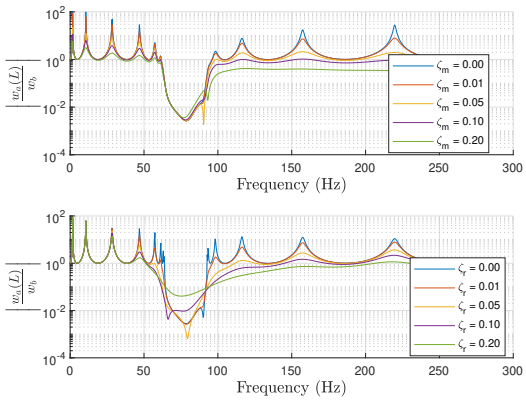

Figure 52: Transmittance showcasing the impact of damping ratios in the main plain and local resonators on the dynamic response of a metastructure, particularly in modifying the bandgap regions.

bandgap region's dynamics, highlighting the critical role of resonator damping in tuning the metastructure's vibration suppression capabilities.

6.1.3 Numerical Studies and Experimental Approaches for Parameter Estimation of Metastructur

This section aims to conduct an examination of structural damping estimation through a dual approach involving both simulated models and experimental validations. The primary aim is to substantiate the accuracy of simulation outcomes within the context of real-world experimental conditions. The methodology involves the calibration of the numerical model to ensure its parameters align with empirical observations, coupled with the use of an experimental framework structured around two simple beams of different lengths and material properties, as well as a metastructure beam. The analysis will include a detailed vibrational analysis for each setup, and identification of natural frequencies, mode shapes, and damping ratios, with a particular focus on conditions that foster the creation of bandgaps. The expected outcome is the validation of theoretical models through empirical data, leading to an enhanced understanding of dynamic behaviors within closed-form presentation of metastructures, particularly through the practical examination of bandgaps. This approach integrates theoretical modeling with practical experiments to deepen the understanding of structural dynamics in metastructures [15].

6.1.4 Noisy Signal: Case Study #1

The initial phase of this investigation involves simulating the transmittance of a metastructure subject to a noisy signal. This scenario is quintessential in real-world applications where operational conditions are rarely ideal and noise is an inherent part of the system dynamics. The primary objective is to develop an algorithm capable of deducing the damping ratio of the resonator within this noisy environment. The challenge here lies in distinguishing the true signal from the noise to accurately identify the system's damping characteristics, which are crucial for predicting the metastructure's behavior and optimizing its performance.

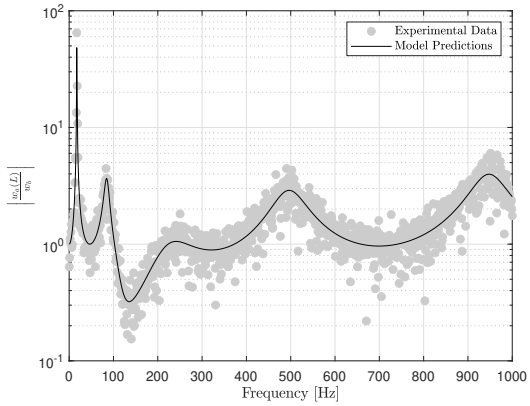

Figure 53: Comparison of the beam's transmittance: noisy signal versus model predictions, highlighting the algorithm's effectiveness in identifying transmittance characteristics within the bandgap frequency range. Parameters as listed in Table 6.

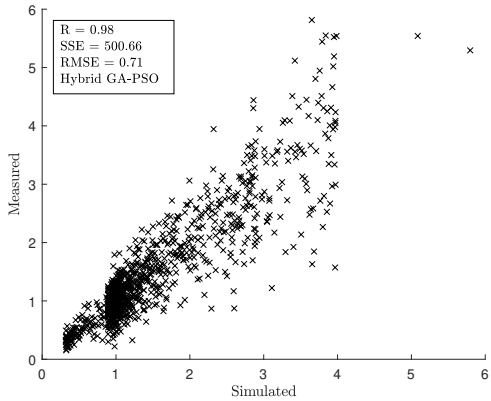

Figure 54: Scatter plot demonstrating the correlation between measured and simulated data via the Hybrid GA-PSO algorithm, evidencing high model accuracy with a correlation coefficient (R) of 0.98.

Table 6: Geometric and material properties of Case Study #1

Parameter	Value	Parameter	Value
L_m	0.3 m	m_r	140 g
w_m	40 mm	k_r	72 kN/m
h_m	3 mm	N_r	8
ρ_m	2710 kg/m^3	N_m	8
E_m	69.5 GP		

The algorithm's performance in calculating ζ_r is illustrated in Fig. 53. The nominal value of the highly damped resonator ζ_r is 0.2, and the results are contextualized within the parameters outlined in Table 6, which details the geometric and material properties of the rectangular aluminum beam under investigation. The findings indicate the algorithm's robustness in parameter estimation amidst experimental uncertainties. Figure 54 presents a scatter plot comparing measured data against values simulated by the Hybrid GA-PSO algorithm. The tight clustering of data points around the line of unity and the high correlation coefficient (R = 0.98) suggest a strong agreement between the model's predictions and the measured data. The scatter plot highlights the algorithm's precision in estimating the damping parameter ζ_r, as evidenced by the low root mean square error (RMSE = 0.71) and the sum of squared errors (SSE = 500.66), which quantify the model's predictive accuracy. This figure substantiates the Hybrid GA-PSO's efficacy in capturing the underlying dynamics of the metastructure under study.

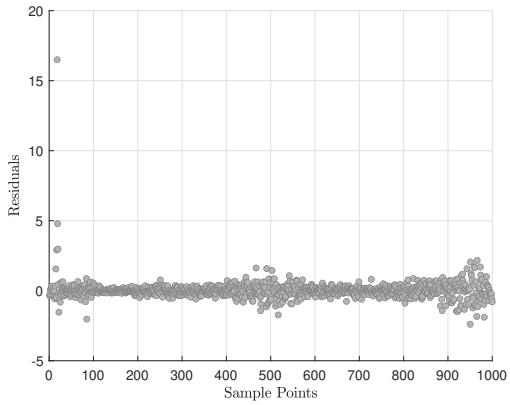

Figure 55: Residual plot from the Hybrid GA-PSO model prediction demonstrating the residuals' distribution against sample points, underscoring the model's accuracy with a high coefficient of determination (R^2).

Figure 55 reveals the model's residual distribution, crucial for evaluating the Hybrid GA-PSO algorithm's accuracy in estimating ζ_r. The residuals, mostly centered around zero, suggest a strong model fit, corroborated by a high R^2 value (0.91). Outliers at the start may signal deviations due to experimental anomalies or noise, warranting further investigation to enhance the algorithm's reliability.

6.1.5 Experimental Setup: Case Study #2

As detailed in Chapter 3, the experimental setup employed a specifically designed cantilever beam configuration. The procedures and equipment used are outlined therein. The current experiments build upon the foundational tests described previously to explore additional variables and their impact on the system's dynamic responses.

The response of the cantilever beam under base excitation generates data on the dynamic behavior of metamaterials. The data obtained from this experimental setup will be further analyzed and compared with model predictions.

Since the resonators are not incorporated into the system for the first part of the experiment, the focus shifts to estimating the modal damping ratio ζ_m of the main structure. The GA algorithm is used for the first case study due to its robustness and to provide a clear baseline for performance evaluation. However, drawing on conclusions from the previous sections, the Hybrid GA-PSO algorithm emerged as a strong candidate for such estimations in the subsequent studies.

To validate the theoretical models and optimization approaches outlined in this study, the first experimental setup was constructed, as illustrated in Fig. 56. The specifications of the prototype are detailed in Table 7.

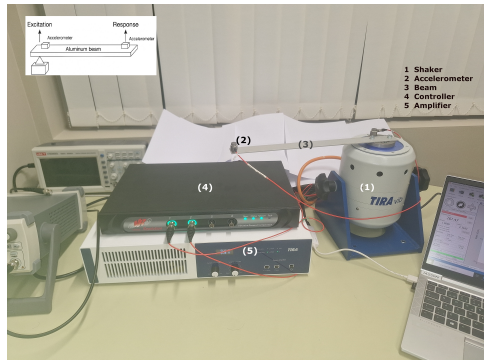

Figure 56: A cantilever beam experimental setup with detailed geometric and material properties listed in Table 7. The setup includes a shaker for base excitation and Dytran accelerometers at the beam's base and tip for dynamic response measurements, all interfaced with a power amplifier and a control system.

Table 7: Geometric and material properties of the studied rectangular aluminum short beam

Parameter	Value	Parameter	Value
L_m	0.3 m	E_m	69.5 GP
w_m	40 mm	ρ_m	2710 kg/m^3
h_m	2 mm	N_m	8

Figure 57 displays a transmittance response curve, comparing GA algorithm estimations to experimental data. This comparison reveals a high degree of accuracy in the lower frequency range, where the GA's predictions and the experimental observations align closely. Nonetheless, as we move to higher frequencies, the model's predictions start to deviate from the empirical data, suggesting that the GA's estimations become less reliable.

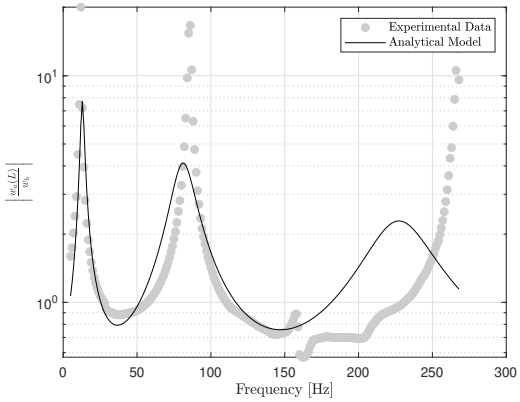

Figure 57: Transmittance response of a cantilever beam with GA algorithm estimations, for structural modal damping ratio ζ_m estimation.

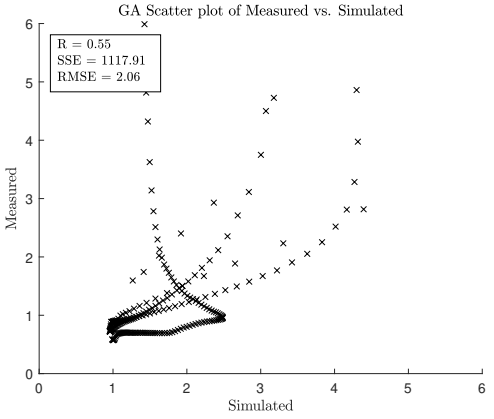

Figure 58: Correlation between the measured and predicted values of the modal damping ratio.

The scatter plot in Fig. 58 demonstrates a spread of data points that reveals the model's limitations, particularly beyond the sixth modal frequency. While the model's estimations align sufficiently with the experimental data within the bandgap frequency region, the coefficient of determination, with an $R^2 \approx 0.3$, indicates a moderate fit. This value, considerably below the ideal of 1 , suggests that the model does not comprehensively explain the variance of the experimental data, especially at higher frequencies.

While most residuals cluster around the baseline in Fig. 59 indicating decent model accuracy for a range of frequencies, the plot also shows significant outliers. These outliers become more pronounced at higher sample points, underlining potential weaknesses in the model, particularly at higher modal frequencies.

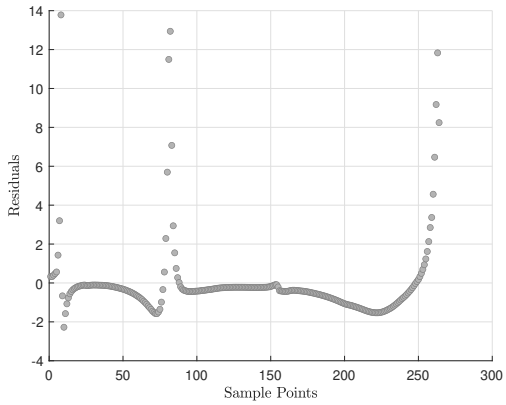

Figure 59: Residual plot of the experimental data versus the model predictions, identifying areas of discrepancy and potential model improvements within the context of Case Study #2.

In this case study, inaccuracies in determining the higher modal frequencies and subsequently modal damping are not solely attributed to the optimization algorithms, but also arise from limitations within the transfer function and modal expansion methodologies employed. These techniques, combined with assumptions such as idealized boundary conditions and material uniformity made during model derivation, contribute to the reduced precision in parameter estimation at higher modal frequencies. The complex dynamic behavior observed at these frequencies underscores the need for advanced modeling techniques to more accurately capture the system's behavior across its entire modal spectrum.

6.1.6 Experimental Setup: Case Study #3

The next configuration is a long beam, as shown in Fig. 60. The specifications of the prototype are detailed in Chapter 2, Table 3. The various optimization algorithms such as GA, PSO, ABC, Hybrid GA-PSO, and Nelder-Mead are utilized to assess their effectiveness in estimating the modal damping ratio.

Figure 61 presents the transmittance response, comparing the experimental data with theoretical model prediction. The plot illustrates the algorithm's effectiveness in estimating ζ_m, crucial for accurate dynamic modeling of the cantilever beam. The close alignment of the model predictions with the experimental data across the frequency spectrum validates the accuracy of all algorithms including Hybrid

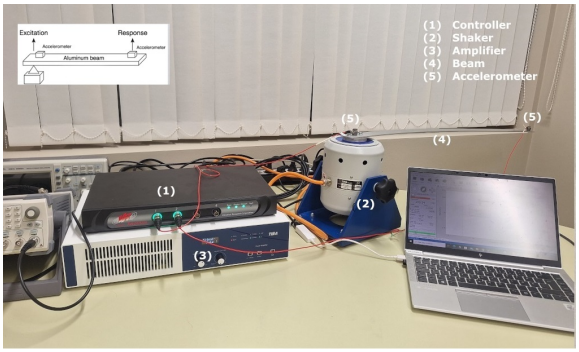

Figure 60: Experimental setup with a longer cantilever beam, reusing the same measurement and control components as the previous experiment. A schematic in the top right illustrates the direction of excitation and response measurement.

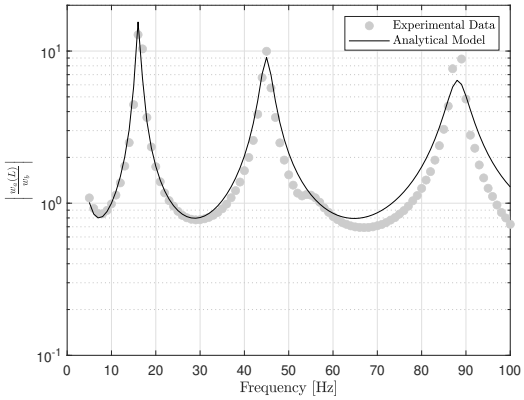

Figure 61: Transmittance response of a cantilever beam: comparison between experimental measurements and analytical predictions incorporating the estimated structural damping ratio ζ_m, identified using the Hybrid GA-PSO algorithm.

GA-PSO algorithm. This successful estimation of ζ_m underscores the potential of hybrid optimization techniques in flexible structures, where accurate damping characterization is essential for designing and controlling dynamic systems.

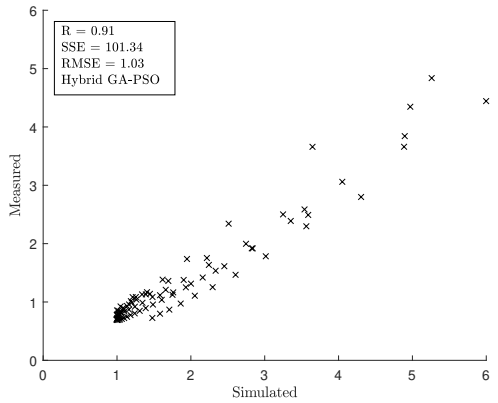

Figure 62: Scatter plot comparing measured data to Hybrid GA-PSO simulated estimations, demonstrating the algorithm's efficacy in predicting the structural modal damping ratio (ζ_m) with a correlation coefficient (R) of 0.91.

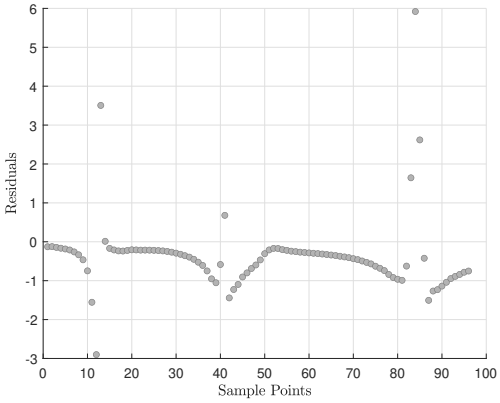

Figure 63: Residual analysis of the Hybrid GA-PSO model predictions showcasing the estimation accuracy across the experimental data set, with a focus on identifying outlier discrepancies for further model refinement.

The scatter plot in Fig. 62 illustrates the correlation between the measured and simulated data points using the Hybrid GA-PSO algorithm for estimating the modal damping ratio. The correlation coefficient (R) of 0.91 indicates a strong positive relationship, suggesting that the algorithm can predict the system's behavior with a high degree of accuracy. The SSE and RMSE provide further insight into the model's precision, with lower values indicating a closer fit to the experimental data. In this case, an RMSE of 1.03 reflects a reasonably accurate model, although there is room for improvement in minimizing the prediction error.

The residuals plot in Fig. 63 predominantly indicates a satisfactory model fit,

as evidenced by the majority of residuals clustering near the zero line. However, the presence of outliers with higher residuals at the structure's modal resonant frequencies suggests that the model's predictions diverge from the experimental data at these critical points. This could be due to the heightened sensitivity of the system's response to parameter variations at resonance.

6.1.7 Experimental Setup: Case Study #4

The experimental setup is captured in Fig. 64, illustrating the prototype of metastructure real-world application. The resonators, integral to the metastructure, were crafted from pure aluminum, featuring a thickness of 2 mm, a width of 20 mm, and a length of 11.3 mm. A set of nuts and bolts served as adjustable tip masses, enabling the fine-tuning of the natural frequency to the target 64 Hz, as determined by FEM analysis.

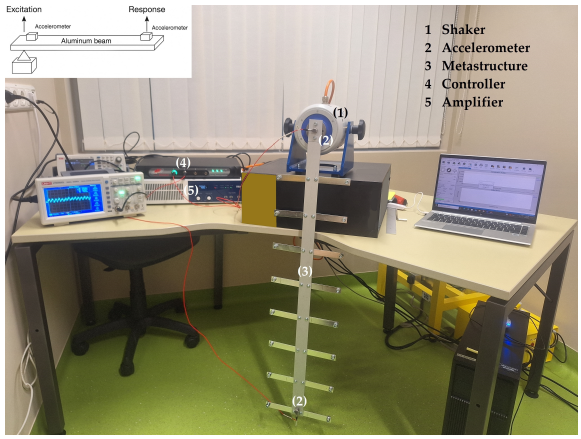

Figure 64: The experimental setup for the metastructure's dynamic analysis. This configuration is instrumental in examining the effects of damping and resonator adjustments on the metastructure's vibrational characteristics.

The data illustrated in Fig. 65 compares experimental data with model predictions that estimate ζ_r using the GA-PSO algorithm. The observed transmittance peaks and troughs align well with the predicted values, particularly in the lower frequency range up to 150 Hz, which includes the designed bandgap region. Beyond this, while the model continues to follow the general trend of the experimental data, some deviations become apparent, suggesting areas for further refinement of the model. Notably, the bandgap's expected impact is clear, with a marked reduction in transmittance indicating effective vibration suppression within the targeted frequency range.

The data depicted in Fig. 66 is indicative of the correlation between the measured and simulated values, obtained through the Hybrid GA-PSO algorithm. The scatter plot, with an R-value of 0.54, suggests a moderate correlation. The SSE of 391.18 and RMSE of 1.21 reflect the discrepancies between the model predictions and the experimental observations. These metrics highlight areas where the model could be further calibrated to enhance its predictive accuracy. Despite these challenges, the model accurately predicts behavior within the critical bandgap frequency region. This indicates that these challenges are influenced more by discrepancies at higher modal frequencies than by those at the targeted bandgap

frequencies.

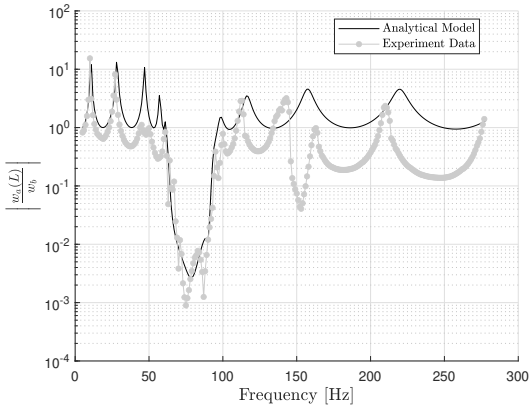

Figure 65: Transmittance response of a metastructure: comparison between experimental measurements and analytical results based on the estimated damping ratios ζ_m and ζ_r.

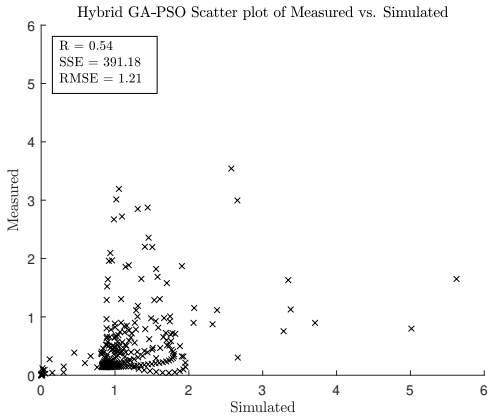

Figure 66: Hybrid GA-PSO Scatter plot of Metastructure's Measured vs. Simulated data in predicting the resonator damping (ζ_r).

Figure 67 presents the residual plot resulting from the algorithm's predictions. The distribution of residuals along the sample points illustrates the model's areas of strength, as well as points where the prediction does not align closely with the experimental data. Together, these figures articulate the performance of the Hybrid GA-PSO algorithm. While the moderate correlation and the residual trends indicate the algorithm's potential, they also suggest that further tuning and validation are necessary for the model to reliably predict dynamic behavior in metastructures.

As compiled in Tables 8 and 9, the different optimization algorithms, while varying slightly in the correlation coefficient (R) and the sum of squared errors (SSE), consistently identified the damping ratios with enough precision for the theoretical model. Upon comparing the results in Table 9, it's evident that the estimated resonator damping ratio values obtained from the Hybrid GA-PSO and Nelder-Mead methods align closely, both indicating a ζ_r of 0.021. This contrasts with the slightly

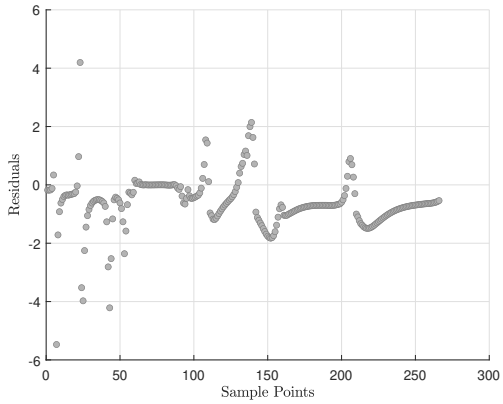

Figure 67: Distribution of residuals from the Hybrid GA-PSO algorithm's predictions.

Table 8: Comparison results of different optimization algorithms in estimating the structural modal damping ratio ζ_m for Case Study #3.

Algorithm	R	SSE	Population size	Estimated ζ_m
GA	0.92	104.57	80	0.0273
PSO	0.92	102.40	80	0.0271
ABC	0.92	103.35	50	0.0268
Hybrid GA-PSO	0.92	101.34	50	0.0273
Nelder-Mead	0.91	101.34	N/A	0.0272

lower estimates from the PSO and ABC algorithms, which may reflect differences in their search strategies or convergence criteria. Notably, the values from the initial table were significantly higher, suggesting a refinement of experimental or algorithmic parameters in the updated analysis. The convergence of estimates in the updated table, particularly for ζ_r, reinforces the robustness of the optimization methods and supports their reliability for accurate metastructure analysis. The hybrid GA–PSO algorithm was configured with crossover and mutation rates of 0.8 and 0.1 respectively, and a PSO inertia weight of 0.7. The fitness function was defined as the Sum of Squared Errors (SSE) between the analytical and experimental transmittance magnitudes. The algorithm terminated after 50 generations or when the fitness change between successive generations fell below 10^{-6}. This hybrid approach was selected to balance exploration and exploitation in the search space, ensuring robust identification of the damping coefficients. The consensus on ζ_m and ζ_r values highlights the algorithms' success in capturing the metastructure's key dynamics. Validation by experimental data emphasizes their potential in designing and optimizing metastructures for enhanced vibration suppression.

6.2 Methodology for Structural Damping Compensation in Distributed Parameter Metastructures through Piezo Actuation with Constant Voltage

In the preceding section, the importance of accurately estimating damping ratios was established, revealing their influence on the dynamic behavior of metastructures, particularly in relation to bandgap efficiency. However, excessive structural

Table 9: Comparison results of different optimization algorithms in estimating the resonator damping ratio ζ_r for Case Study #4.

Algorithm	R	SSE	Population size	Estimated ζ_r
GA	0.93	398.29	80	0.020
PSO	0.92	405.22	80	0.019
ABC	0.91	410.67	50	0.018
Hybrid GA-PSO	0.94	391.18	50	0.021
Nelder-Mead	0.90	420.00	N/A	0.021

damping can adversely affect the depth and efficacy of these bandgaps, leading to diminished vibration suppression capabilities. Recognizing this challenge, the following section explores viable methods to counteract the effects of high damping in metastructures. By integrating piezoelectric elements within the metamaterial structure, it is possible to dynamically adjust the metastructure's characteristics and enhance the bandgap's effectiveness.

Metastructures face the inherent challenge of structural damping, where materials dissipate vibrational energy as heat. This can undermine the effectiveness of the bandgaps crucial for the functionality of metamaterials. To address this issue, piezoelectric actuators are integrated into metamaterial designs. These actuators, which convert electrical energy into mechanical strain and vice versa, can actively modulate mechanical properties such as stiffness. By applying a constant voltage, piezoelectric actuators provide a counterbalancing force that mitigates the effects of structural damping. This helps maintain or restore the desired damping characteristics of the metamaterial. Beyond just countering damping, the actuators also enable adaptive tuning of the bandgaps of the metamaterials to better suit specific operational conditions. Using a constant voltage simplifies the control scheme for actuators, making it easier to implement this damping compensation method across various applications. This approach lays the groundwork for exploring more sophisticated control strategies, such as using variable voltages and notch filters, which will be detailed in further sections of the discussion.

6.2.1 Enabling Methodology for Damping Compensation of Metastructure

The locally resonant metastructure, incorporating piezoelectric actuators, is illustrated in Fig. 68. Employing a distributed parameter model aids in formulating partial differential equations that delineate the system's dynamics, which are subsequently discretized and numerically analyzed to determine the metastructure's modal properties.

The dynamics of the system are captured by unchanged plain beam dynamics (Eq. (67)) and piezo-actuated resonators as follows:

$$m_r \frac{\partial^2 z_r(t)}{\partial t^2} + c_r \frac{\partial z_r(t)}{\partial t} + k_r z_r(t) + m_r \frac{\partial^2 w\left(x_r, t\right)}{\partial t^2} + \vartheta_{p,r} v_{p,r}(t) = \mathcal{F}_{b_r}(t) \tag{152}$$

$$C_{p,r}^* \frac{\partial v_{p,r}(t)}{\partial t} + \vartheta_{p,r} z_r(t) = 0 \tag{153}$$

Equations (67), (152), and (153) address the dynamics of a metamaterial beam system with piezoelectric actuators. Substituting the modal expansion from Eq.

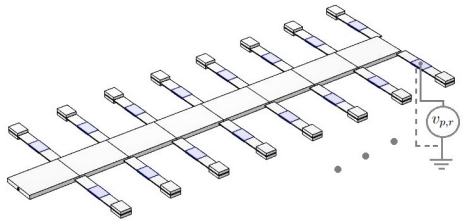

Figure 68: Schematic of a locally resonant metastructure with piezoelectric actuators. Features cantilever beams with tip masses as resonators and piezoelectric elements (with voltage $v_{p,r}$) bonded to alter stiffness dynamically.

(75) into Eq. (67) and Eqs. (152) and (153), and leveraging the orthogonality conditions from Eqs. (70) and (71), simplifies the system dynamics to:

$$\ddot{z}_r(t)+2\zeta_r\omega_r\dot{z}_r(t)+\omega_r^2 z_r(t)+\sum_{m=1}^{N_m}\ddot{z}_m(t)\phi_m(x_r)+\frac{\vartheta_{p,r}}{m_r}v_{p,r}(t)=\mathcal{Q}_{b_r}(t),\quad r=1,2,\ldots,N_r \tag{154}$$

$$C^*_{p,r}\dot{v}_{p,r}(t)+\vartheta_{p,r}z_r(t)=0,\quad r=1,2,\ldots,N_r \tag{155}$$

Here, N_m is the number of structural modes, and N_r is the number of resonators. The term $z_m(t)$ is the modal displacement, while ζ_m and ζ_r are the structural and resonator damping ratios, respectively. The mode shape at the resonator's location is given by $\phi_m(x_r)$. These equations encapsulate the interactions between the structure's modes and the piezo-actuated resonators, forming a solvable system for linear multi-degree-of-freedom dynamics. $C^*_{p,r}$ represents the effective capacitance of the piezoelectric actuator at resonator r, and $\vartheta_{p,r}$ denotes the piezoelectric coupling coefficient, which quantifies the mechanical strain produced by the applied voltage $v_{p,r}(t)$. The term $\vartheta_{p,r}z_r(t)$ reflects the mechanical feedback to the electrical system through the piezoelectric effect, indicating how deformation of the piezo material generates a voltage. This equation links the electrical behavior of the piezoelectric elements with the mechanical vibrations of the resonators, integrating the dynamics of both domains to describe how voltage influences resonator behavior and vice versa, effectively coupling the electrical inputs to mechanical outputs in the metastructure's design.

By applying Laplace transforms and assuming no initial conditions, a set of linear equations in the Laplace domain can be derived.

$$(s^2+2\zeta_m\omega_m s+\omega_m^2)Z_m(s)-\sum_{r=1}^{N_r}Z_r(s)\left(\left(m_r\omega_r^2+2\zeta_r m_r\omega_r s\right)\phi_m(x_r)\right)=\mathcal{Q}_{b_m}(x,s) \tag{156}$$

$$(s^2+2\zeta_r\omega_r s+\omega_r^2)Z_r(s)+\sum_{m=1}^{N_m}Z_m(s)s^2\phi_m(x_r)+\frac{\vartheta_{p,r}^2}{sC^*_{p,r}m_r}Z_r(s)=\mathcal{Q}_{b_r}(s) \tag{157}$$

$$sC^*_{p,r}V_{p,r}(s)+\vartheta_{p,r}Z_r(s)=0 \tag{158}$$

Building on the methodologies and definitions presented in previous chapters, and through mathematical rearrangement, the transfer function for the displacement of the resonator is formulated as:

$$Z_r(s) = \frac{-s^2 w_b - \sum_{m=1}^{N_m} Z_m(s) s^2 \phi_m(x_r)}{s^2 + 2\zeta_r \omega_r s + \omega_r^2 + \frac{k_e^* \omega_r^2}{s}}, \quad r = 1, 2, \ldots, N_r \tag{159}$$

The effective electromechanical coupling of the resonator, denoted as k_e^*, is defined by $k_e^* = \frac{\vartheta_{p,r}^2}{C_{p,r}^* k_r}$. When considering the voltage source as the input, this effective stiffness k_e^* can be expressed through the relationship $k_e^* = \alpha \omega_r v_0 = v_{p,r}$, where ω_r represents the natural frequency of the resonator, v_0 is the voltage applied to the piezoelectric component, and α is an empirical constant with the unit Farads per Coulomb (F/C). After some mathematical manipulation, the transfer function for the displacement of the m-th mode of the structure relative to the excitation force on the same mode is formulated, simplified, and described by Eq. (160). This equation includes terms for modal frequency, damping, and the interaction between the structure's dynamics and the resonator's properties, including the applied voltage.

$$\frac{Z_m(s)}{Q_{b_m}(s)} = \frac{1}{s^2 \left(1 + \frac{\mu(2\zeta_r \omega_r s + \omega_r^2)}{s^2 + 2\zeta_r \omega_r s + \omega_r^2 \left(1 + \frac{v_{p,r}}{s}\right)}\right) + 2\zeta_m \omega_m s + \omega_m^2}, \quad m = 1, 2, \ldots, N_m \tag{160}$$

Here, $Z_m(s)$ and $Q_{b_m}(s)$ represent the Laplace transforms of the displacement response and the external force applied to the m-th mode, respectively. The damping ratios, ζ_r for the resonator and ζ_m for the structure's mode, describe the rate of oscillation decay due to damping, and $v_{p,r}$ represents the voltage applied to the piezoelectric elements of the r-th resonator.

Table 10: Geometric and material properties of the voltage dependant piezo actuation metastructure

Parameter	Value	Parameter	Value
L_m	0.3 m	ζ_r	$0.01 - 0.4$
w_m	40 mm	N_m	8
h_m	3 mm	N_r	8
ρ_m	2710 kg/m^3	v_0	10 V
E_m	69.5 GP	α	0.0976 F/C
ζ_m	0.01	μ	1.39

Adding a piezoelectric actuator to a resonator within a system can indeed influence its stability. The piezoelectric actuator introduces an additional dynamic component to the system, which can modify the system's natural frequencies and potentially introduce new modes of vibration. Depending on how the actuator is applied and controlled, this can lead to changes in the system's stability, due to changing the system's characteristic equations, possibly adding poles to the system's transfer function.

In principle, the actuation can be designed to enhance stability by damping vibrations or controlling specific modes. However, if not carefully managed, the

actuation can also introduce energy into the system at frequencies that resonate with the system's natural frequencies, potentially leading to increased amplitudes of vibration.

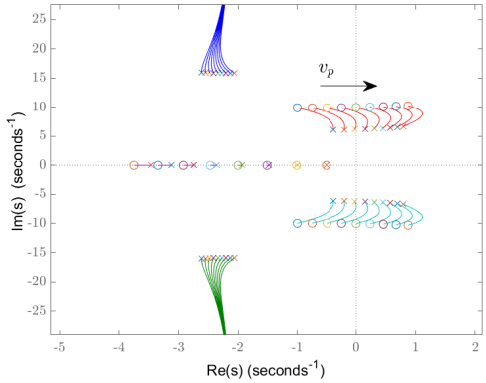

Figure 69: Root locus plot demonstrating the stabilization effect of increasing piezoelectric actuation voltage v_p on stability of metamaterial beam system. System parameters include a mass ratio $\mu = 1$, resonator damping ratio $\zeta_r = 0.1$, resonator natural frequency $\omega_r = 10$, structural damping ratio $\zeta_m = 0.1$, and the first structural natural frequency $\omega_{m_1} = 10$. The plot traces the pole movement across modes, showing enhanced stability with higher v_p, pertinent to the precise dynamic control of metamaterials.

Stability analysis, such as examining the poles' positions in the complex plane or conducting a root locus analysis, becomes essential to predict how variations in control parameters, like the applied voltage, affect stability. The detailed stability analysis of such systems, as well as the dynamic control using variable voltages, have been covered in the associated article [17].

The root locus plot depicted in Fig. 69 provides insight into the dynamic stability of a metamaterial beam with piezoelectric actuators. As shown, varying the applied voltage v_p as a constant voltage (v_0) alters the pole positions within the system, which can lead to instability. The plot reveals that the system's poles respond differently to changes in v_p, with some poles moving toward the instability region (the right-half of the s-plane) as v_p increases. This differential responsiveness underscores the nuanced control that piezoelectric actuation can exert on the system.

Utilizing simulations with the parameters in Table 10, Fig. 70 highlights the impact of high damping $\zeta_r = 0.4$. This level of damping markedly reduces vibration amplitudes and suppresses resonant peaks across the frequency spectrum. Piezoelectric actuation, when used alongside high damping, further reduces peak amplitudes and compensates for the dampened bandgap effect, enhancing the depth of the bandgap. This analysis underscores piezoelectric actuation's superiority over passive damping for vibration reduction and demonstrates its ability to modify dynamic properties like stiffness distribution. Thus, integrating piezoelectric actuators into metamaterial beams emerges as an effective and dynamically tunable strategy for vibration isolation and noise reduction.

While using a constant voltage input on piezoelectric actuators provided initial insights into the metamaterial's behavior, it didn't fully leverage the potential

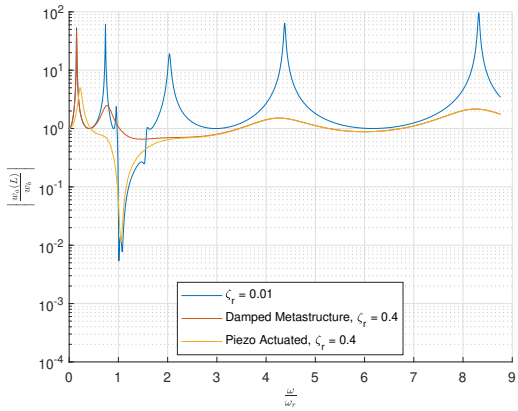

Figure 70: The figure illustrates the effect of constant voltage applied by piezoelectric actuators to compensate for over-damping, as well as the impact of the over-damping resonator on the bandgap properties of the metastructure with unchanged metamaterial structural damping ratio ζ_m. Parameters are sourced from Table 10.

for dynamic control over varying frequencies. Introducing a notch filter alongside the piezoelectric actuator enables frequency-dependent voltage control, which brings several benefits. This setup allows for selective vibration attenuation or amplification at targeted frequencies, improving adaptability and precision in controlling resonant frequencies. Consequently, it broadens the system's bandgap and enhances vibration suppression. This method also permits fine-tuning of the metamaterial's dynamic response, optimizing performance for specific applications that require precise control over narrow frequency ranges.

6.3 Methodology for Structural Damping Compensation in Distributed Parameter Metastructures via Notched Piezo Actuation

To address the challenge of enhancing the bandgap depth within metastructures, this section builds upon the distributed parameter model described in the preceding sections. The equations set forth earlier (67), (152), and (153) provide a robust foundation for understanding and manipulating the interaction between the structural dynamics of the metastructure and the localized piezoelectric actuation implemented on the resonators.

To avoid instability resulting from constant voltage application, and enable precise adjustments to the metamaterial's response across various operational conditions, the introduction of notch filters into the control loop of the piezoelectric actuators is proposed. The design of the notch filter is pivotal, shaping the system's response to diverse frequency components. By attenuating certain frequencies linked with the resonators, the notch filter can proficiently deepen the bandgap while preserving system stability.

This strategy proffers a dual benefit: it deepens the bandgap to enable more effective vibration isolation and upholds system stability by averting excessive amplitudes in the resonators. The forthcoming sections will delineate the design process for the notch filter and the analyses performed to affirm the validity of this

technique.

A notch filter is mathematically represented as:

$$H_{no} = k\frac{s^2 + \frac{\omega_{no}}{Q_\beta}s + \omega_{no}^2}{s^2 + \frac{\omega_{no}}{Q}s + \omega_{no}^2} \tag{161}$$

In this formula, Q and Q_β correlate with the quality factor of the filter, albeit serving distinct functions in the filter's design. The quality factor Q gauges the filter's selectivity or the resonance sharpness. It dictates the bandwidth's width at the notch frequency ω_{no}, with a higher Q yielding a narrower bandwidth, enhancing selectivity and steepening the frequency attenuation near ω_{no}. Conversely, Q_β usually denotes an adjusted quality factor that modulates the notch's depth or the filter's response outside the notch frequency. Although not universally standard, Q_β is employed in certain designs for achieving specific filter attributes.

The notch filter defined here uses k for gain, ω_{no} as the notch frequency, and Q and Q_β to influence the notch's bandwidth and depth. The differentiation of quality factors provides greater control over the filter's frequency response, with adjustments to Q_β allowing for attenuation modulation at the notch frequency or altering the filter's response in ways not feasible by solely manipulating Q.

The integration of the notch filter into the system is evaluated through derived Eq. (162), which now accounts for the notch filter's effects. This revised equation facilitates the analysis of the system's performance, illustrating the modulation of the bandgap via active control, made possible by the inclusion of the notch filter.

$$\frac{Z_m(s)}{Q_{b_m}(s)} = \frac{1}{s^2\left(1 + \frac{\mu(2\zeta_r\omega_r s+\omega_r^2)}{s^2+2\zeta_r\omega_r s+\omega_r^2\left(1+\frac{kv_{p,r}}{s}\frac{s^2+\frac{\omega_{no}}{Q_\beta}s+\omega_{no}^2}{s^2+\frac{\omega_{no}}{Q}s+\omega_{no}^2}\right)}\right) + 2\zeta_m\omega_m s + \omega_m^2} \tag{162}$$

A notch filter with precisely optimized parameters (Q, Q_β, and k) is utilized to counteract the negative effects of damping and deepen the bandgap for each mode $m = 1, 2, \ldots, N_m$. AI algorithms, specifically the Hybrid PSO-GA and a Reinforcement Learning (RL) approach, are employed to find the global minimum and optimally adjust the notch filter parameters. The RL approach uses an unconventional actor-critic method for continuous control parameters, where the actor suggests parameter values and the critic evaluates their impact. The optimization process involves defining the environment and state, action adjustments, reward-based learning, and training of the RL agent using the Deep Deterministic Policy Gradient (DDPG) algorithm. Post-training evaluation checks for convergence to optimal k, Q, and Q_β values. This optimization strategy enhances the vibrational characteristics of the system.

6.3.1 Numerical Studies

The geometric and material characteristics of the examined rectangular aluminum beam are outlined in Table 11. Fig. 71 displays the root locus for the metastructure when a conventional piezoelectric actuated voltage is applied. In this configuration, the poles of the system, which correspond to the system's natural frequencies, can be observed moving towards the right-half of the complex plane as system parameters vary, indicating a potential for instability.

Table 11: Geometric and material properties of the notched-piezo actuation metastructure

Parameter	Value	Parameter	Value
L_m	910 mm	ζ_r	$0.0 - 0.2$
w_m	40 mm	N_m	8
h_m	3 mm	N_r	8
ρ_m	2710 kg/m^3	v_0	10 V
E_m	69.5 GPa	α	0.0976 F/C
ζ_m	0.027	μ	1.04

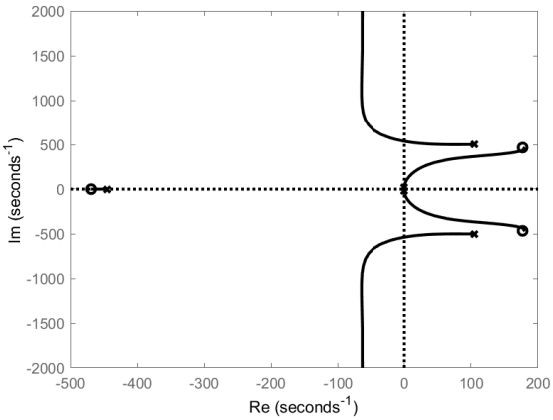

Figure 71: Root locus plot for the first mode of the metastructure with conventional piezoelectric actuation $v_0 = 50$ V, highlighting the stability characteristics without the application of a notch filter

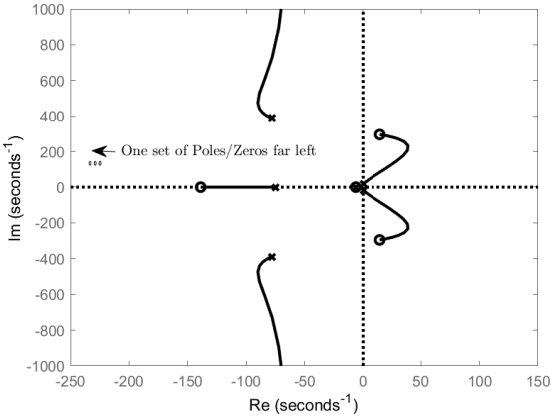

Figure 72: Root locus plot for the first mode of the metastructure with notched piezoelectric actuation for $v_0 = 50$ V, $k = 11.25, Q = 0.001$, and $Q_\beta = 0.021$, demonstrating enhanced stability through the introduction of a notch filter that shifts the poles and zeroes farther from the origin.

In contrast, Fig. 72 illustrates the root locus with a notched piezoelectric actuated voltage. The notch filter's transfer function introduces a new set of poles and zeroes. These new elements in the system's transfer function are strategically placed far from the origin, which contributes to an artificially created stability in the system. By relocating these critical points, the notch filter effectively broadens the stability margins of the metastructure, as indicated by the leftward positioning of the poles on the plot.

The significant difference between the two figures is the introduction of the notch filter, which transforms the stability landscape of the metastructure. The notch filter's impact is particularly evident in the way it modifies the root locus path, steering the system away from the instability regions marked by the right-half plane crossing. This implies that the notch filter, through its parameterization, plays a pivotal role in enhancing the metastructure's stability and, subsequently, its vibration suppression capabilities.

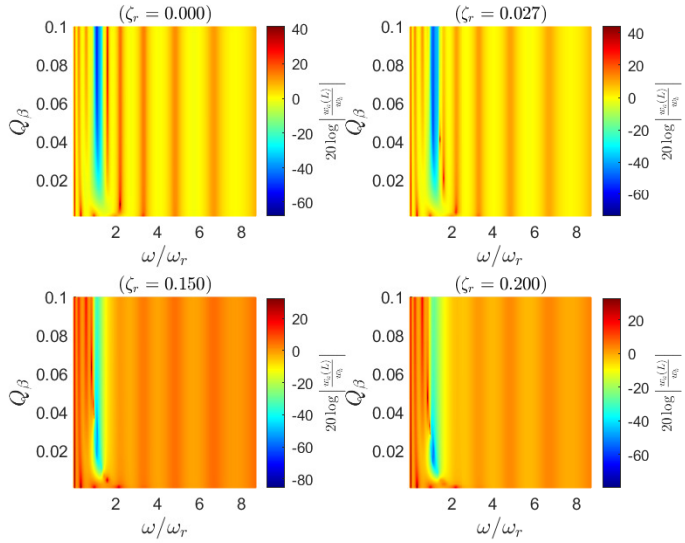

Figure 73: Heatmap demonstrating the bandgap depth's sensitivity to Q_β across different resonator damping levels. This visualization indicates optimal Q_β values for achieving maximum bandgap depth, varying with the level of damping present in the system.

Contrastingly, Fig. 73 depicts the sensitivity of the bandgap depth to changes in the Q_β parameter of the notch filter. The heatmap indicates that the optimal Q_β value that maximizes the bandgap depth shifts depending on the level of damping in the resonators. A key insight from this figure is the interplay between Q_β and the resonator damping, revealing a trend where higher Q_β values are preferable for systems with lower damping to deepen the bandgap, while lower Q_β values are more effective in systems with higher damping.

Fig. 74 illustrates the impact of individual notch filter parameters on the vibration transmittance in a beam metastructure, through a series of contour plots. The top left plot illustrates the variation of gain k while Q and Q_β are held constant. Different levels of attenuation over the frequency spectrum can be observed as k changes, indicating the filter's sensitivity to gain alterations. The top right plot

seems to focus on varying Q_β with fixed values for Q and k. This plot would be particularly useful for understanding how the depth and sharpness of the notch in the filter's response are affected by Q_β. The bottom left plot probably shows the effect of altering Q with Q_β and k remaining constant. Adjusting Q affects the bandwidth of the notch, and this visualization helps in finding the balance between selectivity and attenuation efficiency. The bottom right plot could be a specific case where Q_β, Q, and k are set to optimal values determined by prior optimization algorithms. This plot would exemplify the achieved balance between attenuation depth and bandwidth for effective vibration suppression.

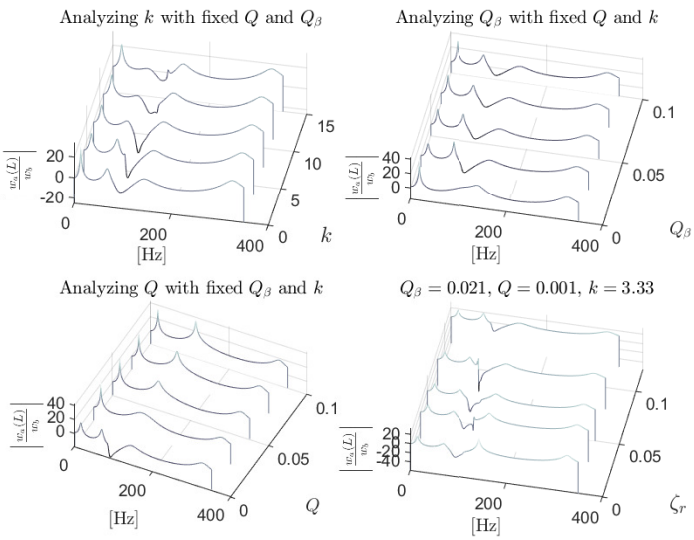

Figure 74: Parameter Sensitivity Analysis of Notch Filter Performance on Metastructure Transmittance, Displaying the Effects of Variations in Gain (k), Quality Factor (Q), and Adjusted Quality Factor (Q_β) Across Frequency Bands.

Fig. 75 illustrates that the notch filter gain (k) significantly affects the depth of the bandgap in the system. At low damping, a low gain results in a deeper bandgap. Higher damping scenarios require an optimal notch filter gain to achieve the best bandgap characteristics. The behavior of the metastructure changes with varying notch filter gain from zero damping to high damping. The selection or design of the notch filter needs to be tailored to the specific damping conditions of the system.

For optimizing the notch filter parameters Q, Q_β, and k, Hybrid PSO-GA and RL algorithms were utilized. The Hybrid PSO-GA identified optimal values of $Q_{\beta_{\text{opt}}} = 0.021, Q_{\text{opt}} = 0.001$, and $k_{\text{opt}} = 11.35$. In parallel, RL found a slightly different optimal set, with $Q_{\beta_{\text{opt}}} = 0.019, Q_{\text{opt}} = 0.001$, and $k_{\text{opt}} = 11.25$. These results demonstrate the effectiveness of both algorithms in fine-tuning the system for enhanced performance, with each algorithm converging on a similar but distinct solution that influences the transmittance and bandgap characteristics of the metastructure.

The transmittance response of the highly damped structure depicted in Fig. 76 illustrates the impact of optimized notch filter parameters on the bandgap in com-

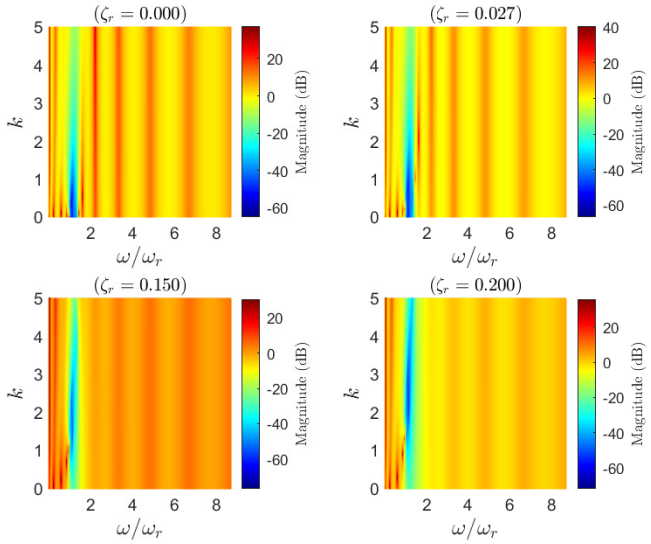

Figure 75: Heatmap showing the influence of notch filter gain (k) on the depth of the bandgap, under different damping conditions. The plot emphasizes how the optimal gain setting for the notch filter is dependent on the specific damping characteristics of the metastructure.

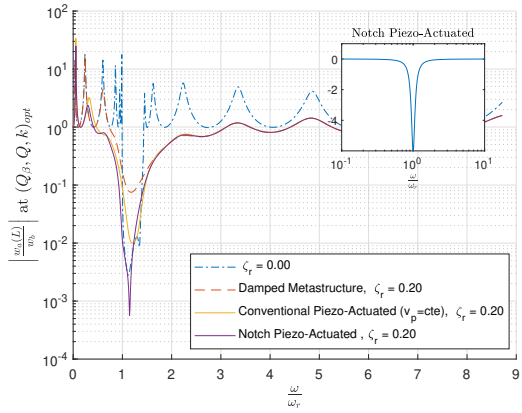

Figure 76: Transmittance response of the beam's tip optimized with Reinforcement Learning, illustrating the effectiveness of notch piezo-actuation in restoring the bandgap at critical resonator frequencies with RL-optimized parameters: $\zeta_m = 0.03$, $\zeta_r = 0.2$, $v_0 = 10$ V, $Q_{\beta_{opt}} = 0.019$, $Q_{opt} = 0.001$, $k_{opt} = 11.25$. The inset depicts the second-order filter frequency response, demonstrating the precision of notch frequency placement.

parison to the conventional piezo-actuated resonators. The graph reveals that at the target frequency, which coincides with the natural frequency of the resonator, the bandgap is significantly affected by the damping levels. Without any intervention, a high amount of damping at this frequency can obliterate the bandgap, impeding the structure's ability to isolate vibrations. The transmittance response, optimized at $Q_{\beta_{opt}}$, Q_{opt}, and k_{opt} via Reinforcement Learning, demonstrates that the notch piezo-actuation method successfully restores the bandgap dampened by resonator energy losses. While the RL method is preferred, the performance between this and the Hybrid PSO-GA optimization is comparable, with both effectively enhancing the bandgap for improved vibration suppression, though with slight differences that may affect the system's overall response.

The inset plot within the figure provides a visual of the Second Order Filter Frequency Responses, with the notch frequency ω_{nt} set at the target frequency. This notch is crucial in creating a deep and well-defined bandgap by attenuating the energy around the resonator's frequency, thereby enhancing the metastructure's vibration isolation capabilities.

This detailed analysis underlines the importance of precise parameter selection for notch filters in engineering applications where vibration control is paramount. The successful enforcement of a bandgap through piezo-actuation stands as a testament to the potential of AI-driven optimization algorithms in fine-tuning complex mechanical systems.

6.4 Summary

This chapter has explored methodologies for modeling and optimizing metastructures through AI-driven techniques, piezoelectric actuation, and the application of notch filters. The integration of these technologies has provided a substantial improvement in the control over bandgap properties, essential for the effective suppression of vibrations and enhancement of structural integrity in engineering applications.

Significant efforts were made to enhance the precision of damping ratio estimations, which play a crucial role in the dynamic behavior of metastructures. The combined use of analytical and experimental methods, supported by sophisticated optimization algorithms, has confirmed the ability of these models to bridge the gap between theoretical predictions and practical, real-world applications.

The introduction of piezoelectric components facilitated the active manipulation of structural properties, offering a promising avenue for compensating for inherent material damping and optimizing the metastructure's response to vibrational energy. Furthermore, the implementation of notch filters allowed for targeted attenuation of vibrations, enhancing the depth and effectiveness of the metastructures' bandgaps.

While the results are promising, the complexities involved in the practical application of these technologies suggest a need for further research. Future studies could focus on refining the integration of AI algorithms to enhance model precision and exploring the scalability of these approaches for larger or more complex structural systems. Additionally, long-term stability and the impact of environmental factors on the performance of piezoelectric actuators and notch filters merit further investigation.

Overall, the methodologies developed and validated in this study contribute significantly to the field of structural engineering, particularly in the design and

optimization of metastructures. The key contributions of this study are summarized as follows:

- The chapter introduces advanced AI-driven optimization techniques for precise estimation of damping ratios, which are critical for effective vibration control in metastructures;
- The mathematical model for metastructures has been refined, enhancing the precision of bandgap optimization. Particularly, the estimation of damping ratios is emphasized as critical for effectively controlling bandgap properties and achieving superior vibration suppression;
- A framework has been presented for addressing variable damping in metastructures, an area not fully explored in current methodologies;
- Explored the use of piezoelectric materials to dynamically modify the structural properties of metastructures to enhance structural response and vibration suppression;
- The study demonstrates the implementation of notch filters in the design of metastructures to selectively control and manipulate frequency responses, thereby improving the effectiveness and depth of bandgaps;
- By combining theoretical models with experimental validations, the chapter helps bridge the gap between conceptual research and practical implementations, enhancing the reliability and applicability of metastructures in various industries;
- It discusses the application of various optimization algorithms, including Hybrid GA-PSO and RL, providing a robust framework for optimizing the complex interactions within metastructures.
- The chapter includes comprehensive experimental setups and validations that confirm the effectiveness of the theoretical models and optimization approaches, ensuring they are grounded in real-world applicability;
- It identifies areas for future research, particularly in refining AI integration, exploring scalability issues, and understanding the long-term stability and environmental impacts on metastructure performance.

7 Conclusions, Contributions, and Future Work

7.1 Summary and Conclusions

This research investigates the dynamics of both mechanical and electromechanical locally resonant metastructures using two complementary modeling approaches: lumped parameter modeling (LPM) and distributed parameter modeling (DPM). The study also explores advanced techniques for enhancing functional diversity in metastructures, with a focus on internally coupled resonators, piezoelectric actuation strategies, and optimization through artificial intelligence.

Key scientific contributions include the development of generalized nonlinear models for complex metastructures, closed-form analytical transfer functions for distributed systems, and the proposal of new theoretical configurations for piezoelectric resonators aimed at improving energy harvesting performance. The thesis also addresses a critical practical challenge—structural damping—by proposing and numerically validating a damping compensation method using piezoelectric actuation. In addition, the work delivers the first experimental validation of internally coupled metastructures and demonstrates how AI-driven optimization techniques can improve parameter estimation and model-experiment agreement.

Throughout this research, a variety of dynamic equations, including Ordinary Differential Equations (ODEs) and Partial Differential Equations (PDEs), are formulated and solved in both time and frequency domains. Methodologies such as modal analysis, finite element analysis, Bloch-Floquet boundary conditions, and the Plane Wave Expansion (PWE) method are applied to address complex challenges in metastructure design.

The primary objective of this study is to develop innovative designs that enhance bandgap width and depth, create multiple bandgaps, and improve energy harvesting capabilities. Through this comprehensive approach, the study advances our understanding of linear and nonlinear mechanical and electromechanical metamaterials, offering new possibilities for practical applications, and address challenges related to instability in varying design contexts.

Understanding the dynamics of metamaterials using simplified lumped parameter models helps to take the next step: novel analytical techniques to develop closed-form transfer functions for finite metamaterial systems using modal analysis. These techniques can accommodate boundary conditions, resonator placement, and other effects that are challenging to capture with unit cell dispersion analysis. This approach enables the derivation of closed-form transfer functions for various functionalities utilized in control engineering, such as internal resonator coupling, and voltage- and frequency-dependent piezo-actuated metastructures. It also addresses challenges associated with metamaterials across diverse design scenarios, facilitating control engineering applications in the field of metamaterials.

7.1.1 Modeling of Flexible Metastructures with Mechanical Resonators

The exploration delves into the modeling of flexible metastructures with mechanical resonators, focusing on their dynamic behaviors and the manipulation of bandgap properties through both lumped and distributed parameter models. This examination is crucial for various engineering applications where controlling vibrational energy and wave propagation is essential.

It begins by applying lumped parameter modeling, which simplifies complex physical systems into discrete elements. This method facilitates an easier under-

standing and preliminary exploration of wave propagation, alongside initial assessments of bandgap characteristics in mechanical metastructures. Conversely, distributed parameter modeling offers a refined analysis by accounting for the continuous distribution of properties across the metastructure, using partial differential equations to provide detailed insights into wave propagation and bandgap formation.

Numerical simulations support these theoretical models, validating the predicted dynamic behaviors and highlighting how structural parameters like mass and stiffness ratios influence the metastructures' bandgap properties. Experimental validations further corroborate the theoretical predictions, demonstrating the actual dynamic responses of metastructures under controlled conditions and confirming the existence and tunability of bandgaps.

Analytical methods, including modal analysis and the frequency determinant method, are employed to analyze the impact of mechanical resonators on the system's dynamics. These methods provide a solid theoretical basis for understanding complex behaviors within metastructures [11]. The research underscores the potential of optimizing mechanical resonators to enhance control over vibrational energy within metastructures. It is demonstrated that nonlinearity, particularly cubic nonlinearity, can be utilized to tailor the metastructures' dynamic responses, offering potential for custom-designed applications [9]. Adjusting bandgap properties by altering structural parameters such as the resonator's mass, stiffness, and placement provides flexibility in designing metastructures for specific needs [18].

7.1.2 Modeling of Flexible Metastructures with Electromechanical Resonators

Modeling flexible metastructures with electromechanical resonators emphasizes their dynamic properties through analytical methods and numerical simulations. The incorporation of piezoelectric materials in these resonators provides distinct benefits for energy harvesting and vibration control due to their electromechanical capabilities.

It is structured into sections on lumped parameter modeling and distributed parameter modeling. In the findings from both modeling approaches, the lumped parameter models demonstrated significant enhancements in energy harvesting efficiency and vibration control through optimized electromechanical coupling coefficients. These simulations indicated that broader bandgaps, resulting from increased coupling, lead to improved vibration isolation and heightened energy conversion capabilities [12]. Particularly, the integration of nonlinear dynamics, such as polynomial and cubic nonlinearity, allowed for a nuanced control over system response, optimizing energy harvesting outputs without compromising the structural integrity of the bandgaps [9].

From the distributed parameter modeling, it was evident that the spatial consideration of piezoelectric elements attached to resonators profoundly affected the wave propagation within the metastructures. The modal analysis revealed that these configurations could significantly alter natural frequencies and mode shapes, thereby modifying the bandgap characteristics essential for targeted energy harvesting and vibration mitigation. Furthermore, numerical studies highlighted the critical role of resonator damping ratios and load resistances, showing that careful tuning of these parameters could lead to optimal conditions for energy harvesting, thus enhancing the overall efficiency of the metastructures in practical applications.

Together, these results underscore the potential of utilizing advanced electromechanical resonators in metastructures for superior control over energy harvesting and vibration damping, aligning theoretical advancements with practical engineering applications.

7.1.3 Streamlining Metastructure Modeling: Internally Coupled Resonator

Detailed lumped and distributed parameter models are introduced to study the dynamic behaviors of metastructures incorporating internally coupled resonators. These models help understand the intricate interactions within the structures and predict the formation of secondary bandgaps. Through theoretical modeling and experimental validation, it is demonstrated how internal coupling can be manipulated to refine bandgap properties, potentially creating new secondary bandgaps [11]. This enhancement is crucial for applications requiring precise control over vibrational energy. Experimental setups and FEM simulations validate the theoretical models, confirming the enhanced performance characteristics and highlighting practical challenges and limitations. The research identifies significant challenges in transitioning from theoretical models to practical applications, such as the need for precise manufacturing and the sensitivity of the system's performance to structural variations [14]. These insights are critical for the future development of metastructures with internally coupled resonators. While several challenges are highlighted, the research also opens avenues for innovations in design and material science to overcome these hurdles and fully harness the capabilities of internally coupled resonators in enhancing vibration control and energy efficiency in engineered structures.

7.1.4 Streamlining Metastructure Modeling: More Techniques for Enhanced Functional Diversity

This research has extensively explored the integration of AI-driven optimization, piezoelectric actuation, and notch filter applications to enhance the functional diversity and control of metastructures. It introduced AI-driven methods, including Genetic Algorithms (GA), Particle Swarm Optimization (PSO), and Hybrid GA-PSO, to optimize metastructures effectively. These algorithms were instrumental in accurately estimating critical damping ratios and enhancing the dynamic behavior of metastructures, confirming their utility in translating theoretical models into practical applications [15]. Piezoelectric materials were utilized to dynamically adjust the structural properties of metastructures. The closed-form transfer function methodology has been utilized, and new mathematical representations have been derived. The numerical implementation of piezoelectric actuation demonstrated how active materials could compensate for inherent material damping, thereby enhancing the effectiveness of vibration suppression techniques. Notch filters were integrated into the metastructure design to selectively attenuate vibrations at specific frequencies [16]. This approach deepened and refined the bandgap properties, leading to more effective control over structural vibrations. The detailed analysis of notch filter parameters through AI-driven methods showcased their impact on improving the metastructure's response to external vibrations.

7.2 Contributions

The following summarizes the major contributions of this dissertation to the current state of the art:

- Introduced advanced lumped and distributed parameter models that provide deep insights into the dynamic behaviors of flexible metastructures, enabling precise prediction of wave propagation and vibration characteristics (Chapter 3);
- Systematized the use of modal analysis to predict and analyze bandgap formation within metastructures, facilitating the strategic design of structures for optimized vibration control and wave manipulation (Chapter 3);
- Explored the impact of nonlinear dynamics, particularly focusing on cubic nonlinearity, on the transmittance spectrum and bandgap properties, thus paving the way for metastructures tailored for specific dynamic response requirements (Chapter 3);
- Validated analytical models for mechanical metastructures through numerical simulations and experimental setups, confirming the practical applicability and reliability of the proposed models in real-world scenarios (Chapter 3);
- Demonstrated practical techniques for tuning the properties of bandgaps by adjusting physical parameters such as mass, stiffness, and placement of resonators, contributing to the field of adaptive and tunable metastructures (Chapter 3);
- Introduced lumped and distributed parameter models that capture the complex dynamics of metastructures with electromechanical resonators. These models provide a deeper understanding of the interaction between mechanical and electrical dynamics, to design more efficient energy harvesting systems (Chapter 4);
- Demonstrated how piezoelectric elements can be effectively integrated within metastructures to enhance energy harvesting and vibration control. The dissertation outlines the impact of piezoelectric coupling on the bandgap properties of metastructures, which is pivotal for improving energy efficiency and suppression of vibrations (Chapter 4);
- Explored the impact of various nonlinearities, including polynomial, voltage-dependent, and cubic forms, on the performance of electromechanical resonators. The dissertation provides a framework for optimizing these nonlinearities to maximize energy harvesting and mitigate vibrations, expanding the practical applications of metastructures in dynamic environments (Chapter 4);
- Conducted extensive numerical analyses to investigate the effects of resonator damping ratios and load resistances on the metastructure's performance. This research contributes optimized strategies for setting these parameters to enhance energy harvesting efficiency and dynamic response under different operational conditions (Chapter 4);

- Introduced comprehensive lumped and distributed parameter models for metastructures with internally coupled resonators. These models enhance understanding of the dynamic interactions within the structures and demonstrate how internal coupling can be used to manipulate and create additional bandgaps, leading to improved performance in vibration control and energy harvesting (Chapter 5);

- Established how internal coupling mechanisms within resonators can be optimized to refine control over bandgap properties, potentially leading to the creation of new secondary bandgaps. This capability is crucial for applications requiring precise control over vibrational energy, such as in building construction, automotive manufacturing, and consumer electronics (Chapter 5);

- Significant challenges in the transition from theoretical models to practical applications, such as the need for precise manufacturing and the sensitivity of system performance to structural variations. These insights are critical for the practical deployment of metastructures in real-world applications (Chapter 5);

- Extensive experimental and numerical studies, including FEM analysis: Validating theoretical models and highlighting practical limitations, thereby guiding future design and implementation strategies (Chapter 5);

- The research opens several avenues for future investigations, particularly in improving the design and integration of internally coupled resonators, exploring new materials and configurations, and overcoming current limitations (Chapter 5);

- Developed and implemented AI-driven optimization strategies, including hybrid algorithms and reinforcement learning, for precise estimation of damping ratios essential for effective vibration control in metastructures (Chapter 6);

- Pioneered the use of piezoelectric materials to dynamically modify structural properties, enabling active control over vibration suppression and structural responses, enhancing the functional capabilities of metastructures (Chapter 6);

- Introduced notch filters in the structural design to selectively manipulate frequency responses, significantly improving the depth and effectiveness of bandgaps in vibration control (Chapter 6);

- Effectively bridged the gap between theoretical research and real-world implementation by validating advanced mathematical models through extensive experimental setups to parameter estimation, enhancing the reliability and industrial applicability of metastructures (Chapter 6);

- Established a robust methodological framework for the analysis and design of metastructures, combining analytical, experimental, and computational approaches to address complex challenges in structural dynamics (Chapter 6).

7.2.1 Practical Engineering and Scientific Impact

The outcomes of this thesis contribute to both scientific understanding and engineering practice in several important ways, as outlined below:

- **Nonlinear Configurations for Enhanced Energy Harvesting:** While prior research has explored various methods for enhancing energy harvesting—such as nonlinear circuit techniques (e.g., SSHI, SECE), graded resonator arrangements, and multi-resonator systems—this thesis contributes by investigating alternative nonlinear structural configurations. These include internal coupling between resonators, nonlinear stiffness elements, and nonlinear piezoelectric capacitance. The proposed configurations are theoretically analyzed in terms of their potential to increase bandgap depth and harvested energy. Although these setups have not yet been implemented experimentally, the work provides a rigorous analytical and stability framework that lays the foundation for future realization and application in smart metastructures.

- **Damping Compensation in Distributed Metastructures:** A common challenge in practical metastructures is the loss of ideal bandgap characteristics due to structural damping. This thesis addresses this issue by proposing a damping compensation strategy based on piezoelectric actuation. Unlike most studies that focus on simplified lumped-mass systems, the proposed approach is developed and validated in the context of distributed (continuous) metastructures, making it more directly applicable to engineering structures such as beams and plates. While the piezoelectric damping compensation strategy was not experimentally implemented, its feasibility and impact were thoroughly analyzed through analytical modeling and simulations.

- **Experimental Validation of Internally Coupled Metastructures:** Although internal coupling in metastructures has received theoretical attention, this work presents one of the first experimental investigations of a beam-based metastructure incorporating internal mechanical coupling. The experimental results align with analytical predictions and offer valuable insights for practical implementation, particularly regarding sensitivity to coupling mismatch and its effect on bandgap behavior.

- **Extension of Closed-Form Modeling to Distributed Systems:** This thesis extends the control-oriented transfer function framework from lumped systems to distributed metastructures, enabling real-time dynamic modeling of continuous systems. These models support advanced vibration control and structural health monitoring applications by bridging the gap between theoretical formulations and practical implementation.

- **AI-Based Parameter Estimation for Metastructure Identification:** This thesis integrates optimization-based parameter estimation techniques into the analytical modeling framework to identify critical system properties—such as structural and resonator damping ratios—that are difficult to measure experimentally. This approach improves agreement between theoretical predictions and experimental results, thereby strengthening the reliability of metastructure models for practical applications.

- **Framework for Future Smart Metastructures:** Although nonlinear piezoelectric configurations could not be physically realized within this work, the proposed concepts, mathematical modeling, and stability criteria establish a robust theoretical foundation for future engineering solutions. These tools support the development of next-generation smart metastructures with integrated sensing, control, and energy harvesting functionalities.

7.3 Future Work

Building on the findings and methodologies developed in this dissertation on flexible metastructures, several key areas for future research are identified. Future studies should integrate more sophisticated modeling techniques that account for multiphysical phenomena and higher-order nonlinearities. Introducing time-dependent boundary conditions and external influences, such as thermal and electromagnetic fields, would provide deeper insights into the dynamic behavior of metastructures under realistic conditions.

The continued development and refinement of algorithms will facilitate the integration of natural frequency and mode shape calculations with finite element analysis (FEA) tools. This integration will improve the precision of metastructure modeling, allowing mode shapes and natural frequencies extracted from FEA to inform analytical derivations of transfer functions for complex designs.

Future development should emphasize creating feedback circuits that automatically adapt to changing conditions, significantly enhancing the performance stability of metastructures. Advanced control loops and Model Predictive Control (MPC) systems should be investigated to improve the responsiveness and adaptability of these structures. Additionally, developing and testing piezo-actuator prototypes specifically tuned for metastructures—especially actuators capable of handling higher loads and stresses suitable for industrial applications—is essential. Further research into complex nonlinear dynamics, including bistable and multistable behaviors and their interactions with other physical phenomena, is recommended.

Advanced circuits surpassing traditional energy harvesting methods should be developed, including synthetic impedance circuits that actively manage energy capture and dissipation processes. By adapting to changes in system dynamics such as load or vibration levels, these circuits could optimize energy harvesting efficiency.

Current one-dimensional (1D) modeling approaches should be extended to three-dimensional (3D) modeling to more accurately represent spatial complexities in metastructures. Exploring advanced materials such as shape-memory alloys and piezoelectric composites can further enhance tunability and responsiveness. Efforts should also be dedicated to establishing industry standards and best practices for the design, testing, and implementation of metastructures, promoting broader acceptance in relevant industries.

Future research should enhance design precision and manufacturing techniques for effectively implementing internal coupling mechanisms. Investigating advanced materials and alternative coupling configurations may overcome current challenges related to stiffness alignment and bandgap merging in practical applications. Developing adaptive control strategies can improve robustness and performance under varying operational conditions.

The complexity of integrating AI, piezoelectric materials, and notch filters suggests that further research is necessary. Future studies should evaluate the scala-

bility of these methods for larger or more complex systems. Additionally, the long-term stability and environmental resilience of piezoelectric actuators and notch filters require further investigation to ensure reliable real-world deployment. Continuous refinement of AI algorithms will enhance the precision of metastructure modeling and optimization, potentially introducing adaptive and self-learning systems for real-time structural dynamics control.

Finally, leveraging cloud computing and high-performance computing (HPC) resources should be explored to handle complex simulations and the optimization of metastructures more effectively. This would accelerate the iterative design process, enabling efficient handling of multi-physics simulations within practical timeframes.

List of Figures

1 Foundational model of linear phononic media: a linear monoatomic chain with linear resonators of masses, spring, and damping. Dashed rectangle is unit cell. 30

2 Foundational model of nonlinear phononic media: a linear monoatomic chain with nonlinear resonators of masses, spring, and damping. Dashed rectangle is unit cell. 31

3 Dispersion in the periodic structure with varying resonance coupling, and mass ratio. The plots demonstrate the profound influence of resonance conditions on the emergence and width of band gaps, highlighting the potential for tuned wave propagation control by adjusting the μ parameter. 33

4 Dispersion in the periodic structure with varying resonance coupling, and stiffness ratio. The plots demonstrate the profound influence of resonance conditions on the emergence and width of band gaps, highlighting the potential for tuned wave propagation control by adjusting the ν parameter..... 34

5 Comparative Analysis of Band Gap Behaviors in a 1-D Chain System: Insights from Mass Chain without Resonators, Conventional Metastructure, Linear, and Nonlinear Resonator Configurations 35

6 Impact of Cubic Nonlinearity on the 1-D Chain System: (a) Transmittance response influenced by cubic nonlinearity, and (b) Nonlinear spring force–displacement relationship for cubic nonlinearities. ... 36

7 Example of standard locally resonant metastructures, where m represents the mass of the resonators, c is the damping, and k is the stiffness of the resonators..... 37

8 Dispersion curves computed using the plane wave expansion method for target frequency f_t=31.2 Hz 44

9 Transmittance plot for a metamaterial beam..... 44

10 A 3D representation of the bandgap frequency shift as a function of the mass positioning along a resonator. Here, delta (δ) is indicative of the mass location on the resonator, increasing from the tip (lower δ) to the base (higher δ) of the cantilever beam. This spatial variation results in a downward shift of the bandgap edge frequency, moving from higher frequencies (approaching $8\omega_r$) to lower frequencies (close to ω_r), as the mass is repositioned towards the base, [18]..... 46

11 Binary mapping of the bandgap presence as a function of mass placement along the resonator, with δ indicating the distance from the cantilever beam's fixed end, versus normalized frequency (ω/ω_r), illustrating how the bandgap shifts with frequency and mass position. White areas denote regions where the transmittance falls below the threshold of 0.2 decibels, signifying the vibration isolation at these frequencies..... 47

12 Experimental setup of a metastructure prototype equipped with 8 resonators, each tuned to a resonator's natural frequency using adjustable mass at the tip. Measurement accuracy is ensured with two Dytran Accelerometers, linked by low-resistance wires. Geometric and material properties of the beam and resonators used in the setup are provided in Table 3. A schematic in the top right illustrates the direction of excitation and response measurement. 48

13 Experimental transmittance data versus excitation frequency for the metastructure, with $\mu = 1.2$. The plot highlights the bandgap region between 64 to 95 Hz, which corresponds to the analytical bandgap boundary $\omega_r\sqrt{1+\mu}$. 48

14 Foundational models of linear phononic media: a linear monoatomic chain with linear resonators of masses, spring, damping, and piezoelectric element, PZ. Dashed rectangle is unit cell. 51

15 An equivalent circuit for piezoelectric device model with internal electrode capacitance and load resistance 51

16 Classical energy harvesting circuit for the standard electronic interfaces. 53

17 Foundational models of nonlinear phononic media: a linear monoatomic chain with nonlinear resonators of masses, spring, damping, and piezoelectric element, PZ. Dashed rectangle is unit cell. 54

18 Band gap illustration for a monochain featuring linear local resonators with $n = 8$ mass chains, demonstrating the influence of k_e on band gap and metastructure response. The results are based on the electromechanical model described by Eq. 55, which corresponds to the schematic shown in Figure 14. 57

19 Electromechanical Coupling's Impact on Energy Harvesting: Illustration of the power harvested across varying k_e in an $n = 8$ unit cell monochain, showcasing the pivotal role of the electromechanical coupling coefficient in optimizing energy conversion and system dynamics. 57

20 Harvested power from a monochain with polynomial nonlinear local resonators in an eight-mass chain configuration. The graph highlights the impact of varying the nonlinearity coefficient β on the piezoelectric response and the resultant band gap behavior. 59

21 Temporal Evolution of Harvested Energy: A depiction of energy harvested from piezoelectric elements over time in a monochain with polynomial nonlinear local resonators, utilizing $n = 8$ mass chains. This visualization underscores the profound influence of polynomial nonlinearity on the system's energy-harvesting trajectory, revealing a substantial enhancement in energy accumulation even in the absence of notable bandgap alterations. 59

22 Influence of quadratic nonlinear piezo capacitance, c_p on transmittance and harvested energy 61

23 Illustrating the Interplay of $v(t)$ and $z(t)$ in the Presence of Cubic Nonlinearities. The figure demonstrates how cubic nonlinearity affects electromechanical coupling in a piezoelectric system, utilizing specific resistances for standard and cubic terms (R = 500 Ω and R = 192 kΩ, respectively) to maintain consistent saturation characteristics across scenarios. 62

24 Schematic of the mechanical locally resonant energy harvesting metastructure. The design features cantilever beams with tip masses, serving as mechanical resonators attached to the primary beam structure. Piezoelectric elements are integrated with a resistive load admittance, denoted as G_r. 63

25 Beam tip response of a mechanical metastructure with variable damping ratios (ζ_r), demonstrating the effect on resonance peaks and bandgaps at optimal power output conditions. The responses are plotted as a function of normalized excitation frequency (ω/ω_r), with parameters set to $\kappa_h = 0.1, g = 1$, and $\mu = 1.4$, for a cantilever beam subjected to base motion. The comparison with a simple beam, which has a damping ratio of $\zeta_m = 0.03$, highlights the influence of the resonators on the formation of the bandgap and the system's pronounced sensitivity to ζ_r. 67

26 Optimal real power output of a cantilever beam in a mechanical metastructure with resistive shunting, presented across a spectrum of normalized metastructure with resistive shunting, presented across a spectrum of normalized excitation frequencies (ω/ω_r). The graph showcases the dependency of power output on various resonator damping ratios (ζ_r), with the parameter $\omega_t = 3\omega_r$ consistent with previous analyses. It highlights the influence of damping on energy harvesting efficiency, notably at and around the resonant frequency. . 68

27 Heatmaps display the power output density variation with normalized excitation frequency and load resistance for different ζ_r. The dashed line indicates the optimal loading condition at each excitation frequency. Notable is the decrease in energy harvesting at higher frequencies with increased damping. Parameters: $g = 1, \kappa_h = 0.1, \omega_t = 3\omega_r, \mu = 1.4, \zeta_m = 0.027$. 69

28 Influence of resonator damping on the beam tip response within a mechanical metastructure, visualized over RC time constant and normalized excitation frequency. The heatmaps depict attenuation effects at lower frequencies and the persistent bandgap stability despite varied damping, with dashed lines marking optimal energy harvesting conditions. Parameters: $g = 1, \kappa_h = 0.1, \omega_t = 3\omega_r, \mu = 1.4, \zeta_m = 0.027$. 70

29 Beam tip response of a mechanical metastructure with varying ζ_r at optimal power output, plotted against normalized excitation frequency. The graph illustrates the impact of damping on the vibrational response of a cantilever beam under base excitation, with parameters set to $g = 1, \kappa_h = 0.1, \omega_t = 3\omega_r, \mu = 1.4$, and $\zeta_m = 0.027$ 70

30 Bandgap frequency shifts and attenuation characteristics across different electromechanical coupling conditions. The heatmaps underscore the transition of the bandgap response with minimal to increased coupling (κ_h), highlighting the narrow bandwidth yet noticeable impact on vibration damping, especially under optimal energy harvester loading. The sensitivity of lower damping ratios to frequency changes and the broadened response at higher ratios are evident. 71

31 Mechanically internally coupled resonators. The dashed rectangle signifies a unit cell. 73

32 Internally coupled with electrical shunt circuit. Forward (dash) and reverse (solid) capacitance shunting configuration. 77

33 Equivalent Electrical System Representation of the Unit Cell Resonators with Capacitance Shunt Circuit Using the Impedance Analogy 78

34 Comparative Analysis of Band Gap Behaviors in a 1-D Chain System: Insights from Linear, Nonlinear, and Internally Coupled Resonator Configurations 84

35 Displacement response of bistable nonlinear mechanical internal coupling resonators. Linear coupling coefficient $k_{c_1} = -20N/m$, and nonlinear coupling coefficient $k_{c_2} = 880N/m^3$. Inset: Resonator's potential energy profile for the specified coupling parameters. 84

36 Stability Area of the Electromechanical Internally Coupled Lumped-Mass System: Exploring the Interplay Between Equivalent Stiffness k_s and Shunt Capacitance c_s. Parameters: $n = 4$, $m_m = 56$ g, $m_r = 33.6$ g, $k_m = 150$ N/m, $k_r = 129.6$ N/m, $\theta = 0.25$ N/V, $R = 500\ \Omega$, $c_p = 1.5 \times 10^{-3}$ F. 86

37 Transmittance Comparison of Electrical Internally Coupling with Shunt Circuit for $\theta = 0.25$ and $c_p = 1.5$mF, Demonstrating the Impact of an Equivalent Negative Stiffness. 86

38 Harvested Power and Energy across Different Shunt Capacitances for $\theta = 0.25$ and $c_p = 1.5$mF 87

39 Locally resonant metastructures with internally coupled resonators. Each pair of resonators forms one unit cell, with m representing the mass of the resonators, c the damping, k the stiffness of the resonators, and κ the internal coupling stiffness between them. 88

40 Left: Conventional metastructure root locus with $\omega_m = 0.5$, $\omega_{2r-1} = \omega_r = 1$, $k_r = 1$, $m_r = 1$, and $\mu = 0.5$. Right: Metastructure with internal coupling, exhibiting a narrow band gap, characterized by $\omega_m = 0.5$, $\omega_{2r} = 1.7$, $\kappa = k_r$ and $\mu = 0.5$. The internal coupling's impact on the system dynamics is highlighted by the additional band gap in the right plot. 91

41 Bode and root locus plots for Eq. (148). (**Left**) Root locus with $K = \omega_m^2$, showing conventional and internally coupled bandgap for $\mu = 0.5$ and $\kappa = 1$. Markers: system poles at $\omega_m^2 = 0$, solid lines: pole trajectory as ω_m^2 increases. Grey region: bandgap frequency range. (**Right**) Bode plot showing frequency response, including resonance from coupling effect. 91

42 Dispersion curve of an internally coupled metamaterial beam, displaying two distinct bandgaps resulting from in-plane and out-of-plane resonator behavior. 92
43 Transmittance plot for a metamaterial beam with internal resonator coupling ($k = k_r$) comprising eight resonators, which equates to four unit cells. 93
44 Analysis of the influence of internal coupling stiffness κ on the metastructure's bandgap frequencies in Eq. (147), showing the consistent edge of the first bandgap and the emergence of narrow higher frequency gaps within certain κ ranges. 93
45 Transmittance contour plot against normalized internal coupling strength and frequency in Eq. (147), highlighting bandgap boundaries and the metastructure's sensitivity to κ variations..... 94
46 Experimental Design for a Prototype Metastructure Comprising Four Unit Cells of Internally Linked Resonators, Constructed from Pure Aluminum. 95
47 Experimental transmittance results for the metastructure with internally coupled resonators. The first bandgap is observed between 90-110 Hz. This shift can be attributed to the enhanced stiffness of the unit cell, which is composed of a pair of resonators. Measurement devices are located at the base and the tip of the metastructure to capture the full spectrum of its response. 96
48 Transmissibility of a cantilever beam for varying stiffness ratios κ, showing system sensitivity and its effects. Subplots detail responses at different κ/ω_r ratios, highlighting a critical condition at $\kappa = k_r$ in the bottom left corner subplot for optimal internal coupling. The y-axis is absolute displacement of beam tip to base displacement, $\ln|w_a(L)/w_b|$, and the x-axis is normalized frequency ω/ω_r. 97
49 Contour plot of transmittance for varying κ, illustrating the frequency-dependent formation and bifurcation of the bandgap. The plot captures the perturbations and potential destabilization inherent to varying internal coupling stiffness, underscoring the need for precise κ calibration. It also highlights the discrepancies between analytical predictions and observed bandgap clarity. 98
50 Metastructure with internally coupled resonators configured as unit cells. 98
51 Visual representation of the mechanism leading to the second bandgap in the internally coupled metastructure. 98
52 Transmittance showcasing the impact of damping ratios in the main plain and local resonators on the dynamic response of a metastructure, particularly in modifying the bandgap regions. 103
53 Comparison of the beam's transmittance: noisy signal versus model predictions, highlighting the algorithm's effectiveness in identifying transmittance characteristics within the bandgap frequency range. Parameters as listed in Table 6. 104
54 Scatter plot demonstrating the correlation between measured and simulated data via the Hybrid GA-PSO algorithm, evidencing high model accuracy with a correlation coefficient (R) of 0.98..... 104

55 Residual plot from the Hybrid GA-PSO model prediction demonstrating the residuals' distribution against sample points, underscoring the model's accuracy with a high coefficient of determination (R^2). 105

56 A cantilever beam experimental setup with detailed geometric and material properties listed in Table 7. The setup includes a shaker for base excitation and Dytran accelerometers at the beam's base and tip for dynamic response measurements, all interfaced with a power amplifier and a control system. 106

57 Transmittance response of a cantilever beam with GA algorithm estimations, for structural modal damping ratio ζ_m estimation. 107

58 Correlation between the measured and predicted values of the modal damping ratio. 107

59 Residual plot of the experimental data versus the model predictions, identifying areas of discrepancy and potential model improvements within the context of Case Study #2. 108

60 Experimental setup with a longer cantilever beam, reusing the same measurement and control components as the previous experiment. A schematic in the top right illustrates the direction of excitation and response measurement. 109

61 Transmittance response of a cantilever beam: comparison between experimental measurements and analytical predictions incorporating the estimated structural damping ratio ζ_m, identified using the Hybrid GA-PSO algorithm. 109

62 Scatter plot comparing measured data to Hybrid GA-PSO simulated estimations, demonstrating the algorithm's efficacy in predicting the structural modal damping ratio (ζ_m) with a correlation coefficient (R) of 0.91. 110

63 Residual analysis of the Hybrid GA-PSO model predictions showcasing the estimation accuracy across the experimental data set, with a focus on identifying outlier discrepancies for further model refinement. 110

64 The experimental setup for the metastructure's dynamic analysis. This configuration is instrumental in examining the effects of damping and resonator adjustments on the metastructure's vibrational characteristics. 111

65 Transmittance response of a metastructure: comparison between experimental measurements and analytical results based on the estimated damping ratios ζ_m and ζ_r. 112

66 Hybrid GA-PSO Scatter plot of Metastructure's Measured vs. Simulated data in predicting the resonator damping (ζ_r). 112

67 Distribution of residuals from the Hybrid GA-PSO algorithm's predictions. 113

68 Schematic of a locally resonant metastructure with piezoelectric actuators. Features cantilever beams with tip masses as resonators and piezoelectric elements (with voltage $v_{p,r}$) bonded to alter stiffness dynamically. 115

69 Root locus plot demonstrating the stabilization effect of increasing piezoelectric actuation voltage v_p on stability of metamaterial beam system. System parameters include a mass ratio $\mu = 1$, resonator damping ratio $\zeta_r = 0.1$, resonator natural frequency $\omega_r = 10$, structural damping ratio $\zeta_m = 0.1$, and the first structural natural frequency $\omega_{m_1} = 10$. The plot traces the pole movement across modes, showing enhanced stability with higher v_p, pertinent to the precise dynamic control of metamaterials. 117
70 The figure illustrates the effect of constant voltage applied by piezoelectric actuators to compensate for over-damping, as well as the impact of the over-damping resonator on the bandgap properties of the metastructure with unchanged metamaterial structural damping ratio ζ_m. Parameters are sourced from Table 10. 118
71 Root locus plot for the first mode of the metastructure with conventional piezoelectric actuation $v_0 = 50$ V, highlighting the stability characteristics without the application of a notch filter 120
72 Root locus plot for the first mode of the metastructure with notched piezoelectric actuation for $v_0 = 50$ V, $k = 11.25, Q = 0.001$, and $Q_\beta = 0.021$, demonstrating enhanced stability through the introduction of a notch filter that shifts the poles and zeroes farther from the origin. 120
73 Heatmap demonstrating the bandgap depth's sensitivity to Q_β across different resonator damping levels. This visualization indicates optimal Q_β values for achieving maximum bandgap depth, varying with the level of damping present in the system. 121
74 Parameter Sensitivity Analysis of Notch Filter Performance on Metastructure Transmittance, Displaying the Effects of Variations in Gain (k), Quality Factor (Q), and Adjusted Quality Factor (Q_β) Across Frequency Bands. 122
75 Heatmap showing the influence of notch filter gain (k) on the depth of the bandgap, under different damping conditions. The plot emphasizes how the optimal gain setting for the notch filter is dependent on the specific damping characteristics of the metastructure. 123
76 Transmittance response of the beam's tip optimized with Reinforcement Learning, illustrating the effectiveness of notch piezo-actuation in restoring the bandgap at critical resonator frequencies with RL-optimized parameters: $\zeta_m = 0.03$, $\zeta_r = 0.2$, $v_0 = 10$ V, $Q_{\beta_{opt}} = 0.019$, $Q_{opt} = 0.001$, $k_{opt} = 11.25$. The inset depicts the second-order filter frequency response, demonstrating the precision of notch frequency placement. 123

List of Tables

1 Defined parameters for the lumped models 34
2 Geometric and material properties of the studied rectangular aluminum beam 43
3 Experimental parameters 47
4 Defined parameters for the lumped models 56
5 Defined parameters for the piezoelectric model 83
6 Geometric and material properties of Case Study #1 105
7 Geometric and material properties of the studied rectangular aluminum short beam 106
8 Comparison results of different optimization algorithms in estimating the structural modal damping ratio ζ_m for Case Study #3. 113
9 Comparison results of different optimization algorithms in estimating the resonator damping ratio ζ_r for Case Study #4. 114
10 Geometric and material properties of the voltage dependant piezo actuation metastructure 116
11 Geometric and material properties of the notched-piezo actuation metastructure 120

References

[1] Jacob Pieter Den Hartog. *Mechanical vibrations*. Courier Corporation, 1985.

[2] Jerome Connor and Simon Laflamme. *Structural motion engineering*. Springer, 2014.

[3] John Brian Pendry. "Negative refraction makes a perfect lens". In: *Physical review letters* 85.18 (2000), p. 3966.

[4] Richard A Shelby, David R Smith, and Seldon Schultz. "Experimental verification of a negative index of refraction". In: *science* 292.5514 (2001), pp. 77–79.

[5] Zhengyou Liu et al. "Locally resonant sonic materials". In: *science* 289.5485 (2000), pp. 1734–1736.

[6] Nicholas Fang et al. "Ultrasonic metamaterials with negative modulus". In: *Nature materials* 5.6 (2006), pp. 452–456.

[7] Ming-Hui Lu, Liang Feng, and Yan-Feng Chen. "Phononic crystals and acoustic metamaterials". In: *Materials today* 12.12 (2009), pp. 34–42.

[8] Manvir S Kushwaha et al. "Acoustic band structure of periodic elastic composites". In: *Physical review letters* 71.13 (1993), p. 2022.

[9] Hossein Alimohammadi et al. "Nonlinear dynamics in PEH for enhanced power output and vibration suppression in metastructures". In: *Nonlinear Dynamics* (2024), pp. 1–23.

[10] Hossein Alimohammadi et al. "Exploring Internally Coupled Resonator's Dynamics and Spatial Variability in Metamaterials for Vibration Suppression". In: *Active and Passive Smart Structures and Integrated Systems XVIII* (2024).

[11] Hossein Alimohammadi et al. "Bandgap Dynamics in Locally Resonant Metastructures: A General Theory of Internal Resonator Coupling". In: *Applied Sciences* 14.6 (2024), p. 2447.

[12] Hossein Alimohammadi et al. "Stability analysis and energy harvesting in lumped parameter systems with internally coupled resonators". In: *Journal of Vibration and Control* (2024).

[13] Hossein Alimohammadi et al. "Harvesting Energy and Stability Insights in Internally Coupled Resonator Systems". In: *2024 IEEE 18th International Conference on Advanced Motion Control (AMC)*. IEEE. 2024, pp. 1–6.

[14] Hossein Alimohammadi et al. "Exploring the Real-World Challenges and Efficacy of Internal Coupling in Metastructures: An Experimental Perspective". In: *The 4th International Conference on Electrical, Computer and Energy Technologies (ICECET)*. 2024, pp. 1–6.

[15] Hossein Alimohammadi et al. "Damping Optimization in Locally Resonant Metastructures via Hybrid GA-PSO Algorithms and Modal Analysis". In: *Conference on Smart Materials, Adaptive Structures and Intelligent Systems (ASME SMASIS)*. 2024, pp. 1–6.

[16] Hossein Alimohammadi et al. "Enhancing Bandgap Depth in Locally Resonant Metastructures via Notch-filtered Piezoelectric Actuation". In: *2024 25th IEEE International Conference on Industrial Technology (ICIT)*. Vol. 1. IEEE. 2024.

[17] Hossein Alimohammadi et al. “Piezoelectric Compensation of Structural Damping in Metamaterial Beams: Stability and Performance Analysis”. In: *Active and Passive Smart Structures and Integrated Systems XVIII* (2024).

[18] H Alimohammadi et al. “Band gap tuning based on adjustable stiffness of local resonators”. In: *13th International Conference on Metamaterials, Photonic Crystals and Plasmonics, META 2023*. 2023.

[19] Ying Li et al. “Design of mechanical metamaterials for simultaneous vibration isolation and energy harvesting”. In: *Applied Physics Letters* 111.25 (2017).

[20] Yuichi Tsujiura et al. “Reliability of vibration energy harvesters of metal-based PZT thin films”. In: *Journal of Physics: Conference Series*. Vol. 557. 1. IOP Publishing. 2014, p. 012096.

[21] Geon Lee et al. “Piezoelectric energy harvesting using mechanical metamaterials and phononic crystals”. In: *Communications Physics* 5.1 (2022), p. 94.

[22] Scott Meninger et al. “Vibration-to-electric energy conversion”. In: *Proceedings of the 1999 international symposium on Low power electronics and design*. 1999, pp. 48–53.

[23] Deepam Maurya, Yongke Yan, and Shashank Priya. *Piezoelectric materials for energy harvesting*. CRC Press, Boca Raton, 2015.

[24] Mickaël Lallart and Daniel Guyomar. “An optimized self-powered switching circuit for non-linear energy harvesting with low voltage output”. In: *Smart Materials and Structures* 17.3 (2008), p. 035030.

[25] Hong Jiang and Yuecheng Wang. “Research Progress on Piezoelectric Energy Harvesting Circuits”. In: *Integrated Ferroelectrics* 231.1 (2023), pp. 9–19.

[26] Daniel Guyomar and Mickaël Lallart. “Recent progress in piezoelectric conversion and energy harvesting using nonlinear electronic interfaces and issues in small scale implementation”. In: *Micromachines* 2.2 (2011), pp. 274–294.

[27] Tao Yang et al. “Nonlinear vibration energy harvesting and vibration suppression technologies: Designs, analysis, and applications”. In: *Applied Physics Reviews* 8.3 (2021).

[28] Tarcisio Marinelli Pereira Silva et al. “An experimental study of a piezoelectric metastructure with adaptive resonant shunt circuits”. In: *IEEE/ASME Transactions on Mechatronics* 25.2 (2020), pp. 1076–1083.

[29] Mohammed Daqaq. “Estimating the State-of-Charge of a Battery Powered by a Weakly Nonlinear Energy Harvester”. In: (2024).

[30] Mohammad Bukhari, Eshagh Farzaneh Joubaneh, and Oumar Barry. “Spectro-spatial wave features in nonlinear metamaterials: theoretical and computational studies”. In: *Journal of Vibration and Acoustics* 143.3 (2021), p. 031010.

[31] A Chaurha, PV Malaji, and T Mukhopadhyay. “Dual functionality of vibration attenuation and energy harvesting: effect of gradation on non-linear multi-resonator metastructures”. In: *The European Physical Journal Special Topics* 231.8 (2022), pp. 1403–1413.

[32] Michael J Frazier and Dennis M Kochmann. “Band gap transmission in periodic bistable mechanical systems”. In: *Journal of Sound and Vibration* 388 (2017), pp. 315–326.

[33] Mohammad A Khasawneh and Mohammed F Daqaq. “Experimental assessment of the performance of a bi-stable point wave energy absorber under harmonic incident waves”. In: *Ocean Engineering* 280 (2023), p. 114494.

[34] Corina Covaci and Aurel Gontean. “Piezoelectric energy harvesting solutions: A review”. In: *Sensors* 20.12 (2020), p. 3512.

[35] Haruhiko Asanuma. “Electromechanical model and simple numerical analysis for a piezoelectric vibration energy harvester considering nonlinear piezoelectricity, nonlinear damping, and self-powered synchronized switch circuit”. In: *Journal of Intelligent Material Systems and Structures* 34.20 (2023), pp. 2360–2378.

[36] Mickaël Lallart and Giulia Lombardi. “Synchronized Switch Harvesting on ElectroMagnetic System: a nonlinear technique for hybrid energy harvesting based on active inductance”. In: *Energy conversion and management* 203 (2020), p. 112135.

[37] Wendi Tian et al. “Analysis on the power and bandwidth improvement of a frequency-tuning optimized SECE circuit”. In: *Sensors and Actuators A: Physical* 332 (2021), p. 113110.

[38] Fahad Faraz Ahmad, Chaouki Ghenai, and Maamar Bettayeb. “Maximum power point tracking and photovoltaic energy harvesting for Internet of Things: A comprehensive review”. In: *Sustainable Energy Technologies and Assessments* 47 (2021), p. 101430.

[39] Di Li et al. “Recent progress and development of interface integrated circuits for piezoelectric energy harvesting”. In: *Nano Energy* 94 (2022), p. 106938.

[40] Sourov Roy et al. “A comprehensive review on rectifiers, linear regulators, and switched-mode power processing techniques for biomedical sensors and implants utilizing in-body energy harvesting and external power delivery”. In: *IEEE Transactions on Power Electronics* 36.11 (2021), pp. 12721–12745.

[41] João Pedro Norenberg et al. “Probabilistic maps on bistable vibration energy harvesters”. In: *Nonlinear Dynamics* 111.22 (2023), pp. 20821–20840.

[42] Tanmoy Chatterjee et al. “Parametric amplification in a stochastic nonlinear piezoelectric energy harvester via machine learning”. In: *Data Science in Engineering, Volume 9: Proceedings of the 39th IMAC, A Conference and Exposition on Structural Dynamics 2021*. Springer. 2022, pp. 283–291.

[43] Alper Erturk and Daniel J Inman. “A distributed parameter electromechanical model for cantilevered piezoelectric energy harvesters”. In: (2008).

[44] Ahmed Elkhashap, Daniel Rüschen, and Dirk Abel. “Distributed parameter modeling of fluid transmission lines”. In: *Journal of Process Control* 106 (2021), pp. 155–172.

[45] Mehran Mirramezani and Shawn C Shadden. “A distributed lumped parameter model of blood flow”. In: *Annals of biomedical engineering* 48 (2020), pp. 2870–2886.

[46] Jian Li, Susan E Luczak, and IG Rosen. “Comparing a distributed parameter model-based system identification technique with more conventional methods for inverse problems”. In: *Journal of inverse and ill-posed problems* 27.5 (2019), pp. 703–717.

[47] Christopher Sugino et al. “A general theory for bandgap estimation in locally resonant metastructures”. In: *Journal of Sound and Vibration* 406 (2017), pp. 104–123.

[48] C Sugino, M Ruzzene, and A Erturk. “Merging mechanical and electromechanical bandgaps in locally resonant metamaterials and metastructures”. In: *Journal of the Mechanics and Physics of Solids* 116 (2018), pp. 323–333.

[49] Shuai Qu et al. “Chiral phononic crystal-inspired railway track for low-frequency vibration suppression”. In: *International Journal of Mechanical Sciences* 274 (2024), p. 109275.

[50] Mostafa Nouh, O Aldraihem, and A Baz. “Wave propagation in metamaterial plates with periodic local resonances”. In: *Journal of Sound and Vibration* 341 (2015), pp. 53–73.

[51] R Zhu et al. “A chiral elastic metamaterial beam for broadband vibration suppression”. In: *Journal of Sound and Vibration* 333.10 (2014), pp. 2759–2773.

[52] Emanuele Baravelli and Massimo Ruzzene. “Internally resonating lattices for bandgap generation and low-frequency vibration control”. In: *Journal of Sound and Vibration* 332.25 (2013), pp. 6562–6579.

[53] Kathryn H Matlack et al. “Composite 3D-printed metastructures for low-frequency and broadband vibration absorption”. In: *Proceedings of the National Academy of Sciences* 113.30 (2016), pp. 8386–8390.

[54] Pai Wang et al. “Harnessing buckling to design tunable locally resonant acoustic metamaterials”. In: *Physical review letters* 113.1 (2014), p. 014301.

[55] Yiwei Xia, Massimo Ruzzene, and Alper Erturk. “Dramatic bandwidth enhancement in nonlinear metastructures via bistable attachments”. In: *Applied Physics Letters* 114.9 (2019).

[56] Yiwei Xia, Massimo Ruzzene, and Alper Erturk. “Bistable attachments for wideband nonlinear vibration attenuation in a metamaterial beam”. In: *Nonlinear Dynamics* 102 (2020), pp. 1285–1296.

[57] Hamed Farokhi, Yiwei Xia, and Alper Erturk. “Experimentally validated geometrically exact model for extreme nonlinear motions of cantilevers”. In: *Nonlinear dynamics* 107 (2022), pp. 457–475.

[58] Deepak K Agrawal, Jim Woodhouse, and Ashwin A Seshia. “Modeling nonlinearities in MEMS oscillators”. In: *IEEE transactions on ultrasonics, ferroelectrics, and frequency control* 60.8 (2013), pp. 1646–1659.

[59] Zhonghua Liu et al. “Amplitude deflection in a nonlinear MEMS resonator under parametric excitation”. In: *International Journal of Non-Linear Mechanics* (2024), p. 104754.

[60] Joshua LeGrande, Mohammad Bukhari, and Oumar Barry. “Effect of electromechanical coupling on locally resonant quasiperiodic metamaterials”. In: *AIP Advances* 13.1 (2023).

[61] Owen Thorp, Massimo Ruzzene, and Amr Baz. “Attenuation and localization of wave propagation in rods with periodic shunted piezoelectric patches”. In: *Smart Materials and Structures* 10.5 (2001), p. 979.

[62] Flaviano Tateo et al. “Design variables for optimizing adaptive metacomposite made of shunted piezoelectric patches distribution”. In: *Journal of Vibration and Control* 22.7 (2016), pp. 1838–1854.

[63] Wanlu Zhou, You Wu, and Lei Zuo. “Vibration and wave propagation attenuation for metamaterials by periodic piezoelectric arrays with high-order resonant circuit shunts”. In: *Smart Materials and Structures* 24.6 (2015), p. 065021.

[64] Gang Wang, Shengbing Chen, and Jihong Wen. “Low-frequency locally resonant band gaps induced by arrays of resonant shunts with Antoniou’s circuit: experimental investigation on beams”. In: *Smart Materials and Structures* 20.1 (2010), p. 015026.

[65] Luca Airoldi and Massimo Ruzzene. “Design of tunable acoustic metamaterials through periodic arrays of resonant shunted piezos”. In: *New Journal of Physics* 13.11 (2011), p. 113010.

[66] Moris Kalderon et al. “Locally resonant metamaterials utilizing dynamic directional amplification: An application for seismic mitigation”. In: *Applied Mathematical Modelling* 110 (2022), pp. 1–16.

[67] Jiong Tang and Kon-Well Wang. “Active-passive hybrid piezoelectric networks for vibration control: comparisons and improvement”. In: *Smart Materials and Structures* 10.4 (2001), p. 794.

[68] Raghavendra C Kamath et al. “Role of Computational Material Science in Improving the Properties of Piezoelectric Smart Materials: A Review”. In: *Engineering Proceedings* 59.1 (2023), p. 21.

[69] Marcin Kaczmarek and Hassan HosseinNia. “Tuneable Bandgap in Active Piezoelectric Metastructures Through Feedback Control”. In: *Available at SSRN 4757923* (2024).

[70] J Dupont, R Christenson, and J Tang. “A locally resonant non-contact absorber based on electromagnetic induction for vibration suppression”. In: *Active and Passive Smart Structures and Integrated Systems XVIII*. Vol. 12946. SPIE. 2024, pp. 23–30.

[71] Mohammed F Daqaq et al. “On the role of nonlinearities in vibratory energy harvesting: a critical review and discussion”. In: *Applied mechanics reviews* 66.4 (2014), p. 040801.

[72] Alper Erturk and Daniel J Inman. *Piezoelectric energy harvesting*. John Wiley & Sons, 2011.

[73] Christopher Sugino et al. “On the mechanism of bandgap formation in locally resonant finite elastic metamaterials”. In: *Journal of Applied Physics* 120.13 (2016).

[74] Alper Erturk and Daniel J Inman. “An experimentally validated bimorph cantilever model for piezoelectric energy harvesting from base excitations”. In: *Smart materials and structures* 18.2 (2009), p. 025009.

[75] Guobiao Hu, Lihua Tang, and Raj Das. “Internally coupled metamaterial beam for simultaneous vibration suppression and low frequency energy harvesting”. In: *Journal of Applied Physics* 123.5 (2018).

[76] Boyan Stefanov Lazarov and Jakob Søndergaard Jensen. "Low-frequency band gaps in chains with attached non-linear oscillators". In: *International Journal of Non-Linear Mechanics* 42.10 (2007), pp. 1186–1193.

[77] Marco Lepidi and Andrea Bacigalupo. "Wave propagation properties of one-dimensional acoustic metamaterials with nonlinear diatomic microstructure". In: *Nonlinear Dynamics* 98.4 (2019), pp. 2711–2735.

[78] WJ Zhou et al. "Spectro-spatial analysis of wave packet propagation in nonlinear acoustic metamaterials". In: *Journal of Sound and Vibration* 413 (2018), pp. 250–269.

[79] Akintoye O Oyelade and Olatunde J Oladimeji. "Coupled multiresonators acoustic metamaterial for vibration suppression in civil engineering structures". In: *Forces in Mechanics* 5 (2021), p. 100052.

[80] Yi Li et al. "Coherent coupling of two remote magnonic resonators mediated by superconducting circuits". In: *Physical Review Letters* 128.4 (2022), p. 047701.

[81] Costas M Soukoulis. *Photonic band gap materials*. Vol. 315. Springer Science & Business Media, 2012.

[82] Mohammed Al Rifaie, Hasanain Abdulhadi, and Ahsan Mian. "Advances in mechanical metamaterials for vibration isolation: A review". In: *Advances in Mechanical Engineering* 14.3 (2022), p. 16878132221082872.

[83] Filippo Casadei et al. "Piezoelectric resonator arrays for tunable acoustic waveguides and metamaterials". In: *Journal of Applied Physics* 112.6 (2012).

[84] Ya Wang and Daniel J Inman. "A survey of control strategies for simultaneous vibration suppression and energy harvesting via piezoceramics". In: *Journal of Intelligent Material Systems and Structures* 23.18 (2012), pp. 2021–2037.

[85] W Merlijn van Spengen. "The electromechanical damping of piezo actuator resonances: Theory and practice". In: *Sensors and Actuators A: Physical* 333 (2022), p. 113300.

[86] Henan Song et al. "Review on the vibration suppression of cantilever beam through piezoelectric materials". In: *Advanced Engineering Materials* 24.11 (2022), p. 2200408.

[87] Chengsi Huang and Hongcheng Li. "Adaptive notch filter for piezo-actuated Nanopositioning system via position and online estimate dual-mode". In: *Micromachines* 12.12 (2021), p. 1525.

[88] Lige Chang et al. "On-demand tunable metamaterials design for noise attenuation with machine learning". In: *Materials & Design* 238 (2024), p. 112685.

[89] Colin Hansen et al. *Active control of noise and vibration*. CRC press, 2012.

[90] Leonard Meirovitch. *Fundamentals of vibrations*. Waveland Press, 2010.

[91] Leonard Meirovitch. *Methods of analytical dynamics*. Courier Corporation, 2010.

[92] Feng-Lian Li, Chuanzeng Zhang, and Yue-Sheng Wang. "Band structure analysis of phononic crystals with imperfect interface layers by the BEM". In: *Engineering Analysis with Boundary Elements* 131 (2021), pp. 240–257.

[93] Lijian Lei et al. “Band gap extending of locally resonant phononic crystal with outward hierarchical structure”. In: *Applied Physics A* 128.6 (2022), p. 492.

[94] YC Shu and IC Lien. “Analysis of power output for piezoelectric energy harvesting systems”. In: *Smart materials and structures* 15.6 (2006), p. 1499.

[95] Peng Li, Chongxiao Zhang, and Lei Zuo. “Review of power electronics for kinetic energy harvesting systems”. In: *Active and Passive Smart Structures and Integrated Systems 2013* 8688 (2013), pp. 58–69.

[96] DJ Mead. “Leonard Meirovitch, Elements of Vibration Analysis , McGraw-Hill Book Company, New York (1986).” In: *Journal of Sound Vibration* 117.3 (1987), pp. 603–604.

[97] Guobiao Hu et al. “Tunable metamaterial beam using negative capacitor for local resonators coupling”. In: *Journal of Intelligent Material Systems and Structures* 31.3 (2020), pp. 389–407.

Acknowledgements

The author expresses his deepest appreciation to Dr. Kristina Vassiljeva, whose meticulous guidance and strategic advice have been invaluable throughout this journey. Special thanks are due to Dr. S. Hassan HosseinNia for his unwavering support and expert technical advice. Gratitude is also expressed to Dr. Aleksei Tepljakov for his insightful suggestions and stimulating discussions. Profound thanks are owed to Drs. Eduard Petlenkov and Peeter Ellervee, whose meticulous revisions and constructive feedback have immensely enhanced the quality of this dissertation. Their support in setting up experiments and test setups has been indispensable. Finally, my deepest gratitude is extended to Katrin Tõemets, for her love, patience, and tireless support.

This work has been supported by the European Union's Horizon Europe research and innovation programm under the grant agreement No 101120657, project ENFIELD (European Lighthouse to Manifest Trustworthy and Green AI), by the Estonian Research Council through the grant PRG658, and by the Estonian Centre of Excellence in Energy Efficiency, ENER (grant TK230) funded by the Estonian Ministry of Education and Research.

Abstract

Dynamics Modeling and Optimization of Locally Resonant Metastructures for Vibration Suppression and Energy Harvesting

This dissertation presents advanced analytical, numerical, and experimental frameworks for the dynamic modeling, optimization, and practical validation of locally resonant metastructures, specifically aimed at vibration suppression and efficient energy harvesting. By combining lumped and distributed parameter modeling, the thesis develops comprehensive and closed-form analytical solutions that allow precise predictions and facilitate real-time adaptive control.

Novel contributions of this work include the in-depth exploration of nonlinear dynamics within resonators, enabling the design of metastructures that robustly suppress vibrations across broader frequency bands. A generalized nonlinear formulation for piezoelectric energy harvesting systems has been developed, significantly enhancing both harvested energy and vibration suppression performance. Additionally, this thesis introduces internally coupled mechanical and electromechanical resonators, deriving closed-form transfer functions suitable for control engineering applications, substantially improving vibration isolation capabilities, and facilitating the generation of multiple bandgaps.

To address practical challenges, advanced techniques were proposed, such as piezoelectric actuation integrated with tailored notch-filtered controllers for structural damping compensation, which substantially deepened and widened the effective bandgaps. Furthermore, the incorporation of AI-driven hybrid optimization algorithms (Genetic Algorithm-Particle Swarm Optimization) provided robust parameter tuning and improved the performance of vibration suppression and energy harvesting.

The theoretical predictions and methodologies have been rigorously validated through comprehensive numerical simulations, employing Finite Element Methods (FEM), and systematically verified with experimental setups, ensuring their effectiveness in realistic engineering contexts. This thesis ultimately provides a versatile and validated framework for systematically designing and optimizing metastructures with significant implications for structural engineering, energy harvesting, and vibration mitigation technologies.

Kokkuvõte
Dünaamiline modelleerimine ja optimeerimine kohalikult resonantsete metastruktuuride jaoks vibratsiooni summutamiseks ja energia kogumiseks

See doktoritöö esitab põhjalikud analüütilised, numbrilised ja eksperimentaalsed raamistikud lokaalsete resonantsete metastruktuuride dünaamiliseks modelleerimiseks, optimeerimiseks ja praktiliseks valideerimiseks, keskendudes vibratsioonide summutamisele ja tõhusale energia kogumisele. Koondatud ja jaotatud parameetrite modelleerimise ühendamisega on töös välja töötatud põhjalikud ja suletud kujul analüütilised lahendid, mis võimaldavad täpseid prognoose ja reaalajas kohanduvat juhtimist.

Selle töö uudsed panused hõlmavad resonaatorite mittelineaarse dünaamika põhjalikku uurimist, mis võimaldab projekteerida metastruktuure, mis tõhusalt summutavad vibratsioone laiemates sagedusvahemikes. Välja on töötatud üldistatud mittelineaarne mudel piesoelektrilistele energia kogumise süsteemidele, parandades märkimisväärselt nii kogutud energia hulka kui ka vibratsioonide summutamise tõhusust. Lisaks esitleb käesolev töö sisemiselt seotud mehaaniliste ja elektromehaaniliste resonaatorite integratsiooni ning nendega seotud suletud kujul ülekandefunktsioonide tuletamist, mis sobivad kasutamiseks juhtimistehnilistes rakendustes, parandavad oluliselt vibratsioonide isoleerimise võimekust ning võimaldavad luua mitmeid sagedusriba vahemikke (bandgaps).

Praktiliste väljakutsete lahendamiseks on töös välja pakutud täiustatud tehnikad, sealhulgas piesoelektrilised täiturid koos spetsiaalselt kohandatud kitsasribafiltritega (notch filters) struktuurse summutuse kompenseerimiseks, mis laiendavad ja süvendavad efektiivseid sagedusriba vahemikke. Lisaks võimaldas tehisintellektil põhinevate hübriid-optimeerimisalgoritmide (geneetiline algoritm – osakeste parvede optimeerimine) rakendamine süsteemi parameetreid tõhusalt häälestada, parandades vibratsioonide summutamise ja energia kogumise tulemuslikkust.

Teoreetilisi prognoose ja meetodeid on põhjalikult kinnitatud numbriliste simulatsioonidega piiratud elementide meetodi (FEM) abil ning süstemaatiliselt valideeritud eksperimentaalsete katsetega, tagades nende tõhususe realistlikes inseneerirakendustes. Kokkuvõttes pakub käesolev doktoritöö mitmekülgset ja valideeritud raamistikku kõrgjõudluslike metastruktuuride süstemaatiliseks disainiks ja optimeerimiseks, omades olulist mõju ehitustehnika, energia kogumise ja vibratsioonide summutamise tehnoloogiate valdkonnas.

Appendix 1

I

Hossein Alimohammadi et al. “Nonlinear dynamics in PEH for enhanced power output and vibration suppression in metastructures”. In: *Nonlinear Dynamics* (2024), pp. 1–23

Nonlinear Dyn (2024) 112:12941–12963
https://doi.org/10.1007/s11071-024-09739-w

ORIGINAL PAPER

Nonlinear dynamics in PEH for enhanced power output and vibration suppression in metastructures

Hossein Alimohammadi · **Kristina Vassiljeva** · **S. Hassan HosseinNia** · **Eduard Petlenkov**

Received: 2 November 2023 / Accepted: 8 May 2024 / Published online: 29 May 2024
© The Author(s), under exclusive licence to Springer Nature B.V. 2024

Abstract This study delves into the nonlinear dynamics of metamaterials, exploring the dual objective of enhancing power output and achieving vibration suppression through piezoelectric energy harvesters (PEHs). Our approach is structured into a sequence of increasingly complex models that bridge mechanical resonators with their electromechanical counterparts. We initiate with (1) modeling mechanical resonators, incorporating nonlinear behaviors that are often overlooked in the linear domain. This lays the groundwork for understanding the fundamental mechanisms of vibration within metamaterials. Subsequently, we progress to (2) electromechanical resonators, where piezoelectric components are integrated, revealing a richer dynamic landscape that is influenced by the interplay of mechanical and electrical energies. The latter sections of our investigation introduce and examine (3) mechanical and (4) electromechanical internally coupled resonators. These segments unveil the role of internal couplings in steering the metamaterial's energy harvesting capabilities and its resilience to vibrational disturbances. Through meticulous simulations and analysis, the research brings to light the significant influence of specific PEH nonlinear parameters on the system's efficiency, offering insights for the optimization of PEHs in practical applications.

Keywords Nonlinear dynamics · Piezoelectric energy harvesting · Electromechanical nonlinearity · Internally coupled resonators · Vibration suppression · Lumped parameter model

H. Alimohammadi ( ) · K. Vassiljeva · E. Petlenkov
Department of Computer Systems, Tallinn University of Technology, 2618 Tallinn, Estonia
e-mail: hossein.alimohammadi@taltech.ee

K. Vassiljeva
e-mail: kristina.vassiljeva@taltech.ee

S. H. HosseinNia
Department of Precision and Microsystems Engineering, Delft University of Technology, 2628CD Delft, The Netherlands
e-mail: s.h.hosseinniakani@tudelft.nl

E. Petlenkov
Department of Computer Systems, Akadeemia tee 15a, 12618 Tallinn, Estonia
e-mail: eduard.petlenkov@taltech.ee

1 Introduction

The advent of mechanical metamaterials, characterized by their unique ability to control vibrational energy, has revolutionized the design and application of energy harvesting systems. For instance, the work by Jiao et al. highlights how modern mechanical metamaterials can interact with their environment and adapt to various conditions, offering insights into the design and optimization of these innovative materials [1]. Central to this innovation are the piezoelectric energy harvesters (PEHs) that form a chain of oscillators, each capable of converting vibrational energy into electrical power. This paper focuses on the detailed study and enhance-

ment of such systems through the lens of nonlinear dynamics, [2,3].

Our investigation begins by defining the mechanical and electromechanical metamaterial system that forms the basis of our theoretical models. We consider a chain of mechanical oscillators, each linked to a piezoelectric resonator, forming an electromechanical system that spans both the mechanical and electrical domains. This interconnected system not only offers the promise of energy harvesting but also presents a platform for vibration suppression-two objectives that are often at odds in traditional materials.

The objective of this study is twofold: to explore the underlying nonlinear dynamic behavior of the metamaterial/electromechanical system and to optimize the design for maximum power output while minimizing vibrational disturbances. To this end, we develop comprehensive theoretical models that capture the intricate behaviors of the resonators and their electromechanical interactions. These models are rigorously validated through a series of numerical simulations that not only ensure the theoretical models align with expected outcomes but also establish comprehensive metrics for evaluating the performance of the energy harvesters.

In summary, this research sets the stage for an in-depth exploration of PEHs within the realm of metamaterials. By addressing the nonlinear dynamics inherent to these systems, we aim to unveil strategies for enhanced energy harvesting and vibration mitigation. The key contributions of this paper are summarized as follows:

- Development of comprehensive theoretical models that integrate both mechanical and electromechanical aspects of piezoelectric energy harvesters within mechanical metamaterials, offering new insights into their nonlinear dynamic behavior.
- A detailed analysis of the impact of various forms of nonlinearity on the performance of energy harvesters, including mechanical and electromechanical nonlinearities, thereby extending the understanding of their operation and optimization.
- Introduction of novel metrics for evaluating the effectiveness of energy harvesters, bridging the gap between theoretical analysis and practical application, and paving the way for future research in optimizing metamaterial-based energy harvesting systems.
- Validation of the theoretical models through rigorous numerical simulations, ensuring their accuracy and reliability, and providing a solid foundation for future experimental investigations.

The structure of the remaining sections of this paper is organized as follows: Sect. 2 delves into the background and relevant literature, laying the groundwork for understanding the current state of research in piezoelectric energy harvesting. Section 3 outlines the methodology employed in this study, including mathematical modeling and simulation approaches. Section 4 presents the results and discussions, where the findings from the application of the proposed models are analyzed and interpreted. Section 5 details the contributions and findings related to nonlinear electromechanical dynamics and their impact on piezoelectric energy harvesters. Section 6 introduces internally coupled resonators with a focus on electromechanical nonlinearity, exploring their implications for energy harvesting. Finally, Sect. 7 concludes the paper with a summary of the findings, contributions to the field, and suggestions for future research directions.

2 Background

The field of energy harvesting has seen significant advancements with the integration of piezoelectric materials into mechanical metamaterials. These materials, capable of converting mechanical vibrations into electrical energy, have opened new avenues for creating efficient energy harvesters. Central to the design of these systems are chain oscillators, which play a dual role in energy conversion and vibration suppression [4,5]. Chain oscillators are fundamental in mechanical metamaterials, designed to control vibrational energy flow through the system while maximizing energy extraction from ambient sources [6].

2.1 The role of nonlinearities in energy harvesting

Nonlinear dynamics play a pivotal role in enhancing the performance of energy harvesting systems [7]. Both mechanical and electromechanical nonlinearities introduce complex behaviors such as bifurcations and chaos, extending the frequency range over which energy can be efficiently harvested. Recent advancements have led

to a deeper understanding and exploitation of nonlinearities within PEHs. Through resonators, the vibration suppression and energy harvesting capabilities of nonlinear models for PEHs have been thoroughly analyzed. These models highlight the role of nonlinear dynamics in enhancing PEH performance, offering insights for more efficient energy solutions. Daqaq et al. [8] found that nonlinear vibratory energy harvesters are more adaptable and efficient in varied environments than their linear counterparts, due to their broader frequency response. This makes them a potentially superior option for powering low-power devices. Furthermore, recent research by Daqaq [9] has extended the nonlinear dynamics to practical applications, specifically focusing on how weakly nonlinear energy harvesters can effectively charge batteries under various excitations, offering a balance between simplicity and accuracy in their analytical models.

2.2 Chain oscillators in mechanical metamaterials

Chain oscillators form the backbone of mechanical metamaterials used in energy harvesting applications. Their primary function is to suppress undesirable vibrations while facilitating the transfer of mechanical energy to piezoelectric elements for conversion into electrical energy. The integration of chain oscillators with piezoelectric resonators exemplifies the synergy between mechanical and electrical components in metamaterials [10]. By designing the oscillators to exploit specific nonlinear dynamics, it is possible to achieve optimal conditions for energy harvesting, wherein the system's natural frequency aligns with prevalent ambient vibrations. Furthermore, the suppression of vibrations through chain oscillators enhances the lifespan and reliability of the harvesting system [11].

In the quest for optimized energy harvesting systems, the exploration of nonlinear dynamics within mechanical and electromechanical systems has emerged as a critical area of research. These nonlinearities, whether inherent in the mechanical structure or introduced through electromechanical coupling, significantly influence the system's ability to harvest energy and suppress vibrations [12]. As such, understanding and leveraging these nonlinear effects can lead to substantial improvements in PEH performance. This backdrop of nonlinear dynamics sets the stage for an in-depth examination of mechanical and electromechanical nonlinearities in PEHs. The following sections delve into the mechanical nonlinearity of resonators, the electromechanical nonlinearity of resonators, and the nuanced dynamics of internally coupled resonators with both mechanical and electromechanical nonlinearities. Each area offers unique insights into the potential for advancing energy harvesting technologies, underscoring the complex interplay between mechanical structures and piezoelectric elements in metamaterials designed for optimized energy conversion

2.3 Nonlinearity in energy harvesters and metamaterial chains

The exploration of mechanical nonlinearities in energy harvesters and metamaterial chains reveals their significant impact on enhancing energy conversion efficiency and vibration control capabilities. This line of inquiry delves into how the introduction of nonlinear properties to resonators, specifically those exhibiting mildly cubic nonlinearities, influences the behavior of acoustic metamaterials and, consequently, the performance of energy harvesting systems (see Fig. 1).

Local resonators within periodic chains, when embedded with nonlinearities, are shown to initiate a detailed wave response, providing an intricate interaction within the system. This interaction is pivotal, as it shapes the system's capability to adapt and respond to vibrational energies more effectively [13,14]. The dynamics of wave propagation in these metamaterials are fundamentally altered by the integration of resonators embedded with mildly cubic nonlinearities, leading to modifications in the frequency domain where energy harvesting and vibration suppression are optimized [15,16]. The study of systems where periodic chains integrate multiple local resonators, each exhibiting nonlinear behavior, has highlighted the potential for expanding the operational bandwidth of energy harvesters. Such systems are adept at adapting to a wider range of vibrational frequencies, thereby enhancing the efficiency of energy conversion. Additionally, the incorporation of bistable systems within these metamaterial chains introduces a dynamic range of wave control, extending the capabilities of these systems beyond conventional linear models [17,18]. The chaotic behavior induced by high-intensity excitations in bistable systems allows for a broader attenuation of vibra-

tions, showcasing the advanced potential of nonlinear mechanical metamaterials in energy harvesting and vibration suppression [19]. However, experimental studies such as those by Khasawneh and Daqaq in [20], have challenged theoretical predictions about bistability in energy harvesters, showing that while bistable systems can shift operational bandwidths to lower frequencies, they may not always enhance the effective bandwidth compared to linear systems.

Bridging the concepts from nonlinear mechanical behaviors to electromechanical nonlinearities, it becomes evident that the complexity of energy harvesters is magnified when electrical components are introduced. This transition from purely mechanical to electromechanical systems opens up a broader spectrum for energy conversion efficiency and dynamic response control, setting the stage for a deeper exploration into the multifaceted nature of piezoelectric energy harvesters.

The exploration of electromechanical nonlinearity in piezoelectric energy harvesters is fundamental for advancing the efficiency and functionality of these systems. The nonlinear interactions between mechanical vibrations and electrical responses in PEHs, often mediated by components such as diodes and piezoelectric materials, play a crucial role in energy conversion dynamics.

Diodes introduce a marked non-linearity in the current–voltage relationship, significantly impacting energy harvesting efficiency. This effect is critical in rectifying the alternating current (AC) generated by piezoelectric elements into direct current (DC), which is more readily used by electronic devices [21–23]. Moreover, the interaction between mechanical structures and embedded piezoelectric materials leads to nonlinear behaviors such as amplitude-dependent frequency shifts, essential for enhancing the energy harvester's bandwidth [24,25].

The integration of data-driven methods, particularly neural networks, into PEH systems, has significantly advanced their performance, [26,27]. By leveraging smart electronic chips programmed based on these models, these systems can dynamically adapt to varying operational conditions, optimizing energy conversion efficiency in real-time. These chips, designed to handle nonlinear dynamics, enhance the adaptability and efficiency of PEHs, ensuring maximum energy extraction from environmental vibrations. This innovative approach, which combines the precision of empirical data analysis with cutting-edge electronic technology, marks a significant step forward in making energy harvesting systems more effective, reliable, and versatile.

2.4 Standard piezoelectric circuit for energy harvesting

The primary goal when integrating metamaterials into energy harvesting systems is to minimize vibrations within the main chain of the device. This minimization leads to the dissipation of the base or excitation energy primarily through the resonators attached to the system. In essence, reducing vibration in the main chain results in increased vibration within the resonators [28]. By effectively transferring energy from the main chain to the resonators, metamaterials not only protect the structural integrity of the system but also enhance the resonator's energy harvesting capabilities. This strategic distribution of vibrational energy is foundational to maximizing the efficiency of energy capture from ambient vibrations, marking a significant advancement in the development of sustainable energy solutions [29].

While metamaterials with resonators can enhance the energy capture capability, the rectifier circuit plays a pivotal role in processing this harvested energy, making it suitable for practical applications. Traditional energy harvesting circuits, characterized by their simplicity, directly connect the load to the harvesting component but often fall short in energy conversion efficiency.

Advanced circuit designs such as Synchronized Switch Harvesting on Inductor (SSHI), Synchronous Electric Charge Extraction (SECE), and Maximum Power Point Tracking (MPPT) [30–32] have been developed to address these limitations, substantially improving energy conversion efficiency. These systems not only surpass traditional models in efficiency but also adapt dynamically to varying environmental conditions to extract optimal energy. Recent progress in this field has been comprehensively reviewed in studies such as the work by Wang et al. [33] highlighting the evolution of interface circuits that significantly contribute to the efficiency and adaptability of PEHs.

Transitioning from the exploration of energy harvesting circuits to the study of internally coupled mechanical resonators, this shift underscores the integration of advanced energy conversion techniques with strategic vibration management. Through this, the

emphasis on mechanical nonlinearity within resonators emerges as a critical factor in enhancing both energy capture efficiency and system stability, signifying a comprehensive approach to optimizing metamaterial-based energy harvesting systems. Introducing nonlinearity into periodic chains with local resonators triggers wave responses that are shaped by the interplay of nonlinearity and local resonance effects. Studies on linear chains with nonlinear resonators [13,15,34] and nonlinear chains with linear resonators [15,35] have demonstrated this phenomenon.

Internally coupled mechanical resonators have emerged recently in modern dynamics and vibration control research. By harnessing the intricate interactions between internal structural elements, these resonators display a diverse range of vibrational behaviors. These characteristics offer unprecedented capabilities in manipulating and controlling wave propagation, making them invaluable assets in areas like structural health monitoring, acoustic metamaterials, and vibration mitigation. One of the pioneering research in this domain, as exemplified by studies like that of Hu et al. [36], has explored metastructures integrated with linearly coupled resonators. Their investigations reveal the presence of an additional narrow bandgap compared to conventional metastructures, highlighting the intriguing prospects of this research area.

Building upon this foundation, recent advancements have seen the development of metastructures incorporating coupled mechanical resonators with inherent nonlinearities. Notably, work by Alimohammadi et al. [37] delves into metastructures that employ a distributed parameter model for the main structure while utilizing a chain or lumped model for resonators. This approach introduces nonlinear internally coupled resonators, demonstrating enhanced wave manipulation capabilities. Their findings, showcasing the frequency response of such systems can affect the performance of metastructures with nonlinear internally coupled resonators compared to their linear counterparts. Nevertheless, a significant research gap persists in the area of nonlinear internally coupled resonators.

Transitioning from mechanical nonlinearity in internal coupled resonators, the focus shifts to electromechanical systems, where piezoelectric elements reveal intricate interactions between mechanical and electrical energies. This area, rich with potential for advancing energy harvesting and vibration control, remains largely unexplored, pointing to significant opportunities for research. In electromechanical resonators, the concept of internally coupled configurations, particularly when piezoelectric elements are interconnected, introduces a captivating complexity. These arrangements initiate a profound interaction between the mechanical and electrical domains, leading to unexpected wave propagation characteristics. Yet, despite the potential they harbor, exploration into nonlinear, internally coupled electromechanical systems remains notably limited.

This gap in the research landscape underscores the need for a comprehensive understanding of such systems, which promises to redefine the boundaries of vibration control and energy harvesting. By leveraging electromechanical nonlinearities, this design strategy enhances the efficiency and adaptability of energy harvesting systems. Studies such as those by Hu et al. and Silva et al. [25,36] underline the potential of this methodology in broadening the bandwidth for vibration suppression and energy harvesting. The integration of piezoelectric shunt techniques not only facilitates the adjustment of system dynamics but also aids in the creation of tunable band gaps.

3 Methodology

The lumped parameters model approach simplifies the analysis of a complex physical system by assuming that the system's physical properties, such as inertia, elasticity, and damping are concentrated at specific points or elements. Each element is characterized by a set of parameters, such as resistance, capacitance, and inductance for electrical circuits, or mass, damping, and stiffness for mechanical systems. These elements are interconnected in a network described by ordinary differential equations. Lumped parameter models are commonly employed when the wavelength of wave propagation is significantly larger than the dimensions of the structure, enabling the use of simplified assumptions.

3.1 Nonlinear mechanical resonators

The simplest lumped model of a 1D nonlinear phononic medium repeating unit cell, as illustrated in Fig. 1, is characterized as a linear atomic chain with embedded nonlinear resonators. This chain comprises an infinite series of uniform unit cells. Each of these unit cells

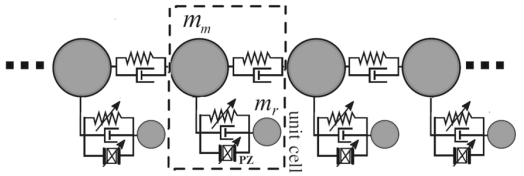

Fig. 1 Foundational models of nonlinear phononic media: a linear monoatomic chain with nonlinear resonators of masses, spring, damping, and piezoelectric element, PZ. Dashed rectangle is unit cell

consists of a mass, m_m, pertaining to the monoatomic chain, interconnected through linear springs. This primary linear chain is interfaced with nonlinear resonators, each identified by its mass, m_r. Both the damping element and the piezoelectric force of the resonators are neglected for simplicity. The net force exerted by the nonlinear spring connecting the resonators can be represented as:

$$f_r = k_r\delta + \sum \gamma_q \delta^q, \tag{1}$$

where δ is the relative displacement between the adjacent masses (chain mass and resonator). Subsequently, the dynamics of the system can be expounded as follows:

$$\begin{aligned} &m_m\ddot{u}_m + k_m\,(2u_m - u_{m^-} - u_{m^+}) \\ &\quad + \sum \gamma_{q_m}\left((u_m - u_{m^-})^q + (u_m - u_{m^+})^q\right) \\ &\quad + k_r(u_m - u_r) + \sum \gamma_{q_r}\,(u_m - u_r)^q = 0 \end{aligned} \tag{2}$$

$$m_r\ddot{u}_r - k_r\,(u_m - u_r) - \sum \gamma_{q_r}\,(u_m - u_r)^q = 0, \tag{3}$$

where for the last mass in the chain: $u_m - u_{m^+} = 0, \quad \dot{u}_m - \dot{u}_{m^+} = 0$, and for the first mass in the chain: $u_{m^-} = u_b$. Here, $\gamma_{q_m}, \gamma_{q_r}$ denote the nonlinear stiffness of the monoatomic chain and resonator, respectively. Here, u_m denotes the displacement of the m^{th} mass, k_m represents the stiffness of that mass, k_r is the resonator's stiffness, while u_{m^+} and u_{m^-} indicate the displacements of the succeeding and preceding masses, respectively, and u_b signifies the displacement of the excitation at the base or first mass chain.

The parameter q can assume values $(0, 1, 2, 3, \ldots)$, denoting the degree of system nonlinearity: linear ($q = 0, 1$), quadratic ($q = 2$), cubic ($q = 3$), and so forth. Weakly and strongly nonlinear systems can be distinguished based on the relative magnitude of the nonlinear force term, expressed as $\sum \gamma_q \delta^q$. Essentially nonlinear systems are characterized by vanishing linear forces ($k_{m,r} \to 0$) but non-zero nonlinear forces ($\gamma > 0$ for all q except $q = 0$ and $q = 1$).

Cubic nonlinearities can manifest as either purely hardening ($\gamma > 0$) or softening ($\gamma < 0$), while quadratic nonlinearities combine both softening and hardening behaviors. The versatility of this elementary discrete model extends to representing more intricate media configurations. These adaptations empower discrete modeling techniques to provide insights into the complexities of nonlinear phenomena.

Considering wave propagation in a system and applying boundary conditions with an input $u_b = e^{i\omega t}$, the transmittance of the system can be quantified as $\tau = \left|\frac{u_m^N}{u_m^1}\right|$, where u_m^{N} represents the displacement of u_m at the end of the chain sequence, while u_m^1 denotes the displacement of the mass at the first position in the sequence or the base excitation or the displacement at the initial position u_b.

The Laplace transform of nonlinear terms, specifically $\gamma_{q_r}\,(u_m - u_r)^q$, is not straightforward. While one could approach this by linearizing around a specific operating point, a more practical solution is often to address it numerically. Essentially, due to the complexities introduced by nonlinearity, numerical methods frequently provide the most feasible approach for analysis.

3.2 Dispersion curve

To elucidate the influence of the resonator's mass and spring within these configurations, the dispersion curve is determined for linear mechanical resonators. A streamlined model, where mechanical damping and the effects of the piezoelectric transducer are neglected (refer to Fig. 1), is employed. In this model, both the stiffness of the monoatomic chain and the resonator are treated as linear. Assuming a harmonic wave solution and incorporating Bloch's theorem, the harmonic displacements of the masses can be expressed as:

$$u_m = u_{m_0} e^{i(G_n a - \omega t)} \tag{4}$$

$$u_r = u_{r_0} e^{i(G_n a - \omega t)}, \tag{5}$$

where u_{m_0} and u_{r_0} are the initial displacements or amplitudes for unit cell or main chain and resonator. Substituting into linear form of Eq. (2) and Eq. (3) results in:

$$m_m m_r \omega^4 - (2k_m m_r(1 - \cos(G_n a)) + k_r m_m$$

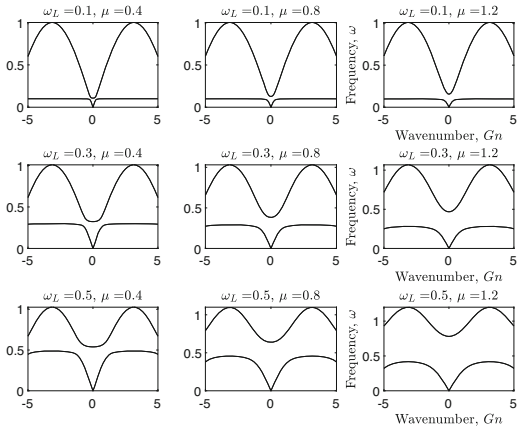

Fig. 2 Dispersion in the periodic structure with varying resonance coupling, and mass ratio. The plots demonstrate the profound influence of resonance conditions on the emergence and width of band gaps, highlighting the potential for tuned wave propagation control by adjusting the μ parameter

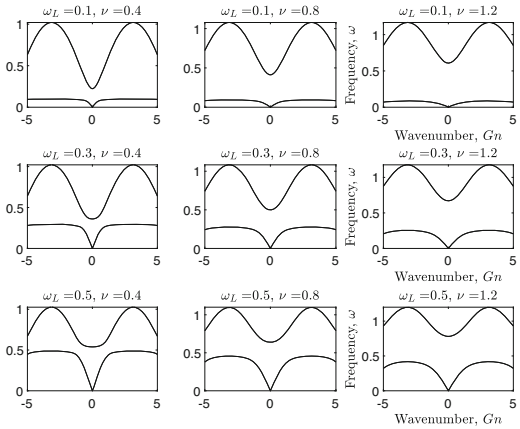

Fig. 3 Dispersion in the periodic structure with varying resonance coupling, and stiffness ratio. The plots demonstrate the profound influence of resonance conditions on the emergence and width of band gaps, highlighting the potential for tuned wave propagation control by adjusting the ν parameter

$$+ k_r m_r)\omega^2 - 2k_m k_r \left(\cos\left(G_n a\right) - 1\right) = 0 \tag{6}$$

For wider scope and easy analysis, the normalized dimensionless parameters are defined as follows:

$$\omega_L = \frac{1}{2}\sqrt{\frac{m_m}{k_m}\frac{k_r}{m_r}},\ \mu = \sqrt{\frac{m_r}{m_m}},\ \nu = \sqrt{\frac{k_r}{k_m}},$$
$$\omega_0 = \sqrt{\frac{4k_m}{m_m}} \tag{7}$$

Solving the Eq. (6) produces four roots for ω, which leads to Eqs. (8) and (9) for the individual derivatives with respect to mass and stiffness ratios, μ and ν.

From Figs. 2 and 3, it becomes evident that the properties of the periodic structure are intricately linked with the resonance conditions. One striking observation is that the emergence of a band gap isn't directly associated with a specific wave vector G_n. Instead, it's bound to certain conditions or parameters, possibly hinting at the importance of resonator properties in dictating wave propagation characteristics. This indicates a more complex interplay between the system parameters than just the wave vector, emphasizing the significance of resonator configurations in the system's acoustic properties.

Another pivotal observation is how the width of the band gap is influenced by ν. As the stiffness ratio

$$\omega_{\pm}(k) = \omega_0 \sqrt{\frac{1}{2}\left\{\frac{1}{2}[1-\cos(G_n)] + \omega_L^2\left(1+\mu^2\right) \pm \sqrt{4\left(\mu\omega_L^2\right)^2 + \left[\frac{1}{2}[1-\cos(G_n)] + \omega_L^2\left(\mu^2-1\right)\right]^2}\right\}} \tag{8}$$

$$\omega_{\pm}(k) = \omega_0 \sqrt{\frac{1}{16}\left\{\sin\left(\frac{G_n}{2}\right)^2 + \frac{1}{4}\nu^2 + \omega_L^2 \pm \sqrt{\left(\frac{1}{4}\nu^2 + \omega_L^2\right)^2 + \left(\frac{\nu^2}{4} - 4\omega_L^2\right)\sin\left(\frac{G_n}{2}\right)^2 + \frac{1}{4}\cos(G_n)^2 - \frac{1}{4}}\right\}} \tag{9}$$

The dispersion relation in Eq. (8) emphasizes the effects of μ, profoundly affecting the value of ω at each wave vector G_n. On the other hand, the dispersion relation Eq. (9) focuses more on the stiffness ratio ν, playing a critical role as well in determining the behavior of the system.

becomes more pronounced, the width of the band gap enlarges. This suggests that by manipulating the stiffness of the resonator, one could have a direct influence on the system's acoustic insulation or filtering capabilities. The stronger the coupling, the more formidable

the band gap, acting as a more robust barrier to certain frequency components.

Figure 3 suggests that controlling the system by adjusting ν is a valuable approach. Online tuning with the mass ratio μ can be challenging and impractical, whereas tuning with ν is straightforward, even in real-time scenarios. This holds significant importance for real-time control applications. Changing the mass ratio typically requires halting the operation to physically modify the system-a process that is both time-consuming and may inadvertently alter other critical parameters like the bandgap width. On the other hand, stiffness can be dynamically altered by implementing mechanisms such as actuators that adjust the position of an attached mass on the resonator, facilitating on-the-fly tuning of the bandgap frequency edges without needing to stop the system. This method provides a streamlined and practical solution for tuning the system's acoustic properties in real time, enhancing its adaptability and effectiveness in various applications.

3.3 Linear electromechanical resonators

Electromechanical systems can incorporate piezoelectric components that introduce additional nonlinearity to the system dynamics. These piezoelectric elements serve a dual purpose: they aid in attenuating vibrations within the unit cell, while simultaneously capturing and enhancing energy harvesting in the resonators. With reference to Fig. 1, let's take a scenario where resonators are equipped with piezoelectric elements. This incorporation couples the mechanical motion of the resonators with electrical dynamics, enriching the behavior and capabilities of the system but also complicating its dynamics.

To derive the dynamic equations of the harvester, the Lagrangian formulation for electromechanical systems is employed. The Lagrangian L is defined as:

$$L = T - U + W_e - D \tag{10}$$

Using Lagrange's equation, the governing dynamics are given by:

$$\frac{d}{dt}\frac{\partial L}{\partial \dot{q}_i} - \frac{\partial L}{\partial q_i} + \frac{\partial D}{\partial \dot{q}_i} = Q_i \tag{11}$$

Here, T represents the kinetic energy of the system, U is the potential energy, W_e denotes the coenergy of the piezoelectric module, and D is the dissipative function capturing both mechanical and electrical energy losses.

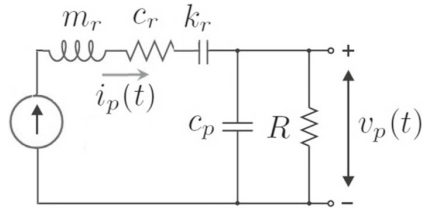

Fig. 4 An equivalent circuit for piezoelectric device model with internal electrode capacitance and load resistance

In this formulation, q_i is the generalized displacement corresponding to a specific degree of freedom in the system. Q_i represents the external force or input acting on the respective degree of freedom. By applying this equation, a set of differential equations governing the behavior of the harvester can be derived, effectively capturing its mechanical and electrical characteristics. The mechanical damping, often referred to as Rayleigh damping, is represented by the term

$$D_m = \frac{1}{2}c_r\,(\dot{u}_r - \dot{u}_m)^2 + \frac{1}{2}c_m\,(\dot{u}_{m^-} - \dot{u}_m)^2 + \frac{1}{2}c_m\,(\dot{u}_m - \dot{u}_{m^+})^2 \tag{12}$$

Piezoelectric devices are often represented by a model where a current source is in parallel with their internal electrode capacitance c_p, as depicted in Fig. 4. Additionally, a simple resistance R is connected to the load in this configuration. The electrical damping arises from the piezoelectric coupling, and it represents the energy dissipation due to electrical losses, denoted by D_p:

$$D_p = \frac{1}{2}\frac{v_p^2}{R} \tag{13}$$

Thus, the total dissipation function for the electromechanical system is given by $D = D_m + D_p$. Considering the piezoelectric transducer integrated into the resonator, the coenergy W_e of the piezoelectric module is given by:

$$W_e = \frac{1}{2}c_p v_p^2 - \theta v_p\,(u_m - u_r) - \frac{1}{2}k_p\,(u_m - u_r)^2 \tag{14}$$

where c_p and k_p denote the equivalent free-body capacitance and stiffness of the piezoelectric element, respectively. θ represents the equivalent force-electric factor of the piezoelectric cantilever beam. The first term corresponds to the electrical coenergy in the capacitance c_p. The second term represents the piezoelectric coenergy. The third term signifies the elastic strain

coenergy in a spring with stiffness k_p. Equatins (11) to (14) detail the electrical behavior of the piezoelectric resonators within the system. It's essential to note that θ and k_p must be experimentally determined to ensure the proposed model aligns with the real setup. In the total mechanical stiffness, $k_r + k_p$, the stiffness contribution from the piezoelectric material, k_p, is significantly smaller in magnitude compared to the resonator's mechanical stiffness, k_r. Therefore, its contribution to mechanical stiffness is often disregarded in the analysis. The energy equations are characterized by linear representations. Given these linear forms of the energy equations, the associated governing equations of motion in metastructure are as follows:

$$\begin{aligned} &m_m\ddot{u}_m(t) + k_m\left(2u_m(t) - u_{m^-}(t) - u_{m^+}(t)\right) \\ &\quad + c_m\left(2\dot{u}_m(t) - \dot{u}_{m^-}(t) + \dot{m}_{m^+}(t)\right) + k_r\left(u_m(t) - u_r(t)\right) \\ &\quad + c_r\left(\dot{u}_m(t) - \dot{u}_r(t)\right) + \theta v(t) = 0 \end{aligned} \tag{15}$$

$$\begin{aligned} &m_r\ddot{u}_r(t) - c_r\left(\dot{u}_m(t) - \dot{u}_r(t)\right) \\ &\quad - k_r\left(u_m(t) - u_r(t)\right) - \theta v(t) = 0 \end{aligned} \tag{16}$$

$$c_p\dot{v_p}(t) + \frac{v_p(t)}{R} - \theta(\dot{u}_m(t) - \dot{u}_r(t)) = 0 \tag{17}$$

Equations (15) to (17) are included with multiple parameters, adding to their complexity. For enhanced clarity and broader applicability, the model's governing equations are recast using the established normalized parameters as follows:

$$\begin{aligned} &\ddot{u}_m(t) + 4\zeta_m\omega_m\dot{u}_m(t) - 2\zeta_m\omega_m\left(\dot{u}_{m^-}(t) + \dot{u}_{m^+}(t)\right) \\ &\quad + 2\omega_m^2 u_m(t) - \omega_m^2(u_{m^-}(t) + u_{m^+}(t)) \\ &\quad + 2\mu\zeta_r\omega_r\left(\dot{u}_m(t) - \dot{u}_r(t)\right) + v^2\omega_m^2\left(u_m(t) - u_r(t)\right) \\ &\quad + k_e^2 v^2\omega_m^2\bar{v}(t) = 0, \end{aligned} \tag{18}$$

where for the last mass $u_m(t) - u_{m^+}(t) = 0$, $\dot{u}_m(t) - \dot{u}_{m^+}(t) = 0$, and for the first mass $u_{m^-}(t) = u_b(t)$. The equation for the resonator becomes:

$$\begin{aligned} &\ddot{u}_r(t) - 2\zeta_r\omega_r\left(\dot{u}_m(t) - \dot{u}_r(t)\right) \\ &\quad - \omega_r^2\left(u_m(t) - u_r(t)\right) - k_e^2\omega_r^2\bar{v}(t) = 0 \end{aligned} \tag{19}$$

Lastly, the equation representing the piezoelectric effect is given as:

$$\dot{\bar{v}}(t) + \frac{\omega\dot{\bar{v}}(t)}{r_g} - (\dot{u}_m(t) - \dot{u}_r(t)) = 0 \tag{20}$$

where $k_e^2 = \theta^2/\left(c_p k_r\right)$ indicates the electromechanical coupling coefficient, $\bar{v} = c_p v_p/\theta$ is the scaled piezoelectric output voltage, and $r_g = Rc_p\omega_r$ designates the proportion of the actual load R to its optimal value R_{opt}. Additionally, $\zeta_m = c_m/(2m_m\omega_m)$ and $\zeta_r = c_r/(2m_r\omega_r)$ are the damping ratios of the main chain and the resonator, respectively. Furthermore, $v^2 = k_r/k_m$ represents the stiffness proportion between the resonator and the chain mass, while $\mu = m_r/m_m$ depicts the mass ratio between the resonator and the chain mass.

3.4 Analysis of power output of standard piezoelectric circuit for energy harvesting

The primary objective of this research is to investigate the inherent properties of various types of nonlinearity in piezoelectric materials, rather than comparing different circuit models. For a consistent evaluation, every type of nonlinearity is paired with the same standard circuit, ensuring each nonlinearity is studied in isolation and without the influence of varying circuit efficiencies. A standard rectifier interface circuit with no electrical losses for energy harvesting is explored using a lumped parameter model. In design analysis for energy harvesting, a simplified circuit is frequently employed, as shown Fig. 5. In this configuration, the regulation circuit and battery are substituted with an equivalent resistor labeled as R, and the rectified voltage across it is denoted as v_e. It is assumed, for the purposes of this study, that the rectifying bridge is in an ideal and faultless state. A rectifying bridge circuit is integrated, targeting a stable output DC voltage v_e, which connects the load directly. It is assumed that the filter capacitor c_e is sufficiently large to render v_e essentially constant. In steady-state operation, the average rectified voltage and displacement are related. Governed by equations, the piezo voltage $v_p(t)$ is proportional to the displacement $u(t)$. Both variables are modeled as $u(t) = u_0\sin(wt-\theta)$ and $v_p(t) = v_{p_0}(wt-\theta)$, where u_0 is the constant displacement magnitude, and $v_{p_0}(t)$ is a periodic function with $|v_{p_0}(t)| \le v_e$.

During a semi-period $\frac{T}{2}$, defined as $T = \frac{2\pi}{w}$, the integral of the rate of change of $v_p(t)$ is $2v_e$. This yields

$$\int_{t_1}^{t_2} I(t)dt = \frac{T}{2}\frac{v_e}{R}, \tag{21}$$

delineating the relationship between the current and average rectified voltage [38]. The integral $\int_{t_1}^{t_2}\dot{v}_p(t)dt$ represents the total change in the piezoelectric voltage $v_p(t)$ from time t_1 to t_2. If $v_p(t)$ oscillates between $-v_e$ and v_e during this semi-period $\frac{T}{2}$, then the total change in $v_p(t)$ is $v_e - (-v_e) = 2v_e$. If $u(t)$ is oscillating from its minimum $-u_0$ to its maximum u_0 during the semi-period from time t_1 to t_2, then the change in $u(t)$ during this period is $u_0 - (-u_0) = 2u_0$.

Assuming the standard linear form and rewriting Eq. (17) yields to:

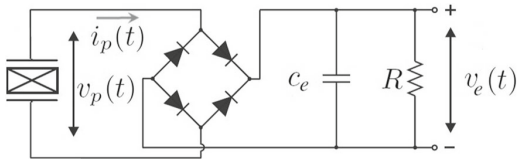

Fig. 5 Classical energy harvesting circuit for the standard electronic interfaces

$$c_p \dot{v}_p(t) + i_p(t) = \theta \dot{z}(t), \tag{22}$$

where $z(t)$ is the relative displacement of the mass chain with respect to the resonator in each unit cell. Integration of Eq. (22) from time t_1 to t_2 gives:

$$2c_p v_e + \frac{T}{2}\frac{v_e}{R} = 2\theta z_0 \tag{23}$$

This equation correlates the changes in stored electric charge, current, and mechanical displacement between times a and b. Given $\frac{T}{2} = \frac{\pi}{\omega}$, the equation for v_e expressed as:

$$v_e = \frac{R\theta\omega}{Rc_p\omega + \frac{\pi}{2}} z_0 \tag{24}$$

Furthermore, the average harvested power P can be well-defined as:

$$P = \frac{v_e^2}{R} = \frac{R\theta^2\omega^2}{\left(Rc_p\omega + \frac{\pi}{2}\right)^2} z_0^2 \tag{25}$$

3.5 Nonlinear electromechanical resonators

The behavior of a linear piezoelectric element is described by Eq. (17). While linearized models offer simplicity and are often adequate for many applications, they may miss critical behaviors and limit our understanding and predictive capabilities. The study of nonlinearity provides a comprehensive and accurate view of systems, essential for both practical applications and scientific inquiry. When introducing any of these nonlinearities into the model, it is essential to ensure that they are grounded in physical reality or experimental observations relevant to the system. Modeling choices should be justified based on the underlying physics, empirical data, or both.

One common approach to introduce nonlinearity is by using a polynomial expansion. When considering the piezoelectric response, one possibility is a nonlinear dependency of the voltage, denoted as $v(t)$, on strain. Adding a simple quadratic nonlinearity to the piezoelectric equation, yields to:

$$\begin{aligned} &c_p \dot{v}(t) + \frac{v(t)}{R} - \theta\left(\dot{u}_m(t) - \dot{u}_r(t)\right) \\ &-\beta\left(\dot{u}_m(t) - \dot{u}_r(t)\right)^2 = 0 \end{aligned} \tag{26}$$

where β is a coefficient of the nonlinear term. In this model, the piezoelectric response starts to deviate from linearity as the strain (differential displacement) increases. The term β dictates the strength of this nonlinearity. If β is zero, the system returns to the original linear behavior. In electronic circuits, transistors, especially MOSFETs, can exhibit polynomial behavior with respect to gate-source voltage and drain current, leading to nonlinear amplification. Moreover, the dynamics of robotic arms can have nonlinear components due to joint friction, and these can be represented as polynomial functions of velocities.

Upon introducing nonlinearity, the system can be numerically simulated using techniques tailored for nonlinear differential equations, such as the Runge–Kutta method. Software packages, like MATLAB's Simulink or COMSOL, can also be employed. Initial conditions and boundary conditions need to be established based on the specific study.

Apart from polynomial expansion, there are several other types to introduce and study nonlinearity in a piezoelectric energy harvester.

3.6 Theoretical models for the nonlinear energy harvesting

The nonlinear behavior in energy harvesting can be succinctly captured in a generalized equation which encompasses multiple facets of nonlinearity. Consider the following expression:

$$\begin{aligned} &\alpha\frac{v(t)}{R(\omega)} + c_p\frac{d}{dt}[f(v(t))] \\ &\quad - \theta\left[g\left(\frac{d^2}{dt^2}u_m(t) - \frac{d^2}{dt^2}u_r(t), v(t)\right)\right] \\ &\quad - h\left(\int v(t)dt\right) = 0 \end{aligned} \tag{27}$$

Here: $R(\omega)$ introduces nonlinearity as a function of frequency. Adjustable parameter, α can be varied to explore different system behaviors and regimes. $f(v(t))$ introduces nonlinearity as a function of the voltage across the impedance.

The term $g\left(\frac{d^2}{dt^2}u_m(t) - \frac{d^2}{dt^2}u_r(t), v(t)\right)$ represents a nonlinear function of the acceleration and voltage. $h\left(\int v(t)dt\right)$ is the nonlinearity introduced by an integral of voltage over time. It is important to note that this is a completely abstract and generalized equation that must be determined based on the system specifications and the physics involved.

The Eq. (27) exemplifies a multi-faceted nonlinear system that integrates various nonlinear dependencies into a comprehensive framework. $R(\omega)$ denotes a frequency-dependent nonlinearity, reflective of materials like semiconductors or piezoelectric elements under resonance. $f(v(t))$ embodies a voltage-dependent nonlinearity, typical in devices like diodes or transistors, where shifting voltage can alter operational regimes. The term $g\left(\frac{d^2}{dt^2}u_m(t) - \frac{d^2}{dt^2}u_r(t), v(t)\right)$ encapsulates a coupled nonlinearity, hinting at a complex relationship between the accelerations of two system components and voltage. Lastly, $h\left(\int v(t)dt\right)$ introduces a memory effect, capturing historical influences on the system, akin to hysteresis or capacitive responses.

To derive the standard linear form of a piezoelectric equation, the resistance is considered as not frequency-dependent, and the capacitance is assumed not to be influenced by voltage variations, simplifying the term $c_p\frac{d}{dt}[f(v(t))]$ to $c_p\dot{v}(t)$ by setting $f(v(t)) = v(t)$. The electromechanical coupling is taken to be linear, meaning the term with $g(\cdot)$ reduces to $\theta\left(\dot{u}_2(t) - \dot{u}_1(t)\right)$, indicating the coupling coefficient isn't influenced by displacement, velocity, or acceleration. Lastly, the term $h\left(\int v(t)dt\right)$ is disregarded, signifying that the integral of voltage over time does not significantly influence the system dynamics. Under these assumptions and simplifications, the generalized Eq. (27) reduces to Eq. (17), which is the standard linear form of a rectifier circuit.

3.7 Internally coupled resonators with mechanical nonlinearity

To clarify the dynamics within the mechanically internally coupled system, the analysis strategically simplifies the system by focusing exclusively on the springs, omitting damping effects and electromechanical elements. This approach allows for a concentrated examination of the system's behavior under the influence of linear springs in the primary chain and resonators, alongside nonlinear springs that facilitate internal coupling between resonators. As depicted in Fig. 6, the

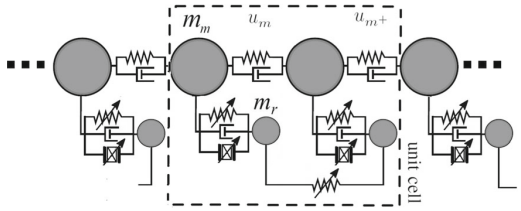

Fig. 6 Nonlinear mechanical internally coupled chain. The dashed rectangle is unit cell

system consists of a nonlinear mechanical internally coupled chain, with the unit cell highlighted by the dashed rectangle. Consequently, the dynamic behavior of the system will be primarily dictated by this nonlinear internal coupling between resonators, even as the rest of the system retains its linearity. This configuration allows for a focused study on the impacts and potential advantages of having a nonlinear inter-resonator spring in an otherwise linear spring system.

The kinetic energy, denoted by T, encompasses the motion of the main chain and the resonators and is given by:

$$T = \frac{1}{2}m_m\left(\dot{u}_m^2 + \dot{u}_{m^+}^2\right) + \frac{1}{2}m_r\left(\dot{u}_r^2 + \dot{u}_{r^+}^2\right) \tag{28}$$

The potential energy, represented by U, captures the energy stored in the main chain's linear springs, the coupling springs between the main chain and resonators, and the nonlinear internal coupling springs of the resonators:

$$\begin{aligned} U =& \frac{1}{2}k_m\left[(u_{m^-} - u_m)^2 + (u_m - u_{m^+})^2 + (u_{m^+} - u_{m^{++}})^2\right] \\ &+ \frac{1}{2}k_r\left[(u_m - u_r)^2 + (u_{m^+} - u_{r^+})^2\right] \\ &+ \frac{1}{2}k_{c_1}(u_r - u_{r^+})^2 + \frac{1}{4}k_{c_2}(u_r - u_{r^+})^4 \end{aligned} \tag{29}$$

Here, k_{c_1} and k_{c_2} are the linear and nonlinear coupling coefficients, respectively. The k_{c_1} term introduces a linear coupling between resonators, while k_{c_2} induces a bistable nonlinearity due to its quartic nature between resonators. When both k_{c_1} and k_{c_2} are positive $\left(k_{c_1} > 0\right.$ and $\left.k_{c_2} > 0\right)$, a classic monostable state is achieved, simplifying the system by avoiding the necessity to find and linearize around a stable point. This selection, while ensuring straightforward and stable system behavior, is often employed to eschew the complexities that arise when dealing with bistable systems, particularly when $k_{c_1} < 0$ and $k_{c_2} > 0$.

Utilizing the Lagrangian formulation, the system's equations of motion are derived as:

$$m_m\ddot{u}_m(t) + k_m\,(2u_m(t) - u_{m^-}(t) - u_{m^+}(t)) + k_r\,(u_m(t) - u_r(t)) = 0 \quad (30)$$

$$m_r\ddot{u}_r(t) - k_r\,(u_m(t) - u_r(t)) + k_{c_1}\,(u_r(t) - u_{r^+}(t)) + k_{c_2}\,(u_r(t) - u_{r^+}(t))^3 = 0 \quad (31)$$

$$m_m\ddot{u}_{m^+}(t) + k_m\,(2u_{m^+}(t) - u_m(t) - u_{m^{++}}(t)) + k_r\,(u_{m^+}(t) - u_{r^+}(t)) = 0 \quad (32)$$

$$m_r\ddot{u}_{r^+}(t) - k_r\,(u_{m^+}(t) - u_{r^+}(t)) - k_{c_1} \times (u_r(t) - u_{r^+}(t)) - k_{c_2}\,(u_r(t) - u_{r^+}(t))^3 = 0 \quad (33)$$

The superscript '$^+$' indicates the two adjacent mass-in-mass structures, where $u_{m^{++}}$ denotes the displacement of the mass or unit that is two positions away from mass m. Utilizing Bloch's theorem, the waveform of the harmonic displacements of masses can be expressed as:

$$\begin{aligned} u_m &= u_{m_0}e^{i(G_n x-\omega t)} \\ u_{m^+} &= u_{m_1}e^{i(G_n x+G_n a-\omega t)} \\ u_r &= u_{r_0}e^{i(G_n x-\omega t)} \\ u_{r^+} &= u_{r_1}e^{i(G_n x+G_n a-\omega t)}, \end{aligned} \quad (34)$$

where G_n represents the wave number or spatial frequency, dictating the spatial periodicity of the wave over the unit cell with the dimension of a. The coefficients u_{m_0}, u_{m_1}, u_{r_0}, and u_{r_1} represent the complex wave amplitudes. Integrating these terms into the provided equations leads to the derivation of the dispersion relation. The associated matrix is determined for this purpose, and by setting its determinant to zero, a relationship between G_n and ω is established. For nonlinear scenarios, as presented in the above equations, a numerical approach is typically employed. From four inertias in a unit cell, an eighth-order dispersion equation arises when the determinant is zero. This results in four curves with three band gaps on the positive real axis, indicating that internally coupled metamaterials offer additional band gaps over conventional ones.

In this study, we focus on a specific frequency range. A comprehensive analysis of the effects of piezoelectric nonlinearities across the entire frequency spectrum is beyond the scope of this work.

3.8 Electromchanical internally coupled resonators

In the previous sections, we explored metamaterials with internal resonator coupling. Given the challenges associated with designing and implementing the internal spring, especially when targeting negative stiffness, an alternative approach is to employ an electrical shunt circuit. Specifically, a prototype capacitance can mimic the behavior of a mechanically internally coupled resonator.

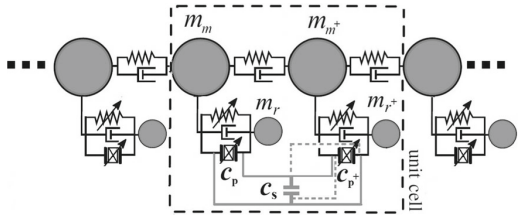

Fig. 7 Internally coupled with electrical shunt circuit. Forward (dash) and reverse (solid) capacitance shunting configuration

3.8.1 Internal coupling via shunt capacitance circuit technique

In this section, the shunt capacitance circuit technique is employed to model a two-degree-of-freedom electrical system with internal coupling, as illustrated in Fig. 7. In this scenario, capacitance is incorporated as a key component instead of utilizing the previously formulated resistance (R).

Figure 7 presents two different configurations of the shunt circuit: the forward and the reverse. For the forward setup, the top and bottom surfaces of the piezoelectric transducer on the left align with the analogous surfaces of its counterpart on the right. Conversely, the reverse configuration has the top and bottom surfaces of the two piezoelectric transducers connected in an opposite fashion. In both setups, a capacitor is connected in parallel to both piezoelectric transducers.

The analytical procedures for both configurations are analogous, leading to comparable conclusions. The distinction in circuit connectivity between these two setups only results in a sign reversal in the ultimate expression for equivalent coupling stiffness. Both forward and reverse connections can achieve the same functionality, albeit with differing capacitance tuning strategies. This investigation primarily focuses on the reverse connection configuration. In its absence of external capacitance, it exhibits characteristics akin to a standard spring with positive stiffness, simplifying its interpretation in an equivalent mechanical context.

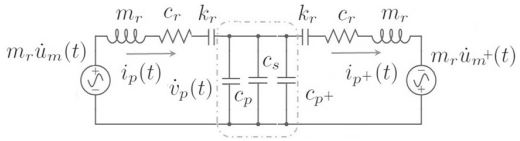

Fig. 8 Equivalent electrical system representation of the unit cell resonators with capacitance shunt circuit using the impedance analogy

Capacitance typically relates the change in electric charge to shifts in electric potential. With positive total capacitance, a discharge of current leads to a voltage decrease across the capacitor, whereas with negative total capacitance, the voltage increases. Utilizing the impedance analogy (current to velocity, charge to displacement, voltage to force), the circuit segments LRC and LRC^+ correspond to the resonators $m_r c_r k_r$ and $(m_r c_r k_r)^+$, respectively, as illustrated in Fig. 8. For simplicity, the mechanical properties of the resonators (mass, stiffness, and damping) are assumed to be identical.

The voltage across the total capacitance represents the force interaction between these resonators. Additionally, the current through total capacitance, representing the difference in currents in the loops' paths, indicates the difference in velocity between the resonators. The charge variation in total capacitance indicates the displacement difference between the resonators. Hence, the capacitor in the electrical system can be envisioned as a spring, k_s coupling the resonators in the mechanical domain, with positive total capacitance acting as a positive-stiffness coupling spring and negative total capacitance as a negative-stiffness spring.

Considering the reversed configuration of the two piezoelectric transducers, the voltages exhibit identical magnitudes but with opposite directions. Factoring in the current passing through the parallel-connected capacitance c_s, the relationship between the voltages is expressed as:

$$\frac{1}{c_s}\int \left(i_p(t) - i_{p^+}(t)\right) dt = v_p(t) \tag{35}$$

The design employs an internal shunt capacitance circuit to optimize the band gap behavior in resonators. When this capacitance acts as a negative capacitor and is finely tuned, it can offset the capacitances of linked piezoelectric transducers, enhancing the coupling between adjacent resonator.

Considering damping in the resonators and assuming identical stiffness, damping coefficients, and masses for all resonators, the governing equations for the motion of the two resonators within a unit cell (refer to Fig. 7) relative to the mass of the chain is as follows:

$$\begin{aligned} &m_r\ddot{z}_r(t) + c_r\dot{z}_r(t) + k_r z_r(t) + \theta_r v_p(t) \\ &\quad = m_r\ddot{u}_m(t) \end{aligned} \tag{36}$$

$$\begin{aligned} &m_r\ddot{z}_{r^+}(t) + c_r\dot{z}_{r^+}(t) + k_r z_{r^+}(t) + \theta_{r^+} v_{p^+}(t) \\ &\quad = m_r\ddot{u}_{m^+}(t) \end{aligned} \tag{37}$$

The relative displacements of these resonators with respect to the main chain structure are denoted by $z_r(t)$ and $z_{r^+}(t)$. The electromechanical coupling coefficients are θ_r and θ_{r^+}, and the voltages across the corresponding piezoelectric transducers are $v_p(t)$ and $v_{p^+}(t)$. The excitation displacements are represented as $u_m(t)$ for the left and $u_{m^+}(t)$ for the right resonators.

The governing electrical domain equations for the piezoelectric transducers are as follows:

$$c_p\dot{v}_p(t) + i_p(t) - \theta_r\dot{z}_r(t) = 0 \tag{38}$$

$$c_{p^+}\dot{v}_{p^+}(t) + i_{p^+}(t) - \theta_{r^+}\dot{z}_{r^+}(t) = 0 \tag{39}$$

By substituting Eq. (35) into Eqs. (38) and (39), expressions for currents $i_p(t)$ and $i_{p^+}(t)$ in the loops are derived as:

$$i_p(t) = \frac{c_{p^+}\theta_r\dot{z}_r + c_p\theta_{r^+}\dot{z}_{r^+} + c_s\theta_r\dot{z}_r}{c_p + c_{p^+} + c_s} \tag{40}$$

$$i_{p^+}(t) = \frac{c_{p^+}\theta_r\dot{z}_r + c_p\theta_{r^+}\dot{z}_{r^+} + c_s\theta_{r^+}\dot{z}_{r^+}}{c_p + c_{p^+} + c_s} \tag{41}$$

Substituting Eqs. (40) and (41) into Eq. (35) and integrating with respect to time for zero initial condition yields:

$$v_p(t) = \frac{(\theta_r z_r - \theta_{r^+} z_{r^+})}{c_p + c_{p^+} + c_s} \tag{42}$$

$$v_{p^+}(t) = -\frac{(\theta_r z_r - \theta_{r^+} z_{r^+})}{c_p + c_{p^+} + c_s} \tag{43}$$

After substituting Eqs. (40) and (41) into Eq. (35) and integrating with respect to time, assuming θ_r is equal to θ_{r^+}, the equations of motion can be simplified as follows

$$\begin{aligned} &m_r\ddot{z}_r(t) + c_r\dot{z}_r(t) + k_r z_r(t) \\ &\quad + k_s\left(z_r(t) - z_{r^+}(t)\right) = m_r\ddot{u}_m(t) \end{aligned} \tag{44}$$

$$\begin{aligned} &m_r\ddot{z}_{r^+}(t) + c_r\dot{z}_{r^+}(t) + k_r z_{r^+}(t) \\ &\quad - k_s\left(z_r(t) - z_{r^+}(t)\right) = m_r\ddot{u}_{m^+}(t), \end{aligned} \tag{45}$$

where

$$k_s = \frac{\theta_r^2}{c_p + c_{p^+} + c_s}. \tag{46}$$

Implementing coupling through piezoelectric transducers and a shunt capacitance circuit is practical, as it serves as an equivalent spring that relates the motions of two resonators via their relative displacements. This coupling mechanism, resulting from local resonances, creates additional band gaps in metamaterials by generating two resonant frequencies.

The piezoelectric transducers, when shunted, act as an analogous internal coupling spring k_s, similar to the mechanical internal coupling that links the movement of two resonators. However, it's important to note that using a negative shunt capacitor, which is a type of positive feedback in op-amp circuits, can increase the risk of system instability without the right parameter choices. Despite this, the design's strength is its tunability and ability to generate multiple band gaps, offering robust vibration suppression.

3.9 Stability analysis

The behavior of the system is largely determined by the parameter k_s, which characterizes the stiffness introduced due to electromechanical coupling via the shunt circuit. To introduce negative stiffness, assuming electromechanical coupling, θ_r is equal to θ_r^+, it is requisite that k_s be negative. This can be expressed mathematically as:

$$k_s = \frac{\theta_r^2}{c_p + c_{p^+} + c_s} < 0 \tag{47}$$

Given that θ_r^2 will always be positive, the denominator must be negative for k_s to be negative. Thus, either c_p and/or c_{p^+}must be negative (which could signify negative capacitance introduced, for instance, by an active circuit) while the magnitude of their sum should be greater than c_s.

Utilizing the Jacobian method and employing the vector $[z_r(t), z_{r^+}(t)]$ for the linear matrix of the system depicted by Eqs. (44) and (45), the eigenvalues are provided as $\lambda_{1,2} = \pm\frac{\sqrt{-k_r m_r}}{m_r}$, and $\lambda_{3,4} = \pm\frac{\sqrt{-m_r(k_r+2k_s)}}{m_r}$. The stability of a system is contingent upon the real parts of its eigenvalues. For the system at hand, when $k_r + 2k_s > 0$, all eigenvalues are purely imaginary, suggesting marginal stability. In this scenario, the system, when perturbed, will oscillate indefinitely without growing unbounded or decaying to zero. Conversely, when $k_r + 2k_s < 0$, the system presents two positive eigenvalues and two negative ones. The presence of positive real eigenvalues clearly indicates an unstable system. This underscores the paramountcy of the interplay between the resonator's spring constant and the feedback shunt capacitance stiffness (associated with k_s). If the feedback's influence is excessively robust and negative, it could push the system into an unstable regime. Therefore, for a stable system, the criterion for c_s is:

$$c_s > \frac{8m_r\theta_r^2}{c_r^2 - 4k_r m_r} - c_p - c_{p^+} \tag{48}$$

For most practical applications, a strictly stable system, where all disturbances decay, is more desirable than a marginally stable one. Exploring stability in lumped parameter systems reveals that maintaining a strictly stable condition, preferable for practical applications, hinges on a fine balance within the system's parameters, as indicated by the derived criterion. For a detailed examination of stability analysis and energy harvesting within lumped parameter systems, particularly those incorporating internally coupled resonators, the study in [39] extends the discussion to encompass a variety of conditions.

4 Simulation analysis and discussion

The behavior of the proposed models is observed through simulations using the case study parameters outlined in Table 1. The system model was developed by formulating a set of interconnected ordinary differential equations that encapsulate both the mechanical and electrical dynamics of the piezoelectric harvesters. Numerical solutions to this system were obtained utilizing the fourth-order Runge–Kutta method with a carefully chosen time step to guarantee precision and stability in the results. The simulation results explore various aspects of the system's dynamic response, including vibration mitigation, energy harvesting, power output, and robustness analysis.

4.1 Nonlinear mechanical resonators and internal coupling dynamics

In Fig. 9, the band gap behaviors for various system configurations are presented. The system's natural fre-

Table 1 Defined parameters for the piezoelectric model

Parameter	Value
Mass of main chain (m_m)	0.056 kg
Mass of resonator (m_r)	0.0336 kg
Spring constant of main chain (k_m)	150 N/m
Spring constant of resonator (k_r)	129.6 N/m
Damping coefficient of main chain (c_m)	0.0464 Ns/m
Damping coefficient of resonator (c_r)	0.0334 Ns/m
Piezoelectric capacitance (c_p)	1.5 mF(C/m)
Electromechanical coupling coefficient (θ)	0.25 N/V
Nonlinear stiffnesses quadratic coefficient (γ_2)	-500 N/m^2
Nonlinear stiffnesses cubic coefficient (γ_3)	15000 N/m^3
Linear coupling coefficient (k_{c_1})	198(-20) N/m
Nonlinear coupling coefficient (k_{c_2})	2386(880) N/m^3
Shunt capacitance (c_s)	-7.9 mF(C/m)
Internal resistance (R)	500 Ω

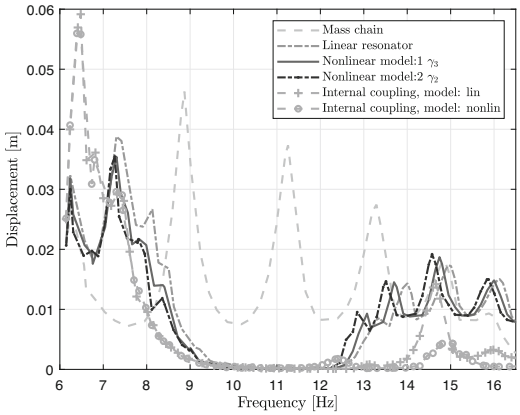

Fig. 9 Comparative analysis of band gap behaviors in a 1-D chain system: insights from linear, nonlinear, and internally coupled resonator configurations

quencies are analyzed within a range from 6 to 17 Hz. The introduction of locally resonating elements distinctly establishes a band gap, differentiating these configurations from the conventional metastructure setup. This band gap characteristic is attributed to the linear local resonance, which undergoes out-of-phase motion when subjected to an external excitation frequency near its local resonance frequency.

The nonlinear analysis focuses primarily on contrasting linear systems with their nonlinear counterparts, in addition to examining internally coupled systems. Effects arising from bifurcation and its influence on frequency sweeps are not explored in this context. Nonlinear resonators, both quadratic and cubic, exhibit a more extensive band gap compared to their linear counterparts. For the quadratic nonlinearity, a modified relation is employed:

$$f_r = k_r u + \gamma_{r_2} u|u| \tag{49}$$

This model facilitates numerical simulations and provides a comparative benchmark against cubic nonlinearities. Both linear and nonlinear internal coupling serve to effectively increase the bandgap within the main chain, as illustrated in Fig. 9. The analysis of mechanical internal coupling reveals that linear and nonlinear internal couplings may not necessarily boost power and energy generation, even when the main chain has a wider bandgap. Surprisingly, energy harvested with internal coupling is sometimes lower than in a single-chain setup. This suggests that interactions between resonators could hinder energy accumulation.

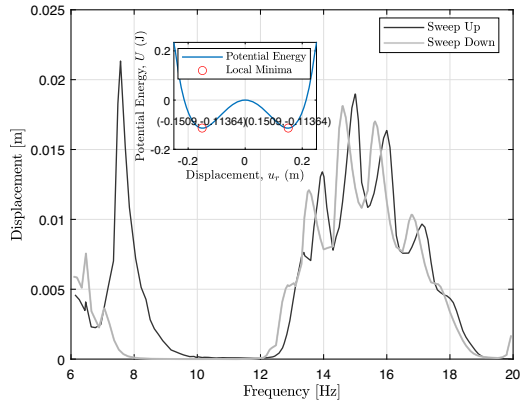

Fig. 10 Displacement response of bistable nonlinear mechanical internal coupling resonators. Linear coupling coefficient $k_{c_1} = -20$ N/m, and nonlinear coupling coefficient $k_{c_2} = 880$ N/m^3. Inset: Resonator's potential energy profile for the specified coupling parameters

Figure 10 shows the transmission response of a metastructure equipped with a nonlinear bi-stable internal coupling resonator. The observed bifurcation is shaped by linear ($k_{c_1} = -20$ N/m) and nonlinear ($k_{c_2} = 880$ N/m^3) coupling coefficients, with the continuous sweep offering a detailed system response. The main graph underlines the system's potential energy dynamics, with an unstable origin indicating negative stiffness. This complexity is further highlighted by bifurcations between 14–16 Hz. The inset reveals var-

ious energy states the system can attain. Multiple local minima suggest system multi-stability, especially during large fluctuations. Hysteresis is evident from discrepancies in sweep traces, particularly in lower frequencies from 6 Hz and 10 Hz. However, it's vital to understand the intent behind the choice of parameters in this study. The deliberate restriction to a specific frequency range serves to mimic negative stiffness phenomena observed in specific electromechanical systems.

Cubic nonlinearities, with their symmetric properties, are observed to manifest either pure hardening or softening behaviors. This stands in contrast to the dual behavior inherent to asymmetric quadratic nonlinearities. The significance of optimal impedance matching is underscored, highlighting its role in achieving enhanced vibration suppression and energy harvesting. However, as theoretical constructs transition to tangible systems, certain compromises are often necessary to accommodate weakly and strongly coupled systems [34,40].

Setting both k_{c_1} and k_{c_2} to be positive (see Table 1) induces a classic monostable state, simplifying the system and avoiding the complications inherent in managing bistable systems, particularly when $k_{c_1} < 0$ and $k_{c_2} > 0$.

Furthermore, when evaluating mechanically internal coupling configurations, there is a discernible decrease in efficiency for energy harvesting. While band gaps are inherent features of these systems, they may sometimes present challenges, especially in terms of wave propagation. The compounded presence of a band gap and internal coupling appears to negatively impact overall energy output. Detailed investigations into the dynamics of these coupled resonators could provide deeper insights into the underlying mechanisms that result in reduced efficiency.

Nonetheless, simulating internally coupled resonators with bistable nonlinearity to observe bifurcation effects was considered valuable. However, due to the inherent complexity and the desire to avoid simulating rapid transitions, this approach was ultimately avoided.

Figure 11 shows the nonlinear spring force-displacement relation for cubic nonlinearities, and transmittance of this nonlinearity. It shows the influence of cubic nonlinearity in the system. Distinctly, the nonlinearity is characterized by the coefficient γ_3, where its sign determines the hardening or softening

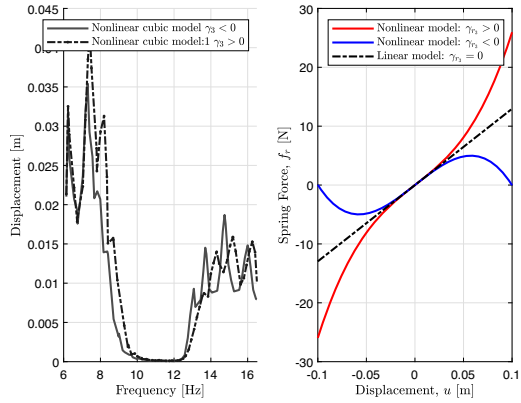

Fig. 11 Nonlinear characteristics of the 1-D chain system: **a** Transmittance response influenced by cubic nonlinearity, and **b** nonlinear spring force-displacement relationship for cubic nonlinearities

nature of the system. For the resonator's equation force:

$$f_r = k_r u + \gamma_{r_3} u^3, \tag{50}$$

The value of γ_{r_3} has been varied as $\pm 15000\ \mathrm{N/m^3}$, pointing to two contrasting behaviors. When $\gamma_{r_3} > 0$, the system exhibits hardening nonlinearity. This means as the amplitude of excitation increases, the natural frequency of the system also escalates. Conversely, for $\gamma_{r_3} < 0$, we observe a softening nonlinearity. Here, an increase in the excitation amplitude leads to a decrease in the system's natural frequency. To reduce the complexity of the system, bistable nonlinearity is deliberately avoided, eliminating the need to perform up and down-frequency simulations. In the broader context, the introduction of diatomic chains, incorporation of nonlinear local resonators (as depicted in Figs. 6, 7), or a transition to 2D setups, allows for deeper exploration and comprehension of the intricate nonlinear phenomena in advanced systems. Building on the findings from the frequency domain analysis, it becomes evident in the time domain that systems with cubic nonlinearity commence vibration suppression earlier compared to those with linear resonators. The duration during which effective suppression occurs depends on multiple factors, including the natural frequency of the system and its inherent physical properties.

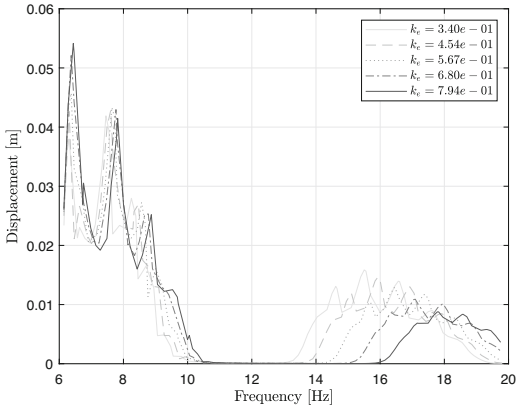

Fig. 12 Band gap illustration for a monochain featuring linear local resonators with $n = 8$ mass chains, demonstrating the influence of k_e on band gap and metastructure response

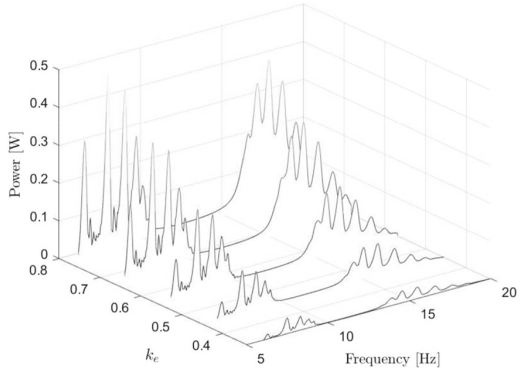

Fig. 13 Electromechanical coupling's impact on energy harvesting: illustration of the power harvested across varying k_e in an $n = 8$ unit cell monochain, showcasing the pivotal role of the electromechanical coupling coefficient in optimizing energy conversion and system dynamics

4.2 Investigation on energy harvesting performance in linear electromechanical metamaterial

In Fig. 12, the transmittance for various values of k_e, representing the piezoelectric coupling coefficient (Eq. 20), is depicted. For the analysis, the stiffness of the piezoelectric element, represented by k_p, is considered negligible compared to the significantly greater stiffness of the resonator, denoted by k_r. This simplification enables a focus on the effects of other parameters without the interference of k_p.

A noticeable broadening of the band gap is observed as the electromechanical coupling coefficient k_e is increased, indicating an enhanced capacity of the system to suppress vibrations. The peaks of the transmittance adjacent to this band gap are notably sensitive to variations in k_e, while those further from the band gap show minimal alternations. This observation emphasizes the crucial role played by k_e in modulating the system's response when using piezoelectric materials, highlighting its significant contribution to vibration control in complex systems. Additionally, the parameter r_g, defined as $r_g = \omega_r c_p R$, can be adjusted to achieve minimal transmittance at each frequency.

As depicted in Fig. 13, the electromechanical coupling coefficient k_e, plays a pivotal role in the energy harvesting performance of a system comprising eight unit cells. This parameter k_e, essentially governs how efficiently piezoelectric materials convert mechanical energy to electrical energy and vice versa, exerting a significant influence on the outcomes of energy harvesting. In scenarios characterized by weak coupling, an increase in k_e results in a notable increase in power output. Conversely, in situations involving strong coupling, an increase in k_e leads to a power level that remains constant, preventing any additional improvements. For our subsequent analysis, a weak coupling value of $k_e = 0.567\,(c_p = 1.5\text{mF})$ is selected to avoid the complex power response patterns observed in strong coupling situations. To comprehensively assess overall energy harvesting performance, we uniformly adjust the resistors R, connected to the piezoelectric transducers, and consolidate power outputs from these resistors. High-capacitance (millifarad-level) piezoelectric materials have a wide range of applications, from energy-harvesting floor tiles in busy areas to vibration damping in machinery, structural monitoring, energy recapture in vehicle suspensions, self-charging personal electronics, and power sources for wearable health monitors. To enhance the capacitance of these materials, strategies include selecting materials with higher dielectric constants, optimizing element geometry, using multi-layer structures, and parallel capacitor configurations, aiming to boost energy harvesting capabilities and efficiency in diverse applications.

5 Nonlinear electromechanical models

This section examines the dynamics of nonlinear electromechanical models, essential for advancing energy

harvesting systems. Various nonlinear phenomena are examined to reveal their significant impact on the performance of piezoelectric devices. By elucidating the interactions between mechanical and electrical components, these nonlinear models demonstrate potential for optimizing energy conversion.

5.1 Model NL: 1-polynomial nonlinearity in resonators

Polynomial nonlinearity finds practical applications in electronic circuits with diodes and in thermostats or temperature controllers. In diodes, the voltage-dependent behavior transitions from an open switch to a closed switch as voltage crosses a threshold, using piecewise linear approximations. In temperature controllers, piecewise linear models are employed to control heaters based on temperature thresholds, resulting in distinct on-off behavior points in the response curve. Introducing polynomial nonlinearity in resonators by adding a term with coefficient β fundamentally alters the voltage-strain relationship within the piezoelectric equation, encapsulating the nonlinear disposition of the piezoelectric material under substantial strains. The primary system equations for m_m and m_r persistently portray the dynamics of the masses along with their reciprocal interactions, which remain unaffected by the inherent nonlinearity of the piezoelectric element. This incorporation of a nonlinearity parameter, β, facilitates a discernable softening behavior when it is positive and a hardening behavior when negative, each having distinct implications on resonance frequency and amplitude of vibration. Optimization of the nonlinear polynomial parameters can be a viable strategy for maximizing energy harvesting within the outlined system. This can be achieved by defining a cost function, an integration of power across a desired frequency span, thereby quantifying the performance. Utilizing computational tools, such as MATLAB, enables optimization of this function concerning the nonlinear coefficient. By examining the system's eigenvalues to extract information about the bandgap, a thorough combination of analytical and numerical methods is used to enhance the system's performance to achieve optimal results.

Figure 14 shows the relationship between the nonlinearity coefficient β and the harvested power in a monochain system. The $n = 8$ mass chain model is instrumental in depicting this correlation, serving as a concise yet representative framework to showcase the trends. Although a larger number of chains could enhance the metamaterial characteristic, the chosen size suffices to capture the essential dynamics for this analysis, aligning with the findings from Eq. (25).

The interaction among β, vibration dynamics, and energy conversion can provide insights for enhancing energy collection in similar systems. Figure 15

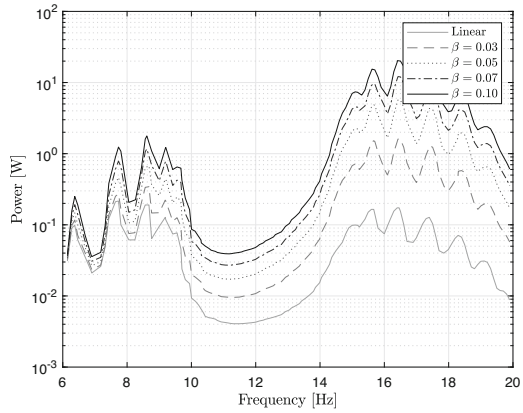

Fig. 14 Harvested power from a monochain with polynomial nonlinear local resonators in an eight-mass chain configuration. The graph highlights the impact of varying the nonlinearity coefficient β on the piezoelectric response and the resultant band gap behavior

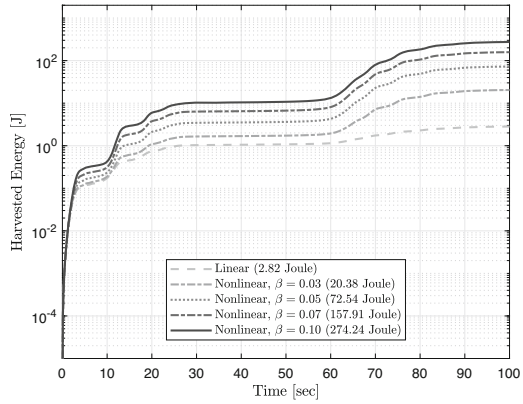

Fig. 15 Temporal Evolution of Harvested Energy: A depiction of energy harvested from piezoelectric elements over time in a monochain with polynomial nonlinear local resonators, utilizing $n = 8$ mass chains. This visualization underscores the profound influence of polynomial nonlinearity on the system's energy-harvesting trajectory, revealing a substantial enhancement in energy accumulation even in the absence of notable bandgap alterations

delves into this concept, demonstrating how energy harvested from piezoelectric elements evolves over time. Although the introduction of polynomial nonlinearity doesn't significantly alter the formation of bandgaps, it noticeably impacts power and energy harvesting because of the increased motion in the presence of nonlinearity.

5.2 Model NL: 2-nonlinear capacitance in voltage-dependent scenarios

Starting with the general nonlinear equation in Eq. (27) and making a few simplifications, such as assuming consistent resistance, introducing voltage-dependent capacitance, transitioning from acceleration nonlinearity to velocity differences, and disregarding memory effects, the following model is derived to describe the nonlinear capacitance in the piezoelectric equation:

$$\frac{v(t)}{R} + c_p(v(t))\frac{dv(t)}{dt} - \theta\left(\frac{du_m(t)}{dt} - \frac{du_r(t)}{dt}\right) = 0 \tag{51}$$

Here, $c_p(v(t))$ represents the voltage-dependent capacitance, mathematically representing scenarios where capacitance shifts with applied voltage.

In practical applications, encountering nonlinear capacitance isn't rare and can be observed in various electronic components and systems like varactors, ferroelectric materials, and memristors. These systems showcase a capacitance that isn't static but modulates with the voltage applied, thereby exhibiting diverse behaviors across assorted operating regimes.

When simulating scenarios where capacitance nonlinearly shifts with voltage, an example relationship might be expressed as:

$$c_p(v(t)) = c_{p0} + k_v \cdot v^2(t), \tag{52}$$

where k_v serves as a proportionality constant, illuminating and predicting how systems respond when capacitance dynamically interacts with applied voltage. In Fig. 16, a specific relationship between capacitance and voltage under the parameters $c_p = 1.5$ mF (base capacitance). The figure, composed of four subplots detailing Transmitance, Power, and Harvested Energy in relation to excitation frequency, and an illustration of the quadratic term coefficient of c_p piezo capacitance, provides a detailed overview of key data points. Notably, there's an evident increase in power when

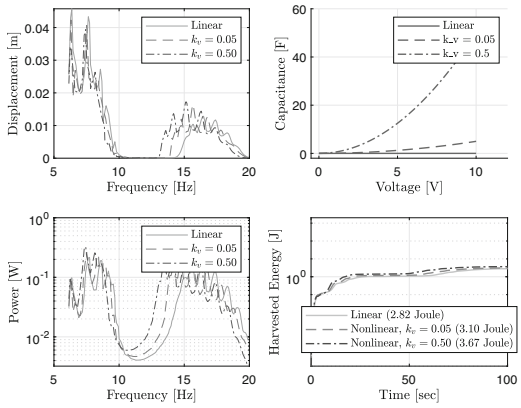

Fig. 16 Influence of quadratic nonlinear piezo capacitance, c_p on transmittance and harvested energy

dealing with nonlinear capacitance compared to linear piezo capacitance. This observation is corroborated by the energy acquired during the simulation time, which is 3.67 Joules, in contrast to the 2.82 Joules observed in a linear framework.

Thus, in this scenario, not only is more energy harvested from the resonators, but there is also an expansion in the transmittance bandgap. The dual advantages of vibration suppression in the main chain and enhanced energy harvesting from the resonator open the door to potentially more effective approaches for optimizing energy extraction in comparable systems.

5.3 Model NL: 3-cubic nonlinearities

Cubic nonlinearities can be found in electromechanical systems, such as sensors and actuators. In micro electromechanical systems (MEMS), such as accelerometers or gyroscopes, cubic nonlinearities can arise due to the miniaturized mechanical components. For nonlinear electromechanical coupling, the piezoelectric equation can be represented as:

$$\frac{v(t)}{R} + c_p\frac{dv(t)}{dt} - \theta\left(\frac{du_m(t)}{dt} - \frac{du_r(t)}{dt}\right)^3 = 0 \tag{53}$$

In Fig. 17, the relation between voltage $v(t)$ and relative displacement z is explored within the context of cubic nonlinearity. The subplot detailing the $v(t) - z(t)$ relationship illustrates that the equation simplifies to:

$$\frac{v(t)}{R} - \theta z(t)^n = 0 \tag{54}$$

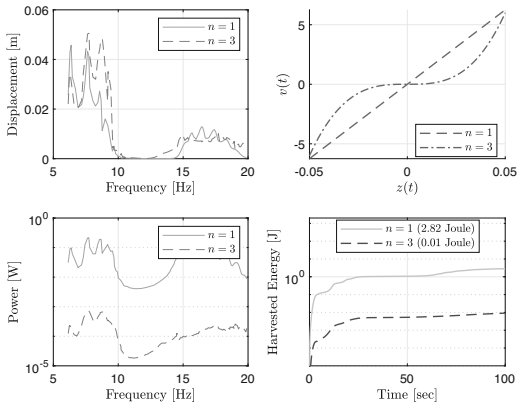

Fig. 17 Illustrating the Interplay of $v(t)$ and $z(t)$ in the Presence of Cubic Nonlinearities. The figure demonstrates how cubic nonlinearity affects electromechanical coupling in a piezoelectric system, utilizing specific resistances for standard and cubic terms (R = 500 Ω and R = 192 kΩ, respectively) to maintain consistent saturation characteristics across scenarios

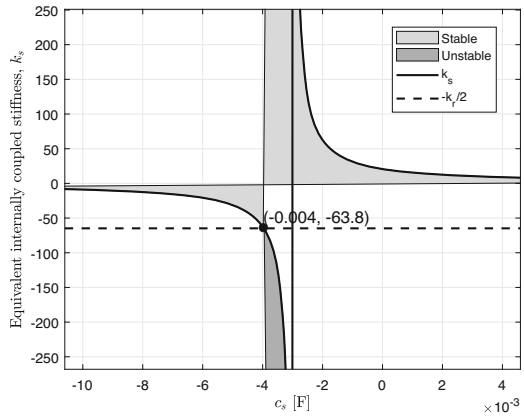

Fig. 18 Stability area of the electromechanical internally coupled lumped-mass system: Exploring the interplay between equivalent stiffness k_s and Shunt Capacitance c_s. Parameters: $n = 4$, $m_m = 56$ g, $m_r = 33.6$ g, $k_m = 150$ N/m, $k_r = 129.6$ N/m, $\theta = 0.25$ N/V, $R = 500\,\Omega$, $c_p = 1.5 \times 10^{-3}$ F

To maintain comparable saturation characteristics between a conventional linear resonator and one with a cubic term, resistances of $R = 500\Omega$ and $192\,\mathrm{k}\Omega$ are utilized, respectively.

The case study demonstrates that introducing cubic nonlinear terms, linked to the relative velocities of the primary chain and resonator, significantly affects both harvested energy and transmittance. Specifically, the observed cubic nonlinearity contributes to a decline in harvested energy, posing noteworthy implications for optimization in energy-harvesting contexts, where strategies to circumvent or offset this reduction are crucial. Simultaneously, the incidence of these nonlinear terms provokes a contraction of the transmittance band gap, which could potentially affect the system's efficacy, inviting further exploration and mitigation strategy development.

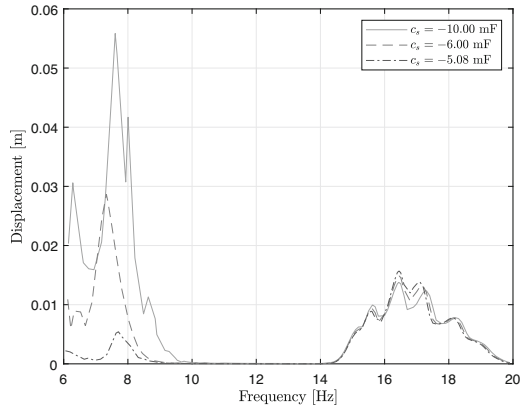

Fig. 19 Transmittance comparison of electrical internally coupling with shunt circuit for $\theta = 0.25$ and $c_p = 1.5$mF, demonstrating the impact of an equivalent negative stiffness

6 Internally coupled resonators with electromechanical nonlinearity

Figure 18 visualizes the derived relationship of Eq. (48) and its implications for system stability. Based on the analysis, the threshold value of the equivalent internally coupled stiffness k_s for stability is given by $k_s > -\frac{k_r}{2}$. The relationship between k_s and shunt capacitance c_s is clearly illustrated, with the light gray region representing system stability and the dark gray region indicating system instability. The dividing threshold between these regions is represented by the line at $k_s = -\frac{k_r}{2}$. For the provided parameters, the system remains stable for c_s values ranging from negative infinity to approximately -0.004 Farad and resumes stability from around -0.003 Farad ($k_s = -3468$ to $5203\,\mathrm{N/m}$) to positive infinity, with a brief interval of instability between these ranges. The magnified view offers a closer perspective on the critical transition points, emphasizing the pivotal c_s values at which the system's dynamical response alternates.

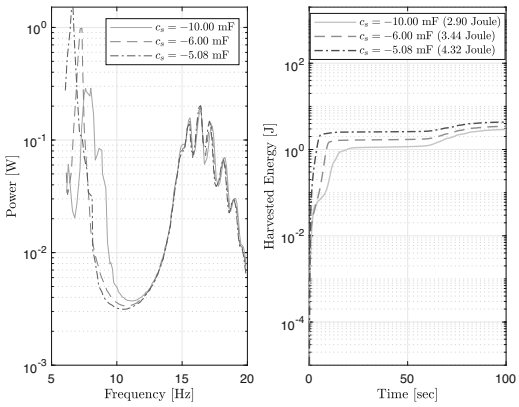

Fig. 20 Harvested power and energy across different shunt capacitances for $\theta = 0.25$ and $c_p = 1.5$mF

Figure 20 presents the harvested power and energy across a range of shunt capacitances. It clearly underscores the influential role of shunt capacitance on the system's overall efficiency. An observation made from the results is the superiority of electrical internal coupling via shunt circuits in terms of tunability. Specifically, electrical coupling seems to allow for easier tuning of the band gap compared to its mechanical counterpart. This is evident in Figs. 19 and 20, where the chosen shunt capacitor facilitates a band gap at a notably lower frequency in comparison to a mechanically internally coupled system, as illustrated in Fig. 9. Choosing a shunt capacitance of $c_s = -5.08$mF results in an equivalent stiffness of k_s = -30. This specific choice not only introduces an equivalent negative stiffness into the system, enhancing energy harvesting capabilities across varied frequency spectrums and enabling the creation of a lower-frequency band gap (see Fig. 19). Compared to mechanical internal coupling, this provides more flexibility in tuning the band gap across different frequencies.

7 Conclusion

This study utilized advanced mathematical modeling to analyze piezoelectric energy harvesters, delving into their mechanical and electrical dynamics. It elucidated the generalized formula for electromechanical nonlinearity and its impact on system performance. The insights gained from examining the interplay between nonlinear dynamics and energy harvesting efficiency have potential implications for optimizing such systems in future practical applications. The main contributions of this research include:

- The development and analysis of a comprehensive theoretical model for electromechanical nonlinearity, elucidating its significant impact on the performance of piezoelectric energy harvesters.
- A detailed examination of the band gap phenomenon in piezoelectric systems, revealing the significant impact of electromechanical parameters such as k_e and γ_3 on the energy harvesting process.
- An investigation into various models of nonlinearity within piezoelectric resonators, shedding light on the correlation between nonlinearity coefficients like β and the system's energy output.
- Insights into the benefits of employing nonlinear mechanical resonators within a mass chain, demonstrating an expansion of the band gap and an increase in energy harvesting potential.
- Observations on the effects of shunt capacitance and its role in internal resonator coupling, with implications for enhancing the energy harvesting capabilities of metamaterials.

The results underscore the intricate balance required between nonlinearity parameters and system efficiency, opening avenues for the optimization of energy harvesters in practical applications. Future studies are anticipated to delve deeper into electromechanical nonlinearity models, with an emphasis on scalability, parameter-specific impacts, and the development of feedback circuits for adaptive systems. The transition to distributed parameter models also stands out as a promising direction for achieving a closer representation of physical systems in piezoelectric energy harvesting research.

Funding This work has been supported by the European Union's Horizon Europe research and innovation program under the grant agreement No 101120657, project ENFIELD (European Lighthouse to Manifest Trustworthy and Green AI), by the Estonian Research Council through the grant PRG658, and by the Estonian Centre of Excellence in Energy Efficiency, ENER (grant TK230) funded by the Estonian Ministry of Education and Research.

Data availability The datasets supporting the conclusion of this article are included within the paper.

Declarations

Conflict of interest The authors declare that they have no conflict of interest.

References

1. Jiao, P., Mueller, J., Raney, J.R., Zheng, X., Alavi, A.H.: Mechanical metamaterials and beyond. Nat. Commun. **14**(1), 6004 (2023)
2. Liang, H., Hao, G., Olszewski, O.Z.: A review on vibration-based piezoelectric energy harvesting from the aspect of compliant mechanisms. Sens. Actuators A **331**, 112743 (2021)
3. Aldin, H.N., Ghods, M.R., Nayebipour, F., Torshiz, M.N.: A comprehensive review of energy harvesting and routing strategies for iot sensors sustainability and communication technology. Sens. Int., p. 100258 (2023)
4. Lee, G., Lee, D., Park, J., Jang, Y., Kim, M., Rho, J.: Piezoelectric energy harvesting using mechanical metamaterials and phononic crystals. Commun. Phys. **5**(1), 94 (2022)
5. Meninger, S., Mur-Miranda, J.O., Amirtharajah, R., Chandrakasan, A., Lang, J.: Vibration-to-electric energy conversion. In: Proceedings of the 1999 International Symposium on Low Power Electronics and Design, pp. 48–53 (1999)
6. Maurya, D., Yan, Y., Priya, S.: Piezoelectric Materials for Energy Harvesting. CRC Press, Boca Raton (2015)
7. Patil, G.U., Matlack, K.H.: Review of exploiting nonlinearity in phononic materials to enable nonlinear wave responses. Acta Mech. **233**(1), 1–46 (2022)
8. Daqaq, M.F., Masana, R., Erturk, A., Dane Quinn, D.: On the role of nonlinearities in vibratory energy harvesting: a critical review and discussion. Appl. Mech. Rev. **66**(4), 040801 (2014)
9. Daqaq, M.: Estimating the state-of-charge of a battery powered by a weakly nonlinear energy harvester (2024)
10. Li, Y., Baker, E., Reissman, T., Sun, C. and Liu, W.K.: Design of mechanical metamaterials for simultaneous vibration isolation and energy harvesting. *Appl. Phys. Lett.* **111**(25) (2017)
11. Tsujiura, Y., Suwa, E., Kurokawa, F., Hida, H., Kanno, I.: Reliability of vibration energy harvesters of metal-based pzt thin films. J. Phys.: Conf. Ser., vol. 557, p. 012096. IOP Publishing (2014)
12. Manktelow, K., Leamy, M.J., Ruzzene, M.: Multiple scales analysis of wave-wave interactions in a cubically nonlinear monoatomic chain. Nonlinear Dyn. **63**, 193–203 (2011)
13. Lepidi, M., Bacigalupo, A.: Wave propagation properties of one-dimensional acoustic metamaterials with nonlinear diatomic microstructure. Nonlinear Dyn. **98**(4), 2711–2735 (2019)
14. Zivieri, R., Garesci, F., Azzerboni, B., Chiappini, M., Finocchio, G.: Nonlinear dispersion relation in anharmonic periodic mass-spring and mass-in-mass systems. J. Sound Vib. **462**, 114929 (2019)
15. Bukhari, M., Joubaneh, E.F., Barry, O.: Spectro-spatial wave features in nonlinear metamaterials: theoretical and computational studies. J. Vib. Acoust. **143**(3), 031010 (2021)
16. Chaurha, A., Malaji, P.V., Mukhopadhyay, T.: Dual functionality of vibration attenuation and energy harvesting: effect of gradation on non-linear multi-resonator metastructures. Eur. Phys. J. Special Top. **231**(8), 1403–1413 (2022)
17. Xia, Y., Ruzzene, M., Erturk, A.: Dramatic bandwidth enhancement in nonlinear metastructures via bistable attachments. Appl. Phys. Lett., **114**(9) (2019)
18. Frazier, M.J., Kochmann, D.M.: Band gap transmission in periodic bistable mechanical systems. J. Sound Vib. **388**, 315–326 (2017)
19. Xia, Y., Ruzzene, M., Erturk, A.: Bistable attachments for wideband nonlinear vibration attenuation in a metamaterial beam. Nonlinear Dyn. **102**, 1285–1296 (2020)
20. Khasawneh, M.A., Daqaq, M.F.: Experimental assessment of the performance of a bi-stable point wave energy absorber under harmonic incident waves. Ocean Eng. **280**, 114494 (2023)
21. Lallart, M., Guyomar, D.: An optimized self-powered switching circuit for non-linear energy harvesting with low voltage output. Smart Mater. Struct. **17**(3), 035030 (2008)
22. Jiang, H., Wang, Y.: Research progress on piezoelectric energy harvesting circuits. Integr. Ferroelectr. **231**(1), 9–19 (2023)
23. Guyomar, D., Lallart, M.: Recent progress in piezoelectric conversion and energy harvesting using nonlinear electronic interfaces and issues in small scale implementation. Micromachines **2**(2), 274–294 (2011)
24. Yang, T., Zhou, S., Fang, S., Qin, W., Inman, D.J.: Nonlinear vibration energy harvesting and vibration suppression technologies: designs, analysis, and applications. Appl. Phys. Rev., **8**(3) (2021)
25. Silva, T.M.P., Clementino, M.A., de Sousa, V.C., De Marqui, C: An experimental study of a piezoelectric metastructure with adaptive resonant shunt circuits. IEEE/ASME Trans. Mechatron., **25**(2):1076–1083 (2020)
26. Norenberg, J.P., Cunha Jr, A., da Silva, S., Varoto, P.S.: Probabilistic maps on bistable vibration energy harvesters. Nonlinear Dyn., **111**(22), 20821–20840 (2023)
27. Chatterjee, T., Karlicic, D., Adhikari, S., Friswell, M.I.: Parametric amplification in a stochastic nonlinear piezoelectric energy harvester via machine learning. In: Data Science in Engineering, Volume 9: Proceedings of the 39th IMAC, A Conference and Exposition on Structural Dynamics 2021, pp. 283–291. Springer (2022)
28. Covaci, C., Gontean, A.: Piezoelectric energy harvesting solutions: a review. Sensors **20**(12), 3512 (2020)
29. Asanuma, H.: Electromechanical model and simple numerical analysis for a piezoelectric vibration energy harvester considering nonlinear piezoelectricity, nonlinear damping, and self-powered synchronized switch circuit. J. Intell. Mater. Syst. Struct. **34**(20), 2360–2378 (2023)
30. Lallart, M., Lombardi, G.: Synchronized switch harvesting on electromagnetic system: a nonlinear technique for hybrid energy harvesting based on active inductance. Energy Convers. Manage. **203**, 112135 (2020)
31. Tian, W., Zhao, Z., Liu, W., Zhu, Q., Zhang, Z., Yuan, Y.: Analysis on the power and bandwidth improvement of a frequency-tuning optimized sece circuit. Sens. Actuators A **332**, 113110 (2021)
32. Ahmad, F.F., Ghenai, C., Bettayeb, M.: Maximum power point tracking and photovoltaic energy harvesting for internet of things: a comprehensive review. Sustain. Energy Technol. Assess. **47**, 101430 (2021)
33. Li, D., Wang, C., Cui, X., Chen, D., Fei, C., Yang, Y.: Recent progress and development of interface integrated circuits for piezoelectric energy harvesting. Nano Energy **94**, 106938 (2022)

34. Boyan Stefanov Lazarov and Jakob Søndergaard Jensen: Low-frequency band gaps in chains with attached non-linear oscillators. Int. J. Non-Linear Mech. **42**(10), 1186–1193 (2007)
35. Zhou, W.J., Li, X.P., Wang, Y.S., Chen, W.Q., Huang, G.L.: Spectro-spatial analysis of wave packet propagation in nonlinear acoustic metamaterials. J. Sound Vib. **413**, 250–269 (2018)
36. Hu, G., Tang, L., Das, R.: Internally coupled metamaterial beam for simultaneous vibration suppression and low frequency energy harvesting. J. Appl. Phys., **123**(5) (2018)
37. Alimohammadi, H., Vassiljeva, K., HosseinNia, S.H., Petlenkov, E.: Exploring internally coupled resonator's dynamics and spatial variability in metamaterials for vibration suppression. In: Active and Passive Smart Structures and Integrated Systems XVIII (2024)
38. Shu, Y.C., Lien, I.C.: Analysis of power output for piezoelectric energy harvesting systems. Smart Mater. Struct. **15**(6), 1499 (2006)
39. Alimohammadi, H., Vassiljeva, K., HosseinNia, S.H., Petlenkov, E.: Stability analysis and energy harvesting in lumped parameter systems with internally coupled resonators. J. Vib. Control (2024)
40. Manimala, J.M., Sun, C.T.: Numerical investigation of amplitude-dependent dynamic response in acoustic metamaterials with nonlinear oscillators. J. Acoust. Soc. Am. **139**(6), 3365–3372 (2016)

Publisher's Note Springer Nature remains neutral with regard to jurisdictional claims in published maps and institutional affiliations.

Springer Nature or its licensor (e.g. a society or other partner) holds exclusive rights to this article under a publishing agreement with the author(s) or other rightsholder(s); author self-archiving of the accepted manuscript version of this article is solely governed by the terms of such publishing agreement and applicable law.

Appendix 2

II

Hossein Alimohammadi et al. “Bandgap Dynamics in Locally Resonant Metastructures: A General Theory of Internal Resonator Coupling”. In: *Applied Sciences* 14.6 (2024), p. 2447

applied sciences

MDPI

Article

Bandgap Dynamics in Locally Resonant Metastructures: A General Theory of Internal Resonator Coupling

Hossein Alimohammadi [1,*], Kristina Vassiljeva [1], S. Hassan HosseinNia [2] and Eduard Petlenkov [1]

[1] Centre for Intelligent Systems, Department of Computer Systems, Tallinn University of Technology, Akadeemia tee 15a, 12618 Tallinn, Estonia; kristina.vassiljeva@taltech.ee (K.V.); eduard.petlenkov@taltech.ee (E.P.)
[2] Department of Precision and Microsystem Engineering, Delft University of Technology, Mekelweg 2, 2628CD Delft, The Netherlands; s.h.hosseinnia@tudelft.nl
* Correspondence: hossein.alimohammadi@taltech.ee

Abstract: The dynamics of metastructures, incorporating both conventional and internally coupled resonators, are investigated to enhance vibration suppression capabilities through a novel mathematical framework. A close-form formulation and a transfer function methodology are introduced, integrating control system theory with metastructure analysis, offering new insights into the role of internal coupling. The findings reveal that precise internal coupling, when matched exactly to the stiffness of the resonator, enables the clear formation of secondary bandgaps, significantly influencing the vibration isolation efficacy of the metastructure. Although the study primarily focuses on theoretical and numerical analyses, the implications of adjusting mass distribution on resonators are also explored. This formulation methodology enables the adjustment of bandgap characteristics, underscoring the potential for adaptive control over bandgaps in metastructures. Such capabilities are crucial for tailoring the vibration isolation and energy harvesting functionalities in mechanically resonant systems, especially when applied to demanding heavy-duty applications.

Keywords: metastructures; internally-coupled resonators; modal analysis; distributed parameter model; spatial variation

check for updates

Citation: Alimohammadi, H.; Vassiljeva, K.; HosseinNia, S.H.; Petlenkov, E. Bandgap Dynamics in Locally Resonant Metastructures: A General Theory of Internal Resonator Coupling. *Appl. Sci.* **2024**, *14*, 2447. https://doi.org/10.3390/app14062447

Academic Editors: Ovidiu Vasile and Mihai Bugaru

Received: 9 February 2024
Revised: 6 March 2024
Accepted: 11 March 2024
Published: 14 March 2024

Copyright: © 2024 by the authors. Licensee MDPI, Basel, Switzerland. This article is an open access article distributed under the terms and conditions of the Creative Commons Attribution (CC BY) license (https://creativecommons.org/licenses/by/4.0/).

1. Introduction

Locally resonant metamaterials have revolutionized the field of material science by enabling the manipulation of mechanical waves through unique structural designs that are not possible with conventional materials. Such metamaterials utilize an intricate arrangement of embedded resonators to selectively amplify or attenuate waves, yielding capabilities like enhanced vibration isolation, targeted wave trapping, and precise steering. The cross-disciplinary value of these materials is evident in their wide-ranging applications, from improving acoustic insulation and energy harvesting to managing seismic waves and developing advanced sensors.

The concept of metamaterials is not exclusive to structural dynamics; its origins can be traced back to research in optics by Shelby et al. [1], and it has since become a subject of extensive study in various fields, including acoustics. Moreover, the concept of mechanical locally resonant metamaterials was first introduced by Liu et al. [2], who demonstrated an elastic locally resonant bandgap phenomenon, akin to a mass-spring oscillator. Since then, various types of mechanical locally resonant metamaterials have been extensively investigated in the literature.

The field of resonator couplings and dispersion has seen substantial progress in recent years. For instance, Hazra et al. [3] innovated a superconducting architecture utilizing a ring resonator for multiqubit connectivity, enhancing the efficiency of quantum processors. In the realm of optics and spectroscopy, Rozenman et al. [4] developed a novel experimental setup to measure the dispersion of organic exciton polaritons, revealing the

quantized interactions between light and matter in organic materials. Additionally, Li et al. [5] demonstrated the coherent internally coupled distant magnonic resonators via superconducting circuits for integrated magnonic networks that can operate coherently at quantum-compatible scales.

From optics and materials science to structural vibration and energy harvesting, these advancements bridge diverse fields to pioneer new applications and efficiencies. Hu et al. [6] proposed a modified metamaterial beam that combined vibration suppression and energy harvesting functions in internally coupled resonators in the low-frequency range. In their design, local resonators were alternately coupled, with piezoelectric elements attached for energy conversion. Oyelade and Oladimeji [7] also contributed by introducing a novel metamaterial with a multiresonator mass-in-mass lattice system, where the internal coupling was achieved through a linear spring, leading to the formation of two additional bandgaps over conventional designs.

The research trajectory in metastructure system formulation has been significantly advanced by Erturk et al. [8], who developed a robust framework that culminates in transfer functions, allowing for nuanced manipulation and control of system responses. Sugino et al.'s mathematical framework, leveraging Laplace transformations, further simplifies the analysis of metastructures, especially in damping low-frequency vibrations, thus enhancing the practical applicability of these complex systems in engineering solutions. Sugino et al. [9] developed the mathematical framework using Laplace transformations for analyzing locally resonant metastructures, simplifying examination of their responses, and deriving a closed-form expression for bandgap frequency range, validated through dispersion analysis and experimental tests.

Traditional methods focus on dispersion analysis and limit the scope of analysis to wave propagation without offering insights into control strategies. This work develops a mathematical framework to derive a close-form formulation for analyzing both conventional and internally coupled resonators in metastructures, integrating control system theory and the transfer function method to provide enhanced control mechanisms and bandgap tuning methods through resonator stiffness adjustments. This advancement has the potential to revolutionize metastructural design for industrial applications, enabling the creation of structures with multiple bandgaps and diverse functionalities.

This framework not only enhances our understanding of metastructures but also provides novel methods for tuning bandgaps, thereby improving vibration isolation and facilitating energy harvesting. With implications spanning industrial machinery and noise cancellation, these advancements promise to revolutionize engineering practices by enabling more efficient and effective control mechanisms in various industrial applications.

This work addresses the knowledge gap in linear internal coupling in metastructures, and aims to improve wave manipulation and dynamic control through a new mathematical framework, expanding the applications and functionalities of metastructures.

It claims that transfer function methodology can model and control metastructure dynamics, including internally coupled resonators. It highlights a gap in understanding linear internal coupling effects on bandgap manipulation, and demonstrates the maintenance of primary bandgaps and the emergence of secondary bandgaps through internal coupling, suggesting adjustable resonator mass distribution for further tuning.

This leads to the following research questions:

- How does internal coupling affect the bandgap characteristics of a metastructure?
- What is the role of internal coupling in enhancing or merging bandgaps for vibration isolation in continuous (distributed) metastructures?
- Can the integration of control system theory and transfer function methodology lead to real-time adaptive tuning of metastructure bandgaps?
- Can an alternative method, such as modifying the mass distribution on resonators, offer a practical way to alter bandgap characteristics without restructuring, while also being suitable for heavy-duty applications where piezoelectric solutions are less viable?

The key contributions of this paper are as follows:

- We enable the transfer function approach as an analysis method for metastructures, enhancing dynamic bandgap characteristics through the use of different functionalities and precise control engineering techniques.
- We develop a mathematical method for formulating closed-form equations describing the behaviors of internally coupled resonators, providing a deeper understanding of their impact on metastructure dynamics.
- We address the challenge of merging bandgaps from internally coupled and conventional resonators, offering insights into continuous vibration control in distributed systems.

The structure of the remaining sections of this paper is as follows: Section 2 delves into the methodology, detailing the theoretical foundations and optimization strategies employed for bandgap generation. Results and discussion are presented in Section 3, where the implications of the applied methodologies are interpreted in the context of mechanical system design and enhancement. A "Finite Element Study" is detailed in Section 4, showcasing the vibrational behaviors and bandgap characteristics of the metastructures under study. This section includes a focused examination of the effects of spatial variations on bandgap properties, emphasizing the utility and implications of these findings for practical applications. Finally, Section 5 concludes the paper, summarizing the key findings and proposing directions for future research.

2. Modal Analysis and Bandgap Formation in Mechanical Metastructures

The research primarily employs modal analysis in the design and optimization of mechanical locally resonant metastructures. This analysis is crucial for identifying key vibration characteristics, such as natural frequencies, mode shapes, and modal damping ratios, under specific conditions. These insights enable the engineering of metastructures with tailored mechanical wave propagation behaviors.

The study employs a distributed parameter model approach, utilizing partial differential equations (PDEs) to capture the system dynamics more precisely than lumped parameter models. This methodology is particularly applicable to systems where spatial variations are non-negligible, affecting phenomena such as wave propagation, heat transfer, and fluid dynamics. Analytical models are derived using modal analysis through the frequency determinant method, providing a solid theoretical foundation for understanding the intricate behavior of internally coupled resonators within metastructures.

The standard distributed model of the metastructure under investigation, subject to base excitation and external forces, is illustrated in Figure 1. Employing Newtonian mechanics and drawing from classical vibration textbooks, the behavior of the metastructure is captured by the following partial differential equation, as detailed in Equation (1).

$$\mathcal{L}w(x,t) + \mathcal{C}\frac{\partial w(x,t)}{\partial t} + \mathcal{M}\frac{\partial^2 w(x,t)}{\partial t^2} - \sum_{r=1}^{N_r}\left(k_r z_r(t) + c_r\frac{\partial z_r(t)}{\partial t}\right)\delta(x - x_r) = \mathcal{F}_{b_m}(x,t) \quad (1)$$

which includes structural flexibility $\mathcal{L}$, damping $\mathcal{C}$, and inertia $\mathcal{M}$. The interaction with the resonators is represented by the summation term, encompassing the stiffness k_r, damping c_r, and location x_r of each resonator. The dynamic of the system is a linear homogeneous differential operator, exhibiting orders of $2p$ and $2q$, respectively, with $q \leq p$. The spatial coordinate x extends over domain D. The function $w(x,t)$ captures the system's relative transverse vibration compared to the base motion, essentially reflecting the displacement at specific points relative to the base's harmonic movement. On the other hand, $z_r(t)$ denotes the resonator's relative vibration in absolute coordinates, providing insight into its displacement to the overall structure's vibration. The $\delta(x - x_r)$ is the Kronecker delta function to pinpoint the resonators' locations on the beam, with x_r specifying the position of the r-th resonator. Moreover, $\mathcal{F}$ symbolizes the external force, distributed across D, and incorporates the impact of the base excitation on the beam.

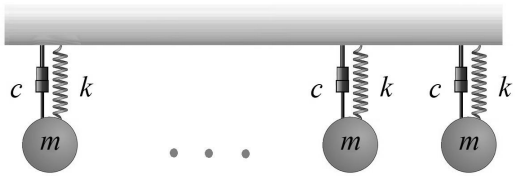

Figure 1. Example of standard locally resonant metastructures, where m represents the mass of the resonators, c is the damping, and k is the stiffness of the resonators.

Similarly, the governing equation for the resonators, derived from Newton's second law of motion, is expressed as follows:

$$m_r \frac{\partial^2 z_r(t)}{\partial t^2} + c_r \frac{\partial z_r(t)}{\partial t} + k_r z_r(t) + m_r \frac{\partial^2 w(x_r, t)}{\partial t^2} = \mathcal{F}_{b_r}(t) \tag{2}$$

The boundary conditions for the system, as outlined in Equation (1), are defined by Equation (3), where each $\mathcal{B}_i$ is a linear homogeneous differential operator of order no greater than $2p-1$.

$$\mathcal{B}_i[w(x,t)] = 0, \quad i = 1, 2, \ldots, p \tag{3}$$

Proportional damping, a method often used in real-world structures for estimating natural frequencies and mode shapes, relates the damping matrix to the mass and stiffness matrices. This concept allows $\mathcal{C}$ to be expressed as a combination of mass and stiffness operators $\mathcal{L}$ and $\mathcal{M}$, as shown in Equation (4), with c_1 and c_2 being non-negative constants, determined based on the physical properties of the system. However, engineers usually use experimental modal analysis or fit data from vibration tests to find them. This approach, as referenced in [10], maintains consistent mode shapes and similar natural frequencies for both damped and undamped systems.

$$\mathcal{C} = c_1 \mathcal{L} + c_2 \mathcal{M} \tag{4}$$

The eigenfunctions $\phi_m(x)$ of the system are derived by solving the eigenvalue problem of the undamped version of Equation (1), presented in Equation (5).

$$\mathcal{L}[\phi_m(x)] = \lambda_m \mathcal{M}[\phi_m(x)], \quad m = 1, 2, \ldots, N_m \tag{5}$$

The symbol λ_m represents an eigenvalue associated with the mth eigenfunction $\phi_m(x)$ of the system. For structures like beams equipped with resonators, the system is defined by coupled differential equations for each resonator and the structure itself. These equations account for the mutual influence of each component on the system's dynamics. The mode shapes of the base structure alone are not the exact mode shapes of the entire metastructure, but using them simplifies the analysis significantly. The solution to Equation (5) is provided in Appendix A.

In the case of an Euler beam spanning domain $D = [0, L]$, assumed to be linearly elastic and homogeneous, the operators $\mathcal{L}$, $\mathcal{M}$, $\mathcal{C}$, $\mathcal{B}_1$, and $\mathcal{B}_2$ are defined in terms of the beam's physical properties: flexural rigidity (EI), density (ρ), and cross-sectional area (A).

$$\begin{aligned} &\mathcal{L} = EI \frac{\partial^4}{\partial x^4}, \quad \mathcal{M} = \rho A, \quad \mathcal{C} = c, \\ &\mathcal{B}_1 = 1, \quad \mathcal{B}_2 = EI \frac{\partial^2}{\partial x^2} \end{aligned} \tag{6}$$

In advancing the understanding of modal expansion in the system, the orthogonality of eigenfunctions is critical for solving Equation (1). The self-adjoint (Hermitian) nature of the eigenvalue problem ensures this orthogonality. For any two eigenfunctions $\phi_m(x)$

and $\phi_n(x)$, the problem is self-adjoint if they satisfy the conditions given in Equation (7), as highlighted by [11].

$$\begin{aligned} \int_D \phi_m(x)\mathcal{L}[\phi_n(x)]dx &= \int_D \phi_n(x)\mathcal{L}[\phi_m(x)]dx \\ \int_D \phi_m(x)\mathcal{M}[\phi_n(x)]dx &= \int_D \phi_n(x)\mathcal{M}[\phi_m(x)]dx. \end{aligned} \tag{7}$$

When considering unique eigenvalues ω_m^2 and ω_n^2 with their respective eigenfunctions $\phi_m(x)$ and $\phi_n(x)$, these functions are normalized with respect to $\mathcal{M}$. This normalization leads to the generalized orthogonality condition outlined in Equations (8) and (9), with δ_{mn} being the Kronecker delta function.

$$\int_D \phi_m(x)\mathcal{M}[\phi_n(x)]dx = \delta_{mn} \tag{8}$$

and

$$\int_D \phi_m(x)\mathcal{L}[\phi_n(x)]dx = \delta_{mn}\omega_m^2 \tag{9}$$

Assuming proportional damping, the structural damping characteristics are captured by Equation (10). Here, ζ_m denotes the damping ratio of the m-th mode, which is precisely defined in Equation (11) utilizing the constants c_1 and c_2. Equations (8)–(10) are integral to constructing a set of orthonormal eigenfunctions, which together form a complete basis for the solution space pertinent to the eigenvalue problem.

$$\int_D \phi_m(x)\mathcal{C}[w_m(x)]dx = c_1\delta_{mn}\omega_m^2 + c_2\delta_{mn} = 2\delta_{mn}\zeta_m\omega_m \tag{10}$$

with

$$\zeta_m = \frac{1}{2\omega_m}\left(c_1\omega_m^2 + c_2\right) \tag{11}$$

Modal decomposition is a method used to describe the structure's vibration across a domain D by representing it as a sum of modal shapes in one direction. This method assumes that the behavior of the structure can be accurately captured using a finite set of modes. For instance, the Euler–Bernoulli beam theory, commonly used in these analyses, may not provide sufficient accuracy in high-frequency situations. This technique, widely used in modal analysis, produces convergent solutions to the boundary value problem as formulated.

Using modal decomposition, the beam's deflection in the domain D is expressed as a sum of modal shapes in one direction. This assumes that the behavior of the beam can be accurately represented by a finite number of modes, as expressed in Equation (12):

$$w(x,t) = \sum_{m=1}^{N_m} \phi_m(x)z_m(t), \tag{12}$$

Here, $\phi_m(x)$ denotes the spatial mode shape, and $z_m(t)$ is the time-dependent modal coordinate for the m-th mode. These modal representations are crucial in modeling the dynamics of a flexible beam with integrated discrete resonators.

Incorporating the modal expansion from Equation (12) into the system's governing differential equation, given by Equation (1), yields Equation (13). This resultant equation effectively combines the modal decomposition with the system's differential operators, capturing the influence of the resonators. It provides a complete representation of the beam's dynamic response, encompassing both the modal characteristics and the interactive effects of the resonators.

$$\mathcal{L}\sum_{m=1}^{N_m}\phi_m(x)z_m(t)+\mathcal{C}\frac{\partial}{\partial t}\sum_{m=1}^{N_m}\phi_m(x)z_m(t)+\mathcal{M}\frac{\partial^2}{\partial t^2}\sum_{m=1}^{N_m}\phi_m(x)z_m(t)-\sum_{r=1}^{N_r}\left(k_r z_r(t)+c_r\frac{dz_r(t)}{dt}\right)\delta(x-x_r)=\mathcal{F}_{b_m}(x,t) \tag{13}$$

Multiplying Equation (13) by $\phi_n(x)$ and integrating over the domain D, and applying the orthogonality conditions Equations (8)–(11) of the mode shapes, gives

$$\ddot{z}_m(t)+2\zeta_m\omega_m\dot{z}_m(t)+\omega_m^2 z_m(t)-\sum_{r=1}^{N_r}m_r\omega_r^2 z_r(t)\phi_m(x_r)=\mathcal{Q}_{b_m}(x,t),\quad m=1,2,\ldots,N_m \tag{14}$$

Similarly for resonators, substituting the modal expansion Equations (12) into (2) yields

$$\ddot{z}_r(t)+2\zeta_r\omega_r\dot{z}_r(t)+\omega_r^2 z_r(t)+\sum_{m=1}^{N_m}\ddot{z}_m(t)\phi_m(x_r)=\mathcal{Q}_{b_r}(t),\quad r=1,2,\ldots,N_r \tag{15}$$

Here, N_m and N_r denote the number of modes and resonators, respectively. Each mode has a specific modal frequency ω_m, and each resonator has a mass m_r and its own natural frequency ω_r. The damping ratios ζ_m for the modes and ζ_r for the resonators quantify energy dissipation.

To simplify, the superscript "dot" indicates time derivatives, and "prime" indicates spatial derivatives. Each equation in the model represents the dynamics of modal coordinates or resonator displacement as a second-order ordinary differential equation. The dynamics are influenced by modal and resonator parameters (natural frequencies ω_m and ω_r, damping ratios ζ_m and ζ_r), their interactions, and base excitation forces ($\mathcal{Q}_{b_m}$ and $\mathcal{Q}_{b_r}$).

Decoupling of these equations is achieved through an orthogonal transformation, involving pre- and post-multiplication by the mode shape matrix. This leads to diagonalization of the mass and stiffness matrices, thanks to the orthogonality of eigenvectors to both matrices. The result is a set of decoupled ordinary differential equations. This normal mode method applies in the absence of damping or with proportional damping, where the damping matrix is a linear combination of the mass and stiffness matrices. The transformation becomes orthonormal when the mode shape is normalized to the mass matrix.

Combining the structural dynamics represented in Equation (14) with the dynamics of resonators from Equation (15) enables the coupling of inertial terms and decoupling of stiffness in the system, facilitating analysis in the frequency domain. This process is expressed in Equation (16), where $\mathcal{H}_{b_m}(x,t)$ is determined by integrating the effects of external forces, base motion, and damping into a net external force, as shown in Equation (17). Equations (15) and (16) together form a set of coupled second-order linear ordinary differential equations, which, upon solving, yield the mode shapes and resonant frequencies of the entire system and its steady-state response to harmonic excitation.

$$\ddot{z}_m(t)+2\zeta_m\omega_m\dot{z}_m(t)+\omega_m^2 z_m(t)+\sum_{r=1}^{N_r}m_r\phi_m(x_r)\sum_{p=1}^{N_m}\ddot{z}_m(t)\phi_p(x_r)+\sum_{r=1}^{N_r}m_r\ddot{z}_r(t)\phi_m(x_r)+2\sum_{r=1}^{N_r}m_r\phi_m(x_r)\zeta_r\omega_r\dot{z}_r(t)=\mathcal{H}_{b_m}(x,t),\quad m=1,2,\ldots,N_m \tag{16}$$

$$\mathcal{H}_{b_m}(x,t)=\int_0^L\mathcal{F}_e(x,t)\phi_m(x)dx-\ddot{w}_b(t)\left(\int_0^L\mathcal{M}\phi_m(x)dx+\sum_{r=1}^{N_r}m_r\phi_m(x_r)\right)-\dot{w}_b(t)\int_0^L\mathcal{C}\phi_m(x)dx \tag{17}$$

The Laplace transform is applied to the system of equations, assuming zero initial conditions, to transition the analysis to the frequency domain, as seen in Equations (18) and (19). In these equations, $Z_m(s)$ and $Z_r(s)$ represent the Laplace transforms of the modal and resonator displacements, respectively. This transformation simplifies the algebraic manipulation and analysis of the system's dynamics.

$$Z_r(s) = \frac{\mathcal{Q}_{b_r}(s) - \sum_{m=1}^{N_m} s^2 Z_m(s)\phi_m(x_r)}{s^2 + 2\zeta_r\omega_r s + \omega_r^2}, \quad r = 1, 2, \ldots, N_r \tag{18}$$

$$\begin{aligned} &s^2 Z_m(s) + 2\zeta_m\omega_m s Z_m(s) + \omega_m^2 Z_m(s) + \sum_{r=1}^{N_r} m_r\phi_m(x_r) \sum_{p=1}^{N_m} s^2 Z_p(s)\phi_p(x_r) + \\ &\sum_{r=1}^{N_r} m_r s^2 Z_r(s)\phi_m(x_r) + 2\sum_{r=1}^{N_r} m_r\phi_m(x_r)\zeta_r\omega_r s Z_r(s) = H_{b_m}(s), \quad m = 1, 2, \ldots, N_m \end{aligned} \tag{19}$$

For a deeper analytical understanding, applying Equation (18) to the Laplace transform of Equation (14) yields the following expression in Equation (20).

$$\begin{aligned} &(s^2 + 2\zeta_m\omega_m s + \omega_m^2) Z_m(s) - \sum_{r=1}^{N_r} m_r\omega_r^2 \left(\frac{\mathcal{Q}_{b_r}(s) - \sum_{p=1}^{N_m} s^2 Z_p(s)\phi_p(x_r)}{s^2 + 2\zeta_r\omega_r s + \omega_r^2} \right) \phi_m(x_r) = \mathcal{Q}_{b_m}(s), \\ &m = 1, 2, \ldots, N_m \end{aligned} \tag{20}$$

The analysis focuses on the transfer function $\frac{Z_m}{\mathcal{Q}_{b_m}}$, particularly when the effect of $\mathcal{Q}_{b_r}$ is ignored. Here, the mass ratio μ, a dimensionless quantity, relates the mass of each resonator to a differential mass element of the system and is defined as $\mu = \frac{m_r}{m(x_r)dx_r}$, where $m(x_r)$ represents the mass per unit length at x_r and dx_r is an infinitesimal segment length at this point. To simplify the system of equations, it is assumed that an infinite number of resonators are distributed throughout the entire domain of x, and the regions represented by x_r become infinitesimally small.

$$\lim_{N_r \to \infty} \sum_{r=1}^{N_r} m(x_r)\phi_m(x_r)\phi_p(x_r)dx_r \approx \int_0^L m(x)\phi_m(x)\phi_p(x)dx = \delta_{mp}, \quad m, p = 1, 2, \ldots \tag{21}$$

Applying these assumptions results in the following expression:

$$\begin{aligned} \frac{Z_m(s)}{\mathcal{Q}_{b_m}(s)} &= \frac{1}{s^2\left(1 + \frac{\mu(2\zeta_r\omega_r s + \omega_r^2)}{s^2 + 2\zeta_r\omega_r s + \omega_r^2}\right) + 2\zeta_m\omega_m s + \omega_m^2} \\ &m = 1, 2, \ldots, N_m \end{aligned} \tag{22}$$

Equation (22) indicates that resonators add a frequency-dependent mass to the system. With the assumption of an infinite resonator distribution, leading to continuous spatial displacements, similar reductions apply to the resonator displacements. By substituting Equations (22) into (18) and transitioning from the discrete x_r to a continuous spatial domain x, a simplified equation emerges as presented in Equation (23).

$$Z_r(x, s) = -\frac{s^2}{s^2 + 2\zeta_r\omega_r s + \omega_r^2} \sum_{m=1}^{N_m} \frac{Q_{b_m}(s)\phi_m(x)}{s^2\left(1 + \frac{\mu(\omega_r^2 + 2\zeta_r\omega_r s)}{s^2 + 2\zeta_r\omega_r s + \omega_r^2}\right) + 2\zeta_m\omega_m s + \omega_m^2} \tag{23}$$

Equation (23) defines the motion $Z_r(x,s)$ of resonators along the beam in the Laplace domain, influenced by modal forces $Q_{b_m}(s)$. The displacement of the resonators is presented as a weighted sum of the beam's modal shapes:

$$Z_r(x,s) = \sum_{m=1}^{N_m} \Psi_m(s)\phi_m(x) \tag{24}$$

Equation (25) expresses the relationship between the modal force $Q_{b_m}(s)$ and the modal coordinate $\Psi_m(s)$ in the Laplace domain. It illustrates how resonator displacements are influenced by the modes of the structure:

$$\frac{\Psi_m(s)}{Q_{b_m}(s)} = \frac{-s^2}{[s^2 + 2\zeta_r\omega_r s + \omega_r^2]\left[s^2\left(1 + \frac{\mu(\omega_r^2 + 2\zeta_r\omega_r s)}{s^2 + 2\zeta_r\omega_r s + \omega_r^2}\right) + 2\zeta_m\omega_m s + \omega_m^2\right]}, \quad m = 1, 2, \ldots, N_m \tag{25}$$

The transfer function in Equation (25) clarifies how the input forces are transformed into modal responses. The function's poles, indicative of the system's natural frequencies, are the points at which the system exhibits peak responses.

By introducing an internal linear coupling term, κ, within the resonators illustrated in Figure 2, the system evolves into internally coupled resonators. This transformation creates an environment where the displacements of the resonators are no longer independent but are coupled. Specifically, the displacement of one resonator influences the displacement of the other, establishing a dynamic interaction. The energy associated with this coupling is quantified by the coupling potential energy, in which each pair of resonators (1 and 2, 3 and 4, 5 and 6, etc.) forms a system with two degrees of freedom: $V_c(t) = \frac{1}{2}\kappa(z_{r_1}(t) - z_{r_2}(t) + w(x_{r_1}, t) - w(x_{r_2}, t))^2$. The equations for the coupled oscillator system can be formulated as follows:

$$\begin{aligned} &\ddot{z}_m(t) + 2\zeta_m\omega_m\dot{z}_m(t) + \omega_m^2 z_m(t) - \sum_{r=1}^{N_r/2}\Big(m_{2r-1}\omega_{2r-1}^2 z_{2r-1}(t)\phi_m(x_{2r-1}) + \\ &m_{2r}\omega_{2r}^2 z_{2r}(t)\phi_m(x_{2r})\Big) = Q_{b_m}, \quad m = 1, 2, \ldots, N_m, \text{ and } N_r \in 2\mathbb{N} \end{aligned} \tag{26}$$

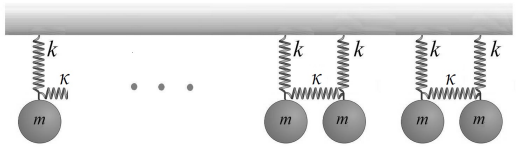

Figure 2. Locally resonant metastructures with internally coupled resonators. Each pair of resonators forms one unit cell, with m representing the mass of the resonators, c the damping, k the stiffness of the resonators, and κ the internal coupling stiffness between them.

Meanwhile, the equation for the resonators is given by the following:

$$\begin{aligned} &\ddot{z}_{2r-1}(t) + 2\xi_{2r-1}\omega_{2r-1}\dot{z}_{2r-1}(t) + \omega_{2r-1}^2 z_{2r-1}(t) + \sum_{m=1}^{N_m}\ddot{z}_m(t)\phi_m(x_{2r-1}) + \\ &\beta\frac{\kappa}{m_{2r-1}} = Q_{b_{2r-1}}, \quad r = 1, 2, \ldots, N_r/2 \end{aligned} \tag{27}$$

$$\begin{aligned} &\ddot{z}_{2r}(t) + 2\xi_{2r}\omega_{2r}\dot{z}_{2r}(t) + \omega_{2r}^2 z_{2r}(t) + \sum_{m=1}^{N_m}\ddot{z}_m(t)\phi_m(x_{2r}) \\ &- \beta\frac{\kappa}{m_{2r}} = Q_{b_{2r}}, \quad r = 1, 2, \ldots, N_r/2 \end{aligned} \tag{28}$$

where

$$\beta = z_{2r-1}(t) - z_{2r}(t) + \sum_{m=1}^{N_m} z_m(t)\phi_m(x_{2r-1}) - \sum_{m=1}^{N_m} z_m(t)\phi_m(x_{2r}) \tag{29}$$

These equations characterize the underlying dynamics of both the beam and the internally linear coupled resonator system. The Laplace transform of Equation (26) with zero initial conditions results in Equation (30).

$$\begin{aligned}(s^2 + 2\zeta_m\omega_m s + \omega_m^2)Z_m(s) - \sum_{r=1}^{N_r/2}\Big(m_{2r-1}\omega_{2r-1}^2 Z_{2r-1}(s)\phi_m(x_{2r-1}) + \\ m_{2r}\omega_{2r}^2 Z_{2r}(s)\phi_m(x_{2r})\Big) = Q_{b_m}(s)\end{aligned} \tag{30}$$

Given that the forces $\mathcal{Q}_{b_{2r-1}}$ and $\mathcal{Q}_{b_{2r}}$ are equal to $-\ddot{w}_b(t)$, and considering that $m_{2r-1} = m_{2r}$ or identical mass m_r for all resonators, along with the distribution of numerous resonators along a beam, it is assumed that the derivative of position within each unit cell is the same, indicated by $dx_{2r-1} = dx_{2r}$. This reflects a uniform position derivative across all resonators. Furthermore, the following relationships are established: $m_{2r-1} = \mu m(x_{2r-1})dx_{2r-1}$, and $m_{2r} = \mu m(x_{2r})dx_{2r}$.

$$\lim_{N_r\to\infty}\sum_{r=1}^{N_r/2} m(x_{2r-1})\phi_m(x_{2r-1})\phi_p(x_{2r-1})dx_{2r-1} = \frac{1}{2}\delta_{mp}, \quad m,p = 1,2,\ldots \tag{31}$$

$$\lim_{N_r\to\infty}\sum_{r=1}^{N_r/2} m(x_{2r})\phi_m(x_{2r})\phi_p(x_{2r})dx_{2r} = \frac{1}{2}\delta_{mp}, \quad m,p = 1,2,\ldots \tag{32}$$

Taking the Laplace transform of Equations (27) and (28), and applying the orthogonality of the mode shapes, as demonstrated in Equations (31) and (32), results in the derivation of the transfer function for a metastructure with internally coupled resonators, as represented in Equation (33).

$$\frac{Z_m(s)}{Q_{b_m}(s)} = \frac{1}{s^2\left(1 + \frac{\mu\omega_{2r-1}^2}{s^2+\omega_{2r-1}^2}\right)\left(1 + \frac{\frac{\mu}{4}\omega_{2r}^2}{s^2+\omega_{2r}^2}\right) + \omega_m^2} \quad m = 1,2,\ldots,N_m \tag{33}$$

The transfer function presented in Equation (33) incorporates coupling effects through the κ parameter, allowing for the interaction between multiple resonators, denoted as ω_{2r-1} and ω_{2r}. This interaction can lead to complex dynamic behavior, including the potential for multiple bandgaps or more pronounced resonant effects. The integration of damping elements for both the plain structure and the resonators can be conveniently executed at this stage.

In distributed parameter systems, such as beams, the resonators are two-degree-of-freedom (2 DOF) systems. It can be proven that $\omega_{2r-1} = \omega_r$, where ω_r is the natural frequency of a resonator when it is not coupled with its adjacent resonator. Additionally, $\omega_{2r} = \sqrt{\omega_{2r-1}^2 + \frac{2\kappa}{m_r}}$, where κ is the mechanical coupling coefficient and m_r is the mass of the resonator. This framework leads to the formation of secondary bandgaps in metastructures with internally coupled resonators. These bandgaps are associated with a 180-degree phase shift in the resonators. Consequently, such metastructures exhibit both primary and secondary bandgaps, a distinct feature compared to traditional structures. The condition of no stretching in the coupling spring essentially renders its influence negligible. Consequently, this scenario simplifies the equation, reducing it to a form that corresponds to the conventional metastructure dynamics, as established in Equation (22). This simplification allows for a more straightforward analysis of the metastructure by reverting to a more basic, yet fundamental, form of the equation. On the other hand, if the resonators differ in frequency or have the same frequency but with a phase difference, the

parameter κ experiences stretching. This results in an additional pole and zero, creating an extra bandgap.

Now, leveraging the transfer function method enables the utilization of the well-known root locus analysis. By considering the modal response as the closed-loop transfer function of a negative feedback system, which incorporates a proportional feedback gain of ω_m^2, and defining the feedforward transfer function as $G(s)$, as specified in Equation (34), one can observe this interpretation.

$$G(s) = \frac{s^2 + \omega_{2r-1}^2}{s^2\left(s^2 + \omega_{2r-1}^2 + \mu\omega_{2r-1}^2\right)} \frac{s^2 + \omega_{2r-1}^2 + \frac{2\kappa}{m_r}}{\left(s^2 + (1 + (\frac{\mu}{4}))(\omega_{2r-1}^2 + \frac{2\kappa}{m_r})\right)} \tag{34}$$

The first transfer function accurately represents what is found in a conventional metastructure. This function has two poles at the origin, characteristic of a system's inherent response dynamics. It includes an additional pole at $\sqrt{1+\mu}\omega_{2r-1}$, influenced by the mass of the resonators. This pole is responsible for creating a bandgap with a length of $\sqrt{1+\mu}$, indicative of the system's frequency-selective behavior. The internal coupling of resonators introduces additional dynamics, particularly influencing the system's behavior near resonant frequencies. The second transfer function introduces terms that model the added poles and zeros in the metastructure due to the internal coupling of resonators. In this function, the roots progress from zero at ω_{2r} to a pole at $\sqrt{1+\frac{\mu}{4}}\omega_{2r}$, creating a bandgap with a length of $\sqrt{1+\frac{\mu}{4}}$.

The comparative analysis of the root locus plots for a conventional metamaterial and a metamaterial with internal resonator coupling, as depicted in Figures 3 and 4, clearly indicate the influence of the coupling term κ on the system dynamics. Figure 3 illustrates the resonance characteristics and bandgap frequencies of a metastructure, as indicated by the poles of its transfer function. The system's resonances correspond to the imaginary components of these poles. Modal responses of the plain beam are modeled as a closed-loop transfer function with proportional feedback. Bandgap edge frequencies are identified using root locus analysis, with specific zeros and poles on the imaginary axis determining these frequencies. Notably, within the bandgap defined by $\omega_{2r-1} < \omega < \omega_{2r-1}\sqrt{1+\mu}$, and $\omega_{2r} < \omega < \omega_{2r}\sqrt{1+\frac{\mu}{4}}$, no poles are present. Root locus analysis is advantageous for evaluating general linear attachments and facilitating the creation of multiple bandgaps.

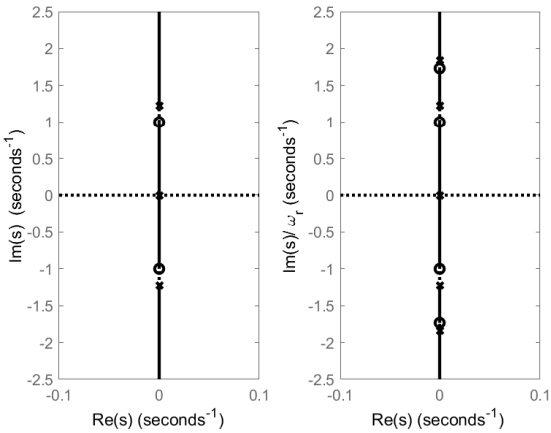

Figure 3. (**Left**) Conventional metastructure root locus with $\omega_m = 0.5$, $\omega_{2r-1} = \omega_r = 1$, $k_r = 1$, $m_r = 1$, and $\mu = 0.5$. (**Right**) Metastructure with internal coupling, showing narrow bandgap with $\omega_m = 0.5$, $\omega_{2r} = 1.7$, $\kappa = k_r$, and $\mu = 0.5$. Internal coupling's impact on system dynamics is highlighted by the additional bandgap in the right plot.

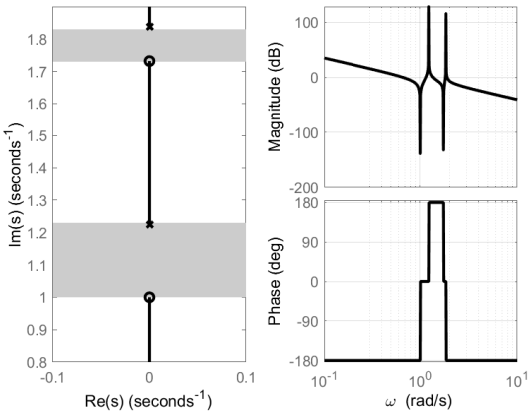

Figure 4. Bode and root locus plots for Equation (34). (**Left**) Root locus with $K = \omega_m^2$, showing conventional and internally coupled bandgap for $\mu = 0.5$ and $\kappa = 1$. Markers: system poles at $\omega_m^2 = 0$, solid lines: pole trajectory as ω_m^2 increases. Grey region: bandgap frequency range. (**Right**) Bode plot showing frequency response, including resonance from coupling effect.

As mentioned earlier, the introduction of κ in the coupled system leads to additional zeros and poles, as evidenced by the second root locus in Figure 4. This modification is characterized by the resonant frequencies $\omega_{2r-1} = 1$ (rad/s) and $\omega_{2r} = 1.7$ (rad/s), suggesting the emergence of a second bandgap. Moreover, the root locus plot in Figure 4 (left) indicates that the internal coupling parameter influences the system's pole trajectories. Conversely, the Bode plot (right) reveals a pronounced resonant peak, suggesting an increased selective sensitivity to certain frequencies. While the phase response indicates the overall system's stability under the new coupling condition, it must be carefully evaluated to ensure robustness, especially in control applications where stability is critical.

Dispersion Analysis and Model Validation of Internally Coupled Resonators by Plane Wave Expansion Method

The plane wave expansion (PWE) method is commonly used for analyzing the propagation of waves in periodic structures, and provides valuable insights into the behavior of these waves, facilitating the design and optimization of these periodic structures for a wide range of applications, such as vibration suppression and energy harvesting [12,13].

The transverse displacement of a metastructure with linearly internally coupled resonators in absolute coordinates is defined as $W_t(x,t) = \hat{W}_t e^{i(G_n x - \omega t)}$ for the beam, $z_{2r-1}(t) = \hat{z}_{2r-1} e^{i(\omega t)}$ for the first resonator, and $z_{2r}(t) = \hat{z}_{2r} e^{i(\omega t)}$ for the second resonator. The dispersion relation emerges from applying periodic boundary conditions to find nontrivial solutions. The relationship between frequency ω and wavevector G_n in one-directional transformation is established by multiplying the variable's amplitude with $\exp(i(G_n x - \omega t))$. With both $k_{r_1} = k_{r_2} = k_r$ and $m_{r_1} = m_{r_2} = m_r$, the equation simplifies as follows:

$$C_1\omega^6 + C_2\omega^4 + C_3\omega^2 + C_4 = 0 \tag{35}$$

where:

$$\begin{aligned} C_1 &= -Am_r^2\rho, \\ C_2 &= m_r^2\left(EIG_n^4 + 2k_r\right) + 2A\rho m_r\kappa + 2A\rho m_r k_r, \\ C_3 &= -\left(2\kappa m_r k_r + A\rho k_r^2 + 2A\rho\kappa k_r + EIG_n^4 m_r^2(\kappa + 2k_r)\right), \\ C_4 &= EIG_n^4\left(2\kappa k_r + k_r^2\right). \end{aligned} \tag{36}$$

3. Results and Discussion

The rectangular beam under investigation has the following dimensions: a length of 0.91 m (L_m), a width of 40 mm (w_m), and a height of 3 mm (h_m). The material used for the beam has a density of 2710 km per cubic meter (ρ_m) and a modulus of elasticity of 52 GPa (E_m). The beam is characterized by a damping ratio of 0.03 (ζ_m), and the analysis considers a total of eight vibration modes (N_m). Each resonator (N_r) within the system has a mass of 80 g (m_r) and a spring constant of 380 kilonewtons per meter (k_r). The damping ratio for the resonators is also set at 0.03 (ζ_r).

Figure 5 depicts the dispersion curve of the internally coupled metamaterial beam ($\kappa = k_r$) using the plane wave expansion method. The target frequency corresponds to the resonator frequency. The diagram illustrates two bandgaps: the first is associated with the in-plane behavior of both resonators within each unit cell, while the second bandgap emerges due to the out-of-plane behavior of the two resonators in each unit cell. Here, G_n represents the wave vector number and a denotes the lattice size.

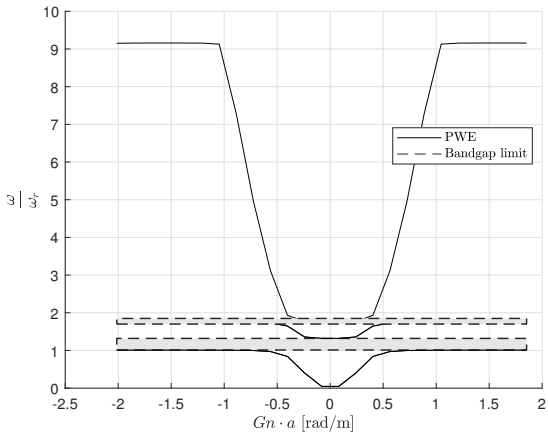

Figure 5. Dispersion curve of an internally coupled metamaterial beam, displaying two distinct bandgaps resulting from in-plane and out-of-plane resonator behavior.

Figure 6 illustrates the transmittance characteristics of a metamaterial beam with internal resonator coupling in terms of tip displacement relative to the base displacement in absolute coordinates. The presence of a common initial bandgap aligns with the theoretical expectations discussed earlier, assuming that all resonators resonate at the same frequency ($\omega_{2r-1} = \omega_{2r} = \omega_r$) and maintain identical phase relationships. In the case of the internally coupled metastructure, an additional bandgap is observed, which substantiates the theoretical premise that variations in resonator frequencies or phase differences can extend the parameter κ. This extension, facilitated by the assumption of a massless coupling spring, introduces new dynamics to the system by adding an extra pole and zero, resulting in the creation of an additional bandgap. The primary bandgap occurs at the target frequency, which corresponds to the resonator's frequency adjusted by the length factor $\sqrt{1+\mu}$. The secondary bandgap's location is contingent upon the stiffness of the internal coupling and is defined by the length factor $\sqrt{1+\frac{\mu}{4}}$. Notably, the dips in the graph signify areas of low transmittance, indicating reduced vibration at the beam's tip and effectively marking the bandgap regions.

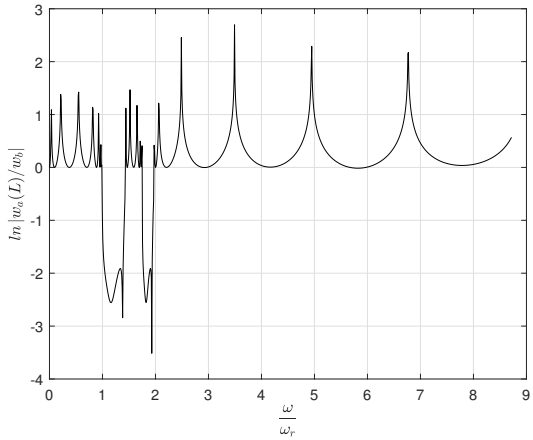

Figure 6. Transmittance plot for a metamaterial beam with internal resonator coupling ($k = k_r$) comprising eight resonators, which equates to four unit cells.

Figure 7 presents a graphical analysis illustrating the influence of varying internal coupling spring constant values, denoted as κ, on the bandgap frequencies within a metastructure. Notably, alterations in κ do not induce substantial shifts in the frequency edges of the primary first bandgap. However, as κ increases, it introduces additional, narrower gaps at frequencies above the rest of the second bandgap. These narrower gaps underscore the sensitivity of the metastructure's dynamic response to specific ranges of internal coupling strength.

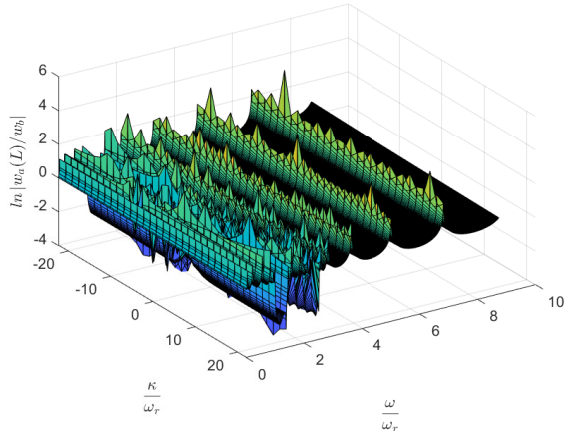

Figure 7. Analysis of the influence of internal coupling stiffness κ on the metastructure's bandgap frequencies in Equation (33), showing the consistent edge of the first bandgap and the emergence of narrow higher-frequency gaps within certain κ ranges.

Figure 8 presents a contour plot of the transmittance across the metastructure as a function of the normalized internal coupling strength, κ/ω_r, and normalized frequency, ω/ω_r. The color gradient represents the logarithmic scale of transmittance, indicating the level of wave attenuation within the metastructure. Dark regions correspond to high attenuation levels, signifying the presence of bandgaps. As observed, the contour lines delineate the boundaries of the bandgaps, which become more distinct with specific values of internal coupling strength. This visualization provides a comprehensive understanding

of how internal coupling affects the bandgap frequencies, offering insights into the precise tuning of the metastructure's vibrational properties. It can be seen that the emergence of additional bandgaps occurs within certain ranges of κ, demonstrating the metastructure's sensitivity to variations in internal coupling. The plot serves as a detailed map for predicting the dynamic behavior of the metastructure under varying conditions of internal coupling, which is critical for applications requiring targeted vibration isolation frequencies.

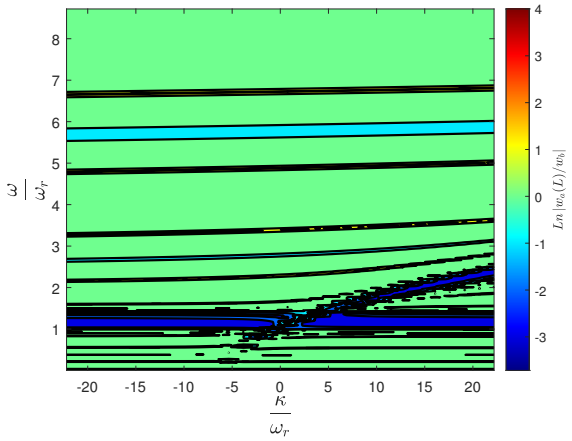

Figure 8. Transmittance contour plot against normalized internal coupling strength and frequency, highlighting bandgap boundaries and the metastructure's sensitivity to κ variations.

The results reveal that metastructures with internally coupled resonators retain the primary bandgap found in conventional metastructures but also introduce an additional, thinner bandgap at a higher frequency. This secondary bandgap remains separate from the primary one, making it challenging to use internal coupling to merge both bandgaps for vibration isolation in continuous and distributed metastructures. This difficulty arises because the second bandgap's nature is linked to a 180-degree phase change in resonators with identical natural frequencies (ω_r). It would be beneficial to investigate the impact of varying ω_r in different unit cells. Despite these challenges, it is noteworthy that in lumped systems, metastructures with internally coupled resonators significantly widen the bandgap compared to conventional configurations.

4. Finite Element Study

The dynamic behavior of metastructures incorporating internally coupled resonators is investigated using finite element method (FEM) simulations, affirming theoretical predictions. The analysis outputs present the vibrational modes of the metastructure. These modes are expressed as amplitude variations across a spectrum of normalized frequencies, with a particular focus on resonant frequencies pertinent to bandgap development. Significant findings from the analysis illustrate the variance in bandgap distribution and intensity of resonant peaks as a function of stiffness ratio. This implies a substantial relationship between internal coupling stiffness and the dynamic response of the metastructure. Visualization of these results not only confirms primary and secondary bandgap presence but also aligns with the theoretical implications of internal resonator coupling. Figure 9 concentrates on the transmissibility for a specific stiffness ratio κ, reflecting a critical scenario where κ is precisely matched with the resonator's stiffness $(\kappa/\omega_r = 0.003)$, an essential condition for optimal bandgap definition. This particular observation underscores the necessity of accurate internal coupling stiffness to achieve the designed dynamic response.

However, deviations from the ideal κ value lead to pronounced disorder within the system's response, emphasizing the metastructure's sensitivity to variations in internal coupling stiffness. Such irregularities pose challenges for ensuring predictability and

consistent performance in practical applications, thus advocating for stringent precision in design and manufacturing processes.

The contour plot depicted in Figure 10 utilizes a binary representation to mark regions of transmittance reduction, set at $log(10^{-0.1})$. The provided binary representation displays two distinct white regions against a cyan background, illustrating the transmittance levels across various stiffness ratios κ and normalized frequencies. The first white region, located at the target resonator frequency ω_r, corresponds to a bandgap typically observed in conventional metamaterials. This bandgap represents a frequency range where the structure prevents wave propagation, thereby indicating a strong vibration isolation capability at the resonant frequency of the metamaterial. The second white region appears at a higher frequency range and signifies the impact of internal coupling within the metamaterial structure. This additional bandgap is a result of the specific design and internal resonator interactions that are a characteristic of the studied metastructures. The emergence of this second bandgap highlights the effect of internal coupling on the extension of vibration isolation performance to higher frequency ranges.

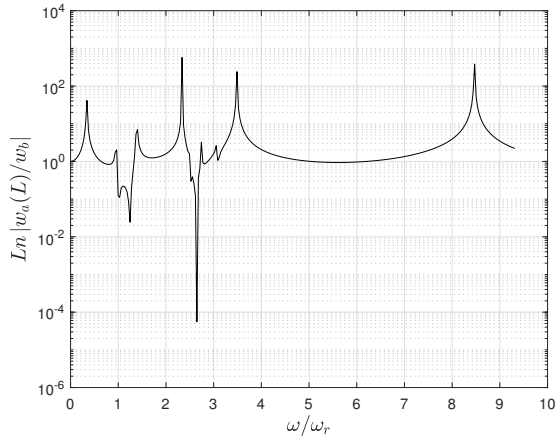

Figure 9. Transmissibility for a cantilever beam with stiffness ratio κ equal to k_r, demonstrating optimal internal coupling for bandgap clarity.

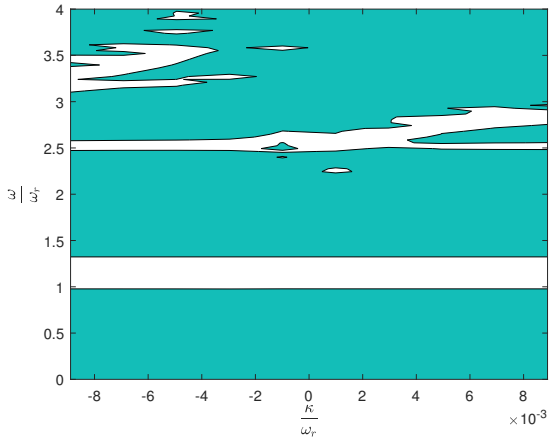

Figure 10. Binary contour plot illustrating the presence and absence of transmittance corresponding to bandgaps as a function of stiffness ratio κ and normalized frequency.

Impact of Spacial Variations on Bandgap Characteristics

The established methodology enables manipulation of the transfer function, thereby permitting exploration into how adjustments in the mass placement on a resonator affect bandgap traits, a key factor for refining bandgap properties within a closed-loop control system.

This section explores adjusting resonator stiffness while maintaining constant mass, a method beneficial for heavy machinery applications where traditional piezoelectric solutions may fall short. Stiffness tuning, as opposed to piezoelectric adjustments, offers a more durable and practical solution for these demanding environments. The current study examines a conventional metastructure that does not incorporate internally coupled resonators. The resonators are of the cantilever type, with a mass that can be positioned along the length from the tip to the base. The specific parameters defining the metastructure and resonators are as follows: eight resonators ($N_r = 8$), with the beam dimensions being 300 mm in length, 25 mm in width, and 3 mm in height. The material density is 2700 kg/m^3, and the modulus of elasticity is 69.5 GPa. The damping ratio of the structure and resonators is the same, at 0.01. An attached mass (m_a) of 3.8 g is placed at distances that vary from 20 to 57.3 mm along the resonator. The natural frequency of the resonator (ω_r), when the attached mass is at the tip, is 32 Hz. This setup allows for an exploration of the resonator stiffness's impact on the bandgap properties of the metastructure.

Figure 11 provides a 3D visualization of how the position of the attached mass along the length of a resonator affects the bandgap frequencies in a metastructure. The natural frequency at which the bandgap starts is denoted as ω_r, corresponding to the case when the mass is located at the tip of the resonator. The graph demonstrates that as the mass moves closer to the base of the resonator—decreasing δ—the resonator's stiffness increases, leading to a rise in ω_r and a subsequent shift of the bandgap towards higher frequencies.

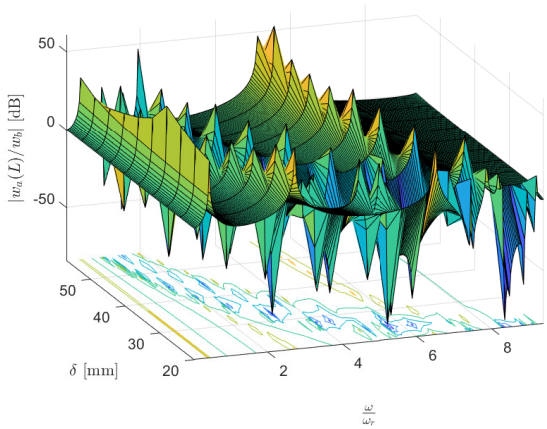

Figure 11. A 3D plot showing the shift in bandgap frequency related to mass positioning on the resonator, with delta (δ) representing the mass location from the resonator's tip to base.

The contour plot in the x–y plane clearly depicts the bandgap's initiation at the initial natural frequency ω_r when the mass is at the resonator's tip. From there, the bandgap expands and moves as the location of the mass changes. This shift is particularly crucial for applications requiring tunable vibration isolation, as it shows the potential to adjust the bandgap frequency by simply repositioning the resonator mass without altering the resonator or structure itself.

The binary representation in Figure 12 illustrates the influence of the mass location along the resonator on the bandgap frequencies. With the bandgap depth limit set at a decibel ratio of output to input displacement of 0.2, the plot shows that when the attached mass is positioned at the tip of the resonator, the bandgap originates at the resonator frequency

ω_r. The white areas in the binary representation correlate to the regions of significant transmittance reduction, effectively mapping the bandgap's presence and evolution as the mass moves closer to the resonator's base.

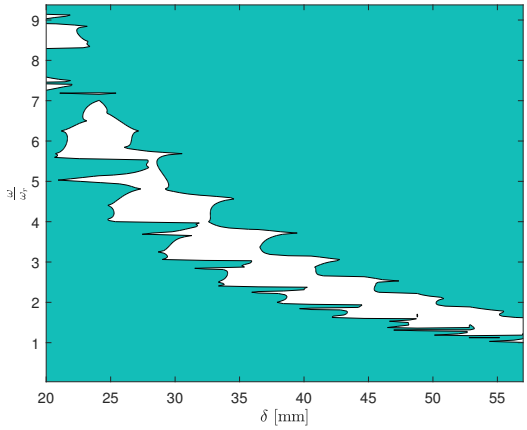

Figure 12. Binary contour plot of bandgap presence against resonator mass placement (δ) and normalized frequency (ω/ω_r), with white areas indicating effective vibration isolation regions.

5. Conclusions

This study explored the dynamic behavior of metastructures, focusing on those with conventional configurations and those augmented with internally coupled resonators, through a theoretical lens. The development of analytical models deepened our understanding of bandgap dynamics, highlighting the prediction of primary and secondary bandgaps as influenced by internal coupling stiffness. Finite element analysis (FEA) corroborated these theoretical insights, yet it also exposed complexities beyond the analytical models' scope. Insights gained from this study stress the importance of accurately accounting for the physical characteristics of internal couplings and achieving exact stiffness ratios. Additionally, this work shows that adjusting the natural frequencies of resonators through stiffness manipulation—via the strategic positioning of mounted masses—provides a viable approach for customizing vibration isolation solutions. This strategy is particularly relevant for environments subjected to heavy loads and extreme conditions, offering tailored responses to complex vibrational challenges.

The principal contributions of this research are as follows:

- We established a novel transfer function approach for the analysis of metastructures, diverging from traditional bandgap investigation methods such as dispersion analysis and wave finite element methods.
- We applied root locus analysis and transfer function modeling, offering new perspectives on metastructure control.
- We demonstrated the enhanced dynamic bandgap characteristics achievable through the use of internally coupled resonators, incorporating control engineering techniques for refined metastructure management.

This research showcases the fusion of control system theory with metastructure analysis, presenting a groundbreaking approach for the precise manipulation of bandgaps. This methodology not only marks a significant advancement in the understanding and application of vibration control technologies but also opens new avenues for energy-efficient solutions across multiple industries. Specifically, in the automotive sector, the integration of metastructures can significantly reduce noise and vibrations, enhancing vehicle durability. In civil engineering, buildings and infrastructure equipped with optimized bandgaps offer enhanced protection against environmental vibrations and seismic activities. Moreover,

the innovative application of these metastructures in energy harvesting from vibrational bandgaps paves the way for smart buildings to achieve superior energy sustainability.

Future studies will prioritize empirical validation through experimentation to confirm the theoretical and numerical models' applicability in real-world scenarios. Subsequent research will focus on fabricating metastructures with internally coupled resonators, with a particular emphasis on manufacturing precision to accurately match the stiffness of the resonators, thereby ensuring optimal system performance. Additionally, the integration of piezoelectric materials for vibration suppression and energy harvesting will be explored, aiming to enhance the functional versatility of these advanced materials.

Author Contributions: The individual contributions of authors to this research article are as follows: Conceptualization, H.A. and K.V.; methodology, H.A.; software, H.A.; validation, H.A., K.V. and S.H.H.; formal analysis, H.A.; investigation, H.A.; resources, S.H.H.; data curation, K.V.; writing—original draft preparation, H.A.; writing—review and editing, K.V. and E.P.; visualization, S.H.H.; supervision, S.H.H.; project administration, E.P.; funding acquisition, E.P. All authors have read and agreed to the published version of the manuscript.

Funding: This work was supported by the Estonian Research Council through the grant PRG658.

Institutional Review Board Statement: Not applicable.

Informed Consent Statement: Not applicable.

Data Availability Statement: The data presented in this study are available on request from the corresponding author. The data are not publicly available due to privacy and ethical considerations pertaining to proprietary information of the university research project.

Conflicts of Interest: The authors declare no conflicts of interest.

Abbreviations

The following abbreviations are used in this manuscript:

$\mathcal{L}$	Structural flexibility parameter (N/m)
$\mathcal{C}$	Damping coefficient (Ns/m)
$\mathcal{M}$	Mass per unit length of the beam (kg/m)
k_r	Stiffness of the resonator (N/m)
c_r	Damping coefficient of the resonator (Ns/m)
x_r	Position of the r-th resonator (m)
$\delta(x - x_r)$	Dirac delta function indicating resonator location
$\mathcal{F}_{b_m}$	External force distributed across the beam due to modals (N)
$\mathcal{F}_{b_r}$	External force distributed across the beam due to resonators (N)
m_r	Mass of the r-th resonator (kg)
ω	Angular frequency of the wave (rad/s)
κ	Internal coupling stiffness (N/m)
z_r	Displacement of the r-th resonator (m)
ϕ_m	Mode shape function of the m-th mode
ϕ_n	Mode shape function of the n-th mode
E	Young's modulus of the beam material (Pa)
I	Moment of inertia of the beam cross-section (m^4)
ρ	Density of the beam material (kg/m^3)
A	Cross-sectional area of the beam (m^2)
N_m	Number of modes
N_r	Number of resonators
δ_{mn}	Kronecker delta function for modes m and n
ζ_m	Damping ratio of the m-th mode
ζ_r	Damping ratio of the r-th resonator
ω_m	Natural frequency of the m-th mode (rad/s)
ω_r	Natural frequency of the r-th resonator (rad/s)
z_m	Modal displacement amplitude
λ_m	Eigenvalue associated with the m-th eigenfunction $\phi_m(x)$

μ	Mass ratio
G_n	Wave number of the n-th mode in the structure (rad/m)
$_{2r-1}$	Subscript notation for odd-numbered resonators
$_{2r}$	Subscript notation for even-numbered resonators

Appendix A

Solution for a Cantilevered Beam

Equation (5) has a general solution of [14]:

$$\phi_m(x) = C_{1m}\cos\beta_m x + C_{2m}\sin\beta_m x + C_{3m}\cosh\beta_m x + C_{4m}\sinh\beta_m x \tag{A1}$$

where

$$\beta_m^4 = \frac{\rho A\omega_m^2}{EI} \tag{A2}$$

The constant coefficients C_{1m}, C_{2m}, C_{3m}, and C_{4m} can be found from the boundary conditions.

The frequency equation can be derived by applying the frequency determinant method to the eigenfunctions given by (A1) and considering the boundary conditions for a cantilever beam with length L, which involve zero displacement and slope at the fixed end, as well as zero shear and moment at the free end.

A nontrivial solution for coefficients C_1 to C_4 is obtained when the coefficient matrix is set to zero. Solving the resulting determinant yields the frequency equation.

$$\cos(\beta L)\cosh(\beta L) = -1 \tag{A3}$$

The roots of this equation can be determined either numerically or graphically. Considering the speed of wave propagation in the material, applying $\beta_m L$ to Equation (A2) gives the natural frequency of vibration.

$$\omega_m = (\beta_m L)^2\sqrt{\frac{EI}{\rho AL^4}}, \quad m = 1, 2, \ldots \tag{A4}$$

This equation provides the natural frequencies for different modes of vibration, where β_m represents the roots of the mode shape equation.

By determining the coefficients C_1 to C_4 and substituting them into Equation (A1), we obtain the normalized equation for the mode shapes in Equation (A5).

$$\phi_m(x) = \frac{1}{\sqrt{\rho LA}}\left[(\sin\beta_m x - \sinh\beta_m x) - \frac{(\sin\beta_m L + \sinh\beta_m L)}{(\cos\beta_m L + \cosh\beta_m L)}(\cos\beta_m x - \cosh\beta_m x)\right] \tag{A5}$$

There is no necessity to numerically solve for a large number of solutions to this equation. For larger solutions, a reliable approximation can be obtained using the following formula:

$$\beta_m L \approx \frac{(2m-1)\pi}{2}, \quad m > 5 \tag{A6}$$

Given the presence of hyperbolic functions in Equation (A3), it becomes crucial to approximate the mode shape for values of m exceeding 10 to circumvent numerical issues. An approximation can be derived by expanding the precise mode shape and presuming a large value for $\beta_m L$. This results in the expression in Equation (A7).

$$\phi_m(x) \approx \frac{1}{\sqrt{\rho AL}}\left[\cos(\beta_m x) - \sin(\beta_m x) - e^{-\beta_m x} - e^{\beta_m x - \beta_m L}\sin\beta_m L\right] \tag{A7}$$

References

1. Shelby, R.A.; Smith, D.R.; Schultz, S. Experimental verification of a negative index of refraction. *Science* **2001**, *292*, 77–79. [CrossRef] [PubMed]
2. Liu, Z.; Zhang, X.; Mao, Y.; Zhu, Y.; Yang, Z.; Chan, C.T.; Sheng, P. Locally resonant sonic materials. *Science* **2000**, *289*, 1734–1736. [CrossRef] [PubMed]
3. Hazra, S.; Bhattacharjee, A.; Chand, M.; Salunkhe, K.V.; Gopalakrishnan, S.; Patankar, M.P.; Vijay, R. Ring-resonator-based coupling architecture for enhanced connectivity in a superconducting multiqubit network. *Phys. Rev. Appl.* **2021**, *16*, 024018. [CrossRef]
4. Rozenman, G.G.; Peisakhov, A.; Zadok, N. Dispersion of organic exciton polaritons—A novel undergraduate experiment. *Eur. J. Phys.* **2022**, *43*, 035301. [CrossRef]
5. Li, Y.; Yefremenko, V.G.; Lisovenko, M.; Trevillian, C.; Polakovic, T.; Cecil, T.W.; Barry, P.S.; Pearson, J.; Divan, R.; Tyberkevych, V.; et al. Coherent coupling of two remote magnonic resonators mediated by superconducting circuits. *Phys. Rev. Lett.* **2022**, *128*, 047701. [CrossRef]
6. Hu, G.; Tang, L.; Das, R. Internally coupled metamaterial beam for simultaneous vibration suppression and low frequency energy harvesting. *J. Appl. Phys.* **2018**, *123*, 055107. [CrossRef]
7. Oyelade, A.O.; Oladimeji, O.J. Coupled multiresonators acoustic metamaterial for vibration suppression in civil engineering structures. *Forces Mech.* **2021**, *5*, 100052. [CrossRef]
8. Erturk, A.; Inman, D.J. A distributed parameter electromechanical model for cantilevered piezoelectric energy harvesters. *J. Vib. Acoust.* **2008**, *130*, 041002. [CrossRef]
9. Sugino, C.; Xia, Y.; Leadenham, S.; Ruzzene, M.; Erturk, A. A general theory for bandgap estimation in locally resonant metastructures. *J. Sound Vib.* **2017**, *406*, 104–123. [CrossRef]
10. Hansen, C.; Snyder, S.; Qiu, X.; Brooks, L.; Moreau, D. *Active Control of Noise and Vibration*; CRC Press: Boca Raton, FL, USA, 2012.
11. Meirovitch, L. *Fundamentals of Vibrations*; Waveland Press: Long Grove, IL, USA, 2010.
12. Li, F.L.; Zhang, C.; Wang, Y.S. Band structure analysis of phononic crystals with imperfect interface layers by the BEM. *Eng. Anal. Bound. Elem.* **2021**, *131*, 240–257. [CrossRef]
13. Lei, L.; Miao, L.; Zheng, H.; Wu, P.; Lu, M. Band gap extending of locally resonant phononic crystal with outward hierarchical structure. *Appl. Phys. A* **2022**, *128*, 492. [CrossRef]
14. Rao, S.S. *Vibration of Continuous Systems*; John Wiley & Sons: Hoboken, NJ, USA, 2019.

Disclaimer/Publisher's Note: The statements, opinions and data contained in all publications are solely those of the individual author(s) and contributor(s) and not of MDPI and/or the editor(s). MDPI and/or the editor(s) disclaim responsibility for any injury to people or property resulting from any ideas, methods, instructions or products referred to in the content.

Appendix 3

Hossein Alimohammadi et al. “Stability analysis and energy harvesting in lumped parameter systems with internally coupled resonators”. In: *Journal of Vibration and Control* (2024)

Check for updates

Original Manuscript

Journal of Vibration and Control
2024, Vol. 0(0) 1–13
© The Author(s) 2024

Article reuse guidelines:
sagepub.com/journals-permissions
DOI: 10.1177/10775463241241161
journals.sagepub.com/home/jvc
Sage

Stability analysis and energy harvesting in lumped parameter systems with internally coupled resonators

Hossein Alimohammadi[1], Kristina Vassiljeva[1], S Hassan HosseinNia[2], and Eduard Petlenkov[1]

Abstract

This article explores internally coupled resonators in metamaterial systems, focusing on mechanical and electromechanical coupling. The article provides a thorough examination of stability within the context of internally coupled resonators. It establishes stability criteria, emphasizing the importance of strictly stable systems in practical applications. Furthermore, it analyzes stability through simulations, revealing how various parameters impact system behavior and highlighting the challenges and benefits of achieving stability in metamaterial systems. Additionally, the article explores the impact of damping coefficients and resonator characteristics, on displacement and power generation profiles. Nonlinear behavior in internally coupled resonators is examined, revealing the presence of bifurcation in simulation and offering insights into multi-stability and system behavior.

Keywords

stability, internally coupled resonators, piezoelectric energy harvesting, vibration suppression, lumped systems

1. Introduction

Internally coupled resonators, integral in wave control, stability, and energy collection, are crucial in lumped parameter systems' engineering. This article emphasizes the role of these resonators, highlighting the benefits of mechanical linear, nonlinear internal coupling, and electromechanical shunt capacitance circuits. These mechanisms allow for negative stiffness and refined system dynamic control. Electrical internal coupling, as shown through simulations, offers tunability and superior energy harvesting. Moreover, the article examines how parameters like damping coefficients and resonator traits influence displacement and energy output at varied frequencies. The nonlinear aspects of these resonators, leading to multi-stability and specific system behaviors, are also explored.

1.1. Internally coupled resonators exhibiting mechanical nonlinearity

The emergence of internally coupled resonators has been identified as a key element in recent dynamics and vibration control research. Through the complex interactions among internal structural components, these resonators exhibit a varied array of vibrational behaviors. These distinctive properties afford unprecedented capabilities in managing and directing wave propagation, establishing themselves as invaluable resources in various fields, such as structural health monitoring, acoustic metamaterials, and vibration mitigation. Notable research in this field, particularly exemplified by the studies of Hu et al. (2018), has traversed through metastructures featuring linearly coupled resonators. The discoveries from such investigations illuminate the existence of an additional narrow band gap in comparison to conventional metastructures, thereby highlighting the fascinating potentialities within this area of research.

While the concept of employing negative stiffness has been explored extensively in past research, Liu et al. (2022) delve into a diatomic-chain locally resonant acoustic metamaterial structure, underscoring the pivotal role of the

[1]Department of Computer Systems, Tallinn University of Technology, Tallinn, Estonia
[2]Department of Precision and Microsystems Engineering, Delft University of Technology, Delft, The Netherlands

Received: 25 October 2023; revised: 13 January 2024; accepted: 27 February 2024

Corresponding author:
E Petlenkov, Department of Computer Systems, Tallinn University of Technology, Akadeemia tee 15a, Tallinn 12618, Estonia.
Email: eduard.petlenkov@taltech.ee

negative-stiffness mechanism in enhancing vibration suppression. By utilizing additional band gaps and Bragg scattering, the structure exhibits superior management of vibration transmission, particularly in managing ultralow frequency vibrations in the lower frequency spectrum. The negative-stiffness mechanism proves vital for fine-tuning the metamaterial's band gap characteristics and potential applications in vibration reduction, especially under specific material parameters.

1.2. Electromechanical internally coupled resonators

Electromechanical resonators, notably those incorporating piezoelectric elements and internal coupling of resonators, manifest a compelling complexity by merging mechanical and electrical aspects, thus enabling unique wave propagation properties. While their promising attributes are evident, an exploration into nonlinear, internally coupled electromechanical systems is relatively untapped. This discernible gap in research accentuates the need for an exhaustive study of these systems, which have the capacity to innovate vibration control and energy-harvesting sectors (Shu and Lien, 2006; Lefeuvre et al., 2005).

Despite their remarkable wave propagation features, metamaterials are often hindered by the limited bandwidth of their band gaps, impacting their performance in broad-spectrum vibration applications. To counteract this, research has pivoted toward developing metamaterial configurations with multiple band gaps and utilizing nonlinearity as a powerful tactic (Fang et al., 2017). The characteristics of piezoelectric shunt methods, marked by their mechanical–electrical conversion capabilities, have spurred research into dynamically tunable metamaterials. However, most studies predominantly utilize independent piezoelectric shunt circuits for each local resonator (Chatziathanasiou et al., 2022; Li et al., 2023).

The primary objective of this study is to comprehensively examine the band gap characteristics of the proposed lumped system, emphasizing the mechanical and electromechanical internal coupling through the shunt capacitance circuit and conceptualizing the circuit as a negative capacitor (Hu et al., 2017). Additional goals involve conducting a stability analysis of the piezoelectric elements model on the resonator and a pivotal comparison of power and energy harvested from the resonators, with a special focus on their impact on band gap formation in the chain mass structure.

1.3. Solution stability

The stability and singularity of nonlinear solutions in mechanical internally coupled resonators, electromechanical internal coupling, and other nonlinear periodic media have been somewhat overlooked. Stability analysis regarding wave responses in phononic media is documented in foundational systems (Newton and Keller, 1987), works addressing geometric nonlinearity (Liu et al., 2022; Murer et al., 2023), and studies on topological modes (Chaunsali et al., 2021). The introduction of nonlinearity often induces bifurcations, leading to dynamic solutions with multiple branches. Without a stability analysis, theoretical responses might not represent physical systems accurately. Investigations into the stability of harmonic excitations have revealed transitions between stable solutions with increasing amplitude, eventually leading to chaotic dynamics (Hoogeboom et al., 2013).

Meanwhile, stability analysis of plane waves in nonlinear phononics remains relatively unexplored. Newton and Keller (Newton and Keller, 1987) introduced an equation to assess the perturbation growth rate to ascertain the start and end of plane wave stability. Further studies by Fronk and Leamy (Fronk and Leamy, 2017, 2019) addressed plane wave stability in monoatomic and diatomic chains. These findings highlight that in 1D systems, stability is amplitude-dependent, and in 2D, it also depends on direction. Recent studies have also analyzed the stability of topologically protected modes (Mančić et al., 2023) in highly nonlinear systems, unveiling specific frequency–energy domains where the protected mode becomes unstable.

This research tackles the challenge of optimizing band gap characteristics and energy harvesting in linear and nonlinear internally coupled resonators, a significant gap in current metamaterial applications crucial for advancing energy efficiency and vibration control.

The primary contributions of this paper are summarized as follows:

- Analyzed band gap and energy harvesting in nonlinear coupled resonators in lumped system.
- Developed new stability analysis for nonlinear resonator systems.
- Identified enhancements in band gaps specifically in internally coupled resonators.
- Illustrated how internal coupling boosts energy harvesting and analyzed damping impacts.
- Provided insights on optimizing metamaterials for energy harvesting.
- Demonstrated advantages of electromechanical shunt circuits in tuning band gaps.

2. Method

Using the lumped parameter model, intricate physical systems are distilled into discrete points defined by parameters such as resistance, capacitance, or mass. This is

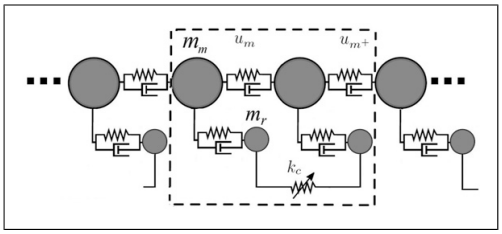

Figure 1. A mechanically internally coupled resonator. The dashed rectangle signifies a unit cell.

suitable for systems where the wave propagation wavelength far exceeds structural dimensions.

Through the Lagrangian energy method, equations of motion are derived for metamaterials interfaced with internally coupled resonators. Given the system's inclusion of negative stiffness, an essential stability analysis is executed, aiming for vibration suppression enhancements while ensuring stability and reliability.

2.1. Linear electromechanical resonators

In electromechanical systems employing piezoelectric elements, additional nonlinearity is introduced to the system dynamics, serving to dampen vibrations and enhance energy harvesting in resonators. When resonators are integrated with piezoelectric elements, a coupling between mechanical and electrical dynamics occurs, which enriches yet complicates system behavior. Utilizing Lagrange's equation, governing dynamics can be obtained, with mechanical damping typically represented via Rayleigh damping and energy equations being linearly characterized. The resulting governing equations of motion are delineated accordingly.

2.2. Analysis of power output of standard piezoelectric circuit for energy harvesting

In investigating the nonlinearity properties in piezoelectric materials, this study utilizes a standard circuit paired with each nonlinearity type. This approach ensures that each nonlinearity is observed in isolation, unaffected by different circuit efficiencies. Here, the piezo voltage, $v_p(t)$, has a direct proportionality to the displacement, $u(t)$. An in-depth analysis yields the average harvested power P in the system as

$$P = \frac{v_c^2}{R} = \frac{R\theta^2\omega^2}{\left(Rc_p\omega + \frac{\pi}{2}\right)^2} z_0^2 \tag{1}$$

This formulation encapsulates the intricate interplay between electric charge storage, current dynamics, mechanical displacement, and the system's power harvesting (Shu and Lien, 2006).

2.3. Internally coupled resonators with mechanical nonlinearity

The system, illustrated in Figure 1, embodies a nonlinear mechanical chain internally coupled, with a unit cell delineated by a dashed rectangle. The analysis simplifies the system dynamics by exclusively considering springs, assuming linearity for both the primary and resonator-associated springs while maintaining nonlinearities in the internally coupled springs, and disregarding damping and electromechanical elements. The primary dynamic behavior emerges predominantly from the nonlinear internal coupling amidst resonators within a generally linear spring system, thereby facilitating a concentrated exploration into the effects and potential benefits of nonlinearity in inter-resonator springs.

The kinetic energy, symbolized by T, includes the dynamic activities of both the main chain and the resonators and is expressed as follows:

$$T = \frac{1}{2}m_m\left(\dot{u}_m^2 + \dot{u}_{m^+}^2\right) + \frac{1}{2}m_r\left(\dot{u}_r^2 + \dot{u}_{r^+}^2\right) \tag{2}$$

The potential energy, denoted by U, encapsulates the energy stored in various components of a mechanically coupled system: the main chain's linear springs, coupling springs between the chain and resonators, and notably, the nonlinear springs internally coupling the resonators provide a comprehensive view of energy distribution and interplay in a predominantly linear mechanical chain with specific nonlinear interactions.

$$\begin{aligned} U = {} & \frac{1}{2}k_m\left[\left(u_{m^-} - u_m\right)^2 + \left(u_m - u_{m^+}\right)^2 + \left(u_{m^+} - u_{m^{++}}\right)^2\right] \\ & + \frac{1}{2}k_r\left[\left(u_m - u_r\right)^2 + \left(u_{m^+} - u_{r^+}\right)^2\right] \\ & + \frac{1}{2}k_{c_1}\left(u_r - u_{r^+}\right)^2 + \frac{1}{4}k_{c_2}\left(u_r - u_{r^+}\right)^4 \end{aligned} \tag{3}$$

Here, k_{c_1} and k_{c_2} serve as the linear and nonlinear coupling coefficients, respectively. While k_{c_1} facilitates a linear coupling between resonators, k_{c_2} introduces a bistable nonlinearity due to its fourth-order nature among the resonators. If both k_{c_1} and k_{c_2} are positive ($k_{c_1} > 0$ and $k_{c_2} > 0$), the system achieves a traditional monostable state, thereby circumventing the need to identify and linearize around a stable point. Opting for this strategy not only guarantees straightforward and stable system dynamics but also commonly serves to sidestep the intricacies encountered when navigating through bistable systems, especially in scenarios where $k_{c_1} < 0$ and $k_{c_2} > 0$. Utilizing the

Lagrangian formulation, and defining $z_r(t)$ as relative displacement between chain mass and resonator, the resonator's equation of motion yields

$$\begin{aligned} &m_m\ddot{z}_r(t) + c_m(2\dot{z}_r(t) - \dot{z}_{r^-}(t) - \dot{z}_{r^+}(t)) \\ &+k_m(2z_r(t) - z_{r^-}(t) - z_{r^+}(t)) + k_r z_r(t) = f_{e_r} \end{aligned} \tag{4}$$

$$\begin{aligned} &m_m\ddot{z}_{r^+}(t) + c_m(2\dot{z}_{r^+}(t) - \dot{z}_r(t) - \dot{z}_{r^{++}}(t)) \\ &+k_m(2z_{r^+}(t) - z_r(t) - z_{r^{++}}(t)) + k_r z_{r^+}(t) = f_{e_{r^+}} \end{aligned} \tag{5}$$

$$\begin{aligned} &m_r\ddot{z}_r(t) + c_r\dot{z}_r(t) + k_r z_r(t) + k_{c_1}(z_r(t) - z_{r^+}(t)) \\ &+k_{c_2}(z_r(t) - z_{r^+}(t))^3 = f_{e_m} \end{aligned} \tag{6}$$

$$\begin{aligned} &m_r\ddot{z}_{r^+}(t) + c_r\dot{z}_{r^+}(t) + k_r z_{r^+}(t) - k_{c_1}(z_r(t) - z_{r^+}(t)) \\ &-k_{c_2}(z_r(t) - z_{r^+}(t))^3 = f_{e_{m^+}} \end{aligned} \tag{7}$$

Here, m_m represents the mass of the main chain, and the coefficient k_m is the main chain's stiffness, interacting with the relative displacements between the resonator and its neighbors, while k_r characterizes the resonator's inherent stiffness. The f_{e_r} is the external excitation force on the primary mass chain. The resonator, with mass m_r, has a damping coefficient c_r and stiffness k_r. k_{c_1} is the linear coupling stiffness, while k_{c_2} is nonlinear. The forces f_{e_r} and $f_{e_{r^+}}$ indicate excitation on the primary mass chain, influenced by the resonator and internal connections. f_{e_m} and $f_{e_{m^+}}$ are the forcing on the resonators, sourced from the main chain mass and internal stiffness interactions.

2.4. Stability analysis for mechanical internally coupled metamaterial

The Jacobian matrix is commonly used to analyze the stability of equilibrium points for nonlinear systems. The idea is to linearize the nonlinear system around its equilibrium points and then analyze the stability of the resulting linear system. This provides insight into the local behavior of the nonlinear system around those points.

Considering equations (6) and (7) without the excitation force, the equilibrium points of the system can be ascertained. Setting the velocities $\dot{z}_r$ and $\dot{z}_{r^+}$, along with the accelerations $\ddot{z}_r$ and $\ddot{z}_{r^+}$, to zero provides the necessary conditions that define these equilibrium positions. The equilibrium points satisfy

$$\begin{aligned} &k_r z_{r_0} + k_{c_1}\left(z_{r_0} - z_{r_0^+}\right) + k_{c_2}\left(z_{r_0} - z_{r_0^+}\right)^3 = 0 \\ &k_r z_{r_0^+} - k_{c_1}\left(z_{r_0} - z_{r_0^+}\right) - k_{c_2}\left(z_{r_0} - z_{r_0^+}\right)^3 = 0 \end{aligned} \tag{8}$$

Introducing small perturbations around these equilibrium points results in the following expressions:

$$\begin{aligned} \delta z_r &= z_r - z_{r_0} \\ \delta z_{r^+} &= z_{r^+} - z_{r_0^+} \end{aligned} \tag{9}$$

Upon linearization of the equations of motion around the equilibrium, terms of higher order in δz_r and δz_{r^+} are neglected, leading to

$$\begin{aligned} &m_r\delta\ddot{z}_r + c_r\delta\dot{z}_r + k_r\delta z_r + k_{c_1}(\delta z_r - \delta z_{r^+}) \\ &+3k_{c_2}\left(z_{r_0} - z_{r_0^+}\right)^2(\delta z_r - \delta z_{r^+}) = 0 \end{aligned} \tag{10}$$

$$\begin{aligned} &m_r\delta\ddot{z}_{r^+} + c_r\delta\dot{z}_{r^+} + k_r\delta z_{r^+} - k_{c_1}(\delta z_r - \delta z_{r^+}) \\ &-3k_{c_2}\left(z_{r_0} - z_{r_0^+}\right)^2(\delta z_r - \delta z_{r^+}) = 0 \end{aligned} \tag{11}$$

A state vector is introduced to convert the second-order system into a system of first order:

$$X = \begin{bmatrix} \delta z_r \\ \delta z_{r^+} \\ \delta\dot{z}_r \\ \delta\dot{z}_{r^+} \end{bmatrix} \tag{12}$$

Differentiating the state vector yields

$$\dot{X} = \begin{bmatrix} \delta\dot{z}_r \\ \delta\dot{z}_{r^+} \\ \delta\ddot{z}_r \\ \delta\ddot{z}_{r^+} \end{bmatrix} \tag{13}$$

The objective is to represent $\dot{X}$ in the form AX, where A is a matrix constructed from the system parameters and possibly the equilibrium point. The matrix A is determined by linearizing the equations of motion. The eigenvalues of A indicate the stability of the system around the equilibrium.

The eigenvalue for the nonlinear internally coupled resonators is determined by equations (14) and (15):

$$\lambda_{1,3} = -\frac{c_r \pm \sqrt{c_r^2 - 4k_r m_r}}{2m_r} \tag{14}$$

$$\begin{aligned} \lambda_{2,4} = -\frac{1}{2m_r}(c_r \pm \\ \sqrt{c_r^2 - 4m_r k_r - 8m_r(k_{c_1} + 3k_{c_2}(\delta z_r - \delta z_{r^+})^2)}\Big) \end{aligned} \tag{15}$$

By omitting the nonlinear term k_{c_2}, the system transitions to a linear internally coupled resonator. This exclusion simplifies the stability analysis by removing the nonlinear component. Consequently, the system's behavior is analyzed linearly around its equilibrium point. After this simplification, the governing equation of motion becomes

$$\lambda_{1,3} = -\frac{c_r \pm \sqrt{c_r^2 - 4k_r m_r}}{2m_r} \tag{16}$$

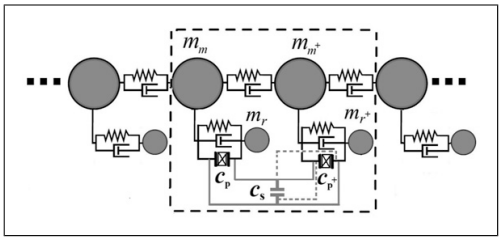

Figure 2. Internally coupled system with electrical shunt circuit: Forward (dashed line) and reverse (solid line) capacitance shunting configurations.

$$\lambda_{2,4} = -\frac{c_r \pm \sqrt{c_r^2 - 4m_r(k_r + 2k_c)}}{2m_r} \tag{17}$$

Stability scenarios for internally coupled systems:

2.4.1. Nonlinear systems:

Case 1: For $c_r^2 - 4k_r m_r < 0$, $\lambda_{1,3}$ imply a stable focus.

Case 2: With $c_r^2 - 4k_r m_r > 0$ and all positive parameters, λ_1 and λ_3 ensure stability.

Case 3: Sign of $\lambda_{2,4}$ depends on term magnitudes and c_r.

Case 4: $c_r^2 - 4k_r m_r - 8m_r(k_{c_1} + 3k_{c_2}(\delta z_r - \delta z_{r^+})^2) < 0$ denotes stability.

2.4.2. Linear systems:

Case 1: For $c_r^2 - 4k_r m_r < 0$, $\lambda_{1,3}$ indicate a stable focus.

Case 2: With $c_r^2 - 4k_r m_r > 0$, signs of λ_1 and λ_3 are determined by c_r.

Case 3: In $c_r^2 - 4k_r m_r - 8k_c m_r > 0$, stability relies on signs of λ_2 and λ_4.

Case 4: Condition $c_r^2 - 4k_r m_r - 8k_c m_r < 0$ signals stability.

2.5. Electromechanical resonators with internal coupling via shunt capacitance circuit technique

In the preceding section, the metamaterial with internal resonator coupling was examined. Due to challenges in constructing and instructing the internal spring, especially when aiming for negative stiffness, an alternative is to utilize an electrical shunt circuit, specifically a prototype capacitance, offering behavior similar to the mechanically internally coupled resonator.

In this section, the shunt capacitance circuit technique is employed to model a two-degree-of-freedom electrical system with internal coupling, as illustrated in Figure 2. In this scenario, capacitance is incorporated as a key component instead of utilizing the resistance (R) as load.

Figure 2 illustrates the forward and reverse shunt circuit setups. The forward pairs the top and bottom surfaces of piezoelectric transducers, whereas the reverse opposes

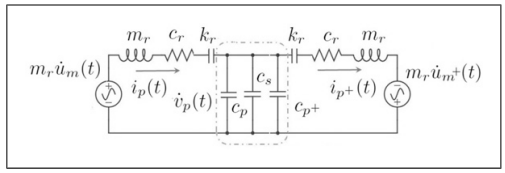

Figure 3. Electrical analog of unit cell resonators with capacitance shunt circuit via impedance method.

them. Both configurations use a parallel capacitor and yield similar analytical conclusions, with the only difference being a sign change in the coupling stiffness. Despite their similarities, this study primarily focuses on the reverse setup due to its straightforward mechanical interpretation when no external capacitance is present. In terms of capacitance, positive values lower voltage during current discharge, while negative ones raise it. Drawing from the impedance analogy, the segments LRC and LRC^+ correspond to resonators $m_r c_r k_r$ and $(m_r c_r k_r)^+$, as displayed in Figure 3.

The voltage across the capacitance reflects force interactions between resonators. Current and charge shifts denote velocity and displacement variations. Essentially, the capacitor acts as a coupling spring, its stiffness determined by the capacitance sign. In the reverse setup for piezoelectric transducers, voltages possess equal magnitude but opposite directions, influenced by the current in the parallel capacitance c_s, as

$$\frac{1}{c_s}\int \left(i_p(t) - i_{p^+}(t)\right)dt = v_p(t) \tag{18}$$

The design uses an internal shunt capacitance, tuned to act as a negative capacitor, to boost resonator performance and strengthen adjacent resonator coupling. Given identical properties for all resonators, including stiffness, damping, and mass, the governing equations for the motion of two resonators within a unit cell, as seen in Figure 2, are

$$m_r\ddot{z}_r(t) + c_r\dot{z}_r(t) + k_r z_r(t) + \theta_r v_p(t) = m_r\ddot{u}_m(t) \tag{19}$$

$$m_r\ddot{z}_{r^+}(t) + c_r\dot{z}_{r^+}(t) + k_r z_{r^+}(t) + \theta_{r^+} v_{p^+}(t) = m_r\ddot{u}_{m^+}(t) \tag{20}$$

Relative displacements of the resonators to the main structure can be defined as $z_r = u_m - u_r$ and $z_{r^+} = u_{m^+} - u_{r^+}$. The coefficients θ_r and θ_{r^+} represent electromechanical coupling, with associated voltages $v_p(t)$ and $v_{p^+}(t)$. The corresponding electrical equations for the transducers are

$$c_p\dot{v}_p(t) + i_p(t) - \theta_r\dot{z}_r(t) = 0 \tag{21}$$

$$c_{p^+}\dot{v}_{p^+}(t) + i_{p^+}(t) - \theta_{r^+}\dot{z}_{r^+}(t) = 0 \tag{22}$$

By substituting equation (18) into equations (21) and (22), expressions for currents $i_p(t)$ and $i_{p^+}(t)$ in the loops are derived as

$$i_p(t) = \frac{c_{p^+}\theta_r\dot{z}_r + c_p\theta_{r^+}\dot{z}_{r^+} + c_s\theta_r\dot{z}_r}{c_p + c_{p^+} + c_s} \tag{23}$$

$$i_{p^+}(t) = \frac{c_{p^+}\theta_r\dot{z}_r + c_p\theta_{r^+}\dot{z}_{r^+} + c_s\theta_{r^+}\dot{z}_{r^+}}{c_p + c_{p^+} + c_s} \tag{24}$$

Substituting equation (23) and equation (24) into equation (18) and integrating with respect to time for zero initial condition yields

$$v_p(t) = \frac{(\theta_r z_r - \theta_{r^+} z_{r^+})}{c_p + c_{p^+} + c_s} \tag{25}$$

$$v_{p^+}(t) = -\frac{(\theta_r z_r - \theta_{r^+} z_{r^+})}{c_p + c_{p^+} + c_s} \tag{26}$$

Substituting equation (25) and equation (26) into equation (19) and equation (20) yields the following expressions:

$$\begin{aligned} &m_r\ddot{z}_r(t) + c_r\dot{z}_r(t) + k_r z_r(t) + k_{s_1} z_r(t) \\ &-k_{s_2} z_{r^+}(t) = m_r\ddot{u}_m(t) \end{aligned} \tag{27}$$

$$\begin{aligned} &m_r\ddot{z}_{r^+}(t) + c_r\dot{z}_{r^+}(t) + k_r z_{r^+}(t) \\ &-k_{s_2} z_r(t) + k_{s_3} z_{r^+}(t) = m_r\ddot{u}_{m^+}(t) \end{aligned} \tag{28}$$

where

$$k_{s_1} = \frac{\theta_r^2}{c_p + c_{p^+} + c_s} \tag{29}$$

$$k_{s_2} = \frac{\theta_r\theta_{r^+}}{c_p + c_{p^+} + c_s} \tag{30}$$

$$k_{s_3} = \frac{\theta_{r^+}^2}{c_p + c_{p^+} + c_s} \tag{31}$$

For identical electromechanical couplings and after substituting the relevant equations into equation (18), the integrated result yields the following condensed motion equations:

$$\begin{aligned} &m_r\ddot{z}_r(t) + c_r\dot{z}_r(t) + k_r z_r(t) \\ &+k_s(z_r(t) - z_{r^+}(t)) = m_r\ddot{u}_m(t) \end{aligned} \tag{32}$$

$$\begin{aligned} &m_r\ddot{z}_{r^+}(t) + c_r\dot{z}_{r^+}(t) + k_r z_{r^+}(t) \\ &-k_s(z_r(t) - z_{r^+}(t)) = m_r\ddot{u}_{m^+}(t) \end{aligned} \tag{33}$$

where

$$k_s = \frac{\theta_r^2}{c_p + c_{p^+} + c_s} \tag{34}$$

2.6. Stability analysis for electromechanical internally coupled resonators via shunt capacitance

The stability of the system hinges on k_s, denoting electromechanical coupling through the shunt circuit. Instability might arise with negative shunt capacitance. For the dual-resonator setup, stability is gauged by linearizing its equations of motion and inspecting the eigenvalues of the Jacobian matrix. A system is stable if all its eigenvalues possess negative real parts. By analyzing the Jacobian matrix derived from linearizing around equilibrium, we discern system behavior. The system remains stable with all eigenvalues in the left-half complex plane. Achieving negative stiffness necessitates k_{s_1}, k_{s_2}, and k_{s_3} to be negative. Uniform electromechanical coupling demands $k_s < 0$.

For a system with positive electromechanical coupling, achieving a negative k_s necessitates the combined c_p and c_s to be negative, indicating a need for negative capacitance. This can be realized using active circuits with operational amplifiers or ferroelectric capacitors. However, this introduces challenges such as potential destabilization. Ensuring system stability, especially with negative capacitance, is paramount, often verified using Jacobian analysis. Mathematically, a corresponding linear system is expressed as

$$m\ddot{z}(t) + c\dot{z}(t) + kz(t) = f(t) \tag{35}$$

with

$$z(t) = \begin{bmatrix} z_r(t) \\ z_{r^+}(t) \end{bmatrix}$$

The system's stability is influenced by the eigenvalues of the Jacobian matrix, determined by equation (36). These eigenvalues are shaped by the damping coefficient c_r and shunt coefficients k_{s_1}, k_{s_2}, and k_{s_3}. While damping can promote stability, spring coefficients introduce potential oscillations. The interplay of couplings k_{s_1}, k_{s_3}, and k_{s_2} deeply impacts the system dynamics. A system is stable when all eigenvalues have negative real parts. If

$$\lambda = \frac{-c_r \pm \sqrt{c_r^2 - 2k_{s_1}m_r - 2k_{s_3}m_r - 4k_r m_r \pm 2m_r\sqrt{k_{s_1}^2 - 2k_{s_1}k_{s_3} + 4k_{s_2}^2 + k_{s_3}^2}}}{2m_r} \tag{36}$$

Table 1. Defined parameters for the piezoelectric model.

Parameter	Value
Mass of main chain (m_m)	0.056 kg
Mass of resonator (m_r)	0.0336 kg
Spring constant of main chain (k_m)	150 N/m
Spring constant of resonator (k_r)	129.6 N/m
Damping coefficient of main chain (c_m)	0.0464 Ns/m
Damping coefficient of resonator (c_r)	0.0334 Ns/m
Piezoelectric capacitance (c_p)	1.5 mF(C/m)
Adjacent resonator's capacitance (c_{p^+})	1.2 mF(C/m)
Electromechanical coupling coefficient (θ_r)	0.25 N/V
Adjacent electromechanical coupling (θ_{r^+})	0.2 N/V
Linear coupling coefficient (k_{c_1})	198 (−20) N/m
Nonlinear coupling coefficient (k_{c_2})	2386 (880) N/m^3
Shunt capacitance (c_s)	−7.9 mF(C/m)
Internal resistance (R)	500 Ω

the discriminant is negative, oscillatory behaviors emerge.

Notably, the real component of λ, defined as $-c_r/2m_r$, predisposes the system to stability, but further analysis is essential for a full understanding.

$$a = c_r^2 - 2k_{s_1}m_r - 2k_{s_3}m_r - 4k_rm_r \tag{37}$$

$$b = 2m_r\sqrt{k_{s_1}^2 - 2k_{s_1}k_{s_3} + 4k_{s_2}^2 + k_{s_3}^2} \tag{38}$$

Case 1: $a < 0$ and $b < 0$, the system is stable if $|a| > |b|$.
Case 2: $a > 0$ and $b > 0$, the system is stable if $a < b$.
Case 3: $a > 0$ and $b < 0$, stability would need to be ascertained by calculating the actual values and verifying the sign of λ. The system can lead to an unstable region.
Case 4: $a < 0$ and $b > 0$, the system is stable if $|a| > |b|$.
Case 5: $a = 0$ or $b = 0$, the system is stable.

For a marginally stable system, damping is typically disregarded to establish boundaries of stability. As per equation (39), when the system's eigenvalues are purely imaginary, it denotes a marginal stability condition. This equation delineates constraints on the stiffness coefficients k_r and k_s, defining the threshold between stable and unstable regimes.

$$2k_r > -k_{s_1} - k_{s3} - \sqrt{k_{s_1}^2 - 2k_{s_1}k_{s3} + 4k_{s_2}^2 + k_{s_3}^2} \tag{39}$$

The associated eigenvalues, representing the system's characteristic frequencies, are given by

$$\lambda = \pm\frac{1}{\sqrt{2}}\sqrt{\frac{-\left(2k_r + k_{s_1} + k_{s_3} \pm \sqrt{k_{s_1}^2 - 2k_{s_1}k_{s_3} + 4k_{s_2}^2 + k_{s_3}^2}\right)}{m_r}} \tag{40}$$

To identify criteria for c_s that ensures a negative equivalent stiffness, equations (29), (30), and (31) are substituted into (37) and (38). The derived expressions are then analyzed to determine the conditions for c_s that satisfy the stability conditions

$$a - b < 0 \tag{41}$$

$$|a| > |b| \tag{42}$$

Substituting a and b into equation (41) for the stability condition of $a - b < 0$ yields

$$c_r^2 - 4k_rm_r < 2m_r\left(\frac{\theta_r^2 + \theta_{r^+}^2 + \sqrt{\theta_r^4 + 2\theta_r^2\theta_{r^+}^2 + \theta_{r^+}^4}}{c_p + c_{p^+} + c_s}\right) \tag{43}$$

Taking into account the absolute values in equation (42), it becomes imperative to explore two scenarios due to the potential positivity or negativity of both a and b.

$$\left|c_r^2 - 4k_rm_r\right| > \left|2m_r\frac{\sqrt{\theta_r^4 + 2\theta_r^2\theta_{r^+}^2 + \theta_{r^+}^4}}{c_p + c_{p^+} + c_s}\right| \tag{44}$$

The inequalities (44) and (43) should be satisfied for stability, and c_s appears in the denominator of the fractions in these expressions, implying that as c_s changes, the values of these expressions will alter, potentially changing the sign of the inequalities. To derive explicit criteria, one could further manipulate these expressions or, depending on the specific application or system, analyze them numerically by substituting values of other parameters (c_r, k_r, m_r, etc.) to explore how varying c_s affects the system's stability. Solving for c_s results in

$$c_s > \frac{2m_r\left(\theta_r^2 + \theta_{r^+}^2 + \sqrt{\theta_r^4 + 2\theta_r^2\theta_{r^+}^2 + \theta_{r^+}^4}\right)}{c_r^2 - 4k_rm_r} - c_p - c_{p^+} \tag{45}$$

In the case of identical electromechanical coupling, and capacitance, the criteria for c_s can be simplified as follows:

$$c_s > \frac{8m_r\theta_r^2}{c_r^2 - 4k_rm_r} - 2c_p \tag{46}$$

In the scenario devoid of damping, the eigenvalues of the system, representing its characteristic roots, are provided as follows:

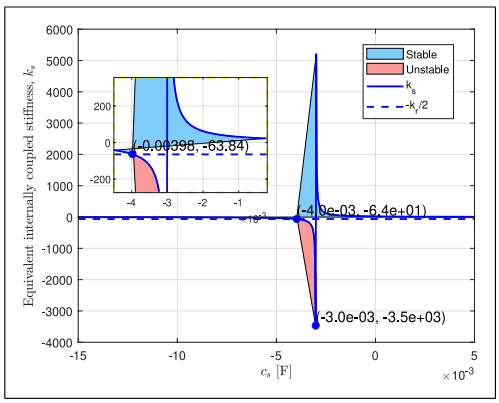

Figure 4. Stability map for the electromechanical lumped system: interplay between equivalent stiffness k_s and shunt capacitance c_s. Parameters: $n = 4$, $m_m = 56$ g, $m_r = 33.6$ g, $k_m = 150$ N/m, $k_r = 129.6$ N/m, $\theta = 0.25$ N/V, $R = 500\ \Omega$, and $c_p = 1.5 \times 10^{-3}$ F.

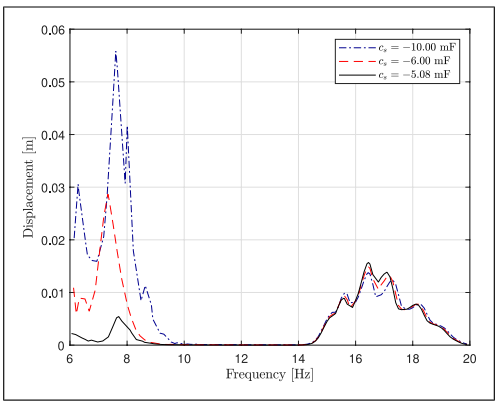

Figure 5. Transmittance comparison of electrical internally coupling with shunt circuit for $\theta = 0.25$ and $c_p = 1.5$ mF, demonstrating the impact of an equivalent negative stiffness of $k_s = -30$.

$$\lambda_{1,2} = \pm\frac{\sqrt{-k_r m_r}}{m_r}$$
$$\lambda_{3,4} = \pm\frac{\sqrt{-m_r(k_r + 2k_s)}}{m_r} \tag{47}$$

The system's stability is defined by the real parts of its eigenvalues. When $k_r + 2k_s > 0$, the system exhibits marginal stability, oscillating continuously without decay or growth. However, if $k_r + 2k_s < 0$, the system has both positive and negative eigenvalues, indicating instability. This highlights the critical relationship between the resonator's spring constant and the shunt capacitance stiffness (k_s). If the feedback from the shunt is overly negative, it can destabilize the system. In most applications, full stability is preferred over marginal stability. The stability criterion for c_s is

$$c_s > -\left(\frac{2\theta_r^2}{k_r} + 2c_p\right) \tag{48}$$

In contrast to purely mechanical internally coupled resonators, electromechanical shunt capacitance circuits provide benefits over solely mechanical resonators by allowing easy adjustments for negative stiffness. The system's flexibility is further amplified by altering parameters like c_p, c_{p^+}, θ_r, and θ_{r^+}, enabling advanced system behaviors and improved dynamic control.

3. Simulation analysis and discussion

The simulation model used in this study has investigated both mechanical and electromechanical dynamics, with a focus on piezoelectric components' key parameters as depicted in Table 1. Differential equations representing the system were solved using the fourth-order Runge–Kutta method. The garnered results have offered profound insights into system performance aspects, notably vibration control, energy capture, and power efficiency.

The model revealed four wavelengths (λ) for creating distinct dispersion curves stemming from the presence of four inertias within a unit cell, suggesting the potential for enhanced band gaps in internally coupled metamaterials as opposed to conventional ones. While our research concentrated on a select frequency range to delineate the variances between mechanical and electromechanical internal coupling, the broader implications of all band gaps across the entire frequency spectrum remain an open field for future exploration.

Incorporating real-world scenarios, our research encapsulates applications that harness high-capacitance piezoelectric materials. These include pedestrian energy-harvesting floor tiles in airports, vibration dampers in industrial machinery, structural health monitors for bridges and buildings, energy-recapturing systems in automotive suspensions, and self-charging phone cases. These case studies demonstrate the practical engineering scenarios where our research can be applied, emphasizing the transformative impact of our findings on sustainable engineering design and operation.

3.1. Shunt capacitance influence on system stability and energy-harvesting efficiency

Figure 4 illustrates the relationship from equation (48). For system stability, the equivalent internal coupling stiffness k_s should exceed $k_s = -k_r/2$. The figure illustrates the

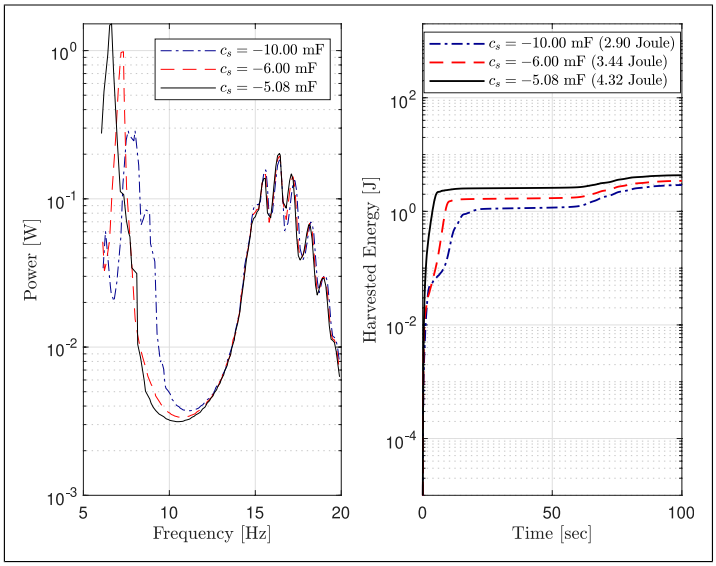

Figure 6. Power and energy harvesting across various shunt capacitances with $\theta = 0.25$ and $c_p = 1.5$ mF.

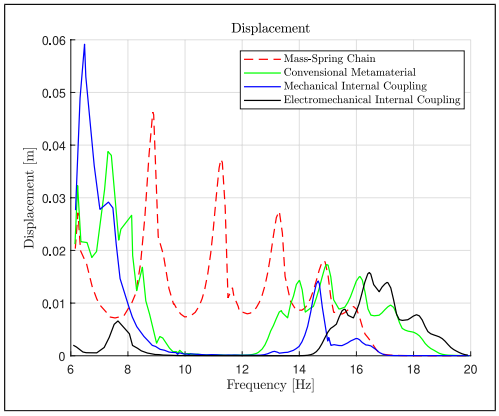

Figure 7. Frequency response analysis: comparative displacement profiles of mechanical, conventional metamaterial, and electromechanical internally coupled systems based on parameters in Table 1.

relationship between k_s and shunt capacitance c_s. The light blue area denotes system stability, while the reddish color signifies instability. Given the parameters, stability is maintained for c_s values from negative infinity to about -0.004 F and from around -0.003 F to positive infinity. However, there's a brief unstable period in between. A zoomed-in view highlights the crucial c_s values where the system behavior changes.

In the study of energy-harvesting systems, understanding the behavior of different parameters is essential for optimization. From the simulations, key insights have emerged. Figure 6 presents the harvested power and energy across a range of shunt capacitances. It clearly underscores the influential role of shunt capacitance on the system's overall efficiency.

A pivotal observation made from the results is the superiority of electrical internal coupling via shunt circuits in terms of tunability. Specifically, electrical coupling seems to allow for easier tuning of the band gap compared to its mechanical counterpart. This is evident in Figures 5 and 6, where the chosen shunt capacitor facilitates a band gap at a notably lower frequency in comparison to a mechanically internally coupled system, as illustrated in Figure 7.

Selecting a shunt capacitance of $c_s = -5.08$ mF results in an equivalent stiffness of $k_s = -30$. This specific choice not only introduces an equivalent negative stiffness into the system, enhancing energy-harvesting capabilities across varied frequency spectrums, but also facilitates the creation of a band gap at a lower frequency (see Figure 5). Compared to mechanical internally coupled resonators, this allows for more flexible and straightforward tuning of the band gap across different frequencies.

3.2. *Electromechanical internally coupled resonators*

Figure 7 illustrates the displacement response across different frequency ranges for four distinct systems: mass–

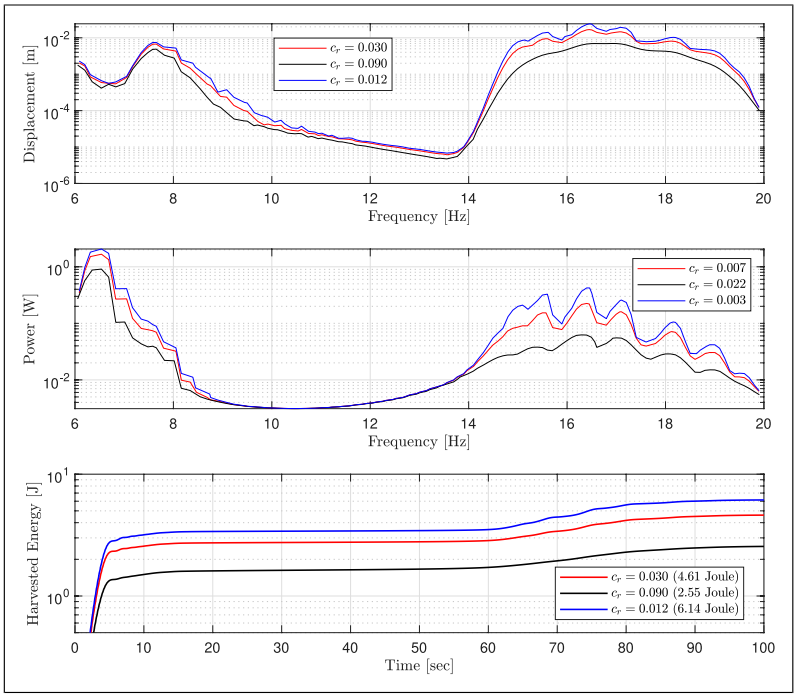

Figure 8. Frequency response showcasing the influence of varying resonator damping coefficients (c_r) on displacement, power generation, and accumulated harvested energy. A higher c_r reveals a smoothed response with broader bandwidth but reduced peak values.

spring chain, conventional metamaterial, mechanical internal coupling, and electromechanical internal coupling. The mechanical internally coupled system has a dominant response at around 7 Hz, peaking at a displacement of approximately 0.06 m, but its effectiveness drops beyond 12 Hz. In contrast, the conventional metamaterial with linear resonators responds at multiple frequencies, especially around 12 Hz and 14 Hz. Both the mechanical and electromechanical internal coupling systems exhibit intricate frequency responses, with the latter demonstrating a wider range of resonances. Displacement magnitudes suggest potential energy-harvesting capabilities, with greater displacements indicating more energy conversion potential. Notably, while the electromechanical system might display a reduced displacement compared to its purely mechanical counterpart, its broader frequency response makes it versatile, though its energy-harvesting efficacy needs further examination as indicated in Figure 9.

From Figures 8 and 9, the damping coefficients of mass chain c_m and resonator c_r alter displacement and power generation profiles across frequencies. A higher damping smoothens the response, lessening peak displacements while broadening the frequency response. This results in decreased peak power but an enhanced ability to harvest energy across a wider frequency range. Observations show that a steeper curve corresponds to more energy harvested over time with a higher c_r. For this case study, the electromechanical parameters, $\theta = 0.25$ N/V, internal resistance $R = 500\ \Omega$, and shunt capacitance $c_s = -5$ mF are selected. As seen in Figure 8, different values of c_r lead to varied displacement, power, and energy profiles. It directly affects the sharpness of the resonance peak and the bandwidth of the system's frequency response. A high c_r broadens the response, suitable for environments with varied frequencies but at the cost of peak performance.

In comparing the displacements from Figures 8 and 9, it's evident that the behaviors of c_m and c_r diverge. Specifically, c_m prominently impacts the system's transient response and settling time. Notably, even with piezoelements on the resonator, increased main chain damping (c_m) leads to reduced energy harvesting. This underlines the intricate dynamics between resonator and mass chain damping in energy-harvesting systems.

Figure 10 shows the displacement response of nonlinear mechanical internal coupling resonators over a frequency sweep. The plot contrasts the displacement during upward and downward frequency sweeps, revealing the nonlinear behavior and hinting at the presence of bifurcation around

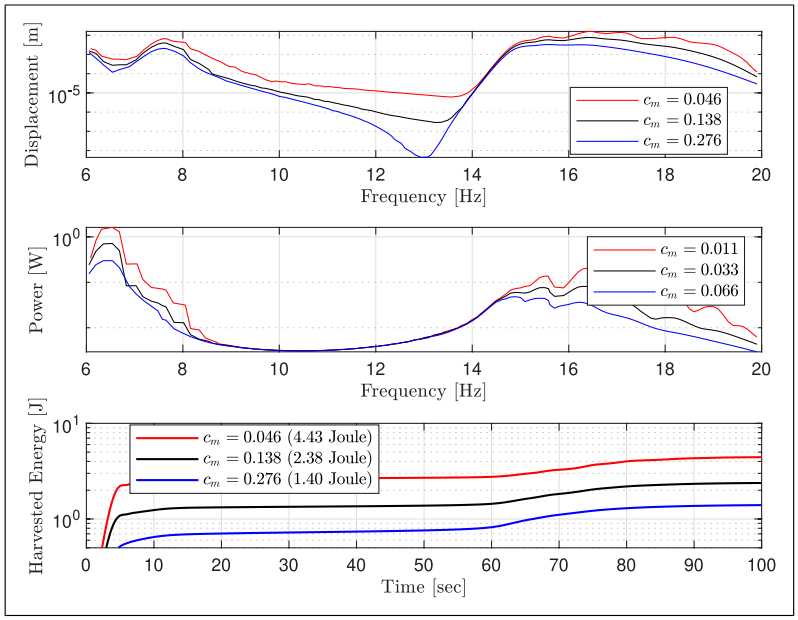

Figure 9. Displacement profiles as influenced by the mass chain damping (c_m). The transient response and settling time of the system are notably affected by c_m. The plot underscores the reduced energy harvesting as c_m increases, despite the presence of piezoelements on the resonator.

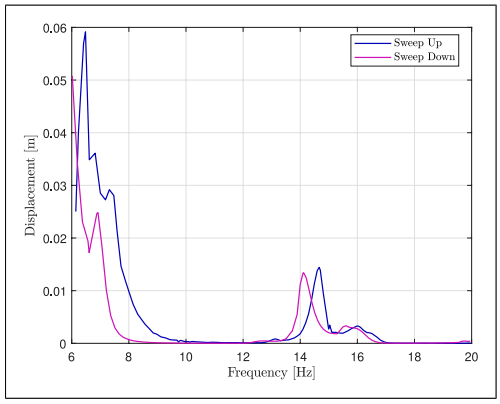

Figure 10. Displacement response of nonlinear mechanical internal coupling resonators over a frequency sweep, with linear coupling coefficient $k_{c_1} = 198$ N/m and nonlinear coupling coefficient $k_{c_2} = 2386$ N/m^3.

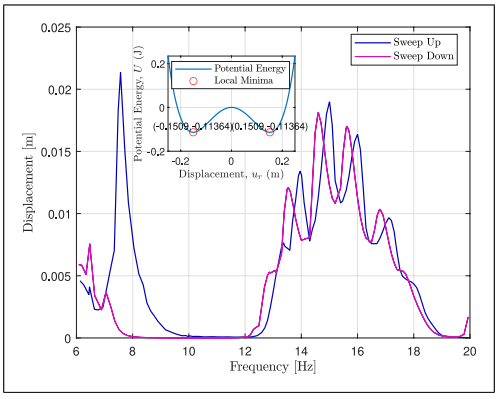

Figure 11. Displacement response of bistable nonlinear mechanical internal coupling resonators: linear coupling coefficient $k_{c_1} = -20N/m$ and nonlinear coupling coefficient $k_{c_2} = 880N/m^3$. Inset: Resonator's potential energy profile for the specified coupling parameters.

15 Hz. This nonlinearity is influenced by the linear coupling coefficient (k_{c_1}) of 198 N/m and the nonlinear coupling coefficient (k_{c_2}) of 2386 N/m^3. The continuous nature of the sweep and the plot's point-connecting methodology give the bifurcation its observed shape.

Figure 11 illustrates bistable-type nonlinear mechanical resonators with internal coupling. The parameters employed include linear coupling coefficient (k_{c_1}) -20 N/m and nonlinear coupling coefficient (k_{c_2}) $0.88e3$ N/m^3. The graph represents the resonator's

potential energy in relation to displacement. It emphasizes the unstable point of origin with negative stiffness. It's worth noting that the system's dynamics are highly sensitive to the value of k_{c_2}. Similar to Figure 10, in the frequency range of 14–16 Hz, bifurcation is observed. The non-coinciding sweep up/down traces indicates the presence of hysteresis, highlighting the system's nonlinear behavior.

The inset plot within the main figure shows a graph of potential energy against displacement. This highlights the energy state of the system for different displacements. The presence of multiple local minima indicates that the system can occupy multiple stable states for specific energy levels. This behavior indicates multi-stability in the system, especially if the resonators encounter large fluctuation range. The peaks, especially those around 8 Hz and 15 Hz, show clear discrepancies between the sweep up/down traces. This difference highlights the system's nonlinear hysteresis behavior. Beyond the 16 Hz mark, multiple peaks and valleys suggest that the system has several resonance frequencies or harmonics. These characteristics can arise due to the interplay of the system parameters and nonlinearities.

Leveraging bistability in phononic media can profoundly alter the wave response within band gaps via supratransmission, a phenomenon documented in bistable periodic chains both with and without resonators (Frazier and Kochmann, 2017), as well as in metastable modular metastructures (Wu and Wang, 2019). Nonetheless, in this context, the parameters of the bistable system are deliberately chosen to operate within a confined frequency range, aiming to exclusively simulate the system akin to negative stiffness found in electromechanical systems utilizing shunt circuits.

To enhance the validity of these findings, supplementary numerical simulations were executed, integrating decreased piezoelectric capacitance values. Specifically, c_p and c_{p+} were adjusted to 800 nF. With other parameters kept constant (k_r, m_r, and c_r), and the electromechanical coupling coefficients θ_r and θ_{r+} set at 0.01 N/V, these simulations were crucial in reinforcing the robustness of the study's findings. Stability analysis revealed that, for system stability, the shunt capacitance c_s must exceed $-3.48\,\mu$F. This criterion was tested with values such as $-1.5\,\mu$F, -200 nF, and -10pF. Conducted within a pragmatic range of piezoelectric capacitance, these simulations not only confirmed the initial results but also underscored the model's practical applicability and relevance. The insights derived from this extended simulation effort are integrated into the study, ensuring that the conclusions drawn are firmly rooted in realistic engineering contexts.

4. Conclusion

In conclusion, this investigation into the dynamics of internally coupled resonators within metamaterial systems has underscored the critical balance between resonator stiffness and shunt capacitance stiffness, k_s. Our stability analysis reveals that excessive negative feedback can lead to system instability, thus necessitating careful parameter tuning.

The simulations have demonstrated the significant advantages of electromechanical shunt capacitance circuits, notably in adjusting negative stiffness and facilitating lower operational frequency band gaps. These insights are invaluable for understanding system efficiency and the effectiveness of electrical internal coupling in energy harvesting. Furthermore, the study of nonlinear characteristics like bifurcation and hysteresis in resonators paves the way for innovative energy-harvesting device designs.

To further validate these findings, additional numerical simulations were conducted with lower piezoelectric capacitance values. This extension of the simulation framework reinforced the robustness of the initial results and confirmed the model's practical applicability and relevance in realistic scenarios.

The applications of high-capacitance (millifarad-level) piezoelectric materials span various sectors. They enable energy-harvesting floor tiles in high-traffic areas like airports, vibration damping in industrial machinery, continuous structural monitoring in buildings and bridges, energy recapture in vehicle suspensions, self-charging solutions for personal electronics, and long-lasting power sources for wearable health monitors. These applications underscore the significant potential and real-world impact of advanced piezoelectric materials in energy harvesting and sustainability.

Guidance for augmenting the capacitance of piezoelectric materials involves selecting materials such as PZT or polymer-based composites with higher dielectric constants, optimizing the geometry of piezoelectric elements, employing multi-layer structures, and connecting multiple capacitors in parallel. These strategies cumulatively increase the overall capacitance available for energy harvesting and other applications.

The key contributions of this research include the analysis of band gaps and energy-harvesting capabilities within linear and nonlinear coupled resonators in lumped systems, a novel stability analysis approach for these systems, and insights into optimizing metamaterials for energy harvesting. A significant discovery is the identification of enhanced band gaps in internally coupled resonators. Our work demonstrates the advantages of electromechanical shunt circuits in fine-tuning band gaps for optimized performance, marking significant steps forward in harnessing the potential of piezoelectric materials for sustainable energy solutions.

5. Future works

This study offers significant insights into the stability and energy harvesting capabilities of internally coupled resonators within lumped parameter systems. Looking ahead, several suggestion for future research emerge: Firstly, there

is a clear necessity for detailed investigation aimed at optimizing coupling parameters, such as capacitance values and nonlinear coefficients, with the aim of maximizing energy harvesting efficiency and bolstering system stability. Furthermore, extending our analysis to encompass networks of internally coupled resonators within distributed parameter systems will be invaluable. Such exploration is critical for deciphering how interactions among multiple resonators affect their collective stability and energy harvesting efficiency. Additionally, the exploration of adaptive control techniques presents an exciting frontier. By dynamically adjusting the coupling parameters in response to fluctuating system conditions, these techniques promise to significantly enhance the adaptability and performance of resonator systems.

Declaration of conflicting interests

The author(s) declared no potential conflicts of interest with respect to the research, authorship, and/or publication of this article.

Funding

The author(s) disclosed receipt of the following financial support for the research, authorship, and/or publication of this article: This work was supported by the European Union's Horizon Europe research and innovation programme under the grant agreement No. 101120657, project ENFIELD (European Lighthouse to Manifest Trustworthy and Green AI), by the Estonian Research Council through the grant PRG658, and by the Estonian Centre of Excellence in Energy Efficiency, ENER (grant TK230) funded by the Estonian Ministry of Education and Research.

ORCID iDs

H Alimohammadi https://orcid.org/0000-0002-8867-8988
K Vassiljeva https://orcid.org/0000-0002-4178-1267
S H HosseinNia https://orcid.org/0000-0002-7475-4628
E Petlenkov https://orcid.org/0000-0003-2167-6280

References

Chatziathanasiou GM, Chrysochoidis NA and Saravanos DA (2022) A semi-active shunted piezoelectric tuned mass damper for robust vibration control. *Journal of Vibration and Control* 28(21-22): 2969–2983.

Chaunsali R, Xu H, Yang J, et al. (2021) Stability of topological edge states under strong nonlinear effects. *Physical Review B* 103(2): 024106.

Fang X, Wen J, Bonello B, et al. (2017) Wave propagation in one-dimensional nonlinear acoustic metamaterials. *New Journal of Physics* 19(5): 053007.

Frazier MJ and Kochmann DM (2017) Band gap transmission in periodic bistable mechanical systems. *Journal of Sound and Vibration* 388: 315–326.

Fronk MD and Leamy MJ (2017) Higher-order dispersion, stability, and waveform invariance in nonlinear monoatomic and diatomic systems. *Journal of Vibration and Acoustics* 139(5): 051003.

Fronk MD and Leamy MJ (2019) Direction-dependent invariant waveforms and stability in two-dimensional, weakly nonlinear lattices. *Journal of Sound and Vibration* 447: 137–154.

Hoogeboom C, Man Y, Boechler N, et al. (2013) Hysteresis loops and multi-stability: from periodic orbits to chaotic dynamics (and back) in diatomic granular crystals. *Europhysics Letters* 101(4): 44003.

Hu G, Tang L, Banerjee A, et al. (2017) Metastructure with piezoelectric element for simultaneous vibration suppression and energy harvesting. *Journal of Vibration and Acoustics* 139(1): 011012.

Hu G, Tang L and Das R (2018) Internally coupled metamaterial beam for simultaneous vibration suppression and low frequency energy harvesting. *Journal of Applied Physics* 123(5).

Lefeuvre E, Badel A, Richard C, et al. (2005) Piezoelectric energy harvesting device optimization by synchronous electric charge extraction. *Journal of Intelligent Material Systems and Structures* 16(10): 865–876.

Li X, Yu Z, Iizuka H, et al. (2023) Observation of an exceptional point with an lr-shunted resonator. *Mechanical Systems and Signal Processing* 196: 110297.

Liu Y, Yang J, Yi X, et al. (2022) Enhanced vibration suppression using diatomic acoustic metamaterial with negative stiffness mechanism. *Engineering Structures* 271: 114939.

Mančić A, Leykam D and Maluckov A (2023) Band relaxation triggered by modulational instability in topological photonic lattices. *Physica Scripta* 98(5): 055513.

Murer M, Guruva SK, Formica G, et al. (2023) A multi-bandgap metamaterial with multi-frequency resonators. *Journal of Composite Materials* 57(4): 783–804.

Newton PK and Keller JB (1987) Stability of periodic plane waves. *SIAM Journal on Applied Mathematics* 47(5): 959–964.

Shu Y and Lien I (2006) Analysis of power output for piezoelectric energy harvesting systems. *Smart Materials and Structures* 15(6): 1499.

Wu Z and Wang KW (2019) On the wave propagation analysis and supratransmission prediction of a metastable modular metastructure for non-reciprocal energy transmission. *Journal of Sound and Vibration* 458: 389–406.

Appendix 4

Hossein Alimohammadi et al. “Harvesting Energy and Stability Insights in Internally Coupled Resonator Systems”. In: *2024 IEEE 18th International Conference on Advanced Motion Control (AMC)*. IEEE. 2024, pp. 1–6

Harvesting Energy and Stability Insights in Internally Coupled Resonator Systems

H. Alimohammadi*, K. Vassiljeva*, S. H. HosseinNia†, and E. Petlenkov*
*Department of Computer Systems
Tallinn University of Technology
Tallinn, Estonia
Email: eduard.petlenkov@taltech.ee
†Department of Precision and Microsystems Engineering
Delft University of Technology
Delft, The Netherlands

2024 IEEE 18th International Conference on Advanced Motion Control (AMC) | 979-8-3503-4281-9/24/$31.00 ©2024 IEEE | DOI: 10.1109/AMC58169.2024.10505680

***Abstract*—This paper presents a comprehensive study on lumped parameter systems with internally coupled resonators, emphasizing stability analysis and energy harvesting potential. Both mechanical and electromechanical coupling mechanisms are explored, revealing the critical role of the resonator's spring constant and feedback shunt capacitance stiffness. Simulation analyses demonstrate the significant advantages of electrical internal coupling, such as enhanced tunability and superior energy harvesting capabilities. By harnessing negative stiffness through electromechanical coupling, the paper highlights possibilities for precise control over system dynamics and the creation of band gaps at lower frequencies. The findings underscore the potential of internally coupled resonators in metamaterial systems, particularly for vibration control and energy harvesting applications.**

***Index Terms*—Lumped Systems, Internally Coupled Resonators, Piezoelectric Energy Harvesting, Vibration Suppression.**

I. Introduction

Internally coupled resonators play a vital role in wave control, stability, and energy collection within lumped parameter systems. The article focuses on the advantages of mechanical linear and nonlinear internal coupling, as well as the electromechanical shunt capacitance circuits. These mechanisms enable the creation of negative stiffness and improved dynamic control of systems. Through simulations, electrical internal coupling is demonstrated to provide better tunability and enhanced energy harvesting capabilities. The impact of parameters such as damping coefficients and the characteristics of the resonators on displacement and energy outputs at different frequencies are analyzed. Additionally, the article delves into the nonlinear attributes of these resonators, which can lead to multiple stable states and unique system behaviors.

II. Background: Internally Coupled Resonators Exhibiting Mechanical Nonlinearity

Internally coupled resonators have recently gained prominence in the realm of dynamics and vibration control, owing to their unique vibrational behaviors resulting from intricate internal structural interactions. These behaviors present novel opportunities in wave propagation management, finding applications in areas like structural health monitoring, acoustic metamaterials, and vibration dampening. While previous studies, such as those by Hu et al. [1], have delved into metastructures with linearly coupled resonators, unveiling an added narrow bandgap compared to traditional metastructures, the work by Y Liu et al. [2] takes a different angle. Liu's research explores a diatomic-chain locally resonant acoustic metamaterial structure, emphasizing the significance of the negative-stiffness mechanism. This mechanism, when leveraged, enhances vibration suppression by introducing additional bandgaps and facilitating Bragg scattering. Consequently, it proves invaluable for mitigating ultralow frequency vibrations in the lower spectrum and fine-tuning the metamaterial's bandgap attributes for specific vibration reduction applications.

III. Background: Electromechanical Nonlinearity in Internally Coupled Resonators

Electromechanical resonators with piezoelectric elements offer unique wave propagation characteristics. However, research on their nonlinear, internally coupled variants remains sparse, highlighting a promising avenue for vibration control and energy harvesting advancements [3]. While metamaterials present wave propagation advantages, they face band gap bandwidth limitations. This study explores a novel design approach, viewing the shunt capacitance circuit as a negative capacitor, as inspired by [4]. The aim is to understand its implications on bandgap behavior and energy harvesting efficiency within the chain mass structure.

IV. Background: Stability Solution

In the realm of mechanical internally coupled resonators and nonlinear periodic media, the stability of nonlinear solutions remains underexplored. While nonlinearity often leads to bifurcations and dynamic solutions with multiple branches, a proper stability analysis is vital to ensure theoretical responses align with physical systems. Specifically, upon amplitude enhancement, there can be transitions between stable solutions, eventually leading to chaotic dynamics at high amplitudes [5]. Regarding the stability of plane waves in nonlinear phononics,

Authorized licensed use limited to: Tallinn University of Technology. Downloaded on September 24,2024 at 09:15:45 UTC from IEEE Xplore. Restrictions apply.

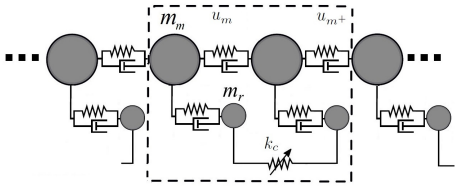

Fig. 1. A mechanically internally coupled resonators. The dashed rectangle signifies a unit cell..

Fronk and Leamy's work [6] highlighted that stability in 1D systems is amplitude-dependent, while in 2D systems, it also depends on direction.

V. Method

The lumped parameters model simplifies complex physical systems by concentrating properties like inertia or elasticity at discrete points, aiding in systems where wave propagation wavelength is much larger than the structure's size. Using the Lagrangian energy method, an equation of motion for metamaterial interfaced with internally coupled resonators is established, blending mechanical and electrical domains for comprehensive wave propagation and stability analysis. As negative stiffness is integrated, a rigorous stability analysis is essential since, while it aids in vibration suppression, it can also introduce stability issues, underlining the importance of ensuring system reliability and safety.

VI. Internally Coupled Resonators with Mechanical Nonlinearity

Fig. 1 presents a schematic representation of a linear mass chain. A unique feature of this chain is the integration of internally coupled resonators that exhibit nonlinear characteristics. The dashed rectangle encompasses a single representative unit cell, providing a clearer view of the chain's arrangement.

The dynamic behavior of these nonlinear resonators, specifically the relationship between their motions and applied forces, can be captured by utilizing the Lagrangian formulation, and defining $z_r(t)$ as relative displacement between chain mass and resonator:

$$\begin{aligned} &m_m\ddot{z}_r(t) + c_m\left(2\dot{z}_r(t) - \dot{z}_{r^-}(t) - \dot{z}_{r^+}(t)\right) \\ &\quad + k_m\left(2z_r(t) - z_{r^-}(t) - z_{r^+}(t)\right) \\ &\quad + k_r z_r(t) = f_{e_r} \end{aligned} \tag{1}$$

$$\begin{aligned} &m_m\ddot{z}_{r^+}(t) + c_m\left(2\dot{z}_{r^+}(t) - \dot{z}_r(t) - \dot{z}_{r^{++}}(t)\right) \\ &\quad + k_m\left(2z_{r^+}(t) - z_r(t) - z_{r^{++}}(t)\right) \\ &\quad + k_r z_{r^+}(t) = f_{e_{r^+}} \end{aligned} \tag{2}$$

$$\begin{aligned} &m_r\ddot{z}_r(t) + c_r\dot{z}_r(t) + k_r z_r(t) + k_{c_1}\left(z_r(t) - z_{r^+}(t)\right) \\ &\quad + k_{c_2}\left(z_r(t) - z_{r^+}(t)\right)^3 = f_{e_m} \end{aligned} \tag{3}$$

$$\begin{aligned} &m_r\ddot{z}_{r^+}(t) + c_r\dot{z}_{r^+}(t) + k_r z_{r^+}(t) - k_{c_1}\left(z_r(t) - z_{r^+}(t)\right) \\ &\quad - k_{c_2}\left(z_r(t) - z_{r^+}(t)\right)^3 = f_{e_{m^+}} \end{aligned} \tag{4}$$

Here, m_m represents the mass of the main chain, and the coefficient k_m is the main chain's stiffness, interacting with the relative displacements between the resonator and its neighbors, while k_r characterizes the resonator's inherent stiffness. The f_{e_r} is the external excitation force on the primary mass chain. The resonator, with mass m_r, has a damping coefficient c_r and stiffness k_r. k_{c_1} is the linear coupling stiffness, while k_{c_2} is nonlinear. The forces f_{e_r} and $f_{e_{r^+}}$ indicate excitation on the primary mass chain, influenced by the resonator and internal connections. f_{e_m} and $f_{e_{m^+}}$ are forcing on the resonators, sourced from the main chain mass and internal stiffness interactions.

A. Stability Analysis for Mechanical Internally Coupled Metamaterial

The Jacobian matrix is used to assess the stability of equilibrium points in nonlinear systems. By linearizing these systems around their equilibrium, we can analyze the stability of the subsequent linear system, revealing the nonlinear system's local behavior. In Eqs. (3) and (4), when external force is absent, the equilibrium points of the system are identified. By setting the velocities $\dot{z}_r$ and $\dot{z}_{r^+}$, as well as the accelerations $\ddot{z}_r$ and $\ddot{z}_{r^+}$, to zero, the conditions for these equilibrium positions are established. These points fulfill the following criteria:

$$\begin{aligned} k_r z_{r_0} + k_{c_1}\left(z_{r_0} - z_{r_0^+}\right) + k_{c_2}\left(z_{r_0} - z_{r_0^+}\right)^3 = 0 \\ k_r z_{r_0^+} - k_{c_1}\left(z_{r_0} - z_{r_0^+}\right) - k_{c_2}\left(z_{r_0} - z_{r_0^+}\right)^3 = 0 \end{aligned} \tag{5}$$

Introducing small perturbations around these equilibrium points results in the following expressions:

$$\begin{aligned} \delta z_r &= z_r - z_{r_0} \\ \delta z_{r^+} &= z_{r^+} - z_{r_0^+} \end{aligned} \tag{6}$$

Linearizing the equations of motion about the equilibrium, higher-order terms in δz_r and δz_{r^+} are disregarded, resulting in:

$$\begin{aligned} &m_r\delta\ddot{z}_r + c_r\delta\dot{z}_r + k_r\delta z_r + k_{c_1}\left(\delta z_r - \delta z_{r^+}\right) \\ &\quad + 3k_{c_2}\left(z_{r_0} - z_{r_0^+}\right)^2\left(\delta z_r - \delta z_{r^+}\right) = 0 \end{aligned} \tag{7}$$

$$\begin{aligned} &m_r\delta\ddot{z}_{r^+} + c_r\delta\dot{z}_{r^+} + k_r\delta z_{r^+} - k_{c_1}\left(\delta z_r - \delta z_{r^+}\right) \\ &\quad - 3k_{c_2}\left(z_{r_0} - z_{r_0^+}\right)^2\left(\delta z_r - \delta z_{r^+}\right) = 0 \end{aligned} \tag{8}$$

To transform the second-order system into a first-order system, a state vector is defined as:

$$X = \begin{bmatrix} \delta z_r \\ \delta z_{r^+} \\ \delta\dot{z}_r \\ \delta\dot{z}_{r^+} \end{bmatrix} \tag{9}$$

Authorized licensed use limited to: Tallinn University of Technology. Downloaded on September 24,2024 at 09:15:45 UTC from IEEE Xplore. Restrictions apply.

with its derivative:

$$\dot{X} = \begin{bmatrix} \delta\dot{z}_r \\ \delta\dot{z}_{r^+} \\ \delta\ddot{z}_r \\ \delta\ddot{z}_{r^+} \end{bmatrix} \tag{10}$$

To determine the stability of the system around its equilibrium, $\dot{X}$ is represented as AX. By linearizing the equations, matrix A is obtained from system parameters. The system's equilibrium stability is indicated by the eigenvalues of A. For nonlinear internally coupled resonators, the eigenvalue is:

$$\lambda_{1,3} = -\frac{c_r \pm \sqrt{c_r^2 - 4k_r m_r}}{2m_r} \tag{11}$$

$$\lambda_{2,4} = -\frac{c_r \pm \sqrt{c_r^2 - 4m_r k_r - 8m_r \left(k_{c_1} + 3k_{c_2}(\delta z_r - \delta z_{r^+})^2\right)}}{2m_r} \tag{12}$$

Removing the nonlinear term k_{c_2} turns the system into a linear internally coupled resonator, streamlining the stability analysis. The system can then be studied linearly around its equilibrium. With this simplification, the resulting equation of motion is:

$$\lambda_{1,3} = -\frac{c_r \pm \sqrt{c_r^2 - 4k_r m_r}}{2m_r} \tag{13}$$

$$\lambda_{2,4} = -\frac{c_r \pm \sqrt{c_r^2 - 4m_r(k_r + 2k_c)}}{2m_r} \tag{14}$$

Stability scenarios for internally coupled systems:

1) Nonlinear Systems: :

Case 1: For $c_r^2 - 4k_r m_r < 0$, $\lambda_{1,3}$ imply a stable focus.

Case 2: With $c_r^2 - 4k_r m_r > 0$ and all positive parameters, λ_1 and λ_3 ensure stability.

Case 3: Sign of $\lambda_{2,4}$ depends on term magnitudes and c_r.

Case 4: $c_r^2 - 4k_r m_r - 8m_r \left(k_{c_1} + 3k_{c_2}\left(\delta z_r - \delta z_{r^+}\right)^2\right) < 0$ denotes stability.

2) Linear Systems: :

Case 1: For $c_r^2 - 4k_r m_r < 0$, $\lambda_{1,3}$ indicate a stable focus.

Case 2: With $c_r^2 - 4k_r m_r > 0$, signs of λ_1 and λ_3 are determined by c_r.

Case 3: In $c_r^2 - 4k_r m_r - 8k_c m_r > 0$, stability relies on signs of λ_2 and λ_4.

Case 4: Condition $c_r^2 - 4k_r m_r - 8k_c m_r < 0$ signals stability.

VII. Electromchanical Internally Coupled Resonators

A. Internal Coupling Via Shunt Capacitance Circuit Technique

The previous section discussed metamaterials with internal resonator coupling. Given the challenges with internal springs, especially for negative stiffness, we turn to an electrical shunt circuit. Specifically, a prototype capacitance mirrors the behavior of mechanically coupled resonators.

This section models a two-degree-of-freedom electrical system using shunt capacitance, as shown in Fig. 2, where

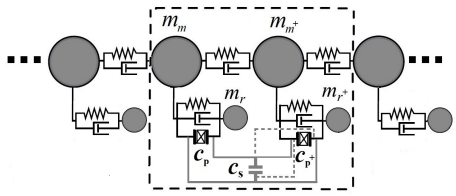

Fig. 2. Internally Coupled System with Electrical Shunt Circuit. Forward (Dashed Line) and Reverse (Solid Line) Capacitance Shunting Configurations.

capacitance plays a central role, replacing the resistance (R) as the primary load.

Fig. 2 illustrates the forward and reverse shunt circuit setups. The forward pairs the top and bottom surfaces of piezoelectric transducers, while the reverse connects them inversely. Both designs include a parallel capacitor. The two configurations discussed share similar analytical methods and results, differentiated mainly by a change in coupling stiffness sign. This study centers on the reverse setup, which inherently acts like a traditional spring without external capacitance, making its mechanics more intuitive. Capacitance links charge shifts to voltage changes: positive capacitance reduces voltage during discharge, while negative increases it. The overall system voltage mirrors resonator force interactions, with current and charge changes indicating velocity and displacement differences. Essentially, the capacitor serves as a mechanical spring with its behavior defined by the capacitance sign. In the reversed setup, voltages on piezoelectric transducers have equal magnitudes but opposing directions.

Utilizing an internal shunt capacitance, tuned as a negative capacitor, enhances resonator performance and intensifies their interconnection. Given similar properties across resonators, the resulting motion equations are:

$$m_r\ddot{z}_r(t) + c_r\dot{z}_r(t) + k_r z_r(t) + \theta_r v_p(t) = m_r\ddot{u}_m(t) \tag{15}$$

$$m_r\ddot{z}_{r^+}(t) + c_r\dot{z}_{r^+}(t) + k_r z_{r^+}(t) + \theta_{r^+} v_{p^+}(t) = m_r\ddot{u}_{m^+}(t) \tag{16}$$

Here, the term k_s, given by

$$k_s = \frac{\theta_r^2}{c_p + c_{p^+} + c_s} \tag{17}$$

which represents the effective spring constant, which arises due to the electrical coupling between the resonators.

B. Electromechanical Resonators' Stability equivalent negative stiffness

Stability hinges on k_s, denoting the electromechanical link through the shunt circuit. A system is stable if its Jacobian matrix's eigenvalues, derived from its linearized motion equations, all have negative real parts. A negative k_s implies the potential of negative capacitance, which might be achieved

Authorized licensed use limited to: Tallinn University of Technology. Downloaded on September 24,2024 at 09:15:45 UTC from IEEE Xplore. Restrictions apply.

with active circuits. Adjusting these parameters necessitates rigorous stability checks, especially when integrating negative capacitance. Eigenvalues, considering identical electromechanical coupling and piezoelectric capacitance, are:

$$\lambda = \frac{-c_r \pm \sqrt{c_r^2 - 4k_r m_r}}{2m_r} \tag{18}$$

$$\lambda = \frac{-c_r \pm \sqrt{c_r^2 - 4m_r(k_r + 2k_s)}}{2m_r} \tag{19}$$

By applying stability criteria, similar to previous mechanical stability analyses, the criterion for c_s to achieve a negative k_s is derived as:

$$c_s > \frac{8m_r\theta_r^2}{c_r^2 - 4k_r m_r} - 2c_p \tag{20}$$

The performance of the system, whether oscillatory or steady, is heavily influenced by the shunt k_s. Electromechanical shunt capacitance resonators provide flexibility, enabling unique behaviors and enhanced control over system dynamics.

VIII. Simulation Analysis and Discussion

A simulation model was employed to investigate the dynamics of piezoelectric components, as detailed in Table I. Differential equations, processed using the fourth-order Runge-Kutta method, outlined the system's behavior. Key performance aspects, such as vibration control, energy capture, and power efficiency, emerged. Notably, four inertias in a unit cell generated distinct dispersion curves with enhanced band gaps in internally coupled metamaterials. The research emphasized distinctions between mechanical and electromechanical internal coupling within a specified frequency domain, omitting an all-encompassing exploration of all band gaps induced by the complexities of internal coupling.

TABLE I
Defined Parameters for the Piezoelectric Model

Parameter	Value
Mass of main chain (m_m)	0.056 kg
Mass of resonator (m_r)	0.0336 kg
Spring constant of main chain (k_m)	150 N/m
Spring constant of resonator (k_r)	129.6 N/m
Damping coefficient of main chain (c_m)	0.0464 Ns/m
Damping coefficient of resonator (c_r)	0.0334 Ns/m
Piezoelectric capacitance (c_p)	1.5 mF(C/m)
Electromechanical coupling coefficient (θ_r)	0.25 N/V
Linear coupling coefficient (k_{c_1})	$198(-20)$ N/m
Nonlinear coupling coefficient (k_{c_2})	$2386(0.88e3)$ N/m^3
Shunt capacitance (c_s)	-7.9 mF(C/m)
Internal resistance (R)	500 Ω

IX. Shunt Capacitance in Band Gap Tuning and System Performance

Fig. 3 demonstrates the correlation from (20), with damping terms omitted to emphasize stability margins. To achieve system stability, k_s must surpass $k_s = -k_r/2$. The diagram shows the link between k_s and shunt capacitance c_s. The light blue region indicates stability, whereas the reddish zone

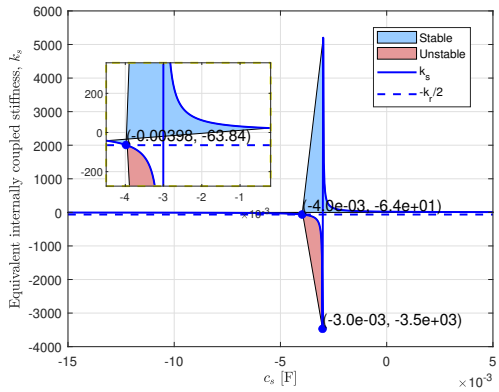

Fig. 3. Stability Map for the Electromechanical Lumped System: Interplay between Equivalent Stiffness k_s and Shunt Capacitance c_s. Parameters: $n = 4$, $m_m = 56$ g, $m_r = 33.6$ g, $k_m = 150$ N/m, $k_r = 129.6$ N/m, $\theta = 0.25$ N/V, $R = 500\ \Omega$, $c_p = 1.5 \times 10^{-3}$ F.

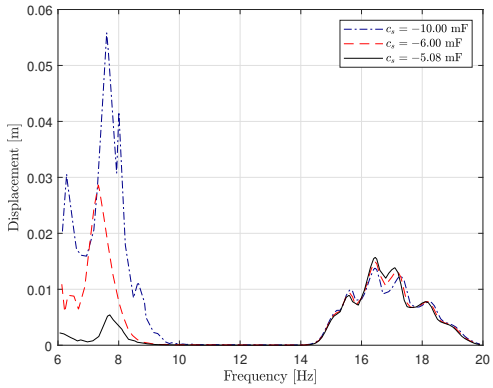

Fig. 4. Transmittance Comparison of Electrical Internally Coupling with Shunt Circuit for $\theta = 0.25$ and $c_p = 1.5$mF, Demonstrating the Impact of an Equivalent Negative Stiffness of $k_s = -30$.

indicates instability. With the provided parameters, stability persists except between approximately -0.004 Farad and -0.003 Farad. A closer view reveals pivotal c_s values where system dynamics shift.

Simulations reveal the pivotal role of shunt capacitance in system efficiency, as depicted in Fig. 5. A notable finding is the enhanced tunability of electrical internal coupling through shunt circuits. This electrical coupling allows for a simpler band gap adjustment than its mechanical counterpart, evident in Figs. 4 and 5. A chosen shunt capacitance of $c_s = -5.08$mF, leading to a stiffness of k_s = -30, provides the system with an equivalent negative stiffness. This boosts energy harvesting across frequencies and facilitates a lower-frequency band gap, seen in Fig.4. Thus, electrical coupling

Authorized licensed use limited to: Tallinn University of Technology. Downloaded on September 24,2024 at 09:15:45 UTC from IEEE Xplore. Restrictions apply.

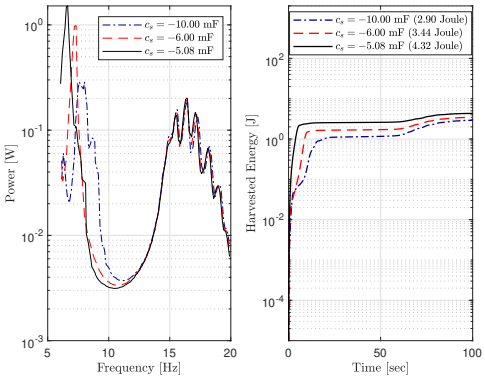

Fig. 5. Power and Energy Harvesting Across Various Shunt Capacitances with $\theta = 0.25$ and $c_p = 1.5$mF.

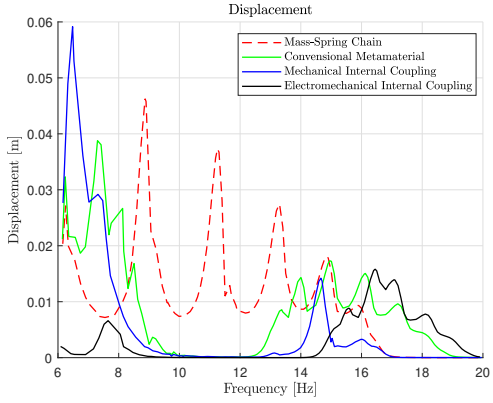

Fig. 6. Frequency Response Analysis: Comparative Displacement Profiles of Mechanical, Conventional Metamaterial, and Electromechanical Internally Coupled Systems based on parameters in Table I.

offers a more adaptable frequency tuning than mechanical counterparts.

Fig. 5 shows power and energy harvesting metrics across various shunt capacitances. In the study of a standard piezoelectric circuit for energy harvesting, a conventional rectifier circuit is analyzed. This assumes an ideal rectifying bridge and models the piezo voltage in proportion to the relative displacement using sine functions. Through integral calculus, relationships among electric charge, current, and displacement are established. The primary outcome is an expression for the average harvested power P as:

$$P = \frac{v_c^2}{R} = \frac{R\theta_r^2\omega^2}{\left(Rc_p\omega + \frac{\pi}{2}\right)^2} z^2 \tag{21}$$

This formula represents the integrated performance of the piezoelectric energy harvesting system, considering mechanical, electrical, and material factors. The left plot illustrates the harvested power for different shunt capacitance values. It can be observed that the power harvested has distinct peaks and troughs, and its behavior varies with the shunt capacitance values. Specifically, there is a notable peak in power harvested around the 7 Hz frequency range, signifying a resonance phenomenon. The right plot delves into the total harvested energy over time for the same capacitance values. It appears that the energy increases steadily with time, with variations in its growth rate based on the capacitance value. Different shunt capacitance values demonstrate varied energy accumulation over time, with certain values, like c_s= -5.08 mF, showing a swift rise, thereby achieving higher harvested energy.

Fig. 6 depicts displacement responses for four systems: Mass-Spring Chain, Conventional Metamaterial, Mechanical Internal Coupling, and Electromechanical Internal Coupling. The Mechanical Internal Coupling peaks at 7 Hz with a 0.06 m displacement but fades past 12 Hz. The Conventional Metamaterial shows multiple peaks, particularly at 12 Hz and

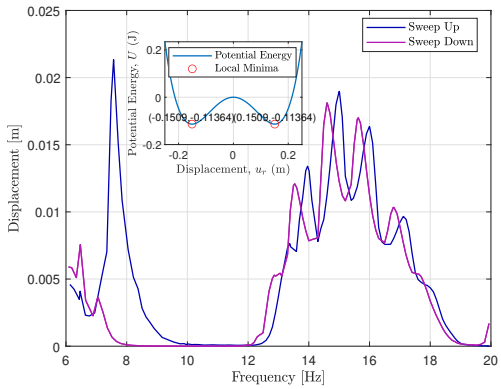

Fig. 7. Displacement response of bistable nonlinear mechanical internal coupling resonators. Linear coupling coefficient $k_{c_1} = -20N/m$, and nonlinear coupling coefficient $k_{c_2} = 880N/m^3$. Inset: Resonator's potential energy profile for the specified coupling parameters.

14 Hz. Both Mechanical and Electromechanical systems have complex frequency responses, but the Electromechanical has broader resonances. Given the linear coupling coefficient k_{c_1} is 198 $\mathrm{N/m}$ and the nonlinear coefficient k_{c_2} is 2386 $\mathrm{N/m\hat{}3}$, higher displacements suggest more energy conversion potential. The Electromechanical system, despite lower peaks, offers versatility with its wide frequency response. Its energy conversion efficiency requires more analysis.

Fig. 7 illustrates bistable-type nonlinear mechanical resonators with internal coupling. The parameters employed include linear coupling coefficient (k_{c_1}) -20 $\mathrm{N/m}$, and nonlinear coupling coefficient (k_{c_2}) 880 $\mathrm{N/m^3}$. The graph represents the resonator's potential energy in relation to displacement. It emphasizes the unstable point of origin with negative stiffness.

Authorized licensed use limited to: Tallinn University of Technology. Downloaded on September 24,2024 at 09:15:45 UTC from IEEE Xplore. Restrictions apply.

It's worth noting that the system's dynamics are highly sensitive to the value of k_{c_2}. In the frequency range of 14-16 Hz, bifurcation is observed. The non-coinciding sweep up/down traces indicates the presence of hysteresis, highlighting the system's nonlinear behavior.

The inset plot within the main figure shows a graph of potential energy against displacement. This highlights the energy state of the system for different displacements. The presence of multiple local minima indicates that the system can occupy multiple stable states for specific energy levels. This behavior indicates multi-stability in the system, especially if the resonators encounter with large fluctuation range. The peaks, especially those around 8 Hz and 15 Hz, show clear discrepancies between the sweep up/down traces. This difference highlights the system's nonlinear hysteresis behavior. Beyond the 16 Hz mark, multiple peaks and valleys suggest that the system has several resonance frequencies or harmonics. These characteristics can arise due to the interplay of the system parameters and nonlinearities.

Leveraging bistability in phononic media can profoundly alter the wave response within band gaps via supratransmission, a phenomenon documented in bistable periodic chains both with and without resonators [7], as well as in metastable modular metastructures [8]. Nonetheless, in this context, the parameters of the bistable system are deliberately chosen to operate within a confined frequency range, aiming to exclusively simulate the system akin to negative stiffness found in electromechanical systems utilizing shunt circuits.

X. Conclusion

This study examined internally coupled resonators in metamaterial systems, focusing on mechanical and electromechanical coupling. The interdependence between the resonator's spring constant and feedback shunt capacitance stiffness (k_s) was emphasized, with stability being a critical concern. Electromechanical shunt capacitance circuits offer adaptability, especially in controlling system dynamics and generating band gaps at lower frequencies. Simulations revealed the system's performance nuances, including the influence of shunt capacitance and the advantages of electrical coupling articulating negative stiffness. Overall, the research underscores the potential of these resonators in applications like vibration control and energy harvesting, emphasizing the promising opportunities from leveraging negative stiffness and tunability.

Acknowledgment

This work has been partially conducted in the project "ICT programme" which was supported by the European Union through the European Social Fund. It was also supported by the Estonian Research Council grant PRG658.

References

[1] G. Hu, L. Tang, and R. Das, "Internally coupled metamaterial beam for simultaneous vibration suppression and low frequency energy harvesting," *Journal of Applied Physics*, vol. 123, no. 5, 2018.

[2] Y. Liu, J. Yang, X. Yi, W. Guo, Q. Feng, and D. Chronopoulos, "Enhanced vibration suppression using diatomic acoustic metamaterial with negative stiffness mechanism," *Engineering Structures*, vol. 271, p. 114939, 2022.

[3] Y. Shu and I. Lien, "Analysis of power output for piezoelectric energy harvesting systems," *Smart materials and structures*, vol. 15, no. 6, p. 1499, 2006.

[4] G. Hu, L. Tang, A. Banerjee, and R. Das, "Metastructure with piezoelectric element for simultaneous vibration suppression and energy harvesting," *Journal of Vibration and Acoustics*, vol. 139, no. 1, p. 011012, 2017.

[5] C. Hoogeboom, Y. Man, N. Boechler, G. Theocharis, P. Kevrekidis, I. Kevrekidis, and C. Daraio, "Hysteresis loops and multi-stability: From periodic orbits to chaotic dynamics (and back) in diatomic granular crystals," *Europhysics Letters*, vol. 101, no. 4, p. 44003, 2013.

[6] M. D. Fronk and M. J. Leamy, "Higher-order dispersion, stability, and waveform invariance in nonlinear monoatomic and diatomic systems," *Journal of Vibration and Acoustics*, vol. 139, no. 5, p. 051003, 2017.

[7] M. J. Frazier and D. M. Kochmann, "Band gap transmission in periodic bistable mechanical systems," *Journal of Sound and Vibration*, vol. 388, pp. 315–326, 2017.

[8] Z. Wu and K.-W. Wang, "On the wave propagation analysis and supratransmission prediction of a metastable modular metastructure for non-reciprocal energy transmission," *Journal of Sound and Vibration*, vol. 458, pp. 389–406, 2019.

Authorized licensed use limited to: Tallinn University of Technology. Downloaded on September 24,2024 at 09:15:45 UTC from IEEE Xplore. Restrictions apply.

Appendix 5

Hossein Alimohammadi et al. “Enhancing Bandgap Depth in Locally Resonant Metastructures via Notch-filtered Piezoelectric Actuation”. In: *2024 25th IEEE International Conference on Industrial Technology (ICIT)*. vol. 1. IEEE. 2024

Enhancing Bandgap Depth in Locally Resonant Metastructures via Notch-filtered Piezoelectric Actuation

H. Alimohammadi*, K. Vassiljeva*, S. H. HosseinNia†, and E. Petlenkov*
*Department of Computer Systems
Tallinn University of Technology
Tallinn, Estonia
Email: eduard.petlenkov@taltech.ee
†Department of Precision and Microsystems Engineering
Delft University of Technology
Delft, The Netherlands

2024 IEEE International Conference on Industrial Technology (ICIT) | 979-8-3503-4026-6/24/$31.00 ©2024 IEEE | DOI: 10.1109/ICIT58233.2024.10540976

***Abstract*—This paper proposes an effective approach to enhance bandgap depth in metastructures with high damping ratios, utilizing piezoelectric actuators coupled with notch filters for improved vibration isolation. The active control strategy focuses on dynamically attenuating specific resonant frequencies through the application of notch filters within the actuator control loops. AI algorithm, in particular Reinforcement Learning, is employed to optimize the notch filter parameters, thereby fine-tuning the system's response. Numerical validation reveals that this approach not only maintains system stability but also significantly deepens the bandgap. The results highlight that utilizing notched piezo-actuation achieves a more pronounced bandgap depth in overdamped systems compared to traditional piezo-actuated resonators, marking a substantial advancement in vibration control technologies.**

***Index Terms*—Metastructures, Notch Filters, Piezoelectric Actuators, Bandgap Enhancement.**

I. Introduction

In the realm of engineering, the quest for efficient vibration control in mechanical structures and metastructures is a perennial challenge that has significant implications for the longevity, safety, and performance of various systems. The ability to manipulate and manage vibrational energy via bandgaps—frequency ranges where wave propagation is inhibited—has emerged as a potent strategy in the design of such structures. However, the presence of high damping ratios within these systems has historically presented a considerable obstacle, as it tends to diminish the effectiveness of the bandgap and thus, the overall vibration isolation capabilities.

The complexity of integrating active vibration control mechanisms that can adapt and respond to varying operational conditions further accentuates the need for innovative solutions. It is within this context that the current research endeavors to bridge the gap, proposing a novel approach that leverages the sophistication of active control strategies to enhance the bandgap depth even in highly damped metastructures.

This paper is structured as follows: Section two provides a literature review and background, setting the stage for the current study by discussing previous work in the field. Section three succinctly describes the methodology used, employing advanced artificial intelligence algorithms to optimize the parameters of notch filters in piezo-actuated systems for improved vibration isolation. Section four presents the results and discussion, delving into the efficacy of the proposed approach through a comparative analysis with traditional methods. Finally, section five offers a conclusion that encapsulates the contributions and insights gleaned from this research and proposes avenues for future work that could expand on the findings presented herein.

II. Literature Review and Background

The literature on vibration isolation in metastructures has extensively covered passive and active control strategies. Passive methods, such as the incorporation of resonators, have been widely researched for their natural bandgap properties. Soukoulis et al. [1] outlined the basic principles of bandgap creation through periodic structuring, while the work of Johnson and Rifaie et al. [2] expanded on the impact of intrinsic material damping on these bandgaps

Active control strategies, including the use of piezoelectric actuators, were explored by Wang and Inman [3] as a means to adaptively tune vibration characteristics. However, these methods often fall short in systems with high damping ratios, as noted by Van Spengen [4], where the active components can introduce additional complexity without significantly improving isolation.

The application of notch filters within the control loop of piezoelectric actuators has been less documented, with pioneering work by Song et al. [5] suggesting potential improvements in bandgap depth. The use of AI algorithms for system optimization is a relatively new approach in this field, with Huang et al. [6] demonstrating the feasibility of machine learning methods for parameter tuning in complex systems.

This study builds on the foundation laid by previous research while addressing the noted gap. By employing an active

Authorized licensed use limited to: Tallinn University of Technology. Downloaded on September 24,2024 at 09:16:49 UTC from IEEE Xplore. Restrictions apply.

control strategy using notch filters, the research provides a novel solution to the challenges posed by high damping ratios in metastructures, a solution that is both robust and adaptable.

The existing research gap is identified in the inadequate performance of current vibration isolation approaches in highly damped metastructures, where traditional methods fall short in fully utilizing the bandgap effect. This study primarily aims to explore whether implementing an active control approach with notch filters can enhance the manipulation of bandgap properties in overdamped systems more efficiently than typical passive or active methods. The research centers on assessing how well these custom-designed notch filters can replicate the vibration isolation capabilities of undamped systems, thereby addressing the difficulties posed by high damping levels.

III. Enhancing Metastructure Bandgap Depth with Notch Filters

In the Method section of your academic article, the dynamics of a metastructure with integrated piezoelectric actuators and resonators are explored through a mathematical model. The model is represented by a set of differential equations that describe the motion of the beam and resonators, their interactions, and the role of the piezoelectric actuators in controlling vibration.

The primary beam's motion is captured by (1), which includes the effects of the flexural rigidity and mass distribution, along with the interactions with attached resonators. The resonators' dynamics are detailed in (2), which accounts for their mass, damping, stiffness, and the influence of the piezoelectric actuators. (3) represents the electrical dynamics of the piezoelectric actuator, linking its voltage to the resonator's motion. The governing equations are as follows [7]:

$$EI\frac{\partial^4 w(x,t)}{\partial x^4} + C\frac{\partial w(x,t)}{\partial t} + \rho A\frac{\partial^2 w(x,t)}{\partial t^2} - \sum_{r=1}^{N_r}\left(k_r z_r(t) + c_r\frac{\partial z_r(t)}{\partial t}\right)\delta\left(x - x_r\right) = \mathcal{F}_{b_m}(x,t) \tag{1}$$

$$m_r\frac{\partial^2 z_r(t)}{\partial t^2} + c_r\frac{\partial z_r(t)}{\partial t} + k_r z_r(t) + m_r\frac{\partial^2 w\left(x_r,t\right)}{\partial t^2} - \vartheta_{p,r} v_{p,r}(t) = \mathcal{F}_{b_r}(t) \tag{2}$$

$$C^*_{p,r}\frac{\partial v_{p,r}(t)}{\partial t} + \vartheta_{p,r} z_r(t) = 0 \tag{3}$$

Parameters EI, ρA, and C represent the beam's flexural rigidity, mass per unit length, and damping coefficient, respectively. Terms $\vartheta_{p,r}, C^*_{p,r}$, and $\mathcal{F}_{b_m}(x,t)$ denote the piezoelectric properties: electromechanical coupling, capacitance, and external force on the main beam. Functions $w(x,t)$ and $z_r(t)$ describe the primary structure's transverse vibrations and the resonators' movements. The Kronecker delta function $\delta(x - x_r)$ positions the resonators on the beam. N_r is the number of resonators, m_r their mass, k_r their stiffness, and c_r their damping coefficient.

Orthogonality conditions are employed to simplify the complex dynamics into a more manageable form, leading to a modal decomposition of the beam's deflection in (4). By substituting this modal expansion into the governing equations and applying orthogonality conditions, a reduced set of equations is obtained, capturing the interactions between the structure's modes and the resonators.

$$w(x,t) = \sum_{m=1}^{N_m}\phi_m(x) z_m(t), \tag{4}$$

Where $\phi_m(x)$ represents the spatial configuration of the m-th mode shape, and $z_m(t)$ corresponds to its time-dependent amplitude. This approach simplifies the intricate dynamics of a flexible structure with embedded resonators into a set of more comprehensible modal elements.

The application of Laplace transforms to these equations, assuming no initial conditions, provides a linear set of equations in the Laplace domain, which are used to derive the transfer function for the resonator's displacement, as shown in (5). This equation demonstrates the effect of applying voltage to the piezoelectric actuator on the dynamics of the resonator.

The influence of the resonators' mass distribution on the structure is taken into account, leading to the approximation of the mass distribution across the structure in terms of a mass ratio. This mass ratio ensures that the resonator masses are synchronized with the structural dynamics.

The transfer function for the displacement of the resonator is derived from the aforementioned definitions and mathematical rearrangement, as follows:

$$Z_r(s) = \frac{-s^2 w_b - s^2\sum_{m=1}^{N_m} Z_m(s)\phi_m\left(x_r\right)}{s^2 + 2\zeta_r\omega_r s + \omega_r^2 + \frac{v_a\omega_r^2}{s}}, \quad r = 1, 2, \ldots, N_r \tag{5}$$

Here, the active voltage applied to the piezo, v_a, equals κ_e^* and assumed that κ_e^* is defined as $\kappa_e^* = \frac{\vartheta_{p,r}^2}{C^*_{p,r}k_r}$. When considering the voltage source as an input in piezoelectric as an actuator, we assume that the effective coupling stiffness, κ_e^*, can be represented by the $\kappa_e^* = \alpha\omega_r v_0 = v_a$. In this equation, ω_r denotes the resonator's natural frequency, v_0 is the voltage applied to the piezoelectric element, and α is an empirical coefficient with units of Farads per Coulomb (F/C). Equation (5) represents the Laplace transform of the displacement of the r-th resonator, $Z_r(s)$, in a dynamic system. It incorporates Z_m, the modal displacement for each of the N_m number of modes of the system, and w_b, the base excitation displacement. The term $\phi(x_r)$ indicates the mode shape at the location of the r-th resonator.

Further mathematical manipulation brings to light the interaction between structural modes and resonators in the Laplace domain, as demonstrated in equation (6). This equation incorporates $Z_m(s)$, representing the Laplace-transformed displacement of the m-th structural mode, and $\mathcal{Q}_{b_m}(s)$ for the transformed external disturbances affecting the system. Here, ζ_m and ζ_r denote the modal and resonator damping ratios,

Authorized licensed use limited to: Tallinn University of Technology. Downloaded on September 24,2024 at 09:16:49 UTC from IEEE Xplore. Restrictions apply.

$$\left(s^2+2\zeta_m\omega_m s+\omega_m^2\right)Z_m(s)+\frac{s^2\left(\omega_r^2+2\zeta_r\omega_r s\right)\sum_{r=1}^{N_r} m_r\phi_m(x_r)\sum_{p=1}^{N_m}\phi_p(x_r)Z_p(s)}{s^2+2\zeta_r\omega_r s+\omega_r^2\left(1+\frac{v_a}{s}\right)}=\mathcal{Q}_{b_m}(s),\quad m=1,2,\ldots,N_m \quad (6)$$

respectively. The equation thus underscores the resonators' dynamic response to applied voltage and delineates the effect of piezoelectric actuation on the system, taking into account the damping characteristics of both the modes and the resonators.

The masses of the resonators, represented by (m_r), are calculated based on the structure's mass distribution at the points where resonators are installed. This calculation uses a mass ratio, denoted as (μ), to define the resonator mass in relation to the total mass of the primary structure. The formula $m_r = \mu m\left(x_r\right) dx_r$ links resonator masses to the structure's mass distribution, ensuring their behavior aligns with the structural dynamics. In systems with many resonators, their distribution can be approximated by $\sum_{r=1}^{N_r} m\left(x_r\right)\phi_m\left(x_r\right)\phi_p\left(x_r\right)dx_r \approx \int_0^L m(x)\phi_m(x)\phi_p(x)dx = \delta_{mp}$. This approximation considers the cumulative impact of resonators over the entire structure, in line with the orthogonality expressed by the Kronecker delta function δ_{mp}.

Enhancing the bandgap depth with notch filters introduces an innovative approach to mitigate the challenges posed by high damping ratios in mechanical systems that affect the performance of the bandgap, especially its depth. The utilization of notch filters is proposed as a means to fine-tune the system, deepening the bandgap and improving vibration isolation.

The method involves integrating a notch filter, represented by (7), into the piezoelectric actuator circuit to refine the performance and stabilize the system. The notch filter's parameters, such as the quality factor Q, the adjusted quality factor Q_β, and the gain k, are key to its function. These parameters allow the filter to selectively attenuate specific frequencies, which corresponds to the resonant frequencies that contribute to excess damping.

$$H_{no} = k\frac{s^2+\frac{\omega_{no}}{Q_\beta}s+\omega_{no}^2}{s^2+\frac{\omega_{no}}{Q}s+\omega_{no}^2} \quad (7)$$

Where H_{no} describes the filter's response, with k as its gain, and ω_{no} as the notch frequency. The quality factor Q determines the filter's selectivity and bandwidth width at ω_{no}, with a higher Q leading to narrower bandwidth and sharper resonance. In contrast, Q_β is an adjusted quality factor that controls the depth of the notch and the filter's response outside the notch frequency. This differentiation between Q and Q_β allows for precise control over the filter's frequency response, with changes in Q_β enabling modulation of attenuation at the notch frequency and altering the filter's behavior in specific ways. The use of Q_β varies based on the filter design and the engineer's objectives.

The integration of the notch filter into the system is evaluated through the derived (8), which now accounts for the notch filter's effects. This revised equation facilitates the analysis of the system's performance, illustrating the modulation of the bandgap via active control, made possible by the inclusion of the notch filter.

Equation (8) incorporates the dynamics of a notch filter, enabling the analysis of its influence on the system's performance (eliminating modal damping for simplicity). This includes examining how the filter affects the depth of the system's bandgap through active control using piezoelectric actuators. This equation provides a framework for understanding how the notch filter's parameters interact with the system dynamics, especially in terms of modifying bandgap characteristics.

To deepen the bandgap, Reinforcement Learning (RL) with an actor-critic method is utilized, focusing on optimizing notch filter parameters. This RL approach refines control parameters by iteratively adjusting actions based on the environmental state and corresponding rewards. The optimization leverages the Deep Deterministic Policy Gradient (DDPG) algorithm to target optimal values for parameters k, Q, and Q_β, which are critical for enhancing the bandgap depth and achieving superior vibration isolation.

IV. Results and Discussion

The parameters of this study are detailed in Table I, that presents the geometric and material properties of the rectangular aluminum beam.

TABLE I
GEOMETRIC AND MATERIAL PROPERTIES OF THE STUDIED RECTANGULAR ALUMINUM BEAM

Parameter	Value	Parameter	Value
L_m	300 mm	w_r	87 Hz
w_m	40 mm	ω_m	$18, 114, 319, ..$ Hz
h_m	2 mm	ζ_r	0.08
ρ_m	2700 kg/m^3	N_m	8
E_m	69.5 GPa	N_r	8
ζ_m	0.02	v_0	1 V
μ	0.66	α	0.098 F/C

Fig. 1 illustrates the sensitivity of the notch filter with varying parameters Q, Q_β, and k. The graph demonstrates the filter's frequency response, highlighting the attenuation levels across a range of frequencies. The shaded areas represent the variation in attenuation due to changes in the notch filter parameters, providing insight into the filter's effectiveness in suppressing specific frequency bands. The notch depths and bandwidths at various frequencies show how the system's response can be fine-tuned for enhanced vibration isolation. A comparison of the optimized parameters obtained through the Reinforcement Learning algorithm demonstrates their impact on the system's performance. The sensitivity analysis confirms that precise adjustments of Q, Q_β, and k are crucial for achieving the desired bandgap depth, validating the RL approach's efficacy in optimizing the metastructure's dynamic behavior.

Authorized licensed use limited to: Tallinn University of Technology. Downloaded on September 24,2024 at 09:16:49 UTC from IEEE Xplore. Restrictions apply.

$$\frac{Z_m(s)}{Q_{b_m}(s)} = \frac{1}{s^2\left(1+\frac{\mu(2\zeta_r\omega_r s+\omega_r^2)}{s^2+2\zeta_r\omega_r s+\omega_r^2\left(1+\frac{kv_a}{s}\frac{}{\frac{s^2+\frac{\omega_{no}}{Q_\beta}s+\omega_{no}^2}{s^2+\frac{\omega_{no}}{Q}s+\omega_{no}^2}}\right)}\right)+2\zeta_m\omega_m s+\omega_m^2} \tag{8}$$

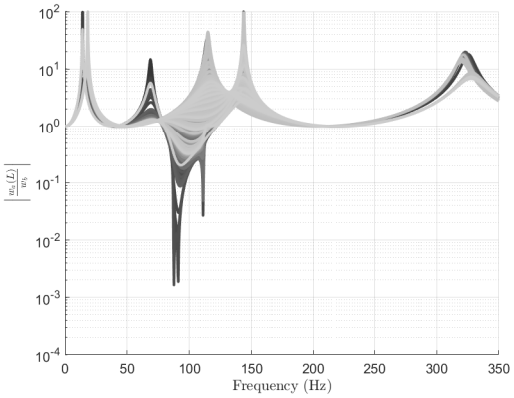

Fig. 1. Sensitivity of Transmittance from the Base to the Tip of the Aluminum Beam Metastructure, Illustrating Attenuation Variability with Parameter Adjustments of Q, Q_β, and k.

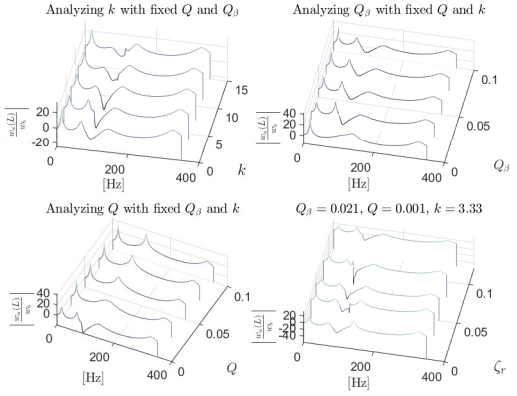

Fig. 2. Parameter Sensitivity Analysis of Notch Filter Performance on Metastructure Transmittance, Displaying the Effects of Variations in Gain (k), Quality Factor (Q), and Adjusted Quality Factor (Q_β) Across Frequency Bands.

Fig. 2 illustrates the impact of individual notch filter parameters on the vibration transmittance in a beam metastructure, through a series of contour plots. The top left plot illustrates the variation of gain k while Q and Q_β are held constant. Different levels of attenuation over the frequency spectrum can be observed as k changes, indicating the filter's sensitivity to gain alterations. The top right plot seems to focus on varying Q_β with fixed values for Q and k. This plot would be particularly useful for understanding how the depth and sharpness of the notch in the filter's response are affected by Q_β. The bottom left plot probably shows the effect of altering Q with Q_β and k remaining constant. Adjusting Q affects the bandwidth of the notch, and this visualization helps in finding the balance between selectivity and attenuation efficiency. The bottom right plot could be a specific case where Q_β, Q, and k are set to optimal values determined by prior optimization algorithms. This plot would exemplify the achieved balance between attenuation depth and bandwidth for effective vibration suppression.

For optimizing the notch filter parameters Q, Q_β, and k, Artificial Intelligence algorithms were utilized. The Reinforcement Learning (RL) approach pinpointed an optimal parameter set, achieving a structural damping ratio ζ_m of 0.03 and a resonator damping ratio ζ_r of 0.08. The parameters were determined to be $Q_{\beta_{\text{opt}}}$ at 0.021, Q_{opt} at 0.001, and k_{opt} at 33.3. These values are indicative of the RL algorithm's capability to finely adjust the system, enhancing its performance and demonstrating a similar yet uniquely effective solution compared to other algorithms for influencing the metastructure's transmittance and bandgap properties.

Fig. 3 compares transmittance across a range of frequencies for different damping treatments and system configurations. It includes four scenarios: an undamped metastructure, a damped system, a conventional piezo-actuated system with constant voltage, and a notch piezo-actuated system with optimized parameters. The optimized notch parameters, obtained through a Reinforcement Learning algorithm to reduce structural damping to $\zeta_m = 0.03$, illustrate the notch filter's effectiveness in decreasing transmittance at resonant frequencies, thereby deepening the bandgap and enhancing vibration isolation. This comparison underscores the enhanced vibration suppression of the notch piezo-actuated system compared to other configurations. The results highlight that in an overdamped metastructure, a piezo-actuator with constant voltage is less effective. However, integrating a notch filter significantly improves bandgap characteristics, even surpassing an undamped system's performance. This finding is pivotal in addressing the research objective of augmenting bandgap depth in highly damped metastructures, demonstrating that an

Authorized licensed use limited to: Tallinn University of Technology. Downloaded on September 24,2024 at 09:16:49 UTC from IEEE Xplore. Restrictions apply.

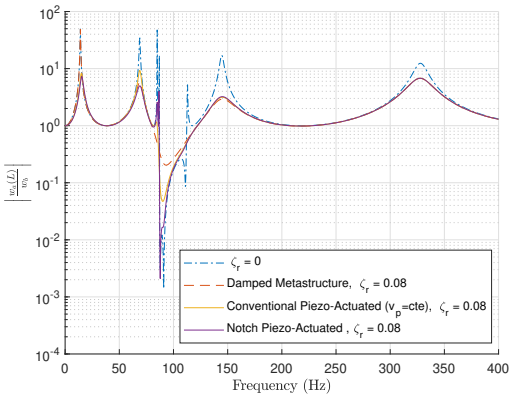

Fig. 3. Performance Comparison of Transmittance in High Damping Metastructures, Demonstrating the Effectiveness of Notch Filter Application in Piezo-Actuated Systems Versus Constant Voltage Application, with parameters: $\zeta_m = 0.02$, $\zeta_r = 0.08$, $v_0 = 1$ V, $Q_{\beta_{opt}} = 0.021$, $Q_{opt} = 0.001$, $k_{opt} = 33.3$. Achieving Bandgap Characteristics Comparable to Conventional and Undamped System.

actively controlled piezo-actuated system with a notch filter can achieve favorable bandgap properties in an overdamped system.

V. Conclusion

This research has made significant contributions to the field of vibration control in mechanical metastructures. Through the integration of notch filters in piezo-actuated systems, the study has demonstrated an innovative approach to enhancing bandgap characteristics in systems with high damping ratios. The use of Reinforcement Learning algorithms to optimize the parameters of the notch filter represents a noteworthy advance, enabling the precise tuning of the system's dynamic response. Results have shown that the application of a notch filter in an overdamped metastructure can effectively emulate the bandgap features of an undamped system, thereby achieving superior vibration isolation.

The insights gained from this study underscore the potential of smart materials and control strategies in engineering applications where vibration suppression is crucial. It affirms the viability of using advanced AI algorithms for system optimization, setting a precedent for their application in more complex dynamic systems.

Looking forward, future research could explore the scalability of this approach to larger structures or those with varying damping characteristics. Further investigation into the long-term stability and robustness of the control system under different operational conditions would also be valuable. Additionally, the integration of this approach with other smart material technologies could lead to the development of even more sophisticated vibration control systems, broadening the scope of practical applications in industries ranging from aerospace to civil engineering.

The principal contribution of this paper is the introduction of an active control strategy using notch filters to enhance the bandgap depth within highly damped metastructures. This approach has proven to be more effective than traditional piezo-actuated methods that employ constant voltage. The study demonstrates that by carefully adjusting the notch filter parameters, it is possible to achieve bandgap characteristics similar to those in undamped systems, thus providing a significant improvement in vibration isolation. This methodology represents a substantial advancement in metastructural design, offering a sophisticated tool for engineers to optimize dynamic responses in a variety of practical applications.

Acknowledgment

This paper was supported by the European Union's HORIZON Research and Innovation Programme under grant agreement No 101120657, project ENFIELD (European Lighthouse to Manifest Trustworthy and Green AI). It was also supported by the Estonian Research Council grant PRG658.

References

[1] C. M. Soukoulis, *Photonic band gap materials*. Springer Science & Business Media, 2012, vol. 315.

[2] M. Al Rifaie, H. Abdulhadi, and A. Mian, "Advances in mechanical metamaterials for vibration isolation: A review," *Advances in Mechanical Engineering*, vol. 14, no. 3, p. 16878132221082872, 2022.

[3] Y. Wang and D. J. Inman, "A survey of control strategies for simultaneous vibration suppression and energy harvesting via piezoceramics," *Journal of Intelligent Material Systems and Structures*, vol. 23, no. 18, pp. 2021–2037, 2012.

[4] W. M. van Spengen, "The electromechanical damping of piezo actuator resonances: Theory and practice," *Sensors and Actuators A: Physical*, vol. 333, p. 113300, 2022.

[5] H. Song, X. Shan, R. Li, and C. Hou, "Review on the vibration suppression of cantilever beam through piezoelectric materials," *Advanced Engineering Materials*, vol. 24, no. 11, p. 2200408, 2022.

[6] C. Huang and H. Li, "Adaptive notch filter for piezo-actuated nanopositioning system via position and online estimate dual-mode," *Micromachines*, vol. 12, no. 12, p. 1525, 2021.

[7] S. S. Rao, *Vibration of continuous systems*. John Wiley & Sons, 2019.

Authorized licensed use limited to: Tallinn University of Technology. Downloaded on September 24,2024 at 09:16:49 UTC from IEEE Xplore. Restrictions apply.

Appendix 6

H Alimohammadi et al. “Band gap tuning based on adjustable stiffness of local resonators”. In: *13th International Conference on Metamaterials, Photonic Crystals and Plasmonics, META 2023*. 2023

Band gap tuning based on adjustable stiffness of local resonators

Hossein Alimohammadi[1], Kristina Vassiljeva[1], S. Hassan HosseinNia[2], Eduard Petlenkov[1]
[1]Computer Systems Department, Tallinn University of Technology, 12618 Tallinn, Estonia
[2]Precision and Microsystems Engineering Department, Delft University of Technology, 2628 Delft, The Netherlands
*corresponding author, E-mail: Hossein.alimohammadi@taltech.ee

Abstract

This research article employs the finite element method to simulate the system and investigates the mechanisms for achieving broadband vibration suppression through adjustable stiffness by tuning the bandgap of beam-type resonators. The method involves changing the center of mass of the cantilever-type resonator to achieve piezo-free tuning of stiffness. The study explores the effect of varying the center of masses of attached masses (δ) on the bandgap and vibration suppression performance of a non-uniform beam-type resonator within a phononic structure. The results suggest that the cantilever-type resonator beam can be used for tunability and real-time control and demonstrate that varying the center of masses significantly impacts the bandgap and transmittance response. The research also examines the feasibility of using the first and second modes of resonators for tunability and real-time control, providing insights into the design and optimization of metamaterial beams for vibration suppression applications.

1. Introduction

The recent development of advanced vibration has made it possible to create innovative and resilient structures that can withstand extreme environmental and operating conditions. To protect critical components and sensitive equipment from excessive vibration in extreme operating conditions, engineers need to develop innovative solutions. The use of metamaterials has gained significant attention in recent years due to their unique properties that enable the control of electromagnetic and acoustic waves. In particular, the Locally Resonant (LR) mechanism has been found to be suitable for obtaining band gaps in the low-frequency range. This is in contrast to the Brag Scattering (BS) mechanism, which is more commonly used for band gaps in higher frequencies. One advantage of LR is that it eliminates the dependence of the band frequency on the lattice constant of the metamaterial. This section focuses on the approaches used to regulate the LR band gap, which can be achieved through adjusting the stiffness of the resonator. By understanding these fundamental strategies, it becomes possible to design and optimize metamaterials for specific applications in areas such as noise reduction, vibration control, and energy harvesting.

An approach for tuning the band gap in metamaterials involves the manipulation of the mass of the resonators. This can be achieved through direct mass variation, where a portion of mass is transferred between the resonator and the primary structure, or through introducing an inertial amplification mechanism that creates a large effective mass based on a small resonator mass. Direct mass variation can be accomplished using various methods, including electromagnets and pumps. Electromagnetic mass switching involves manipulating the current to attach or detach electromagnets, which alters the resonator's mass. Pump-based mass switching relies on pumping fluid to modify the resonator's mass. In contrast, the inertial amplification mechanism involves amplifying the resonator's mass by using a non-linear coupling between the resonator and the surrounding medium.

The tuning of the resonator mass is a fundamental strategy for adjusting the edge frequency of the band gap in metamaterials. Tuning the band gap through this method finds its application in various fields such as noise reduction, energy harvesting, sensing, and vibration control. By comprehending these techniques, researchers can optimize and design metamaterials with specific properties that meet the requirements of particular applications.

Another way to tune the bandgap of metamaterials is by adjusting the stiffness of the resonator. This can be achieved through two approaches: changing the mechanical structure of the material or adjusting the stiffness in real-time. Mechanical approaches include introducing negative stiffness mechanisms, decreasing the cross-section of elastic materials, or adjusting the amount of compression.

Nonetheless, implementing alterations to these techniques after material design is typically challenging, thus making real-time adjustments difficult This can be a significant limitation in situations where the desired resonant frequency changes, or where there is a need to adjust the properties of the resonator to improve its performance. Although mechanical structures can be useful in achieving the desired resonator properties, it is crucial to carefully weigh the trade-offs associated with their design, including the challenges involved in modifying them once they are installed.

Alternatively, metamaterials can be designed with real-time controllable configurations, allowing for more precise and dynamic adjustments to the resonator stiffness. Controllable variables include electrical elements such as current, voltage, inductance, and resistance, air pressure, and temperature. Piezoelectric actuators and electromagnets are two primary electronic components used to adjust the stiffness of the material based on electrical elements. By adjusting the

inductance or resistance, these components enable the creation of intelligent metamaterials that can simultaneously open multiple types of band gaps and easily tune the frequency of band gaps. Overall, the ability to tune metamaterial properties in real-time makes them promising candidates for a wide range of applications, including communication devices, energy harvesting, and sensing technologies.

There are two main mechanisms for creating bandgaps due to LRs: mechanical and electromechanical. Mechanical LR bandgap formation is based on the principle of periodic structures. It involves changing the physical characteristics of the structure, such as the size, shape, and material composition of the structure. By changing these characteristics, it is possible to create a periodic pattern of dielectric and metallic layers that form a bandgap. This type of bandgap is used in applications such as filters, interconnects, and antennas.

Most electromechanical LR can be divided into two categories: those that use piezoelectric unit cells and inductive circuits, and those that use magnetic motors. LR bandgaps do not rely on periodic lattice arrangements and can be controlled and tuned in different spatial configurations. With the advent of new technologies, it is now possible to create more efficient and powerful electromechanical LR. The ability to adjust the bandgap of a material via an external mechanical force paves the way for novel material and device development with enhanced performance. Numerous types of mechanical locally resonant metastructures have been studied in the past. Bilal et al. [1] studied the way sound waves travel through elastic metastructures made up of a periodic array of pillars with and without holes. They found that the presence of holes in the pillars caused an increase in bandgap. Tsung-Tsong Wu et al. [2] demonstrated through both numerical analysis and physical experiments that a periodic stubbed surface can create a complete band gap. They found that when the stub height is roughly three times the plain thickness, the band gap is created formed precisely. Xudong Wu et al. [3] suggested a locally resonant beam that incorporated an aperiodic mass distribution. They utilized an optimization algorithm to identify the desired bandgap, and demonstrated through finite element simulations that this configuration could effectively expand the frequency range of bandgaps in flexural vibrations. Despite the potential of mass distribution, the desired rigidity of the system remains unchanged in this study. Zhi Tao et al. [4] studied two-dimensional phononic metamaterials consisting of plates with resonant cylinders that have a negative Poisson's ratio structure. Their study showed that this design could achieve a lower frequency, wider bandgap, and tunable bandgap than traditional designs. Nonetheless, similar to most other works, this approach necessitates design at the outset and cannot be fine-tuned or adjusted during its operation.

Jian et al. [5] proposes a novel method of broadband vibration attenuation using a graded piezoelectric metamaterial beam. The term "graded" refers to a variation in the natural frequencies of the resonators. This means that the resonators are designed or arranged in such a way that they have different natural frequencies across a certain range or spectrum. By applying electrode pairs with varying lengths connected to an identical shunt resonant circuit, the proposed graded metamaterial can broaden the vibration attenuation region through varying spatial profiles. The results show that the graded piezoelectric metamaterial beams achieve the widest theoretical attenuation area and increase the bandwidth compared to conventional methods.

The concept of graded materials is based on the assumption of “gradual” changes, which makes it suitable for certain systems, for example considering the allowable variations in dimensions or properties of a resonator that are inevitable during the manufacturing process. However, the use of graded metamaterials may not be practical or feasible for achieving real-time controller tunability in some systems. Therefore, it is important to carefully consider the specific requirements of each application before choosing to use graded materials. Hence, it is crucial to meticulously evaluate the particular needs of each application before deciding to employ graded materials. It may not be appropriate to use the term "graded" in the present research context. Instead, "graded disorder" or center of mass (CM) variation could be utilized as a substitute.

As it is mentioned in the introduction, tuning the band gap based on the adjustable stiffness is done through two methods: changing the mechanical structure or adjusting the stiffness in real time. The first has a limited operating range due to initial design, and the second has a limited actuator that uses piezo to change the stiffness.

This research proposes a method for tuning the band gap of beam-type resonators based on adjustable stiffness to achieve broadband vibration suppression. The study explores the possibility of piezo-free tuning of the resonator's stiffness by changing its CM. It is noteworthy that this method does not involve mass tuning, but rather adjusts the stiffness of the resonator by altering its mass. The article examines the viability of this technique and its potential for enhancing the performance of the resonator. The main research question is how the δ affects its frequency behavior via adjusting the stiffness when the resonator is clamped to a host beam. The results of this study will allow us to continue our efforts to enhance the metastructure for future work.

2. Method

First, we analyze propagation of acoustic waves through a phononic structure with one, two, and four beams connected to a non-uniform beam-type resonator. By using a reduced wave factor, the unit cell is able to disperse waves in a way that the attenuation can be achieved. The frequency response of the tip of the Euler–Bernoulli beam is than monitored to verify the outcomes found in the dispersion curves. To determine the bandgap of a structure, typically, one unit cell and a resonator are examined, as this reduces the computational workload. In this study, these waves propagate along the unit cell, and their propagation is restricted to the ΓX direction.

Solving the equation of motion involves applying a harmonic input force, while taking into account the entire beam with periodic boundary conditions and Floquet periodicity to obtain precise outcomes. Due to forced

vibration, it can be assumed transverse displacement $z(t)$ for define location, x, on beam is equal to

$$z(t) = z_a e^{-i(\omega t)}, \quad (1)$$

where z_a is the displacement amplitude.

Moreover, if we consider that the transverse displacement $z(t)$ is also a function of position, x, we can obtain the periodic function $z(x)$. This function can be represented by a set of base vectors, a_i in a real space. This function follows the wave propagation of an infinite periodic structure.

$$z(x) = z(x_0 + r) = z(x_0), \quad (2)$$

Here, $r=a_iS$, where x represents the global location, and $x0$ is the relative location in the primitive unit cell. S is an integer (the number of resonators). If an elastic wave travels through a structure with repeating patterns, it must satisfy the Bloch condition at the edges of the repeating unit. This condition ensures that the wave can propagate through the structure without any disruption. By combining the properties of waves, we can define the wave equation with respect to temporal and spatial frequencies as follows:

$$z(x,t) = z_a e^{-i(\omega t - kx)}, \quad (3)$$

Where k is the Bloch wave vector confined in the first Brillouin zone in the spatial position (rad/m). The considered physical model is a square lattice of rectangular resonators of a thin homogeneous beam as shown in Fig.1.

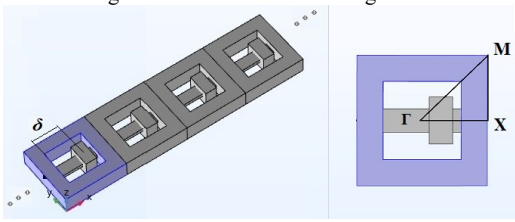

Fig. 1. Schematic of studied phononic structure by a square lattice dots deposited on both sides of a thin beam. The geometrical parameters are as: unit cell outer/inner length=20, 12mm, width=20mm, hight=5mm. The resonator parameters are: length=12mm, width=3.6mm, hight=1mm. The attached mass: length=3.6mm, width=7.2mm, hight=5mm, Number of resonators, S=8.

The reference position of the attached mass is located at the CM of the resonator. Shifting the position of the attached mass alters the CM of resonator from δ_{min}=-3.6 mm to δ_{max}=+3.6 mm. The z axis is perpendicular to the beam axis, x. The modulus of elasticity is E=2.8 GPa and mass density of the material is ρ=992 Kg/m^3, which is relatively low compared to some other common 3D printing materials like ABS and Nylon. It is important to recognize that various factors such as printing temperature, print speed, and cooling can also affect the final properties of the object. Moreover, the infill density during printing process can alter the rigidity of the structure. In this manner, a spring-mass resonator is designed within the unit cells, which are connected to the beam by one, two and four slender beams, which serve as the spring. Then, local resonance at some particular frequencies may be stimulated.

An acceptable and continent approach to analyzing the acoustic bandgaps in the proposed structure is to calculate the dispersion curve. The amount of wave that passes through a metamaterial beam is measured as the transmittance ratio. This ratio is determined as follows:

$$TR(\omega) = \frac{z_{tip}(\omega)}{z_{base}(\omega)}, \quad (4)$$

The ratio TR is a measure of how much the vibration of the free end is reduced compared to the vibration of the base. TR less than 1 indicates that the vibration at the free end is smaller than at the base, meaning the vibration is being attenuated.

The dominant attenuation bandwidth X_{BW} is defined

$$X_{BW} = \max(|\Im|), \{\forall \omega \ni \Im, 20\log(TR(\omega)) \leq -40\}, \quad (5)$$

which measures the largest bandwidth in the attenuation region. Less than 1% of the base amplitude is allocated in this work for complete suppression, which means X_{BW} = 20log(TR) < -40 dB. For an infinite number of resonators on a plain (simple) structure, (6) can be used to calculate the mass ratio.

$$\mu = \frac{\sum_{res=1}^{S} x_{res}}{m_p}, \quad (6)$$

This ratio represents the total mass of the resonators to the total mass of the planar structure. Here, m_p refers to the mass of the plain structure, and S represents the number of resonators.

The total mass of the resonator is sum of beam-type resonator and attached mass. Equation (6) was derived using an undamped model that is infinitely long. In a practical metamaterial system with limited cells, the effective range of attenuation frequencies may be smaller than what was predicted. To overcome this, the natural frequency due to CM variation δ can be intentionally changed so that each resonator operates within overlapping frequency ranges. This can overcome the difficulties of changing mass in real-time tuning control, where the mass ratio is fixed. The resonator's CM is a key factor in determining the system's resonance frequency. The CM is presented as δ and determined by the mass, the location, and the shape of the resonator. The reference point of δ is located in the initial center of mass of a plain beam-type resonator without any attached mass. The host beam is lattice shaped metastructure. At its minimum value, the δ on the resonator is located close to the base, and at its maximum, it is near the tip of the resonator. This can impact the width of the X_{BW}, causing it to become narrower or wider.

3. Results and Discussion

A parametric study was conducted to investigate how the δ affects the bandgap and transmittance of the host beam. The COMSOL software is used to simulate wave propagation and analyze bandgaps. MATLAB scripts are written to facilitate the related steps of modeling and calculations. The Bloch

calculation produces eigenfrequencies and corresponding eigenvectors by varying the wave vector in the first irreducible Brillouin zone, allowing the dispersion curves to be obtained. A study was conducted on how the dispersion curves evolve along the direction from ΓX, by arranging the resonators from a lower equivalent stiffness distribution to a higher distribution. The objective of this study is to analyze the impact of the attached mass's δ on the bandgap and vibration suppression performance. The investigation concentrates on a beam consisting of eight resonators with a μ value of 0.1 to 0.9.

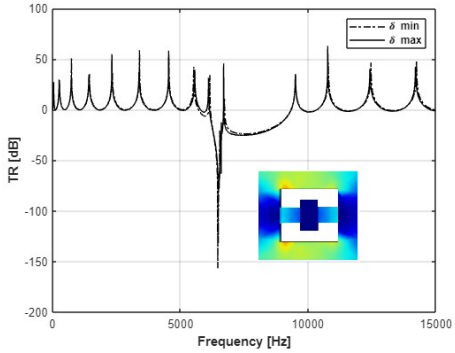

Figure 2: Transmittance responses of the fixed-fixed type resonator beam with μ=0.1 for different δ.

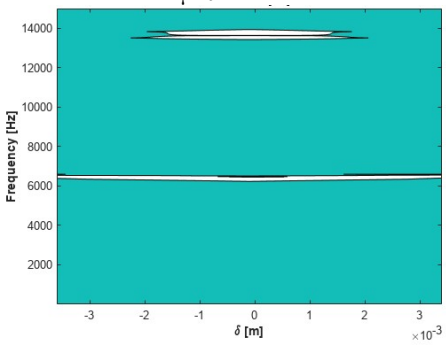

Figure 3: Binary representation of the transmittance pattern evolution in response to the variation of δ, and μ=0.1. The unshaded, X_{BW}=-40 dB.

The results presented in Fig. 2 and Fig. 3 demonstrate the impact of the δ on the transmittance response of the fixed-fixed resonator beam with μ = 0.1. Fig. 2 shows that varying δ does not result in any noticeable changes in the X_{BW} or edge frequency. This lack of dependence is attributed to the symmetry of the first Brillouin zone, which causes the dispersion curve for waves traveling in the ΓX direction to remain consistent regardless of δ.

To further investigate the effect of δ on the transmittance pattern, Fig. 3 represents the binary representation of the transmittance pattern evolution with changes in δ. The unshaded region in the figure denotes the dominant attenuation region below -40 dB. It is evident that the X_{BW} remains consistent regardless of the value of δ, indicating that δ has no impact on the transmittance pattern in the dominant X_{BW}.

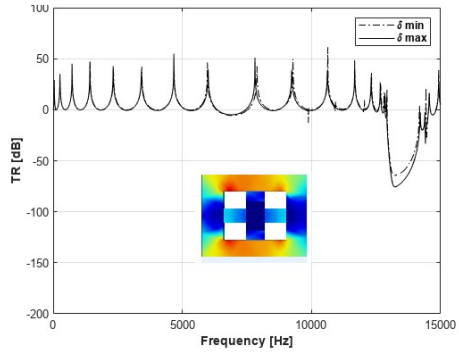

Figure 4: Transmittance responses of the cross type resonator beam with μ=0.1.

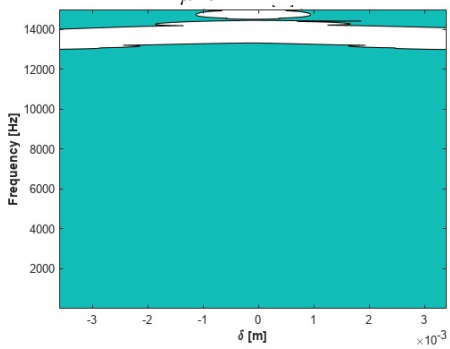

Figure 5: Binary representation of the transmittance pattern evolution contour in response to the variation of δ, and μ=0.1

The results presented in Fig. 4 and Fig. 5 demonstrate the impact of the δ on the transmittance response of the cross-type resonator beam with a μ= 0.1. Fig. 3 shows that the transmittance response changes with variations in δ, but the bandgap characteristics remain constant. Similar to fixed-fixed beams resonator, this is attributed to the symmetry of the first Brillouin zone, which results the dispersion curve to remaining consistent regardless of δ. However, the rigidity is enhanced because, in a cross configuration, two extra stiffnesses are added in parallel to what existed before. This configuration leads to a change in the edge of the bandgap towards higher frequencies. Fig. 4 shows the binary representation of the transmittance contour pattern evolution with changes in δ for -40dB. The area without shading in the plot represents the X_{BW}, and it can be observed that the transmittance response is not greatly influenced by δ. This independence implies that the position of the resonator's center of mass does not have a significant impact on the beam's bandgap properties. Therefore, it is difficult to adjust or manipulate the beam in real-time by modifying δ. Based on these findings, it can be concluded that the center of mass location of the attached masses has little effect on the vibration suppression capabilities of the metamaterial beam in this particular scenario.

To overcome this issue, the fixed-fixed beams were converted into cantilever-type resonators. To determine the possibility of creating a bandgap, the dispersion curve was

calculated and plotted in Fig. 6. These results suggest that the cantilever-type resonator beam can be used to achieve tunability and real-time control by utilizing the second mode shape for specific bandgap tuning purposes. Overall, these findings provide insights into the design and optimization of graded metamaterial beams for vibration suppression applications.

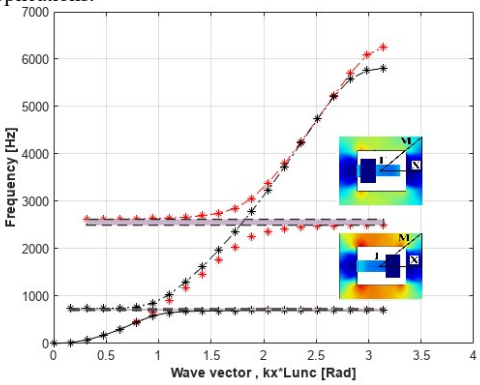

Figure 6: The dispersion curves along the ΓX direction with the δ variation, and μ=0.1. The filled area denotes the bandgap region.

Fig.6 displays the dispersion relations for waves travelling in the ΓX direction within the first Brillouin zone. The plot depicts the relationship between the wave vector and the frequency of the wave as it propagates through the zone. The result demonstrates that the bandgap characteristics of the graded disorder metamaterial beam can be influenced by the value of δ. Specifically, the figure reveals that increasing δ leads the formation of a bandgap at lower frequencies, while decreasing δ produces a bandgap at higher frequencies. This observation is significant as it suggests that the bandgap characteristics can be tuned by adjusting the value of δ. Moreover, the results suggest that the value of δ can be used as a tuning parameter to adjust the bandgap characteristics of graded disorder metamaterial beams. This information can be helpful in optimizing the design of such beams for specific applications where a certain bandgap frequency range is desired. By varying the value of δ, researchers can achieve the desired bandgap characteristics and improve the overall performance of the metamaterial beam.

Fig. 7 provides additional insight into the transmittance responses of the metamaterial beam with 8 cantilever resonators for different values of δ. The results show that there are significant changes in the edge of the bandgap, which indicates the potential for practical applications of this metamaterial beam. It is also important to consider the effect of δ on the mass ratio μ mathematically called CM ratio, and how it impacts the edge of the bandgap. Further analysis of these parameters can provide a more comprehensive understanding of the behavior of the metamaterial beam.

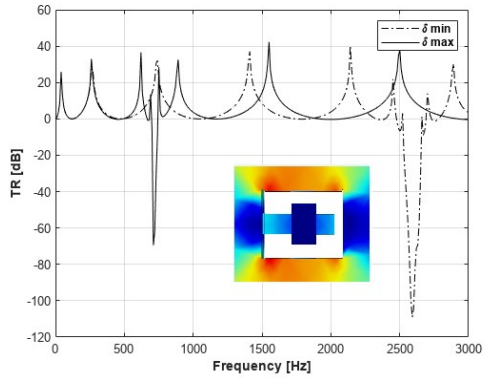

Figure 7: Transmittance responses of the first and second mode of resonator with μ=0.1 for different δ.

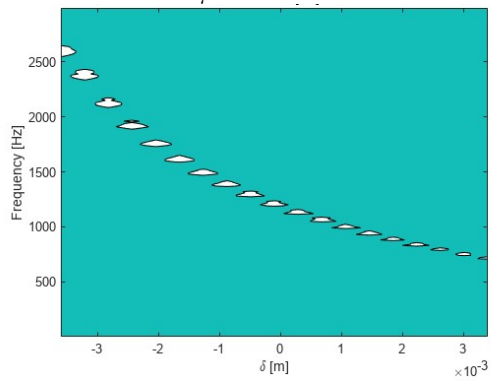

Figure 8: Image binarization contour of the transmittance using -40 dB as reference in response to the variation of δ, and μ=0.1.

Fig. 8 provides a visual representation of how the bandgap edge is affected by changes in δ for the region below -40 dB. This plot helps to visualize the dependence of the edge of bandgap on the variation of δ. It is clear that δ has a significant impact on the location of the bandgap edge, indicating that the resonator's center of mass location is crucial in determining the beam's bandgap characteristics. This discovery enables real-time control and tuning of the beam's bandgap characteristics, which is a significant advantage. Additionally, the discrete zones in the plot can be attributed to the small value of μ and the selected attenuation level of -40 dB. It is important to note that selecting different values of μ or attenuation levels would yield different plot features.

By using a cantilever-type resonator instead of a lumped mass spring, it becomes feasible to examine other modes of the resonator. Fig. 9 shows the transmittance responses of the first and second mode of the resonator with a high mass ratio of μ=0.9 for different values of δ. The second mode is observed in the transverse vibration of the beam, and the attached mass on the resonator material is replaced from PLA to steel to decrease the natural frequency of the resonator to the desired frequency range. The result shows the same behaviour in the second mode as well, and the variation of δ

changes the bandwidth X_{BW} and edge of bandgap similar to first mode.

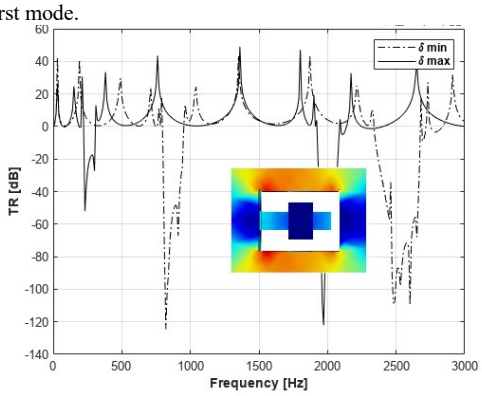

Figure 9: Transmittance responses of the first and second mode of resonator with μ=0.9 for different δ.

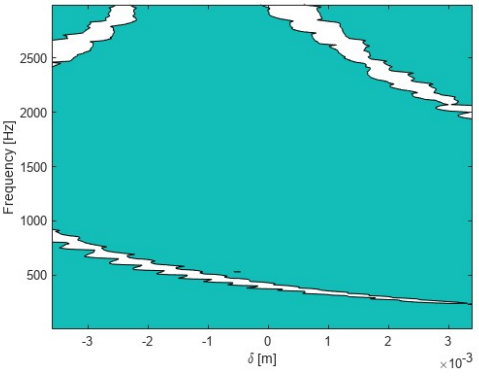

Figure 10: Image binarization contour of the transmittance using -40 dB as reference in response to the variation of δ, and μ=0.9.

Fig.10 shows the binary representation of the transmittance contour pattern evolution with changes in δ for a high mass ratio of μ=0.9. The image binary contour of the transmittance for μ=0.9 and -40 dB as reference is shown in Fig. 10. The second mode of resonator creates an additional gap in higher frequencies, as shown in the top part of Fig. 10. Using a cantilever-type resonator instead of a lumped mass spring enables the investigation of additional resonator modes, as indicated by this result. Additionally, the ability to alter the attached mass and mass ratio permits real-time control and tuning of the bandgap characteristics of the beam. The results presented in this study demonstrate the impact of the δ on the transmittance response of graded disorder metamaterial beams. Additionally, the study highlights the importance of considering the resonator mode shape when designing and optimizing graded disorder metamaterial beams for specific bandgap applications. By using a cantilever-type resonator instead of a lumped mass spring, other modes of the resonator can be studied, providing greater flexibility in designing the bandgap characteristics. The ability to tune and control the bandgap characteristics in real-time experiments makes this type of metamaterial beam a promising candidate for various applications, including vibration and noise suppression in mechanical system.

4. Conclusion

In conclusion, this research has examined the possibility of tuning the band gap of beam-type resonators based on adjustable stiffness to achieve broadband vibration suppression. Through the analysis of dispersion relations and the binary representation of transmittance contour patterns, it has been demonstrated that the center of masses of attached masses does not significantly affect the vibration suppression performance of the metamaterial beam. However, by using a cantilever-type resonator instead of a lumped mass spring, it has become possible to examine other modes of the resonator and to tune and control the bandgap characteristics of the beam in real-time experiments. This research proposes a piezo-free method for tuning the adjustable stiffness of beam-type resonators to achieve broadband vibration suppression. The study explores the feasibility of changing the center of mass to tune the resonator's stiffness and discusses its potential for improving performance. This study has provided valuable insights into the design and optimization of graded metamaterial beams for vibration suppression applications. Additionally, further research could be conducted to investigate the potential of using graded disorder metamaterial beams for other applications beyond vibration suppression, such as energy harvesting or acoustic insulation. Overall, the findings of this study provide a promising avenue for the development of advanced metamaterial beams with tailored bandgap characteristics for a wide range of applications.

Acknowledgements

This work has been partially conducted in the project "ICT programme" which was supported by the European Union through the European Social Fund. It was also supported by the Estonian Research Council grant PRG658.

References

[1] O. R. Bilal and M. I. Hussein, "Trampoline metamaterial: Local resonance enhancement by springboards," *Applied Physics Letters*, vol. 103, no. 11, 2013.

[2] T. Wu, Z. G. Huang, T. C. Tsai, and T. C. Wu, "Evidence of complete band gap and resonances in a plate with periodic stubbed surface," *Applied Physics Letters*, vol. 93, no. 11, 2008.

[3] X. Wu, Y. Li, and S. Zuo, "The study of a locally resonant beam with aperiodic mass distribution," *Applied. Acoustics.*, vol. 165, 2020

[4] Z. Tao et al., "A novel auxetic acoustic metamaterial plate with tunable bandgap," *The International Journal of Mechanical Sciences*, vol. 226, p. 107414, Jul. 2022.

[5] Y. Jian, L. Tang, G. Hu, Z. Li, and K. C. Aw, "Design of graded piezoelectric metamaterial beam with spatial variation of electrodes," *The International Journal of Mechanical Sciences*, vol. 218, 2022.

Appendix 7

Hossein Alimohammadi et al. "Piezoelectric Compensation of Structural Damping in Metamaterial Beams: Stability and Performance Analysis". In: *Active and Passive Smart Structures and Integrated Systems XVIII* (2024)

Piezoelectric Compensation of Structural Damping in Metamaterial Beams: Stability and Performance Analysis

H. Alimohammadi[a], K. Vassiljeva[a], S. H. HosseinNia[b], P. Ellervee[a], and E. Petlenkov[a]

[a]Department of Computer Systems, Tallinn University of Technology, Tallinn, Estonia
[b]Department of Precision and Microsystems Engineering, Delft University of Technology, Delft, The Netherlands

ABSTRACT

This paper examines the stability implications of integrating piezoelectric actuators into metamaterial beams, focusing on the compensation of structural damping and its effect on the system's dynamic performance. Metamaterials, characterized by their unique bandgap properties, offer potential in various engineering applications, including vibration control and energy harvesting. However, structural damping inherent in such systems can degrade these properties, prompting the use of piezoelectric actuators as a compensatory mechanism. Through a distributed parameter model and modal analysis, this study explores the temporal and spatial dynamics of the metamaterial beam and investigates how piezoelectric actuation influences the natural frequencies and mode shapes, with a particular emphasis on stability thresholds. Employing root locus analysis, the paper visualizes the transition of system stability across different levels of actuation voltage, highlighting the delicate balance between enhanced performance and stability. The findings delineate a clear operational voltage range, within which piezoelectric actuation improves bandgap properties without compromising system stability.

Keywords: Damping Compensation, Stability Analysis, Piezoelectric Actuation, Distributed parameter model of metastructures, Bandgap Engineering

1. INTRODUCTION

In this study, we delve into the stability analysis of metamaterial beams incorporating piezoelectric actuators, a subject that sits at the intersection of advanced materials science and dynamic system control. The crux of this investigation lies in understanding how the integration of active control elements affects the overall stability of these sophisticated structures.

Metamaterial beams, known for their unique mechanical properties and dynamic behaviors, present a complex challenge when augmented with piezoelectric actuators. These actuators, capable of precise manipulation of the beam's response, introduce a new dimension to the system's dynamics. Thus, a rigorous stability analysis becomes paramount to ensure that such modifications do not lead to detrimental outcomes like system instability or resonance failures.

Our approach begins with constructing a distributed parameter model for the metamaterial beam. This model, essential for capturing the continuous spatial variation of mechanical properties along the beam, is governed by a nuanced set of partial differential equations. These equations are the backbone of our analysis, allowing us to explore the temporal and spatial dynamics of the beam in detail.

We employ modal analysis to uncover the natural frequencies and mode shapes of the beam. Understanding these characteristics is crucial for predicting the emergence of bandgaps—a phenomenon where certain frequency ranges are blocked or altered by the structure of the metamaterial. Modal analysis also aids in assessing how active control via piezoelectric actuators can be used to tailor these bandgaps effectively.

To visualize and understand the implications of varying control parameters, specifically the applied voltage v_a, we utilize root locus analysis to track the movement of the poles in the complex plane as the applied voltage changes, offering a clear depiction of the stability landscape of the system under different operational scenarios.

Further author information: (Send correspondence to E. Petlenkov)
E.P.: E-mail: eduard.petlenkov@taltech.ee, Telephone: 1 234 567 890

Active and Passive Smart Structures and Integrated Systems XVIII, edited by Serife Tol, Guoliang Huang, Xiaopeng Li, Mostafa A. Nouh, Shima Shahab, Jinkyu Yang, Proc. of SPIE Vol. 12946, 129460J · © 2024 SPIE · 0277-786X · doi: 10.1117/12.3024120

A focal point of our study is the exploration of the potential risks associated with using piezoelectric actuation to counteract damping effects. We rigorously investigate whether this approach introduces new poles or zeros in the transfer function, potentially leading to instability. Through comprehensive simulations, we aim to establish stability thresholds, providing a concrete framework for evaluating the system's resilience to various levels of piezoelectric actuation.

This research is not just an academic exercise but a practical guide for engineers and designers. By identifying and understanding the boundaries of stability in such complex systems, we aim to inform the design and operational protocols of metamaterial beams, ensuring they achieve their intended dynamic performance without compromising their structural integrity.

2. LITERATURE REVIEW AND BACKGROUND

The study of bandgaps in metamaterials has garnered considerable attention from engineers and researchers due to its potential in various practical applications. This Literature Review and Background section will delve into the existing research and identify the gap that our study aims to address.

Metamaterials, known for their extraordinary mechanical properties, have been a focal point in materials science research. One of the key features of these materials is their ability to exhibit bandgaps - frequency ranges in which wave propagation is significantly reduced or entirely inhibited. The control over bandgap characteristics, such as width and depth, has important implications for noise reduction, vibration control, and energy harvesting applications.[1]

In practical scenarios, the effectiveness of these bandgaps is often compromised due to the inherent damping characteristics of the structure. Damping, a natural phenomenon in materials, leads to the dissipation of energy, thereby affecting the depth of the bandgaps and diminishing their effectiveness.[2]

To counteract this issue, one approach has been the integration of piezoelectric actuators. These actuators, leveraging the piezoelectric effect, are employed to enhance the resonator's performance, thereby compensating for the damping and potentially restoring the depth of the.[3,4]

However, the introduction of piezoelectric actuators alters the dynamic properties of the system, potentially leading to instability. The interaction between the piezoelectric elements and the mechanical structure can introduce changes in the system's natural frequencies and mode shapes, which in turn might affect its stability.[5,6]

While previous studies have explored the influence of piezoelectric actuation on metamaterial bandgaps, there is a lack of comprehensive understanding of how this actuation affects the stability of the system. This leads us to the primary research question of our study: How does the use of piezoelectric actuators to compensate for damping in metamaterial beams influence the stability of the system, and what are the implications for the practical application of these enhanced bandgaps?

Our research aims to investigate this stability, or potential instability, introduced by piezoelectric actuation in metamaterial beams. By addressing this question, we seek to bridge the gap in current understanding and provide insights that are crucial for the practical application and optimization of piezoelectrically enhanced metamaterials.

3. DISTRIBUTED PARAMETER MODEL USING MODAL ANALYSIS

In this study, a distributed parameter model is employed to analyze the behavior of a metamaterial system. This model is crucial for understanding spatial variations in physical properties and their impact on wave propagation. Modal analysis is utilized to determine the natural frequencies and mode shapes of the metastructure, which are essential for identifying and manipulating bandgaps.

The locally resonant metastructure, incorporating piezoelectric actuators, is illustrated in Fig. 1. This diagram emphasizes the deliberate placement of piezoelectric elements crucial for the actuation approach. Employing a distributed parameter model aids in formulating partial differential equations that delineate the system's dynamics, which are subsequently discretized and numerically analyzed to determine the metastructure's modal properties.

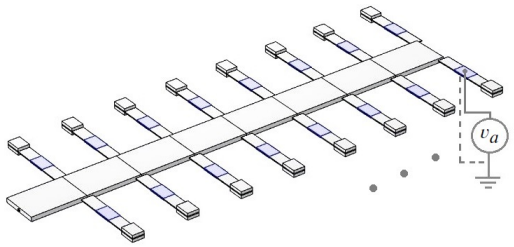

Figure 1. Schematic of a locally resonant metastructure with piezoelectric actuators. Features cantilever beams with tip masses as resonators and piezoelectric elements (with voltage v_{p_r}) bonded to alter stiffness dynamically.

The dynamics of the system are captured by a set of partial differential equations as follows:[7]

$$\mathcal{L}w(x,t) + \mathcal{C}\frac{\partial w(x,t)}{\partial t} + \mathcal{M}\frac{\partial^2 w(x,t)}{\partial t^2} - \sum_{r=1}^{N_r}\left(k_r z_r(t) + c_r\frac{\partial z_r(t)}{\partial t}\right)\delta\left(x - x_r\right) = \mathcal{F}_{b_m}(x,t) \tag{1}$$

$$m_r\frac{\partial^2 z_r(t)}{\partial t^2} + c_r\frac{\partial z_r(t)}{\partial t} + k_r z_r(t) + m_r\frac{\partial^2 w\left(x_r,t\right)}{\partial t^2} - \vartheta_{p,r}v_{p,r}(t) = \mathcal{F}_{b_r}(t) \tag{2}$$

$$C^*_{p,r}\frac{\partial v_{p,r}(t)}{\partial t} + \vartheta_{p,r}z_r(t) = 0 \tag{3}$$

Equations (1), (2), and (3) in the study address the dynamics of a metamaterial beam system with piezoelectric actuators. Equation (1) focuses on the primary beam's displacement and its interaction with resonators, while Equation (2) details the resonators' motion and the influence of the piezoelectric actuator force. Equation (3) links the actuator voltage to the resonator motion through capacitance and a coupling coefficient.

The parameters $\mathcal{L}, \mathcal{C}$, and $\mathcal{M}$ represent the system's flexural rigidity, damping, and mass distribution. The piezoelectric properties defined as electromechanical coupling (ϑ_r), capacitance ($C^*_{p,r}$), and the shunt circuit admittance (G_r) on each resonator. The functions $w(x,t)$ and $z_r(t)$ describe the main structure's and resonators' transverse vibrations, respectively. The Kronecker delta function $\delta\left(x - x_r\right)$ denotes resonator locations, with N_r being the total number.

The system's boundary conditions are determined by linear homogeneous differential operators, and damping is often modeled based on the mass and stiffness matrices. This approach simplifies analysis using common mode shapes for both damped and undamped scenarios, albeit as an approximation.

Orthogonality conditions involving these operators, as indicated by δ_{mn} in Equations (4) and (5), confirm that the mode shapes are orthogonal in terms of the system's stiffness and mass. Proportional damping links damping characteristics to these orthogonal eigenfunctions, defining the damping ratio ζ_m for each mode as a linear combination of the system's mass and stiffness.

$$\int_D \phi_m(x)\mathcal{M}\left[\phi_n(x)\right]dx = \delta_{mn} \tag{4}$$

and

$$\int_D \phi_m(x)\mathcal{L}\left[\phi_n(x)\right]dx = \delta_{mn}\omega_m^2 \tag{5}$$

In modal decomposition, the deflection of an Euler beam over the domain $D = [0, L]$ is represented as a sum of modal contributions:

$$w(x,t) = \sum_{m=1}^{N_m} \phi_m(x) z_m(t), \tag{6}$$

The deflection of an Euler beam in modal decomposition is expressed through a series of modal contributions, where $\phi_m(x)$ illustrates the spatial pattern of each mode shape, and $z_m(t)$ indicates the time-dependent development for each mode. This method effectively reduces the intricate dynamics of a flexible beam with embedded resonators to simpler, more understandable elements.

The modal expansion from Eq. (6) is substituted into Eqs. (1) and (2), using the orthogonality conditions from Eqs. (4) and (5). By reorganizing these equations and applying Laplace transforms (assuming no initial conditions), a set of linear equations in the Laplace domain is derived. This process leads to the formulation of a transfer function for the displacement of the resonator.

In this framework, the resonator masses (m_r) are proportionally defined relative to the mass distribution of the structure at resonator attachment points, scaled by a mass ratio (μ). This ratio represents the total mass of the resonators compared to the base structure's mass. The relationship is expressed as $m_r = \mu m\left(x_r\right) dx_r$, ensuring that the resonator masses are integrally linked to the structure's mass distribution.

For systems with a large number of resonators, the expression involving the sum of resonator masses can be approximated by an integral over the structure's length. This approximation aligns with the orthogonality condition represented by the Kronecker delta function δ_{mp}.

Using the defined terms and after rearranging the equations mathematically, the transfer function that describes the displacement of the resonator is constructed as follows:

$$Z_r(s) = \frac{-s^2 w_b - \sum_{m=1}^{N_m} Z_m(s) s^2 \phi_m\left(x_r\right)}{s^2 + 2\zeta_r \omega_r s + \omega_r^2 + \frac{k_e^* \omega_r^2}{s}}, \quad r = 1, 2, \ldots, N_r \tag{7}$$

where $Z_r(s)$ signifies the Laplace transform of the displacement response for the r-th resonator in a metamaterial system, where ω_b represents the base excitation. The term $\phi_m\left(x_r\right)$ indicates the mode shape at the location x_r of the resonator, N_r is the total number of resonators, ζ_r is the damping ratio signifying energy dissipation efficiency, and ω_r is the resonator's natural frequency.

The effective electromechanical coupling of the resonator, denoted as k_e^*, is defined by $k_e^* = \frac{\vartheta_{p,r}^2}{C_{p,r}^* k_r}$. When considering the voltage source as the input, this effective stiffness k_e^* can be expressed through the relationship $k_e^* = \alpha \omega_r v_0 = v_a$, , where ω_r represents the natural frequency of the resonator, v_0 is the voltage applied to the piezoelectric component, and α is an empirical constant with the unit Farads per Coulomb (F/C). After some mathematical manipulation, the transfer function for the displacement of the m-th mode of the structure relative to the excitation force on the same mode is formulated, simplified, and described by Eq. (8). This equation includes terms for modal frequency, damping, and the interaction between the structure's dynamics and the resonator's properties, including the applied voltage.

$$\frac{Z_m(s)}{Q_{b_m}(s)} = \frac{1}{s^2\left(1 + \frac{\mu(2\zeta_r \omega_r s + \omega_r^2)}{s^2 + 2\zeta_r \omega_r s + \omega_r^2\left(1 + \frac{v_a}{s}\right)}\right) + 2\zeta_m \omega_m s + \omega_m^2}, \quad m = 1, 2, \ldots, N_m \tag{8}$$

Here, $Z_m(s)$ and $Q_{b_m}(s)$ represent the Laplace transforms of the displacement response and the external force applied to the m-th mode, respectively. ω_r and ω_m are the natural frequencies of the resonator and the m-th mode of the structure. The damping ratios, ζ_r for the resonator and ζ_m for the structure's mode, describe the rate of oscillation decay due to damping. v_a is the voltage applied to the piezoelectric elements, influencing the system's response. N_m indicates the number of modes in the analysis.

4. STABILITY ANALYSIS

The theoretical framework for the stability analysis of a piezoelectrically actuated metamaterial beam is rooted in a distributed parameter model and modal analysis. These models illuminate the system's natural frequencies and mode shapes, crucial for evaluating dynamic manipulation and potential bandgaps. The stability is assessed by the poles' locations of Eq. (8) in the complex plane, with stability indicated by poles residing in the left-half plane.

Root locus analysis is used to visualize how the poles shift with varying applied voltages v_a, offering a graphical perspective of stability regions against the control parameter changes. This analysis becomes particularly significant when examining the effects of piezoelectric actuation meant to counteract damping. The introduction of an additional s term in the transfer function's denominator, indicative of a new pole, poses a critical inquiry into whether such compensation might inadvertently lead to instability. Further, a specific stability criterion is set where the system is considered stable if the weighted average of the real parts of the poles is less than the threshold of $w_a(L)/w_b = 0.1$. This benchmark, both theoretical and empirical, allows for a pragmatic assessment of stability, taking into account the practical operational limits.

The methodological framework outlined in this study serves as the foundation for the subsequent numerical simulations aimed at exploring the stability characteristics of the metamaterial beam under various actuation strategies. The outcomes of this theoretical analysis will inform the design decisions and operational procedures to ensure that the system can achieve the desired dynamic behavior without succumbing to instability.

5. RESULTS AND DISCUSSION

This section presents a numerical analysis using defined geometric and material properties of a rectangular beam, detailed in Table 1. This table provides the parameters for the simulations and calculations, offering a precise depiction of the beam's properties for the study.

Table 1. Geometric and material properties of the studied rectangular aluminum beam

Parameter	Value	Parameter	Value
L_m	0.3 m	m_r	17 g
w_m	40 mm	k_r	9 kN/m
h_m	3 mm	ζ_r	0.01
ρ_m	2700 kg/m^3	N_m	8
E_m	69.5 GP	N_r	8
ζ_m	0.01		

The root locus plot in Fig. 2 demonstrates the stability of a flexible structure with varying modes. It illustrates the pole trajectories for a system considering one mode versus eight modes. As the plot shows, including more modes in the analysis captures a more complex stability behavior, indicated by the poles' paths moving into the left-half plane, which suggests increased stability. This highlights the critical importance of accounting for multiple modes in flexible structures to ensure a robust stability analysis and accurate prediction of the system's dynamic response. Neglecting higher modes could omit essential details, potentially compromising the effectiveness of stability enhancement strategies like the implementation of deep bandgaps with controlled damping.

The root locus plot depicted in Fig. 3 provides insight into the dynamic stability of a metamaterial beam with piezoelectric actuators. As shown, varying the applied voltage v_p alters the pole positions within the system, which can lead to instability. The plot reveals that the system's poles respond differently to changes in v_p, with some poles moving toward the instability region (the right-half of the s-plane) as v_p increases. This differential responsiveness underscores the nuanced control that piezoelectric actuation can exert on the system.

By finely adjusting v_p, it is possible to tune the dynamic stability of the beam, which is a critical aspect of enhancing the performance of metamaterials. The ability to control stability through piezoelectric actuation is particularly valuable in applications where material properties must be precisely managed to achieve desired dynamic behavior. Conversely, if the approach involves using piezoelectric actuators to offset the damping effect

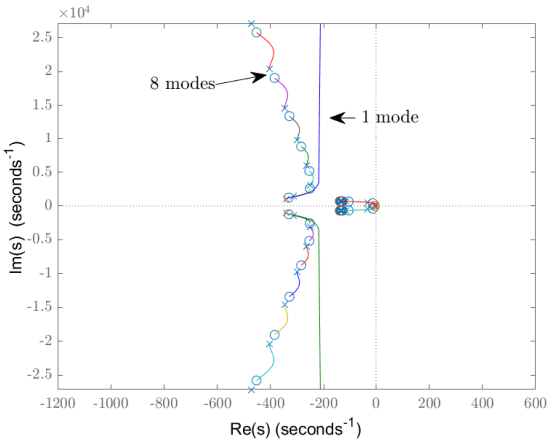

Figure 2. Root locus plot illustrating the pole trajectories for one mode versus eight modes in a piezoelectrically actuated metamaterial beam, highlighting the impact of mode inclusion on system stability. The sourced parameters from Table 1.

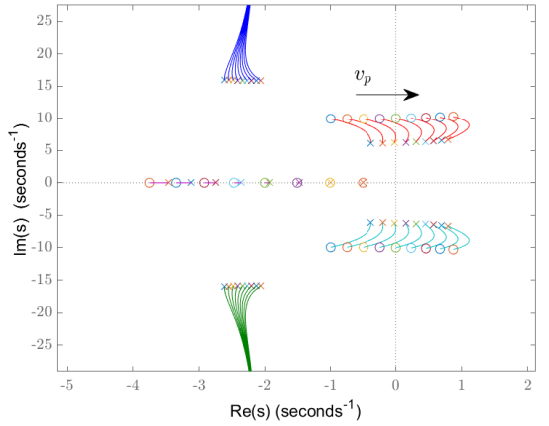

Figure 3. Root locus plot demonstrating the stabilization effect of increasing piezoelectric actuation voltage v_p on stability of metamaterial beam system. System parameters include a mass ratio $\mu = 1$, resonator damping ratio $\zeta_r = 0.1$, resonator natural frequency $\omega_r = 10$, structural damping ratio $\zeta_m = 0.1$, and the first structural natural frequency $\omega_{m_1} = 10$. The plot traces the pole movement across modes, showing enhanced stability with higher v_p, pertinent to the precise dynamic control of metamaterials.

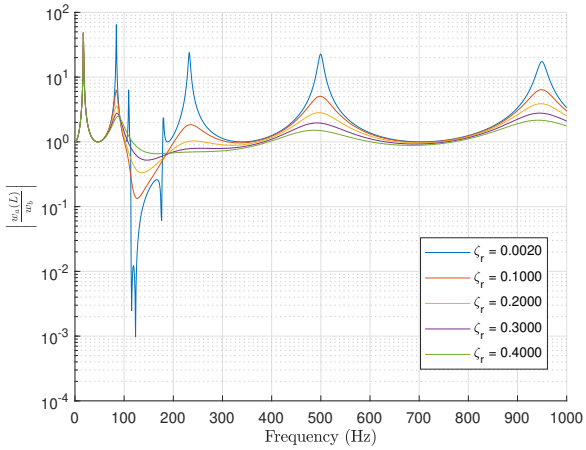

Figure 4. This figure illustrates the effect of varying resonator damping ratios ζ_r on the bandgap properties of the metastructure, considering a constant metamaterial damping ratio of $\zeta_m = 0.01$ in the frequency response analysis. The sourced parameters from Table 1.

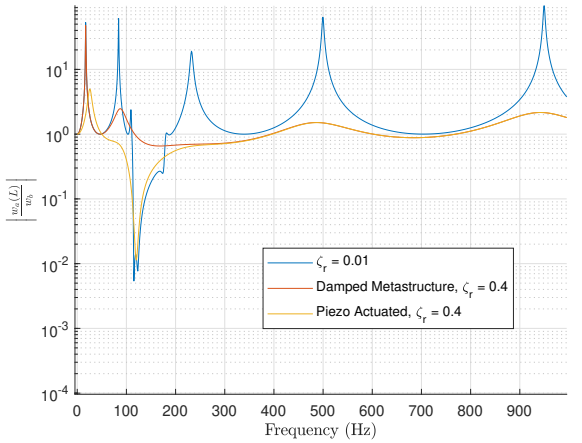

Figure 5. This figure illustrates the effect of varying resonator damping ratios ζ_r on the bandgap properties of the metastructure, considering a constant metamaterial damping ratio of $\zeta_m = 0.01$ in the frequency response analysis. The sourced parameters from Table 1.

and thus deepen the bandgap, the figure reveals that such use of piezoelectric actuators to counterbalance the damping in a metamaterial beam might result in instability. This is shown in Fig. 4, where it's clear that altering the resonator's structural damping significantly influences the behavior of the bandgap.

Fig. 5 graphically demonstrates the impact of high damping $\zeta_r = 0.4$ in a practical application, where it significantly diminishes the amplitude of vibrations across the frequency spectrum and effectively suppresses resonant peaks. When piezoelectric actuation is applied in conjunction with this high damping rate, there is a notable further reduction in peak amplitudes. Importantly, it also compensates for the reduced bandgap effect caused by increased damping and modifies the resonant frequencies, showcasing the capacity for active vibration

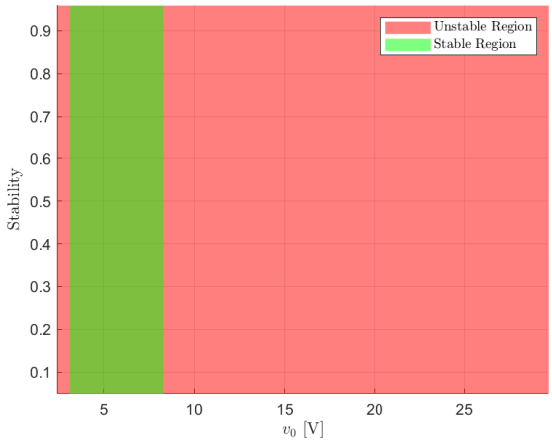

Figure 6. Stability landscape of a metamaterial beam with piezoelectric actuation, showcasing the stable (green) and unstable (red) voltage regions. Stability is quantified by the defined threshold, for balancing piezoelectric damping compensation and maintaining system stability

control. This comparative analysis confirms that piezoelectric actuation not only surpasses passive damping in vibration reduction but also implies that it can adjust the system's dynamic properties, such as stiffness or mass distribution. Consequently, the utilization of piezoelectric actuators in metamaterial beams is a promising strategy for vibration isolation and noise reduction, offering a dynamically tunable solution to control undesirable vibrations.

The chart in Fig. 6 depicts how the stability of a metamaterial beam responds to different applied voltages to piezoelectric actuators. Stability is defined by the weighted average of the pole real parts, with a threshold set at $w_a(L)/w_b = 0.1$. The green area represents stable voltage levels, while the red indicates voltages that cause instability. Maintaining applied voltage within the green region is essential to ensure stable operation while enhancing the bandgap depth using piezoelectric damping.

Fig. 7 illustrates the relationship between the cost function and the applied voltage v_0 in a piezoelectrically actuated system. It shows a rapid decline in cost as v_0 increases, which then levels off, indicating an optimal voltage range for system operation. This data is critical for determining the most efficient voltage for system performance, highlighting the effectiveness of piezoelectric actuation within a specific voltage range.

The 3D plot in Fig. 8 illustrates the effect of the applied voltage v_0 on the transmittance response of a metamaterial beam's tip displacement with length L to the base excitation displacement over a range of frequencies. The plot's valley depth signifies a pronounced attenuation, indicating the optimization of v_0 enhances the bandgap due to compensated damping effects in the presence of over-damping. The response surface reveals that v_0 not only modulates the bandgap's depth but also its frequency position, which is critical for applications that require precise control of vibrational characteristics.

Fig. 9 illustrates the variation in the maximum ratio of tip displacement $w_a(L)$ to base excitation displacement w_b as a function of applied voltage v_0. The plot shows a notable decrease in the displacement ratio when v_0 rises from 0 to about 5 volts, indicating a significant improvement in the beam's response, likely due to the influence of actuation on the system dynamics. Beyond 5 volts, the ratio levels off and increases gradually, implying limited benefits from further voltage increases. This behavior aids in determining the optimal operational voltage range where the piezoelectric actuation has the most significant impact on the beam's vibrational characteristics. The sharp peaks indicate resonant frequencies where the system's response is highly sensitive to changes in v_0. In practice, such a plot is essential for system designers to set appropriate actuation voltages that balance

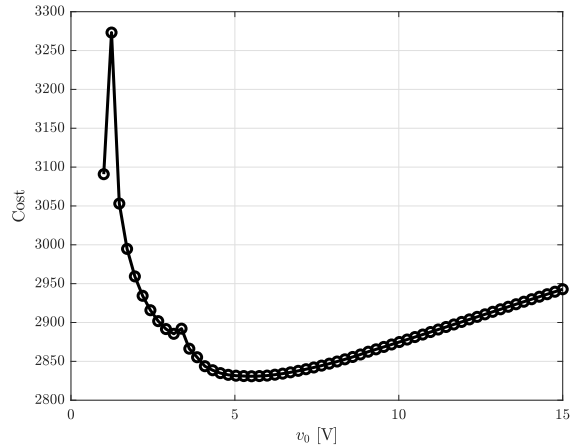

Figure 7. The cost function's variation with applied voltage v_0, displaying a sharp decrease and subsequent stabilization. This identifies an optimal voltage range for the piezoelectric actuation system, beyond which no significant cost benefit is observed.

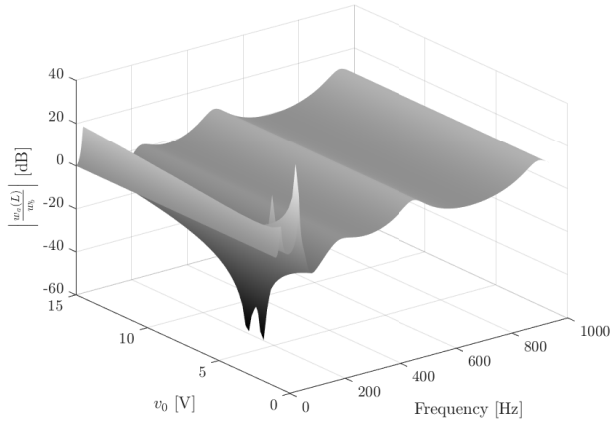

Figure 8. Transmittance response of the beam's tip displacement to base excitation across frequencies, depicting the effect of applied voltage v_0. The pronounced valley indicates an optimized bandgap within the structure, adjusted by v_0 to mitigate overdamping effects. This plot is key for identifying optimal v_0 settings to control the metamaterial's vibrational characteristics effectively.

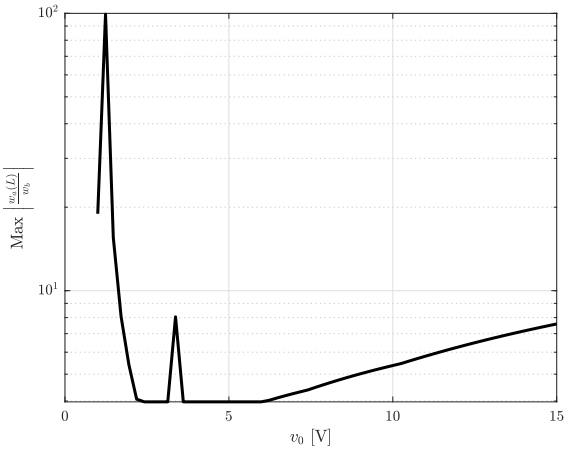

Figure 9. Variation of maximum $|w_a(L)/w_b|$ with applied voltage v_0, highlighting resonant frequencies and the impact of piezoelectric actuation on the beam's vibrational response.

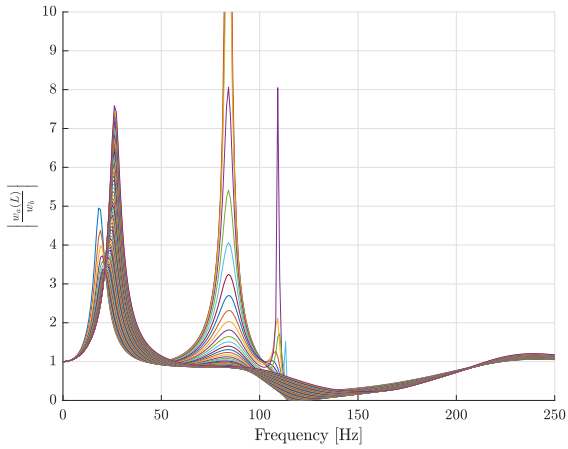

Figure 10. Transmittance variation with frequency for different applied voltages v_0 on a piezoelectrically actuated damped system, illustrating the modulation of resonant peaks and the adjustment of bandgap frequencies due to piezoelectric effects.

performance with energy efficiency and ensure the structural integrity of the beam under dynamic loading conditions.

Fig. 10 shows transmittance responses for varying applied voltages v_0, demonstrating the tunability of the system's resonant frequencies. The curves shift in response to different v_0 levels, which is indicative of the piezoelectric effect's impact on the damped system. Such control is essential for optimizing dynamic behaviors like vibration suppression and bandgap frequency adjustments. The visualization captures the nuanced influence of voltage on the system's ability to manage and refine the depth of its bandgap in response to external damping forces.

6. CONCLUSION

This research investigated the dynamic stability of a metamaterial beam system with integrated piezoelectric actuators, designed to compensate for the structural damping of resonators. Central to this investigation was the implementation of piezoelectric actuation as a means to counteract damping effects, represented by the introduction of an additional pole term in the denominator of the system's transfer function (Eq. (8)).

The study's findings indicate that while piezoelectric actuation can effectively compensate for damping and enhance the system's performance, it introduces a complexity that can lead to instability. The root locus analyses provided a clear depiction of how the system's poles migrate with varying applied voltage v_a, highlighting the delicate balance between achieving desired damping compensation and maintaining system stability.

Through numerical simulations, we delineated the stability regions, revealing that there is an optimal range of applied voltages within which the system can operate stably while benefiting from the damping compensation provided by the piezoelectric actuators. However, surpassing this range may lead to instability, as evidenced by the poles' transition across the critical boundary in the complex plane.

In conclusion, the study confirms that piezoelectric actuation, when carefully applied, is a potent tool for managing the dynamic response of metamaterial beams. The critical contribution of this work lies in the identification of stability thresholds for applied voltages, enabling the use of piezoelectric actuators to control damping without compromising the system's stability.

Acknowledgments

This paper is supported by the European Union's HORIZON Research and Innovation Programme under grant agreement No 101120657, project ENFIELD (European Lighthouse to Manifest Trustworthy and Green AI). It was also supported by the Estonian Research Council grant PRG658.

REFERENCES

[1] Cummer, S. A., Christensen, J., and Alù, A., "Controlling sound with acoustic metamaterials," *Nature Reviews Materials* **1**(3), 1–13 (2016).

[2] Smith, D. R., Pendry, J. B., and Wiltshire, M. C., "Metamaterials and negative refractive index," *science* **305**(5685), 788–792 (2004).

[3] Erturk, A. and Inman, D. J., [*Piezoelectric energy harvesting*], John Wiley & Sons (2011).

[4] Sirohi, J. and Chopra, I., "Fundamental understanding of piezoelectric strain sensors," *Journal of intelligent material systems and structures* **11**(4), 246–257 (2000).

[5] Li, F., Zhang, C., and Liu, C., "Active tuning of vibration and wave propagation in elastic beams with periodically placed piezoelectric actuator/sensor pairs," *Journal of Sound and Vibration* **393**, 14–29 (2017).

[6] Saravana Jothi, N. and Hunt, A., "Active mechanical metamaterial with embedded piezoelectric actuation," *APL Materials* **10**(9) (2022).

[7] Mead, D., "Leonard meirovitch, elements of vibration analysis , mcgraw-hill book company, new york (1986).," *Journal of Sound Vibration* **117**(3), 603–604 (1987).

Appendix 8

Hossein Alimohammadi et al. “Exploring Internally Coupled Resonator’s Dynamics and Spatial Variability in Metamaterials for Vibration Suppression”. In: *Active and Passive Smart Structures and Integrated Systems XVIII* (2024)

Exploring Internally Coupled Resonator's Dynamics and Spatial Variability in Metamaterials for Vibration Suppression

H. Alimohammadi[a], K. Vassiljeva[b], S. H. HosseinNia[b], and E. Petlenkov[a]

[a]Department of Computer Systems, Tallinn University of Technology, Tallinn, Estonia
[b]Department of Precision and Microsystems Engineering, Delft University of Technology, Delft, The Netherlands

ABSTRACT

Metamaterials have marked notable advancements in vibration damping and energy harvesting. However, the specific impact of internal coupled resonators, encompassing both linear and nonlinear types, has received limited attention from researchers. This study aims to delve into this underexplored area. Utilizing a distributed parameter model grounded in modal analysis, our research investigates the effects of these coupled resonators on metamaterial functionality. We particularly emphasize the influence of varying the position of attached masses and its consequent impact on the bandgap properties. Through developing theoretical and mathematical models for metastructural beams with internally coupled resonators, our approach facilitates future simulations and analyses. This investigation not only provides pivotal insights for the design and optimization of metamaterials but also underscores the possible potential of manipulating resonator properties to broaden their practical applications.

Keywords: Distributed parameter model, Modal analysis, Nonlinear internally coupling, Spatial variation

1. INTRODUCTION

Locally resonant metamaterials are engineered materials designed with unique vibrational properties that allow them to selectively amplify or dampen mechanical waves within certain frequency ranges. Through the strategic arrangement and geometry of resonators within these materials, they can control wave propagation, enabling effects such as wave trapping, vibration isolation, and wave guiding. These materials are applied in various fields, including acoustic and vibration control, energy harvesting, and advanced sensing technologies. A key feature of locally resonant metamaterials is their ability to create low-frequency bandgaps, where wave propagation is blocked, differentiating them from phononic crystals that use Bragg scattering for this purpose. This characteristic makes them particularly valuable for research in vibration attenuation and offers a broad spectrum of potential applications in related fields.

In the field of locally resonant metastructures, various methods have been identified to expand bandgaps, such as utilizing multiple periodic arrays, employing multi-degree-of-freedom local resonators, and integrating Bragg-type with resonance-type bandgaps. Techniques like internal coupling between resonators, quasi-periodic arrangements, and leveraging smart materials and actuators are underscored for their contributions to enhanced vibrational control.

The study of transverse vibrations in cantilever beams, as presented by Frank Pai et al.,[1] underlines the advantages of multi-frequency vibration absorbers in establishing effective stopbands for wave absorption. This research emphasizes the critical role of boundary conditions and the distribution of absorbers, especially significant at low frequencies.

The inclusion of mass within a system is identified as beneficial for enhancing damping, vibration control, and structural stability. The investigation conducted by Skoblar et al.[2] focuses on the effects of additional mass

Further author information: (Send correspondence to E. Petlenkov)
E. Petlenkov: E-mail: eduard.petlenkov@taltech.ee, Telephone: 1 234 567 890

Active and Passive Smart Structures and Integrated Systems XVIII, edited by Serife Tol, Guoliang Huang, Xiaopeng Li, Mostafa A. Nouh, Shima Shahab, Jinkyu Yang, Proc. of SPIE Vol. 12946, 1294614 · © 2024 SPIE · 0277-786X · doi: 10.1117/12.3024067

on the dynamic response of cantilever beams, providing insights into the vibration characteristics and overall system behavior. Piezoelectric materials' capability for energy conversion is exploited in adjusting the resonant frequency of cantilever beams, with Yuejuan Li et al.[3] offering a methodology for modifying frequency sensitivity through the strategic placement of attached masses. Magnetic actuators are highlighted for their broad frequency range and robustness. Hyunseok Song et al.[4] introduce a magneto-mechano-electric generator that features self-resonance tunability, illustrating its use in consistently powering IoT sensor systems in variable conditions. The formulation of a general mathematical model for analyzing locally resonant metastructures by Sugino et al.[5] establishes a systematic approach for predicting structure behavior and facilitating design optimization, with a particular emphasis on modal analysis to delineate bandgap properties.

The exploration of metastructures with internal coupling and nonlinear resonators is motivated by their potential to improve bandgap formation and vibration suppression. Research by Hu et al.[6] and Xia et al.[7] delves into novel designs for energy harvesting and vibration attenuation, highlighting the efficacy of alternate coupling mechanisms and the influence of excitation intensity on vibrational modes.

1.1 Internally coupled resonators

The subsection on internally coupled resonators delves into the advancements in metamaterial beam designs that significantly enhance energy harvesting capabilities in the low-frequency range while also marginally improving vibration suppression through the introduction of an additional band gap. Bao et al.[8] explored the enhancement of vibration suppression performance in the low-frequency region by using a locally resonant metamaterial beam coupled with horizontal springs. Their findings indicate that variables such as the number of units, damping ratio, mass, and stiffness critically influence the bandgap, leading to improved vibration suppression in locally resonant metamaterial beams.

Moreover, Hu et al.[6] introduced a modified metamaterial beam designed for dual purposes: vibration suppression and energy harvesting. This design features local resonators that are alternately coupled, with each resonator equipped with a piezoelectric element to convert vibrations into electrical energy. Furthermore, Oyelade and Oladimeji[9] presented an innovative metamaterial with a multiresonator mass-in-mass lattice system, where inner masses are interconnected by a linear spring. Their research highlighted the critical role of the additional spring and mass ratio in creating two extra bandgaps, showcasing a significant advancement over traditional multiresonator lattice systems.

Despite these developments, there has been limited research on the effects of nonlinear coupling between internal resonators within metamaterials. While comprehensive reviews like Patil et al.[10] have investigated various nonlinear characteristics of metamaterials and metastructures, there remains a gap in the focused study of nonlinear internal coupling and its potential impacts on metamaterial performance.

This study aims to bridge a significant gap in metamaterial research by focusing on the effects of nonlinear coupling between internal resonators, a topic largely overlooked despite its potential to enhance system dynamics and application efficiency. Nonlinear behaviors, intrinsic to most physical systems, can lead to improved vibration control and energy harvesting mechanisms, yet their impact remains underexplored. By investigating both linear and nonlinear internal coupling, this research seeks to uncover new insights into resonator behavior, potentially advancing metamaterial design and functionality.

Additionally, the study addresses the minimal investigation into how spatial variations in resonator properties, such as changes in attached mass positions on beam-type resonators, affect natural frequencies and bandgap characteristics. Exploring these aspects could offer novel tuning methods, optimize performance, and broaden metamaterial applications, marking a pivotal step toward mitigating production tolerances and enhancing material versatility.

2. DISTRIBUTED PARAMETER MODEL USING MODAL ANALYSIS

The section discusses the utilization of modal analysis in the design and optimization of mechanical locally resonant metastructures. Modal analysis is essential for identifying vibration characteristics such as natural frequencies, mode shapes, and modal damping ratios, enabling the creation of metastructures tailored for specific

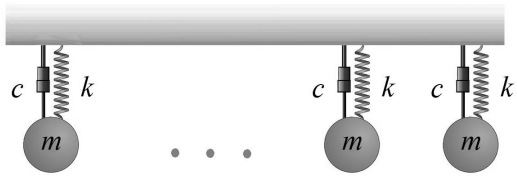

Figure 1. Example of locally resonant metastructures

wave propagation behaviors. Unlike lumped parameter models that use ordinary differential equations, distributed parameter models employ partial differential equations (PDEs) to account for the spatial distribution of physical properties within the material or structure. These models are crucial for systems where dimensions match or exceed the wavelength of wave propagation, offering insights into phenomena where spatial variations significantly influence behavior, including wave propagation, heat transfer, and fluid dynamics. Through modal analysis and the frequency determinant method, analytical models are derived to understand the dynamics of systems under base excitation and external forces, as illustrated by a typical distributed model.

Let's explore a standard distributed model that governs the oscillations of a system subjected to base excitation and external forces (refer to Figure 1). This model is formulated as a partial differential equation, drawing upon principles from Newtonian mechanics and classical references on vibration analysis.

$$\mathcal{L}w(x,t) + \mathcal{C}\frac{\partial w(x,t)}{\partial t} + \mathcal{M}\frac{\partial^2 w(x,t)}{\partial t^2} - \sum_{r=1}^{N_r}\left(k_r u_r(t) + c_r\frac{du_r(t)}{dt}\right)\delta\left(x - x_r\right) = \mathcal{F}_{b_m}(x,t) \tag{1}$$

with associated equations for the resonators:

$$m_r\frac{\partial^2 u_r(t)}{\partial t^2} + c_r\frac{\partial u_r(t)}{\partial t} + k_r u_r(t) + m_r\frac{\partial^2 w\left(x_r,t\right)}{\partial t^2} = \mathcal{F}_{b_r}(t) \tag{2}$$

The operators $\mathcal{L}, \mathcal{C}$, and $\mathcal{M}$ in the equations represent the flexural rigidity, damping, and mass distribution of the system. The main structure's transverse vibrations and those of individual resonators are denoted by $w(x,t)$ and $u_r(t)$, respectively, while $\delta\left(x - x_r\right)$ indicates the resonators' locations. N_r is the number of resonators, m_r their mass, k_r the stiffness, and c_r the damping coefficient. The mode and resonator external force is denoted by $\mathcal{F}_{b_{m,r}}(t)$, which is distributed over D, and the effects of the base excitation on which the beam is supported.

The boundary conditions corresponding to Eq. (1) can be expressed as

$$\mathcal{B}_i[w(x,t)] = 0, \quad i = 1, 2, \ldots, p \tag{3}$$

where $\mathcal{B}_i$ is a linear homogeneous differential operator of the order less than or equal to $2p-1$.

In many real-world structures, the concept of proportional damping often provides sufficient accuracy for estimating the natural frequencies and mode shapes of these structures.[11] Proportional damping is a distinctive kind of damping where the damping matrix is directly related to the mass and stiffness matrices. Under the assumption of proportional damping, $\mathcal{C}$ can be depicted as a blend of the mass and stiffness operators, denoted as $\mathcal{L}$ and $\mathcal{M}$.

$$\mathcal{C} = c_1\mathcal{L} + c_2\mathcal{M} \tag{4}$$

Here, c_1 and c_2 are non-negative constants determined by the physical properties of the system or through an engineering approach involving modal analysis experiments and data fitting. A benefit of employing proportional damping is the consistent mode shapes (eigenfunctions) for both the damped and undamped scenarios, and the

natural frequencies (eigenvalues) remain nearly identical.[11] As a result, the eigenfunctions $\phi_m(x)$ can be derived by solving the eigenvalue problem associated with the undamped version of Eq. (1).

$$\mathcal{L}\left[\phi_m(x)\right] = \lambda_m \mathcal{M}\left[\phi_m(x)\right], \quad m = 1, 2, ..., N_m \tag{5}$$

For a flexible structure (like a beam) with a set of resonators, the system would indeed be described by a set of coupled differential equations: one for each resonator and the flexible structure itself. Each of these components contributes to the overall dynamic behavior of the system, and they can influence each other. Since the force exerted by the resonators depends on the displacement of the structure, the mode shapes of the original structure without resonators are no longer the exact mode shapes of the full metastructure. Nevertheless, an expansion using the mode shapes of the plain structure provides significant simplification.

In the context of an Euler beam, the domain $D = [0, L]$, where the beam is assumed to be linearly elastic and homogeneous, the operators $\mathcal{L}$ and $\mathcal{M}$ can be defined as follows:

$$\mathcal{L} = EI\frac{\partial^4}{\partial x^4}, \quad \mathcal{M} = \rho A, \quad \mathcal{C} = c, \quad \mathcal{B}_1 = 1, \quad \mathcal{B}_2 = EI\frac{\partial^2}{\partial x^2}, \tag{6}$$

where EI is flexural rigidity of the beam, which is the product of Young's modulus E and the second moment of area I. ρ is the density of the beam material. A is the cross-sectional area of the beam.

Employing the modal expansion method, it becomes necessary for the eigenfunctions to be orthogonal to serve as the basis function for determining the solution of Eq. (1). In order to formalize the overarching principle of orthogonality, the self-adjoint (Hermitian) eigenvalue problem is outlined. For any two arbitrary eigenfunctions $\phi_m(x)$ and $\phi_n(x)$ within a one-dimensional domain, the eigenvalue problem is deemed to be self-adjoint if the following criterion is satisfied:[12]

$$\int_D \phi_m(x)\mathcal{L}\left[\phi_n(x)\right] dx = \int_D \phi_n(x)\mathcal{L}\left[\phi_m(x)\right] dx \tag{7}$$

and

$$\int_D \phi_m(x)\mathcal{M}\left[\phi_n(x)\right] dx = \int_D \phi_n(x)\mathcal{M}\left[\phi_m(x)\right] dx. \tag{8}$$

Let us now consider ω_m^2 and ω_n^2 as two unique eigenvalues with their corresponding eigenfunctions $\phi_m(x)$ and $\phi_n(x)$, these being the result of solving the self-adjoint eigenvalue problem. For convenience, the eigenfunctions are generally normalized with respect to $\mathcal{M}$. Consequently, the generalized condition of the orthogonality equation can be established.

$$\int_D \phi_m(x)\mathcal{M}\left[\phi_n(x)\right] dx = \delta_{mn} \tag{9}$$

and

$$\int_D \phi_m(x)\mathcal{L}\left[\phi_n(x)\right] dx = \delta_{mn}\omega_m^2 \tag{10}$$

Here, δ_{mn} is recognized as the Kronecker delta function, which yields a value of 1 when $m = n$, and maintains a value of zero in all other situations.

Under the assumption of proportional damping, the following equation is obtained:

$$\int_D \phi_m(x)\mathcal{C}\left[w_m(x)\right] dx = c_1\delta_{mn}\omega_m^2 + c_2\delta_{mn} \tag{11}$$

which can be reformulated to yield:

$$\int_D \phi_m(x)\mathcal{C}\left[w_m(x)\right] dx = \delta_{mn}2\zeta_m\omega_m \tag{12}$$

with

$$\zeta_m = \frac{1}{2\omega_m}\left(c_1\omega_m^2 + c_2\right) \tag{13}$$

Here, ζ_m denotes the damping ratio of m-th mode, and c_1 and c_2 are non-negative constants. Eq. (9) through to Eq. (12) constitute a set of orthonormal eigenfunctions. These eigenfunctions serve as a comprehensive basis that encapsulates the entire solution space of the eigenvalue problem.

In cases where the domain D is two-dimensional, it is often more straightforward to separate the modal summation into individual summations over the two modal indices. However, it is always feasible to re-frame the double summation as a single summation over all possible combinations of the two indices. This technique, widely used in modal analysis, produces convergent solutions to the boundary value problem as formulated. The effectiveness of these solutions, undoubtedly, depends on the assumptions made during the formulation of the boundary value problem. For example, the Euler-Bernoulli beam theory might not yield accurate results at high frequencies. Furthermore, the existence of resonators in the structure creates discontinuities in the internal forces, making it necessary to use a large number of modes as a general guideline.

Using modal decomposition, the beam's deflection in the domain D is expressed as a sum of modal shapes in one direction. This assumes that the behavior of the beam can be accurately represented by a finite number of modes:

$$w(x,t) = \sum_{m=1}^{N_m} \phi_m(x) z_m(t), \tag{14}$$

where $\phi_m(x)$ represents the spatial mode shape and $z_m(t)$ represents the time-dependent modal coordinate of the $m-th$ mode of the plain. These equations are to be PDEs that are used to model the dynamics of a flexible beam system integrated with discrete resonators.

Substituting the modal expansion Eq. (14) into Eq. (1), yields to:

$$\begin{aligned} &\mathcal{L}\sum_{m=1}^{N_m}\phi_m(x)z_m(t) + \mathcal{C}\frac{\partial}{\partial t}\sum_{m=1}^{N_m}\phi_m(x)z_m(t) + \mathcal{M}\frac{\partial^2}{\partial t^2}\sum_{m=1}^{N_m}\phi_m(x)z_m(t) \\ &\quad - \sum_{r=1}^{N_r}\left(k_r u_r(t) + c_r\frac{du_r(t)}{dt}\right)\delta\left(x - x_r\right) = \mathcal{F}_{b_m}(x,t) \end{aligned} \tag{15}$$

Multiplying Eq. (15) by $\phi_n(x)$ and integrating over the domain D, and applying the orthogonality conditions Eq. (9) to Eq. (13) of the mode shapes gives

$$\ddot{z}_m(t) + 2\zeta_m\omega_m\dot{z}_m(t) + \omega_m^2 z_m(t) - \sum_{r=1}^{N_r} m_r\omega_r^2 u_r(t)\phi_m\left(x_r\right) = \mathcal{Q}_{b_m}(x,t), \quad m = 1,2,\ldots,N_m \tag{16}$$

Similarly for resonators, substituting the modal expansion Eq. (14) into Eq. (2) yields to:

$$\ddot{u}_r(t) + 2\xi_r\omega_r\dot{u}_r(t) + \omega_r^2 u_r(t) + \sum_{m=1}^{N_m}\ddot{z}_m(t)\phi_m\left(x_r\right) = \mathcal{Q}_{b_r}(t), \quad r = 1,2,\ldots,N_r \tag{17}$$

For ease of representation, the superscript *dot* denotes the derivative with respect to time, while the superscript *prime* signifies the derivative with respect to spatial location. Each equation characterizes the dynamics of the corresponding modal coordinate or resonator displacement through a second-order ordinary differential equation. The motion is influenced by the modal or resonator parameters (natural frequencies ω_m and ω_r, damping ratios

ζ_m and ζ_r), the interaction between the beam modes and resonators, and the effective forces due to base excitation ($\mathcal{Q}b_m$ and $\mathcal{Q}b_r$).

The accomplishment of decoupling can be attained by executing an orthogonal transformation, which comprises pre- and post-multiplication of the mode shape matrix. This transformation process results in the diagonalization of the mass and stiffness matrices, as the eigenvectors are orthogonal to both matrices. As a consequence, a set of decoupled ordinary differential equations is derived. The normal mode method is applicable only when there is no damping or when the damping matrix is proportional, as previously assumed, implying it can be presented as a linear combination of the mass and stiffness matrices. The practice of pre- and post-multiplying the mode shape matrix with the mass and stiffness matrices is often referred to as an orthogonal transformation. When the mode shape is normalized to the mass matrix, this transformation is known as an orthonormal transformation.

By merging the basic structure depicted in Eq. (16) and the resonators represented in Eq. (17), the inertial terms of the system can be coupled, the stiffness can be decoupled, which enables further examination of the system in the frequency domain. This integration process leads to :

$$\begin{aligned}\ddot{z}_m(t) + 2\zeta_m\omega_m\dot{z}_m(t) + \omega_m^2 z_m(t) + \sum_{r=1}^{N_r} m_r\phi_m(x_r)\sum_{p=1}^{N_m}\ddot{z}_m(t)\phi_p(x_r) + \\ \sum_{r=1}^{N_r} m_r\ddot{u}_r(t)\phi_m(x_r) + 2\sum_{r=1}^{N_r} m_r\phi_m(x_r)\zeta_r\omega_r\dot{u}_r(t) = \mathcal{H}_{b_m}(x,t), \quad m = 1,2,\ldots,N_m\end{aligned} \tag{18}$$

where

$$\mathcal{H}_{b_m}(x,t) = \int_0^L \mathcal{F}_e(x,t)\phi_m(x)dx - \ddot{w}_b(t)\left(\int_0^L \mathcal{M}\phi_m(x)dx + \sum_{r=1}^{N_r} m_r\phi_m(x_r)\right) - \dot{w}_b(t)\int_0^L \mathcal{C}\phi_m(x)dx \tag{19}$$

Eqs. (17) and (18) represent a set of $N_m + N_r$ coupled second-order linear ordinary differential equations. The simultaneous solution of these equations enables the estimation of the mode shapes and resonant frequencies of the complete system, as well as the analysis of its steady-state response to harmonic excitation.

Laplace Transform facilitates the system's analysis in the frequency domain, which often proves simpler to handle algebraically than the original time-domain equations. Therefore, applying the Laplace Transform to Eqs. (17) and (18), under the assumption of zero initial conditions, results in:

$$U_r(s) = \frac{\mathcal{Q}_{b_r}(s) - \sum_{m=1}^{N_m} s^2 Z_m(s)\phi_m(x_r)}{s^2 + 2\xi_r\omega_r s + \omega_r^2} \tag{20}$$

$$\begin{aligned}s^2 Z_m(s) + 2\zeta_m\omega_m s Z_m(s) + \omega_m^2 Z_m(s) + \sum_{r=1}^{N_r} m_r\phi_m(x_r)\sum_{p=1}^{N_m} s^2 Z_p(s)\phi_p(x_r) + \\ \sum_{r=1}^{N_r} m_r s^2 U_r(s)\phi_m(x_r) + 2\sum_{r=1}^{N_r} m_r\phi_m(x_r)\zeta_r\omega_r s U_r(s) = H_{b_m}(s), \quad m = 1,2,\ldots,N_m\end{aligned} \tag{21}$$

Here, $Z_m(s)$ and $U_r(s)$ symbolize the Laplace Transforms of the modal coordinates and the resonator displacements, respectively. For further analytical understanding, the Laplace Transform is applied to Eq. (17), following the assumptions made in:[5]

$$\sum_{r=1}^{N_r} m_r\phi_m(x_r)\phi_m(x_r) \approx \mu, \quad Q_{b_r}(s) = 0 \tag{22}$$

where μ represents the mass ratio, which is the sum of the resonators' mass to the mass of the plain beam. Applying these assumptions results in the following expression:

$$U_r(s) = -\frac{s^2}{s^2 + 2\zeta_r\omega_r s + \omega_r^2} \sum_{r=1}^{N_r} Z_m(s)\phi_m(x_r), \quad r = 1, 2, \ldots, N_r \tag{23}$$

Applying the Laplace transform to Eq. (16) and substituting from Eq. (23) gives the following result:

$$\frac{Z_m(s)}{Q_{b_m}(s)} = \frac{1}{s^2\left(1 + \frac{\mu\omega_r^2}{s^2+2\zeta_r\omega_r s+\omega_r^2}\right) + 2\zeta_m\omega_m s + \omega_m^2} \quad m = 1, 2, \ldots, N_m \tag{24}$$

Eq. (24) reveals that the presence of resonators brings about a frequency-dependent mass term. Assuming an infinite number of resonators, which results in continuous displacements throughout the space, similar simplifications can be made for the resonator displacements. Substituting Eq. (24) into Eq. (23) and replacing the discrete variable x_r with the continuous variable x, the following equation can be derived:

$$U_r(s) = -\frac{s^2}{s^2 + 2\zeta_r\omega_r s + \omega_r^2} \sum_{m=1}^{N_m} \phi_m(x_r) \frac{Q_{b_m}(s)}{s^2\left(1 + \frac{\mu\omega_r^2}{s^2+2\zeta_r\omega_r s+\omega_r^2}\right) + 2\zeta_m\omega_m s + \omega_m^2} \tag{25}$$

This provides a continuous equation for the motion $U_r(s)$ of the resonators along the beam, expressed in terms of the modal force inputs $Q_{b_m}(s)$.

The resonators' displacement can now be expressed as a linear combination of the plain structure's mode shapes in Laplace form:

$$U_r(s) = \sum_{m=1}^{N_m} \Psi_m(s)\phi_m(x) \tag{26}$$

Equation (26) can be associated with Eq. (25) by identifying the modal coordinates within the Laplace domain, given by $\Psi_m(s)$, as follows:

$$\frac{\Psi_m(s)}{Q_{b_m}(s)} = -\frac{s^2}{[s^2 + 2\zeta_r\omega_r s + \omega_r^2]\left[s^2\left(1 + \frac{\mu\omega_r^2}{s^2+2\zeta_r\omega_r s+\omega_r^2}\right) + 2\zeta_m\omega_m s + \omega_m^2\right]}, \quad m = 1, 2, \ldots, N_m \tag{27}$$

The transfer function depicted in Eq. (27) elucidates the relationship between the modal force $Q_{b_m}(s)$ and the modal coordinate $\Psi_m(s)$. It provides insight into the system's dynamics. The poles of this function, where the function's values reach their maximum, correspond to the system's resonant frequencies.

Investigating the system stability further, as outlined by Eq. (24), demands an exploration of the system poles. As shown in Figure 2, the impact of resonators and damping on the frequency response and stability of the system. The introduction of the resonator results in frequency splitting, manifesting as a distinct frequency bandgap in the Bode plot. The exhibited splitting, regardless of the system's damping characteristics, underscores the substantial impact of the resonators. They shape the system's behavior by engaging with the intrinsic dynamics of the beam, thereby underscoring the importance of considering resonator influence in the modeling and analysis of such systems. Damping emerges as a crucial element in ensuring system stability. In the absence of damping, poles reside on the imaginary axis or the right half of the complex plane, indicating marginal stability or instability. However, with the inclusion of damping, these poles effectively shift to the left half of the complex plane, denoting system stability as seen in Root Locus plot in Figure 2. This pivotal transition is evident in various analyses, such as the Lyapunov stability criterion, reinforcing the fundamental role of damping in stabilizing the system and optimizing its performance. Moreover, in the damped system, both the beam and

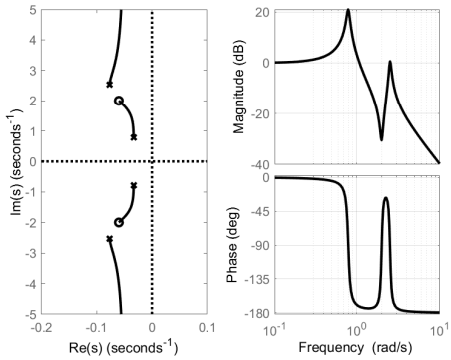

Figure 2. Root Locus and Bode plot analysis of Eq.(24) with parameters $\omega_m = 1$, $\omega_r = 2$, $\zeta_m = 0.05$, $\zeta_r = 0.03$, $\mu = 0.5$.

Figure 3. Locally resonant metastructures with internally coupled resonators

resonator's resonant frequencies are slightly lower than their undamped counterparts. This reduction in resonant frequencies results in smaller peaks in the frequency response, while damping also introduces a phase shift in the system's frequency response, further altering its characteristics. These effects underscore the importance of understanding and considering damping in system design and control strategies, as it not only ensures stability but also influences the magnitude and phase aspects of the system's response. It is clearly depicted from Root Locus in Figure 2 that there are no poles within the locally resonant bandgap zone, which falls within the frequency range of $\omega_r < \mathrm{Im}(s) < \omega_r\sqrt{1+\mu}$.

Further investigation of the effects of mass ratio, μ, and root locus interpretation of the bandgap, taking into account the neglect and exclusion of effects of base excitation on resonators (Q_{b_r}), and for undamped system can be found in the work by Sugino et al.[5]

3. INTERNALLY COUPLED RESONATORS MODELING

3.1 Linear system

By incorporating a linear coupling term, k_c, into the resonators depicted in Fig. 3, the system transforms into a connected duo of resonators. This alteration leads to a scenario where the movements of the resonators are intertwined rather than independent. In particular, the motion of one resonator directly affects the motion of its counterpart, fostering a dynamic interplay. The energy stemming from this coupling is captured by the coupling potential energy, where each resonator pair (1 and 2, 3 and 4, 5 and 6, etc.) constitutes a system characterized by two degrees of freedom.

$$V_c(t) = \frac{1}{2}k_c\left(u_{r_1}(t) - u_{r_2}(t) + w\left(x_{r_1}, t\right) - w\left(x_{r_2}, t\right)\right)^2 \tag{28}$$

The equations governing the coupled resonator system are derived as follows:

$$\ddot{z}_m(t) + 2\zeta_m\omega_m\dot{z}_m(t) + \omega_m^2 z_m(t) - \sum_{r=1}^{N_r/2}\left(m_{2r-1}\omega_{2r-1}^2 u_{2r-1}(t)\phi_m\left(x_{2r-1}\right) + m_{2r}\omega_{2r}^2 u_{2r}(t)\phi_m\left(x_{2r}\right)\right) = \mathcal{Q}_{b_m}, \quad m = 1, 2, \ldots, N_m, \text{ and } N_r \in 2\mathbb{N} \tag{29}$$

Meanwhile, the equation for the resonators is given by:

$$\ddot{u}_{2r-1}(t) + 2\xi_{2r-1}\omega_{2r-1}\dot{u}_{2r-1}(t) + \omega_{2r-1}^2 u_{2r-1}(t) + \sum_{m=1}^{N_m}\ddot{z}_m(t)\phi_m\left(x_{2r-1}\right) + \beta\frac{k_c}{m_{2r-1}} = \mathcal{Q}_{b_{2r-1}}, \quad r = 1, 2, \ldots, N_r/2 \tag{30}$$

$$\ddot{u}_{2r}(t) + 2\xi_{2r}\omega_{2r}\dot{u}_{2r}(t) + \omega_{2r}^2 u_{2r}(t) + \sum_{m=1}^{N_m}\ddot{z}_m(t)\phi_m\left(x_{2r}\right) - \beta\frac{k_c}{m_{2r}} = \mathcal{Q}_{b_{2r}}, \quad r = 1, 2, \ldots, N_r/2 \tag{31}$$

where

$$\beta = u_{2r-1}(t) - u_{2r}(t) + \sum_{m=1}^{N_m}\ddot{z}_m(t)\phi_m\left(x_{2r-1}\right) - \sum_{m=1}^{N_m}\ddot{z}_m(t)\phi_m\left(x_{2r}\right) \tag{32}$$

These equations delineate the fundamental dynamics of the beam along with the system of internally linearly coupled resonators.

3.2 Nonlinear system

In the case of a nonlinear coupling, the nature of interaction between the resonators becomes more intricate and more interesting dynamics can emerge. This nonlinearity could arise from various sources such as mechanical, magnetic, or electrical interactions. The equations governing the system behavior in this case would contain nonlinear terms and could potentially give rise to phenomena like bifurcations, chaos, or complex oscillatory behaviors. The analysis and understanding of such systems often requires advanced mathematical techniques and may involve numerical simulations. The exact form of the equations would depend on the specific form of nonlinearity in the coupling.

In the case of bistable nonlinearity (quadratic and quartic terms), the energy associated with this coupling can be formed as:

$$V_c(t) = \frac{1}{2}k_{c_1}\left(u_{r_1}(t) - u_{r_2}(t) + w(x_{r_1}, t) - w(x_{r_2}, t)\right)^2 + \frac{1}{4}k_{c_2}\left(u_{r_1}(t) - u_{r_2}(t) + w(x_{r_1}, t) - w(x_{r_2}, t)\right)^4 \tag{33}$$

The quadratic term represents the linear coupling between the resonators, while the quartic term introduces an additional nonlinearity that leads to bistability for negative k_{c_1}. The quartic term can create a double-well potential energy landscape, allowing for the presence of two stable equilibrium positions for the resonators. The dynamic of resonators forms to:

$$\ddot{u}_{2r-1}(t) + 2\xi_{2r-1}\omega_{2r-1}\dot{u}_{2r-1}(t) + \omega_{2r-1}^2 u_{2r-1}(t) + \sum_{m=1}^{N_m} \ddot{z}_m(t)\phi_m\left(x_{2r-1}\right) + \frac{k_{c_1}\beta}{m_{2r-1}} + \frac{k_{c_2}\beta^3}{m_{2r-1}} = \mathcal{Q}_{b_{2r-1}}, \quad r = 1, 2, \ldots, N_r/2 \tag{34}$$

$$\ddot{u}_{2r}(t) + 2\xi_{2r}\omega_{2r}\dot{u}_{2r}(t) + \omega_{2r}^2 u_{2r}(t) + \sum_{m=1}^{N_m} \ddot{z}_m(t)\phi_m\left(x_{2r}\right) - \frac{k_{c_1}\beta}{m_{2r}} - \frac{k_{c_2}\beta^3}{m_{2r}} = \mathcal{Q}_{b_{2r}}, \quad r = 1, 2, \ldots, N_r/2 \tag{35}$$

Equations (29) to (35) present a more comprehensive formulation that is compatible with the approach taken in[5] when neglecting the coupling effects, and damping of the structure and resonators. Moreover, this equation advances the previous work by incorporating a modal representation for both the structure and resonators, a detail overlooked in reference,[5] thereby providing a more complete representation of the system.

4. DISPERSION ANALYSIS AND MODEL VALIDATION OF INTERNALLY COUPLED RESONATORS BY PLANE WAVE EXPANSION METHOD

Linear system

The Plane Wave Expansion (PWE) method is commonly used for analyzing the propagation of waves in periodic structures, and provides valuable insights into the behavior of these waves, facilitating the design and optimization of these periodic structures for a wide range of applications, such as vibration suppression and energy harvesting.[13,14]

Let's define the transverse displacement of metastructure and resonators with linear internally coupled in absolute coordinate as $W_t(x,t) = \hat{W}_t e^{i(G_n x - \omega t)}$ for the beam, $z_{r_1}(t) = \hat{z}_{r_1} e^{i(\omega t)}$ for the first resonator, and $z_{r_2}(t) = \hat{z}_{r_2} e^{i(\omega t)}$ for the second resonator.

$$EIG_n^4 \hat{W}_t\left(G_n\right) - \rho A\omega^2 \hat{W}_t\left(G_n\right) + k_{r_1}\hat{W}_t\left(G_n\right) + k_{r_2}\hat{W}_t\left(G_n\right) - k_{r_1}\hat{z}_{r_1} - k_{r_2}\hat{z}_{r_2} = 0 \tag{36}$$

$$-k_{r_1}\hat{W}_t\left(G_n\right) + k_c\hat{z}_{r_1} - k_c\hat{z}_{r2} + k_{r_1}\hat{z}_{r_1} - m_{r_1}\omega^2\hat{z}_{r_1} = 0 \tag{37}$$

$$-k_{r_2}\hat{W}_t\left(G_n\right) - k_c\hat{z}_{r_1} + k_c\hat{z}_{r2} + k_{r_2}\hat{z}_{r_2} - m_{r_2}\omega^2\hat{z}_{r_2} = 0 \tag{38}$$

The equations capture the interactions within a metastructure, highlighting the dynamics between the main beam and resonators via coupling constants and mass effects, crucial for understanding wave propagation. The internal coupling term, k_c, is uniquely present in the resonators' equations, indicating that the coupling directly links the two resonators, rather than connecting them with the main beam. This setup points to a direct interaction between resonators, although it implies that forces resultant from this coupling can still transfer to the main beam, affecting its overall dynamics.

The dispersion relation is obtained by imposing periodic boundary conditions and seeking non-trivial solutions. In one-direction transformation the relation between the frequency ω and the wavevector G_n is achieved by multiplying the amplitude of the variable by a complex exponential function $\exp(i(G_n x - \omega t))$, which can be written in the form:

$$C_1\omega^6 + C_2\omega^4 + C_3\omega^2 + C_4 = 0 \tag{39}$$

where:

$$
\begin{aligned}
C_1 &= -Am_{r_1}m_{r_2}\rho, \\
C_2 &= m_{r_1}m_{r_2}\left(EIG_n^4 + k_{r_1} + k_{r_2}\right) + A\rho\left(m_{r_1} + m_{r_2}\right)k_c + A\rho m_{r_2}k_{r_1} + A\rho m_{r_1}k_{r_2}, \\
C_3 &= -\left(k_c\left(m_{r_1} + m_{r_2}\right)\left(k_{r_1} + k_{r_2}\right) + A\rho\left(k_{r_1}k_{r_2} + k_c\left(k_{r_1} + k_{r_2}\right)\right) + EIG_n^4 m_{r_1}m_{r_2}\left(k_c + k_{r_2} + k_{r_1}\right)\right), \\
C_4 &= EIG_n^4\left(k_c\left(k_{r_1} + k_{r_2}\right) + k_{r_1}k_{r_2}\right).
\end{aligned}
\tag{40}
$$

Nonlinear system

$$
EIG_n^4\hat{W}_t\left(G_n\right) - \rho A\omega^2\hat{W}_t\left(G_n\right) + k_{r_1}\hat{W}_t\left(G_n\right) + k_{r_2}\hat{W}_t\left(G_n\right) - k_{r_1}\hat{z}_{r_1} - k_{r_2}\hat{z}_{r_2} = 0 \tag{41}
$$

The first and second nonlinear internally coupled resonators are:

$$
-k_{r_1}\hat{W}_t\left(G_n\right) + k_{c_1}\hat{z}_{r_1} - k_{c_1}\hat{z}_{r_2} + k_{r_1}\hat{z}_{r_1} + k_{c_2}\hat{z}_{r_1}^3 - k_{c_2}\hat{z}_{r_2}^3 - m_{r_1}\omega^2\hat{z}_{r_1} + 3k_{c_2}\hat{z}_{r_1}\hat{z}_{r_2}^2 - 3k_{c_2}\hat{z}_{r_1}^2\hat{z}_{r_2} = 0 \tag{42}
$$

$$
-k_{r_2}\hat{W}_t\left(G_n\right) - k_{c_1}\hat{z}_{r_1} + k_{c_1}\hat{z}_{r_2} + k_{r_2}\hat{z}_{r_2} - k_{c_2}\hat{z}_{r_1}^3 + k_{c_2}\hat{z}_{r_2}^3 - m_{r_2}\omega^2\hat{z}_{r_2} - 3k_{c_2}\hat{z}_{r_1}\hat{z}_{r_2}^2 + 3k_{c_2}\hat{z}_{r_1}^2\hat{z}_{r_2} = 0 \tag{43}
$$

Due to the system's nonlinearity, the utilization of the determinant of the matrix approach failed. These transforms are computed numerically.

5. NUMERICAL STUDY

The complexity of such equations is increased due to the coupling induced by resonators, which obstructs a straightforward analytical solution for $Z_m(s)$. Therefore, numerical methods become necessary to determine the system response. In cases of non-linear equations which may not have closed-form solutions, state-space representation proves advantageous. This method involves casting the system in matrix form, complete with an associated vector $[Z_m(s), U_r(s)]$ of size $[N_m + N_r]$. Subsequently, numerical methods like the Newton-Raphson algorithm can assist in computing the Fourier series expansion coefficients. However, when the Newton-Raphson method fails to converge, the Runge-Kutta method served as an effective alternative, especially in situations where the system exhibits high nonlinearity and a large number of degrees of freedom.

The geometric and material properties of the investigated rectangular beam are detailed in Table 1. The attached mass m_a is positioned at various locations along the resonator, with their distances ranging from 20 to 57.3 mm. The coupling spring constants are k_c and k_{c_1}, with a second nonlinear coupling constant k_{c_2} being studied, providing a basis for further analysis and simulations.

Table 1. Geometric and material properties for the studied rectangular beam

Parameter	Value	Parameter	Value
L_m	0.3 m	m_r	5.9 g
w_m	25 mm	k_r	374 N/m
h_m	3 mm	ζ_r	0.003
ρ_m	2700 kg/m^3	N_r	8
E_m	70 GP	m_a	3.8 g
ζ_m	0.01	k_{c_1}	-37.4 N/m
N_m	10	k_{c_2}	102 N/m^3
k_c	374 N/m	δ	[20...57.3] mm

Fig. 4 presents the simulation of the linear transmissibility characteristics of a clamped-free beam without any attachments, referred to in this context as a plain beam. Notably, the distinct separation of the first three

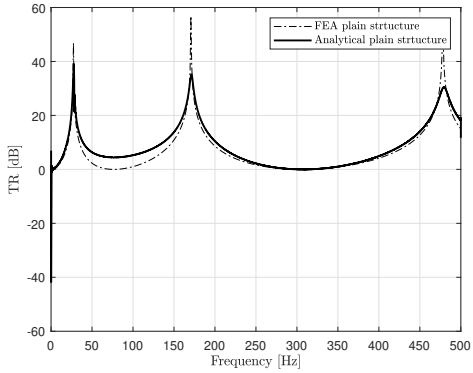

Figure 4. Validation of studies plain structure

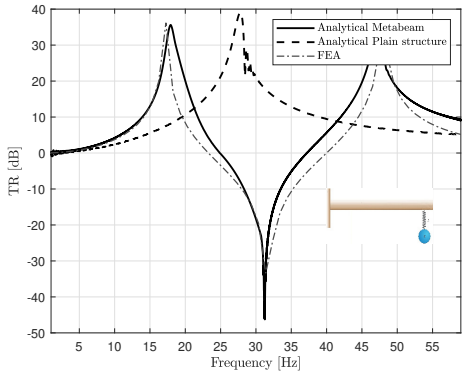

Figure 5. Bandgap formation and anti-resonance phenomena in a vibration absorber structure with an additional resonator

modes can be clearly observed. The outcomes from this simulation align well with the results obtained from finite element analysis (FEA) for the plain beam, underscoring the validity of the simulation approach. The parameters for this study were carefully selected to mirror the conditions in the FEA model, thus boosting the validity of the simulation.

Fig. 5 demonstrates the impact of introducing an additional resonator into the system. This addition induces the formation of a bandgap, mimicking the attributes of a traditional vibration absorber structure. Consequently, an anti-resonance event is noted around the resonator's natural frequency. This occurrence is instrumental in attenuating specific frequencies in the vibration spectrum, reflecting the response of a single resonator, comparable to a classical vibration absorber structure. The figure depicts the resonator at the end of the beam, with the simulated results exhibiting a high degree of agreement with the FEA outcomes. This concurrence validates the precision of the simulation and the reliability of the modeling assumptions employed. The dash-solid line in Fig. 5 corresponds to the case of a plain beam without an attached local resonator. This case provides a stark contrast, as no bandgap phenomenon is observed, highlighting the pivotal role local oscillators play in the system's vibrational properties. Such insights are crucial when it comes to designing systems to control and manipulate desired vibrational behaviors.

Fig. 6 demonstrates the bandgap extracted from the plane wave expansion dispersion analysis for a conventional metamaterial. The displayed curve outlines the relationship between wave frequency and wavenumber,

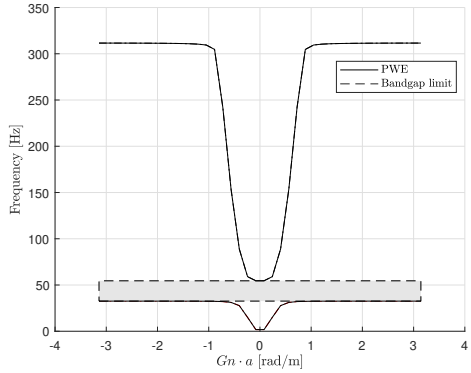

Figure 6. Dispersion curves computed using the plane wave expansion method for target frequency f_t=31.2 Hz

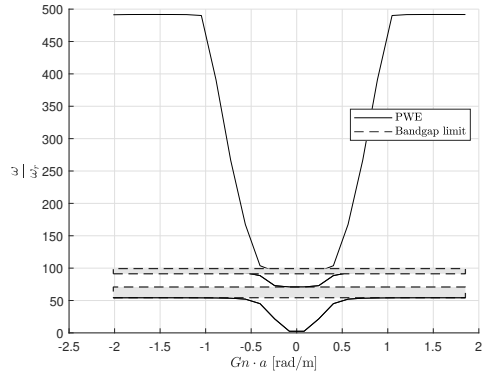

Figure 7. Dispersion curve of internally coupled metamaterial beam using the plane wave expansion method for target frequency $k_c = k_r$ and f_t=31.2 Hz.

providing insight into the spatial variation of the wave within the structure. Based on the design parameters, the curve reveals that wave propagation occurs within a frequency range of 31.5 Hz to 52.4 Hz. The figure identifies the presence of bandgaps within this range, where specific frequencies are prevented from propagating through the structure. The target mode is selected at f_r=31.2 Hz. This mode signifies frequency ranges where the wave propagation is strongly influenced by local resonance, leading to the opening of a bandgap in the out-plane phase. Understanding this interaction between local resonance and wave propagation provides critical information for the effective design and application of metamaterials.

Fig. 7 illustrates the bandgap derived from the plane wave expansion dispersion analysis outlined in Eq. (41). This figure highlights the first bandgap (indicated by the shaded area), which aligns with that of the conventional metamaterial beam in Fig. 6. Furthermore, a second, narrower bandgap is observed at a slightly higher frequency range. Notably, this additional bandgap is a result of internal coupling within the metamaterial structure. The presence of this second bandgap, brought about by internal coupling, could profoundly impact the wave propagation characteristics and subsequent design strategies of such metamaterials.

The bandgap depicted in Fig. 8 aligns well with the plane wave expansion dispersion analysis presented in Fig. 6 and Fig. 7. This consistency lends credence to the analytical approach and validates the findings of the study. Compared to Fig. 5, a significant observation is that the width of the bandgap expands with

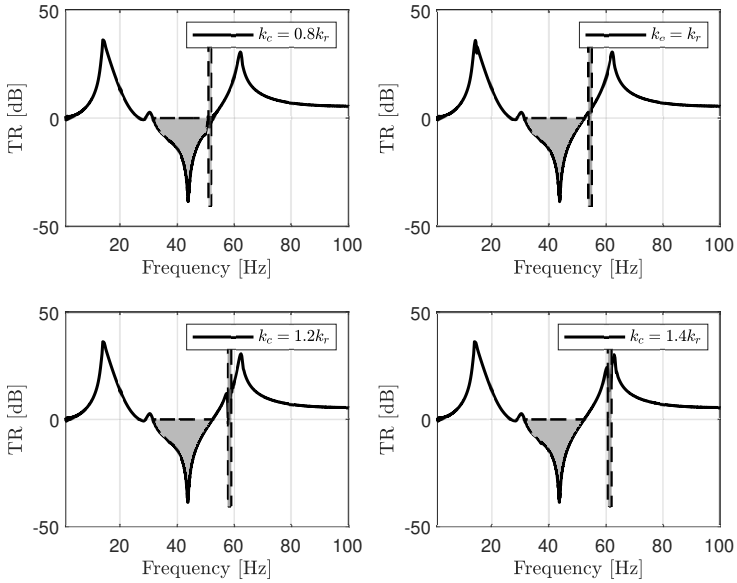

Figure 8. Transmittance of internally linear coupled N_r=8 resonators metamaterial beam for different k_c/k_r ratios: (a) $k_c = 0.8k_r$, (b) $k_c = k_r$, (c) $k_c = 1.2k_r$, (d) $k_c = 1.4k_r$.

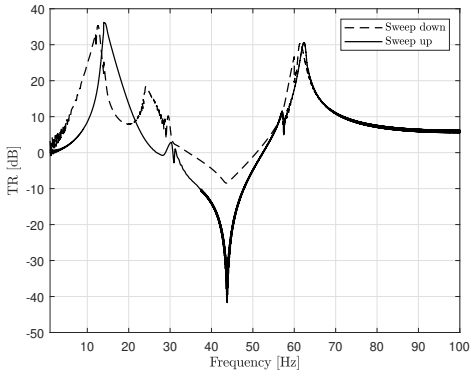

Figure 9. Transmittance of internally nonlinear coupled metamaterial beam with N_r=8 resonators, $k_{c_1} = 0.1k_r$ and $k_{c_2} = 0.27k_r$

the increase in the number of resonators. This expansion enhances vibration suppression, indicating that the incorporation of more resonators could lead to improved vibration control in such structures. Interestingly, it's found that an increase in the coupling spring stiffness (k_c) does not affect the first bandgap. On the other hand, the position of the second bandgap migrates towards higher frequencies, and its width fluctuates. However, given the relative narrowness of the second bandgap when compared to the first, alterations in its width, either increasing or decreasing, are not significantly noticeable. This suggests that changes in coupling spring stiffness may not substantially affect the overall system behavior via the width of the second bandgap.

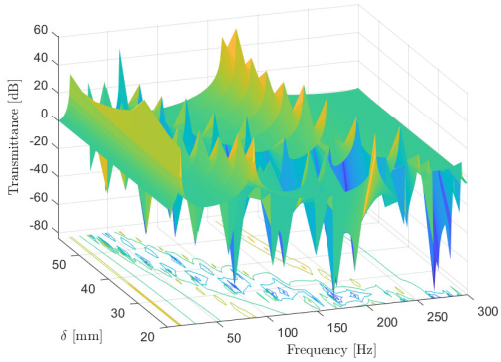

Figure 10. The transmittance pattern evolution in response to the variation of δ

Fig. 9 presents the behavior of nonlinear coupled resonators, the parameters of which are selected to mirror the behavior of linear coupled resonators. As the figure depicts, the bandgap created during the frequency sweep-up matches that of the linear case. However, during the sweep-down process, the bandgap behavior diverges due to the nonlinearity of the coupled spring, resulting in a narrower bandgap compared to the linear or sweep-up frequency operation. A significant observation from the figure is the notable reduction of the first side peak around 15 Hz, accompanied by a visible softening behavior exhibited on the second side peak. These findings underline the substantial influence of nonlinearity on the vibrational behavior of the coupled resonators. Interestingly, no remarkable increase in the bandgap is observed in this case, despite the introduced nonlinearity. This observation could have significant implications for the design and control of such systems with selected parameters.

Given these observations, it is valuable to further explore nonlinear dynamics through analyses like bifurcation, chaos theory, Lyapunov exponents, or investigations into regimes far removed from linear or stable conditions. Extending this work into more complex nonlinear analyses could unveil deeper insights into the behavior and control of nonlinear coupled resonator systems, potentially leading to advanced applications and optimization techniques for managing vibrational phenomena.

Impact of Variations in Resonator Natural Frequencies on Bandgap Characteristics

This section delves into the influence of variations in resonator natural frequencies on resonant bandgap edge frequencies. Theoretical frameworks frequently assume identical target frequency ω_t for all resonators. However, real-world resonators exhibit small variations, inevitably resulting from manufacturing inconsistencies, the distinct interfaces connecting resonators to the primary structure, and other factors. Notably, apart from these unavoidable minor variations, it is possible to intentionally adjust ω_t. Such tuning of the structure enables operation within different frequency ranges, a capability crucial for broader real-world applications such as in heavy-duty machinery. This tunability presents a solution to the limitations of piezoelectric metamaterials, whose applicability is otherwise constrained. Furthermore, the location of the attached mass (δ) can be varied, resulting in changes to the resonator's natural frequency due to adjustment in the effective stiffness. This ability to individually and distinctly alter each resonator's natural frequency introduces a new dimension of tunability to the system. Consequently, this approach can potentially circumvent the performance issues commonly associated with graded metamaterials, as noted in recent studies.[15,16]

In Fig. 10, the transmittance pattern evolution of a metastructural beam equipped with eight resonators is depicted in response to the variation of δ, which represents the position of the attached mass. The parameters for these resonators can be referred to in Table 1. The graph displays a frequency range from 0 to 300 Hz, concurrent with the alteration in the attached mass position δ from 20 mm to 57.3 mm. The value of δ effectively quantifies

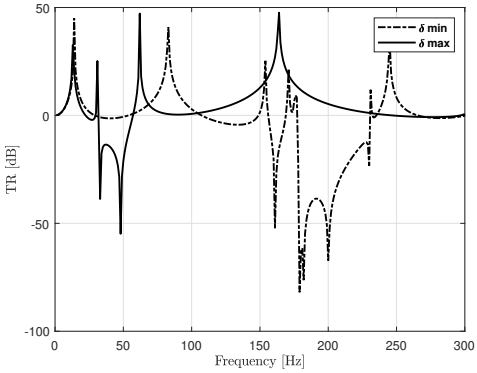

Figure 11. Effects of attached mass position on resonator natural frequencies and bandgap characteristics: comparing maximum and minimum δ scenarios

the location of the attached mass along the beam-type resonator. As δ decreases, indicating the mass is closer to the base of the resonator, a resulting increase in resonator stiffness is observed. This further escalates the resonator's natural frequency, ω_r.

A key observation from the plot in Fig. 10 is that the bandgap shrinks as δ increases. This suggests that there is a maximum allowable variation in δ. Moreover, the impact of δ on the width of the bandgap is of paramount importance, as visualized in Fig. 11. An attached mass moving towards the resonator's tip (an increase in δ) results in a narrower bandgap. Conversely, if the mass is attached farther from the tip (a decrease in δ), a broader bandgap is achieved. These insights highlight the crucial role of the attached mass position in enhancing the performance of a metastructural beam. They also propose an exciting possibility of manipulating both the central frequency and width of the bandgap by finely adjusting the location of the attached mass on each resonator.

6. CONCLUSION

In conclusion, the research outlined provides an expansive theoretical insight into bandgap generation within internally coupled, locally resonant metastructures. By investigating both linear and nonlinear coupled resonators, this work sheds light on the significant impact of varying resonator properties, notably the natural frequency variation of resonators and the stiffness of coupling springs. This study also unveils the substantial effect of the position of an attached mass on resonators, which dictates the natural frequency and thus governs the central frequency and width of the bandgap.

While the number of resonators can result in a wider bandgap, the impact of the stiffness of the coupling spring on the first bandgap is negligible. However, it induces a shift in the second bandgap towards higher frequencies, while also causing fluctuations in its width. Additionally, in the context of nonlinear coupled resonators, unique bandgap formation patterns were observed during sweep-up and sweep-down frequency operations, which can be attributed to the inherent nonlinearity present.

This study further examined the effects of the position of an attached mass on the natural frequency and bandgap characteristics of a cantilevered beam, highlighting a promising avenue for system tunability. While these findings offer a critical leap towards comprehensive knowledge of bandgap generation in metamaterials, it is important to note that these conclusions are bound by the assumptions of the theoretical model used. Empirical validation through future experimental studies is thus highly recommended to confirm these findings' real-world application viability.

Furthermore, the study's findings highlight the potential of metamaterials compared to conventional piezoelectric devices. The ability to finely adjust bandgap characteristics and manipulate wave propagation properties

within these metastructures offers superior vibration suppression, benefiting the maintenance and performance of various machinery, in particular heavy-duty machinery. Additionally, the design flexibility and tunability of these metastructures enhance their potential for efficient energy harvesting applications, contributing to sustainability and cost-effectiveness. By establishing a strong foundation for further exploration and optimization of metamaterial parameters, this research opens doors for broader practical applications of these innovative structures.

Acknowledgments

This paper is supported by the European Union's HORIZON Research and Innovation Programme under grant agreement No 101120657, project ENFIELD (European Lighthouse to Manifest Trustworthy and Green AI). It was also supported by the Estonian Research Council grant PRG658.

REFERENCES

[1] Pai, P. F., "Metamaterial-based broadband elastic wave absorber," *Journal of intelligent material systems and structures* **21**(5), 517–528 (2010).

[2] Skoblar, A., Žigulić, R., Braut, S., and Blažević, S., "Dynamic response to harmonic transverse excitation of cantilever euler-bernoulli beam carrying a point mass," *FME Transactions* **45**(3), 367–373 (2017).

[3] Li, Y., Hou, X., Qi, W., Wang, Q., and Zhang, X., "Modeling and analysis of multiple attached masses tuning a piezoelectric cantilever beam resonant frequency," *Shock and Vibration* **2020**, 1–12 (2020).

[4] Song, H., Hwang, G.-T., Ryu, J., and Choi, H., "Stable output performance generated from a magneto-mechano-electric generator having self-resonance tunability with a movable proof mass," *Nano Energy* **101**, 107607 (2022).

[5] Sugino, C., Xia, Y., Leadenham, S., Ruzzene, M., and Erturk, A., "A general theory for bandgap estimation in locally resonant metastructures," *Journal of Sound and Vibration* **406**, 104–123 (2017).

[6] Hu, G., Tang, L., and Das, R., "Internally coupled metamaterial beam for simultaneous vibration suppression and low frequency energy harvesting," *Journal of Applied Physics* **123**(5) (2018).

[7] Xia, Y., Erturk, A., and Ruzzene, M., "Topological edge states in quasiperiodic locally resonant metastructures," *Physical Review Applied* **13**(1), 014023 (2020).

[8] Bao, H., Wu, C., Zheng, W., and Yan, B., "Vibration bandgap of a locally resonant beam considering horizontal springs," *Journal of Vibration and Control* **28**(3-4), 452–464 (2022).

[9] Oyelade, A. O. and Oladimeji, O. J., "Coupled multiresonators acoustic metamaterial for vibration suppression in civil engineering structures," *Forces in Mechanics* **5**, 100052 (2021).

[10] Patil, G. U. and Matlack, K. H., "Review of exploiting nonlinearity in phononic materials to enable nonlinear wave responses," *Acta Mechanica* **233**(1), 1–46 (2022).

[11] Hansen, C., Snyder, S., Qiu, X., Brooks, L., and Moreau, D., [*Active control of noise and vibration*], CRC press (2012).

[12] Rao, S. S., [*Vibration of continuous systems*], John Wiley & Sons (2019).

[13] Li, F.-L., Zhang, C., and Wang, Y.-S., "Band structure analysis of phononic crystals with imperfect interface layers by the bem," *Engineering Analysis with Boundary Elements* **131**, 240–257 (2021).

[14] Lei, L., Miao, L., Zheng, H., Wu, P., and Lu, M., "Band gap extending of locally resonant phononic crystal with outward hierarchical structure," *Applied Physics A* **128**(6), 492 (2022).

[15] Zhao, B., Thomsen, H. R., De Ponti, J. M., Riva, E., Van Damme, B., Bergamini, A., Chatzi, E., and Colombi, A., "A graded metamaterial for broadband and high-capability piezoelectric energy harvesting," *Energy Conversion and Management* **269**, 116056 (2022).

[16] Hu, G., Austin, A. C., Sorokin, V., and Tang, L., "Metamaterial beam with graded local resonators for broadband vibration suppression," *Mechanical Systems and Signal Processing* **146**, 106982 (2021).

Appendix 9

Hossein Alimohammadi et al. “Exploring the Real-World Challenges and Efficacy of Internal Coupling in Metastructures: An Experimental Perspective”. In: *The 4th International Conference on Electrical, Computer and Energy Technologies (ICECET)*. 2024, pp. 1–6

IV. International Conference on Electrical, Computer and Energy Technologies (ICECET 2024)
25-27 July 2024, Sydney-Australia

Exploring the Real-World Challenges and Efficacy of Internal Coupling in Metastructures: An Experimental Perspective

Hossein Alimohammadi
Department of Computer Systems
Tallinn University of Technology
Tallinn, Estonia
0000-0002-8867-8988

Kristina Vassiljeva
Department of Computer Systems
Tallinn University of Technology
Tallinn, Estonia
0000-0002-4178-1267

S. Hassan HosseinNia
Precision and Microsystem Engineering
Delft University of Technology
Delft, Netherlands
0000-0002-7475-4628

Peeter Ellervee
Department of Computer Systems
Tallinn University of Technology
Tallinn, Estonia
0000-0002-0745-6743

Eduard Petlenkov
Department of Computer Systems
Tallinn University of Technology
Tallinn, Estonia
0000-0003-2167-6280

***Abstract*—Metastructures with internally coupled resonators promise enhanced vibration control and energy harvesting capabilities by theoretically enabling multiple bandgaps. This paper investigates the feasibility of these theoretical benefits under practical constraints, particularly the challenge of merging multiple bandgaps in continuous systems. Employing a closed-form analytical approach alongside FEM simulations and experimental validation, the study reveals that while internal coupling can modify bandgap behavior, achieving precise stiffness alignment and bandgap merging remains challenging. The findings indicate that practical applications may not fully realize the predicted advantages and also present more challenges in merging multiple bandgaps created in such metastructures, even for metastructures with advanced manufacturing precision and design optimization. The paper contributes to the understanding of the dynamic behavior of internally coupled metastructures and outlines directions for future research to bridge the gap between theory and application.**

***Index Terms*—Locally Resonant Metastructure, Experimental Exploration, Bandgap Engineering, Internal Coupling, Vibration Suppression**

I. Introduction

Recent advancements in the field of metastructures have opened new frontiers in materials science, particularly in the realms of vibration suppression and energy harvesting. They have garnered substantial research attention due to their potential in low-frequency applications at scales smaller than the wavelength. However, a major limitation is the relatively narrow widths of their band gaps, which restricts their utility in environments experiencing broadband spectrum vibrations. To address this challenge, researchers have investigated various strategies to broaden the band gap of metastructures. These strategies include the creation of novel structural configurations aimed at producing multiple band gaps [1], combining Bragg Scattering and local resonance band gaps [2], and incorporating nonlinearities for broadband capabilities [3].

Among the various innovations, the concept of internal coupling within resonators presents a promising avenue for enhancing the performance of these structures. Theoretically, internal coupling facilitates the formation of multiple bandgaps, potentially broadening the bandgap width and offering substantial benefits in terms of energy dissipation and conversion efficiency [4], [5].

This phenomenon has been highlighted in seminal works, such as those by Hu et al. [6], who have demonstrated the potential of internal coupling on the dynamic properties of metastructures. Li et al. [7] have demonstrated the coherent internally coupled distant magnonic resonators via superconducting circuits, for integrated magnonic networks that can operate coherently at quantum-compatible scales. Oyelade and Oladimeji [8] also contributed by introducing a novel metastructure with a multiresonator mass-in-mass lattice system, where the internal coupling was through a linear spring, leading to the formation of two additional bandgaps over conventional designs.

A wider bandgap allows resonators to operate over a broader frequency range, enhancing their effectiveness. Integrating sensors like piezoelectric devices can transform this mechanical energy into electrical energy, increasing the efficiency of energy harvesting. Thus, a wider bandgap not only improves vibration control but also enhances the metastructure's energy harvesting capabilities.

Despite theoretical advancements and computational validations, a significant gap remains in the experimental inves-

XXX-X-XXXX-XXXX-X/XX/$XX.00 © 20XX IEEE

tigation of metastructures with internal coupling. The theoretical benefits of such designs, including enhanced vibration suppression and energy harvesting, rely on precise internal coupling mechanisms which, if not accurately implemented, may not yield the expected performance improvements in practical settings. Moreover, the real-world applicability of merging multiple bandgaps to extend the bandgap width remains underexplored, leaving unanswered questions about the feasibility and effectiveness of these advanced metastructural designs under operational conditions.

Addressing these challenges requires a focused investigation into the practical implementation of internally coupled resonators within metastructures. This study aims to bridge the gap between theoretical predictions and experimental realities, offering insights into the challenges of realizing the proposed benefits of internal coupling in metastructural designs. By examining the limitations and potential discrepancies in the performance of these structures, this research contributes to a deeper understanding of the factors that influence the efficacy of metastructures in achieving desired vibration control and energy harvesting outcomes.

This work asserts that the theoretical benefits of using internally coupled resonators in metastructures, such as enhanced vibration suppression and energy harvesting, are currently limited by practical constraints in bandgap creation mechanism.

The primary contributions of this paper are summarized as follows:

- Utilizes a closed-form formulation for analyzing bandgaps in metastructures with internally coupled resonators, moving away from traditional methods like Bloch theory and dispersion curve analysis;
- Illustrates that the bandgap observed in experiments aligns with those in standard metastructures, underscoring its importance for structural dynamics and wave manipulation;
- Demonstrates the practical challenges associated with achieving the theoretical benefits of internally coupled resonators in metastructures, as discussed by researchers in earlier studies;
- Provides empirical evidence on the difficulties of merging multiple bandgaps to increase the overall bandgap width in continuous metastructures with internally coupled resonators;
- Analyzes the effectiveness of internally coupled resonators in real-world applications, questioning the practicality of their implementation for vibration suppression and energy harvesting;
- Offers insights into the limitations and considerations necessary for the successful application of internally coupled resonators in distributed or continuous systems.

The remaining sections of this paper are as follows:

The structure of the remainder of this paper is organized as follows: In Section 2, the Methodology is presented, outlining the experimental design, analytical techniques, and the steps taken to investigate internal coupling effects in metastructures. Section 3, Results and Discussion, presents the data from the experiments and FEM simulations, analyzes the dynamic behavior of metastructures with varying coupling, and assesses the findings against the backdrop of existing theories and their practical implications. The final section, Section 4, Conclusion, encapsulates the main discoveries, situates them within the broader research landscape, and proposes for future inquiry.

II. Methodology

This section outlines the experimental setup designed to investigate the creation of band gaps and their impact on the dynamic behavior of metastructures. The methodology is bifurcated into two primary investigative thrusts: firstly, to validate the theoretical predictions concerning the standard metastructure through tangible observations; and secondly, to delineate the practical challenges and limitations inherent in the implementation of internally coupled resonators within real-world applications.

Before diving into the experimental setup, it's crucial to understand the theoretical underpinnings that guide the investigation of mechanical metastructures and their dynamic behaviors. Mechanical metastructures with local resonances manipulate wave propagation and dynamic responses by combining structural modes and integrated resonators. The modeling methodology employs modal analysis within a distributed parameter model to accurately describe the intricate interplay of mass, damping, and stiffness. The expression, which represents the transfer function of the m-th mode in response to an external force, is detailed as [9]:

$$\frac{Z_m(s)}{Q_{b_m}(s)} = \frac{1}{s^2\left(1+\frac{\mu(2\zeta_r\omega_r s+\omega_r^2)}{s^2+2\zeta_r\omega_r s+\omega_r^2}\right)+2\zeta_m\omega_m s+\omega_m^2} \quad (1)$$

Here, s is the Laplace transform's complex frequency variable, $Z_m(s)$ denotes the transverse vibration displacement of the main structure, $Q_{b_m}(s)$ represents the Laplace Transform of the external force applied to the m-th mode of the main structure, and the parameters μ, ζ_r, ζ_m, ω_r, and ω_m represent the mass ratio, damping ratios, and natural frequencies of both the resonators and the modal structure. This equation highlights how resonator properties impact the metastructure's resonance behavior, allowing for the design of systems with desired dynamics, such as band gaps for wave control and vibration suppression.

Ignoring the damping ratios of both the structure and the resonator, the transfer function in (1) features two poles at the origin, reflecting the fundamental response dynamics of the system, and reveals a bandgap within the frequency spectrum due to its unique pole-zero configuration. Specifically, it features zeros at $s = \pm i\omega_r$ and poles at $s = \pm i\omega_r\sqrt{1+\mu}$, with a second-order pole at $s = 0$. This arrangement ensures that no poles between ω_r and $\omega_r\sqrt{1+\mu}$, defining a bandgap in $\omega_r < \omega < \omega_r\sqrt{1+\mu}$. The transfer function formulation represents a shift from traditional metastructure analysis methods like Bloch theory towards a more practical approach. By developing a closed-form solution that leads to a transfer

function model, makes it easier to tailor these structures for specific applications by directly relating input forces to system behavior, offering a useful tool for engineers. Although the approach enhances practical analysis, it's an evolutionary step in metastructure research, focusing on application rather than theoretical novelty.

A. Experimental Setup

Experimental investigations were carried out using a carefully designed cantilever beam arrangement, aiming to provide empirical validation for the theoretical findings discussed earlier and the numerical ones discussed later.

1) Standard Metastructure Validation: For the initial phase of the experiment, a standard metastructure prototype without internal coupling was constructed to serve as a baseline. The beam's dimensions and material properties are specified in Table I. The experiment was conducted using a cantilever beam setup (see Fig. 1). The cantilever beam was fabricated from aluminum and had the following dimensions: 3mm thickness, 4cm width, and 0.91m length. To adjust the resonator's natural frequency, a nut and screw with a combined mass of 19 grams were attached to the tip of the beam. This modification successfully achieved a natural frequency of 64 Hz. For generating base motion, we utilized a 100N TIRA 51110 Shaker. Acceleration at the beam tip was measured using a Dytran Accelerometer 3055D21, which has a sensitivity of 100 mV/g. To measure transmissibility, another accelerometer of the same model was positioned at the base of the cantilever beam. The input signals to the shaker were amplified using the Power Amplifier BAA 120. The Vibration Controller VR9500 was employed for base control and monitoring of vibrational inputs and responses throughout the experiment.

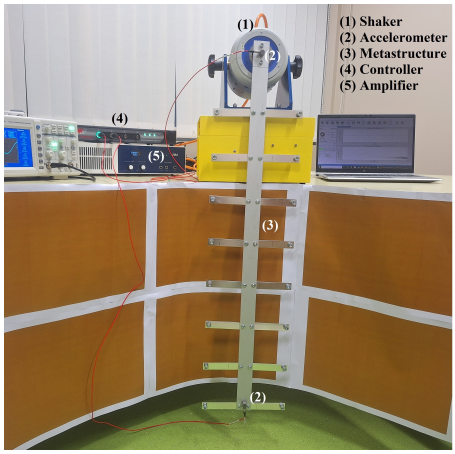

Fig. 1. Experimental setup of a metastructure prototype equipped with 8 resonators, each fine-tuned to a 64 Hz natural frequency using adjustable mass at the tip. Measurement accuracy is ensured with two Dytran Accelerometers, model 3055D2, linked by low-resistance, high-fidelity wires.

2) Investigating Internally Coupled Resonators: Furthermore, an additional experiment involving the metstructure with internally coupled resonators is detailed in Fig. 2. Each resonator was meticulously crafted and integrated into the metastructure, with particular attention paid to the precision of internal coupling to examine its impact on the system's dynamic response. In this setup, each internally coupled resonator is composed of pure aluminum, featuring a thickness of 2 mm, a width of 20 mm, and a length of 11.3 mm.

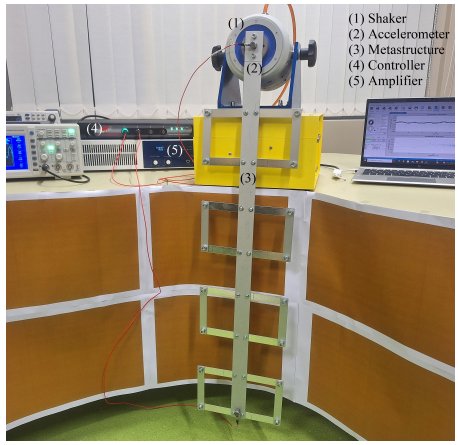

Fig. 2. Experimental Design for a Prototype Metastructure Comprising Four Unit Cells of Internally Linked Resonators, Constructed from Pure Aluminum. Each Coupled Beam has a Thickness of 2 mm, a Width of 20 mm, and a Length of 113 mm.

TABLE I
EXPERIMENTAL PARAMETERS

Symbol	Parameter	Value
L	Length of the beam	91 cm
b	Width of the beam	4 cm
h	Thickness of the beam	3 mm
E	Young's modulus of the beam	70 GPa
ρ	Density of the beam	2700 kg/m^3
ω_r	Resonator's natural frequency	64 Hz
ω_{r_κ}	Coupled resonator's natural frequency	85 Hz
N_r	Number of Resonators	8

3) Standard Metastructure Transmittance Measurements: The experimental results displayed in Fig. 3 demonstrate the transmittance spectrum, which corresponds to the resonant frequencies of the standard metastructure with $\mu = 1.2$. The regions of low transmittance, which signify the bandgaps, commence at a frequency of $\omega_r = 64$ Hz, in line with theoretical predictions. Additionally, the observed width of the bandgap is consistent with the anticipated value of $(1+\mu) = 2.2$. This data shows the existence of a bandgap between frequencies ω and $\omega_r\sqrt{1+\mu}$, corresponding to the calculated bandgap limit of $\sqrt{1+\mu} = 1.484$. This observation confirms

the presence of the primary bandgap, illustrating the dynamic behavior of the system across the spectrum.

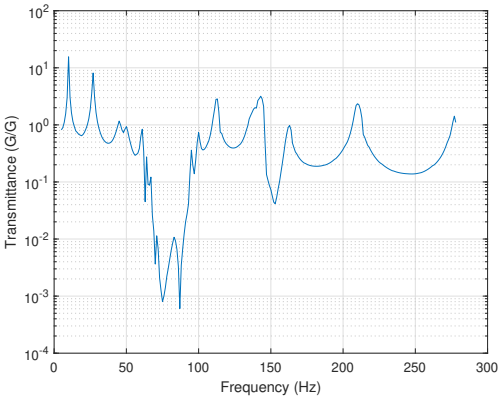

Fig. 3. Experimental transmittance data versus excitation frequency for the metastructure, with $\mu = 1.2$. The plot highlights the bandgap region between 64 to 95 Hz, which corresponds to the theoretical bandgap boundary $\omega_r\sqrt{1+\mu}$.

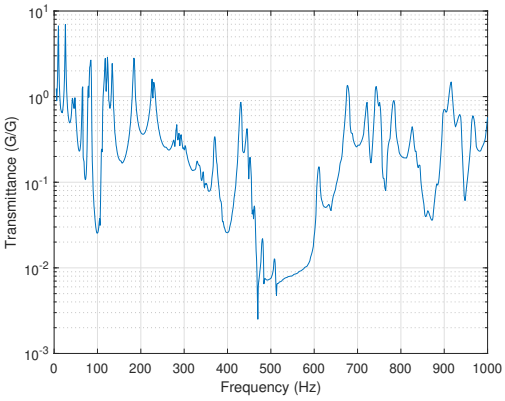

Fig. 4. Experimental transmittance results for the metastructure with internally coupled resonators. The first bandgap is observed between 90-110 Hz. This shift can be attributed to the enhanced stiffness of the unit cell, which is composed of a pair of resonators. Measurement devices are located at the base and the tip of the metastructure to capture the full spectrum of its response.

4) Internally Coupled Metastructure Transmittance Measurements: While the experimental outcomes for the standard metastructure corroborated the theoretical forecasts, the scenario markedly diverged with the introduction of internally coupled resonators. Fig. 4 encapsulates the experimental transmittance data, evidencing a distinct behavioral pattern for the metastructure endowed with internal coupling mechanisms. The manifestation of the initial bandgap at 85 Hz, slightly higher than what is observed in the standard metastructure (Fig. 3), aligns with the natural frequency of the coupled resonators. This is indicative of increased stiffness within the unit cell, a direct result of the resonators' collective configuration.

This measurement uncovers a scenario marked by chaos and irregularities in the transmittance spectrum, diverging from the uniform patterns expected based on theoretical projections by researchers in earlier studies, as highlighted in the introduction. Such manifestations underscore the sensitivity of the metastructure's dynamic behavior to the precise integration and configuration of internally coupled resonators, highlighting the challenges inherent in translating theoretical advantages into practical applications. It raises questions about the practical realization of internally coupled resonator benefits, such as significant bandgap widening or enhanced energy dissipation. The results imply that while the concept of internal coupling holds promise in theory, the transition to tangible applications faces challenges that may limit the effectiveness of such designs in real-world vibration control scenarios. Further investigation and refinement of the metastructure design and manufacturing processes are necessary to harness the full potential of internal coupling in metastructures for practical vibration suppression and energy harvesting applications. This claim is further supported by FEM analysis in the following section.

III. Finite Element Study

Following the experimental investigation, the focus moves to Finite Element Method (FEM) simulations, aimed to offer an analytical view complementary to the experimental insights, especially concerning metastructures with internally coupled resonators. This shift towards numerical modeling serves as a crucial phase in corroborating experimental findings, with the primary aim of substantiating the observed behaviors in experiments, thereby deepening our comprehension of the metastructure's dynamic characteristics.

A. Observations from FEM Analysis:

Fig. 5 depicts the transmissibility across different internal coupling stiffness, κ, as a function of normalized frequency. These results highlight the appearance of a pronounced second bandgap at a specific internal coupling stiffness, κ, matched to the resonator's stiffness ($\kappa/\omega_r = 0.003$), pinpointing this condition as essential for optimal bandgap definition (see bottom left corner subplot). Such precise matching between the internal coupling and resonator stiffness is key to achieving the desired dynamic behavior in the metastructure.

However, deviations from this optimal κ value lead to significantly disordered responses, underlining the metastructure's acute sensitivity to variations in internal coupling stiffness. Such behavior showcases the challenges associated with achieving and maintaining this precision in stiffness alignment in practical applications. The observed irregularities and chaotic dynamics for non-optimal κ values highlight potential difficulties in predictability and replicability of the metastructure's performance in real-world settings.

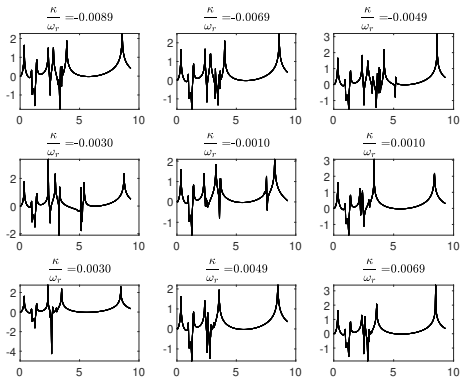

Fig. 5. Transmissibility of a cantilever beam for varying stiffness ratios κ, showing system sensitivity and its effects. Subplots detail responses at different κ/ω_r ratios, highlighting a critical condition at $\kappa = k_r$ in the bottom left corner subplot for optimal internal coupling. The y-axis is absolute displacement of beam tip to base displacement, $\ln|w_a(L)/w_b|$, and the x-axis is normalized frequency ω/ω_r.

Figure 6 confirms the importance of precisely tuning the internal coupling stiffness κ in metastructures to achieve effective vibration isolation. The contour plot shows significant transmittance variations and bandgap formations, represented by cooler colors, which are crucial for blocking wave propagation. This visualization emphasizes the need for meticulous parameter optimization, as even small deviations from the ideal stiffness ratio can substantially alter the system's behavior.

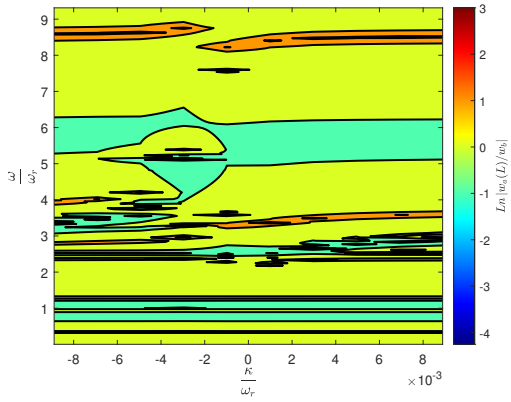

Fig. 6. Contour plot of transmittance for varying κ, illustrating the frequency-dependent formation and bifurcation of the bandgap. The plot captures the perturbations and potential destabilization inherent to varying internal coupling stiffness, underscoring the need for precise κ calibration.

Achieving the exact bandgap properties requires careful adjustment of the metastructure's internal stiffness. While analytical models predict clear transitions and bandgap formations, the observed data might show more gradual changes and less distinct boundaries between bandgap regions. This disparity highlights the challenges in translating theoretical models into experimental or real-world scenarios. The irregularities and variations presented in the FEM results underscore the imperative for experimental studies to authenticate and fine-tune the theoretical models, thereby confirming their relevance and effectiveness in real-world applications.

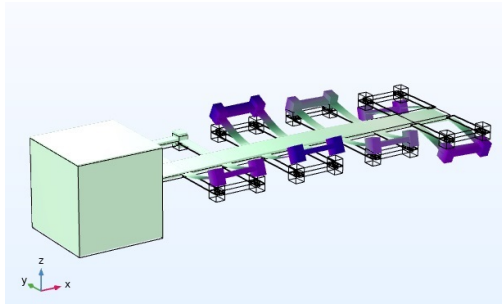

Fig. 7. Metastructure with internally coupled resonators configured as unit cells.

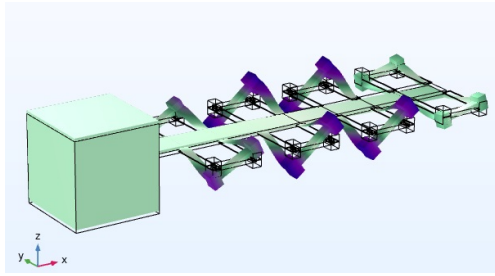

Fig. 8. Visual representation of the mechanism leading to the second bandgap in the internally coupled metastructure.

In Figs. 7 and 8, an internal coupling mechanism is demonstrated at work within the metastructure, where each pair of resonators acts as a unit cell. Fig. 7 demonstrates the initial out-of-plane oscillations that give rise to the primary bandgap, analogous to the behavior observed in conventional metastructures. As the excitation frequency increases, the system temporarily reverts to normal vibrational modes before encountering a specific frequency where the resonators within each cell commence vibration in opposing directions. This antiphase motion, depicted in Fig. 8, signifies the onset of the secondary bandgap due to the stiffness matching between the resonator and the internal coupling. However, the crucial insight is that despite the exact stiffness alignment (resonators and internal couple stiffness), merging the primary and secondary bandgaps to expand the bandgap width is not feasible. The inherent nature of the secondary bandgap's

formation in such metastructures prevents the amalgamation of multiple bandgaps, thus questioning the practical application of internally coupled resonators in continuous metastructures.

The experimental outcomes for standard metastructures aligned well with theoretical predictions, confirming the models' reliability. However, experiments with internally coupled metastructures revealed discrepancies, emphasizing the need for precise matching of internal coupling and resonator stiffness (κ to k_r). Practical implementation faced challenges due to manufacturing limitations. Additionally, attempts to merge multiple bandgaps into a broader one were hindered by the inherent characteristics of the second bandgap, questioning the feasibility of using internally coupled resonators in practical applications.

IV. Conclusion

This paper has addressed the practical implications of utilizing internally coupled resonators within continuous metastructures for enhanced vibration suppression and energy harvesting. Through the experimental validation, and Finite Element Method simulations, we have illuminated both the potential advantages and the notable challenges posed by the implementation of internal coupling mechanisms. While the pioneering research by Hu et al. [6], and related studies [10], have highlighted the theoretical benefits of internal coupling in creating secondary bandgaps and boosting energy harvesting efficiency, our findings underscore the difficulties faced when translating these concepts into practical applications. The challenges identified, such as the precision required in assembly and the limitations in merging multiple bandgaps, were substantiated through experimental observations and reinforced by FEM analysis, revealing a nuanced understanding of the real-world applicability of internally coupled resonator metastructures.

The contributions of this paper are:

- Demonstrated the practical challenges in implementing internally coupled resonators within continuous metastructures.
- Provided evidence that achieving the theoretical benefits of such systems is non-trivial and highly sensitive to precise manufacturing and assembly conditions.
- Shown that while internal coupling can indeed create additional bandgaps, merging these to broaden the overall bandgap width remains problematic due to inherent structural behavior.
- Confirmed that despite identical stiffness of resonators and internal coupling, the anticipated increase in bandgap width may not be practical for real-world applications, as evidenced by experimental and FEM analysis.
- The exploration of internal coupling in metastructures presents a unique case study of how advanced material concepts transition from theory to practical realization. While our findings have highlighted several limitations, they also pave the way for future research opportunities.

Future research could focus on developing new manufacturing techniques or material configurations that mitigate the current limitations. Innovations in precision engineering and design optimization may hold the key to successfully harnessing the full potential of internally coupled resonators. Further studies could also explore alternative mechanisms for bandgap manipulation that may offer more practical and flexible solutions for real-world applications.

In closing, we must acknowledge that while our findings are promising, they are not without their caveats. The results should not be overinterpreted as the complexities of real-world applications may yield different outcomes. Additionally, while our data is robust, we caution against speculation and inflation of these results. We must recognize the limitations of our current study and refrain from drawing conclusions not fully supported by the data. Instead, we should consider these findings as stepping stones towards more comprehensive and applied research in the field of metastructures.

Acknowledgment

This work has been supported by the European Union's Horizon Europe research and innovation programme under the grant agreement No 101120657, project ENFIELD (European Lighthouse to Manifest Trustworthy and Green AI), by the Estonian Research Council through the grant PRG658, and by the Estonian Centre of Excellence in Energy Efficiency, ENER (grant TK230) funded by the Estonian Ministry of Education and Research.

References

[1] C. Xu, Y. Yang, C. H. Wang, and L. Zhao, "Simultaneous low-frequency vibration suppression and energy harvesting using a metastructure with alternately combined nonlinear local resonators," *Mechanical Systems and Signal Processing*, vol. 211, p. 111241, 2024.

[2] F. Liang, Y. Chen, H. Kou, and Y. Qian, "Hybrid bragg-locally resonant bandgap behaviors of a new class of motional two-dimensional metastructure," *European Journal of Mechanics-A/Solids*, vol. 97, p. 104832, 2023.

[3] J. Zhou, L. Dou, K. Wang, D. Xu, and H. Ouyang, "A nonlinear resonator with inertial amplification for very low-frequency flexural wave attenuations in beams," *Nonlinear Dynamics*, vol. 96, pp. 647–665, 2019.

[4] C. Li, B. Qiu, Y. Yoshioka, K. Hirakawa, and Y. Zhang, "Mechanical control of nonlinearity in doubly clamped mems beam resonators using preloaded lattice-mismatch strain," *Physical Review Applied*, vol. 19, no. 2, p. 024025, 2023.

[5] L.-Q. Chen and Y. Fan, "Internal resonance vibration-based energy harvesting," *Nonlinear Dynamics*, vol. 111, no. 13, pp. 11 703–11 727, 2023.

[6] G. Hu, L. Tang, and R. Das, "Internally coupled metamaterial beam for simultaneous vibration suppression and low frequency energy harvesting," *Journal of Applied Physics*, vol. 123, no. 5, 2018.

[7] Y. Li, V. G. Yefremenko, M. Lisovenko, C. Trevillian, T. Polakovic, T. W. Cecil, P. S. Barry, J. Pearson, R. Divan, V. Tyberkevych *et al.*, "Coherent coupling of two remote magnonic resonators mediated by superconducting circuits," *Physical Review Letters*, vol. 128, no. 4, p. 047701, 2022.

[8] A. O. Oyelade and O. J. Oladimeji, "Coupled multiresonators acoustic metamaterial for vibration suppression in civil engineering structures," *Forces in Mechanics*, vol. 5, p. 100052, 2021.

[9] H. Alimohammadi, K. Vassiljeva, S. H. HosseinNia, and E. Petlenkov, "Bandgap dynamics in locally resonant metastructures: A general theory of internal resonator coupling," *Applied Sciences*, vol. 14, no. 6, p. 2447, 2024.

[10] G. Hu, J. Xu, L. Tang, C. Lan, and R. Das, "Tunable metamaterial beam using negative capacitor for local resonators coupling," *Journal of Intelligent Material Systems and Structures*, vol. 31, no. 3, pp. 389–407, 2020.

Appendix 10

Hossein Alimohammadi et al. “Damping Optimization in Locally Resonant Metastructures via Hybrid GA-PSO Algorithms and Modal Analysis”. In: *Conference on Smart Materials, Adaptive Structures and Intelligent Systems (ASME SMASIS)*. 2024, pp. 1–6

Proceedings of the ASME 2024
Conference on Smart Materials, Adaptive Structures and Intelligent Systems
SMASIS2024
September 9-11, 2024, Atlanta, GA

SMASIS2024-XXXX

DAMPING OPTIMIZATION IN LOCALLY RESONANT METASTRUCTURES VIA HYBRID GA-PSO ALGORITHMS AND MODAL ANALYSIS

Hossein Alimohammadi[1,*], Kristina Vassiljeva[1], S. Hassan HosseinNia[2], Peeter Ellervee[1], Eduard Petlenkov[1,*]

[1]Department of Computer Systems, Tallinn University of Technology, Tallinn, Estonia
[2]Department of Precision and Microsystems Engineering, Delft University of Technology, Delft, The Netherlands

ABSTRACT

This study explores the optimization of bandgap characteristics in locally resonant metastructures through advanced artificial intelligence (AI) and optimization algorithms, focusing on the accurate estimation of resonator damping ratios. By developing a novel mathematical framework for metastructure analysis, this research diverges from traditional methods, offering a more nuanced approach to bandgap manipulation. This research significantly improves metastructure modeling accuracy by precisely estimating resonator and structural damping ratios, enhancing model fidelity crucial for analysis, control strategies, and design optimization. Through a combination of model simulations and experimental validation, the efficacy of the Hybrid Genetic Algorithm-Particle Swarm Optimization (GA-PSO) algorithm is demonstrated, highlighting its potential for practical applications in engineering metastructures. This paper not only provides a robust method for estimating damping ratios but also opens new avenues for future research, including the application of machine learning techniques and the development of intelligent materials. The findings of this study contribute to the foundational understanding necessary for the advancement of mathematical modeling metamaterials, with broad implications for industries where precise vibration control is crucial.

Keywords: Bandgap Optimization, Modal Expansion Method, Experimental Damping Estimation

1. INTRODUCTION

The burgeoning field of metamaterials has revolutionized engineering and material science by offering properties not found in nature, particularly in controlling wave phenomena. These engineered materials are notable for their bandgaps-specific frequency ranges where wave propagation is hindered. These bandgaps are critical in applications aimed at reducing vibration and noise. However, the inherent damping in metamaterials, originating from their structural components and embedded resonators, poses a challenge. The resonator's damping ratio, denoted as ζ_r, is a key determinant of bandgap efficacy and thus a focus for enhancing the vibration suppression capabilities of these materials.

The exploration of metamaterials has advanced significantly in recent years, with a particular focus on their unique wave manipulation capabilities. Research by Valipour et al. [1] and Dalela et al. [2] has demonstrated how metamaterials can be designed to exhibit bandgaps, effectively blocking specific frequency ranges. These bandgaps are pivotal in applications requiring vibration suppression and noise control.

The role of AI in material science has grown exponentially, with studies like Diao et al. [3] showcasing how machine learning algorithms can predict and optimize material properties. The application of AI in metamaterials, as explored by Song et al. [4], is an emerging field that promises to revolutionize the design and functionality of these materials.

The complexity of metamaterials, especially those exhibiting bandgaps, necessitates sophisticated optimization techniques. The works of Zagaglia et al. [5] and Meng et al. [6] have highlighted the efficacy of algorithms like Genetic Algorithms, Particle Swarm Optimization, and others in fine-tuning the properties of dynamic systems for optimal performance.

The integration of AI with optimization algorithms in the context of metamaterials is a relatively new concept. Recent studies, such as those by Xiong et al. [7], and Salsa et al [8] have begun to explore this integration, showing promising results in the dynamic manipulation of bandgaps and enhancing the functionality of metamaterials.

This work breaks new ground by developing a fresh mathematical formulation for the analysis of metastructures, moving beyond conventional Bloch and dispersion curve methodologies. This innovative framework allows for a more nuanced AI and optimization algorithm-based analysis of bandgap phenomena.

The importance of this research lies in its capacity to significantly enhance the accuracy of mathematical models for metas-

*Corresponding author: eduard.petlenkov@taltech.ee
Documentation for `asmeconf.cls`: Version 1.37, June 27, 2024.

Copyright © 2024 by ASME

tructures through precise estimation of both resonator and structural damping ratios. This improvement in model fidelity is vital for in-depth analysis, robust control strategies, and efficient design optimization of metastructures.

The current approaches to metastructure analysis are limited in their ability to adapt to variable damping scenarios, presenting a challenge in the real-world application of bandgaps. This research proposes a solution to this limitation by enabling precise damping ratio adjustments within the bandgap optimization process.

The effectiveness of this new framework is demonstrated through a combination of model predictions and real-world experiments. This validation supports the claim that AI-driven optimization can more effectively tailor bandgap properties for practical use, providing a clear path to bridge the gap between theoretical and applied metamaterials research.

The article is structured as follows: Section 2 discusses the research methods, incorporating modal expansion and optimization algorithms to model the metamaterial and identify critical parameters influencing its bandgap properties. Section 3 analyzes the results from these optimization algorithms, assesses their effectiveness in capturing the dynamics of the metastructure, and examines their implications for vibration suppression. Section 4 offers conclusions and suggests directions for future work.

2. ANALYTICAL AND EXPERIMENTAL APPROACHES FOR METASTRUCTURE OPTIMIZATION

This study refines the analysis of metastructures using a distributed parameter model, focusing on modal dynamics and system transfer functions. It simulates real-world conditions by integrating noise into theoretical models and employs optimization algorithms like the Hybrid GA-PSO for parameter estimation. This approach balances traditional modal analysis with modern computational techniques, enhancing our grasp of metastructural dynamics for more effective design and vibration suppression strategies. The incorporation of actual experimental data further validates the optimization methods, ensuring their practical applicability in complex system analysis.

2.1 Modal Transfer Function Dynamics of Structure

The study employs modal analysis within a distributed parameter model to explore the dynamic characteristics of a metastructure, consisting of an aluminum rectangular beam with integrated local resonators. This analytical approach facilitates the identification of natural frequencies and mode shapes, which are used for the control of the structure's bandgap properties.

Equations (1) and (2) elucidate the interaction between the beam's displacement and the resonators' movement, as well as the influence of external excitations. These equations are derived from a comprehensive modal decomposition approach, leveraging the system's orthogonality conditions to simplify the complex dynamics.

$$\begin{aligned} &\ddot{z}_m(t) + 2\zeta_m\omega_m\dot{z}_m(t) + \omega_m^2 z_m(t) \\ &\quad - \sum_{r=1}^{N_r} m_r\omega_r\left(\omega_r z_r(t) + 2\zeta_r\dot{z}_r(t)\right)\phi_m(x_r) \\ &\quad = \mathbb{Q}_{b_m}(x,t), \quad m = 1,2,\ldots,N_m \end{aligned} \tag{1}$$

Equation (1) captures the modal dynamics of the beam, incorporating the effects of damping and resonator interaction. It presents a detailed account of how the resonators' characteristics and positioning influence the beam's response to dynamic loads.

$$\begin{aligned} &\ddot{z}_r(t) + 2\xi_r\omega_r\dot{z}_r(t) + \omega_r^2 z_r(t) + \\ &\quad \sum_{m=1}^{N_m}\ddot{z}_m(t)\phi_m(x_r) = \mathbb{Q}_{b_r}(t), \quad r = 1,2,\ldots,N_r \end{aligned} \tag{2}$$

Conversely, Equation (2) details the resonators' dynamics, highlighting the interaction between resonator movements and the structural modes. The approach discussed more in [9] to identify natural frequencies and mode shapes within a metastructure. The analysis involves developing partial differential equations through a distributed parameter model to describe the system's dynamics. These equations are then discretized and solved numerically to gain a better understanding of the metastructure's modal characteristics, enabling the precise manipulation of bandgaps within the structure.

In reaching the stage of formulating the transfer function, the analysis first considers the resonator masses (m_r), which are proportionally determined by the structure's mass distribution at the resonators' attachment points. This relationship is quantified by a mass ratio (μ), reflecting the resonators' total mass relative to the base structure's mass, as represented by the formula $m_r = \mu m(x_r)\,dx_r$. This ensures that the resonator masses directly correspond to the structural mass distribution, thereby aligning resonator behavior with the overall dynamics of the structure. For systems incorporating numerous resonators, an approximation is employed, equating the summation over discrete resonators to a continuous integral over the structure's length. Taking the Laplace transform of equations (1) and (2), followed by mathematical manipulation, leads to the derivation of a transfer function. This function elucidates the relationship between the displacement of the structure's m-th mode and the corresponding excitation force as [9]:

$$\begin{aligned} \frac{Z_m(s)}{Q_{b_m}(s)} = \frac{1}{s^2\left(1 + \frac{\mu\left(2\zeta_r\omega_r s + \omega_r^2\right)}{s^2 + 2\zeta_r\omega_r s + \omega_r^2}\right) + 2\zeta_m\omega_m s + \omega_m^2}, \\ m = 1,2,\ldots,N_m \end{aligned} \tag{3}$$

In this context, $Z_m(s)$ represents the Laplace-transformed displacement of the structure's m-th mode, $Q_{b_m}(s)$ symbolizes the Laplace-transformed external force, ζ_m and ζ_r are damping ratio of structure's m-th mode and resonator, respectively. ω_m and ω_r are the natural frequencies of the structure's m-th mode and the resonators, respectively.

2.2 Estimation of Damping Ratio in Metastructures

In the study of metastructures, estimating the damping ratio ζ_r from experimental data is pivotal for the effective modeling of vibration suppression and dynamic response tuning. Various methods can be employed for this estimation, each with its specific advantages and requirements. These include Frequency Response Analysis, System Identification Techniques, Energy Decay Method, Optimization Algorithms, and Bayesian Inference.

Copyright © 2024 by ASME

To estimate the damping ratio, optimization algorithms are utilized due to their ability to navigate complex, multidimensional parameter spaces. These algorithms are particularly effective in situations where the objective function is non-linear or nonsmooth, as often encountered in real-world data from metastructures. An objective function is defined to quantify the error between the experimental data and theoretical model predictions. Several algorithms are considered for algorithm Selection and configuration:

Nelder-Mead Simplex Algorithm: A heuristic search method ideal for non-smooth functions, enabling robust initial parameter estimation without derivatives. Genetic Algorithm (GA): This algorithm excels in finding global solutions in complex problems characterized by multiple local minima.

Particle Swarm Optimization (PSO): It simulates a social process, effectively honing in on global optima, especially in continuous optimization scenarios.

Artificial Bee Colony (ABC) Algorithm: Inspired by the foraging behavior of bees, it balances local and global search effectively, useful for complex parameter estimation tasks.

Hybrid GA-PSO: Combining GA's exploration and PSO's exploitation efficiency, this approach aims to quickly and reliably find global optima in multi-modal data landscapes.

For implementation, each algorithm is configured with appropriate parameters such as learning rate, population size, mutation rates, and particle velocities. The choice and configuration of the algorithm depend on the specific requirements of the problem and the nature of the experimental data. The selected algorithm is run to optimize the ζ_r, using the objective function to guide the search. This process is iterative, involving continuous evaluation and refinement based on performance metrics.

2.3 Integration in Metastructure Damping Estimation

These algorithms are particularly suited for metastructure analysis due to their ability to handle non-linearities and discontinuities in the objective function, which commonly arise from complex modal interactions within the structure. To estimate ζ_r, the mentioned algorithms can be configured to:

- Define an initial range of possible damping values based on physical constraints and preliminary data.
- Evaluate the fitness of each candidate solution by integrating the damping values into the metastructure model and comparing the resulting dynamic response with experimental measurements.
- Iteratively refine the population of algorithms based on the fitness evaluations, converging on a solution that best fits the experimental data.

The Sum of Squared Errors (SSE) is a statistical measure commonly used to quantify the difference between predicted values and observed data, especially useful in optimizing damping ratios in metastructures. SSE is calculated by summing the squares of the differences between observed experimental responses (y_i) and model predictions ($\hat{y}_i$) across n data points at various excitation frequencies. This formula provides a scalar value indicating the magnitude of error across all frequencies.

In the context of damping ratio estimation for metastructures, minimizing SSE helps in fine-tuning the parameters of optimization algorithms. The process includes simulating the metastructure model across a range of frequencies, comparing the predicted responses to the actual observed responses, and using SSE as the objective function to guide optimization.

Given a dataset consisting of n observed experimental data points y_i at different excitation frequencies, and corresponding model predictions $\hat{y}_i$, the SSE is calculated as follows:

$$\text{SSE} = \sum_{i=1}^{n} (y_i - \hat{y}_i)^2$$

Where y_i is the observed experimental response of the metastructure at the i-th excitation frequency. $\hat{y}_i$ is the predicted response from the metastructure model using the estimated damping ratios at the same frequency. n is the total number of data points, encompassing various excitation frequencies used during the experimental testing and simulations.

By minimizing the SSE, the optimization algorithms adjust the damping ratios ζ_r and ζ_m to achieve a closer match between the model predictions and the experimental results.

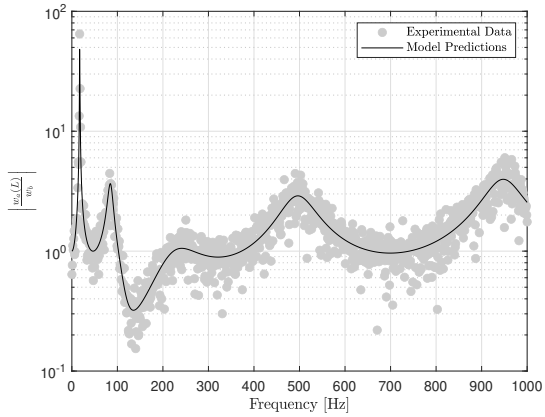

FIGURE 1: Comparison of the beam's transmittance: noisy signal versus model predictions, highlighting the algorithm's effectiveness in identifying transmittance characteristics within the bandgap frequency range. Parameters are as listed in Table 1 with initial simulations for noisy signal evaluation, using parameters L_{m_0}, m_{r_0} and k_{r_0}.

3. RESULTS AND DISCUSSION

In this section, the analysis extends to incorporating noise within theoretical models to closely mimic real-world scenarios, aiming to estimate the damping ratio ζ_r in systems characterized by a locally resonant bandgap. This study further delves into the utilization of actual experimental data, segmented into two distinct parts: a simple beam and a metastructure. Each segment is examined to determine the structural modal damping ratio ζ_m, demonstrating the efficacy and adaptability of the Hybrid

Copyright © 2024 by ASME

TABLE 1: Geometric and material properties of the studied rectangular aluminum beam

Parameter	Value	Parameter	Value
L_{m_0}	0.3 m	m_{r_0}	17 g
L_m	0.91 m	k_{r_0}	9kN
w_m	40 mm	m_r	10 g
h_m	3 mm	k_r	1.65 kN/m
ρ_m	2700 kg/m^3	N_r	8
E_m	69.5 GPa	N_m	8

GA-PSO algorithm across diverse experimental contexts. The outcomes of this investigation affirm the model's capability to accurately predict dynamic behavior, emphasizing its relevance and potential in enhancing vibration suppression techniques in metastructures.

The use of different beam lengths in our study—0.3 meters for preliminary tests to assess basic dynamic responses and modal analysis under controlled conditions, and 0.9 meters for comprehensive experimental validation—allows us to explore metastructure behavior across various scenarios. The shorter beam facilitates detailed observation of higher frequency dynamics for initial model validations, while the longer beam helps simulate more realistic operational conditions, revealing the impact of beam length on modal damping and bandgap behavior in settings akin to real-world applications.

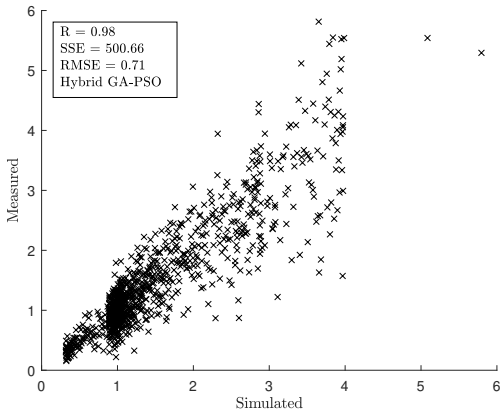

FIGURE 2: Scatter plot demonstrating the correlation between measured and simulated data via the Hybrid GA-PSO algorithm, evidencing high model accuracy with a correlation coefficient (R) of 0.98.

The algorithm's performance in calculating ζ_r is illustrated in Figure 1. The nominal ζ_r is 0.2 as an initial guess, and the results are contextualized within the parameters outlined in Table 1, which details the geometric and material properties of the rectangular aluminum beam under investigation. The findings indicate the algorithm's robustness in parameter estimation amidst experimental uncertainties. Figure 2 presents a scatter plot comparing measured data against values simulated by the Hybrid GA-PSO algorithm. The horizontal axis (Simulated) represents the predicted values of the dynamic response of the metastructure, normalized to the same scale as the experimental measurements, which are depicted on the vertical axis (Measured). Each data point corresponds to a specific excitation frequency used during the simulations and experimental testing, ranging from 0 to 5 arbitrary units reflecting normalized response magnitudes. The tight clustering of data points around the line of unity and the high correlation coefficient (R = 0.98) suggest a strong agreement between the model's predictions and the measured data. The scatter plot highlights the algorithm's precision in estimating the damping parameter ζ_r, as evidenced by the low root mean square error (RMSE = 0.71) and the sum of squared errors (SSE = 500.66), which quantify the model's predictive accuracy. This figure substantiates the Hybrid GA-PSO's efficacy in capturing the underlying dynamics of the metastructure under study.

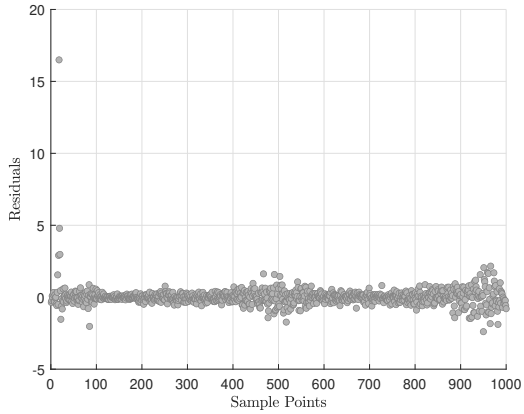

FIGURE 3: Residual plot from the Hybrid GA-PSO model prediction demonstrating the residuals' distribution against sample points, underscoring the model's accuracy with a high coefficient of determination (R^2).

Figure 3 reveals the model's residual distribution, crucial for evaluating the Hybrid GA-PSO algorithm's accuracy in estimating ζ_r. The residuals, mostly centered around zero, suggest a strong model fit, corroborated by a high R^2 value (0.91). Outliers at the start may signal deviations due to experimental anomalies or noise, warranting further investigation to enhance the algorithm's reliability.

3.1 Empirical Analysis of a Basic Beam Structure

To substantiate the theoretical model and optimization approaches proposed in this study, an experimental validation was conducted using a cantilever beam setup. This setup is depicted in Figure 4. The experiment involved a cantilever beam composed of aluminum, with 3 mm in thickness, 4 cm in width, and 0.91 m in length. This beam, representative of a standard metamaterial structure, was devoid of any locally resonant subsystems.

The experimental rig included a 100N TIRA 51110 Shaker, which provided base motion to excite the beam. The response

Copyright © 2024 by ASME

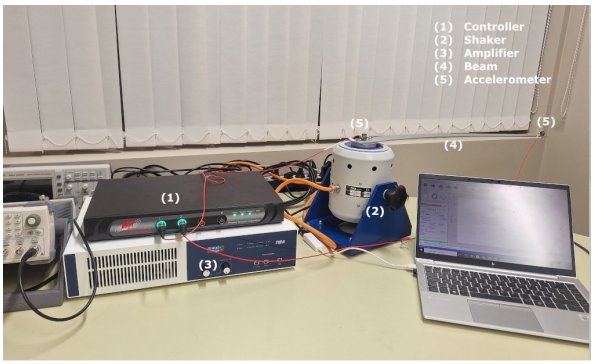

FIGURE 4: Experimental setup showcasing the simple cantilever beam attached to the Shaker, with the Dytran Accelerometers positioned at the base and tip, and connected to the Power Amplifier and Controller.

of the beam was meticulously measured using a Dytran Accelerometer 3055D21, a single-axis TEDS accelerometer capable of 100mV/g. This accelerometer, weighing 10 grams, was employed to capture the tip acceleration, while a second accelerometer of the same model was used at the base for control purposes. The Power Amplifier BAA 120 was utilized to amplify the input signals to the Shaker. The Vibration Controller VR9500, was employed to regulate, control the base, and monitor the vibrational inputs and responses. It is worth noting that the addition of hardware, specifically the low-noise accelerometer wire, introduced additional mass to the system. This added mass, assumed to be approximately 1% of the accelerometer's mass, was factored into the experimental analysis to ensure accurate representation of the beam's response.

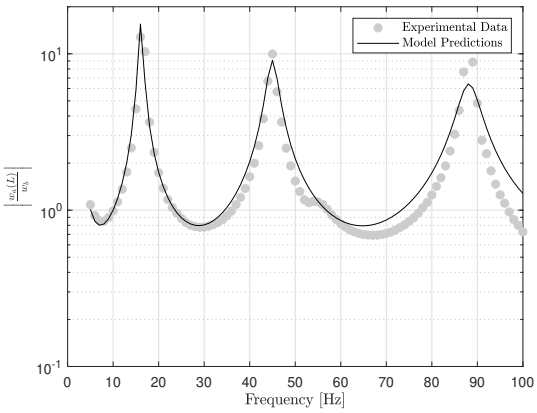

FIGURE 5: Transmittance response of a cantilever beam with Hybrid GA-PSO algorithm estimations, highlighting the model's alignment with experimental data for structural modal damping ratio (ζ_m) estimation.

The response of the cantilever beam under base excitation generates data on the dynamic behavior of metamaterials. The data obtained from this experimental setup will be further analyzed and compared with model predictions.

Since the resonators are not incorporated into the system for the first part of the experiment, the focus shifts to estimating the modal damping ratio (ζ_m) of the main structure. Drawing on conclusions from the previous sections, the Hybrid GA-PSO algorithm emerged as a strong candidate for such estimations. In this phase of the research, this algorithm is employed to determine ζ_m, leveraging its demonstrated proficiency in parameter estimation within complex dynamic systems.

Figure 5 presents the transmittance response, comparing the experimental data with theoretical model prediction. The plot illustrates the algorithm's effectiveness in estimating ζ_m, crucial for accurate dynamic modeling of the cantilever beam. The close alignment of the model predictions with the experimental data across the frequency spectrum validates the accuracy of all algorithms including Hybrid GA-PSO algorithm. This successful estimation of ζ_m underscores the potential of hybrid optimization techniques in flexible structures, where accurate damping characterization is essential for designing and controlling dynamic systems.

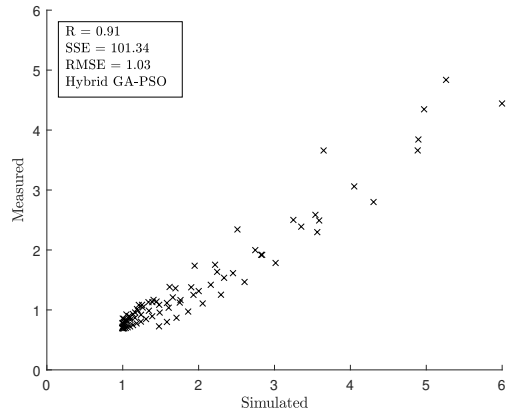

FIGURE 6: Scatter plot comparing measured data to Hybrid GA-PSO simulated estimations, demonstrating the algorithm's efficacy in predicting the structural modal damping ratio (ζ_m) with a correlation coefficient (R) of 0.91.

The scatter plot in Figure 6 illustrates the correlation between the measured and simulated data points using the Hybrid GA-PSO algorithm for estimating the modal damping ratio. The correlation coefficient (R) of 0.91 indicates a strong positive relationship, suggesting that the algorithm can predict the system's behavior with a high degree of accuracy. The SSE and RMSE provide further insight into the model's precision, with lower values indicating a closer fit to the experimental data. In this case, an RMSE of 1.03 reflects a reasonably accurate model, although there is room for improvement in minimizing the prediction error.

The residuals plot in Figure 7 predominantly indicates a sat-

Copyright © 2024 by ASME

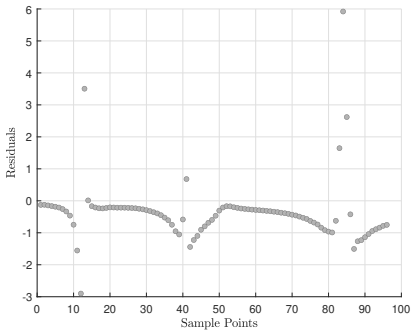

FIGURE 7: Residual analysis of the Hybrid GA-PSO model predictions showcasing the estimation accuracy across the experimental data set, with a focus on identifying outlier discrepancies for further model refinement.

isfactory model fit, as evidenced by the majority of residuals clustering near the zero line. However, the presence of outliers with higher residuals at the structure's modal resonant frequencies suggests that the model's predictions diverge from the experimental data at these critical points. This could be due to the heightened sensitivity of the system's response to parameter variations at resonance.

3.2 Empirical Assessment of Metastructural Dynamics

An integral aspect of designing metastructures for vibration suppression is understanding the sensitivity of bandgaps to damping ratios. To investigate this, a series of simulations were conducted to observe the effects of varying damping ratios on the bandgap's efficacy. Figure 8 depicts the frequency response functions illustrating the impact of varying damping ratios on the dynamic response of a metastructure. The upper plot reveals that altering the structural damping ratio influences the overall dynamic response but leaves the bandgap region largely unaffected. In contrast, the lower plot indicates that changes in the resonator damping ratio significantly alter the bandgap region's dynamics, highlighting the critical role of resonator damping in tuning the metastructure's vibration suppression capabilities.

Building upon the simulation insights, an experimental analysis was conducted on an actual metastructure to validate the theoretical findings and assess the practicality of bandgap manipulation through damping variations. This experiment aims to corroborate the simulation results with real-world data, establishing the reliability of the proposed models and the feasibility of achieving targeted vibration suppression through bandgap engineering. The experimental setup is captured in Figure 9, illustrating the prototype of metastructure real-world application. The resonators, integral to the metastructure, were crafted from pure aluminum, featuring a thickness of 2 mm, a width of 20 mm, and a length of 11.3 mm. A set of nuts and bolts served as adjustable tip masses, enabling the fine-tuning of the natural frequency to the target 64 Hz, as determined by Finite Element Method (FEM) analysis.

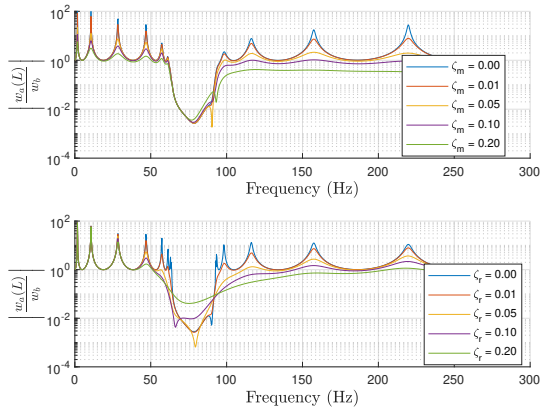

FIGURE 8: Transmittance highlighting the effects of damping ratio variations on a metastructure's dynamic response, with a focus on bandgap region alterations.

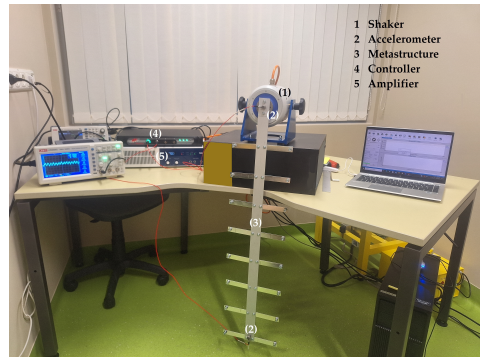

FIGURE 9: The experimental setup for the metastructure's dynamic analysis. This configuration is instrumental in examining the effects of damping and resonator adjustments on the metastructure's vibrational characteristics.

Copyright © 2024 by ASME

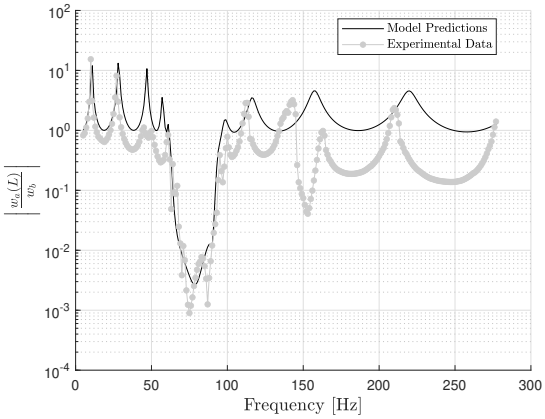

FIGURE 10: Comparison of experimental data with theoretical model employing estimated damping ratio

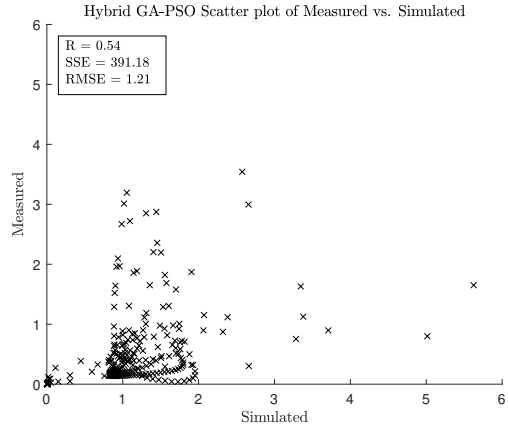

FIGURE 11: Hybrid GA-PSO Scatter plot of Metastructure's Measured vs. Simulated data in predicting the resonator damping (ζ_r).

This experimental arrangement was utilized to invoke the bandgap phenomenon and study its sensitivity to the damping ratios in a controlled environment. By systematically altering the tip mass, the resonant frequency of the metastructure could be adjusted, thereby shifting the bandgap. The data illustrated in Figure 10 compares experimental data with model predictions that estimate ζ_r using the GA-PSO algorithm. The observed transmittance peaks and troughs align well with the predicted values, particularly in the lower frequency range up to 150 Hz, which includes the designed bandgap region. Beyond this, while the model continues to follow the general trend of the experimental data, some deviations become apparent, suggesting areas for further refinement of the model. Notably, the bandgap's expected impact is clear, with a marked reduction in transmittance indicating effective vibration suppression within the targeted frequency range.

The data depicted in Figure 11 is indicative of the correlation between the measured and simulated values, obtained through the Hybrid GA-PSO algorithm. The scatter plot, with an R-value of 0.54, suggests a moderate correlation. The SSE of 391.18 and RMSE of 1.21 reflect the discrepancies between the model predictions and the experimental observations. These metrics highlight areas where the model could be further calibrated to enhance its predictive accuracy.

Figure 12 presents the residual plot resulting from the algorithm's predictions. The distribution of residuals along the sample points illustrates the model's areas of strength, as well as points where the prediction does not align closely with the experimental data. Together, these figures articulate the performance of the Hybrid GA-PSO algorithm. While the moderate correlation and the residual trends indicate the algorithm's potential, they also suggest that further tuning and validation are necessary for the model to reliably predict dynamic behavior in metastructures.

As compiled in Tables 2 and 3, the different optimization algorithms, while varying slightly in the correlation coefficient (R) and the sum of squared errors (SSE), consistently identified the damping ratios with enough precision for the theoretical model. Upon comparing the results in Table 3, it's evident that the estimated resonator damping ratio values obtained from the Hybrid GA-PSO and Nelder-Mead methods align closely, both indicating a ζ_r of 0.021. This contrasts with the slightly lower estimates from the PSO and ABC algorithms, which may reflect differences in their search strategies or convergence criteria. Notably, the values from the initial table were significantly higher, suggesting a refinement of experimental or algorithmic parameters in the updated analysis. The convergence of estimates in the updated table, particularly for ζ_r, reinforces the robustness of the optimization methods and supports their reliability for accurate metastructure analysis.

TABLE 2: Comparison results of different optimization algorithms in estimating the structural modal damping ratio (ζ_m)

Algorithm	R	SSE	Population size	Estimated ζ_m
GA	0.92	104.57	80	0.0273
PSO	0.92	102.40	80	0.0271
ABC	0.92	103.35	50	0.0268
Hybrid GA-PSO	0.92	101.34	50	0.0273
Nelder-Mead	0.91	101.34	N/A	0.0272

The consensus on ζ_m and ζ_r values highlights the algorithms' success in capturing the metastructure's key dynamics. Validation by experimental data emphasizes their potential in designing and optimizing metastructures for enhanced vibration suppression.

4. CONCLUSION

This research represents the design and optimization of locally resonant metastructures for vibration suppression. Through the integration of advanced AI and optimization algorithms, a new methodology for estimating damping ratios has been established, shedding light on the sensitivity of bandgap characteristics to these critical parameters. The key contributions of this paper are summarized as follows:

Copyright © 2024 by ASME

TABLE 3: Comparison results of different optimization algorithms in estimating the resonator damping ratio (ζ_r)

Algorithm	R	SSE	Population size	Estimated ζ_r
GA	0.93	398.29	80	0.020
PSO	0.92	405.22	80	0.019
ABC	0.91	410.67	50	0.018
Hybrid GA-PSO	0.94	391.18	50	0.021
Nelder-Mead	0.90	420.00	N/A	0.021

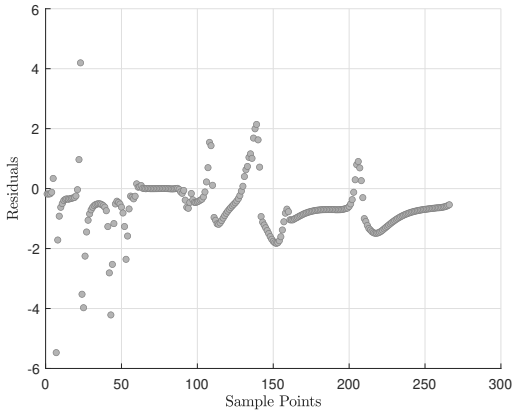

FIGURE 12: Distribution of residuals from the Hybrid GA-PSO algorithm's predictions.

- A novel mathematical formulation for the analysis of metastructures is utilized to enhance the precision of bandgap optimization;
- The study demonstrated the significance of accurately estimated damping ratios in the manipulation of bandgap properties for effective vibration suppression;
- A reliable framework was established to address the gap in current methodologies regarding variable damping scenarios within metastructures;
- The efficacy of the Hybrid GA-PSO algorithm was validated against experimental data, reinforcing its potential for real-world applications in the engineering of metastructures.

The insights from this study suggest promising avenues for future research, such as developing adaptive control mechanisms that dynamically adjust damping ratios based on varying conditions and exploring the scalability of these methodologies for larger and more complex metastructures. Future efforts may focus on refining these algorithms for greater precision, testing more complex metastructural configurations, and integrating broader experimental data to enhance the robustness and real-world applicability of the models. This research moves the field of metastructure optimization forward by effectively integrating AI and optimization techniques, although it also highlights the need for careful interpretation of results due to the limitations of the current methodologies.

ACKNOWLEDGMENTS

This paper is supported by the European Union's HORIZON Research and Innovation Programme under grant agreement No 101120657, project ENFIELD (European Lighthouse to Manifest Trustworthy and Green AI). It was also supported by the Estonian Research Council grant PRG658 and COST Action CA22151 Cyber-Physical systems and digital twins for the decarbonisation of energy-intensive industries (CYPHER).

REFERENCES

[1] Valipour, Ali, Kargozarfard, Mohammad H, Rakhshi, Mina, Yaghootian, Amin and Sedighi, Hamid M. "Metamaterials and their applications: an overview." *Proceedings of the Institution of Mechanical Engineers, Part L: Journal of Materials: Design and Applications* Vol. 236 No. 11 (2022): pp. 2171–2210.

[2] Dalela, Srajan, Balaji, PS and Jena, DP. "A review on application of mechanical metamaterials for vibration control." *Mechanics of advanced materials and structures* Vol. 29 No. 22 (2022): pp. 3237–3262.

[3] Diao, Yupeng, Yan, Luchun and Gao, Kewei. "A strategy assisted machine learning to process multi-objective optimization for improving mechanical properties of carbon steels." *Journal of Materials Science & Technology* Vol. 109 (2022): pp. 86–93.

[4] Song, JunHo, Lee, JaeHoon, Kim, Namjung and Min, Kyoungmin. "Artificial intelligence in the design of innovative metamaterials: A comprehensive review." *International Journal of Precision Engineering and Manufacturing* (2023): pp. 1–20.

[5] Zagaglia, Luca, Demontis, Valeria, Rossella, Francesco and Floris, Francesco. "Particle swarm optimization of GaAs-AlGaAS nanowire photonic crystals as two-dimensional diffraction gratings for light trapping." *Nano Express* Vol. 3 No. 2 (2022): p. 021001.

[6] Meng, Shengguo, Tang, Wankai, Yu, Zhexuan, Wang, Jinghe, Lan, Jifeng, Su, Xin, Yuan, Yifei, Li, Xiao, Jin, Shi, Cheng, Qiang et al. "An Efficient Multi-Beam Generation Method for Millimeter-Wave Reconfigurable Intelligent Surface: Simulation and Measurement." *IEEE Transactions on Vehicular Technology* (2023).

[7] Xiong, Yuanhao, Xu, Andi, Wen, Shurui, Li, Fengming and Hosseini, Seyed Mahmoud. "Optimization of vibration bandgap characteristics of a periodic elastic metamaterial plate." *Mechanics of Advanced Materials and Structures* Vol. 30 No. 15 (2023): pp. 3204–3214.

[8] Salsa Junior, Rubens Gonçalves, Sales, Thiago de Paula and Rade, Domingos Alves. "Optimization of vibration band gaps in damped lattice metamaterials." *Latin American Journal of Solids and Structures* Vol. 20 (2023): p. e493.

[9] Alimohammadi, Hossein, Vassiljeva, Kristina, HosseinNia, Hassan, Ellervee, Peeter and Petlenkov, Eduard. "Bandgap Dynamics in Locally Resonant Metastructures: A General Theory of Internal Resonator Coupling." *Applied Sciences* (2024).

Copyright © 2024 by ASME

Curriculum Vitae

1. Personal data

Name	Hossein Alimohammadi
Date and place of birth	16 December 1978 Tehran, Iran
Nationality	Iranian

2. Contact information

Address	Tallinn University of Technology, School of Information Technologies, Department of Computer Systems, Ehitajate tee 15a, 12618 Tallinn, Estonia
E-mail	hossein.alimohammadi@taltech.ee

3. Education

2020–2024	Tallinn University of Technology, Tallinn, Estonia, PhD in Computer Engineering
2018–2020	Tallinn University of Technology, Tallinn, Estonia, MSc in Mechatronics Engineering, *Cum Laude*
2001–2004	Tarbiat Modares University, Tehran, Iran, MSc in System Dynamic and Control Engineering

4. Language competence

Farsi (Persian)	Native
English	Professional working proficiency

5. Professional employment

2019–2024	Center for Intelligent Systems, TalTech, Estonia, Early Stage Researcher

6. Computer skills

- Programming: Matlab (Professional), AVR Microcontrollers (Professional), Python (Intermediate), C/C++ (Intermediate)
- Software: Comsol Multiphysics (Structural Vibration, Magnetics, Fluid and Heat Transfer), Solidworks, LabVIEW, Altium Designer
- Others: PLC programming, VHDL, Embedded systems

7. Honours and awards

- European Dora Scholarship
- Top 1st-ranked student in Mechatronics Department at Tallinn University of Technology

8. Defended theses

- 2020, Parameter estimation in nonlinear dynamic systems using optimization methods based on experimental data, MSc.

Elulookirjeldus

1. Isikuandmed

Nimi	Hossein Alimohammadi
Sünniaeg ja -koht	16 detsember 1978, Teheran, Iraan
Kodakondsus	Iraani

2. Kontaktandmed

Aadress	Tallinna Tehnikaülikool, Infotehnoloogia teaduskond, Arvutisüsteemide osakond, Ehitajate tee 15a, 12618 Tallinn, Eesti
E-post	hossein.alimohammadi@taltech.ee

3. Haridus

2020–2024	Tallinna Tehnikaülikool, Tallinn, Eesti, PhD arvutitehnika alal
2018–2020	Tallinna Tehnikaülikool, Tallinn, Eesti, Mehatroonika alal magistrikraad, *Cum Laude*
2001–2004	Tarbiat Modaresi Ülikool, Teheran, Iraan, Magistrikraad süsteemide dünaamika ja juhtimistehnika erialal

4. Keelteoskus

Pärsia keel	Emakeel
Inglise keel	Professionaalse töö keel

5. Töökogemus

2019–2024	Arukate süsteemide keskus, TalTech, Eesti, Nooremteadur

6. Computer skills

- Programmeerimine: Matlab (Professionaalne), AVR Microcontrollers (Professionaalne), Python (Kesktase), C/C++ (Kesktase)
- Tarkvara: Comsol Multiphysics (Structural Vibration, Magnetics, Fluid and Heat Transfer), Solidworks, LabVIEW, Altium Designer
- Muud: PLC programmeerimine, VHDL, Sisseehitatud süsteemid

7. Autasud

- Euroopa Dora stipendium
- Parim üliõpilane Mehatroonika osakonnas Tallinna Tehnikaülikoolis

8. Kaitstud lõputööd

- 2020, Parameetrihinnangud mittelineaarsetes dünaamilistes süsteemides optimeerimismeetodite abil eksperimentaalsete andmete põhjal, MSc.

ISSN 2585-6901 (PDF)
ISBN 978-9916-80-397-4 (PDF)